The Determination of Rock Mass Strength for Engineering Design

Anthony G. Meyers

Thesis Submitted For The Degree of
Doctor of Philosophy
in
The University of Adelaide
(Faculty of Engineering)

Contents

Figures

Tables

Abstract

The Determination of Rock Mass Strength for Engineering Design

In this thesis, a technique based upon the rigorous principles of discontinuity analysis is proposed for increasing the objectivity of the Rock Mass Rating (RMR) system developed by Bieniawski [19], a laboratory testing procedure for obtaining the relevant data is described and the proposed technique is applied to a design situation. The RMR system is widely used to provide input parameters for the rock mass yield criterion of Hoek and Brown [65]. There is evidence that the yield strength predicted with this criterion can be conservative. The modifications to the RMR system that are proposed in this thesis enable the Hoek-Brown yield criterion to provide a better estimate of rock mass yield strength for underground design situations.

A detailed laboratory programme conducted on discontinuous specimens is described. These tests were used to obtain data necessary for the development of the modified RMR system. The technique developed for manufacturing the test specimens is shown to be capable of producing any number of identical cylindrical models comprised of distinct blocks suitable for triaxial testing. The models can possess virtually any discontinuity geometry and incorporate discontinuities that fully intersect the cylinder or terminate, instead, at other discontinuities. A modelling material was selected from which to manufacture the specimens after unconfined compression tests, triaxial tests, brazil tests and shear box tests under constant normal stress conditions, confirmed that the material reasonably satisfied similitude requirements with natural rock.

The development of a linear displacement pump and associated micro-processor based controller, used as an integral part of the triaxial testing, is described. This pump was used to provide precise regulation of cell pressure during the triaxial tests and to provide a means by which specimen volume changes could be accurately monitored.

The results obtained from the triaxial testing are used to validate a proprietary two-dimensional distinct element method of numerical analysis. This validation procedure highlights the limitations of this method of numerical analysis when used to predict the elasto-plastic response of the discontinuous specimens under triaxial conditions.

The methodology for applying the modified RMR system to practical situations is presented by way of a case study.

The results presented in this thesis should aid in the understanding of the elasto-plastic response of discontinuous rock masses. The methodology developed for determining a modified RMR should provide the geotechnical engineer with an improved tool for obtaining an initial estimate of the yield conditions in the rock mass adjacent to proposed underground excavations.

Statement of Originality.

This work contains no material which has been accepted for the award of any other degree or diploma in any University or other tertiary institution and, to the best of my knowledge and belief, contains no material previously published or written by another person, except where due reference has been made in the text.

I give consent to this copy of my thesis, when deposited in the University Library, being available for loan and photocopying.

SIGNED: DATE: 4.2.93

Acknowledgments.

The work described in this thesis was carried out in the School of Civil Engineering at the University of Adelaide during the period 1989 to 1993. The candidate was supervised for the first half of his candidature by Professor S.D. Priest and, after Professor Priest transferred to another University, by Dr. W.S. Kaggwa and Professor R.F. Warner. The author is indebted to Professor Priest for providing the opportunity for this research to be carried out and for seeing it to fruition. As much appreciation is also shown to Dr. Kaggwa for being generous with his advice, assistance and guidance.

The author is grateful for the discussions with Dr. George Sved, Honorary Visiting Research Fellow in Civil Engineering. No amount of thanks would be enough to give to the technical staff in the Department of Civil Engineering, University of Adelaide for without their assistance and encouragement this project would not have been completed. In particular the author would like to give special mention to:

* Mr. Colin Haese for making enough sense of the technical drawings to enable him to construct the linear displacement pump,

* Mr. Bob Marcussen for providing invaluable assistance with the construction of the discontinuous specimens and for always having a solution to every problem,

* Mr. Stan Woithe and Mr. Bruce Lucas for being able to take a block diagram and from it design and meticulously produce the micro-processor based pressure controller and

* Mr. Peter Cotton in the Department of Mining Engineering, University of South Australia for constructing the mould for the initial specimen, his photographic skills and his patience.

The author is thankful for the valuable friendship provided by fellow postgraduates over the period of his candidature.

Synopsis

In this thesis any material or idea derived or obtained from other sources has been acknowledged in the text. Those sections of the thesis for which, to the best of his knowledge, the Author claims originality are as follows:

- In Chapters 3 and 9, the development of the methodology for incorporating the statistically based principles of discontinuity analysis into the Rock Mass Rating scheme using orientation and a spacing weighting theory.

- In Chapter 3, the design of a series of cylindrical specimens comprised of discontinuous blocks and the technique for relating these designs to hypothetical rock masses.

- In Chapter 4, the development of the methodology for fabricating distinct blocks from which discontinuous specimens can be constructed in collaboration with Mr. B. Marcussen (see Meyers and Priest [102]).

- In Chapter 5, the development of a linear displacement pump using micro-processor technology in collaboration with Mr. S. Woithe, Mr. B. Lucas and Mr. C. Haese (see Meyers and Priest [101]).

- In Chapter 6 and Appendix C, the detailed laboratory testing to determine the properties of intact gypsum based modelling materials and clean and infilled discontinuities intersecting the material. The analyses and discussion of the test results.

- In Chapter 7, the development of the laboratory procedure required for triaxial testing cylinders comprised of distinct blocks.

- In Chapter 7, the use of the linear displacement pump to highlight the volumetric change that occurs when discontinuous specimens are axially deformed. The analyses and discussion of the test results (see Meyers and Priest [100]).

- In Chapter 7, the development of the technique for photographing deformed specimens through a thin rubber membrane and the use of the paper jacket as a means for recording relative block displacements.

- In Chapter 8, the validation of the elasto-plastic response predicted by UDEC against test results.

- In Chapter 9, the case study demonstrating the use of the modified RMR procedure in a design situation.

Principal Notations

Many of the symbols that are commonly used throughout the thesis are presented below. For convenience, the symbols are divided up according to the English and Greek alphabets. Each symbols is also defined when it is first encountered in the text.

English Symbols

a	= Distance from base to apex of a triangular asperity (m).
A	= Cross sectional area of a cylindrical specimen (m^2).
A_x	= Cross sectional area of an excavation (m^2).
c_i, c_w	= Cohesion of intact material and a discontinuity respectively (N/m^2).
d_r	= Proportion of N_R to N_S.
f	= Thickness of infill material within a discontinuity (m).
g	= Gravitational acceleration (m/s^2).
E, G, K	= Young's, shear and bulk moduli (N/m^2).
F, M	= Force and moment acting at a point (N, Nm).
i	= Angle of inclination of an asperity (degrees).
I	= Moment of inertia of a block (m^4).
J_v	= Average *in situ* block size (m^3).
JCS	= Joint wall Compressive Strength (N/m^2).
JRC	= Joint Roughness Coefficient.
K_a	= Stiffness in the direction of the major principal stress (N/m^3).
K_n, K_s	= Normal and shear stiffness of a discontinuity (N/m^3).
L	= Length of drill core recovered (m). Used in RQD determination.
L_e	= Length of a straight section of an excavation within a rock mass (m).
L_i	= Distance at which a discontinuity intersects a scanline (m).
L_s	= Length of a scanline (m).
m, s	= Hoek-Brown empirical constants.
m_i	= Value of m for intact rock in the Hoek-Brown rock mass yield criterion.
N	= Total number of discontinuities sampled in a scanline survey.
N_a	= Total number of active discontinuities to intersect an excavation.
N_R	= Total number of sampled discontinuities that cannot be allocated to a set.
N_s	= Total number of sampled discontinuities that can be allocated to a set.
$N_{s(k)}$	= Total number of discontinuities from set k to intersect an excavation.
$N_{(k)total}$	= Total number of discontinuities to intersect an excavation.
NJS	= Total number of discontinuity sets in a rock mass.
P_w	= Water pressure acting on a discontinuity (N/m^2).

RMR = Rock Mass Rating (after Bieniawski [23])

$RMR_{(space)}$ = Rating applicable for discontinuity spacing in RMR system.

$RMR_{(orient)}$ = RMR adjustment for discontinuity orientation.

RQD = Rock Quality Designation (%) (after Deere et al. [45]).

r^2 = Correlation coefficient.

s_i = Length of a section of drill core (m). Used in RQD determination.

$S_{\mu(a)}$ = Mean discontinuity spacing of a population (m).

$S_{\mu(k)}$ = Mean discontinuity spacing of set k (m).

SPW = Single Plane of Weakness (theory).

t, T = Time (s).

u, v = Displacement parallel and normal to a discontinuity (m).

U = Angular displacement of the linear displacement pump motor armature (degrees).

UDEC = Universal Distinct Element Code ©.

V = Volume (m^3).

w_i = Weighting applied to a discontinuity to correct for orientation sampling bias.

$w_{i(limit)}$ = Maximum value of w_i.

w_i' = Normalized w_i.

w_θ = Orientation weighting applicable to a discontinuity.

$w_{\theta(mass)}$ = Orientation weighting applicable to a rock mass.

$w_{\theta(\phi)}$ = The value of the orientation weighting when β_w is equal to the friction angle.

W = Mass (kg).

Greek Symbols

α_d, β_d = Trend and plunge of the line of maximum dip within a discontinuity plane (degrees).

α_e, β_e = Trend and plunge of an excavation within a rock mass (degrees).

α_L, β_L = Trend and plunge of a scanline (degrees).

α_n, β_n = Trend and plunge of the upward unit vector normal to a discontinuity (degrees).

$\alpha_{r(k)}$,$\beta_{r(k)}$ = Trend and plunge of the vector defining the mean orientation of discontinuity set k (degrees).

α_σ, β_σ = Trend and plunge of the major principal stress (degrees).

α = Damping coefficient.

β_w = Acute angle between the major principal axis and a unit vector normal to a discontinuity (degrees).

β_{crit} = The value of β_w at which $\sigma_{1(peak)}$ is minimised.

δ_a, δ_θ, δ_v = Axial, circumferential and volumetric deformation, respectively (m, m, m^3).

δ_{pump} = Linear displacement of pump piston (m).

Δ_v = Volumetric deformation ratio.

ε_a, ε_θ, ε_v = Axial, circumferential and volumetric strain at a point, respectively.

ν = Poisson's ratio of a material.

λ = Mean discontinuity frequency of the population (/m).

ϕ_i, ϕ_w = Instantaneous friction angle of intact material and a discontinuity (degrees).

ϕ_p, ϕ_r = Peak and residual friction angles for discontinuities conforming to a linear Mohr-Coulomb relationship (degrees).

ρ = Density of a material (kg/m^3).

σ_c = Uniaxial compressive strength of a material (N/m^2).

σ_n = Stress acting normal to a plane (N/m^2).

σ_1, σ_2, σ_3 = Principal stresses acting at a point (N/m^2).

$\sigma_{1(n)}$, $\sigma_{3(n)}$ = Normalized principal stresses acting at a point (N/m^2).

$\sigma_{1(peak)}$ = Major principal stress acting at a point at yield (N/m^2).

$\bar{\sigma}_1$, $\bar{\sigma}_3$ = Average major and minor principal stresses (N/m^2).

θ_k = Acute angle between discontinuity set k and the major principal axis (degrees).

$\theta_{Ln(i)}$ = Angle between a scanline and the normal to discontinuity i (degrees).

$\theta_{Lr(k)}$ = Angle between a scanline and the normal to discontinuity set k (degrees).

$\theta_{er(k)}$ = Angle between an excavation and the normal to discontinuity set k (degrees).

$\theta_{en(i)}$ = Angle between an excavation and the normal to discontinuity i (degrees).

τ = Shear stress acting at a point (N/m^2).

τ_{ult}, τ_{res} = Ultimate and residual shear strength of a material (N/m^2).

Ω = Angular velocity (rad/s).

Definitions

Some of the more common terms encountered in the thesis are defined below. Many of these terms are defined in more detail in the text.

Aperture. The space between the walls of a discontinuity.

Apparent cohesion. The shear strength of a discontinuity at zero normal stress obtained by extrapolating the tangent at a point on the shear stress versus normal stress envelope at a point back to zero normal stress. A discontinuity can only have a true cohesive strength at zero normal load if there is a rock bridge or cementation along the discontinuity.

Asperity. A point of roughness, usually assumed to be triangular, on the surface of a discontinuity.

Discontinuity. Any break in the mechanical properties of a rock mass, such as a joint, bedding plane or fault. A discontinuous mass is a rock mass containing discontinuities.

Discontinuity friction angle, ϕ_w. The frictional component of shear strength. This component may not be constant, varying with the normal stress on the discontinuity.

Discontinuity stiffness. (1) Shear Stiffness, K_s. The ratio of shear stress to shear deformation, (2) Normal Stiffness, K_n. The ratio of normal stress to normal deformation.

Infill. Material occupying space between the walls of the discontinuity. This material may take the form of a depositional soft gouge or the material that results from the grinding of the wall rock.

Peak shear strength. The limiting value of shear stress for a discontinuity for a particular normal stress. This value may be equivalent to the residual shear strength.

Rock mass. A three-dimensional volume of intact rock which may be intersected by discontinuities.

Residual shear strength. The value of shear stress at which plastic behaviour occurs for a particular normal stress.

Volumetric deformation ratio, Δ_v Studies into the fracture in intact rock have used the volumetric strain versus axial strain relationship as a key indicator of crack initiation and

growth (Brace et al. [26], Cain et al. [34], Crouch [38], Wawersik [152]). In cylindrical specimens of intact rock, the volumetric strain, ε_v, is traditionally calculated with the equation

$$\varepsilon_v = \varepsilon_a + 2\varepsilon_\theta$$

where ε_a is the average strain along the principal axis and

ε_θ is the average circumferential strain at mid-height of the specimen.

In contrast to an intact specimen, the change in volume of a discontinuous specimen undergoing compression is due, not only to the change in volume of the intact material, $\delta_{v(i)}$, but also to the change in volume due to the normal and shear deformation of the discontinuities, $\delta_{v(d)}$ and $\delta_{v(w)}$, respectively. Once the individual blocks of intact material begin to displace relative to each other, the total volume of the specimen may, owing to block rotation, also include a volume, $\delta_{v(a)}$, in which there is no material. In this study the ratio of the change in the total volume of a discontinuous specimen to the original volume of the specimen, V_i, is referred to as the volumetric deformation ratio, Δ_v, defined as,

$$\Delta_v = \frac{\delta_{v(i)} + \delta_{v(d)} + \delta_{v(w)} + \delta_{v(a)}}{V_i}$$

Chapter 1
Introduction

Chapter 1. Introduction.

1.1. Introduction.

The increased degree of specialisation within the field of rock mechanics reflects the intractability of rock masses to rational engineering design. Man-made materials often have easily definable homogeneous and isotropic properties and well-understood yield mechanisms. Rock masses are often heterogeneous and anisotropic, contain discontinuities and have unpredictable spatial variability in the engineering properties of the intact material and the discontinuities, all of which affect the strength and deformability of the rock mass. The influence of the properties of the discontinuities on the strength and deformability of a rock mass has been researched for many years by many diverse approaches. The number of the hypotheses investigated reflects the number of independent and dependent variables involved in the problem.

The two essential elements of research are the hypothesis and the validation. In order to validate the hypothesis, a number of logical processes are followed. Initially the hypothesis is broken down into a number of component parts. This break down generally requires assumptions concerning the nature, or the behaviour, of certain components to be made. These assumptions are important if an analytical model that satisfies the physical laws is to be developed as the act of 'simplification' tends to deviate the solution away from the original hypothesis. If analytical solutions are to be obtained, the complexity of many problems in Rock Mechanics makes simplification necessary. This complexity is, in part, due to the spatial variabitity that occurs in the construction material. In order to incorporate this variability into the analytical model, parametric studies are required. These studies have

pragmatically led to the formulation of numerical models. The basic algorithms used in the numerical models are generally no different from those of the analytical formulations.

In order to obtain realistic input data for and validation of, the analytical and numerical models, experimental studies should be conducted on natural rock and rock masses. The difficulties involved in conducting representative experimental studies on naturally fractured rock, due to the variability of the material and the cost of conducting these tests, has led researchers for a number of years to conduct experimental tests on geometrically symmetrical, ideal models of discontinuous masses. Much of this research has successfully resulted in the development of analytical yield criteria for geometrically uniform specimens. The natural variability of discontinuous rock masses, the infinite number of possible discontinuity orientations and the need to base analytical solutions upon a set of assumptions, has restricted the adoption of a simple analytical equation for predicting rock mass strength and deformability for practical engineering design purposes.

An alternative approach to the process of validating a hypothesis by developing an analytical model, which is itself validated by an experimental study, is to develop a solution to the original hypothesis directly from the results of the experimental study. This technique is the basis for an empirical model. By collating data from a large number of tests, relationships are established between particular parameters. These relationships are established more through trial and error than by a consideration of the physical relationship that exists between them. An empirical model can be assumed to be useable for practical design purposes, in or upon a rock mass, on the basis of two main requirements. The first requirement is that the mechanical characteristics of the design situation are 'assumed' to be adequately represented by the model. Unlike an analytical model, which is developed after a number of assumptions and simplifications are made, the empirical model is derived directly from a large number of similar practical design situations to which the model *did* apply. The second requirement for the empirical model is that it should be sensitive to the natural variability in the rock mass properties. These properties can only be determined by measuring the mechanical and geometrical properties of the discontinuities at exposed faces of the rock mass and/or from

borehole core and then combining these data with the material and mechanical properties of the intact rock determined from laboratory tests. The combined data are then input into the model. The first of these requirements has been satisfied by the widely accepted empirical rock mass strength criterion developed by Hoek and Brown [65]. This criterion does not, however, fully satisfy the second requirement, that of being sensitive to the variability in rock mass properties. This latter requirement must be considered if an accurate assessment is to be made of the deformability and strength of a discontinuous rock mass upon, or within, which engineering structures are constructed.

1.2 Aim of the Study

There are advantages and disadvantages in the use of either analytical, numerical or empirical methods for determining the yield strength of rock masses, many of which will be further discussed in Chapter 2. The use of empirical methods is seen to be a valuable tool for this purpose. The major shortcoming with these methods, of insensitivity to the variability in the rock mass properties, was mentioned previously and will be discussed in Chapter 2. This study aims to address this shortcoming by developing a rational approach for predicting the yield strength of a discontinuous rock mass using an empirical yield strength criterion incorporating three basic considerations. The first consideration is concerned with the classification of the mass according to the rigorous principles of discontinuity analysis. The second consideration is the determination of the material and mechanical properties of the discontinuities and the intact material by laboratory tests. The third consideration incorporates these parameters into a rock mass rating system used as input to the yield criterion. The outcome of this study is an improvement in the method currently used to assess the strength of discontinuous rock masses for engineering design purposes.

These aims are addressed in the following manner,

(1) Develop a non-subjective procedure for rating a discontinuous rock mass in order to obtain input parameters for a rock mass yield strength criterion.

(2) Design specimens containing randomly orientated discontinuities and classify them

according to the principles developed in (1).

(3) Produce these specimens from a number of materials having known properties.

(4) Conduct experimental studies on the specimens in order to investigate the yield behaviour of specimens containing random discontinuities.

(5) Use the results of the experimental study to validate a two-dimensional distinct element method of numerical analysis.

(6) Use the results of (4) to complete the procedure developed in (1).

(7) Apply the techniques developed in (6) to an *in situ* site.

1.3. Layout of the Thesis.

This thesis is made up of two main sections comprising a total of 10 chapters including this Introduction and a Summary presented in Chapter 10. The first and largest section, containing Chapters 2 to 7, discusses procedures for determining the yield strength of rock masses and deals with the laboratory component of the study. The second section, containing Chapter 8 and 9, deals with the numerical analysis and subsequent validation of the procedures developed in the first section.

The current techniques for determining the strength and deformability of discontinuous rock masses using analytical, experimental, empirical and numerical methods have evolved over the last century. In Chapter 2 the evolution and shortcomings in each of these methods are discussed. Very few of these approaches have been specifically aimed at combining the rigorous principles of discontinuity analysis with a rock mass yield criterion.

A technique for classifying a rock mass, based on the rigorous principles of discontinuity analysis, is presented in Chapter 3. The rating applied to the rock mass is suitable as input data for the Hoek-Brown [65] rock mass yield criterion. This technique attempts to overcome much of the subjectivity that exists with the popular Rock Mass Rating procedure developed by Bieniawski [23]. The predominant amount of research by other researchers into the strength of discontinuous rock has tended to be concentrated on models comprised of

geometrically similar parallelepipedal blocks. In contrast, the current research designed and classified four cylindrical specimens containing up to eight 'randomly' orientated discontinuities in order to investigate the mechanical characteristics of specimens comprised of distinct blocks and to provide data required for the rock mass rating procedure developed in Chapter 3.

In Chapter 4 an original procedure for fabricating moulds used in the manufacture of the four cylindrical specimens is described. A review of past research that has utilised a particular modelling material is used in this chapter as a basis for the selection of two materials used to construct the intact blocks, and a third material used as infill in the discontinuities. The preparation of the modelling material is then followed by a discussion of the method used to construct the specimens.

Chapter 5 describes the test equipment developed for this project and the techniques used to investigate the behaviour and define the properties of the intact specimens and the discontinuous specimens. It was essential that the properties of the intact material and the discontinuities in the specimens were determined accurately if the relationship between these properties and the behaviour of the specimens was to be established. A comprehensive series of uniaxial, triaxial and shear box tests were, therefore, conducted. The details of these tests are presented in Chapter 6 and Appendix C.

Chapter 7 describes triaxial testing of the discontinuous specimens. The techniques used to process the test data and apply the necessary corrections are discussed. A comprehensive analysis of the results is presented, accompanied with a series of graphical plots of the test results. From these plots, relationships defining the strength and deformability of the specimens are established.

Due to the lack of suitable test data, little work has been done previously by other researchers to validate the effectiveness of the distinct element method of numerical analysis for modelling the behaviour of rock masses. The availability of the laboratory results obtained

in Chapter 7 presented an opportunity to carry out this validation. In Chapter 8 the principles upon which the distinct element method is based are discussed. The distinct element method was used to model the triaxial tests and the results of the two-dimensional numerical analysis are compared to those obtained in the three-dimensional experimental study.

In Chapter 9, many of the diverse activities carried out in this study are linked together. The validity of the classification technique presented in Chapter 3 is ascertained with reference to the triaxial test data obtained in Chapter 7. The classification technique is then applied to an *in situ* rock mass in order to demonstrate its use as a tool for providing input data for the Hoek-Brown rock mass yield criterion.

The main findings from this study and recommendations for future work are presented in Chapter 10.

Chapter 2.
Previous Research into Methods for Determining the Strength of Discontinuous Rock Masses

Chapter 2. Previous Research into Methods for Determining the Strength of Discontinuous Rock Masses.

2.1. Introduction.

This chapter reviews the historical developments in analytical, numerical, experimental and empirical methods for the determination of the strength and the deformability of discontinuous rock masses. Much of this development has occurred in chronological succession and the review will approximately follow this sequence.

2.2. Analytical Studies.

The classical equation, derived from the work of Coulomb [35] in 1776 and later modified by Patton [115], defined the shear strength, τ, along a plane within a material, in terms of a cohesive strength, c_w, a frictional component, *tan* $(\phi + i)$ and the normal stress, σ_n, on the plane as,

$$\tau = c_w + \sigma_n \, tan \, (\phi + i) \qquad (2.1)$$

The Single Plane of Weakness (SPW) theory of Jaeger [78] formed a cornerstone for later research into the influence of discontinuities on the strength and deformability of a rock mass. Jaeger investigated the two-dimensional case of a material having single or multiple parallel planes of weakness subjected to uniaxial compression in which the planes were assumed to have a different shear strength from the remainder of the material. Jaeger

concluded that the material failed either along the plane of weakness or along planes cutting across it, depending on the angle between the unit vector orientated normal to the discontinuity and the direction of the major principal stress. It is a straight forward process to extend the uniaxial theory of Jaeger's to include the major and the minor principal stresses acting on the rock mass by applying the two-dimensional stress transformation equations. By substituting these equations into Equation 2.1 the limiting major principal stress to cause yielding, either through intact material or along a pre-existing discontinuity, can be determined. Brady and Brown [27] presented this result as:

$$\sigma_{1(peak)} = \sigma_3 + \frac{2(c + \sigma_3 \tan\phi)}{\sin 2\beta\,(1 - \tan\phi \cot\beta_w)} \qquad (2.2)$$

where $\sigma_{1(peak)}$ is the major principal stress on the mass at yield,

σ_3 is the minor principal stress on the mass,

ϕ and c are the friction angle and cohesion of the plane (Note: If the plane intersects intact material, $\phi = \phi_i$ and $c = c_i$. If the plane is a pre-existing discontinuity, $\phi = \phi_w$ and $c = c_w$) and

β_w is the acute angle between the unit vector orientated normal to the plane and the major principal axis.

Equation 2.2 is minimized by maximising the denominator, differentiating the result and equating it to zero. This minimum occurs when $\beta_w = \beta_{crit}$ i.e.

$$\beta_{crit} = 45^\circ + \frac{\phi_w}{2} \qquad (2.3)$$

By substituting Equation 2.3 into Equation 2.2 and solving, the minimum value for $\sigma_{1(peak)}$ as a function of β_w is found to occur when:

$$\sigma_{1(peak)} = 2c_w \tan\beta_w + \sigma_3 \tan^2\beta_w \qquad (2.4)$$

Jaeger [78] and McLamore and Gray [98] noted that the shear strength parameters, ϕ_w and c_w, were not constants as shown in Equations 2.2 and 2.4, but varied with changes in σ_3. McLamore and Gray [98] addressed this problem and established relationships for ϕ_w and c_w

as functions of σ_3. The relationships were, however, insufficiently developed to be applicable to practical design situations.

The two-dimensional analysis of anisotropic rock strength of Jaeger [78] was extended by Attewell and Woodman [3], Amadei [4] and Landriani and Taliercio [129] who developed methodologies for determining the strength of a rock mass containing a single discontinuity set. The studies assumed that the shear strength of the discontinuity set conformed to the Coulomb yield criterion (Equation 2.1) and the analyses allowed for the three-dimensional orientation of the plane and the intermediate principal stress, σ_2. Attewell and Woodman combined this analysis with a statistical analysis of discontinuity orientation and presented the results on a hemispherical projection. The use of hemispherical projection techniques enhanced the practical applicability of Attewell and Woodman's study.

Landriani and Taliercio [129] based their analysis on a 'homogenisation technique' that involved summing the behaviour of each individual discontinuity to determine the behaviour of the whole. This procedure, also referred to as an analytical decomposition procedure, will be discussed further later in this chapter. The input parameters for the strength criterion developed by Landriani and Taliercio were obtained after they conducted a series of triaxial tests on anisotropic rock and substituted the shear strength parameters for the rock into the criterion. The criterion was, however, more of an analytical curve fitting model than a practical tool for predicting the strength of an anisotropic rock.

Amadei [4] considered a rock mass orientated with respect to a set of Cartesian co-ordinate axes as shown in Figure 2.1. The mass was subjected to three principal stresses σ_1, σ_2 and σ_3, creating a uniform stress distribution throughout the mass. The principal stresses were parallel to the Cartesian axes respectively and the Y axis was assumed to lie in the vertical plane. The major principal stress that would cause the intact mass to yield was assumed to be defined by the empirical strength criterion of Hoek and Brown [65] which is discussed in Section 2.5.

The limiting shear strength along a given plane, τ_{ult}, was defined by a Coulomb yield criterion with respect to the positive, normal stress on the plane, the shear strength components of the plane and the water pressure, P_w, acting on the plane. The limiting strength was expressed in terms of the stress differential, SD, where:

$$SD = \tau_{ult}^2 + (P_w \tan \phi_w)^2 - (\sigma_n \tan \phi_w)^2 - c_w^2 \qquad (2.5)$$

By the application of the standard three-dimensional stress transformation equations, to substitute for σ_n and τ_{ult}^2 in Equation 2.5, the stress differential was expressed as:

$$\begin{aligned} SD = {} & \sigma_1^2 (\bar{y}^2 - \bar{y}^4 T) + \sigma_2^2 (\bar{y}^2 - \bar{x}^4 T) + \sigma_3^2 (\bar{z}^2 - \bar{z}^4 T) \\ & - 2\sigma_1 \sigma_2 \bar{x}^2 \bar{y}^2 T - 2 \sigma_2 \sigma_3 \bar{x}^2 \bar{z}^2 T - 2\sigma_1 \sigma_3 \bar{y}^2 \bar{z}^2 T \\ & + P_w^2 \tan^2 \phi_w - c_w^2 \end{aligned} \qquad (2.6)$$

where $T = (1 + \tan^2 \phi_w)$ and

$\bar{x}$, $\bar{y}$ and $\bar{z}$ are the direction cosines of a unit vector normal to the set.

A positive value for SD in Equation 2.6 indicates that a situation exists in which the activating stresses on the discontinuity exceed the restraining stresses. The behaviour of the mass may therefore be dominated by slip on the discontinuity. Alternatively, a negative value of SD indicates that the behaviour of the mass will not be dominated by slip on the discontinuity but rather by the shear strength properties of the intact material.

Attewell and Woodman, Landriani and Taliercio, and Amadei concluded that the limiting strength of a specimen subjected to polyaxial stress conditions (ie. $\sigma_1 > \sigma_2 > \sigma_3$) was strongly dependent on the value of the intermediate principal stress and on the orientation of the discontinuity set. In contrast to these analytically obtained results, laboratory based studies discussed later in this section (Hojem and Cook [68], Paterson [114]) have tended to down-play the significance of the intermediate principal stress on rock mass behaviour. It is important to note that the results obtained by the application of Equation 2.6 are only applicable where the rock mass is intersected by a single set of parallel discontinuities since, as noted by Amadei, it is mechanically incorrect to superimpose the effect of several non-parallel sets to determine rock mass yield strength.

A logical progression from SPW theory research was the development of analytical models that were appropriate for situations in which the rock mass was intersected by more than one set of discontinuities. These models were investigated by Fossum [53] who derived a constitutive model to determine the shear and bulk modulus of a rock mass containing randomly orientated discontinuities. Fossum demonstrated how the moduli reduce with an increase in the discontinuity spacing. By assuming the discontinuities to be randomly orientated this relationship was insensitive to the influence of discontinuity orientation on the deformability of a rock mass and therefore limited in its applicability.

Rock masses containing multiple sets of discontinuities were also investigated by Gerrard [54] [55] and Singh and Huck [135] who presented a series of equations for calculating the elastic moduli for a rock mass containing orthogonal discontinuity sets. Singe developed a set of constitutive equations for a two-dimensional rock mass containing an orthogonal set of discontinuities, intersecting an anisotropic rock mass. A set of 'joint stress concentration' factors, defined as the ratio between the stress along the discontinuities to the overall stresses in the rock, were used to describe the mass in terms of a continuum. Hart et al. [61] and Makurat et al. [97] used these continuum equations to estimate joint stiffness properties in their particular studies. These two studies are discussed in Sections 2.3 and 2.4.1 respectively. Gerrard [55] also defined a discontinuous rock mass in terms of an equivalent continuum by developing a set of relationships that defined a three-dimensional rock mass containing three sets of approximately equally spaced orthogonal discontinuity sets in terms of an equivalent homogeneous orthorhombic material. These equivalent material properties could be used to calculate the distribution of stresses in the rock mass. The analyses of Singe and Huck and Gerrard were restricted to highly theoretical discontinuity geometries and were, therefore, limited in practical applicability.

The necessity to develop analytical models that were applicable for practical design purposes was highlighted by Kulhawy [86] who developed an analytical model for determining the deformability of a rock mass containing up to three sets of orthogonal discontinuities loaded by a rectangular or circular footing on the surface. Kulhawy used an analytical

decomposition model that assumed that a discontinuous system could be represented by an equivalent continuum under the same stress system, in order to calculate the deformation of the mass. This model was, however, limited to pre-yield conditions.

The input parameters for Kulhawy's model were the elastic properties for the intact rock, the shear and normal stiffness of the discontinuities and the RQD coefficient developed by Deere [44] [45] for the rock mass. The RQD (%) coefficient is an approximate measure of the degree of jointing in a rock mass determined from an investigation of diamond drill core and is given by:

$$RQD = \frac{100\sum_{i=1}^{n} s_i}{L} \qquad (2.7)$$

where s_i are the lengths of the individual pieces of drill core in a total length of core, L, having lengths greater than 0.1m.

If an estimate of the mean spacing of the discontinuities is known, the RQD rating for the rock mass can be estimated by the equation (Priest and Hudson [121]),

$$RQD = 100\, e^{-0.1\lambda}(0.1\lambda + 1) \qquad (2.8)$$

where $\lambda = 1/ S_{\mu(a)}$ is the mean discontinuity frequency of the population.

Kulhawy and Goodman [87] investigated the problem of determining the deformation of a rock mass into which a footing has been socketed and Kulhawy and Ingraffea [88] extended the work of Kulhawy [86] to include strip footings, such as those below long dams. The bearing capacity of the footings on the discontinuous rock was determined by Kulhawy and Goodman in terms of the dimensions of the footings, the shear and compressive strength parameters of the intact rock and the discontinuity spacing. No allowance was made in these analyses for the orientation of the discontinuities as the analyses assumed that the discontinuities were parallel and orientated either parallel or perpendicular to the applied load. This assumption limited the practicality of the technique to these specific cases. As with most analytical solutions of discontinuous rock masses, the authors did not consider the

situation in which the rock mass contained several discontinuity sets at various orientations to the applied load. This result is understandable, as an infinite number of possible combinations of discontinuity geometries and imposed stress states exist, each requiring a characteristic model. The positive influence of the effect of block interlocking on the strength of a discontinuous mass, investigated by Lajtai [91], was also not considered and therefore the estimate for bearing capacity could only be considered to be a lower bound.

The complexity of any analytical models increases substantially as the number of discontinuities increases. Numerical techniques have proved increasingly popular because of the difficulties involved in developing a closed form analytical model that is appropriate to all discontinuity geometries and design situations.

2.3. Numerical Studies.

In Civil and Mining Engineering, numerical methods of analysis have been used successfully in a wide range of design situations. For example, finite element analysis is an important design tool for the structural engineer who deals with materials having properties that are accurately known and structures whose yield mechanisms are well understood. A different approach must, however, be adopted when designing a numerical model of a discontinuous rock mass because of:

(1) the limitations in available data defining the stress state and the geometric properties of the discontinuities and the uncertainty and variability of these data,

(2) the tendency for discontinuous rock masses to behave in a chaotic and therefore unpredictable manner and

(3) the complex, heterogeneous nature of rock masses.

A numerical model describing a rock mass, therefore, needs to be used as a tool to assist in the understanding of the mechanisms involved in a particular problem rather than as a means to predict accurately the behaviour of the rock mass.

The commonly used methods of numerical analysis of rock masses are categorised as either integral or differential methods with each of these methods containing several sub-classes. While most of these methods have been developed to a state where they can handle most problem domains, the fundamental differences between the methods mean that, often, one category of analysis is more suitable for analysing a particular problem than the other.

One method of analysis that has gained popularity is the boundary element method which falls into the category of an integral method. For two-dimensional problems, this method assumes a problem domain to be included within an infinite plate. Far-field behaviour can be correctly modelled because this method does not require an arbitrary boundary to be defined along with the boundary conditions acting upon it. The infinite plate assumption eliminates the need to incorporate the uncertainties associated with the boundary conditions into the analysis. Another feature of the boundary element method is that it enables stress and displacement to vary continuously throughout the domain without the need to discretise the domain as required with other formulations.

The boundary element method of numerical analysis is inefficient if used to analyse domains comprising heterogeneous material characterised by non-linear behaviour. The method is also inappropriate for modelling domains intersected by a large number of discontinuities along which large displacements are likely to occur. The deformability of discontinuous rock masses is influenced, to a major extent, by the non-linear stress versus deformation characteristics of the discontinuities. Depending on the boundary conditions and the geometric and material properties of the discontinuities, the deformability of the rock mass may be due to large deformations occurring along the discontinuities. The need to model the non-linear behaviour of discontinuities and large deformations suggested that alternative numerical methods to the boundary element method would be more suitable for the present study.

With differential methods of numerical analysis, such as the finite element and the finite difference methods, the problem domain is divided into a mesh of individual elements,

connected at nodes, that maintain displacement compatibility with neighbouring elements. In order to obtain a solution, the nodal forces and displacements are solved for a known series of boundary forces applied to the domain. This process is undertaken by solving a set of equations that describe all elements and constraints using standard matrix methods. Discontinuities in the domain can be allowed for by modifying the stiffness of the elements along the discontinuity.

A comprehensive analytical analysis into the shear strength versus deformation behaviour of discontinuities was conducted by Goodman et al. [59] who used their results to develop one of the first finite element models of a system of intact blocks separated by discontinuities. Goodman et al. compared the results obtained from their model with the experimental results of Trollope [144] and concluded that their finite element model was able to handle discontinuity behavioural features such as failure in tension or shear, rotation of blocks, development of arches and the collapse pattern of structures in discontinuous rock. Pinnaduwa and Kulatilake [118] used a finite element analysis combined with a Monte-Carlo simulation in order to investigate the strength and deformability of a discontinuous rock mass. This simulation allowed the natural variability in discontinuity geometry that occurs throughout a mass to be incorporated into the model. This variability had been ignored by many researchers up to that time. By allowing for this variability Pinnaduwa and Kulatilake were able to quantify ranges of behaviour for the rock mass and thereby provide an indication of upper and lower bounds for design purposes. The researchers used a bi-linear elastic constitutive model, in which the pre- and post-yield behaviour for the block was linear. The limitations of this model were accepted by the researchers who concluded that more accurate results could have been achieved if an elasto-plastic relation, that could accurately model strain softening behaviour, had been used for the intact material and an elasto-plastic constitutive relation, with perfect plastic behaviour beyond peak stress, used for the discontinuities.

Differential methods of numerical analysis are suitable for systems that behave as a continuum. It becomes numerically inefficient to use these methods to model systems, such

as those being investigated in the present study, in which large inelastic displacements occur. These inefficiencies arise out of the necessity to re-formulate the stiffness matrix each time the connections between elements are broken or reformed as displacements occur along the discontinuities. Alternative methods of numerical analysis that could handle large deformations more efficiently were therefore investigated for the purposes of the present study.

Explicit methods of numerical analysis do away with the need to manipulate matrices to solve a set of equations that describe the problem domain. An explicit formulation is an algebraic technique in which all the values on one side of all equations are known and the equations can be solved without the need to solve a set of simultaneous equations. This procedure forms the basis of the discrete element method of numerical analysis. The discrete element method is particularly suitable for modelling problem domains in which the response of the problem domain to a set of boundary conditions is governed by the behaviour of discontinuities intersecting the domain rather than the behaviour of the intact material. The discontinuities divide the domain into a series of distinct blocks that can contact neighbouring blocks or separate from the continuum. A number of formulations of the method have been developed (Mustoe et al. [106], Walton [150]) and the method developed by Cundall [39] which he referred to as the distinct element method has gained wide spread acceptance. Cundall used the term distinct element method to describe the implementation of the discrete element method in which equations are solved in the time domain. While it is not intended to discuss fully the theoretical basis behind the discrete element method a general overview of the principles is presented in Chapter 8 (Note: The discrete element method is fully discussed by Williams et al.[157]).

A number of researchers have successfully used the distinct element method for modelling problem domains involving discontinuous rock masses. Starfield and Cundall [139] and Wei et al. [154] used the method to analyse rock slope failure due to block slip and toppling. Starfield and Cundall were able to use the results obtained using the distinct element method to identify the mechanisms that were causing yield. Wei et al. concluded that the method

gave results that were consistent with those obtained from films using a high speed camera in laboratory tests. The suitability of the distinct element method for modelling the behaviour of discontinuous rock masses in a high stress environment underground was demonstrated by Makurat et al. [97] who used the method as a design tool for a road tunnel in a rock mass containing three orthogonal joint sets.

Bardet and Scott [9] and Omachi and Arai [110] used the distinct element method to simulate the effect of earthquakes on a soil and rock-fill dam. It was concluded that the distinct element method appeared to be a viable tool for simulating the non-linear stress versus strain behaviour of the dam that occurred during an earthquake simulation. While the present study did not require the distinct element method to be used to model dynamic behaviour, the ability of the method to simulate non-linear behaviour was considered advantageous. Mustoe et al. [106] showed that early implementations of the distinct element method could be used to model the fracturing of intact brittle plates under dynamic impact loading. This study highlighted the ability of the distinct element method to model the fracture of intact material, an important requirement of a numerical method for the present study. Regrettably this feature of the distinct element method was found to be theoretically flawed (Coulthard [36]) and has been eliminated from recent versions of the computer code.

Many of the early implementations of numerical methods were based around models developed in other disciplines. This practice was particularly true of finite element techniques. While these formulations appeared to provide reasonable results, widespread acceptance of the methods was slow. One reason for this slow acceptance was that only a limited number of studies had attempted to validate the results obtained from, what were primarily, two-dimensional numerical methods with those obtained from three-dimensional field and laboratory testing. The validation of the distinct element method of numerical analysis was, therefore, considered to be one of the goals of the present study. Efforts were made during the laboratory studies on discontinuous specimens to obtain results suitable for the validation process. A historical overview of some of the experimental studies that have previously been conducted in this area is presented in the next section.

2.4. Experimental Studies.

Much of the detail regarding the engineering behaviour of discontinuous rock masses for use in numerical or analytical studies has been based upon examination and testing of core samples recovered from the field. Although these cores might have contained discontinuities, deformability and strength tests were often conducted on intact specimens according to the method detailed in the ISRM guidelines, as described by Vogler and Kovari [74]. The fact that these tests were conducted in preference to conducting tests on cores of the discontinuous rock according to the method detailed in the ISRM guidelines, as described by Natau and Mutschler [76], was a reflection on the difficulties associated with conducting laboratory experiments on discontinuous material in order to obtain accurate and reproducible data.

One of the traditional experimental methods for investigating the behaviour of geo-materials has been to subject a specimen to a similar stress state to that existing *in situ*. The response of the specimen to variations in the stress state is monitored. A test in which $\sigma_1 > \sigma_2 > \sigma_3$ is known as a polyaxial test. The principles behind such a test were presented as early as 1902 by Foppl [52], who loaded concrete cubes to failure in order to study the effect of boundary conditions on material strength. Since that time, various methods have been investigated and equipment developed for conducting the tests. In general these tests have been conducted on cubic specimens with three independent hydraulic devices for applying the stress state (Bieniawski et al. [22], Desai et al. [46], Hojem and Cook [68], Hoskins [69], Lenoe [96], Michelis [103], Mogi [105] and Paterson [114]). According to Brady and Brown [27] the research has tended to produce inconsistent results due to the difficulties associated with ensuring uniformity in the applied stress states.

As an alternative to the polyaxial test, a vast number of researchers have chosen to conduct investigations into the behaviour of cylindrical specimens under triaxial conditions, where $\sigma_1 \geq \sigma_2 = \sigma_3$ or $\sigma_1 = \sigma_2 \geq \sigma_3$. By definition, the stress states imposed on a cylindrical specimen is not truly triaxial but is, instead, axi-symmetrical. A true triaxial test, that is, one

in which the three principal stresses are applied along three orthogonal axes, requires similar procedures to those adopted in the polyaxial test. The accepted use of the term triaxial will be continued in this thesis. In a triaxial test, an isotropic stress, referred to as the cell pressure, is applied to the cylindrical specimen by a hydraulic fluid confined in the annulus between the specimen and the triaxial cell barrel. An axial stress is applied with a piston. A triaxial compression test is carried out by applying a compressive load on the piston whereas an extension test is carried out by applying tensile strains while maintaining the cell pressure constant or by increasing the cell pressure while maintaining the axial load constant.

Under triaxial conditions the assumption is made that the intermediate principal stress, σ_2, has little effect on the behaviour of the specimen. Brady and Brown [27], citing the work of Paterson [114], reported that this assumption was incorrect as an increase in the intermediate principal stress tended to increase the strength of the specimen. Paterson found that an increase in the minor principal stress of the same magnitude produced a greater increase in the strength of the specimen. A comparison of polyaxial and triaxial test results by Hojem and Cook [68] found that triaxial conditions often produced very similar results to those obtained under polyaxial conditions.

For the present study, triaxial tests were chosen in preference to polyaxial tests because,

(1) triaxial testing is the most commonly accepted procedure of multi-axial testing and the results obtained from this study would therefore be reproducible by the greatest number of investigators,

(2) triaxial test equipment could be readily purchased in contrast to polyaxial test equipment which had to be designed and fabricated,

(3) the International Society for Rock Mechanics has prepared guidelines for triaxial testing of intact and discontinuous rock (ISRM [74] [76]) but not for polyaxial testing and

(4) triaxial conditions simulate adequately those existing in many natural situations.

Historically, experimental studies on discontinuous rocks have been conducted on specimens of natural rock material or upon specimens of discontinuous material manufactured from an

idealised synthetic material. The following two sections will discuss the results from several significant studies.

2.4.1. Tests on Natural Material.

Attewell and Sandford [2], McLamore and Gray [98], Ramamurthy et al. [123], Reik and Hesselmann [124], Sargand and Hazen [133] and Singh et al. [136] are among a number of researchers who have investigated the influence of transverse isotropy on the strength of natural sedimentary rocks.

McLamore and Gray conducted triaxial tests on cylindrical specimens (25 x 13mm diameter) of slate and shale. The rock material was drilled in such a manner that transversely isotropic specimens, in which the angle, β_w, between a unit vector normal to the anisotropy and the major principal axis was varied. Confining pressures ranging from 7MPa to 170MPa were applied to the specimens and the major principal stress at yield was determined in terms of β_w. The results of these tests were plotted as a series of curves shown in Figure 2.2. It should be noted that McLamore and Gray defined the orientation of the anisotropy in terms of the acute angle, α, between the discontinuity and the major principal axis. In this study, discontinuity orientation is defined in terms of the acute angle, β_w, between the normal to the discontinuity and the major principal axis. The results shown in Figure 2.2 indicate that the minimum strength of an anisotropic material could be predicted according to Equation 2.2. In contrast to SPW theory, discussed in Section 2.2, McLamore and Gray found that as $\beta_w \rightarrow 0$, when $\beta_w \leq \phi_w$, the strength of an anisotropic specimen progressively approached that of the intact material. In contrast, the SPW theory predicts that for all values of $\beta_w \leq \phi_w$ the strength of the specimen would be equivalent to the strength of the intact material. The studies of McLamore and Gray will be further discussed in Section 3.2.

A series of polyaxial tests was conducted by Sargand and Hazen [133] on 100mm cubic specimens of shale. The specimens were orientated so that the plane of anisotropy was either normal, perpendicular or at 45° to the major principal axis. The main purpose of this study was to develop a compliance matrix expressing the axial strain of the specimen, ε_a, for the

material in terms of the axial stress, σ_1, of the form,

$$\varepsilon_a = S_{ij}\,\sigma_1 \qquad (2.9)$$

where S_{ij} contains five elastic constants, Young's modulus and Poisson's ratio, E_1 and ν_1 in the plane of isotropy and E_2, ν_2 and the shear modulus, G_2, in a plane orientated normal to the isotropy.

Large diameter specimens (60mm to 120mm in diameter) of calcite interspersed with parallel beds of soft clay were subjected to triaxial compression by Reik and Hesselmann [124] in order to determine the influence of the soft beds of clay on the strength and deformability of the stronger calcite material. Reik and Hesselmann made a number of conclusions regarding the behaviour of the specimens, yet they did not attempt to establish a relationship between the orientation of the anisotropy and the strength of the specimens. The researchers tended to concentrate their conclusions, instead, on the influence that variations in the thickness of the softer layers had on the strength of the specimens. Had they varied the angle between the major principal stress and the plane of anisotropy, they then could have included the influence of the orientation of the discontinuity with respect to the major principal axis in their analysis.

The results of tests by Reik and Hesselmann, McLamore and Gray, Sargand and Hazen and Attewell and Sandford indicated that for a transversely isotropic material,

(1) the compressive strength is related to the orientation of the anisotropy, although, the influence of the anisotropy on the strength of the material decreases as the confining pressure increases,

(2) the strength of an anisotropic specimen is similar to that for an intact specimen if the loading is in a direction normal to the anisotropy. If the anisotropy is due to soft layers of material then the strength of the specimen would depend on the properties of the individual layers. If the difference in these properties was large then the strength of the specimen would depend almost entirely on that of the weakest material.

(3) If the loading were parallel to the layering then the strength of the specimen would depend on the ratio of the total volume of each of the layers,

(4) the shear strength parameters, ϕ_w and c_w, vary with the orientation of the anisotropy,

(5) the yield behaviour of transversely isotropic rock can reasonably be described by Jaeger's SPW theory [78] and

(6) the elastic constitutive equations for a transversely isotropic material can be adequately represented by a relationship of the form of Equation 2.9.

A structure engineered with respect to a discontinuous rock mass behaves very differently from predictions based on laboratory testing of intact and transversely isotropic specimens. Accordingly, large scale *in situ* and laboratory tests (ISRM [76]) have been conducted by several researchers in an attempt to determine the strength and deformability of a rock mass. An excellent example of such tests was those by Jaeger [79] who tested 150mm diameter cores of discontinuous andesite. The intricate network of discontinuities and filled veins in these specimens resulted in them being highly fragile and it was therefore necessary for Jaeger to confine the specimens in thin copper jackets in order for them to maintain their integrity. The specimens were subjected to triaxial compression at six confining pressures ranging from 0.7MPa to 41.0MPa.

The axial stress versus axial deformation relationship at all confining pressures was characterised by an initial linear rise in the deviator stress followed by non-linear behaviour. Thereafter, plastic behaviour was observed. Jaeger concluded that the strength of the discontinuous specimens, described in terms of a linear shear stress, τ, versus normal stress, σ_n, relationship, could be defined by a power law of the form,

$$\tau = A\,\sigma_n^{B} \qquad (2.10)$$

where A and B were experimentally determined coefficients.

The results obtained by Jaeger were in contrast to the results of tests that he had conducted previously on specimens containing single discontinuities that exhibited clearly defined peak and residual shear strengths. Both series of tests highlighted the differences in the stress versus deformation behaviour of a specimen containing a single discontinuity and one

containing multiple discontinuities. By comparing the shear strength results for the two series of tests Jaeger concluded that the discontinuous rock mass was significantly stronger than the individual discontinuities. He attributed this occurrence to the interlocking of the blocks of intact material as deformation occurs. Jaeger also found that the strength of the discontinuous specimens was significantly less than the strength of intact specimens of the same material subjected to the same confining pressure.

Many rock masses contain discontinuities that do not fully intersect the mass. In these cases deformations of the mass cannot occur due solely to slip along discontinuities but rather due to a combination of mechanisms. An example was the large *in situ* block (2.3 x 2.3 x 4.5m) of highly discontinuous basalt composed almost entirely of undulating, well-developed vertical, hexagonal basalt columns, of approximately 200mm diameter, studied by Hart et al. [61] and tested by Cramer and Black [37]. Hart et al. analysed the results of a triaxial test conducted on the block in order to establish a logical approach that could be used for describing linear and non-linear rock deformation behaviour for the purpose of numerical modelling. A major principal stress of 12.5MPa was applied to the block with one flat jack while minor principal stresses of up to 5MPa were applied with another jack. The deformation characteristic of the block was found to be highly non-linear and hysteretic for all values of deformation. Hart et al. concluded that an adequate mechanical description of the rock mass had to account for not only slip, as described by other authors, but also rotation of the columns.

It is possible for rotation to occur not only in columnar materials but in any discontinuous rock mass. As shear deformations occur, 'steps' appear in many once planar discontinuities. Blocks can only negotiate these 'steps' by rotating. This rotational mechanism contributes to increases in the volumetric deformation of a rock mass. In regions where a high stress state exists such as those encountered underground, the volumetric deformation is resisted by the constant shear and normal stiffness of the far field rock. As the shear and normal deformation of the discontinuities increase, so too does the shear and normal stress opposing

the deformation. Increases in the stresses act to restrict further shear and normal deformation.

The practice of conducting tests on discontinuous samples of natural rock material can yield valuable results to aid the understanding of the strength and deformation characteristics of the material. The studies cited in this section have highlighted the following points.

(1) The spatial variability of the properties of the discontinuities and the highly variable stress distribution in a discontinuous mass, necessitates that large volumes of material be tested if results that are representative of the total mass are to be obtained. These tests can be a prohibitively expensive and logistically difficult operation and can only be justified for major projects.

(2) It can be extremely difficult to obtain specimens of undisturbed natural rock and ensure that they remain undisturbed while installing the specimen into the laboratory equipment prior to testing.

(3) The size of the specimen that can be tested is limited by the size of the available test equipment which is generally small in relation to the rock mass. A number of studies (Bandis et al. [8], Blejwas and Hanson [24]) have shown that the process of interpreting field results in terms of laboratory test results can be problematical owing to the difference in scale. These studies have shown a reduction in shear stiffness and strength of individual discontinuities and a reduction in the modulus of deformation of the rock mass with increasing specimen size. One of the most essential areas in which future research needs to be concentrated is to quantify the influence of scale on the properties of a rock mass.

The problems involved with conducting tests on natural discontinuous material have led researchers to substitute an idealised modelling material for the natural rock as an important method of obtaining information concerning the behaviour of discontinuous rock masses.

2.4.2. Tests on Models of Discontinuous Rock.

The practice of conducting geotechnical tests as part of the design process for proposed engineering structures has a long history. In 1916 Young and Stoek [161] summarised over

100 papers that had been written in the previous 60 years dealing purely with subsidence related testing. Many of these and subsequent papers reported results of laboratory studies conducted on models of proposed structures. By observing the responses of a model fabricated from a material having a set of accurately defined properties and subjected to a set of boundary conditions, the responses of the prototype to a similar set of conditions could be better understood.

An early study was one conducted by Trollope [144] when he investigated the behaviour of a rock mass, intersected by a staggered set of discontinuities, in which a tunnel was progressively constructed. The rock mass was represented by a series of 16mm plastic cubes stacked to form a trapezium 700mm at the base by 400mm high. A tunnel in the shape of a 175mm x 90mm high trapezium was formed by progressively removing the blocks and the behaviour of the mass was monitored. Trollope concluded that two regions occurred from the tunnelling operation, a triangular 'suspended' compression zone above the opening, surrounded by a stable zone. This model highlighted the formation of an arch that had been used for centuries to support engineering structures. Unfortunately the unrealistic network of discontinuities limited the practical applicability of the results obtained by Trollope.

Many researchers considered that the use of model studies could, not only be used to provide valuable information about the response of a particular rock mass to a proposed structure but could also, be used to provide information about the behaviour of discontinuous rock masses in general. Even with the infinite number of possible discontinuity orientations there are some common conclusions that arise from all studies. Several of these studies and the respective conclusions will be discussed.

Brown and Trollope [33] described a series of triaxial tests conducted on prismatic specimens (100 x 100 x 200mm) made up of assemblies of 25mm cubes of gypsum based modelling material. These cubes were arranged so that specimens were formed having three sets of orthogonal discontinuity planes. Each specimen had one of four discontinuity geometries. Confining pressures ranging from 1.4MPa to 13.8MPa were applied to the

specimens. The axial load versus axial deformation characteristics of the material at all confining pressures was characterised by an initial linear increase in load followed by a non-linear increase, with stick-slip oscillations, up to a maximum load. Thereafter, for larger deformations, the behaviour became plastic and the load carrying capacity of the specimen either remained constant or gradually decreased. Brown and Trollope concluded that the yield strength of each specimen was markedly less than that of the intact material except when discontinuities were parallel and/or perpendicular to the major principal axis. From their results, the authors found that the yield strength could be described by a power law in the form of Equation 2.10. They concluded that the equation should be modified to allow for the cohesion of the material. The authors were concerned also that this equation did not take into account the observed variations in the coefficients A and B with the inclination of the discontinuities. They therefore proposed the following dimensionless equation to describe the peak strength of a discontinuous specimen,

$$\frac{\tau - c_w}{\sigma_c} = Z\left(\frac{\sigma_n}{\sigma_c}\right)^{\xi} \qquad (2.11)$$

where σ_c is the uniaxial compressive strength of the intact material and $Z = Z'\sigma_c^{\xi - 1}$.

The parameters Z' and ξ were experimentally determined coefficients that varied according to the orientation of the discontinuities, (ie $0 \leq \xi \leq 1$). The authors concluded that, at the time, a satisfactory method for estimating the coefficients Z' and ξ had not been developed.

The work of Brown and Trollope [33] was extended by Brown [31] who manufactured prismatic specimens from blocks having parallelepipedal and hexagonal shapes as shown in Figures 2.3(a) and (b). The hexagonal configuration represented a similar orientation to the previously described columnar basalt block studied by Hart et al. [61]. Brown conducted a rigorous programme of triaxial testing on these specimens and produced the axial stress versus axial deformation curves indicated in Figure 2.3(b). The strength of the specimens was defined by an equation similar to Equation 2.11. Brown presented a comprehensive discussion of the test results and concluded that the mode of failure of the specimens was different from that presented previously in the literature. The results clearly demonstrated

the significance of discontinuity orientation on the yield strength of a specimen and highlighted how failure modes ranged from axial cleavage fracture through intact material, to slip along discontinuities and to combinations of the two. Brown considered that the axial cleavage fracture was significant for design situations involving underground openings in brittle rock. Brown concluded that failure, other than the types observed in his research, would occur in natural discontinuous masses owing to the presence of tensile stresses.

Einstein and Hirschfeld [50] conducted a comprehensive programme of triaxial tests on prismatic specimens (50x100x200mm) composed of individual blocks of modelling material arranged so that different geometries from those studied by Brown [31] and Brown and Trollope [33] were formed. The blocks were arranged so that specimens had the following discontinuity configuration at various spacings (refer Figure 2.4(a));

(1) intact specimens,

(2) a single set of discontinuities inclined at 45° to the major principal axis,

(3) a single set of discontinuities perpendicular to the major principal axis,

(4) a single set of discontinuities parallel to the major principal axis,

(5) a single discontinuity at various inclinations to the major principal axis,

(6) two orthogonal sets of discontinuities inclined at 45° to the major principal axis and

(7) two orthogonal sets of discontinuities parallel and perpendicular to the major principal axis.

Einstein and Hirschfeld concluded that for cases (3), (4) and (7) failure was not due to shear deformation occurring along pre-existing discontinuities but rather to shear deformation occurring along failure planes that developed through intact material. For these tests there was a systematic increase in strength with an increase in the discontinuity spacing at all confining pressures. At low confining pressures, the strongest specimen was that with vertical discontinuities whereas the weakest specimen had horizontal discontinuities. At higher confining pressures (σ_3 > 20MPa) the strengths of all specimens tended to the same value. Axial deformation of the specimens was due to slip along a failure plane having a similar orientation to that which developed through an intact specimen of the same material.

It was also found that the specimens became less deformable with increasing confining stress and increasing discontinuity spacing. The least deformable specimen was that with the vertical discontinuities and the orthogonal specimen was the most deformable.

For cases (2) and (6) it was concluded that at low confining pressures failure occurred in a few blocks due to shear failure through intact material, although the predominant mode of failure was due to slip along the pre-existing discontinuities. The predominant mode of failure at higher confining pressures was due to shear through intact material. As the confining pressure increased, the number of fracture surfaces also increased. It was also shown that at all confining pressures, the strength of a specimen containing multiple sets of parallel fractures was similar to that of a specimen containing a single fracture at an orientation that represented the mean orientation of the discontinuity set. The deviator stress versus axial deformation curves for the specimens with discontinuity configuration (6), shown in Figure 2.4(b), contains three distinct regions. The first region is essentially linear. This region is followed by a region in which stick-slip oscillations are prevalent indicating that slip is occurring. The third region shows either constant plastic flow or initial plastic flow followed by a gradual decrease in the load carrying capacity of the specimen.

Ladanyi and Archambault [89] constructed a cubic specimen from 62mm long rods having a square cross section. The rods were stacked so that the angle between the discontinuities and the major and minor principal stresses could be varied as shown in Figure 2.5(a). Ladanyi and Archambault compared the yield strength of the specimen to that predicted by Equation 2.2 and found that there was poor agreement between the predicted (Figure 2.5(b)) and the measured (Figure 2.5(c)) results. It was concluded that the degree of interlocking of the blocks had a major influence on the strength and deformability of the specimen because it affected the ability of the blocks to rotate. The influence of block interlocking on the strength of discontinuous rock masses was also mentioned in Section 2.4.1. in relation to the studies of Jaeger [79] on discontinuous natural rock. Another conclusion by Ladanyi and Archambault was that an increase in the number of discontinuities would cause the system to

behave more like a homogeneous, isotropic system similar to that of a tightly compacted rock fill.

Generally, the predicted strengths were higher than those achieved in the specimen tests and Ladanyi and Archambault were unable to achieve the material strength predicted by Equation 2.2. It is suggested that there are two possible causes for the differences. From the test results, it appears that localised internal displacements occurred along the discontinuities, possibly the same displacements that Brown [31] referred to as post peak sliding. These displacements, which occurred irrespective of the orientation of the discontinuities with respect to the boundary conditions, might have been due to localised stress variations. Had the discontinuities not been present, any internal displacement would have had to be accompanied with fracturing of the intact material. The second possible cause for the variation between theory and measurement is that the analytical results assume the discontinuity to be planar. Planarity is extremely difficult to achieve in practice. The effect of these imperfections would have caused stress concentrations and localised yielding (Bray [28] Lajtai [91]). With the onset of yielding, stresses are re-distributed away from the yielding zone, thereby increasing stresses elsewhere in the specimen. The result of this occurrence is failure at lower loads than expected.

Similar tests to those carried out by Brown and Trollope [33] and Einstein and Hirschfeld [50] were conducted by Reik and Zacas [125] on large prismatic specimens (600 x 600 x 1300mm) composed of blocks of modelling material (40 x 60 x 100mm). The authors were able to orientate the discontinuity planes at different angles with respect to the principal axes by arranging the blocks in different configurations. The relationship between the specimen and the principal axes is indicated in Figure 2.6(a). The blocks were arranged in a similar pattern to bricks in a wall in that only one set of discontinuities, referred to as the main set, intersected the entire specimen while each discontinuity in the other two sets was terminated by another discontinuity. Reik and Zacas subjected the specimens to polyaxial testing (ie. $\sigma_1 > \sigma_2 > \sigma_3$) within an elaborate test cell in order to determine the influence of the intermediate

principal stress, σ_2, on the deformation behaviour of the specimen. Polyaxial testing on specimens of discontinuous rock had not, previously, been widely discussed.

The result of one of these tests is shown in Figure 2.6(b). Reik and Zacas concluded that the most unfavourable discontinuity orientation was one in which the main discontinuity set was parallel to the intermediate principal axis. In this case, the magnitude of σ_2 had little influence on the strength of the specimen. For other orientations, an increase in the magnitude of σ_2 led to increases in strength as high as 200%. The authors also concluded that the stiffness and the ductility of the specimen were highly dependent on the orientation of the discontinuities. Depending on the orientation of the discontinuities and to a lesser degree the magnitude of σ_2, the modes of failure for the specimens were similar to those observed by Einstein and Hirschfeld [50]. These modes included shear fracture through intact material, composite shear failure partly through intact material and partly along discontinuities and sliding along pre-existing discontinuity planes. Another mode of failure that the authors recognised was indicated by the occurrence of wide shear zones accompanied with bending of the layers, rotation and plastic flow. Many of the characteristics observed in this mode of failure were the result of the process referred to as localisation. The influence of localisation on rock strength was reported previously in relation to the studies by Reik and Zacas [125]. In relation to the influence of localisation on rock strength, Cundall [41] discussed the studies of Vermeer [147]. These studies concluded that the possibility for localisation occurs when one or more stress components at a point in the material decreases with increasing strain due to,

(1) large geometric distortions,

(2) material softening in which the intrinsic material becomes weaker or

(3) a change occurs in the stress state at the point such that at least one stress component decreases.

Subsequent straining tends to be concentrated at the point of localisation.

Models of horizontally layered discontinuous rock, containing weak inclusions, were investigated by Zacas and Knox [163]. The researchers fabricated a specimen from

individual concrete blocks placed one upon another within a frame in a similar manner to that used when building a brick wall. Three orthogonal sets of discontinuities were, thereby, formed by this method. An inclusion composed of a mixture of plaster, Kieselguhr and water was placed between one of the horizontal layers. The blocks were then subjected to a vertical uniformly distributed load and no horizontal stresses (Figure 2.7). The authors concluded that the extent to which the weak inclusions influenced the behaviour of a layered rock mass was inversely proportional to the distance of the inclusion from the loading surface and to the strength characteristics of the inclusion. The presence of the weaker inclusions tended to influence the deformation behaviour of those blocks in proximity to the inclusion which in turn influenced the behaviour of the entire specimen. The authors did not, however, attempt to quantify the influence of the inclusions on the deformation or strength of the specimen.

Yoshinaka and Yamabe [162] conducted shear and compression tests on single discontinuities in order to investigate the influence of specimen size and roughness on stiffness. Following these tests, the authors extended the investigation and conducted a series of tests on cubic specimens (500 x 500 x 300mm) of soft welded tuff, intersected by two sets of orthogonal discontinuities arranged at various angles to the principal axes. The results of a series of biaxial loading tests on the specimen, using the apparatus shown in Figure 2.8(a), showed that the stress versus strain behaviour of the specimen was dependent on the state of stress, was anisotropic and non-linear (Figure 2.8(b)). The authors noted that these characteristics were essentially due to the compression and shear deformation characteristics of the discontinuities. From the results of the tests, Yoshinaka and Yamabe showed that the deformation of a specimen constructed from parallelepipedal blocks could be estimated by simple summation. Based on the relationships between the deformability of the rock mass and the properties of the intact material and the discontinuities, Yoshinaka and Yamabe found that the stiffness of a rock mass in the direction of the major principal stress, K_a, could be estimated from,

$$K_a = L\left(\frac{1}{E} + \sum_{k=1}^{NJS} \frac{\cos^2\theta_k}{S_{\mu(k)}}\left(\frac{\sin^2\theta_k}{K_{s(k)}} + \frac{\sin^2\theta_k}{K_{n(k)}}\right)\right)^{-1} \qquad (2.12)$$

where L is the unit length of rock mass considered,

$S_{\mu(k)}$ is the spacing of discontinuity set k,

θ_k is the acute angle between discontinuity set k and the major principal axis, defined by $\theta_k = 90^\circ - \beta_w$,

$K_{s(k)}$ and $K_{n(k)}$ are the shear and normal stiffness of discontinuity set k,

E is Young's modulus for the intact material and

NJS is the total number of discontinuity sets.

The validity of Equation 2.12 is investigated in Chapter 7.

Experimental studies are an essential tool for determining the behaviour of a rock mass when subjected to a set of boundary conditions. Although an infinite number of possible discontinuity geometries exist in a rock mass, most of the studies cited utilised specimens having discontinuity geometries that could be classified as having,

(1) parallel discontinuities (Einstein and Hirschfeld [50]),

(2) two or three sets of orthogonal discontinuities each of which fully intersected the specimen (Brown and Trollope [33], Einstein and Hirschfeld [50]),

(3) two sets of non-orthogonal discontinuities each of which fully intersect the specimen (Yoshinaka and Yamabe [162]),

(4) three sets of orthogonal discontinuities with two sets that fully intersected the specimen and one set staggered to create a 'brick wall' effect (Reik and Zacas [125], Zacas and Knox [163]),

(5) three sets of discontinuities made up of two orthogonal sets that fully intersected the specimen and one non-orthogonal staggered set (Brown [31]) or

(6) discontinuities orientated so that hexagonal blocks were formed (Brown [31]).

Groups 1, 2 and 3 represent possible configurations for rock masses, Groups 2 and 3 representing a specific situation in which a blocky rock mass is composed of at least two orthogonal sets. Group 6 represents a discontinuity configuration such as that encountered in columnar jointing. It is unlikely that the 'brick wall' formed by staggering a discontinuity set

as done in Groups 4 and 5, creates a specimen that is a good representation of a rock mass. The discontinuities in a rock mass are the product of the tectonic history to which the rock mass has been subjected. Each tectonic occurrence creates a fingerprint of discontinuities in the rock mass that appears as an intricate network of discontinuity sets. None of the groups listed above addressed the fact that, because of this history, many rock masses are intersected by two or more sets of non-orthogonal discontinuities. This present study considers this matter.

Conducting laboratory or *in situ* tests on discontinuous rock masses is impractical and inefficient except for the largest projects. If these tests are carried out, the spatial variability in the properties of the mass requires that sufficient tests be conducted in order to gather statistically representative results. Recognising these problems has led a number of researchers to propose empirical relationships for predicting the strength and deformability of discontinuous rock masses.

2.5. Empirical Methods and Rock Mass Classification Schemes.

One of the earliest rock mass classification schemes was that developed by Terzaghi [142] when he presented a method for classifying the support capability of rock in tunnels for the purpose of choosing steel support sets. Bieniawski [21] reviewed this classification scheme and concluded that it was too general for evaluating rock quality and provided little information on the properties of the mass.

In an attempt to base a classification scheme on a number of rigorously defined parameters McMahon [99] attempted to quantify the strength and deformation characteristics of discontinuous rock in terms of two indices, a Joint Breakage index and a Joint Dispersion index. McMahon related the Joint Breakage index to the two-dimensional extent of a joint set and the Joint Dispersion index to the degree of 'randomness' of a joint system. These indices did not have a precise relationship to the strength or deformability of the rock mass yet McMahon hoped that once correlations were established with large scale tests they could

form the basis for the transfer of test results obtained in one area to the prediction of behaviour in another. This scheme was not developed sufficiently at that stage to be a practical rock mass classification tool for the purposes of engineering design.

One empirical approach to modelling the relationship between shear and normal stress was that developed by Barton [10] and expanded by Barton and Choubey [13]. The empirical shear strength criterion relates the residual shear strength, τ_{res}, to the normal stress on the discontinuity using the relationship,

$$\tau_{res} = \sigma_n \tan\left(\text{JRC} \log_{10}\left(\frac{\text{JCS}}{\sigma_n} \right) + \phi_{(r)} \right) \qquad (2.13)$$

where JRC is the Joint Roughness Coefficient,

JCS is the compressive strength of the joint wall material and

$\phi_{(r)}$ is the residual friction angle of discontinuities conforming to Equation 2.1.

The magnitude of the joint wall compressive strength, JCS, is equivalent to the unconfined compressive strength of the wall material in a completely unweathered discontinuity. This value will decrease as weathering of the discontinuity increases. The JCS can be estimated from the results of a point load test on the discontinuity wall or obtained from uniaxial compressive strength test data. The value of the joint roughness component, JRC, is either obtained by reference to a chart showing typical discontinuity roughness profiles such as that provided by Barton and Choubey or, preferably, obtained by back substitution into the equation,

$$\text{JRC} = \frac{\phi_{(p)} - \phi_{(r)}}{\log_{10}\left(\frac{\text{JCS}}{\sigma_n} \right)} \qquad (2.14)$$

where $\phi_{(p)}$ is the peak friction angle of discontinuities conforming to Equation 2.1.

Barton [10] suggested that the components $\phi_{(p)}$ and $\phi_{(r)}$ in Equation 2.14 could be obtained from a tilt test. In this test, the block of material intersected by the discontinuity is tilted until the upper half of the block begins to slide. The value of $\phi_{(p)}$ is the angle measured from

the horizontal at which slip occurred. The value of the normal stress acting on the discontinuity is obtained by resolving the self weight of the upper half of the block. Owing to the small size of the upper block, the resulting normal stress may be small relative to *in situ* conditions. For discontinuities in which the shear stress is defined in terms of the normal stress by a non-linear relationship, the friction angle predicted by this method may be larger than that applicable at higher values of normal stress. The predicted friction angle would, therefore, be non-representative of that applying *in situ*. A tilt test should, therefore, only be considered for discontinuities in which the shear strength can be defined in terms of a linear Mohr-Coulomb relationship or after due consideration is given to the normal stresses conditions applicable in the test and *in situ* conditions.

An *in situ* discontinuity having surface roughness features, subjected to a high normal stress, can be mobilised after the shear strength of the roughness features is realised. Discontinuity dilation is minimised under these conditions. At low values of normal stress, such as those applied in the tilt test, mobilisation can be due to over riding of the asperities. Discontinuity dilation is maximised under these conditions. The value of shear stress to cause mobilisation under these conditions is not what is traditionally defined as being the peak or the residual value.

A final concern with the use of the tilt test or, for that matter, any laboratory shear tests on small specimens, is that these tests cannot incorporate the effect of discontinuity curvature into the test. Subsequent to the onset of shearing of a discontinuity, small scale asperities are sheared off. The effective friction angle of the discontinuity is then equivalent to the residual friction angle of the discontinuity plus a component accounting for the curvature. An *in situ* design, based upon a residual friction angle obtained in a laboratory, is likely to be conservative if the influence of curvature on discontinuity shear strength is not considered. The residual strength of the discontinuity can, however, be suitably estimated from laboratory shear box tests if an *in situ* discontinuity is predominantly planar (Baczynski et al. [5]).

The Rock Structure Rating system developed by Wickham et al. [156] was designed for determining the steel rib spacing, shotcrete thickness and bolt spacing in tunnels on the basis of a summation of three parameters. These parameters relate to the general geology, the discontinuity pattern and the ground water inflow. The first parameter was not well defined by Wickham et al. and the remaining two, even though they were measurable, were insensitive to the variation in the respective properties that could most significantly influence the performance of the rock mass. Kaiser et al. [83] found this system to have limited applicability to tunnel design purposes as it was developed on the basis of a too simplistic load bearing capacity model.

During 1972-73, Bieniawski [17] noted the deficiencies in a number of the classification schemes that had been developed and presented a Rock Mass Rating (RMR) system for assessing, on a partly subjective basis, the quality of rock masses for the purpose of preliminary support design in tunnelling. The RMR system has been modified a number of times over the years (Bieniawski [19]) and has been adapted and extended by a number of authors to make it appropriate for their particular application (Gonzalez de Vallejo [56], Kendorski et al. [84], Laubscher [93][94], Newman and Bieniawski [107], Romana [126], Serafim and Pereira [134] and Weaver [153]). The large number of case histories involving the use of the classification system attests to the acceptance of the system and its inherent ease of use and versatility in engineering practice.

A criticism of the RMR system is that the data base used for its development, shallow tunnels in sedimentary rocks, limited its applicability to other design situations. This criticism was addressed by Bieniawski [23] who referred to 351 tunnelling and mining case histories that successfully used the system in a wide variety of rock formations.

To apply the RMR system to a rock mass, the mass is divided into a number of structural units, each unit having similar material or discontinuity properties. Each unit is rated according to the uniaxial compressive strength of the intact rock, the RQD coefficient (Deere [44] [45], defined in Equation 2.7), the discontinuity spacing and condition and the ground

water inflow. Each of these parameters is given a rating and the ratings are summed, thereby, providing the basic RMR rating for the structural unit.

The next procedure is to apply an adjustment, given in Table 2.1, to adjust the basic rating for the orientation of the discontinuities. This procedure involves qualitatively describing the discontinuity orientation with respect to a proposed excavation and providing a rating adjustment accordingly. For tunnels, the appropriate description is based on the work of Wickham et al. [155] and, for slopes and foundations, on the work of Bieniawski and Orr [18] and Romana [126]. For example, the description of the discontinuity orientation for tunnels ranges from 'Very Favourable' to 'Very Unfavourable' according to the parameters detailed in Table 2.2. If more than one discontinuity set is present Bieniawski [23] suggests that, if no one set is dominant, the ratings from each set are averaged for the appropriate individual classification parameter. By this method, the basic RMR is adjusted for orientation, thereby, providing a RMR for each structural unit. In the situation where the behaviour of the rock mass may be influenced by features not covered by the basic classification procedure, Bieniawski suggested that a procedure should be applied that is based on the studies of Kendorski et al. [84] and Laubscher [93]. This procedure applies a further series of rating adjustments to the basic RMR to allow for the presence of major faults and fractures, blasting damage and *in situ* stress or change of stress.

After all adjustments have been applied to the basic RMR, the structural unit is designated to one of five classes ranging from 'very good rock' to 'very poor rock'. Various authors have provided physical significance to these classes (unsupported stand up time and the maximum unsupported span, Bieniawski [23]; support load, Unal (1983) and TBM rippability, Lauffer (1988) cited by Bieniawski [23]). Serafim and Pereira [134] proposed the empirical relationship, based on approximately 40 case studies, relating the RMR to the modulus of deformation, E (GPa), for the rock mass as:

$$E = 10^{(RMR - 10)/40} \qquad (2.15)$$

Table 2.1. RMR discontinuity orientation reduction factors (after Bieniawski [19])

Strike and Dip Orientations of Discontinuities		Very Fav.	Fav.	Fair	Unfav.	Very Unfav.
Ratings	Tunnels and mines	0	-2	-5	-10	-12
	Foundations	0	-2	-7	-15	-25
	Slopes	0	-5	-25	-50	-60

Table 2.2. Qualitative description of discontinuity orientation with respect to tunnelling (after Wickham et al. [155]).

Strike perpendicular to tunnel axis				Strike parallel to tunnel axis		Irrespective of strike
Drive with dip Dip		Drive against dip Dip		Dip		Dip
45°-90°	20°-45°	45°-90°	20°-45°	20°-45°	20°-45°	0°-20°
very favourable	favourable	fair	unfavourable	very unfavourable	fair	unfavourable

The influence of discontinuity orientation on the behaviour of a discontinuous rock mass has been discussed in Sections 2.2 and 2.4. Studies cited in these sections have indicated that changes in the orientation of the discontinuities can produce significant changes in the strength and the deformability of a rock mass. These changes are poorly reflected in the 7 subgroups indicated in Table 2.2.

The process of grouping the discontinuities into one of 3 orientation groups, $0°\rightarrow20°$, $20°\rightarrow45°$ and $45°\rightarrow90°$ is an over-simplification of the influence of orientation on rock mass strength. There is little evidence that 20° or 45° are meaningful limiting conditions. Evidence has, however, been presented in Section 2.4. that indicates that if limiting conditions were to be linked to the strength and deformability of the rock mass then they should incorporate the friction angle of the discontinuities and the angle between the discontinuities and the direction of the major principal stress into their determination.

The suggestion by Bieniawski [23] that, in cases where the classification procedure is used to estimate rock mass strength, the ratings for each discontinuity set can be averaged in order to obtain the rating for the mass as a whole, is a debatable one. As an extreme example, assume a rock mass is intersected by two discontinuity sets one having a RMR of 80 and the other having a RMR of 20. The average rating of the rock mass is therefore 50 and the rock mass would be classified as consisting of 'fair' rock in which a 5m span would have an average stand up time of 1 week. The studies on specimens of discontinuous rock cited in Section 2.4 showed that even in cases where the specimen was intersected by more than one discontinuity set, axial deformation of the specimen would occur predominantly along the set in which a unit vector normal to the set had the closest orientation to β_{crit} (where $\beta_{crit} = 45^{o} + \phi_{w}/2$). It is likely that the set having the RMR of 20 satisfied this criterion. The RMR for the rock mass should, therefore, have been 20 that would classify the rock mass as consisting of 'Very Poor' rock with an average stand up time of only 30 minutes for a 1m span. It would have been incorrect to expect larger spans to stand for longer. A more appropriate procedure would be to consider the influence of each set in turn and the 'worst case' situation to be considered as the norm. It is understood that this procedure may lead to over conservatism in design but, for most engineering projects, long term stability cannot be compromised in terms of short term economies.

One property of the rock mass, discontinuity frequency, is rated twice in the RMR system. The RQD rating of the rock mass and the discontinuity spacing are given maximum possible ratings of 20 points each which, in effect, gives the discontinuity frequency a maximum possible rating of 40 points. The relationship between RQD and discontinuity frequency was clearly demonstrated by Priest and Hudson [121]. In the case of underground mines and tunnels and footings, the RMR system attaches a higher rating to the influence of discontinuity frequency on the strength and deformability of a rock mass than it does to discontinuity orientation. This practice is not consistent with rock mass behaviour. A desirable modification to the RMR system would be one that gives a more suitable priority to those factors that most influence rock mass behaviour.

The use of the RQD parameter as an indicator of discontinuity frequency is of questionable merit. The RQD is an unreliable indicator of frequency because its determination is based on the quality of core obtained from diamond drilling. The quality of diamond drill core is, itself, an unreliable indicator of discontinuity frequency because it is influenced by,

(1) the shear strength of the intact material being drilled,

(2) the drilling practice (vibration, speed, penetration rate, experience of driller) and

(3) the ability of the person logging the core to discriminate between natural fractures and those caused by blasting or drilling.

There is an inconsistency in Bieniawski's rating method between discontinuity spacing and RQD that can be summarised as shown in Table 2.3. Column 1 lists the bounds used to assign a rating for discontinuity spacing. Column 2 presents the rating suggested by Bieniawski for discontinuities having a mean spacing within these bounds. Column 3 inverts the values in Column 1 thereby presenting the spacing bounds as frequency bounds. Priest and Hudson found that the RQD value could be estimated in terms of the discontinuity frequency according to Equation 2.8. These estimations are listed in Column 4. Column 5 presents the range of ratings suggested by Bieniawski appropriate to the particular frequency boundaries. In most cases, the ratings in Column 2 do not fall within the boundaries listed in Column 5. Without further investigation, it is difficult to be definitive about the source of this discrepancy. Equation 2.8 is, however, empirically derived from a large data base whereas the source of the relationship between RQD and rating suggested by Bieniawski is unknown.

The behaviour of rock masses under low stress conditions, such as surface outcrops, is influenced more by the shear strength properties of the discontinuities than by the compressive strength of the intact material. The RMR system, however, assigns a maximum rating of 15 points to the uniaxial compressive strength of the intact material while the shear strength of the discontinuities is only incidentally considered owing to its relationship to the, subjectively assessed, discontinuity roughness.

Table 2.3. Comparison of RMR values derived from discontinuity spacing and RQD values.

(1) Discontinuity Spacing (mm)	(2) Rating for Discontinuity Spacing	(3) Discontinuity Frequency (/m)	(4) RQD (%)	(5) Rating for RQD
< 60	5	> 16.7	< 50.4	3 - 10
60 - 200	5.0 - 8.2	5 - 16.7	50.4 - 91	10 - 18
200 - 600	8.1 - 11.7	1.7 - 5	91 - 98.7	18 - 19.5
600 - 2000	11.7 - 20	0.5 - 1.7	98.7 - 99.9	19.5 - 20
> 2000	20	< 0.5	> 99.9	20

A desirable modification to the RMR system would be to incorporate into it a parameter that allows for the frictional properties of the discontinuities.

The Hoek-Brown rock mass strength criterion developed by Hoek and Brown [65] represents the best developed empirical method for determining the strength of discontinuous rock masses. The criterion was developed after analysing a wide range of experimental data for intact rock and rock discontinuities and a limited amount of data for discontinuous rock masses. This analysis showed that the relationship between the major effective principal stresses at yield could be described by the equation:

$$\sigma_1 = \sigma_3 + \sqrt{m\,\sigma_3\,\sigma_c + s\sigma_c^2} \qquad (2.16)$$

where σ_1 and σ_3 are the major and minor principal stresses at yield,

σ_c is the uniaxial compressive strength of the intact material,

s is an empirical parameter relating to the degree and nature of fracturing in the rock mass and

m is an empirical parameter related to the rock type, ranging from 7 for carbonate rocks with well-developed crystal structure, to 25 for coarse grained polyminerallic igneous and metamorphic crystalline rocks.

Hoek and Brown [65] recognised that the characteristics that define the strength and deformability of a rock mass were included in the RMR classification system of Bieniawski [17] and by combining the yield criterion with the classification system, they were able to

develop a practical tool for estimating the strength of a discontinuous rock mass. Hoek and Brown [66] defined relations between m, s and the RMR as,

Disturbed Rock Masses

$$\frac{m}{m_i} = e^{\frac{RMR - 100}{14}} \qquad s = e^{\frac{RMR - 100}{6}} \qquad (2.17(a)\text{-}(b))$$

Undisturbed Rock Masses

$$\frac{m}{m_i} = e^{\frac{RMR - 100}{28}} \qquad s = e^{\frac{RMR - 100}{9}} \qquad (2.18(a)\text{-}(b))$$

where m_i is the value of m for the intact rock.

The principal stress acting upon a rock mass at yield can be estimated by determining the RMR for the rock mass, substituting this value into Equations 2.17(a)-(b) or 2.18(a)-(b) as appropriate and determining the Hoek-Brown parameters m and s. These parameters are substituted, in conjunction with σ_c for the intact rock and the value for the minor principal stress at the point of concern, into Equation 2.16 and an estimate obtained of the major principal stress at yield.

Hoek [64] noted that the estimate of the yield strength of a rock mass obtained by this method tended to be conservative yet could be used to predict a lower bound for design purposes. One of the few studies that reported similar conclusions was that by Trueman and Follington [145]. The researchers used the RMR/Hoek-Brown yield criterion system to estimate the strength of an underground coal and limestone pillar containing two sets of discontinuities. The mean orientation of the two discontinuity sets was such that $\beta_w \approx 0^\circ$ and $\beta_w \approx 90^\circ$ respectively. Trueman and Follington found the yield criterion estimated the pillars to have a strength of between 55% and 63% of the *in situ* yield strength. They concluded that it was not the Hoek-Brown yield criterion that caused the discrepancy but that it was the

result of the RMR value being insensitive to those geometric properties of the discontinuities that influenced rock mass strength.

2.6. Summary.

This chapter has reviewed analytical, numerical, experimental and empirical methods for determining the strength and deformability of discontinuous rock masses. Reviews of other aspects pertinent to the present study are presented where appropriate.

Analytical solutions are restricted to fairly simple domains having a small number of discontinuity sets. The variability in the properties of the rock mass and the simplistic design domains can be allowed for by including the analytical techniques within a numerical model. The use of numerical models is becoming widespread and will continue to grow as the strength and deformation predictions of the numerical methods are further validated by laboratory and *in situ* testing.

Well planned *in situ* testing provides valuable data on the engineering properties of a rock mass. These field tests can, however, be prohibitively expensive for all but the largest projects.

Laboratory studies can be conducted on specimens of the intact and discontinuous rock, however,

(1) the natural variability in the properties of the intact rock and the discontinuities requires that large volumes of material are tested if statistically significant test results are to be obtained,

(2) laboratory studies are restricted to specimens having a size which is limited by the capacity of the available test equipment and

(3) the influence of scale must be considered when extrapolating laboratory results to *in situ* dimensions.

Tests conducted on models of discontinuous rock have provided valuable information regarding the behaviour of discontinuous rock particularly in relation to the influence of discontinuity orientation and spacing on the strength and deformability of a rock mass. Many of these studies tended to concentrate upon specimens having non-representative discontinuity geometries and further work is required to study specimens having more representative geometries. Further work is also required to compare the results obtained from these specimen tests with those obtained from numerical models.

The use of the empirically derived rock mass yield strength criterion, developed by Hoek and Brown [65], using input parameters derived from the Rock Mass Rating (RMR) system, developed by Bieniawski [23], has gained widespread acceptance for Civil and Mining Engineering applications as a practical tool for estimating the yield strength of a discontinuous rock mass. There are, however, deficiencies in the combined Hoek-Brown yield criterion/RMR system procedure. Many of these deficiencies have been discussed in this chapter and are related more to the use of the RMR system for obtaining input for the Hoek-Brown yield criterion than to the yield criterion itself.

The tendency for the RMR/Hoek-Brown yield criterion procedure to provide only a lower bound to rock mass yield strength as noted by Hoek [64] may lead to conservatism in design. The insensitivity of the procedure to those discontinuity properties that most influence rock mass behaviour such as discontinuity shear strength and orientation is of more concern for structural stability reasons. These discontinuity properties can be obtained from shear box tests conducted either in the laboratory or *in situ* and by classifying the rock mass according to the rigorous principles of discontinuity analysis. While these techniques are well documented (ISRM [72], Priest [119]) it is essential that methods are established for incorporating this information into the RMR/yield criterion procedure if it is to provide an acceptable estimate of rock mass yield strength. Such a method is suggested in the following chapter.

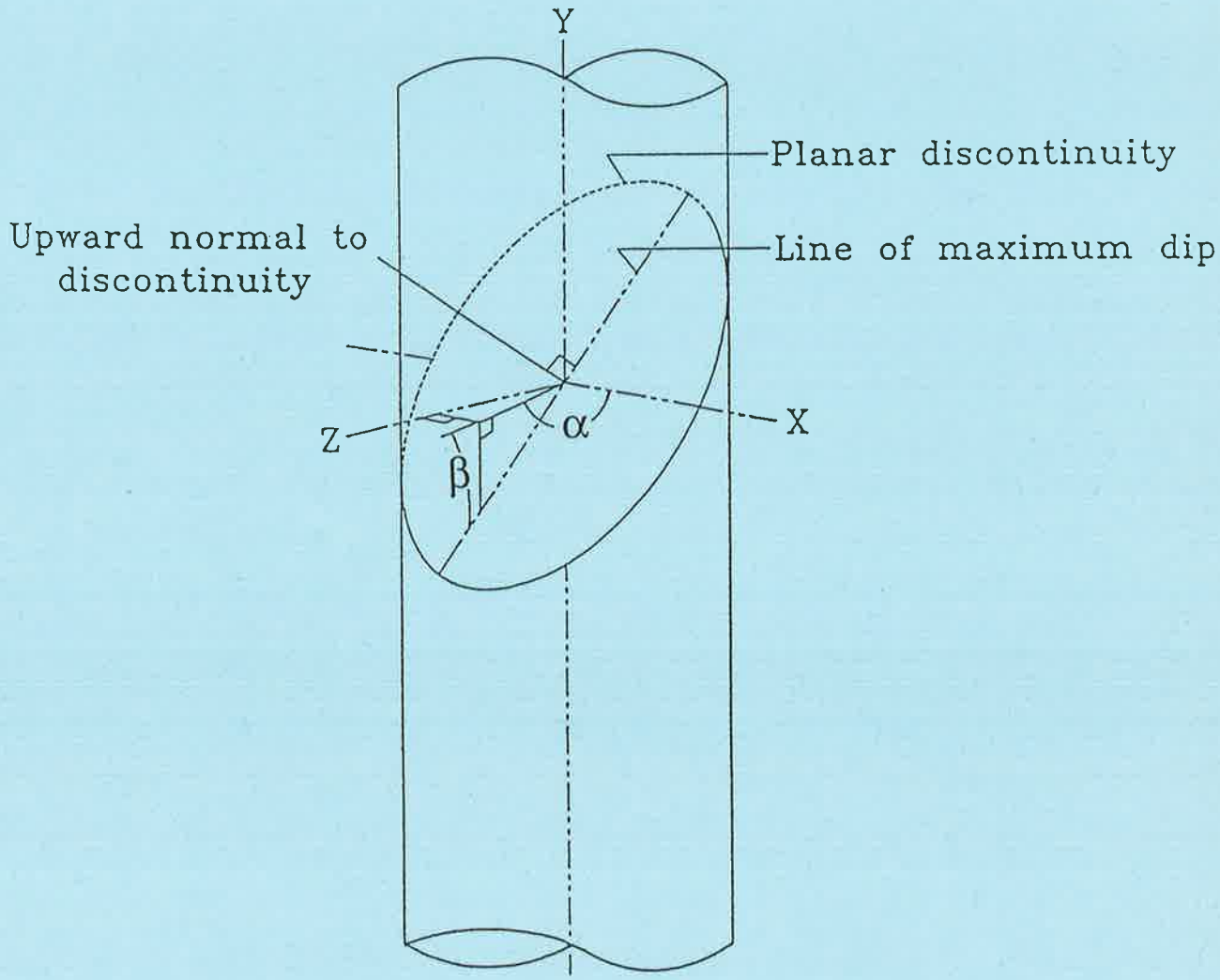

Figure 2.1. Specimen containing a single discontinuity set represented by a single planar discontinuity.

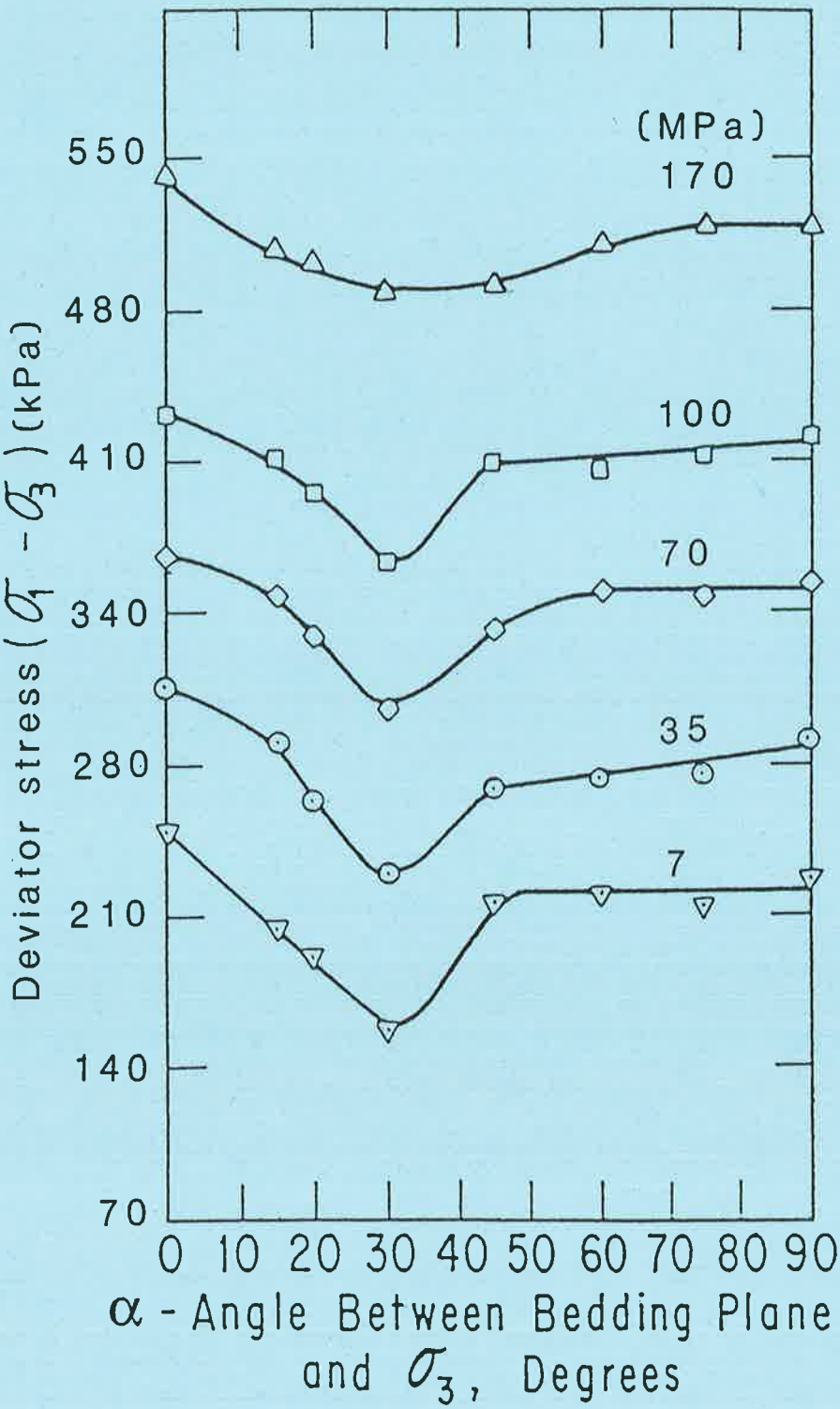

Note: In the notation system of McLamore and Gray [98], $\alpha = \beta_w - 90^o$

Figure 2.2. Plot showing the influence of changes in β_w upon the deviator stress (after McLamore and Gray [98]).

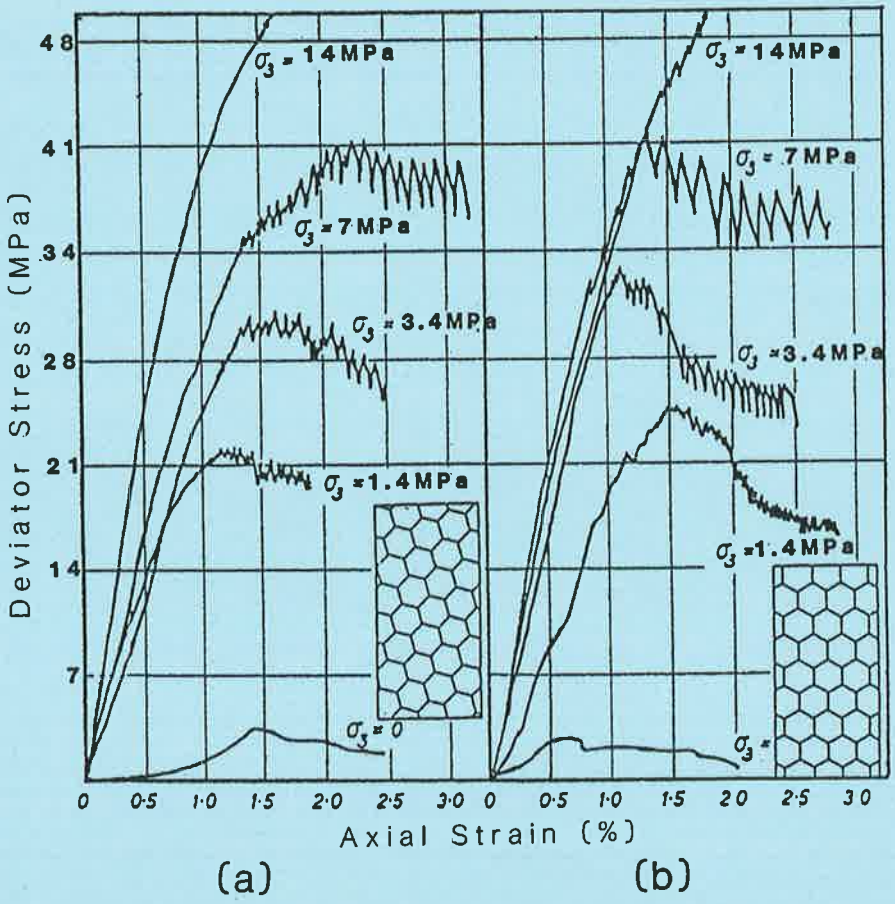

Figure 2.3. (a) Block jointed sample geometry. (b) Principal stress difference versus axial strain curves (after Brown [31])

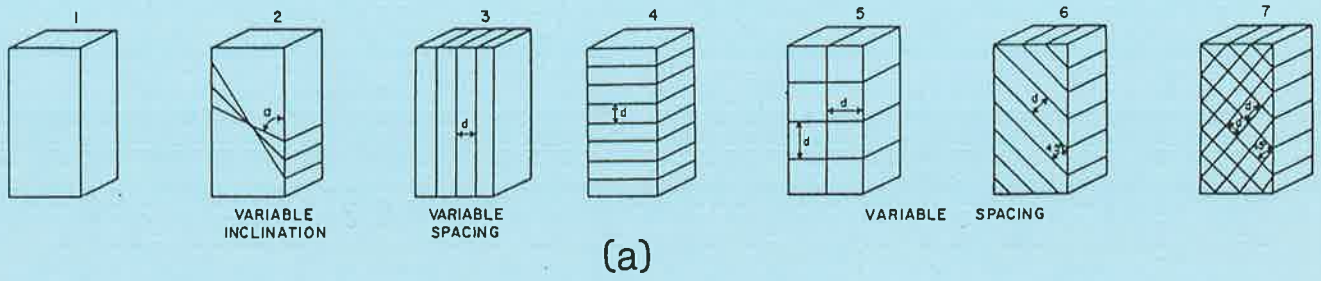

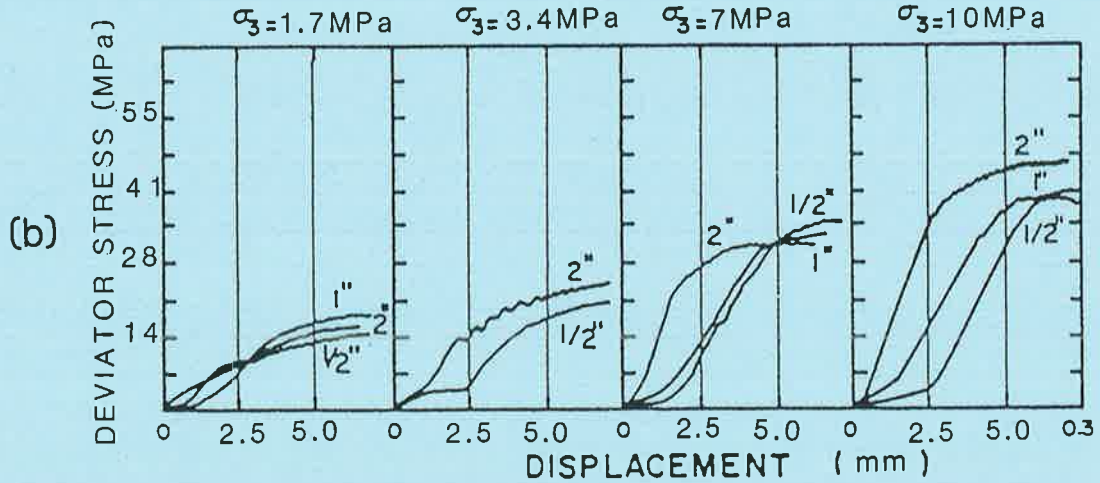

Figure 2.4. (a) Discontinuity configuration. (b) Behaviour of specimens with two sets of orthogonal discontinuities (after Einstein and Hirschfeld [50])

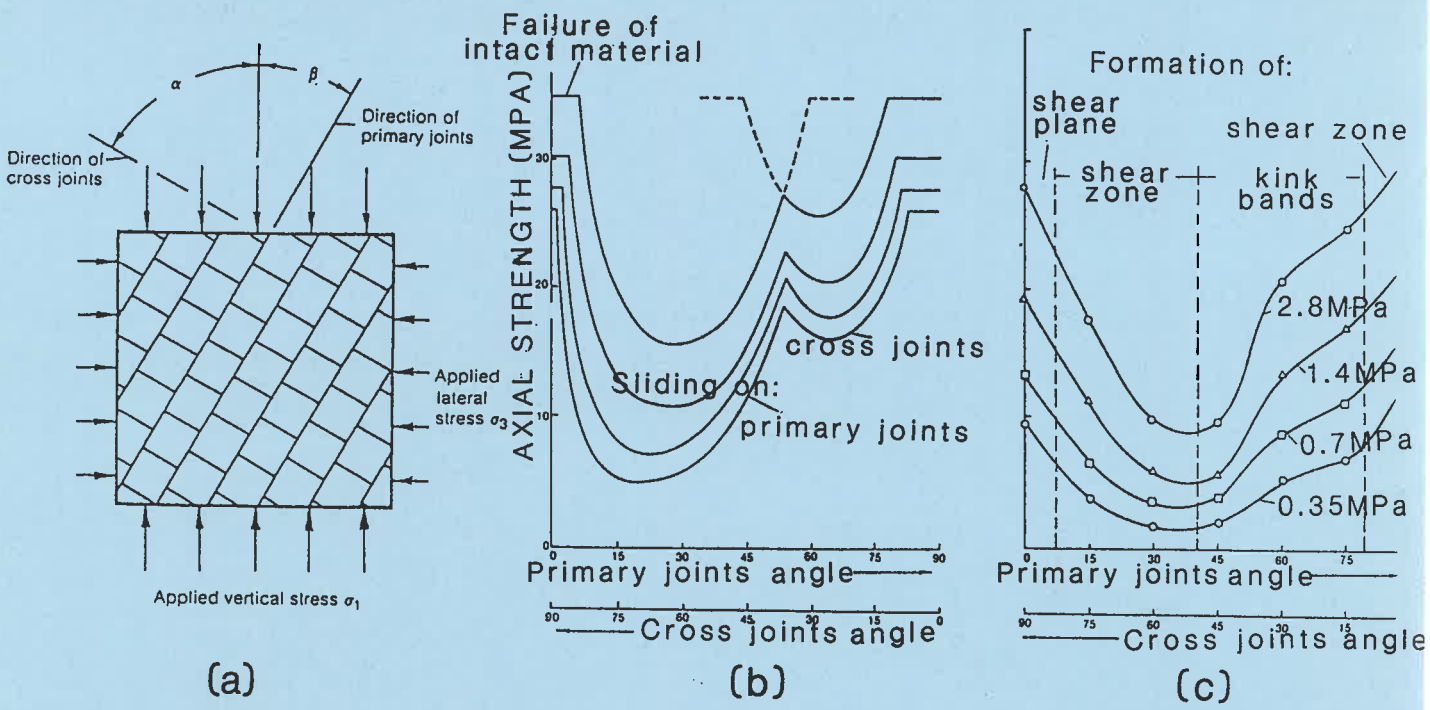

Figure 2.5.(a) Model configuration. (b) Predicted results (c) Observed results (after Ladanyi and Archambault [89])

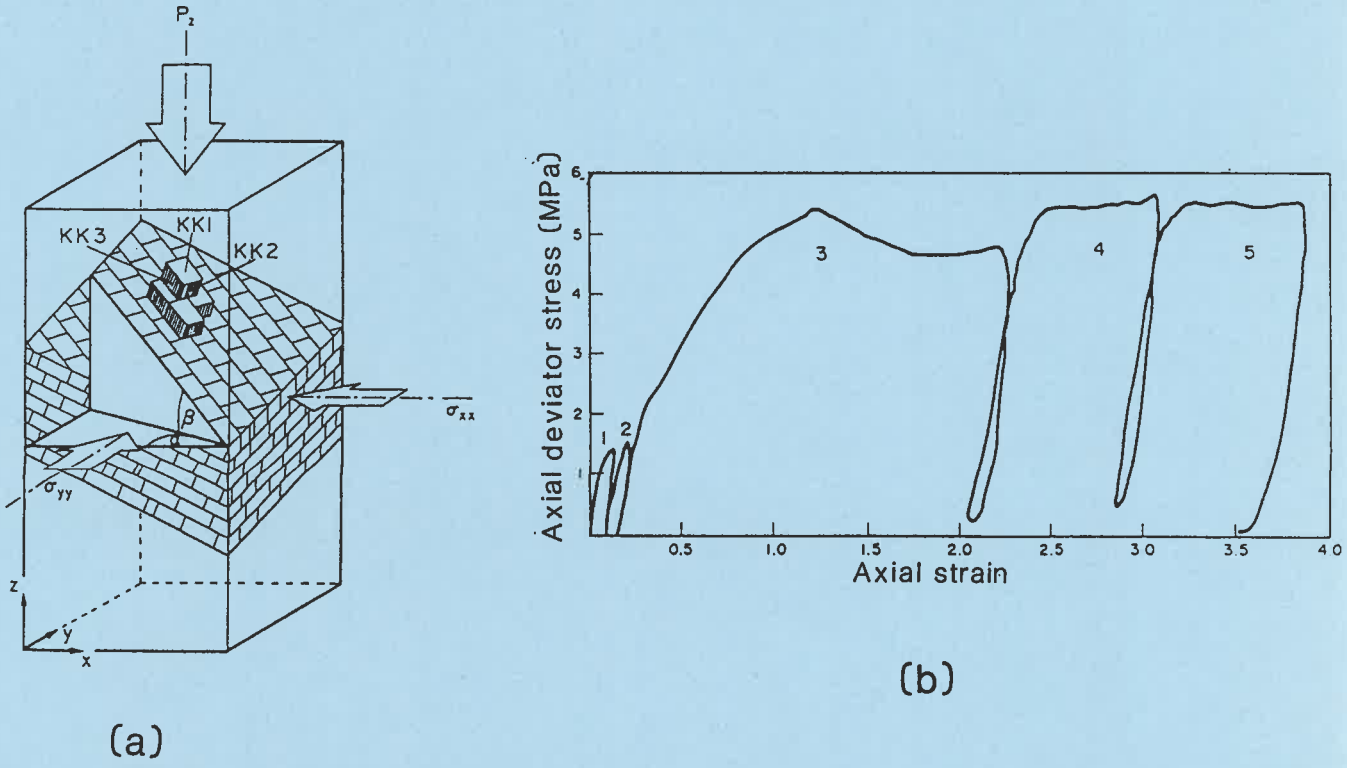

Figure 2.6. (a) Discontinuity configuration. (b) Axial stress versus axial strain curves (after Reik and Zacas [125])

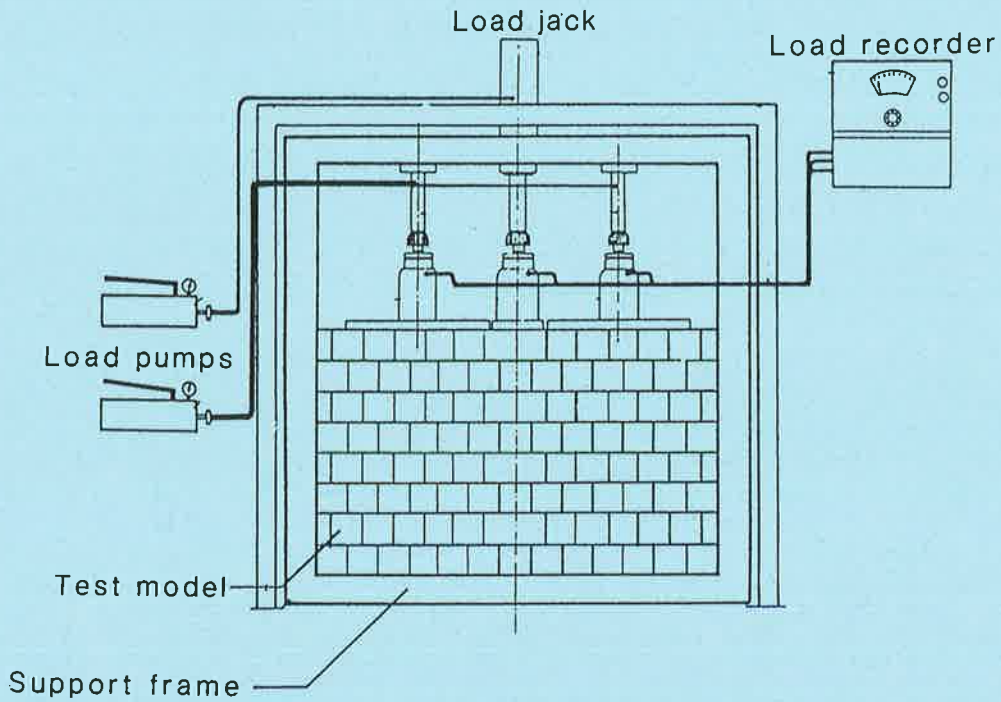

Figure 2.7.Experimental test apparatus (after Zacas and Knox [163])

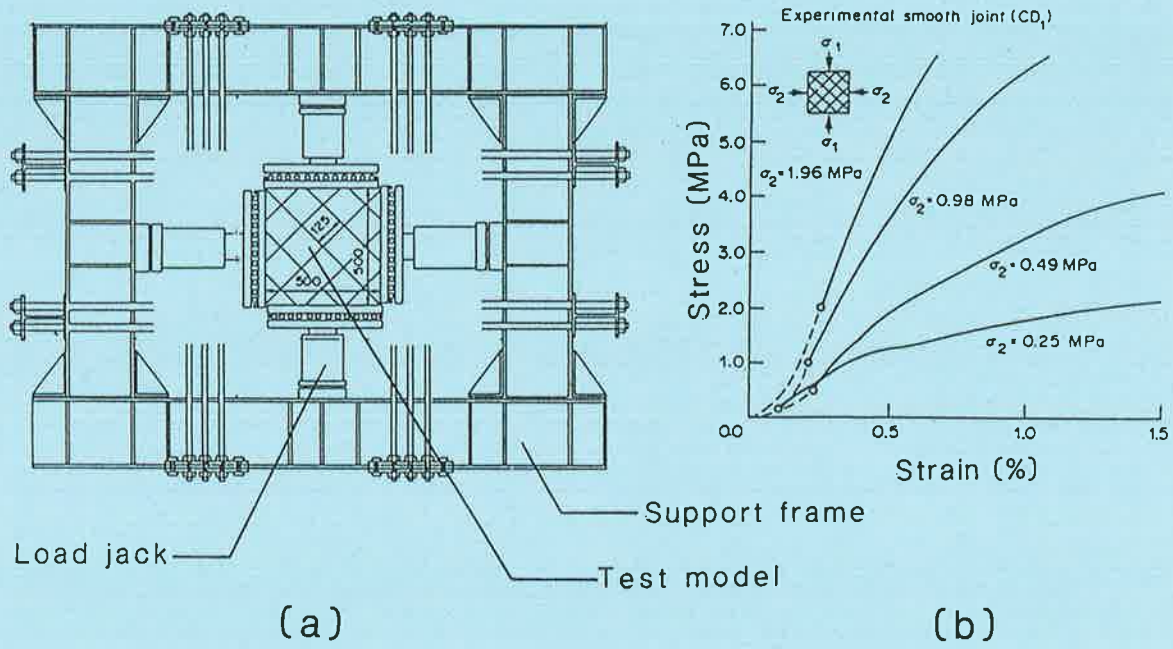

Figure 2.8. (a) Experimental configuration. (b) Experimental stress versus strain curves. (after Yoshinaka and Yamabe [162])

Chapter 3.
Quantification of Discontinuity Geometry.

Chapter 3. Quantification of Discontinuity Geometry.

3.1. Introduction.

A set of relationships used to define the yield strength of discontinuous rock masses must have input parameters derived from the properties of the intact material and the discontinuities. In Chapter 2 the rock mass yield criterion of Hoek and Brown [65] was shown to be a simple, versatile and well-accepted method for estimating the yield strength of discontinuous rock masses. In order to obtain input parameters for the yield criterion, Hoek and Brown established tentative links with the Rock Mass Rating (RMR) procedure developed by Bieniawski [19].

While the RMR procedure is basically sound, as shown in Section 2.5, there are a number of drawbacks with the procedure. In this Chapter, modifications to the basic procedure are suggested to make it a better input source for the Hoek-Brown criterion. These modifications consider how the yield strength of the rock mass is influenced by the geometrical properties of the discontinuities and the proposed excavation and by the orientation of the major principal stress acting on the rock mass. Data on the geometric properties of the rock mass are obtained from a scanline survey conducted on an exposed face of the rock mass.

A series of laboratory tests on discontinuous specimens, assumed to represent diamond drill core obtained from four hypothetical rock masses, is proposed. These tests are designed to

provide data necessary for the development of the modified RMR procedure and to assess the effectiveness of the Hoek-Brown yield criterion when combined with the basic RMR procedure for estimating yield strength.

3.2. Discontinuity Orientation Weighting.

In Section 2.2 and 2.4, the concept was introduced that the strength of a rock mass and the deformations that occur within the rock mass were highly dependent on the orientation of the discontinuities. It was emphasised that it was mechanically incorrect to estimate the strength of rock masses containing more than one set of parallel discontinuities using relationships, such as Equations 2.2, developed for anisotropic rock masses. The reason for this result is that the deformation of a discontinuous rock mass is the result of a number of complex localised deformations occurring within the intact material and along the discontinuities as a result of the interaction between discontinuity sets. These deformations were observed in the experimental studies of Einstein and Hirschfeld [50] and Ladanyi and Archambault [89]. Parallels do, however, exist between anisotropic rock and rock containing multiple discontinuities with respect to the influence of discontinuity geometry on rock mass behaviour.

Assume that an unbalanced stress state is applied to a rock mass containing multiple discontinuities. Prior to shear deformations occurring along any discontinuity, due to the orientation of each discontinuity within the local stress space, each discontinuity will possess a particular potential for shear deformation to occur along it. Let the potential for the discontinuity to slip be expressed as a weighting, referred to as an orientation weighting, w_θ, ranging from 0 to 1. A weighting close to 1 indicates that the discontinuity has a high potential to slip while a weighting close to 0 indicates a potentially stable discontinuity.

In a number of the studies cited in Sections 2.2, 2.4 and 2.5 it was shown that the angle, β_w, between a unit vector normal to a discontinuity and the major principal axis had a major influence on the behaviour of the discontinuity. It is therefore reasonable to assume that the

value of the orientation weighting appropriate for a particular discontinuity should be a function of β_w. It is also reasonable to assume that proportional changes in w_θ should be related to the proportional changes in the strength of the rock mass that occur with changes in β_w. One study cited in Section 2.4 was that by McLamore and Gray [98] in which the researchers conducted triaxial tests on cylindrical cores of slate and shale in order to investigate the influence of discontinuity orientation on the strength of anisotropic rock. The series of tests produced the experimental data illustrated in Figures 2.2 relating the deviator stress at yield to β_w. Similar results were obtained in the studies of Donath [48] and Jaeger [78].

Two sets of test data from McLamore and Gray [98] have been reproduced in Figure 3.1. In this figure, the confining pressure on the slate specimens was 210MPa and that on the shale specimens was 35MPa. The friction angle, ϕ_w, for the shale was 30° and for the slate was 10°. Several features defining the relationship between the deviator stress at yield and β_w, notable in the test data illustrated, are similar to those features required to express the orientation weighting coefficient, w_θ, in terms of β_w. These similar features are,

(1) As $\beta_w \rightarrow 0^\circ$, when $\beta_w \leq \phi_w$ and as $w_\theta \rightarrow 0$ the deviator stress on an anisotropic specimen at yield progressively approaches that for the intact material, that is:

$$\frac{\partial(\sigma_{1(peak)} - \sigma_3)}{\partial\beta_w} \rightarrow 0 \text{ and } \frac{\partial w_\theta}{\partial\beta_w} \rightarrow 0 \qquad \text{for } 0^\circ \leq \beta_w \leq \phi_w, \qquad (3.1)$$

(2) As $\beta_w \rightarrow \beta_{crit}$ and as $w_\theta \rightarrow 1$ the deviator stress on an anisotropic specimen at yield decreases, that is:

$$\frac{\partial(\sigma_{1(peak)} - \sigma_3)}{\partial\beta_w} < 0 \text{ and } \frac{\partial w_\theta}{\partial\beta_w} < 0 \qquad \text{for } \phi_w \leq \beta_w \leq \beta_{crit} \qquad (3.2)$$

where $\beta_{crit} = \frac{\phi_w}{2} + 45^\circ$

(3) As $\beta_w \rightarrow \beta_{crit}$ and as $w_\theta \rightarrow 1$ the change in the rate of decrease in the deviator stress at yield with changes in β_w decreases, that is:

$$\frac{\partial^2(\sigma_{1(peak)} - \sigma_3)}{\partial\beta_w^2} < 0 \text{ and } \frac{\partial^2 w_\theta}{\partial\beta_w^2} < 0 \qquad \text{for } \phi_w \leq \beta_w \leq \beta_{crit} \qquad (3.3)$$

(4) When $\beta_w = \beta_{crit}$ and when $w_\theta = 1$ the deviator stress at yield is a minimum, that is:

$$\frac{\partial(\sigma_{1(peak)} - \sigma_3)}{\partial\beta_w} = 0 \text{ and } \frac{\partial w_\theta}{\partial\beta_w} = 0 \qquad \text{for } \beta_w = \beta_{crit} \qquad (3.4)$$

(5) As $\beta_w \rightarrow 90^\circ$ and as $w_\theta \rightarrow 0$ the deviator stress on an anisotropic specimen at yield increases, that is:

$$\frac{\partial(\sigma_{1(peak)} - \sigma_3)}{\partial\beta_w} > 0 \text{ and } \frac{\partial w_\theta}{\partial\beta_w} > 0 \qquad \text{for } \beta_{crit} \leq \beta_w \leq 90^\circ \qquad (3.5)$$

(6) As $\beta_w \rightarrow 90^\circ$ and as $w_\theta \rightarrow 0$ the change in the rate of decrease in the deviator stress at yield with changes in β_w increases, that is:

$$\frac{\partial^2(\sigma_{1(peak)} - \sigma_3)}{\partial\beta_w^2} > 0 \text{ and } \frac{\partial^2 w_\theta}{\partial\beta_w^2} > 0 \qquad \text{for } \beta_{crit} \leq \beta_w \leq 90^\circ \qquad (3.6)$$

The relationship between the deviator stress on an anisotropic specimen at yield and β_w, illustrated in Figure 3.1, can be approximated by a half cycle of an equation of the form,

$$\xi = (cos\ 2\Phi)^n \qquad (3.7)$$

where $\Phi = f(\beta_w)$,

$\xi = (\sigma_{1(peak)} - \sigma_3)$, the deviator stress at yield and

n is a constant.

The relationship defining w_θ in terms of β_w represents a phase shift of 180° beyond that defining the deviator stress at yield for the anisotropic rock in terms of β_w. For example, when Equation 3.7 is a maximum, the latter relationship is a minimum. Based on this

conclusion, it was found empirically that w_θ could be defined as:

$$w_\theta = (cos\ 2\Phi)^n \qquad (3.8)$$

where $\Phi = \beta_w - \beta_{crit}$,

$\beta_{crit} = \frac{\phi_w}{2} + 45^\circ$ (degrees),

ϕ_w is the friction angle (degrees) for the discontinuity and

$n = 0.175\ \phi_w - 0.250$.

Equation 3.8 has a maximum value of 1 which occurs when $\beta_w = \beta_{crit}$. This result is consistent with the preceding theory that a discontinuity having a weighting of 1 has the greatest potential to slip. It should be noted that Equation 3.8 becomes indeterminate at values of $\beta_w - \beta_{crit} < -45^\circ$. In these cases it is consistent with the preceding theory to set $w_\theta = 0$. Similarly, as $\beta_w \rightarrow 90^\circ$ and the potential for the discontinuity to slip decreases, $w_\theta \rightarrow 0$.

The value for the orientation weighting when β_w is equal to the friction angle, ϕ_w, is here designated $w_{\theta(\phi)}$. A discontinuity for which β_w is greater than ϕ_w is referred to as an active discontinuity. The orientation of an active discontinuity with respect to the direction of the major principal stress is such that the discontinuity has the potential to mobilise.

Figure 3.2 graphically illustrates the relationship between the orientation of a discontinuity intersecting a rock mass and the orientation weighting. A feature of Equation 3.8, highlighted in the figure, is that the deviation of the bell shaped curve increases as the friction angle for the discontinuity increases. This occurrence has been reported by several authors (Donath [48], McLamore and Gray [98]).

The experimental data from the triaxial tests on the shale and the slate by McLamore and Gray are compared in Figure 3.1 to analytical curves. These curves were obtained by scaling Equation 3.8 so that a weighting of 1 was equivalent to the minimum deviator strength at yield, occurring when $\beta_w = \beta_{crit}$, and a weighting of 0 was equivalent to the maximum deviator strength at yield, occurring when $\beta_w = 90^\circ$. For values of $\beta_w > \phi_w$, Equation 3.8 can

be seen to be broadly validated by the test data. The results highlight the tendency for the deviator stress to approach the strength of the intact material as $\beta_w \rightarrow 90^o$.

Single plane of weakness theory, discussed in Section 2.2, predicts that parallel discontinuities having a value of $\beta_w < \phi_w$ do not influence the strength of a specimen. McLamore and Gray found this result to be incorrect when he showed that for an anisotropic specimen there was a gradual increase in strength as $\beta_w \rightarrow 0^o$ for values of $\beta_w < \phi_w$. Likewise, for specimens containing discontinuities with multiple orientations, the results of Einstein and Hirschfeld [50] and Reik and Zacas [125] showed that the presence of discontinuities will always reduce the strength of an intact material. This influence of discontinuities on intact strength is embodied in the orientation weighting principle by ensuring that for all values of $\beta_w < \phi_w$ the weighting was not assumed to be zero. Instead, as highlighted in Figures 3.1 and 3.2, Equation 3.8 allows w_θ to gradually reduce to zero for values of $\beta_w < \phi_w$.

It can be seen in Figure 3.1 that the deviator stress at yield is over-estimated for values of $\beta_w < \phi_w$. This over-estimation occurs as a result of w_θ being assumed to equal 0 when $\beta_w - \beta_{crit} < -45^o$. The curves were scaled so that a value of $w_\theta = 0$ corresponded to the maximum deviator stress at yield for the specimen. In single plane of weakness theory this maximum strength occurs when β_w is close to 90^o and when $\beta_w < \phi_w$. As shown in experimental studies on discontinuous specimens, such as those by Einstein and Hirschfeld and McLamore and Gray, the deviator stress at yield in the latter case is often less than it is in the former. Considering that the orientation weighting technique was not intended to be used to provide an estimate of the strength of an anisotropic rock but rather to provide an easily determinable indication of the propensity of a discontinuity to slip due to its orientation, it is encouraging that there is reasonable agreement between predicted and measured strength data.

3.2.1 Application of Orientation Weighting Theory

In Section 2.5, the procedure for determining the RMR value in the classification system of Bieniawski was discussed. One of the input parameters in the classification system was a

rating adjustment for discontinuity orientation, $RMR_{(orient)}$, selected according to the information presented in Tables 2.1 and 2.2. It is proposed in this study that the procedure described by Bieniawski be modified to incorporate the data obtained from a scanline survey of the rock mass and the orientation weighting applicable to the rock mass.

The suggested procedure provides a first estimate of rock mass stability, around underground excavations, using data obtainable from an initial survey of the rock mass. The procedure is not intended to provide a rigorous analysis of the behaviour of the rock mass as excavation proceeds. A more rigorous approach would require numerical methods to be applied to the problem. The procedure is based upon a number of simplifying assumptions. These assumptions are:

(1) The discontinuity spatial characteristics (orientations, spacing, size) and shear strength properties are homogeneous throughout the rock mass

(2) The discontinuities have a dilation in shear due to surface roughness that can be represented by an angle, i. The dilation can be allowed for by increasing the residual friction angle for the discontinuities, ϕ_w, to $(\phi_w + i)$.

(3) The discontinuities have negligible apparent cohesion and tensile strength and a shear strength that can be defined in terms of the linear Mohr-Coulomb equation.

(4) The discontinuities are assumed to be planar and large scale curvature is ignored.

(5) The intact blocks behave rigidly and cannot crack or collapse. Therefore, only those discontinuities present prior to the application of an unbalanced principal stress state can exist. Intact block strength is, however, included in the analysis.

(6) The rock mass in the vicinity of the excavation is assumed not to be subjected to cyclic changes in the stress state during progressive drill and blast cycles as the excavation progresses.

Steps (2) to (5) in the following procedure represent variations of statistical methods, described in detail by Priest [119], for quantifying the population of discontinuities intersecting a rock mass. Steps (1) and (6)-(20) extend the use of these procedures to enable a modified RMR (Rock Mass Rating) to be applied to the rock mass. The term 'modified'

RMR is used extensively throughout this report to distinguish between the proposed rating and that obtained by the application of the basic RMR procedure developed by Bieniawski.

The procedures are sufficiently straight forward to apply to most rock masses but the repetitive nature of the calculations requires that the discontinuity data be processed using computer methods. An example of the use of the procedure is presented in the next section and a computer coding of the procedure, WEIGHT, is presented in Appendix A. The relative orientation of many of the planes discussed in the procedure is highlighted in Figure 3.3. This figure shows a two-dimensional body in a global XY Cartesian space. The major and minor axes refer to the geometry of the body. The major and minor principal axes refer to the orientation of the principal stresses acting on the body. The modified RMR procedure is as follows:

(1) Ascertain the following data required to define the rock mass, excavation and stress state:

(1.1) The orientation, length and cross sectional area of the proposed tunnel, drive or decline through the rock mass.

The orientation of the excavation is defined in terms of the trend, α_e, and plunge, β_e, of the major axis of the excavation and the length, L_e, refers to the total length of a straight section of the excavation. If the excavation is comprised of a number of straight sections, each having a different orientation, each section can be investigated individually.

(1.2) Data defining the basic geometrical properties of a representative sample of the discontinuities intersecting the rock mass.

Discontinuities are inaccessible in three-dimensions and the two-dimensional linear traces of the discontinuities on exposed faces of the rock mass must be used to estimate the properties of the planar discontinuities. A scanline survey is an accepted method by which an exposed rock face can be rigorously logged (Priest [119], Villaescusa and Landmark [149], Windsor and Robertson [159]). In a scanline survey a number of scanlines are established across the rock face. In order to obtain suitable data it is desirable to conduct at least three orthogonal

scanline surveys. The limited amount of exposure of most rock masses often means that only two orthogonal surveys are possible. Data is gathered in a systematic manner on only those discontinuities that intersect the scanline. The minimum number of characteristics that must be recorded for each discontinuity for this procedure are,

(i) the distance, L_i, at which the discontinuity intersects the scanline (i = 1 to N, where N is the total number of discontinuities sampled) and

(ii) the orientation of the discontinuity (ie. trend, α_d, and plunge, β_d, of the line of maximum dip within the discontinuity. A line normal to the discontinuity has orientation α_n, β_n in which $\alpha_n = \alpha_d \pm 180°$ and $\beta_d = 90° - \beta_n$.)

(1.3) The residual friction angle, ϕ_w, for the discontinuities.

This discontinuity property is determined by carrying out shear box tests on a representative unweathered discontinuity. This discontinuity is preferably obtained from diamond drill core. (Note: Different sets of discontinuities may have different friction angles.)

(1.3.1) Determine β_{crit} from Equation 2.3

(1.3.2) Determine the exponent, n, in Equation 3.8

(1.4) The orientation of the major principal stress within the rock mass in the area of the proposed excavation (defined by trend, α_σ, and plunge, β_σ).

Data defining the major principal stress are obtained using well-established techniques incorporating devices such as the CSIRO hollow inclusion stress measurement cells, biaxial yoke stress monitoring gauges or biaxial rigid inclusion stress meters. The methodology for determining the orientation of the principal stresses is beyond the scope of this study.

Stages (2) to (4) are carried out to enable the mean orientation of the individual discontinuity sets to be determined.

(2) Apply a normalised weighting appropriate to each discontinuity sampled to correct for the orientation bias introduced during the scanline logging procedure.

Orientation bias occurs because those discontinuities in which a unit vector normal to the

discontinuity is orientated parallel to the scanline are more likely to be sampled than are those discontinuities in which the unit vector is perpendicular to the scanline. The likelihood that a scanline intersects a discontinuity is, therefore, inversely proportional to the angle between a unit vector normal to the discontinuity and the scanline. To compensate for this bias, a normalised weighting, w_i' (i = 1 to N), is applied to each of the N discontinuities sampled. This weighting represents an estimate of the number of discontinuities that would have been sampled if the scanline had been orientated normal to the respective discontinuity. The weighting is defined with respect to the angle, $\theta_{Ln(i)}$, between the scanline and the unit vector normal to the discontinuity as:

$$w_i' = \frac{w_i N}{\sum_{i=1}^{N} w_i} \tag{3.9}$$

where $w_i = \dfrac{1}{|cos\ \theta_{Ln(i)}|}$ and

θ_{Ln} is the angle between the scanline and the unit vector normal to the discontinuity. This angle is given by Equation 3.10 in which $\theta = \theta_{Ln(i)}$, $\alpha_1 = \alpha_{n(i)}$, $\beta_1 = \beta_{n(i)}$, $\alpha_2 = \alpha_L$ and $\beta_2 = \beta_L$.

$$cos\ \theta = cos\ (\alpha_1 - \alpha_2)\ cos\ \beta_1\ cos\ \beta_2 + sin\ \beta_1\ sin\ \beta_2 \tag{3.10}$$

where $\alpha_{n(i)}$ and $\beta_{n(i)}$ are the dip direction and dip angle respectively of a unit vector orientated normal to the planar discontinuity i.

A discontinuity with a value of β_n close to 90° will result in a large value for w_i. Such a value may result in the discontinuity being over represented within the rock mass during the subsequent procedure. In order to adopt caution until the true frequency of the discontinuity can be substantiated, an upper limit, $w_{i(limit)}$, is often imposed on w_i. This upper limit is often set at a constant value. It would be more satisfactory to make the limit proportional to the length of the scanline. Therefore, based on the recommendation by Priest [119] that $w_{i(limit)}$=10 for a 30-40m long scanline, $w_{i(limit)}$ will be defined as:

$$w_{i(limit)} = 0.35L_s \tag{3.11}.$$

where L_s is the length of the scanline.

(3) Allocate each discontinuity to its respective set.

The unit vectors normal to each discontinuity, along with their associated normalised weighting factors, are plotted onto a lower-hemispherical equal angle projection. This procedure enables each set of discontinuities to be identified and an unbiased estimate of the mean orientation of the set to be obtained. The k individual sets (k = 1 to NJS, where NJS is the total number of sets) can be identified and each discontinuity sampled can be allocated to a particular set by the use of an appropriate clustering algorithm. In brief, clustering algorithms count the number of discontinuities that fall into a specified cone angle around each discontinuity. Concentrations of discontinuities are then identified. Clustering algorithms are implemented in numerical programs such as DIPS (Diederichs and Hoek [47]) and CANDO (Priest [119]) and will not be described further.

It should be noted that there will always be a number of discontinuities having random orientations that cannot be allocated to any set. It is important that these discontinuities, referred to as the random component, are not ignored in the subsequent analysis. A mean orientation cannot be obtained for these discontinuities in Stage (4) because of the random nature of the discontinuities. What is determined, however, is the ratio, d_r, between the number of random discontinuities and the number of discontinuities that could be allocated into a set, i.e.

$$d_r = \frac{N_R}{N_s} \tag{3.12}$$

where N_R is the total number of discontinuities that form the random component intersecting the scanline and

N_s is the total number of discontinuities that can be allocated into particular sets.

(4) Determine the mean orientation of each set.

The mean orientation of each set can be represented in the Cartesian system by a single vector R_k having length, r_k, from the origin and having the orientation, $\alpha_{r(k)}$, and $\beta_{r(k)}$ such that:

$$\alpha_{r(k)} = arctan\left(\frac{r_{x(k)}}{r_{y(k)}} + q\right) \tag{3.13(a)}$$

$$\beta_{r(k)} = arctan\left(\frac{r_{z(k)}}{\sqrt{r_{x(k)}^2 + r_{y(k)}^2}}\right) \qquad (3.13(b))$$

where

$$r_{x(k)} = \sum_{i=1}^{N} w_i' \sin \alpha_{n(i)} \cos \beta_{n(i)},$$

$$r_{y(k)} = \sum_{i=1}^{N} w_i' \cos \alpha_{n(i)} \cos \beta_{n(i)},$$

$$r_{z(k)} = \sum_{i=1}^{N} w_i' \sin \beta_{n(i)} \text{ and}$$

$$q = 0^\circ \text{ if } r_{x(k)} \geq 0 \text{ and } r_{y(k)} \geq 0$$
$$= 360^\circ \text{ if } r_{x(k)} < 0 \text{ and } r_{y(k)} > 0$$
$$= 180^\circ \text{ otherwise.}$$

Stages (5) to (12) estimate the number of discontinuities intersecting the excavation. This estimate, based upon the mean orientation of each of the discontinuity sets, provides a measure of the quality of the rock mass in the vicinity of the excavation.

(5) Determine the mean spacing of the discontinuities in each set.

The average true discontinuity spacing, $S_{\mu(k)}$, along the normal to each set is determined by the equation (refer Figure 3.4),

$$S_{\mu(k)} = \frac{\sum_{i(k)=1}^{N_k - 1} (L_{(i(k)+1)} - L_{i(k)}) \cos \theta_{Lr(k)}}{N_k - 1} \qquad (3.14)$$

where $(L_{(i(k)+1)} - L_{i(k)})$ is the distance between two adjacent discontinuities from set k,

N_k is the total number of discontinuities in set k and

$\theta_{Lr(k)}$ is the angle between the vector R_k and the scanline given by Equation 3.10 in which $\theta = \theta_{Lr(k)}$, $\alpha_1 = \alpha_{r(k)}$, $\beta_1 = \beta_{r(k)}$, $\alpha_2 = \alpha_L$ and $\beta_2 = \beta_L$.

The use of Equation 3.14. to estimate the mean true spacing of the discontinuities within a particular set assumes that the set can be represented as parallel planes all having the orientation appropriate to the particular set. For the random component, this assumption is not valid. The best estimate of a mean spacing that can be applied to the discontinuities forming this component, is that of the apparent spacing, determined as the average spacing of

the intersections of these discontinuities with the scanline as follows,

$$S_{\mu(R)} = \frac{\sum_{i(R)=1}^{N_R - 1} L_{(i(R)+1)} - L_{i(R)}}{N_R - 1} \qquad (3.15)$$

The value for the spacing of the random set obtained with Equation 3.15 is required in Stage 10.

(6) Determine the angle between the mean normal to a set and the excavation.

The angle, $\theta_{er(k)}$, between the mean normal to a set and the excavation is determined using Equation 3.10 in which $\theta = \theta_{er(k)}$, $\alpha_1 = \alpha_e$, $\beta_1 = \beta_e$, $\alpha_2 = \alpha_{r(k)}$ and $\beta_2 = \beta_{r(k)}$ where α_e and β_e define the orientation of the excavation and $\alpha_{r(k)}$ and $\beta_{r(k)}$ define the mean orientation of discontinuity set k.

(7) Estimate the number of discontinuities, $N_{s(k)}$, from the set that will intersect the excavation based on the mean orientation of the individual sets.

Referring to Figure 3.5, an estimate of $N_{s(k)}$ based upon the mean orientation of each set, is determined with the equation:

$$N_{s(k)} = \frac{L_e \cos \theta_{er(k)}}{S_{\mu(k)}} \qquad (3.16)$$

where L_e is the length of excavation under consideration.

(8) Estimate the total number of discontinuities that will intersect the excavation, $N_{(k)total}$.

Repeat step (7) for each set and sum the results:

$$N_{(k)} = \sum_{k=1}^{NJS} N_{s(k)} \qquad (3.17)$$

where NJS is the total number of sets and

$N_{(k)}$ is the total number of discontinuities that will intersect the excavation based on the mean orientation of the individual sets.

It is important that the random component of discontinuities determined in Stage (3) is included in this estimation. The easiest way that this result can be achieved is to assume that the same proportion of the random component that were present in the scanline survey will intersect the excavation. An estimate of the total number of discontinuities that will intersect the excavation is, therefore, given by:

$$N_{(k)total} = N_{(k)} + d_r N_{(k)} \qquad (3.18.)$$

The procedures carried out in Stages (6)-(8) were based on the mean orientation of the discontinuity sets rather than on the orientation of the individual discontinuities within each of those sets. The procedures carried out in Stages (9)-(12) to determine the orientation weighting, w_θ, appropriate to each discontinuity and hence for the rock in the vicinity of the excavation, are based upon the properties of the individual discontinuities sampled. This procedure is not based on the assumption that the discontinuities intersecting the excavation are the same discontinuities that were sampled in the scanline survey. In fact, it is quite likely that the scanline survey will have been conducted on a cross section through the rock mass quite remote from the immediate volume surrounding the excavation. What is assumed is that the statistical properties defining the spatial characteristics of the sampled discontinuities are the same in the region of the excavation as they are in the area sampled.

(9) Determine the angle, $\theta_{en(i)}$, between a single discontinuity sampled in the scanline survey and the excavation.

The angle, $\theta_{en(i)}$, between a single discontinuity sampled in the scanline survey and the excavation (refer to Figure 3.6) is determined using Equation 3.10 in which $\theta = \theta_{en(i)}$, $\alpha_1 = \alpha_e$, $\beta_1 = \beta_e$, $\alpha_2 = \alpha_{n(i)}$ and $\beta_2 = \beta_{n(i)}$ where α_e and β_e define the orientation of the excavation and $\alpha_{n(i)}$ and $\beta_{n(i)}$ define the mean orientation of discontinuity i.

(10) Estimate the number, $N_{e(i)}$, of discontinuities having the same orientation as the discontinuity in (9), that will intersect the excavation.

In order to estimate $N_{e(i)}$, each discontinuity is allocated a spacing equivalent to the mean spacing of the set to which the discontinuity belongs. In the case of those discontinuities that

form the random component, the spacing is $S_{\mu(R)}$, as determined in Equation 3.15. The estimate of $N_{e(i)}$ applicable to each discontinuity is determined using the equation,

$$N_{e(i)} = \frac{L_e \cos \theta_{en(i)}}{S_{\mu(k/R)}} \tag{3.19}$$

where $S_{\mu(k/R)}$ is the mean spacing of the set, or the random component, to which the discontinuity belongs.

(11) Find the total number of discontinuities that will intersect the excavation.

Repeat stages (9)-(10) for every discontinuity sampled in the scanline survey including the random component and sum the results:

$$N_{total} = \sum_{i=1}^{N} N_{e(i)} \tag{3.20}$$

The estimated total number of discontinuities that will intersect the excavation will be significantly greater than the total number determined in Stage (8). The reason for this discrepancy is that Stage (8) involved summing the results obtained in Stage (7). In Stage (7) only one discontinuity was considered per set, a discontinuity having the mean orientation for the particular set. Stage (11) involved summing the results obtained in Stage (10). In Stage (10) every discontinuity assigned to the particular set was considered. Assume, for example that 500 discontinuities sampled in a scanline survey could all be assigned to one set. Depending on the length of the excavation and the mean orientation of the set, by applying Equation 3.17, $N_{(k)total}$ may be found to be 750. When Equation 3.19 is applied to each of the discontinuities in the set, N_{total} would be in the order of 375,000 (500 x 750) which clearly provides an inaccurate picture of the quality of the rock mass in the region of the excavation. In order to correct this over estimation, the values obtained from Equation 3.19 must be normalised.

(12) Normalise the value of $N_{e(i)}$ determined for each discontinuity.

A normalised value of $N_{e(i)}$ is determined for each discontinuity with the equation:

$$N_{e(i)}' = \frac{N_{e(i)} N_{(k)total}}{N_{total}} \qquad (3.21)$$

where $N_{e(i)}'$ is the normalised value of $N_{e(i)}$.

At the end of Stages (9)-(12), each of the N discontinuities sampled in the scanline survey has a weighting, $N_{e(i)}'$, applicable to it. This weighting is a measure of how many discontinuities having an orientation the same as the discontinuity will intersect the excavation. Stages (13) to (15) apply a second weighting to each of the discontinuities to describe the potential for each of the $N_{e(i)}'$ discontinuities to mobilise in the region of the excavation.

(13) Determine the angle, β_w, between a discontinuity sampled in the scanline survey and the major principal axis.

The potential for a rock mass to deform as a result of shear deformation occurring along a particular discontinuity is related to the acute angle, β_w, between the major principal axis (defined by α_σ and β_σ) and the unit vector defining the normal to the discontinuity (defined by α_n and β_n). This angle is determined for each of the N discontinuities sampled using Equation 3.10 in which $\theta = \beta_w$, $\alpha_1 = \alpha_s$, $\beta_1 = \beta_s$, $\alpha_2 = \alpha_n$ and $\beta_2 = \beta_n$.

(14) Determine the orientation weighting, $w_{\theta\phi}$, applicable if $\beta_w = \phi_w$.

A discontinuity in which $\beta_w \geq \phi_w$ is referred to as an active discontinuity. The minimum orientation weighting applicable to an active discontinuity, $w_{\theta\phi}$, is determined by letting $\beta_w = \phi_w$ in Equation 3.8.

(15) Determine the orientation weighting, w_θ, for the discontinuity.

A value of the orientation weighting, w_θ, is determined for each of the sampled discontinuities using Equation 3.8. If $\beta_w - \beta_{crit} < -45^o$, the discontinuity is assigned a value of $w_\theta = 0$. If $w_\theta \geq w_{\theta\phi}$ the discontinuity is an active discontinuity. A record is maintained ofthe number, N_a, of active discontinuities expected to intersect the excavation ie.:

$$N_a = N_a + N_{e(i)}' \tag{3.22}$$

Stages (13)-(15) are repeated for all discontinuities.

(16) Produce a histogram of orientation weightings for the rock mass.

After completing Steps (12) to (15) each discontinuity sampled has four parameters defining it. The first two parameters, α_n and β_n, define the orientation of a unit vector normal to the discontinuity. The third parameter, $N_{e(i)}'$, is an estimate of the number of discontinuities having the particular orientation that are expected to intersect the excavation. The fourth parameter, the orientation weighting coefficient, w_θ, quantifies the potential for the discontinuity to mobilise.

The distribution of orientation weightings can be graphically represented in the form of a histogram. The abscissa of the histogram, representing the orientation weightings, is divided into a number of equally spaced class intervals. The ordinate axis gives the respective number of discontinuities having a value for w_θ within each class interval. Examples of these histograms are shown in Figure 3.7(a)-(c).

(17) Determine the ultimate orientation weighting for the rock mass

The ultimate orientation weighting for the rock mass is defined with respect to the mean weighting for all discontinuities intersecting the excavation as:

$$w_{\theta(mass)} = \frac{\sum_{i=1}^{N_{total}} N_{e(i)}' \, w_\theta}{N_{total}} \tag{3.23}$$

and the mean weighting value for the active discontinuities intersecting the excavation is defined as:

$$w_{\theta\alpha(mass)} = \frac{\sum_{i=1}^{N_a} N_{e(i)}' \, w_\theta}{N_a} \tag{3.24}$$

where N_a is the number of active discontinuities intersecting the excavation.

Neither Equation 3.23 nor Equation 3.24 should be used to provide a definitive value for the ultimate orientation weighting for the rock mass without interpreting the results in the histogram. The histogram provides the design engineer with a powerful visual aid for assessing the integrity of the rock mass in the vicinity of the excavation. By considering the distribution of weightings and the positions of $w_{\theta\alpha(mass)}$ relative to $w_{\theta(mass)}$ the design engineer can choose whether to increase the ultimate orientation weighting for the rock mass from $w_{\theta(mass)}$ closer to $w_{\theta\alpha(mass)}$. This choice should be based on the following considerations:

(1) In cases where there is a fairly uniform distribution, as shown in Figure 3.7(a), it is preferable that the ultimate weighting for the mass be $w_{\theta\alpha(mass)}$.

(2) In cases where there is a clustering of weightings towards $w_\theta = 1$, as shown in Figure 3.7(b), the ultimate weighting should be chosen between $w_{\theta\alpha(mass)}$ and 1 depending on the mean of the clustering.

(3) In cases where there is a clustering of weightings towards $w_\theta = 0$, as shown in Figure 3.7(c), the ultimate weighting should be $w_{\theta(mass)}$. As $w_{\theta\alpha(mass)} \rightarrow 1$, the ultimate weighting should be increased accordingly.

In Bieniawski's [23] rock mass classification scheme the classification applicable to a rock mass is adjusted for the orientation of the discontinuities. In Section 2.5 a number of problems with this system were discussed. In the modified RMR procedure being presented in this study, it is recommended that a factor analogous to Bieniawski's reduction factor be referred to as $RMR_{(orient)}$ in which $RMR_{(orient)} = f(w_{\theta(mass)})$. A relationship between $w_{\theta(mass)}$ and $RMR_{(orient)}$ is presented in Chapter 9, determined on the basis of a series of tests conducted on discontinuous specimens. Details of the specimens are presented in Section 3.4 and of the tests in Chapters 4 to 7.

3.3. Discontinuity Spacing Rating.

In Bieniawski's [19] basic RMR classification system, the influence of discontinuity spacing on the behaviour of a rock mass is acknowledged by assigning a maximum of 40 points, out of a possible total of 100 points, to the parameter. Spacing is directly assigned a maximum of 20 points while the RQD rating of the rock mass, which is directly related to discontinuity

spacing (Priest and Hudson [121]), is assigned a further 20 points. Discontinuity spacing, therefore, takes a higher priority than discontinuity orientation for tunnels with respect to rock mass stability.

In Section 2.4, several cited studies highlighted the influence of the spacing between discontinuities on the strength and deformability of discontinuous rock masses (Einstein and Hirschfeld [50], Reik and Hesselmann [124]). These studies indicated that while discontinuity spacing does have an influence on the mechanical behaviour of a rock mass, this influence is more indirect than that of discontinuity orientation. The size of intact blocks, which is directly related to the spacing of the discontinuities, will influence the ease with which a rock mass can be excavated (ie. blasting characteristics) and the stability of individual blocks in the area adjacent to the excavation.

The classification system of Bieniawski does not acknowledge that any difference exists in the mechanical behaviour of a slabby rock mass comprising a single set of parallel discontinuities spaced 0.25m apart and a blocky rock mass containing three sets of orthogonal discontinuities each set spaced at 0.25m. The need for the RMR system to consider block sizes, rather than average discontinuity spacing, was partially addressed by Laubscher [93] who developed a table for estimating the RMR spacing value based on the average spacing of the three most closely spaced sets of discontinuities. The solution of Laubscher was based on a standard excavation diameter of 3 metres and did not consider the relationship between block size and excavations of other sizes. For cases of large mining or civil projects (eg. stopes, declines, power stations and waste storage repositories) this approach is inappropriate.

The approach that will be adopted in the modified RMR system is to consider the number of blocks that could fit into a chosen length of excavation. This procedure is carried out by determining the rating, $RMR_{(space)}$, as a function of the block volume, the cross sectional area of the excavation and the maximum set spacing, using the equation:

$$RMR_{(space)} = f\left(\frac{J_v}{A_x \times S_{\mu(max)}}\right) \tag{3.25}$$

where J_v is the mean volume of a block (m^3),

A_x is the cross sectional area of the excavation (m^2) and

$S_{\mu(max)}$ is the maximum spacing (m) of all discontinuity sets determined from Equation 3.14.

The approach adopted in this study for using $RMR_{(space)}$ as a measure of the significance of block size and shape on the stability of the excavation does not consider whether the shape of the blocks is such that blocks could be removed from the rock mass. Non-removable blocks are generally stable and of far less concern during excavation than removable blocks. A number of methods for determining whether blocks are removable are available (Goodman and Shi [58], Priest [119], Warburton [151]) and the respective theories are referred to as 'block theories'. The vectorial techniques for assessing block removability developed by Warburton has been incorporated into the numerical code BLOCKS. The technique developed by Priest utilises an inclined hemisphere projection whereas the technique developed by Goodman and Shi utilises stereographic projections. The software SAFEX by Thompson and Windsor [143] presents the theories of Warburton, Priest, Goodman and Shi in a user friendly manner.

While the simplistic approach adopted in this study for incorporating block size into the rock mass classification procedure does not have the sophistication of the techniques cited, it is in keeping with the basic philosophy adopted by Bieniawski with his RMR system. This philosophy has been to present a procedure that can be used to obtain an initial estimate of rock mass strength. The acceptability of the RMR system is proof that this philosophy is reasonable. The procedures recommended in this study aim to improve the basic RMR system but do not aim to make the system so complex that its usefulness would be in question. It is assumed that once the engineer obtains an initial feel for the integrity of the rock mass they would then use more sophisticated techniques, such as those cited, in the design process.

The parameter $RMR_{(space)}$, takes the place of the separate ratings for spacing and RQD used in the basic RMR system of Bieniawski. While it may seem useful to include the RQD rating as a separate identity in the modified rock mass classification system, owing to the relative simplicity with which it can be determined, the number of concerns raised in Section 2.5 regarding the suitability of this parameter as an indicator of discontinuity frequency makes it preferable that the parameter should not be included.

Miles [104] discussed the methodology for estimating the volume of polyhedra formed by the intersection of random planes in space. This methodology was clearly appropriate to the intersection of a rock mass by discontinuities. Miles showed that, if it were assumed that discontinuity frequency, λ, along any line within the rock mass were constant, mean volume, J_v, could be estimated from:

$$J_v = \frac{6}{\pi\lambda^3} \tag{3.26}$$

In the case of the present study, the excavation is analogous to a line through the rock mass. The frequency, λ, along this line is defined as:

$$\lambda = \frac{N_{k(total)}}{L_e} \tag{3.27}$$

where N is the total number of discontinuities intersecting the excavation (see Procedure 8) and L_e is the length of the excavation.

For ratios of $\left(\frac{J_v}{A_x S_{\mu(max)}}\right) \geq 1$, $RMR_{(space)}$ is given a rating of 20. This value is half that of the combined value for RQD and spacing in the basic RMR system. In this procedure, the 20 additional points are allocated to the orientation weighting. By doing this, the influence of discontinuity spacing on rock mass yield strength, with respect to the influence of discontinuity orientation on rock mass yield strength, is effectively accounted for.

For the purposes of the present study a relationship between the ratio $\left(\frac{J_v}{A_x S_{\mu(max)}}\right)$ and

$RMR_{(space)}$ would have to satisfy the following criteria:

(1) When $\left(\frac{J_v}{A_x S_{\mu(max)}}\right)$ is greater than 1 the likelihood that a block will enter the excavation is reduced. In this case, $RMR_{(space)}$ is set to 20.

(2) As the volume of the block decreases, $\left(\frac{J_v}{A_x S_{\mu(max)}}\right) \rightarrow 0$ and, as the excavation will potentially require additional support to secure unstable blocks, $RMR_{(space)}$ also decreases.

(3) The influence of large blocks entering the excavation can be more of a problem than if smaller blocks enter. This influence can be modelled by choosing a non-linear curve in which $\frac{\partial RMR}{\partial\left(\frac{J_v}{A_x S_{\mu(max)}}\right)} > 0$ and $\frac{\partial^2 RMR}{\partial\left(\frac{J_v}{A_x S_{\mu(max)}}\right)^2} < 0$.

Requirements (1)-(3) can be satisfied by a relationship for $RMR_{(space)}$ in terms of $\left(\frac{J_v}{A_x S_{\mu(max)}}\right)$ of the form:

$$RMR_{(space)} = 20\left(\frac{J_v}{A_x S_{\mu(max)}}\right)^{0.36} \qquad (3.28)$$

The exponent in Equation 3.28 influences the rate at which $RMR_{(space)}$ changes with changes in $\left(\frac{J_v}{A_x S_{\mu(max)}}\right)$. The choice of the magnitude of this exponent was based on the work of Santos [132]. Santos developed a relationship of a similar form to that in Equation 3.28 to describe the average discontinuity spacing for a rock mass, S_μ, in terms of the spacing rating in the basic classification system of Bieniawski. Santos chose the value for the exponent to be 0.36. Owing to a lack of data to the contrary and as A_x is constant and $J_v = f(S_\mu)$, the same value was chosen in this study. While this choice satisfies the requirements (1)-(3), further investigation could, possibly, improve the choice. The relationship between $RMR_{(space)}$ and $\left(\frac{J_v}{A_x S_{\mu(max)}}\right)$ for a unit discontinuity spacing is shown in Figure 3.8.

It is recognised that, rather than considering the ratio between the block volume and an excavation volume, it may be appropriate to consider the ratio between the block volume and the area of the excavation normal to the cross section of the development. This latter area

would be equivalent to W_e x $S_{\mu(max)}$ where W_e is the width of the excavation. This ratio considers whether a block of rock could 'fit' into an excavation. For the purposes of applying a weighting for discontinuity spacing, it is considered preferable that the ratio be dimensionless.

A small value for $RMR_{(space)}$ does not necessarily indicate that the rock mass is either slabby or blocky. A small block size is, however, generally the result of a complex network of intersecting discontinuities whereas larger block sizes tend to be the result of the intersection of parallel or near parallel sets of discontinuities or sets having large average spacings. The mechanical behaviour of rock masses containing discontinuities is different for both of these cases and this difference is, therefore, acknowledged to some extent by the rating.

The procedure for determining $RMR_{(space)}$ continues on from the procedure for determining $RMR_{(orient)}$ as follows,

(18) Specify the three sets with the minimum spacing determined from Equation 3.14.

(19) Determine the average block size, J_v, using Equations 3.26 and 3.27.

(20) Determine RMR(space) using Equation 3.28.

It is one thing to propose a modification to an established system with the aim of improving it especially with geotechnical problems. It is quite another thing to prove that the modification is valid. The next section establishes the methodology used in this study to demonstrate that the modified Rock Mass Rating system is a better input source for the Hoek-Brown yield criterion than is the basic system developed by Bieniawski.

3.4. Design and Characterisation of Discontinuous Models

This section discusses the design of a series of discontinuous specimens used in a rigorous programme of laboratory testing conducted with the aim of,

(1) establishing the link between $w_{\theta(mass)}$ and $RMR_{(orient)}$,

(2) validating the effectiveness of the Hoek-Brown rock mass yield criterion when used in conjunction with the modified RMR system for estimating rock mass yield strength and

(3) highlighting the influence that various intact material and discontinuity properties have on the strength and deformability of discontinuous rock masses composed of distinct blocks.

In Section 2.4.2, the advantages of conducting research into the behaviour of discontinuous specimens comprised of modelling material, compared to using specimens of discontinuous rock, were discussed. These tests have traditionally involved subjecting specimens comprised of geometrically similar parallelepipedal blocks to triaxial stress conditions and monitoring their response. For the present research project, this simplification of a discontinuous rock mass was avoided and specimens comprised of distinct blocks were used in a programme of triaxial testing.

Four, 150mm diameter x 300mm, cylindrical specimen geometries, shown in Figure 3.9, were designed. The major principal stress acting on the specimen during triaxial testing was applied parallel to the major axis of the specimen. The line of maximum dip within each discontinuity was considered to plunge downwards from a plane having the major axis as a normal. Table 3.1 tabulates the plunge, β_d, of each of the discontinuities and assigns each of the discontinuities to a set.

Geometry 1 included 6 discontinuity sets comprising 8 discontinuities in which β_w ranged from 20° to 40°. Discontinuities 6, 7 and 8 were designed to be parallel. The orientations of Discontinuities 1 to 5 were designed to range in increments of 5° from 20° with the aim of investigating the influence of discontinuity orientation on the deformability and strength of the specimen in cases where $\beta_w < \phi_w$. As $\beta_w > \phi_w$ for Discontinuity 5, it was assumed that, during triaxial testing, axial deformation of the specimen would primarily result from shear deformations occurring along this discontinuity. In order to prevent this shear deformation, the discontinuity was removed in Geometry 2 specimens to force the specimen to deform through intact material.

Table 3.1. Plunge of the line of maximum dip within each discontinuity intersecting cylindrical specimens.

Geom.	Discontinuity							
	1	2	3	4	5	6	7	8
	Plunge/Set							
1 set:	20° 1	25° 2	30° 3	35° 4	40° 5	35° 6	35° 6	35° 6
2 set:	20° 1	25° 2	30° 2	35° 4	35° 5	35° 5	35° 5	
3 set:	40° 1	47° 2	54° 3	60° 4				
4 set:	45° 1	52° 2	59° 3	34° 4	28° 5	15° 6		

Discontinuities in the Geometry 3 specimen were orientated so that $\phi_w \leq \beta_w \leq \beta_{crit}$ (where $\beta_{crit} = \phi_w/2 + \pi/4 \approx 60^\circ$) In this case it was assumed that axial deformation of the specimen would result from shear deformations occurring in varying amounts along all discontinuities. A similar range of orientation to that chosen for Geometry 3 was chosen for Geometry 4 specimens. Geometry 4 specimens differed from the other geometries in that non-persistent discontinuities, that is discontinuities that did not fully bisect the specimen, were included with the aim of investigating the influence of rock bridges on the strength and deformability of the specimens. The orientation of the non-persistent discontinuities was such that $\phi_w \leq \beta_w \leq \beta_{crit}$ and of the fully cutting discontinuities was such that $\beta_w \leq \phi_w$.

In order to highlight the influence of intact material strength on the strength and deformability of the specimens, two materials were chosen from which to construct the specimens. The choice and properties of the materials are discussed in Chapters 4 and 6. The influence of infill on the mechanical behaviour of the specimens was also demonstrated by manufacturing a series of specimens in which a coating material had been applied to the discontinuities to modify their frictional properties.

In order to obtain a RMR for each of the geometries, four hypothetical rock masses having similar discontinuity characteristics to the test specimens were proposed. Cross sections through each of these rock masses were drawn to scale and are shown in Figures 3.10 to

3.13. The outline of the respective test specimen is indicated on each cross section. The cross section was designed by repeating this outline the required number of times while randomly varying the orientation of each of the discontinuities through $\pm\approx5^{\circ}$ and the discontinuity spacing by $\pm\approx5$mm for each new discontinuity. A one metre section of a scanline is also shown in each figure. This scanline is used in Chapter 9 to enable each rock mass to be 'logged'.

The basic criterion for each two-dimensional cross section was that it had to represent a three-dimensional population from which a 'random' sample, the cylindrical specimen, could have been obtained. This result was achieved by assuming that each cross section represented a two-dimensional slice through its respective population, in a similar way that a rock face represents a two-dimensional slice through a three-dimensional rock mass. The irregularities on an *in situ* rock face allow the three-dimensional orientation of the discontinuities to be logged during a scanline survey whereas only two-dimensional orientations were observable in the cross sections. To allow for this difference, the assumption was made that the normal to each discontinuity in the designs had a trend, α_n, parallel to a line within the observed plane. A discontinuity sloping down to the right was assumed to have $\alpha_n = 0^{\circ}$ whereas one sloping down to the left was assumed to have $\alpha_n = 180^{\circ}$.

In order to estimate either a basic or a modified Rock Mass Rating for the four hypothetical rock masses, details regarding the strength of the intact material and the discontinuities are required. These properties are determined in Chapter 6. The relationship between $RMR_{(orient)}$ and $w_{\theta(mass)}$ required in the modified rating system, are established on the basis of the triaxial test results on the discontinuous specimens. These results are presented in Chapter 7.

3.5. Summary.

In this chapter, two modifications to the RMR classification system of Bieniawski [17] were proposed to make the system more sensitive to the mechanical and geometric properties that most influence the strength and deformability of a rock mass. These modifications, based upon data obtained from a scanline survey of the rock mass, quantify the orientation of the discontinuities with respect to the orientation of the major principal stress within the rock mass and the average size of the rock blocks.

Four, two-dimensional, hypothetical rock masses that could be classified according to the procedures developed in the chapter were proposed and cross sections through these rock masses were designed. Four cylindrical specimens were designed, having similar discontinuity properties to those in the four hypothetical rock masses, to be used in a comprehensive series of triaxial tests. The techniques for manufacturing the specimens are discussed in the next chapter.

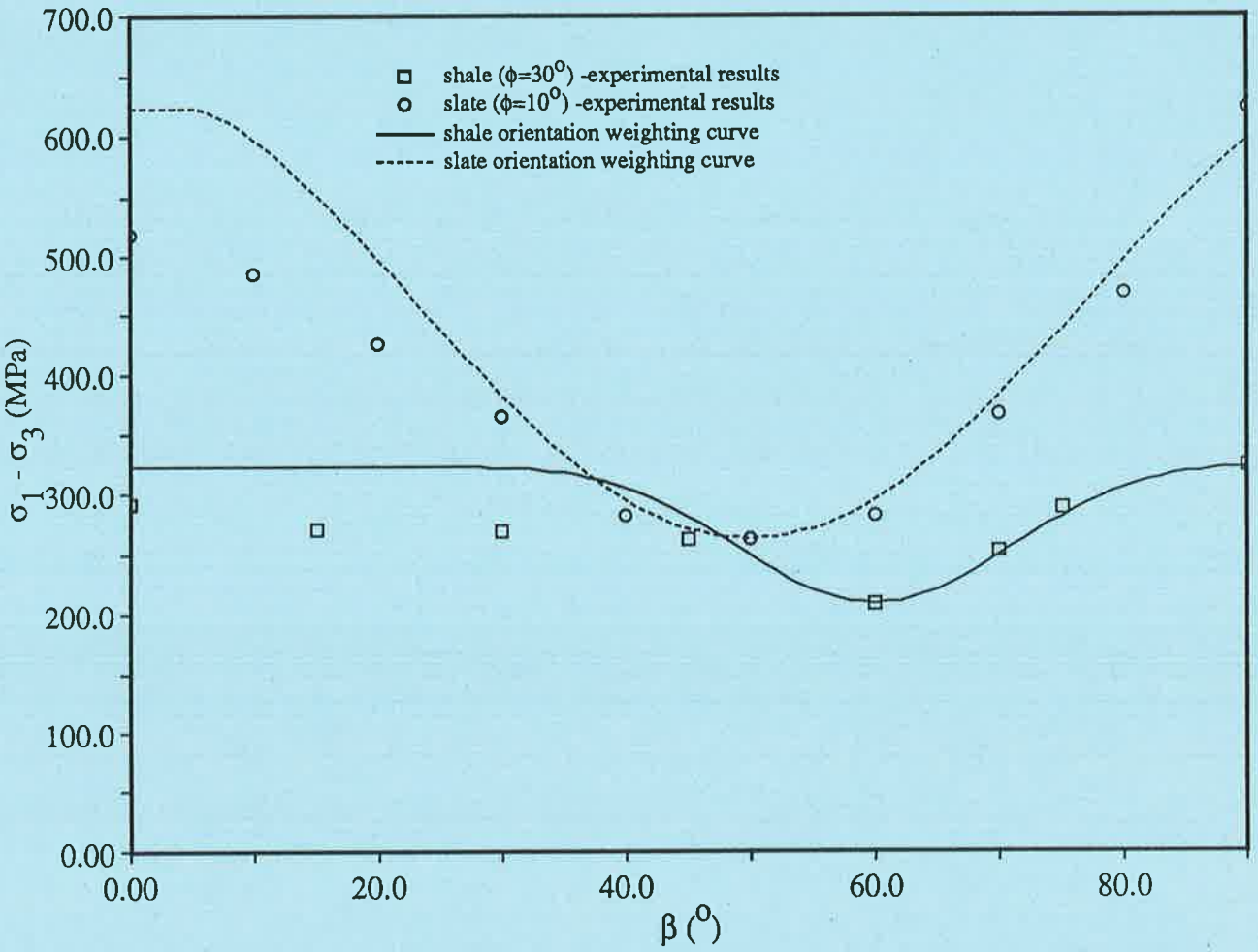

Figure 3.1. Comparison of experimental (after McLamore [98]) and analytical deviator stress versus anisotropy angle plot.

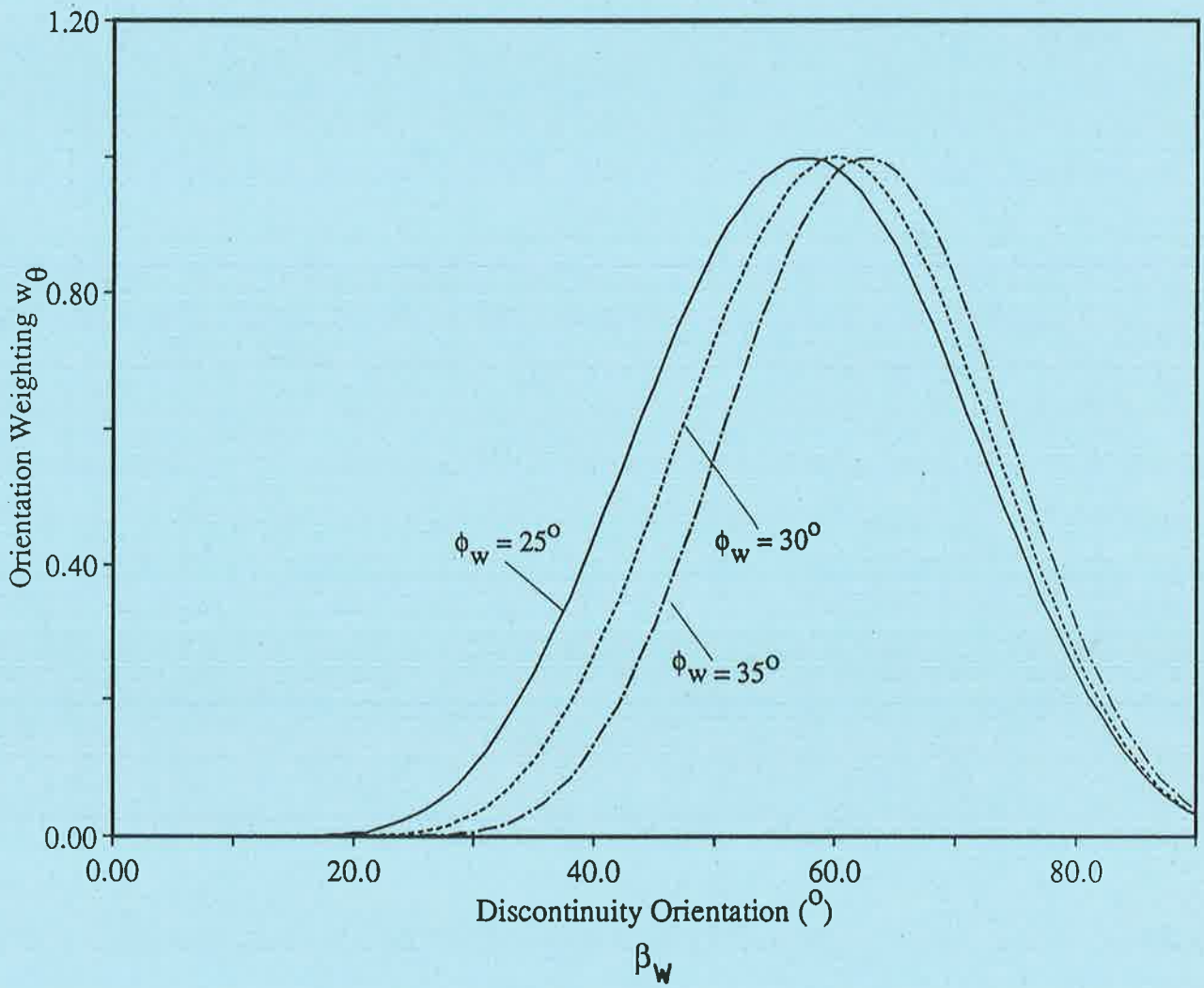

Figure 3.2. Plot highlighting the variation in the orientation weighting, w_θ, that occurs with changes in β_w.

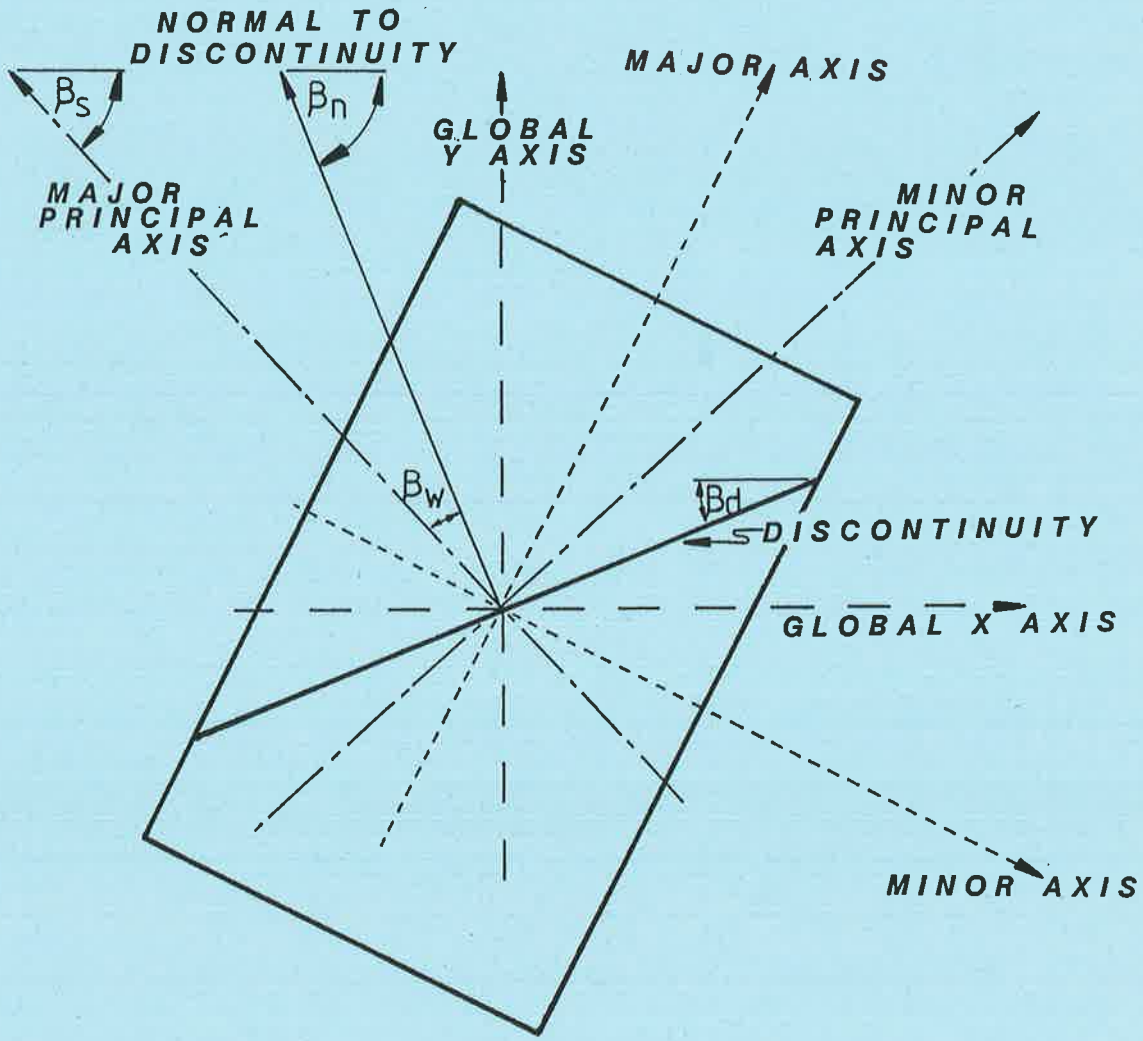

Figure 3.3. Representation of axes in two-dimensional Cartesian space used in the modified Rock Mass Rating procedure.

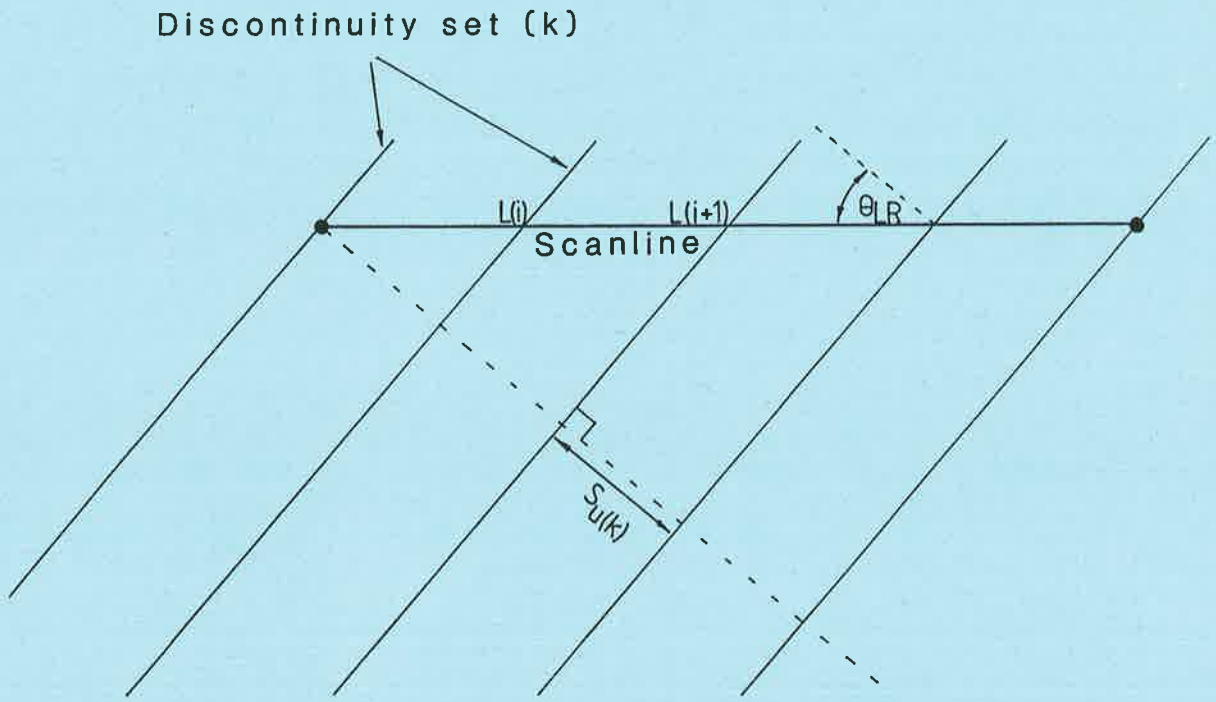

Figure 3.4. Representation of a single discontinuity set (k) intersecting a scanline.

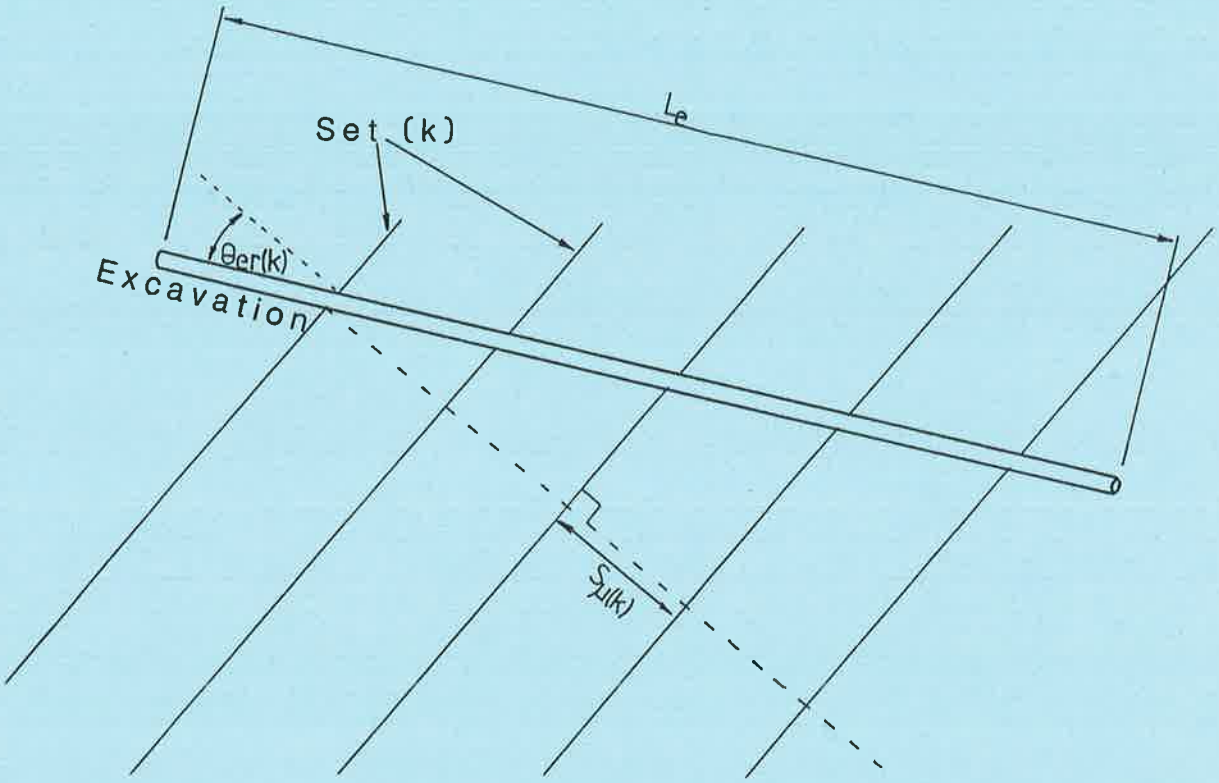

Figure 3.5. Representation of a single discontinuity set (k) intersecting an excavation.

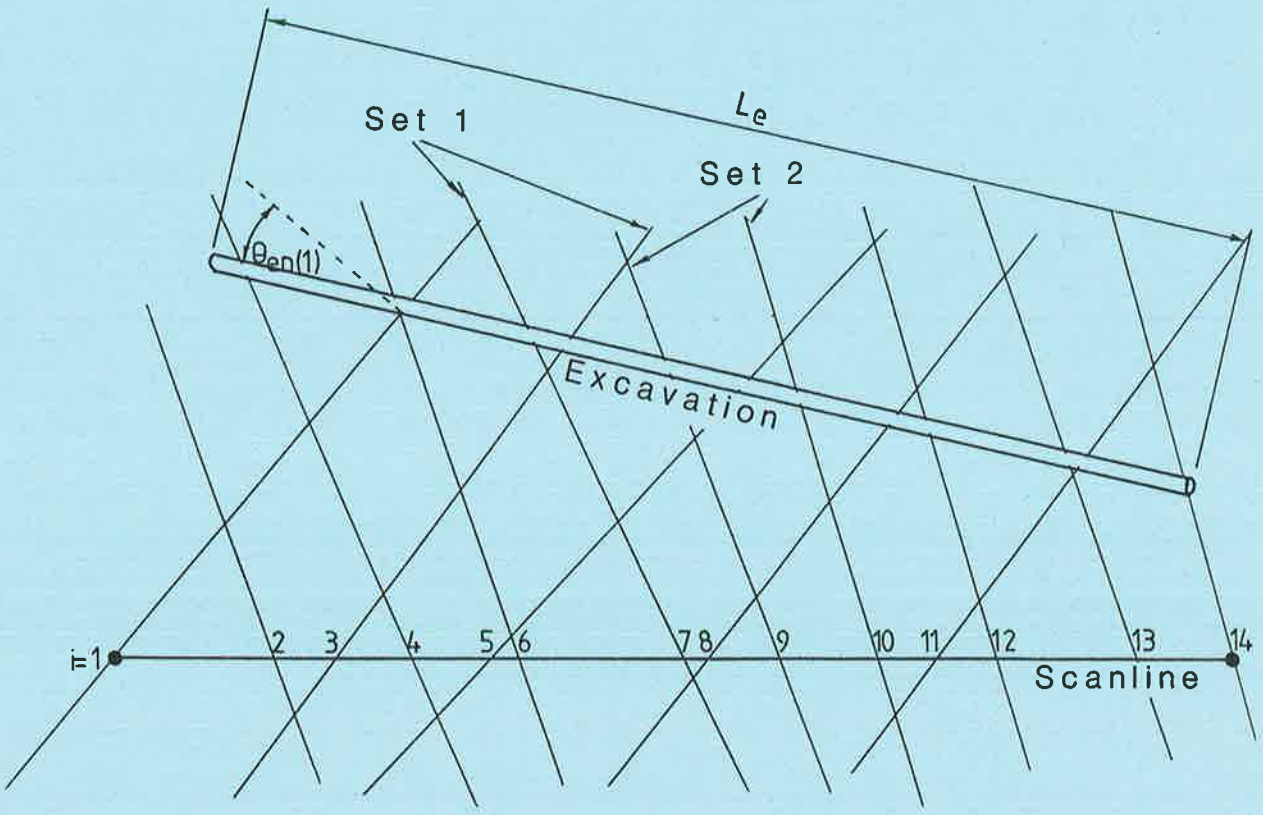

Figure 3.6. Representation of individual discontinuities intersecting the scanline and the excavation.

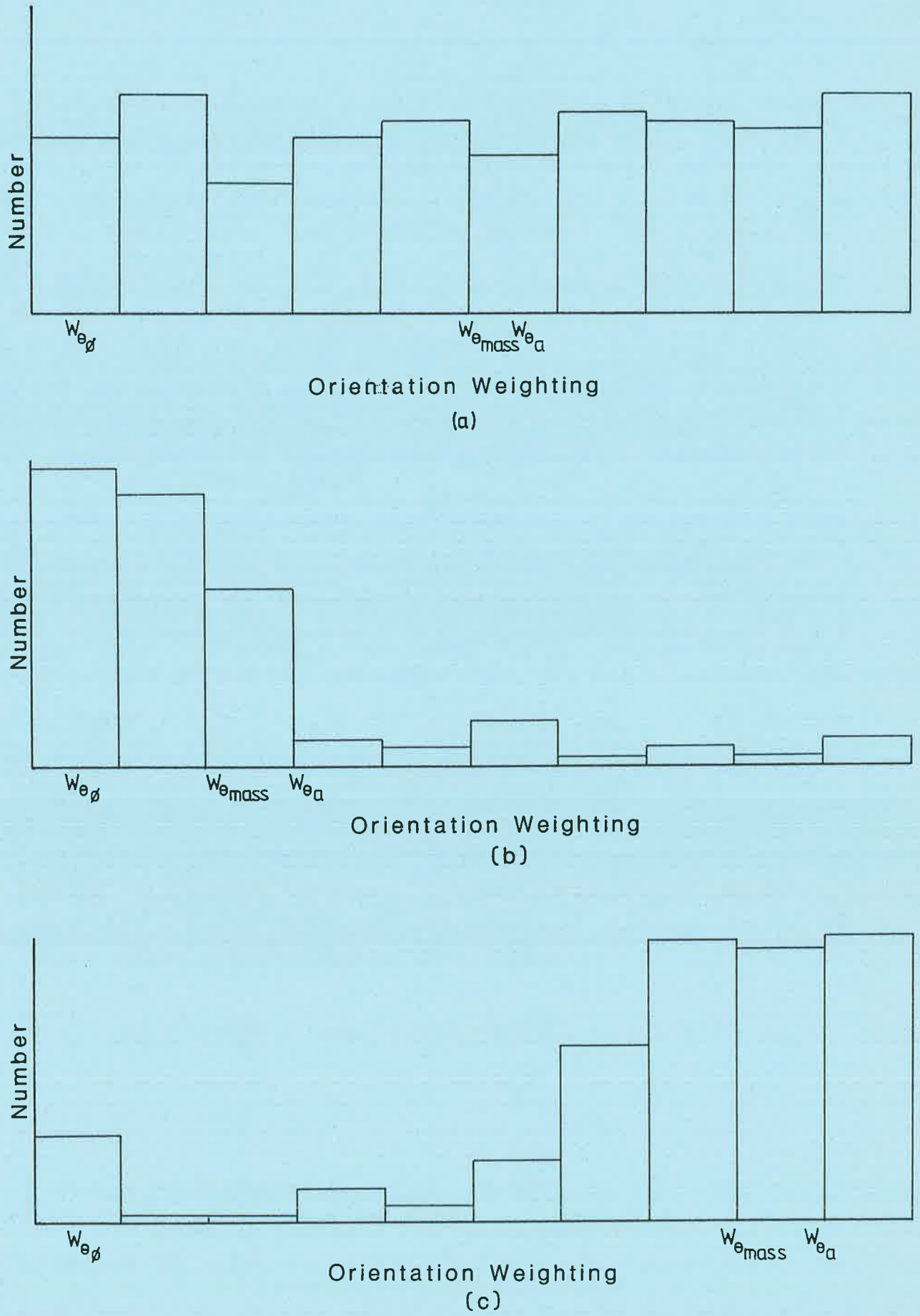

Figure 3.7(a)-(c). Examples of theoretical orientation weighting histograms.

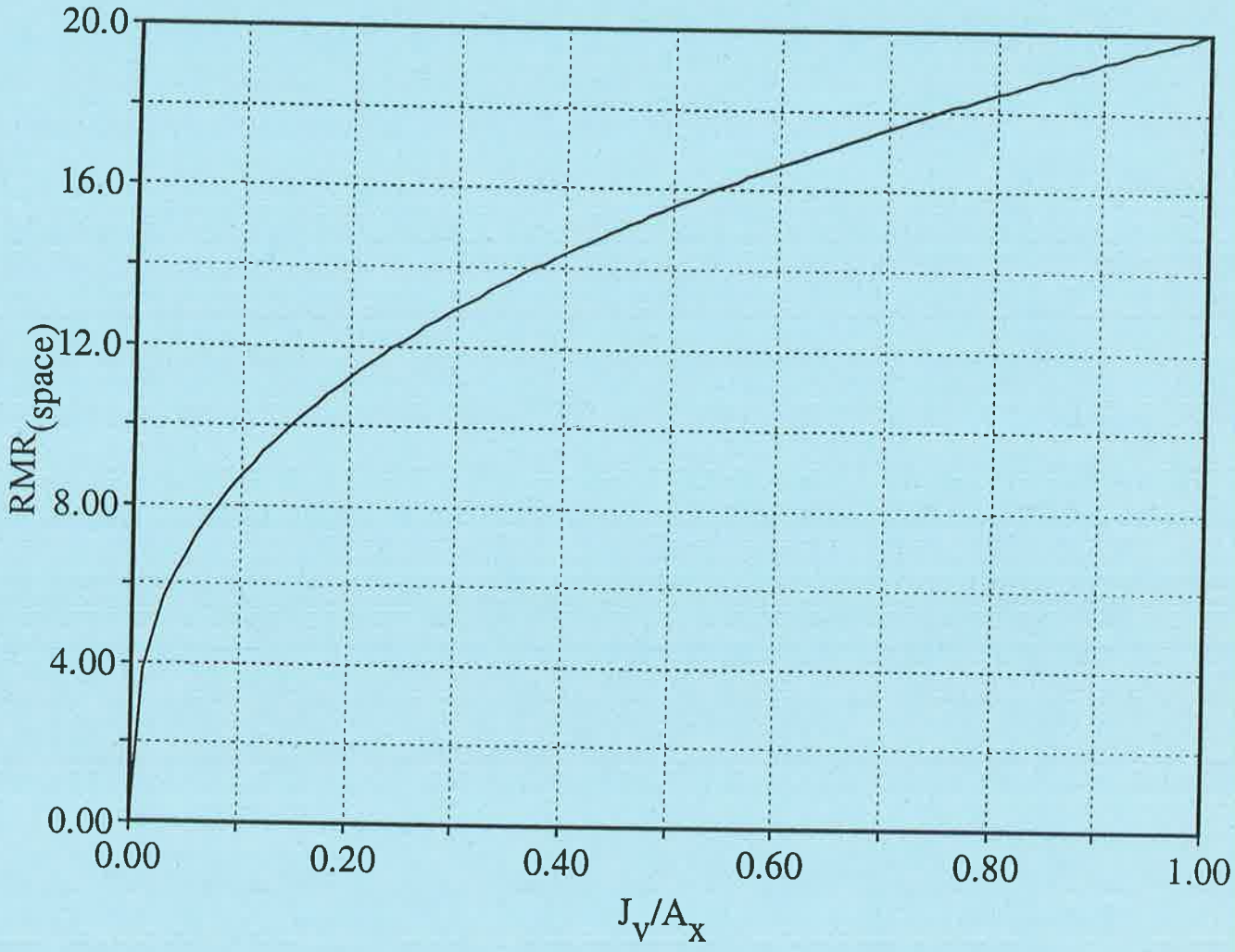

Figure 3.8. Relationship between $RMR_{(space)}$ and J_v/A_x for a unit discontinuity spacing.

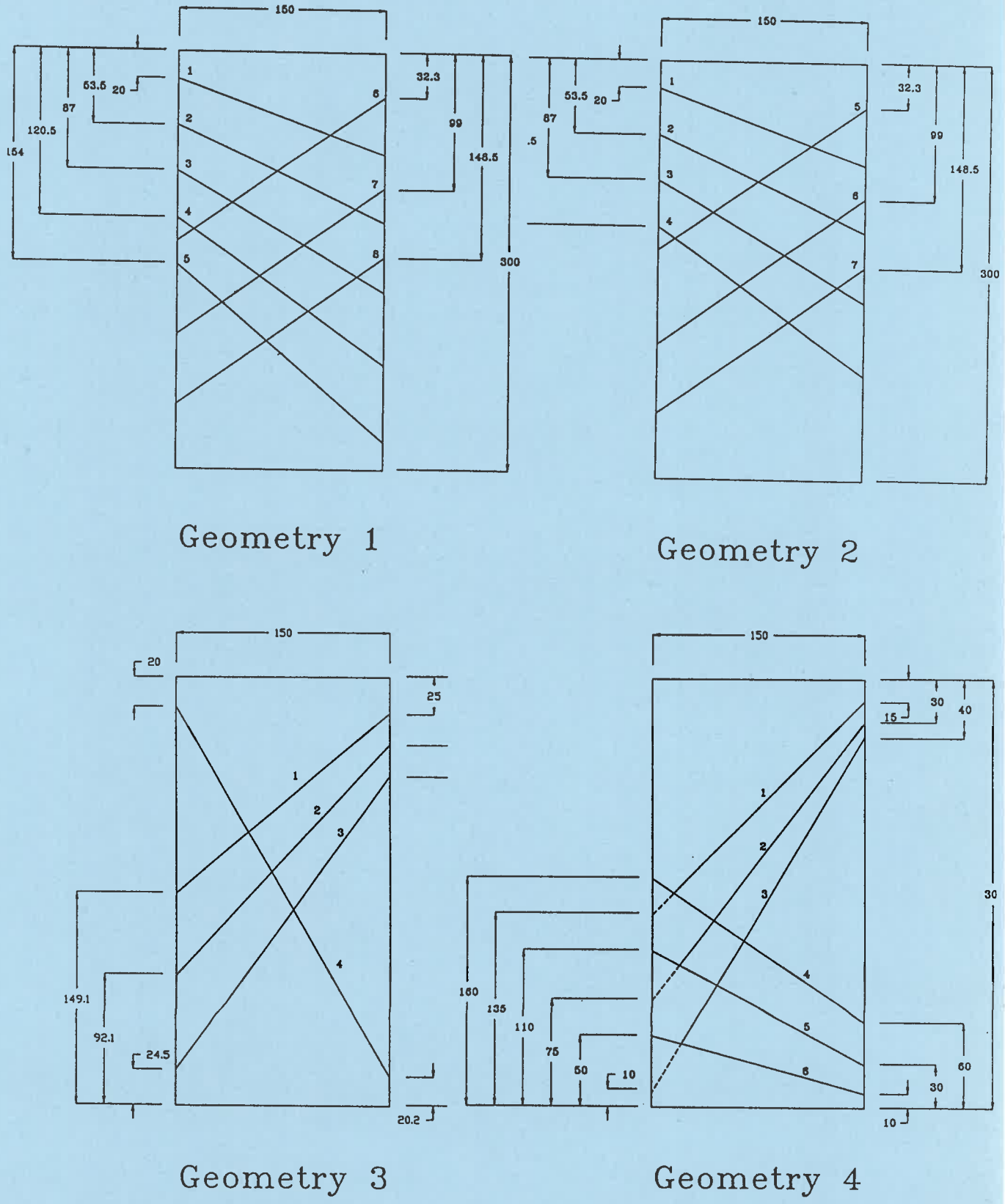

Figure 3.9. Diagram showing details of the laboratory specimens

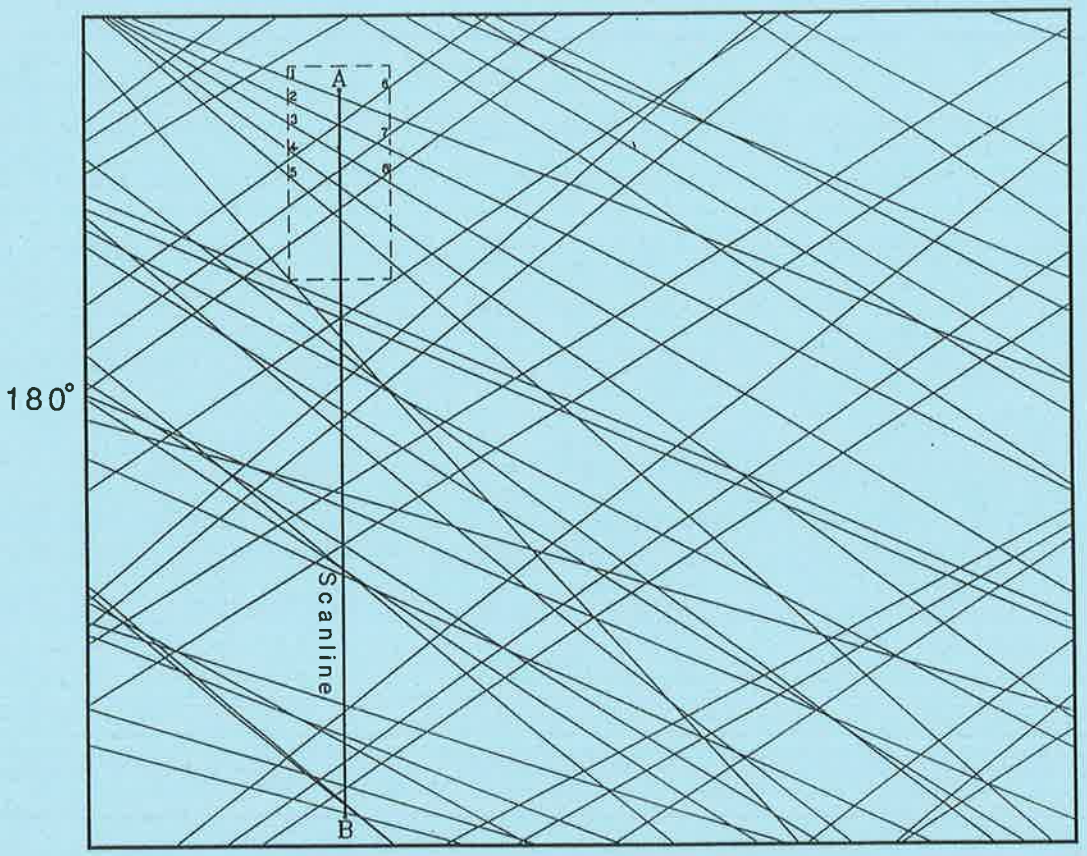

Figure 3.10. Hypothetical rock mass for Geometry 1 RMR assessment. A 1m section of scanline is shown.

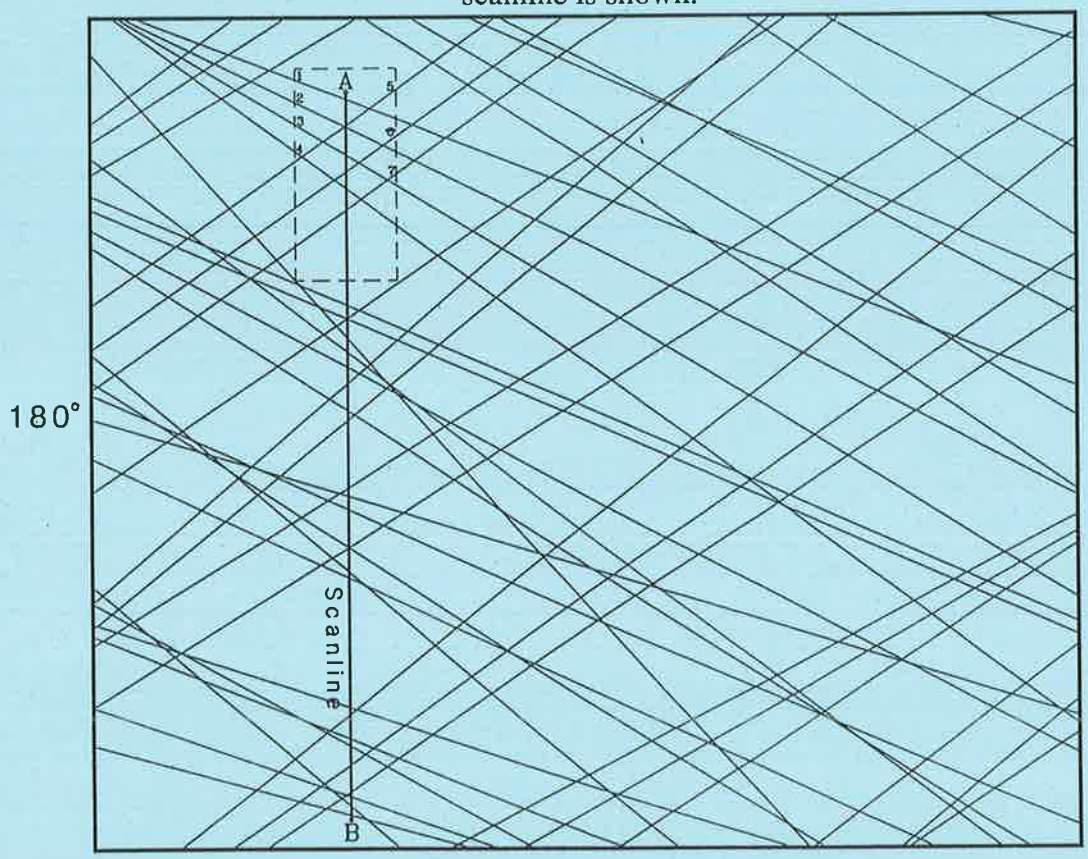

Figure 3.11. Hypothetical rock mass for Geometry 2 RMR assessment. A 1m section of scanline is shown.

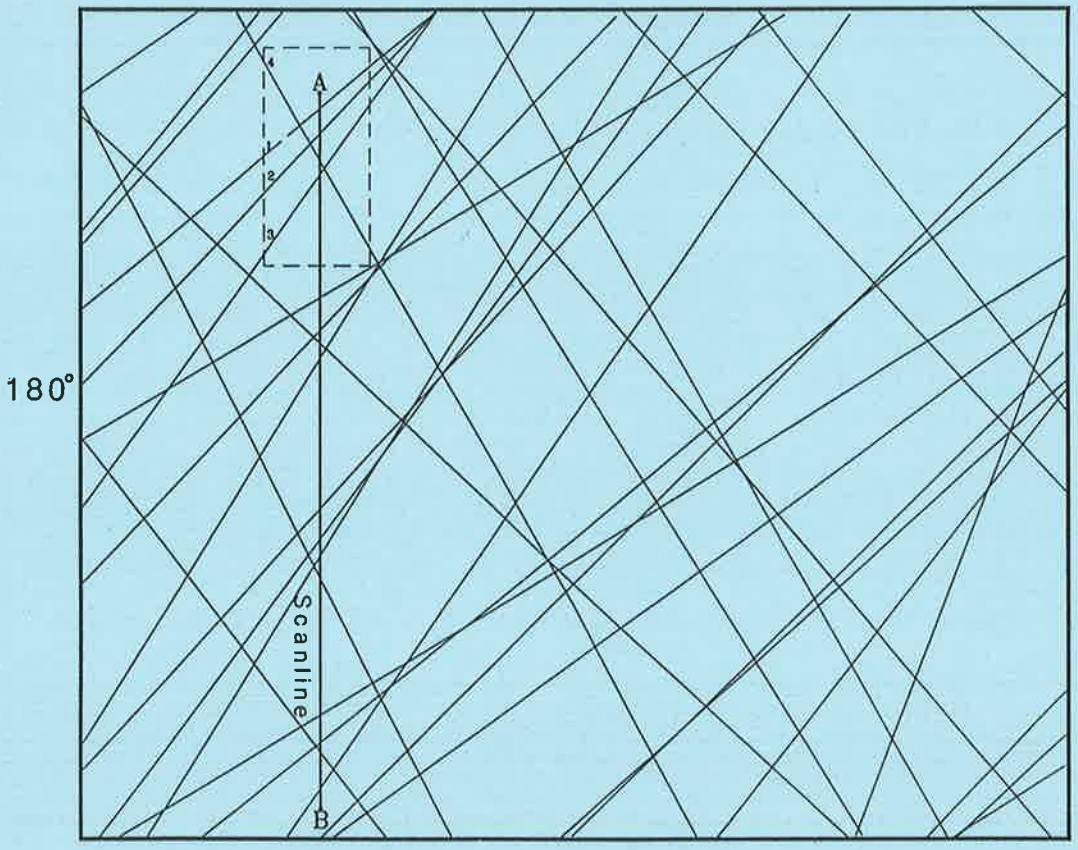

Figure 3.12. Hypothetical rock mass for Geometry 3 RMR assessment. A 1m section of scanline is shown.

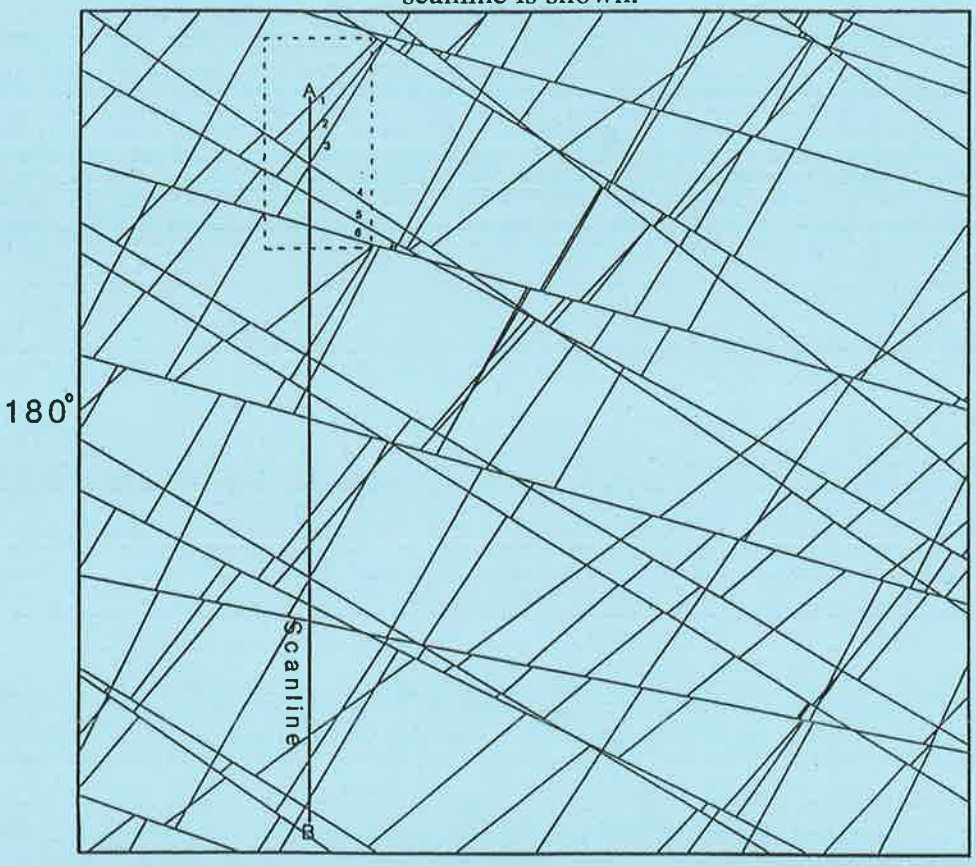

Figure 3.13. Hypothetical rock mass for Geometry 4 RMR assessment. A 1m section of scanline is shown.

Chapter 4.
Development and Manufacture of Specimens.

Chapter 4. Development and Manufacture of Specimens.

4.1. Introduction.

Previous research into the strength and deformability of discontinuous rock was discussed in Section 2.4. This research often involved the use of specimens fabricated from uniformly shaped blocks. One reason for this practice was the difficulties involved in producing specimens comprised of distinct blocks suitable for testing. In Chapter 3, the design of four specimens of discontinuous rock formed from distinct blocks, was described. These four specimens, shown in Figure 3.9, contained 20, 17, 8 and 10 distinct blocks, respectively. This chapter will describe the techniques developed in this project for overcoming some of the difficulties encountered by other researchers in manufacturing such specimens. Many of the researchers, cited in Section 2.4, composed their blocks from a range of natural and synthetic modelling material that had many of the properties of real rock without the natural variability. The basis for selecting a suitable modelling material for this project and the manner that these materials were prepared, will also be discussed.

4.2. Constructing Models.

Before discontinuous specimens could be tested, a method had to be developed for manufacturing dimensionally similar specimens that could be reproduced in large numbers. Constructing a mould to produce an intact cylindrical specimen for material property testing was a fairly simple process that utilised a split plastic tube having the correct internal

diameter. A more complex operation was required in order to construct the moulds required to reproduce the dimensionally complex blocks in the discontinuous specimens.

A model of a discontinuous rock mass is, in effect, an assemblage of individual intact blocks each of varying dimensions separated by discontinuities. The complexity of the block shapes used in this study ruled out the possibility of manufacturing the blocks by machining techniques. A more appropriate method was to construct moulds of the individual blocks into which a modelling material could be poured.

For the Geometry 1 specimen, a 165 x 165 x 300mm block of high density 'Craftwood' timber was obtained and turned down to a diameter of 160mm. In order to create a discontinuity, the cylinder was sawn at the required angle with a radial arm saw. The thickness of the cut was built back up with masonite after the saw cut was completed. The two halves of the cylinder were then lightly glued together to ensure that there would be no movement along the discontinuity. The procedure was repeated until all the required discontinuities were cut and glued. The oversize cylinder was next turned down to the required diameter of 150mm and cut to a length of 300mm. The glue bonds were then broken, leaving a set of blocks. These blocks were carefully sanded to remove any excess glue and any imperfections were corrected with automotive body filler. This method of creating the Geometry 1 cylinder proved extremely time consuming and so an alternative construction method was employed for the other geometries.

A cylinder suitable for forming moulds for Geometries 2, 3 and 4 began as a rectangular block of high density styrofoam having the dimensions, 160 x 160 x 300 mm. The foam block was shaped by a hot wire as shown in Figure 4.1. A similar procedure for producing foam blocks having variable dimensions for use in rock mass modelling was carried out by Bro [30]. Unlike this study, Bro did not progress beyond the use of foam blocks. The hot wire used in the current study comprised a 350mm length of 5Ω/m NiChrome wire, supported in a lightweight frame and connected to an 18V power supply. The wire had a diameter of 0.23mm, thereby, ensuring that the thickness of a cut was minimal. This

consideration was important as a thick cut would have removed material and produced a specimen that did not assemble correctly. The hot wire method allowed the discontinuities to be cut quickly, accurately and smoothly because of the tendency for the styrofoam to be sealed by the heat after it was cut.

The styrofoam block was secured in a jig, shown in Figure 4.2, designed to allow the block to be slowly rotated next to the hot wire. The hot wire was orientated parallel to and 75 mm away from, the major axis of the block. This rotation produced a 150 mm diameter cylinder. The cylinder was placed in a second jig designed to orientate the axis of the styrofoam cylinder at the angle required for cutting a discontinuity. The discontinuity was cut and the halves of the cylinder were joined together with tape. Subsequent discontinuities were cut in a similar manner. When all the required discontinuities had been cut, the tape was removed, leaving a set of individual styrofoam blocks. The blocks were next coated with several coats of shellac to seal the foam and act as a release agent. An example of the foam blocks assembled to form a cylinder is shown in Figure 4.3.

Each of the foam blocks was placed on a smooth wooden base and a timber frame was constructed around the edges of the base to confine the moulding material as shown in Figure 4.4. A two-part mixture of RTVE silicone moulding rubber was used as a moulding medium because of its durability, ability to cure at room temperature and high tear and tensile strength. This material was easy to pour, capable of filling crevices and reproducing sharp edges. The rubber mixture was prepared in batches according to the manufacturer's instructions. In order to de-air the mixture, each batch was placed in a vacuum chamber connected to a two stage pump shown in Figure 4.5. A pump capable of applying a vacuum of 0.13Pa was found to be suitable. When subjected to the vacuum, the mixture expanded to three times its original volume before contracting back to its original volume. It was therefore important to ensure that the size of the vessel containing the mixture was of sufficient volume to contain this expansion. After 3 minutes of vacuum application the liquid rubber was poured into each wooden frame until the selected block was covered with rubber to a minimum depth of 6 mm. Slight tapping on the frame ensured that the rubber

flowed to all parts of the mould. The liquid rubber was allowed to set for 24 hours after which time the rubber moulds, shown in Figure 4.6, were removed from their frames. After a further 48 hours the rubber moulds reached full strength and were ready for use in the manufacture of the individual blocks. It was then necessary to choose a suitable material from which to construct the blocks.

4.3. Modelling Material.

Stimpson [140] [141] reviewed the properties of a wide range of modelling materials and concluded that, with the large range of materials available, it should be possible to choose a material to satisfy the requirements of most projects. The major requirements for a modelling material to satisfy this research were:

(1) The material had to enable homogeneous specimens to be manufactured. Homogeneity ensured that specimens produced from the same batch of modelling material had statistically similar properties.

(2) The material had to enable specimens to be produced having properties that satisfied the requirements for similitude with natural rock. This requirement was not necessarily invalidated if all the engineering properties of the specimen were not the same as those of natural rock. The requirements for similitude are discussed in the following section.

(3) It was desirable that the material could be combined with a range of materials, so that specimens having a range of engineering properties could be produced.

(4) The material had to be readily available, reasonably priced and capable of being stored under similar conditions to those recommended for bagged cement.

(5) The viscosity of the prepared mixture had to be low enough to ensure that the material could be prepared with basic equipment.

(6) The material had to be capable of being moulded to the desired shape and have minimal shrinkage during curing.

4.3.1. Similitude Requirements.

One of the requirements for a geotechnical modelling material is that it has similitude with

natural rock. This requirement establishes the relationship that should exist between the dimensions and the engineering properties of a specimen and those of the mass being modelled. These laws were expressed by Einstein et al. [49] in terms of the major principal stress acting on the specimen by the function:

$$\sigma_1 = f(\sigma_c, \sigma_t, \sigma_3, \phi_w, \phi_i, E, \nu, \rho, S, \beta_w, \varepsilon, g, \varepsilon') \qquad (4.1)$$

where σ_c and σ_t are the uniaxial compressive strength and the tensile strength, respectively,
σ_1 and σ_3 are the major and minor principal stresses, respectively,
ϕ_w is the discontinuity friction angle,
ϕ_i is the friction angle of the intact material,
E and ν are Young's modulus and Poisson's ratio, respectively,
ρ is the density,
S is the discontinuity spacing,
β_w is the angle between the normal to the discontinuity and the major principal stress,
ε and ε' are the strain and the strain rate and
g is the acceleration of gravity.

Obert and Duvall [108] expressed this function in terms of the following set of dimensionless factors (π factors):

$$\frac{\sigma_1}{\rho g S} = f\left(\frac{\sigma_c}{\rho g S}, \beta_w, \frac{\sigma_t}{\rho g S}, \frac{\sigma_3}{\rho g S}, \phi_w, \phi_i, \frac{E}{\sigma_c}, \nu, \varepsilon, \varepsilon'\sqrt{\frac{S}{g}}\right) \qquad (4.2)$$

Indraratna [71] noted that similitude with respect to the shear and normal stiffness and the joint roughness coefficient should also be ensured, but considered these to be of secondary importance.

With the large variety of modelling materials available, it would have been difficult to select a suitable material from which to produce specimens that had specific engineering properties while at the same time satisfying the laws of similitude. The approach adopted in this investigation was, therefore, to select a particular modelling material that had wide spread

acceptance, determine the properties of specimens manufactured from this material and then establish the range of natural materials that this material could successfully model.

4.3.2. The Use of Hydrated Gypsum as a Modelling Material.

A common modelling material that has been used for many years is one based upon hydrated gypsum. Some examples of the use of this material and the conclusions of the various authors regarding the suitability of the material for modelling purposes will be discussed.

White and Sabnis [158] conducted a series of tests in which they investigated the occurrence of strength variations in partially dried specimens with changes in specimen size. The specimens were manufactured from mixtures of 'Hydrocal' type gypsum cement and sand. It was concluded that, if precautions were taken to eliminate the effects of differential drying on the strength of the mortar, then the material represented a suitable material for modelling those materials that exhibited a non-linear compressive stress versus strain curve. White and Sabnis noted that these results were only applicable to partially dried specimens.

Stimpson [141] conducted a comprehensive summary of modelling materials used in geomechanics research and commented on the wide-spread acceptance of gypsum-based materials up to that time (1968). Stimpson claimed that some researchers found such material to possess a linear stress strain curve while others found it to be non-linear. Stimpson concluded that the stress versus strain behaviour for gypsum based materials appeared to be influenced by the rate of strain and he could not conclude that there was any difference in fracture behaviour between these materials and brittle rock. He did concede, that there were very few fracture criteria available for brittle materials and that available evidence suggested that the fracture processes may not be the same for gypsum based materials and brittle rock. Some of this evidence was the tendency for rock to display an exponential decrease in strength of the order of 100% with increasing length/diameter ratio during uniaxial testing, compared to a linear decrease of only 20% with gypsum based materials. Stimpson found that these materials displayed very similar characteristics to rock during triaxial testing. One such characteristic was the tendency for the yield condition to

pass from axial fracture to shear and multiple failures and the tendency for a cylindrical specimen comprised of the modelling material to barrel. Stimpson stressed the need to remove all free water during curing of the gypsum based materials, because small changes in moisture content tended to cause significant changes in the compressive strength of the modelling material.

The work of Brown [31] and Brown and Trollope [33] has been described in Section 2.4.2. Brown and Trollope used a 'Hydrocal' type gypsum based material because of the ease with which it could be moulded and machined. The researchers commented on the similarity between the properties of the gypsum based materials and those found in many natural rocks yet noted that these properties tended to be size dependent.

Einstein and Hirschfeld [50] used specimens made from a mixture of 'Hydrocal' type gypsum based material and diatomaceous earth. This mixture was used because it was considered to simulate reasonably the characteristics and behaviour of brittle rock.

Reik and Zacas [125] using similar techniques to those adopted by Brown [31] and conducted a series of tests on samples built up from a gypsum based cement/sand mixture. The authors chose this material because they considered it to produce specimens that had the properties of a competent, layered sedimentary rock in terms of the Mohr strength envelopes, joint friction properties and the elastic properties.

Oda et al. [109] conducted a series of tests on 200mm diameter cylindrical specimens made from gypsum based material containing non-persistent discontinuities. These discontinuities were formed in the specimen with strips of greased paper. The authors investigated the influence of crack geometry on acoustic wave velocity and found that the acoustic properties for the specimens were consistent with those obtained for jointed granites.

Johnston and Choi [82] reviewed Stimpson's earlier summary and considered all currently available model materials as being unsuitable for modelling mudstone. A gypsum based

material was initially considered because of its price, availability, curing time and ease of fabrication. After experimenting with the material the researchers decided that the brittle nature and high void ratio of the plaster made it unsuitable for their purposes. They were also concerned about the heterogeneous characteristics exhibited by large specimens of plaster. In light of the deficiencies in existing materials for modelling soft rocks, Johnston and Choi developed a synthetic soft rock they referred to as Johnstone. The material represented a considerable advancement in the nature of modelling materials. This advancement was due partly to the machineability of Johnstone that allowed blocks having a wide variety of dimensions to be produced but predominantly because Johnstone was homogeneous and isotropic and it could be produced at a wide range of saturated water contents. Haberfield and Johnston [60] carried out an extensive series of tests on this material and were able to demonstrate how Young's modulus for soft rocks was dependent on the nature of the applied loads. Johnstone appears to be an excellent material for simulating soft rock. A material having a higher compressive strength than Johnstone was, however, preferable for the present research. The compressive strength of Johnstone was similar to that of mudstone, in the order of 8MPa. For the present research it was also desirable that a material was used that could be moulded in order to produce the desired block shapes rather than having to be machined as was the case with Johnstone.

Indraratna [70] [71] studied the properties of intact and discontinuous specimens composed of Hydrocal gypsum cement and sand in order to investigate the behaviour of reinforced composites and rock joints. He concluded that the material effectively simulated the behaviour of an array of weak, sedimentary rocks characterised by homogeneous and isotropic properties.

The question of the suitability of gypsum based materials as a modelling material to simulate natural hard rock has produced mixed reactions among researchers. The general opinion suggested that, if the limitations of such materials were recognised then, they could provide a reasonable simulation of natural rock. For this reason a Hydrocal type gypsum based cement marketed under the name of Patternstone F was chosen as a base from which to mould

specimens for this research. A second material comprising a 50/50 gypsum cement/sand mixture was also investigated.

4.3.3. Choice of Infill Material.

The research work discussed in the previous section concerning the behaviour of discontinuous rock masses tended to be concentrated on rock masses containing clean discontinuities. Ladanyi and Archambault [89] and Papaliangas et al. [113] extended this research to include infill material into the discontinuity. This contribution was important because the research concluded that infill material altered the strength and deformation behaviour of a discontinuity. The influence of discontinuities on rock mass behaviour was, therefore, investigated as a component of this research.

Celite was used as an infill material. Celite is the proprietary name for diatomaceous silica, also known as diatomite. Diatomite is in the SiO_2 group of the tectosilicates. Included in this group are minerals having similar structures to either quartz, tridymite, cristobalite or opal. Diatomite has the structure of opal having the general chemical composition,

$$SiO_2 \cdot nH_2O$$

The H_2O fraction ranges between 4% and 9%. Diatomite resembles chalk in appearance and has the particle size distribution of a fine to coarse silt as shown in Figure 4.7. The material is formed from the sedimentation at the sea bed of diatoms, which are single cell algae, which are consolidated with time.

4.4. Preparation of the Modelling Material.

Although gypsum based mortars have been used for many years, some of the techniques for preparing them, that are specific to the present project, will be briefly outlined in this thesis.

Sufficient dry gypsum cement for the specimens was accurately weighed. The weight of water required to produce the chemical reaction that causes the calcium sulphate semihydrate to recrystallise as the dihydrate under the following reaction,

$$CaSO_4.\tfrac{1}{2}H_2O + \tfrac{3}{2}H_2O = CaSO_4.2H_2O$$

is equivalent to 19% of the weight of the gypsum cement. The mixture would, however, have been virtually unworkable at this moisture content and so 40% water by mass was specified by the manufacturer of the cement (Boral [25]). Therefore, every 100g of cement required 40ml. of water to produce a workable mixture.

In the case of the cement/sand mixture, sand passing the #16 BS. sieve (0.85mm) was mixed thoroughly with an equal mass of cement. The sand was a fine to coarse orange sand having a dry unit weight of 13.4kN/m^3. The grading curve for the sand is shown in Figure 4.8. Tests revealed that the volume of water required to saturate the dry sand was equivalent to 8.5% of the dry mass of the sand. Therefore, 0.1kg of the cement/sand mixture required 20ml (40% x 0.05kg) of water for the cement and 4.25ml (8.5% x 0.05kg) of water to saturate the sand giving a total water requirement of 24.25ml. In order to construct a 150mm x 300mm cylindrical specimen having a density of 1.734 kg/m^3, 9.4kg of the cement/sand mixture was required. The water requirement was, therefore, 2279ml $\left(\frac{9.4kg}{0.1} \text{ x } 24.25ml\right)$.

The dry powder was slowly sprinkled into a measured quantity of the water. If the water had been added to the dry powder, heterogeneous specimens could have been produced as the outer layer of any lumps in the powder formed impermeable shells once wetted. When these shells cured, an uncured region could have remained within.

The mixture was soaked for ten minutes, to allow the powder to saturate, after which time the mixture was stirred manually with a spatula. The results obtained by manual stirring were superior to those produced by an electric mixer which was unable to remove material that bonded to the sides of the mixing vessel. Another disadvantage with an electric mixer was that the speed at which it agitated the mixture generated a small amount of heat that tended to reduce the setting time. After approximately two minutes of mixing, when the mortar achieved the consistency of thick cream, the mixture was poured slowly into the clean

rubber moulds. During the pouring process the mixture formed layers that, if allowed to remain, would have trapped air bubbles. It was necessary, therefore, continuously to move the pouring vessel to reduce the possibility of layering. During pouring, the moulds were lightly tapped to expel any air bubbles present in the mixture. These bubbles were removed by lancing them with a pointer. If the moulds had been vibrated excessively, vibro-compaction could have occurred causing the water to bleed out of the mixture and form a thin layer at the top. Excessive vibration of the cement/sand mixture could also have caused the denser sand particles to settle out of the mixture. These undesirable situations, if allowed to occur, would have introduced heterogeneous regions into the blocks.

After 30 minutes, when the mixture had reached an initial set, the solid blocks of mortar were stripped from the moulds and the blocks allowed to cure as shown in Figure 4.9. After 12 hours, the blocks were transferred to a thermostatically controlled ventilated drying oven maintained at a constant temperature of 40°C. Indraratna [70] reported that at temperatures greater than about 50°C the bonded water of hydration tends to dissociate from the calcium sulphate dihydrates. This results in the disintegration of the complex monoclinic crystal structure of the dihydrate, thereby adversely affecting the strength and deformation properties of the material.

The curing process occurred quickly. As the strength of specimens composed of gypsum based materials is influenced by the presence of free water, it was important to ensure that sufficient additional time was provided to remove as much excess liquid as possible. In order to determine this time, drying tests were conducted on cured blocks. These tests involved recording the mass of a specimen (100mm long x 42mm diameter) at different times throughout the drying process. The minimum drying time was considered to be that time at which the mass of the specimen approached within 2% of the asymptote of the dry mass. The plot of the tests, shown in Figure 4.10, shows that the blocks could be considered dry after a minimum of 20 hours. On the basis of results obtained by other researchers and owing to the increased humidity that occurred in the oven when a large number of blocks

were being dried concurrently, the blocks were left to cure in the oven for a minimum of seven days.

4.5. Preparation of Infill Material.

The infill material, Celite, was prepared by soaking a quantity of the material in sufficient distilled water to ensure that the suspension had the consistency of cream. The exact quantity of water added was not of critical importance because Celite is an inert material. The solution was then poured onto every surface of a block that would become a discontinuity to a thickness of approximately 0.5mm. Cured gypsum mortar has an affinity for water and so most of the water in the Celite solution was rapidly absorbed by the mortar, thereby enabling the Celite to be screeded to produce a planar surface. The specimen was then placed in the oven for at least two days to fully dry.

4.6. Assembly of Specimens.

After curing, the individual blocks for the discontinuous specimens were placed into a (300mm long x 150mm diameter) paper jacket in their respective positions to form a cylinder. Care was taken to ensure that the individual blocks fitted closely together. Any misalignment could result in stress concentrations and inhibit sliding. The jacket was used for two reasons. Firstly, it provided lateral confinement to the specimen so it could be transferred into the triaxial cell for testing. Secondly, the deformation of the paper provided a permanent record of any block displacements that occurred during triaxial testing. An alternative to using a plain paper jacket would have been to construct one from waxed paper similar to that used in borehole impression devices. Waxed paper has the advantage over plain paper of being able to record even finer detail.

Jaeger [79] obtained satisfactory results from a series of triaxial tests in which each specimen was encased in a thin copper jacket. He determined that the jacket provided approximately 480kPa of confining pressure to the specimen. The paper jacket used for a 150mm diameter

cylinder was 0.25mm thick and had a tensile strength of 59MPa that would have imposed an additional confining pressure of approximately 299kPa $\left(\frac{2 \times 59\times10^{6} \times 0.25\times10^{-3}}{150\times10^{-3}}\right)$ on the specimen. In order to prevent this additional confining pressure from influencing the results, the jacket was joined with Sellotape. This adhesive on the tape had a low tensile strength and, once this strength was realised, the cylinder provided negligible additional constraint to the specimen.

A total of 157 discontinuous specimens, containing clean discontinuities and discontinuities containing a Celite infill were prepared in the manner described. Even though each block of a particular shape was formed from the same mould, small differences in the preparation procedure and the elastic nature of the rubber moulds used, would have resulted in each specimen being unique. These differences between specimens of the same geometry might not have been observable to the eye, but precise measurement of the overall dimensions of each block and the contour of the faces of a block, would have revealed geometric dissimilitude. Care was taken when the blocks were placed into the paper cylinder to ensure that all blocks fitted closely together and that the discontinuities were planar. With up to 20 blocks in a specimen, any irregularity in the position or movement of an individual block affected every other block which in turn produced unique specimens.

The slight variation between seemingly identical specimens meant that the initial conditions that applied to each laboratory test were dissimilar. A slight variation in initial conditions is one reason why seemingly identical systems behave in a random manner. Cundall [41], when discussing the effect of the initial conditions on the behaviour of a discontinuous rock mass, presented the example shown in Figure 4.11. This figure represents a small part of a much larger discontinuous mass. Assume that the upper block is forced to move down relative to the lower block. Whether the upper block slides to the left or to the right of the lower block will ultimately be decided at the microscopic level at the point of intersection of the two blocks. The cylindrical specimens contained many such pairs of blocks and the behaviour of the specimens would have been influenced by the microscopic irregularities of any one pair.

The behaviour of the specimens would also have been influenced by the presence of minute heterogeneities in the material forming the individual blocks. If these heterogeneities resulted in stress concentrations, the region immediately surrounding the heterogeneity might have suffered larger strains than the bulk of the material. These excess strains might have resulted in further stress concentrations that could have caused further strains and so on. Eventually the deformation behaviour of the specimen would have been influenced to a significant degree by the initial microscopic heterogeneity.

The combined influences of the heterogeneities in the individual blocks that formed the specimens and the subtle differences in the placement of the blocks were likely to result in the specimens behaving in an apparently random manner. The discontinuous specimens were intended to simulate, albeit in a simplified manner, the behaviour of a rock mass under triaxial conditions. Both the specimen and a rock mass are influenced by variability in the initial conditions. It would, therefore, appear pointless to have attempted to obtain repeatability between tests. Instead, care was taken to reduce the variability between the specimens, where possible, in the hope that the range of behaviour observed during the experimental programme would have been analogous to that seen in rock masses.

4.7. Summary.

A set of moulds was constructed from which individual blocks were formed and assembled into discontinuous specimens. Two materials, one composed of gypsum cement and the other, a 50/50 combination of gypsum cement and sand, were selected as suitable material from which to manufacture specimens. In order to investigate the properties of the modelling material, to ensure that it satisfied the requirements for similitude with natural rock and to enable the characteristics of the discontinuous specimens to be tested under triaxial conditions, suitable test equipment was developed as the next stage of the research.

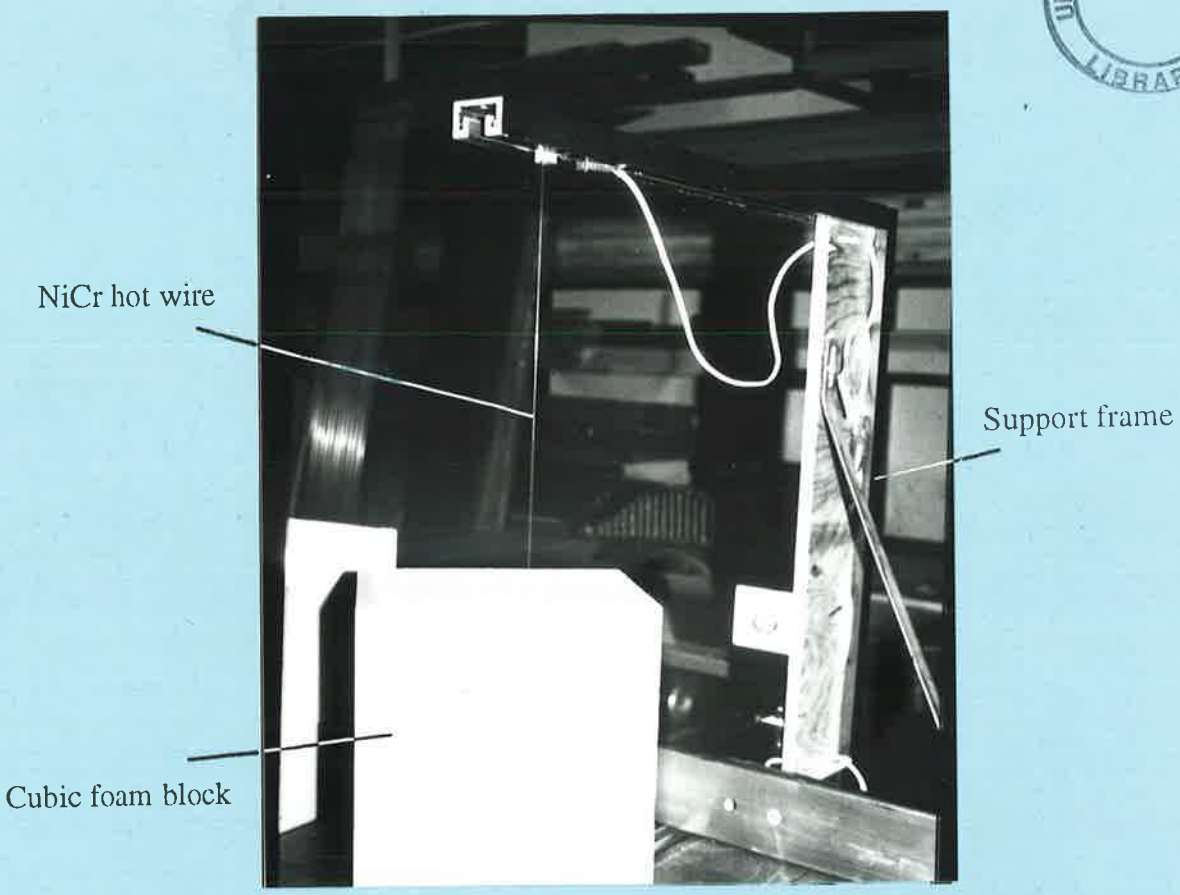

Figure 4.1. Cubic block of foam in hot wire cutting apparatus

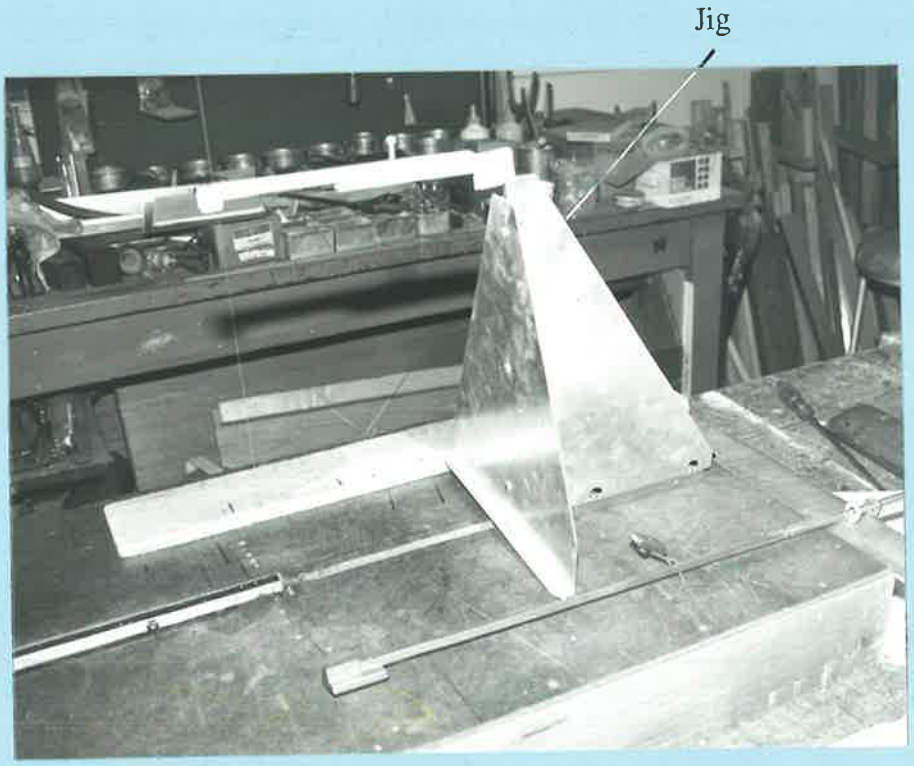

Figure 4.2. Pressed metal jig used to hold foam block so it can be cut into a cylinder.

Figure 4.3. Individual foam blocks assembled into a cylinder.

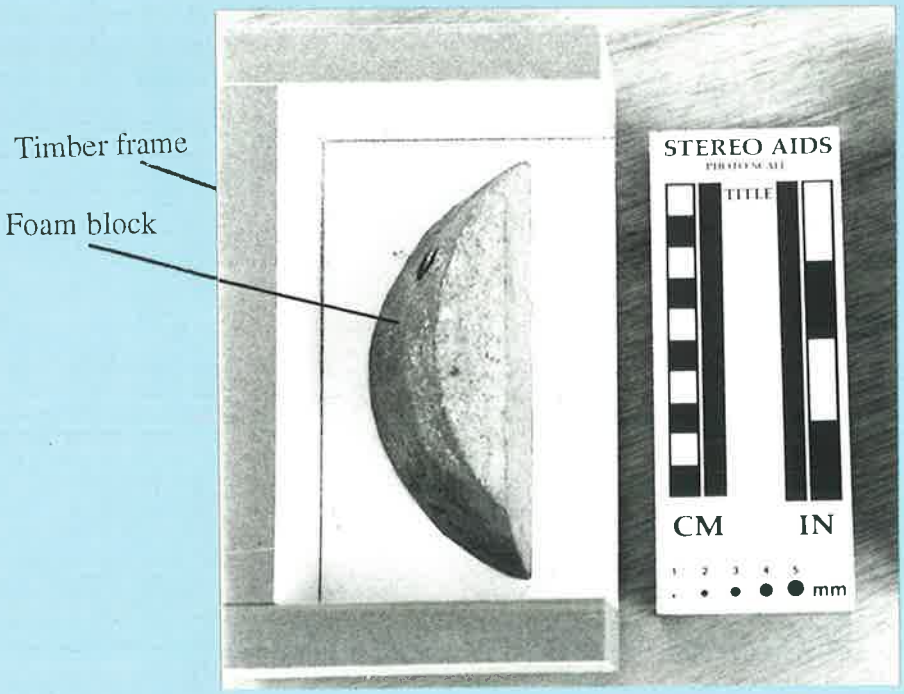

Figure 4.4. Timber frame being assembled around foam block to retain liquid rubber.

Figure 4.5. Vacuum pump used to de-aerate liquid rubber mixture.

Figure 4.6. Cured rubber moulds ready to accept modelling material.

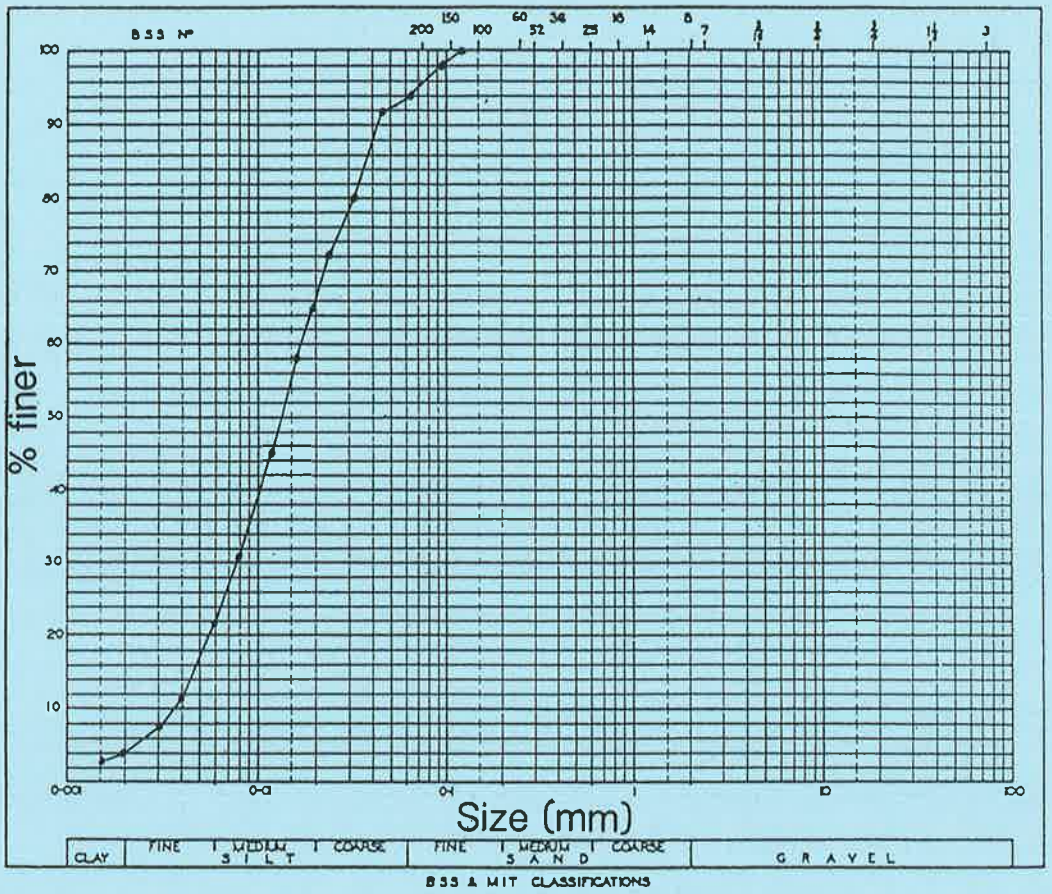

Figure 4.7. Grading Curve for Celite.

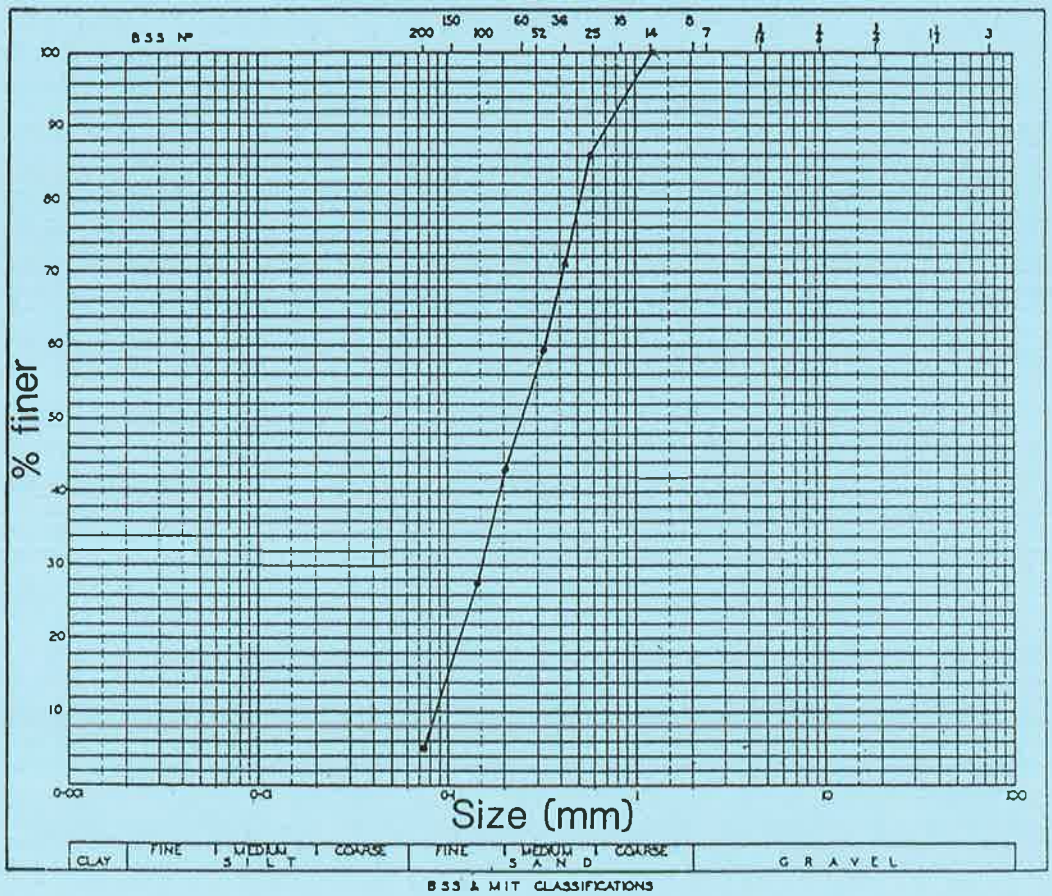

Figure 4.8. Grading Curve for Sand.

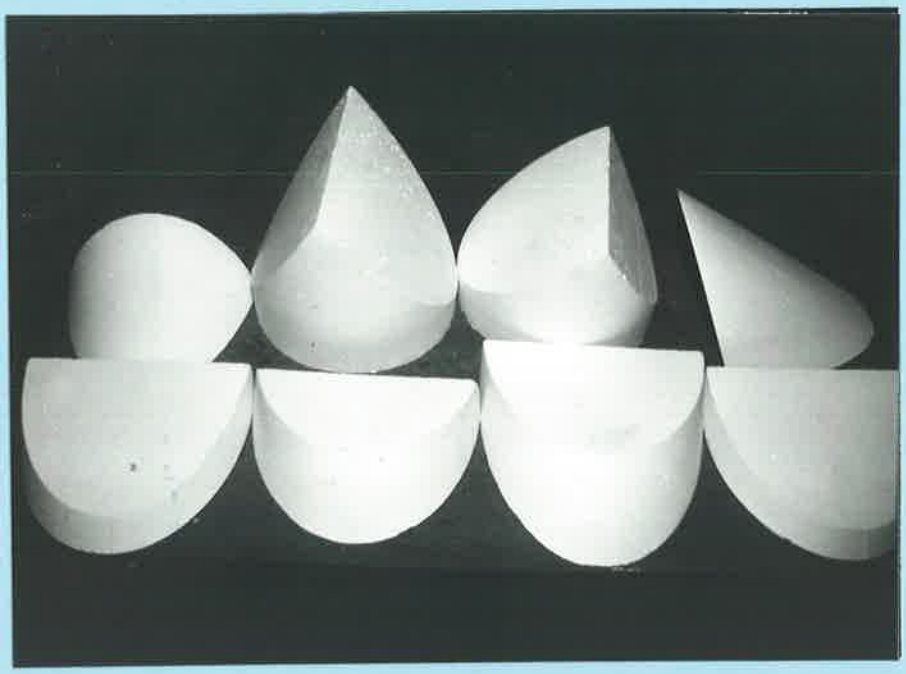

Figure 4.9. Cured blocks of modelling material after having been stripped from the rubber moulds.

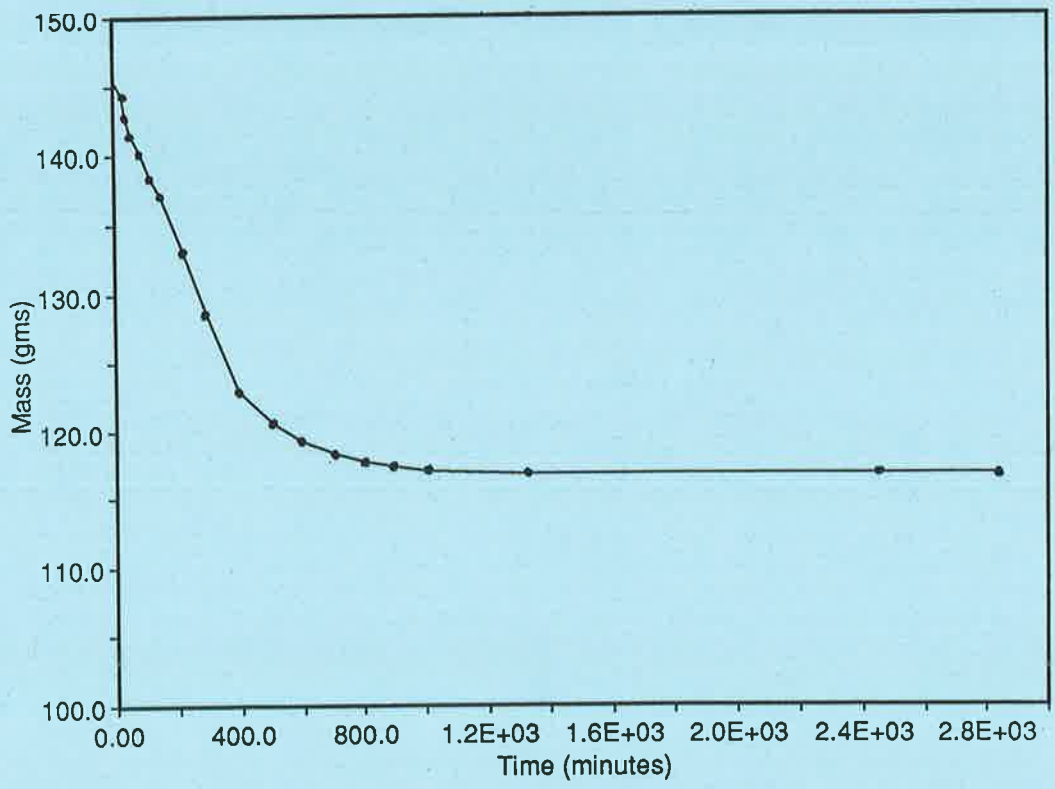

Figure 4.10. Plot of mass versus drying time for a small specimen drying at a constant 40°C.

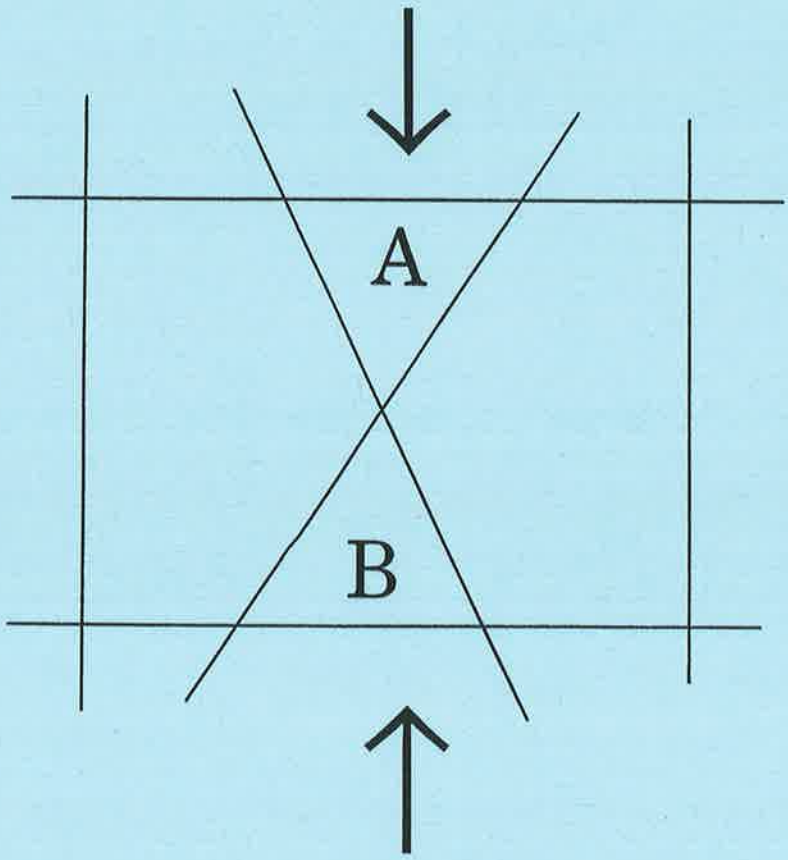

Figure 4.11. A chaotic system (after Cundall [41]).

Chapter 5.
Test Equipment.

Chapter 5. Test Equipment.

5.1. Introduction.

This chapter details the equipment developed and used in order to determine the response of the intact material and the discontinuous specimens when they were subjected to various stress conditions. The original nature of the research, in subjecting 150mm diameter cylindrical discontinuous specimens comprised of distinct blocks to triaxial stress conditions, meant that a substantial amount of work was required in order to select and develop suitable equipment and establish test procedures.

5.2. Loading Frame.

Two loading frames were used in the course of this study, a 5000MN Amsler and a 3000kN Seidner. The physical dimensions of the Seidner loading frame and compression platens were smaller than those of the Amsler and so the Seidner loading frame was more convenient to use.

The axial force on the triaxial cell used for all triaxial tests on 150mm diameter discontinuous specimens was provided by the Amsler loading frame driven from the console of a pendulum dynamometer. The frame consisted primarily of a high pressure hydraulic cylinder constructed beneath the floor, which supported the lower compression platen and an upper platen, supported by an electrically driven crosshead, that moved along a threaded column. The platens were supported on spherical seats that were fixed to remain parallel.

An electrically driven oil pump, within the pendulum dynamometer, provided the hydraulic pressure via an oil delivery valve to the high pressure cylinder. An increase in pressure in this cylinder caused the ram and hence the lower compression platen to rise, thereby, causing the specimen to be progressively loaded. The load on the specimen was a function of the hydraulic pressure within the cylinder and the cross sectional area of the ram. The cross sectional area of the ram was fixed and, therefore, a dial gauge on the dynamometer displayed the pressure in terms of the load on the specimen. A full bridge load cell, located beneath the lower platen, provided an analog signal to the data logger.

In order to calibrate the load cell, it was connected to the data logger which provided a stable excitation voltage. The load cell was calibrated using the load indicated on the load frame dial gauge as the reference load. As the dial gauge was regularly calibrated to conform to NATA[1] specifications it was considered suitably accurate. The calibration was carried out by applying a load to a steel, dummy specimen and noting the load cell output voltage indicated on the data logger. The results of this calibration, shown in Figure 5.1, indicated that the force versus voltage characteristics of the load cell could be described by the linear relation,

$$F = 0.829 \times V + 6.572 \qquad (5.1)$$

where V is the output voltage (mV) from the load cell and F is the axial force (kN) applied to the load cell.

The load on a test specimen was released by closing the delivery valve and opening a bleed off valve thereby causing the oil to be forced from the cylinder back to the holding tank in the dynamometer by the weight of the ram and by the elastic strain energy stored within the specimen and the load frame.

---

[1] National Association of Testing Authorities

The Seidner loading frame provided the axial force on the 42mm diameter intact specimens specimens used in the triaxial and the uniaxial compression tests. This frame was physically smaller than the Amsler and more suited to testing specimens of smaller overall dimensions. The frame primarily consisted of four rigid columns that supported the upper and lower compression platens. For this project, the upper platen was fixed so that it remained parallel to the lower platen. The hydraulic pressure was generated by an electric multi-piston pump that was immersed in the oil reservoir. An oil delivery valve operated by a hand wheel regulated the flow of oil from the pump to a hydraulic cylinder. This cylinder contained the ram upon which the lower compression platen was fixed.

The load on the specimen was monitored by a full bridge load cell and displayed as a digital readout on the control panel. The panel included an integrator that enabled the loading rate on the specimen to be calculated and displayed as a percentage of the full scale deflection of the load frame controller. This facility was valuable as it ensured that the loading rate on the specimens was uniform and kept within the limits recommended by the ISRM [74]. The recommended loading rate for a specimen undergoing triaxial compression is 1.0MPa/s which is equivalent to a rate of 83.1kN/min on a 42mm diameter specimen. The full scale deflection (FSD) of the loading frame controller was set at 1500kN and therefore, the specimens were loaded at a rate of 5.5% $\left(\frac{83.1 \times 10^3 \times 100}{1500 \times 10^3}\right)$ of FSD/min.

5.3. The Triaxial Cell.

The stress state at a point can be defined by the three mutually independent principal stresses, σ_1, σ_2, σ_3, acting at the point. In a rock mass these stresses vary in magnitude and direction. In Section 2.4.2 the principle of modelling these triaxial test conditions using axi-symmetrical conditions, ie. $\sigma_1 \geq \sigma_2 = \sigma_3$, on a cylindrical specimen was described. Such a test is traditionally referred to as a triaxial test. In this study, triaxial tests on specimens of intact material and discontinuous specimens were conducted in a Hoek cell.

A 150mm diameter Hoek cell[2] (Hoek and Franklin [67]) was purchased for use in this research. The cell is shown in Figure 5.2 set up in the Amsler load frame. A Hoek cell was selected because it had design, practicality and price advantages over the alternative styles of triaxial cells. The design of the Hoek cell is in contrast to the more traditional rock testing cells (Elliott [51]) which shall be referred to as 'high pressure' cells in this discussion. The name 'high pressure' is used, not because such a cell is capable of withstanding higher pressures than the Hoek cell but because the 'high pressure' cell was designed as a high pressure version of the standard soils triaxial cell. In the 'high pressure' cell, a specimen is totally enclosed in a thin protective membrane similar to that used for soils testing and is placed into the cell that is subsequently totally sealed. The 'high pressure' cell is then completely filled with hydraulic fluid prior to a test. At the completion of the test, the cell must be totally drained of fluid before the specimen can be removed and inspected. The process of assembling and dismantling the 'high pressure' cell and transferring fluid into and out it invariably leads to contamination of the fluid, the seals and the surrounding environment and requires a significant amount of time.

A Hoek cell consists of a steel cylinder with threaded end caps as shown in Figure 5.3. A confining pressure is applied to the specimen using hydraulic fluid that is retained within the annular space between the outer body of the cell and a flexible Adiprene urethane rubber membrane. In a 'high pressure' cell, a lengthy procedure is required to prepare the cell for testing. In a Hoek cell it is possible to load a specimen into the cell, conduct the test and remove the specimen without having to break the seal or drain the hydraulic fluid. The membrane only needs to be removed if it is damaged during testing. A simple method was developed in this study for replacing a damaged membrane as the method recommended by the manufacturer was unsuitable for a cell of such a mass (290 kg without the spherical seats). This procedure is presented in Appendix B. During a test there is no need to be concerned about the integrity of the membrane as any rupture is immediately obvious by a drop in cell pressure and the sight of fluid leaking from the cell. This result is in contrast to a

---

[2] Manufactured by Robertson Research, Deganwy, Conwy, Gwynedd LL31 9PX UK

test conducted with a 'high pressure' cell in which the operator is generally unaware if the thin membrane is damaged and the specimen contaminated with fluid.

In the Hoek cell, the axial force is applied to the specimen through opposing, hardened steel, spherically seated pistons. The spherical seats are designed to compensate for slight angularity between the ends of the specimen and then lock together while loading continues. It should be noted that the use of spherical seats does not substitute for correctly preparing the ends of the specimen as discussed in the ISRM recommendations [74]. In a Hoek cell it is easy to apply the stress state $\sigma_1 = \sigma_2 > \sigma_3$, which places a cylindrical specimen into tension. Alternatively, in the 'high pressure' cell it would be necessary to use fixed end platens and only low tensile stresses could be applied to the specimen if this same stress state were required.

5.3.1. Pressure Distribution Calibration Test.

It is important when using a Hoek cell to ensure that the specimen is placed at the correct height within the cell in order to ensure a uniform radial stress distribution on the specimen. This stress distribution was achieved using a rigid support stand, shown in Figure 5.2. The height of this stand ensured that the specimen sat upon the lower piston at the correct height with respect to the membrane.

As the thickness of a membrane around a triaxial test specimen increases, the difference between the radial stress on the outer surface of the membrane and that applied to the specimen also increases. The rubber membrane used in the Hoek cell is 3mm thick which is significantly thicker than the membranes used in either a triaxial cell for soil or a 'high pressure' cell. It was, therefore, considered prudent to conduct tests to determine if a radial stress differential existed across the membrane. In order to do this, two plates, 20 x 270mm in diameter, were fabricated and secured over either end of the cell. The top plate contained a tapped hole through which the inner volume of the membrane was filled with water. A large rubber O-ring seated within each plate ensured that no water was lost through leakage. A calibrated pressure transducer monitored the pore pressure response of the water inside the

membrane to changes in pressure within the annulus. The pressure in the annulus was monitored by a second transducer incorporated into the cell pressure hydraulic system. This transducer and the hydraulic system will be discussed in detail in Section 5.5. The annulus was slowly pressurised with a hydraulic hand pump up to 1000kPa and the pressure on each side of the membrane was constantly tabulated. The results of this test, plotted in Figure 5.4, showed that, for the range of pressures investigated, the pressure on the inside of the membrane could be defined in terms of the pressure in the annulus by the equation,

$$\sigma_3 = 0.99\ \sigma_{3(sys)} - 8.43 \qquad (5.2)$$

where σ_3 is the confining pressure on the specimen (kPa) and
σ_{sys} is the pressure in the annulus of the triaxial cell (kPa).

The pressure differential across the membrane was allowed for when the test data was processed subsequent to each test.

5.3.2. Specimen Transfer Frame.

A major advantage of a Hoek cell for this project, over a 'high pressure' cell, was the ease with which specimens could be placed into it and removed from it. The physical dimensions and mass of the cell made this process far more difficult than if a smaller Hoek cell had been used. This problem was addressed by developing a specimen transfer frame. The frame comprised a 15mm thick, hardened steel plate placed between the specimen and the lower piston. A 1mm deep x 16mm wide rectangular channel was milled into the lower face of the plate and each surface of the plate was ground and polished.

A stainless steel strap, having a 680MPa tensile strength, passed between the upper piston and the cell cap, down the side of the specimen, along the channel and back up the opposite side of the specimen. The dimensions of the rectangular channel in the base matched those of the strap to ensure that, when the combination was subjected to an axial load, it had no effect on the complex system of shear and normal stresses that developed between the base of the specimen and the upper surface of the plate. The slight differences in the elastic

properties of the plate and the strap meant that there was a possibility of the plate deforming under load. In order to investigate this possibility, a finite element analysis was conducted on the plate/strap combination. Two limiting cases were studied because of the difficulties involved with modelling the effect of friction between the plate and the specimen. The first of these cases assumed that there was no friction between the surfaces by placing the nodes on the upper surface of the plate on rollers to allow movement parallel to each surface. The second case assumed that both surfaces were bonded together by fixing the nodes on the upper surface of the plate. The actual case was considered to be intermediate between these two extremes. The objective of the analysis was to determine the normal stress distribution acting on the specimen as a result of a uniformly distributed load (modelled as a set of equivalent nodal forces) being applied to the base of the plate. The results of this analysis indicated that the strap/channel combination produced no significant stress variations from the uniform stress distribution acting on the specimen.

At the completion of a test, the upper spherical seat and piston were removed and a second plate was placed on the upper surface of the specimen. Two small clamps attached to this upper plate were used to grip the strap. An eye bolt threaded into the plate was used to lift the specimen from the cell with a portable crane.

5.4. Specimen Axial Deformation Monitoring.

One disadvantage of the Hoek cell, compared to a 'high pressure' cell, is that it is difficult to attach transducers to specimens inside the cell to monitor the axial deformation of the specimen. The method suggested by the manufacturer of the Hoek cell, for monitoring strains in intact specimens, is to use electrical resistance strain gauges. While it was not a priority to measure these strains for this research, consideration was briefly given to the problem.

The method recommended by the manufacturer for routing the wires attached to the strain gauges through a small channel in the upper piston is unsuccessful generally because the

wires from the strain gauges are often cut at the piston/cell body interface. An alternative method for routing the wires was, therefore, investigated that involved routing the strain gauge lead wires through a small covered tube cut into the side of the upper piston. This method was more successful except that in some tests the lead wires were cut at the piston/specimen interface.

Even if the problem of severed lead wires could be eliminated, there are still some fundamental problems with the use of strain gauges on rock. A strain gauge can only provide accurate readings if it is secured firmly to the surface of the material. Rock often tends to be porous, rough or powdery thereby providing an ineffective base for a strain gauge. Yielding of intact rock may be accompanied with the onset of micro-cracks. These cracks can result in stress concentrations at the tips of the cracks and lead to the development of localised straining. If this result occurs, the localised straining can cause a strain gauge to inaccurately monitor total axial strain of the intact material. As compression continues and the crack extends to the boundaries of the specimen, subsequent axial deformation of the specimen may be due to shear deformation occurring along the crack rather than through axial deformation of the intact material.

The problem of monitoring the axial deformation of an intact or a discontinuous specimen in a 'high pressure' cell is accomplished by monitoring the relative axial displacement of the upper piston with respect to the lower piston. LVDTs, placed adjacent to the specimen within the cell, are used for this purpose. The design of the Hoek cell does not, however, allow LVDTs to be placed adjacent to the specimen. This problem was overcome by monitoring, instead, the relative displacement of the upper piston with respect to the upper cap of the cell. This procedure involved using up to four LVDTs mounted in a bracket, shown in Figure 5.1, orientated parallel to the major axis of the piston. It was assumed that the LVDTs provided a reasonable estimate of the axial displacement of the specimen because of the large difference between the stiffness of the piston and that of the specimen.

When monitoring the axial deformation of discontinuous specimens in triaxial compression,

Brown [33], Einstein and Hirschfeld [50], Jaeger [79], Reik and Zacas [125] and Yoshinaka and Yamabe [162], found that, on average, discontinuous specimens tended to deform plastically after about 5% axial deformation. In relation to the present study on 300mm long specimens, this strain equates to an axial deformation of 15mm. The LVDTs used in the present study had a stroke length of 20mm that was, therefore, considered to be adequate.

The type of LVDTs used consist of a conductive carbon film bonded to a flexible substrate within a solid housing. The wiper was of the form of a multi-finger contact consisting of a group of fine contact springs that provided a group of individual contacts. This arrangement minimised friction and ensured linearity in the voltage versus displacement characteristics. In order to establish these characteristics for the particular input voltage used, a drum micrometer mounted in a jig was used to apply an axial displacement to each LVDT. The output voltage was measured with a digital multi-meter. A typical calibration curve from one of the LVDTs is shown in Figure 5.5. For this particular LVDT, the linear equation fitted to the test data, using a standard regression method, was:

$$\delta_a = 3168 \times 10^{-6} V - 0.51 \qquad (5.3)$$

where δ_a is the axial displacement of the LVDT (mm) and
V is the output voltage (mV) for a 10V excitation.

5.5. Specimen Volumetric Deformation Monitoring.

The change in the volume of a discontinuous specimen with axial deformation can be used to indicate the mode of deformation, that is, whether deformation is occurring as a result of compression of the intact material or sliding along discontinuities. In a triaxial test, where it is generally impossible to observe the deformation of a specimen, the ratio can provide a 'set of eyes' for the operator.

The change in the volume of a discontinuous specimen is a function of the axial deformation and the circumferential deformation of the specimen. For small values of axial deformation,

prior to any shear deformations occurring along discontinuities, the volumetric deformation ratio, Δ_v, can be estimated by the equation:

$$\Delta_v = \frac{\delta_a}{L_i} + \frac{2\delta_\theta}{L_\theta} \qquad (5.4)$$

where L_i is the original axial length of the specimen,
L_θ is the original circumferential length of the specimen and
δ_θ is the change in the circumferential length of the specimen.

When a discontinuous specimen is subjected to axial deformation, the individual blocks that make up the specimen displace relative to each other in a complex manner. The task of measuring anything other than an average value for δ_θ is, therefore, difficult. In this study, a method of estimating δ_θ was addressed by noting that strain compatibility existed between the cell rubber membrane and the specimen as long as the cell pressure was greater than ≈100kPa. Under these conditions, the membrane/specimen combination behaved as a composite material. The average value of δ_θ around a particular circumference of the specimen was, therefore, related to the circumferential strain at the same height on the annular surface of the membrane. In a 'high-pressure' type cell it would have been possible to incorporate 'dog collar' type extensometers into the cell in order to monitor this strain. Such a device cannot be used in a Hoek cell because of the limited space in the annulus.

The use of four, high elongation, strain gauges wired in series and placed equi-distant around the external surface of the membrane was investigated as a means for monitoring the average circumferential strain in the membrane. The gauges were found to bond to the membrane successfully with an epoxy glue. The strain gauge wires were joined to two thin, lacquer coated wires that passed out of the cell through a bushing. Lacquer coated wires were found to provide excellent adhesion to the high strength, metal filled, epoxy resin used to seal the bushing. The bushing was screwed into a tee-piece connected externally to the hydraulic fluid outlet of the cell. The wires that passed out of the bushing were connected to a bridge circuit with an appropriate balancing resistor. During initial trials this method of monitoring δ_θ appeared promising.

The major problems with the apparatus and the theory were, however,

(1) The high elongation strain gauges were more suitable for use on plastics than the Adiprene rubber used for the membrane. Stress concentrations therefore occurred in the area of the strain gauges which resulted in the strain gauges monitoring strain that was not equivalent to the average strain around the circumference of the membrane.

(2) As axial deformation of the specimen occurred and individual blocks moved relative to each other, voids formed within the specimen. Voids also resulted from the inflexible membrane being forced away from certain blocks by other slipping blocks. Equation 5.4 made no allowance for the influence of these voids on the volumetric deformation of the specimen.

(3) Equation 5.4 assumes that the cross sectional area of a cylindrical specimen remains circular. While this assumption may be satisfactory for specimens intersected by a large number of discontinuities with a wide range of dip directions, it becomes less satisfactory as the number of discontinuities decreases.

Problem (1) might have been solved if equipment suitable for monitoring large strains could have been obtained. Problems (2) and (3), however, tended to invalidate the use of Equation 5.4 with discontinuous specimens. Alternative techniques for monitoring changes in the volume of the specimens during axial deformation were therefore investigated.

5.6. Confining Pressure Control System.

The simplest and cheapest means of applying cell pressure in the triaxial cell is with a single stage hand pump. In this case, pressure fluctuations are controlled by manual manipulation of a bleed-off valve. This system is generally unsatisfactory because,

(1) it is difficult to ensure repeatability of cell pressure,

(2) two operators are required for tests, one operator to maintain the system pressure while the other operates the loading frame,

(3) it is difficult to maintain system pressure during specimen dilation or contraction within the limits specified in the ISRM guidelines [74],

(4) manual operation of the bleed off valve and the hydraulic pump produces unacceptable cyclic pressure fluctuations and

(5) the volume of fluid added to or subtracted from the cell in order to achieve constant pressure conditions cannot be accurately monitored.

These problems with manual control of the cell pressure highlighted the necessity for researchers to develop automated pressure control equipment. Wawersik [152] developed a system for automatically controlling pressure based on a manual system developed by Crouch [38]. The main pressure control components of this apparatus consisted of a motor driven servo controlled linear displacement pump and a differential pressure gauge for feedback control. This apparatus allowed volume changes in the hydraulic fluid to be monitored to within 6.5mm^3 and system pressure controlled to ±20.7kPa. Better pressure control was achieved by utilising electronic control systems such as those used by Elliott [51]. This system enabled the pressure in the hydraulic system to be monitored continuously by the electronic controller. If an error existed between the existing and the required pressure, the controller switched on an electric motor that either advanced or retracted a pump accordingly. Elliott was able to control the pressure in the hydraulic system to within ±19.5kPa with this equipment and monitor changes in volume to within 4mm^3. If triaxial tests were being conducted with pressure control equipment such as that used by Crouch or Elliott, at low confining pressures, ie. $\sigma_3 < 300$kPa, the system pressure could be in error by greater than 6.5%. This error exceeds the limits suggested in the ISRM guidelines [74].

Baleshta and Dusseault [6] found that, by using a micro-processor based controller acting upon an 'intensifier-accumulator', pressure could be maintained within 0.1% of that required up to a maximum working pressure of 70MPa. The system, developed by Baleshta and Dusseault, was particularly suitable for applications in which small changes in specimen volume occurred over a long period. An internal volume of 48cc meant, however, that the system was limited in its suitability as a pressure control device for applications involving rapid large changes in specimen volume as may occur when discontinuous specimens are subjected to triaxial test conditions.

The following section discusses details of a micro-processor controlled linear displacement pump developed during the present research. The equipment enabled the pressure in a triaxial cell to be regulated during a test to within 1% of that required and specimen volume changes to be accurately monitored. Robust construction and straightforward controls ensured that the pump was reliable and simple to operate and the use of micro-technology and readily available components ensured that the pump was fairly inexpensive to construct.

The basic component of the linear displacement pump was a cylindrical pressure vessel in which a plunger advanced or retracted along the bore, thereby removing or adding a volume of hydraulic fluid to the system. The movement of the plunger served either to maintain an existing pressure, fluctuating as a result of volume changes occurring in the hydraulic system, or to increase the pressure to a required pressure.

In order for the membrane in the triaxial cell to produce a competent seal against the cell cap, there needed to be a pressure slightly greater than atmospheric in the cell annulus. Between tests, when no pressure was applied to the hydraulic system, a small volume of hydraulic fluid occasionally leaked passed this seal. If the linear displacement pump was to be used to replace this leaked volume, the pressure vessel would have required a larger internal volume than if the pump were to have been used purely to ramp the system to the desired pressure and then maintain the pressure. In order to minimise the dimensions of the pressure vessel, the linear displacement pump was designed to operate as part of a dual system. This system used a proprietary electric hydraulic reciprocating pump to fill the system rapidly. Once the initial fill was achieved, the linear displacement pump was used to ramp up to and maintain the required pressure. Details of the hydraulic circuit are shown in Figure 5.6 and the linear displacement pump in Figure 5.7. The major components of the hydraulic circuit were:

(1) the triaxial cell,

(2) the reciprocating and the linear displacement pump

(3) a safety pressure relief valve to ensure that the hydraulic circuit could not be pressurised by the reciprocating pump beyond the design pressure of the linear displacement pump and

(4) a pressure transducer and a Bourdon tube gauge.

The major components of the linear displacement pump were:

(1) the pressure vessel containing the hydraulic fluid,

(2) the power tube and power screw which caused the cup piston to linearly displace and

(3) the motor/gearbox and flexible coupling combination providing the driving force.

The linear displacement pump pressure vessel consisted of a steel cylinder and a piston. A 28mm cylinder bore was selected to provide an internal volume of 155cc. This volume was sufficiently large to accommodate a major proportion of the volumetric deformation of a 150mm diameter discontinuous specimen undergoing triaxial testing. The bore diameter was selected by considering the influence that bore size had on the axial load carried by the components and the torque available from the motor. The maximum operating pressure of the pump was 20MPa.

A cup seal was attached to the piston to ensure a high pressure seal. On the high pressure side of the piston, the cylinder was sealed in the mounting block with an O-ring. High strength tubing was used to connect the cylinder mounting block to the hose connection block. 'Swagelock' fittings were used for all tubing connections as these fittings were found previously to provide quality seals. 'Swagelock' fittings are connected onto a tube with an axial, rather than a rotary motion, and therefore no torque is applied to the tube. This motion reduced the initial strain in the tube that could otherwise have led to premature failure. 'Enerpac' quick release, high flow couplings were used to connect the external pump and the triaxial cell to the linear pump. These couplings allowed the hoses to be easily connected and disconnected and provided a leak proof seal when they were not in use. The couplings were also designed to minimise flow restriction when they were in use. It was considered important that pressure head losses from the cylinder to the triaxial cell, due to back pressure, were reduced as much as possible. The hoses used were composed of heavy duty rubber reinforced with two layers of braided steel webbing. The hoses, therefore, remained flexible and strong up to a rated working pressure of 70MPa, far in excess of that required. During

this research, expansion of the internal volume of the hoses as a result of an increase in pressure was minimal because the maximum pressure to which the hoses were subjected to was only 2% of the rated working pressure of the hoses.

The power screw connected to the piston in the cylinder was threaded through a nut fixed to the cylinder end of the power tube. Phosphor bronze was used for the nut primarily to reduce the friction between the power screw and the nut and to ensure that the nut would be sacrificed for the power screw. The power screw linearly translated within the bore of the rotating nut by the rotation of the power tube. This tube was supported at both ends and rotated freely on roller bearings. The thrust exerted axially along the power screw was resisted by a thrust bearing. The power tube was connected to the shaft of an in-line reduction gearbox via a flexible coupling. The gearbox reduced the maximum output speed of an electric motor by a factor of 10 while providing a constant torque under varying load. Tests conducted on the motor/gearbox combination by Russack [128] suggested that the manufacturer's quoted torque value was conservative, ensuring that the motor would readily supply the pressure.

5.6.1. Specimen Volume Change Measurement.

During a triaxial test a specimen is compressed axially as the upper platen of the triaxial cell is displaced into the body of the triaxial cell. At high strain levels these effects cause the specimen to volumetrically dilate. The increase in the total volume, due to the upper platen advancing into the cell, combined with the dilation of the specimen, causes the pressure in the hydraulic system to increase. In order for the confining pressure to be maintained constant, the volume of the hydraulic system must be increased by an amount equal to the volume change within the cell. Therefore, by determining the change in the volume of the hydraulic system, V_p, and the change in the volume of the upper piston within the cell, it was possible to determine the change in the volume of the specimen. Allowances did, however, have to be made for any hydraulic fluid leaked from the cell during a test. As the confining pressure was maintained constant during a test, elastic volume changes in the hydraulic

system were insignificant and could be ignored. The change in the volume of the specimen, δ_v, was determined by

$$\delta_v = V_l - V_c - V_p \qquad (5.5)$$

where V_l is the volume of fluid leaked from the system,

V_c is the volume of penetration of the triaxial cell piston into the cell which is equivalent to δ_a x the cross sectional area of the piston and

V_p is the volume of fluid withdrawn from or added to the system by the pump.

The volume of fluid added to, or withdrawn from, the linear displacement pump was a function of the linear displacement of the piston within the cylinder. The linear piston displacement was a function of the angular displacement of the gear box shaft. The gearbox shaft contained an in-line spur gear that was coupled to a 10 turn rotary potentiometer via a driven gear producing a 5:1 ratio between the gearbox shaft and the potentiometer. The linear displacement of the pump piston was therefore directly related to the angular displacement of the potentiometer wiper and, hence, to the output voltage of the potentiometer. The output voltage from the potentiometer was monitored in parallel by the data logger and, via an isolating amplifier, by a moving coil meter. This meter produced a visual indication of the piston position at any time as a percentage of the full travel of the piston within the cylinder.

The potentiometer was calibrated to establish the output voltage versus piston displacement characteristics for the input voltage used. A 10V supply was connected across the potentiometer and the linear displacement pump was advanced in one revolution cycles (Note: One cycle was equivalent to a piston displacement of 5mm). The output voltage from the potentiometer was monitored with a digital multi-meter. The calibration curve, shown in Figure 5.8, provided a calibration coefficient for the potentiometer of 0.122mm/mV. For a 1mV change in the output of the potentiometer, the 28mm diameter linear displacement pump piston, therefore, swept a volume of $75.12\text{mm}^3 \left(0.122\text{mm} \times \frac{\pi \times (28\text{mm})^2}{4}\right)$.

The accuracy with which a change in specimen volume could be monitored during a triaxial test was dependent on the minimum resolution of the data logging equipment. The particular

data logger used had a minimum resolution of 0.05mV. The minimum volume change that could be monitored was, therefore, 3.8mm^3 (75.12mm^3 x 0.05mV).

5.6.2. Calibration Tests for Hydraulic System Leakage.

In order to effectively use Equation 5.5, the volume of fluid leaked from the hydraulic system during a test had to be determined. Leakage was negligible, however, owing to the close tolerances of all seal surfaces within the hydraulic system. A small amount of leakage did occur, however, between the triaxial cell membrane and the end caps until a pressure was achieved sufficient to cause the seal to become effective. It was, therefore, considered prudent to attempt to quantify this rate of leakage.

A series of calibration tests was conducted in order to establish the relationship between the volume of hydraulic fluid leaked from the system over time and the pressure in the hydraulic system. For these tests a thick walled steel cylinder was placed in the triaxial cell. The dimensions of the cylinder were chosen using thick cylinder theory to ensure that the cylinder did not significantly deform as a result of the maximum confining pressure that would be applied during the calibration tests. All seal surfaces in the triaxial cell were cleaned to the same standard as for the test conditions. A series of five different pressures was then applied to the system with each pressure being monitored for 20 minutes. The pressure was released after each test and the system allowed to contract before the next pressure was applied.

Figure 5.9 shows the pressure versus time data obtained from the calibration tests. Allowance was made for the decrease in radial pressure transferred to the steel cylinder because of the thick rubber membrane (discussed in Section 5.3). These results show that the system pressure decreased non-linearly for approximately four minutes after which time, the pressures decreased approximately linearly with time. This non-linear behaviour is typical of that expected across the rubber membrane/cell cap interface. The rate of pressure decrease was determined as the slope of the linear region of each of these curves. Figure 5.10 shows the relationship between the rate of pressure decrease and the system pressure which can be

described by the equation:

$$\frac{d\sigma_{3(sys)}}{dt} = 6.057 \times 10^{-5}\sigma_{3(sys)} + 0.015 \qquad (5.6)$$

where $\frac{d\sigma_{3(sys)}}{dt}$ is the rate of decrease in pressure with respect to time (kPa/s) and

$\sigma_{3(sys)}$ is the pressure in the hydraulic system (kPa).

In order to relate the decrease in pressure over time to the volume leaked over that period of time, it was first necessary to determine the total volume of fluid that was required to be added to the hydraulic system in order to increase the pressure from atmospheric to a particular system pressure. This volume was influenced by:

(1) expansion in the hydraulic system,

(2) compression of the hydraulic fluid and the air in the system and

(3) leakage of hydraulic fluid from the system during the test.

It was not, however, necessary to quantify items (1) and (2) as, once a desired system pressure was achieved and maintained constant, there was no cumulative change in the value of these parameters with time during a test.

In this test, as much air as possible was removed from the system by circulating fluid with the external gear pump and by bleeding air from the top of the triaxial cell using the techniques described in Appendix B. The linear pump was then advanced rapidly and the linear displacement relating to each particular pressure achieved was recorded, thereby allowing the volume of fluid displaced to be calculated. The test was repeated a number of times to confirm the results. Figure 5.11 shows the relationship between the volume pumped and the system pressure, which can be described by the equation:

$$V_p = 146.85\ \sigma_{3(sys)}^{0.04469} \qquad (5.7)$$

where V_p is the volume of fluid pumped.

The total volume of fluid leaked from the hydraulic system during a test was determined by the following procedure:

(1) The leakage rate, $\frac{d\sigma_{3(sys)}}{dt}$, appropriate for the particular system pressure, $\sigma_{3(sys)}$ was determined from Equation 5.6.

(2) The total volume of fluid pumped from the system at a particular pressure was determined from Equation 5.7.

(3) The time elapsed since the beginning of the test was determined.

(4) The pressure, $\sigma_{3(f)}$, that the hydraulic system would have reduced to had the linear displacement pump not been maintaining the pressure, was determined with the equation,

$$\sigma_{3(f)} = \sigma_{3(sys)} - \left(t_{elapsed} \times \frac{d\sigma_{3(sys)}}{dt} \right) \qquad (5.8)$$

where $t_{elapsed}$ was the time elapsed since the start of the test (sec) and

(5) Equation 5.7 was applied to determine the volume of fluid appropriate to $\sigma_{3(f)}$.

(6) The difference in the volume of fluid determined in (2) and (5) provides an estimate of the total volume of fluid leaked from the system, V_l, during the elapsed time.

5.6.3 Design and Fabrication of Pressure Controller.

In order to control the linear displacement pump a pressure controller utilising a microprocessor was designed and fabricated. In this section the major components of this controller will be discussed. Figure 5.12 shows the block diagram of the controller circuit which can be divided into 3 parts;

(1) the pressure transducer,

(2) the micro-controller and

(3) the drive motor and power control circuits.

5.6.3.1. Pressure Transducer.

The pressure in the linear displacement pump cylinder and hence the hydraulic circuit, was monitored by an electronic pressure transducer. These transducers incorporate piezo-resistive strain gauges bonded to the diaphragm wired in a full bridge. Even though the series of triaxial tests were conducted up to a maximum pressure of only 1.5MPa, a transducer rated to 70MPa was chosen to ensure that it was capable of operating within the

capacity of the triaxial cell. The transducer was calibrated over the pressure range used in the triaxial tests.

The calibration was carried out by applying a 10V excitation voltage to the transducer and measuring the output voltage with a digital multi-meter. Pressure was applied to the transducer in stages with a dead weight tester. The results of this calibration, shown in Figure 5.13, indicated that the pressure versus voltage characteristics of the transducer could be described by the equation:

$$\sigma_{3(sys)} = 14.247V + 17.872 \qquad (5.9)$$

where $\sigma_{3(sys)}$ is the pressure acting on the transducer (kPa) and
V is the output voltage from the transducer at 10V excitation (mV).

A pressure transducer operating within the lower regions of its operating range is often susceptible to the effect of temperature fluctuations even though the balanced bridge configuration of the strain gauges on the diaphragm should provide temperature compensation. As the transducer was operated within a laboratory that was fairly insensitive to outside temperature fluctuations it was considered unlikely that the temperature of the transducer would vary significantly over the duration of the test. It was, therefore, assumed that the linear calibration curve would apply during a test and only the intercept on the pressure axis of the calibration curve, referred to as the transfer function, would vary between tests. The intercept was, therefore, checked before the start of each test by referring to the Bourdon tube pressure gauge as this gauge was found to be suitably insensitive to small temperature fluctuations. The effects of any changes in the temperature of the laboratory on the calibration was compensated for when the test data was subsequently analysed

5.6.3.2. Micro-Controller.

The micro-controller contained the analogue to digital (A/D) converter, the microprocessor and the multiplexer in a single chip. A 10 bit A/D converter was selected for the system to

provide an accuracy of conversion of one bit in 1023 (2^{10}-1) at a reference voltage of 200mV. The limits, $\sigma_{3(limit)}$, within which the controller were able to maintain the pressure were determined by determining the pressure represented by a single count, with the equation,

$$\sigma_{3(limit)} = \frac{V_{ref} \times \sigma_{3(FSD)}}{V_{A/D} \times C} \qquad (5.10)$$

where V_{ref} is the reference voltage for the A/D converter = 200 x 10^{-3}V,
$V_{A/D}$ is the maximum input voltage into the A/D from the transducer = 5V,
$\sigma_{3(FSD)}$ is the maximum (Full Scale) range of the transducer = 70MPa and
C is the maximum number of counts of the A/D = 1023.

By solving Equation 5.10 one count on the A/D converter can be seen to be equivalent to 2.73kPa $\left(\frac{200\text{x}10^{-3}\text{V} \times 70\text{x}10^{6}\text{Pa}}{5\text{V} \times 1023}\right)$. During the triaxial tests, for a particular set pressure, $\sigma_{3(set)}$, the pressure could, therefore, vary within the limits $\sigma_{3(set)} \pm$ 2.73kPa. If the system pressure exceeded 273kPa, the pump and controller were able to maintain the pressure within the 1% limit recommended by the ISRM [74].

The micro-processor monitored the state of the control switches on the front panel (Figure 5.14) of the controller and the digital signals from the pressure transducer and pump position potentiometer. The speed and direction of the pump drive motor could therefore be controlled. The state of the "forward" and "reverse" direction switches was continually monitored when the "manual/automatic" switch was in the "manual" state. If the direction switches were activated by the operator, the drive motor was driven accordingly. Since the reversing relay was mechanically operated, it had a much slower response time than the solid state switch. This response time was allowed for by a delay sequence in the microprocessor that prevented the solid state switch turning on while the reversing relay was changing over. Furthermore, the microprocessor prevented the reversing relay changing state before the motor has stopped after the power had been disconnected from the motor by the solid state switch. During the "manual" mode, any signals into the microprocessor were ignored except

for the system pressure value that was continually updated for later use as a reference pressure.

Changing the front panel "manual/automatic" switch to the "automatic" position, caused the system to operate in the automatic pressure regulating mode, where the set pressure was the last pressure measured by the micro-controller before the change over. The "forward" and "reverse" switches were inoperative in this mode. The micro-controller maintained the set pressure in the system for as long as the pump piston travel limits were not exceeded or until pressure changes occurred in the system at such a rate that they could not be followed by the pump and the controller. Limit switches were incorporated into the linear displacement pump in order to prevent the drive motor from attempting to displace the piston in the linear displacement pump beyond the limits of its travel.

5.6.3.3. Drive Motor and Power Control.

The piston of the pressure pump was driven by a 240V DC, reversing motor with a separate shunt field. In this system, the field was wired in parallel with the armature and the motor speed was controlled by the micro-controller switching the applied DC voltage on and off. Further speed control was possible by manually changing the setting of a proprietary variable mains transformer used to control the voltage applied to the motor and, indirectly, the maximum response speed of the system.

The output voltage from the transformer was applied to a solid state switch that contained semiconductor devices called TRIACs. Other components caused the TRIACs to turn on or off only when the AC mains voltage passed through the zero crossing point. This system provided low switching noise but it required that the minimum motor 'on time' was 10ms (half the mains period). Since the speed of the motor was controlled by the duration it was on compared to the duration it was off, this minimum 'on time' caused the system to display the characteristic sawtooth behaviour known as "hunting" if the voltage applied from the transformer was too high. As the pressure in the hydraulic system was increased, the load opposing the momentum of the armature also increased. 'Hunting' was, therefore, observed

only when the regulated pressure was less than a particular pressure, in this case, about 1500kPa. The characteristic of 'hunting' is highlighted in the following extreme example.

Assume that the system pressure fell below the desired pressure of 250kPa. The motor switched on and accelerated to an angular velocity of 10rev/min when the pressure decreased to the lower pressure limit. The motor caused the pump to advance and the pressure in the system to increase. When the pressure had returned to the set pressure the motor switched off. Depending on the pressure in the system and the speed of the motor, Russack [128] determined that the motor might have required up to 0.5 seconds to come to a standstill after switching off as a result of the angular momentum of the armature. The angular displacement of the armature, U, that occurred within this time could be determined using the equation:

$$U = 0.5\ (\omega_o - \omega_t)\ (t_T - t_o) \qquad (5.11)$$

where t is time (t_o = 0s, t_T = 0.5s),

U is angular displacement of the armature over the time period $t = 0 \rightarrow t = T$ and

ω is the angular velocity of the armature (ω_o =167.7 x 10^{-3}rev/s, ω_T = 0 rev/s)

Using Equation 5.11 it can be estimated that, because of momentum, the armature advanced by 0.04 revolutions. This movement caused the pump piston to linearly advance by approximately 0.21mm. The excess volume of fluid pumped by this over-run was estimated from Equation 5.7 to be 0.13cc. When the motor finally came to a standstill, the pressure of the system would have been 254kPa and above the upper pressure limit. The excess pressure would result in the motor switching on again, this time in the reverse direction, to reduce the pressure.

The effect of 'hunting' is illustrated in Figure 5.15. This figure, based on a record of pressure changes over a time duration of 400sec, shows three distinctive regions. The far left region shows the system pressure remaining steady at a pressure of approximately 1230kPa. This pressure remains within the limits of the controller for about 30 seconds. The system pressure was then decreased by inducing leakage through the bleed off valve. This activity is

highlighted by the second region in the figure. With the mains transformer set at 80V, the motor advanced whenever the pressure fell to the lower bound of the limit. Occasionally the response speed of the motor was high enough to cause the system pressure to overshoot the upper bound necessitating the motor to reverse until the pressure was within the limits. The disadvantage of selecting a low motor speed is that a low response rate can limit the ability of the pump to maintain the required pressure if the system pressure is rapidly changing. In the third region in the figure the mains transformer was set to 200V. With the speed of the motor now significantly faster, the system pressure fluctuated as the motor attempted to keep the pressure within the limit. This example highlighted the importance of selecting the most suitable motor speed to match the rate of change of system pressure and, under normal test conditions, a single voltage adjustment generally sufficed to provide the optimum performance.

5.7. Shear Box Apparatus.

The traditional method for obtaining discontinuity shear property data has been to use a shear box apparatus as described in the ISRM guidelines [72]. This method involves the application of a constant normal load perpendicular to a discontinuity while the shearing force is slowly increased and the resulting shear displacements recorded. If one half of the specimen has a smaller surface area than the other half, it is possible to shear the specimen under conditions of constant normal stress. If the two halves of the specimen are symmetric then the normal stress on the discontinuity, σ_n, is not constant but must instead be calculated from the equation:

$$\sigma_n = \frac{F_n}{(b - u)l} \qquad \tau = \frac{F_s}{(b - u)l} \qquad (5.12(a)\text{-}(b))$$

where F_n is the normal force on the discontinuity,

F_s is the shear force on the discontinuity,

u is the shear displacement,

b is the linear dimension of the specimen parallel to the shear force and, prior to shearing and

l is the linear dimension of the specimen perpendicular to the shear force.

It should be noted that the contact area of the discontinuity will, in reality, be significantly smaller than that calculated from the denominators in Equations 5.13(a)-(b) as contact across a discontinuity generally occurs at asperities.

In many rock mechanics situations such as slope stability problems, it is reasonable to assume that sliding occurs under conditions of constant normal stress. In many situations the normal stress on the discontinuity is, however, not constant but tends to vary with normal deformation. These situations are ones in which the sliding blocks are constrained, as may occur in a tunnel wall, or those in which sliding is accompanied with contraction or dilation of the blocks. Under these conditions it is more realistic to model the behaviour under conditions of constant normal stiffness rather than constant normal stress. If normal stiffness conditions are not present, then the peak shear strength of a discontinuity is found to be conservative (Goodman [57], Saeb and Amadei [130] Skinas et al. [137]). Equipment suitable for conducting shear box tests under conditions of constant normal stiffness has been developed by Archambault et al. [1], Benjelloun et al. [15], Johnston and Lam [81], Ohnishi and Dharmaratne [111], Ooi and Carter [112], Skinas et al. [137] and Van Sint Jan [146]. Ohnishi and Dharmaratne [111] reported that the residual shear strength obtained under constant normal stress and normal stiffness conditions approached each other as the normal stress across the discontinuity increased.

If a triaxial test is conducted on a discontinuous specimen at low to moderate confining stresses, constant normal stress conditions can apply. Under low normal stress conditions, there is little possibility that dilation of a discontinuity can be prevented as the individual blocks within the specimen are free to translate and rotate. It can, therefore, be assumed that shear box tests conducted under constant normal stress conditions can simulate the behaviour of a discontinuity in a triaxial tests.

The shear box tests were initially conducted in a proprietary portable rock shear box apparatus of the type developed at Imperial College and described by Ross-Brown and Walton [127]. In this apparatus, a hydraulic jack on the upper box acts upon a wire rope

attached to the lower box. By raising the jack, the two halves of the box are compressed together and apply a normal force to the specimen. A second jack and cable are used to apply a shear displacement to the specimen.

The initial series of shear box tests showed that the portable rock apparatus was insensitive to the stick-slip oscillations that occurred as the two halves of the specimen were displaced relative to each other. This result was, in part, caused by the difficulties associated with maintaining a constant rate of shear displacement. Manually pumping the shear displacement pump tended to jerk the specimen. The jerking made it impossible to obtain suitable data required for determining the shear stiffness of the discontinuities. The portable shear box apparatus is designed to accommodate normal stresses up to 150MPa and therefore most of the equipment tended to be insensitive to the range of normal stresses required for this investigation.

Difficulties were also encountered with the use of this apparatus in maintaining constant normal stress conditions because the cable applying the normal force moved away from vertical as shear displacement occurred. This result caused the pressure in the jack and hence the normal stress across the discontinuity, to increase. If specimens possessing surface roughness had been tested the pressure in the normal jack would have needed correcting each time the discontinuity dilated. These problems were addressed by Hencher and Richards [63] and Bandis et al. [8] proposed modifications to the portable apparatus in an attempt to improve its effectiveness.

To obtain satisfactory results, direct shear tests were carried out using a Casagrande soils shear box apparatus (shown in Figure 5.16(a)). This apparatus was capable of applying a constant rate of shear displacement with a geared electric motor and a constant normal force through a system comprising a hanger, lever arm and masses. This apparatus was, however, incapable of providing as large a normal force to the specimen as the portable rock apparatus.

For example, in the present research the average normal stress state on a discontinuity

intersecting a discontinuous specimen was 5.8MPa (σ_1=8.5MPa, σ_3=0.69MPa, $\bar{\beta}_w$=36°). On a 60mm x 60mm direct shear test specimen, this stress is equivalent to a normal force of 21kN. Referring to Figure 5.16(a) the total force applied to a specimen is the sum of the forces resulting from the self weight of the primary hanger and the weights placed upon it. In addition there is a force transferred to the primary hanger from the secondary hanger due to its eccentricity along the extension arm. By resolving the forces, the normal force on the discontinuity is found by solving the equation:

$$F_n = (W_A + 5W_B + 183.3)\ cos\ \theta \qquad (5.13)$$

where W_A and W_B are the additional mass on hangers A and B (N),

θ is the angle through which the primary hanger has moved due to the shear displacement of the specimen, δ_s, ie. $\theta = arcsin\ \frac{\delta_s}{L}$ and

L is the length of the primary hanger from the pivot to the discontinuity.

For the shear box apparatus used, $W_{A(max)}$ =20N and $W_{B(max)}$ =640N and therefore, the maximum shear force that could be applied to a specimen was 3.4kN. This normal force is 16% of that required. Owing to a lack of suitable shear test apparatus, the assumption had to be made in this study that any relationships developed on the basis of results obtained using this apparatus would be consistent at the stress states required.

Modifications to the shear box apparatus can be seen in Figure 5.16(b). These modifications included installing calibrated LVDTs for monitoring shear and normal displacement and proving ring compression. This modification enabled the shear and normal displacement and the shear force to be monitored by a data logger. The specimen carrier was also modified to enable 60 x 60 x 35mm specimens of the modelling material to be installed.

5.8. Data Logging.

During the shear box tests and the triaxial tests on the intact and the discontinuous specimens a Kyowa data logger, model UCAM-5AT, was used to monitor all analog outputs. The logger scanned each input at a rate of 0.45 seconds per input and, because it contained a

micro-processor, all analog inputs could be multiplied by a calibration coefficient that enabled the value of each input to be displayed in the desired units on an LED display. The output signals were passed through an A/D converter and the digital signals channelled through the RS232 serial port to a Toshiba, model T1100, laptop computer. The computer displayed the test output in real time and stored it in RAM. The computer dumped the stored data to the hard disk when the RAM was full.

5.9. Summary.

Considerable time was devoted in this study to develop equipment that could be used to conduct reliable and well-controlled tests. A 150mm Hoek cell was commissioned and instrumented. Methods were developed to insert and remove discontinuous specimens from the cell and to change the rubber membrane when damaged. A cell pressure control system was developed that was capable of maintaining pressure within closer limits than those required by the ISRM. The pressure control system was also capable of accurately monitoring changes in the volume of a specimen to within $3.8mm^3$, representing an improvement on the cited systems of other researchers. In order to conduct shear box tests on single discontinuities, a soils shear box apparatus was modified and instrumented. The next two chapters discuss the tests that were conducted using this equipment.

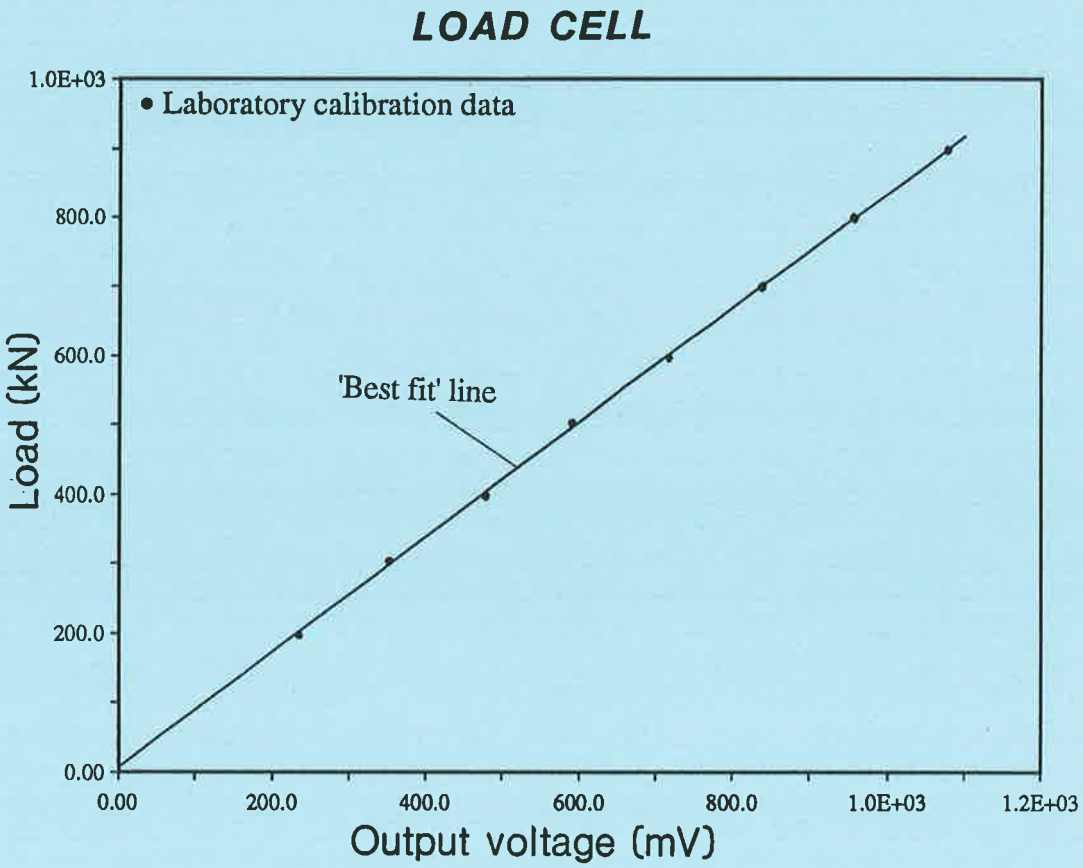

Figure 5.1. Load cell calibration curve.

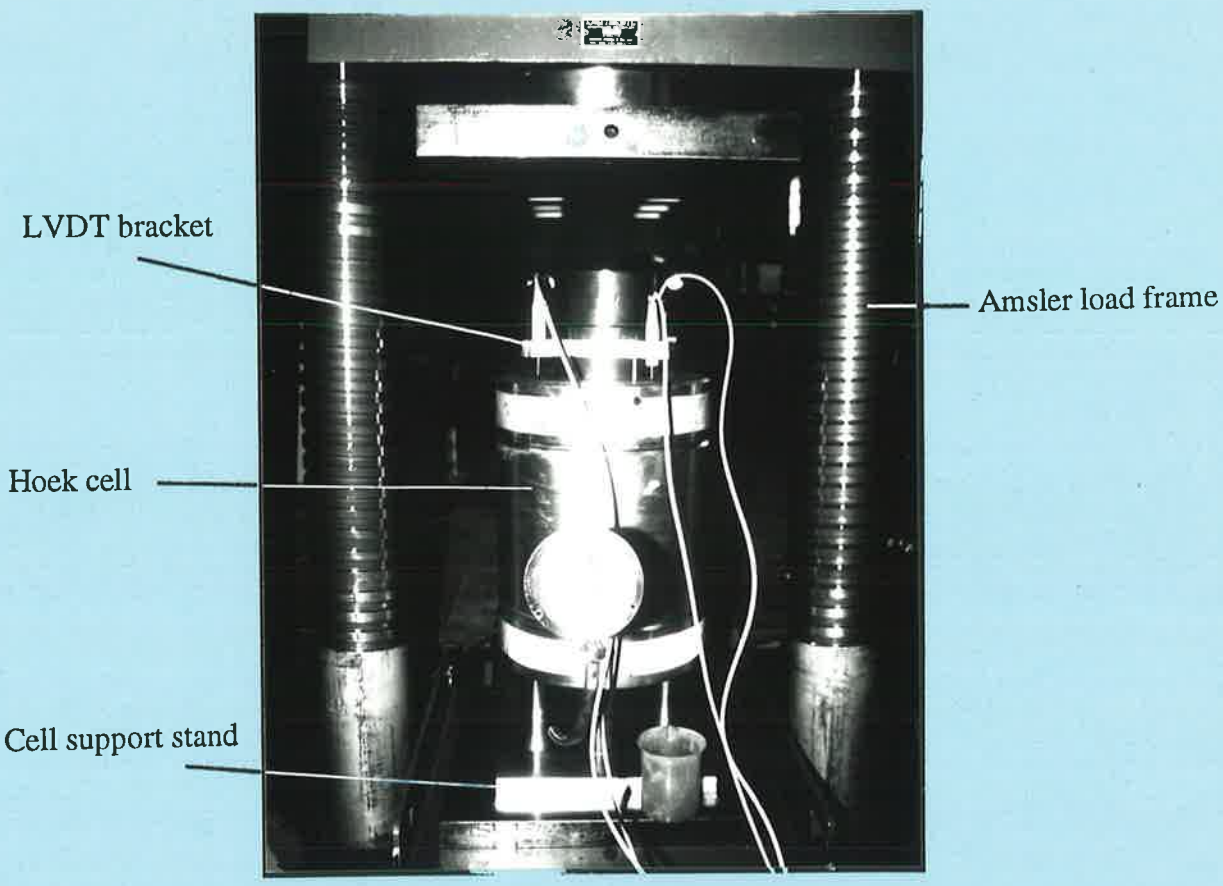

Figure 5.2. Hoek cell in Amsler load frame.

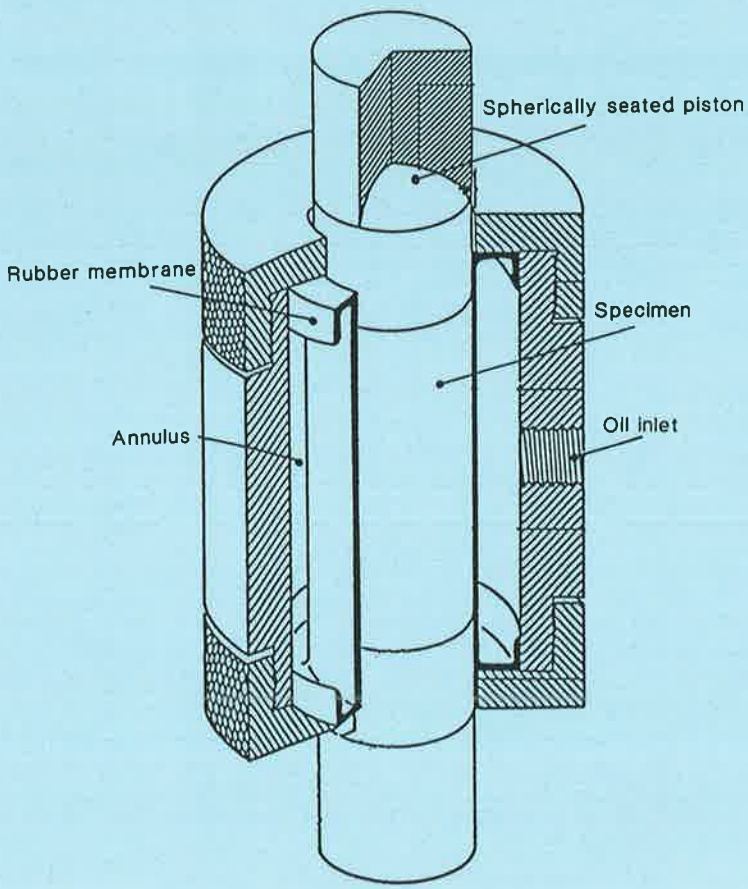

Figure 5.3. Hoek cell internals.

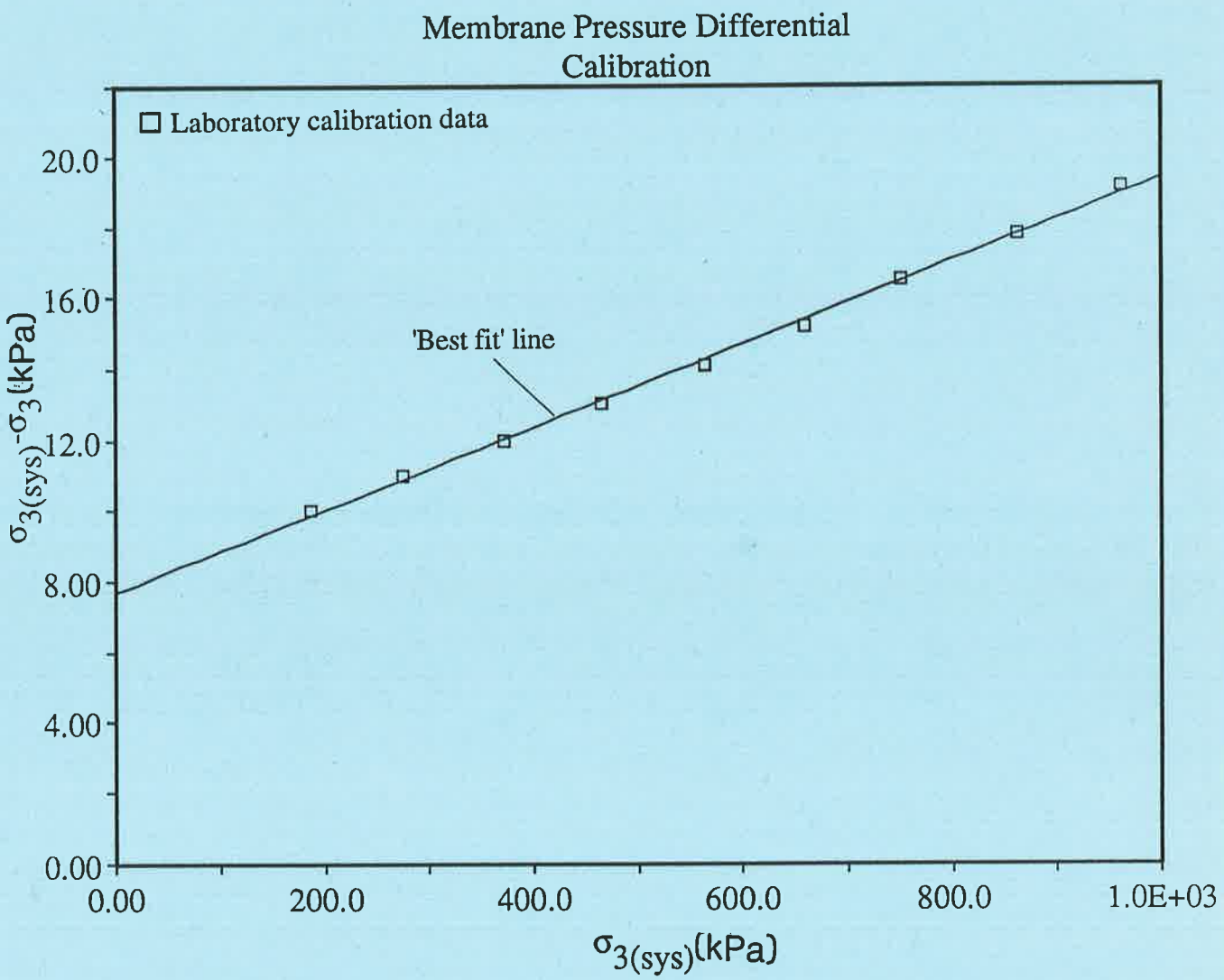

Figure 5.4. Plot showing pressure differential across membrane.

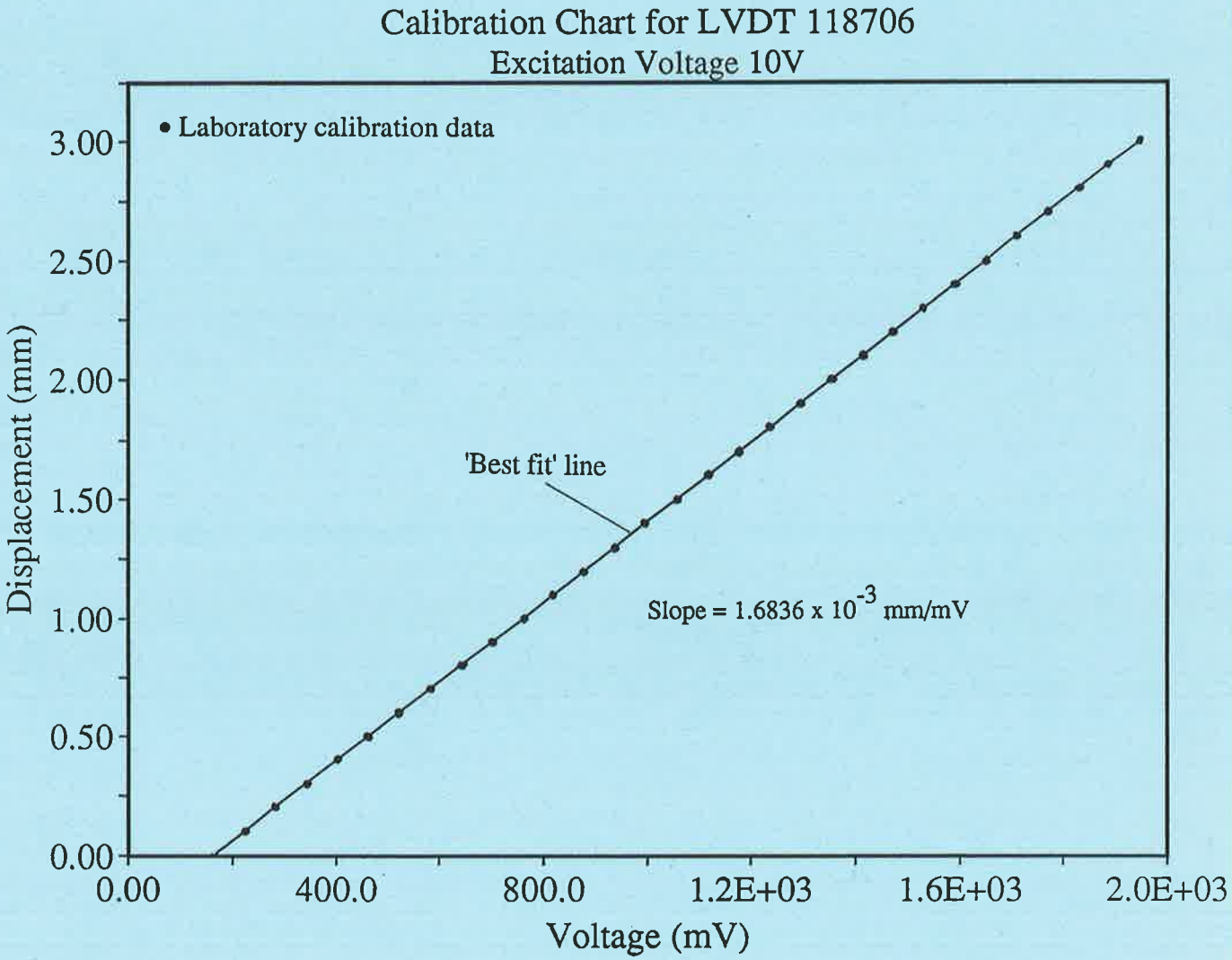

Figure 5.5. A typical LVDT calibration curve.

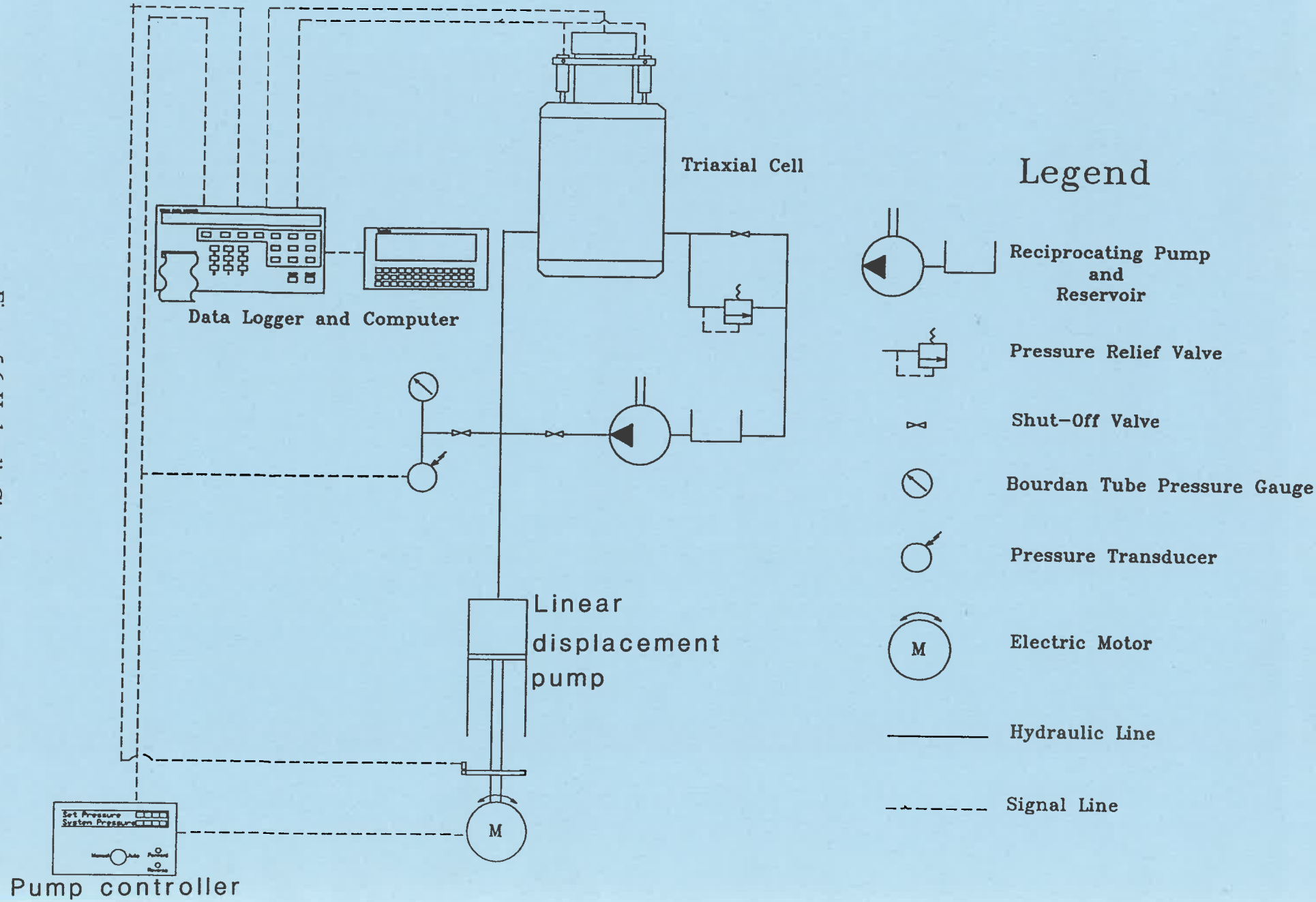

Figure 5.6. Hydraulic Circuit.

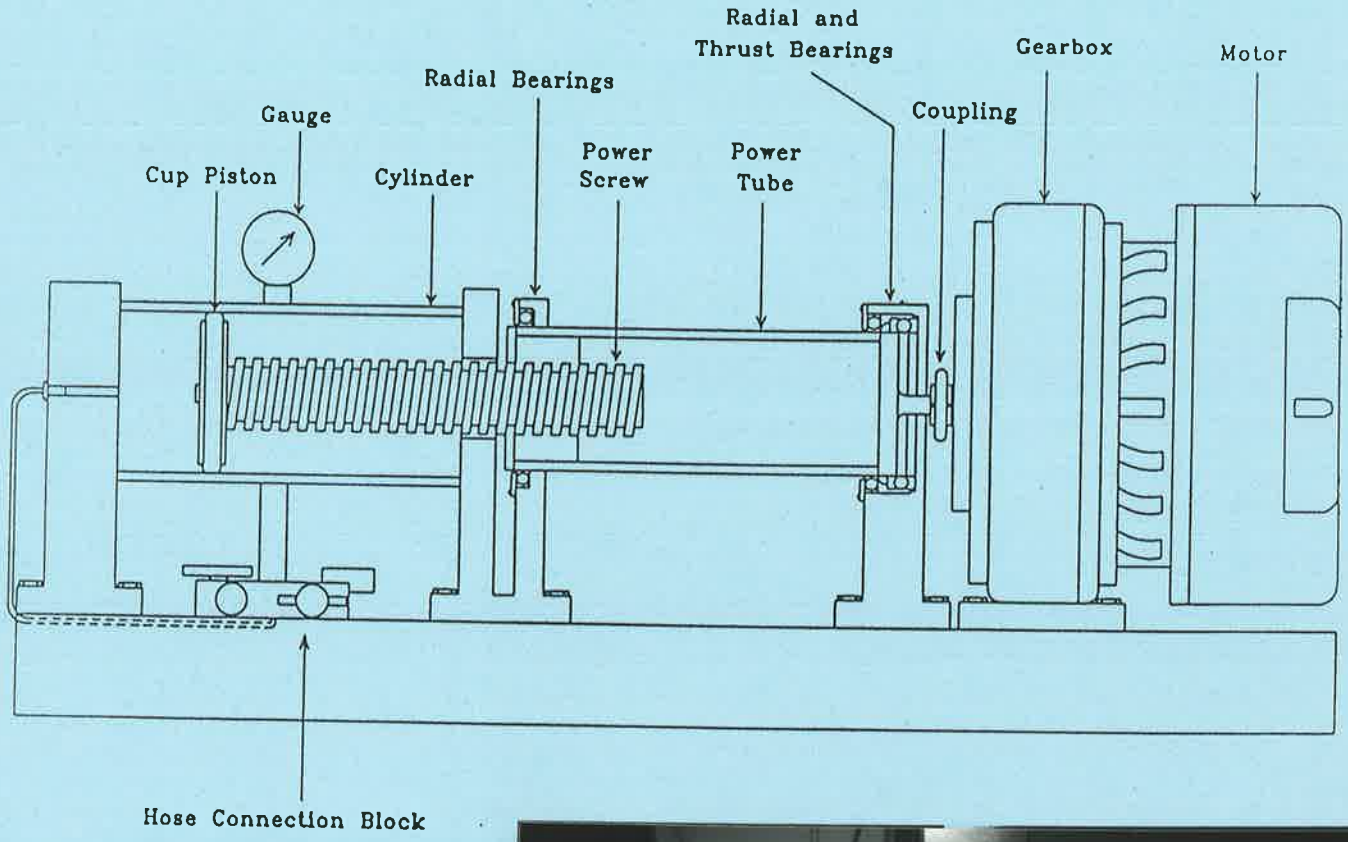

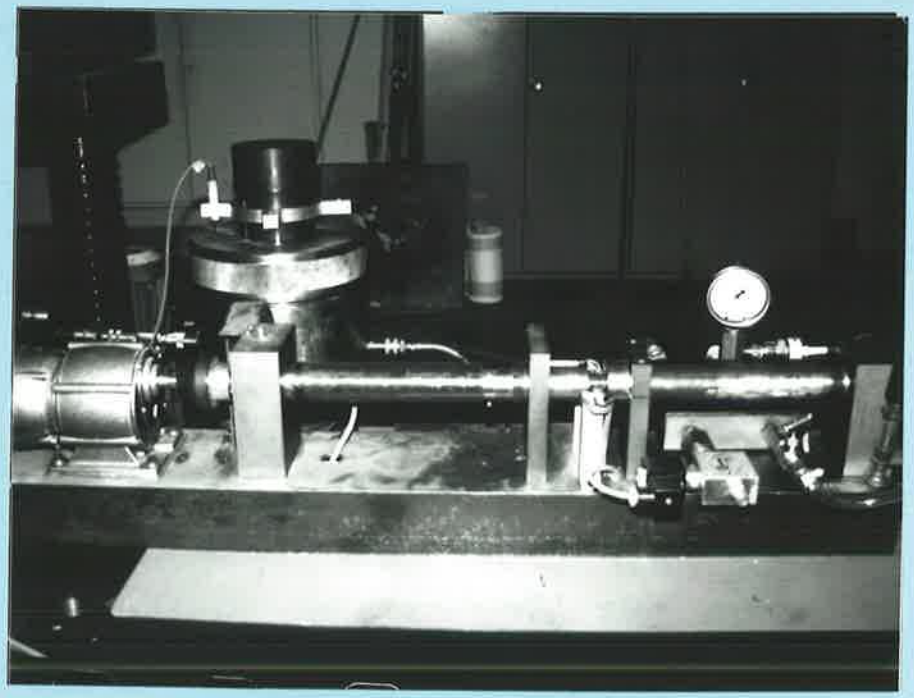

Figure 5.7. Linear displacement pump. (Note: A 2:1 vertical/horizontal ratio was used in the drawing).

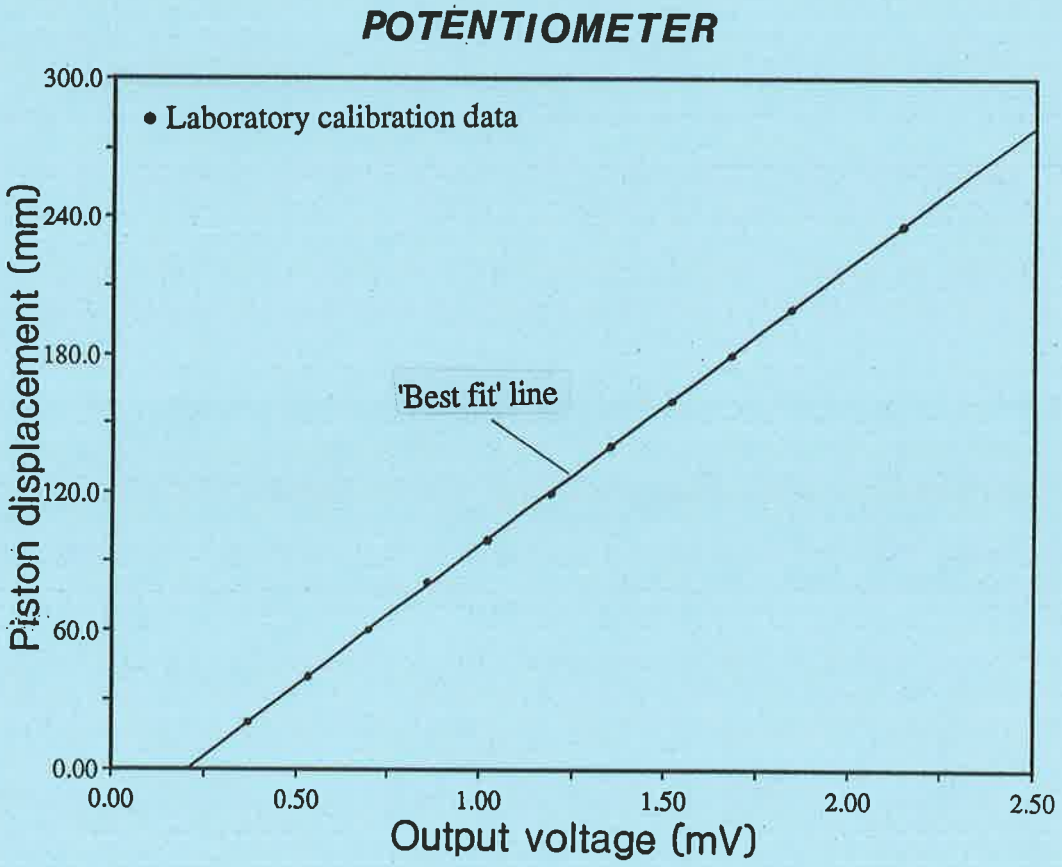

Figure 5.8. Potentiometer Calibration Curve

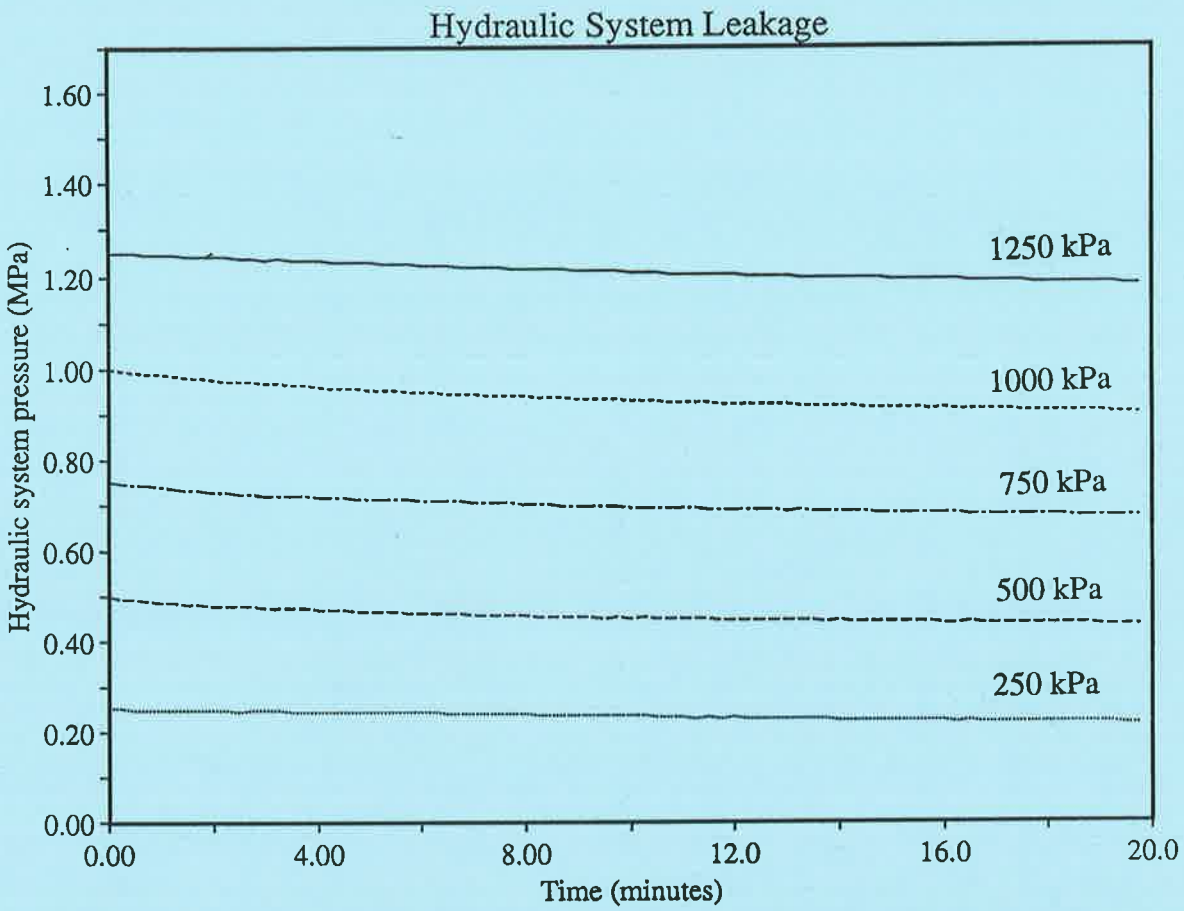

Figure 5.9. Plot showing hydraulic system pressure versus time curves obtained from system leakage calibration tests.

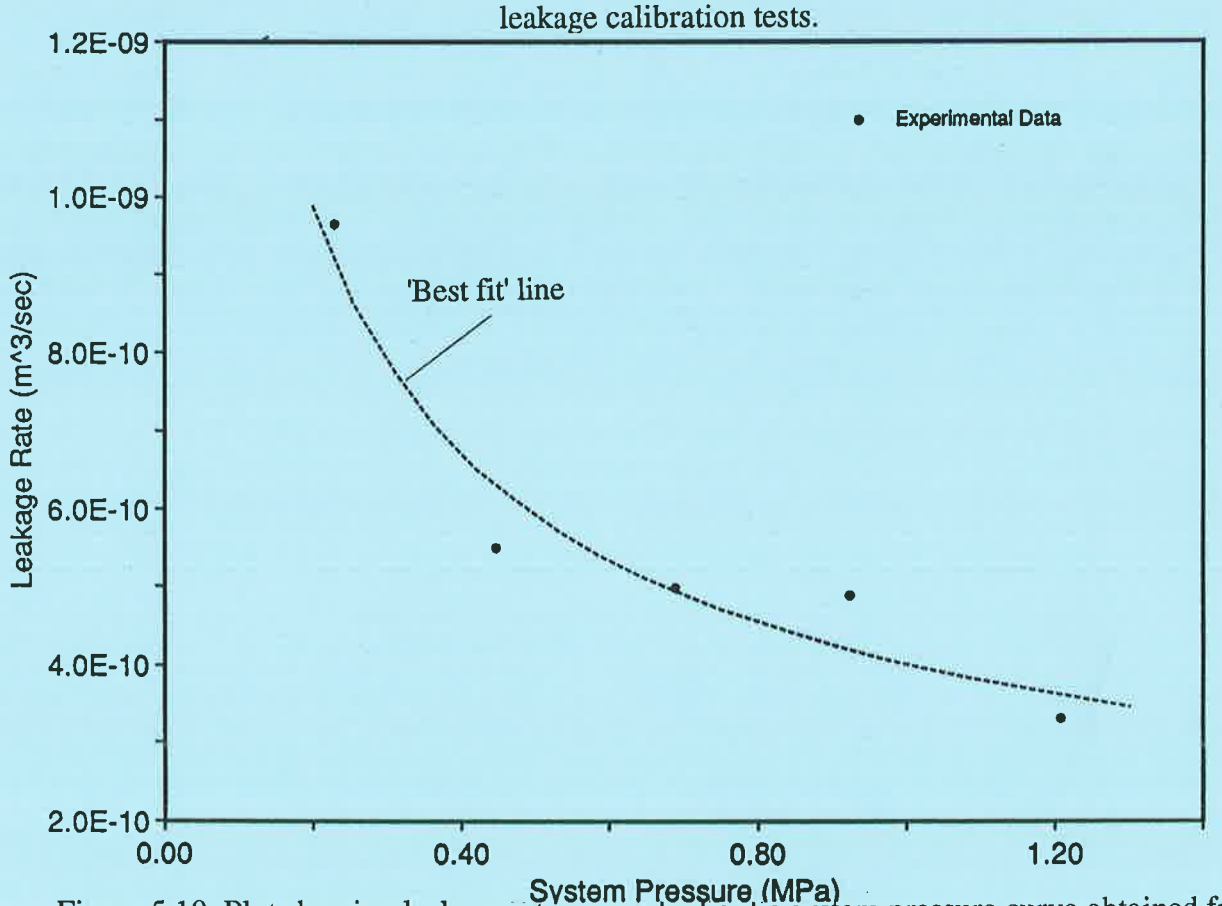

Figure 5.10. Plot showing leakage rate versus hydraulic system pressure curve obtained from envelope gradients in previous plot.

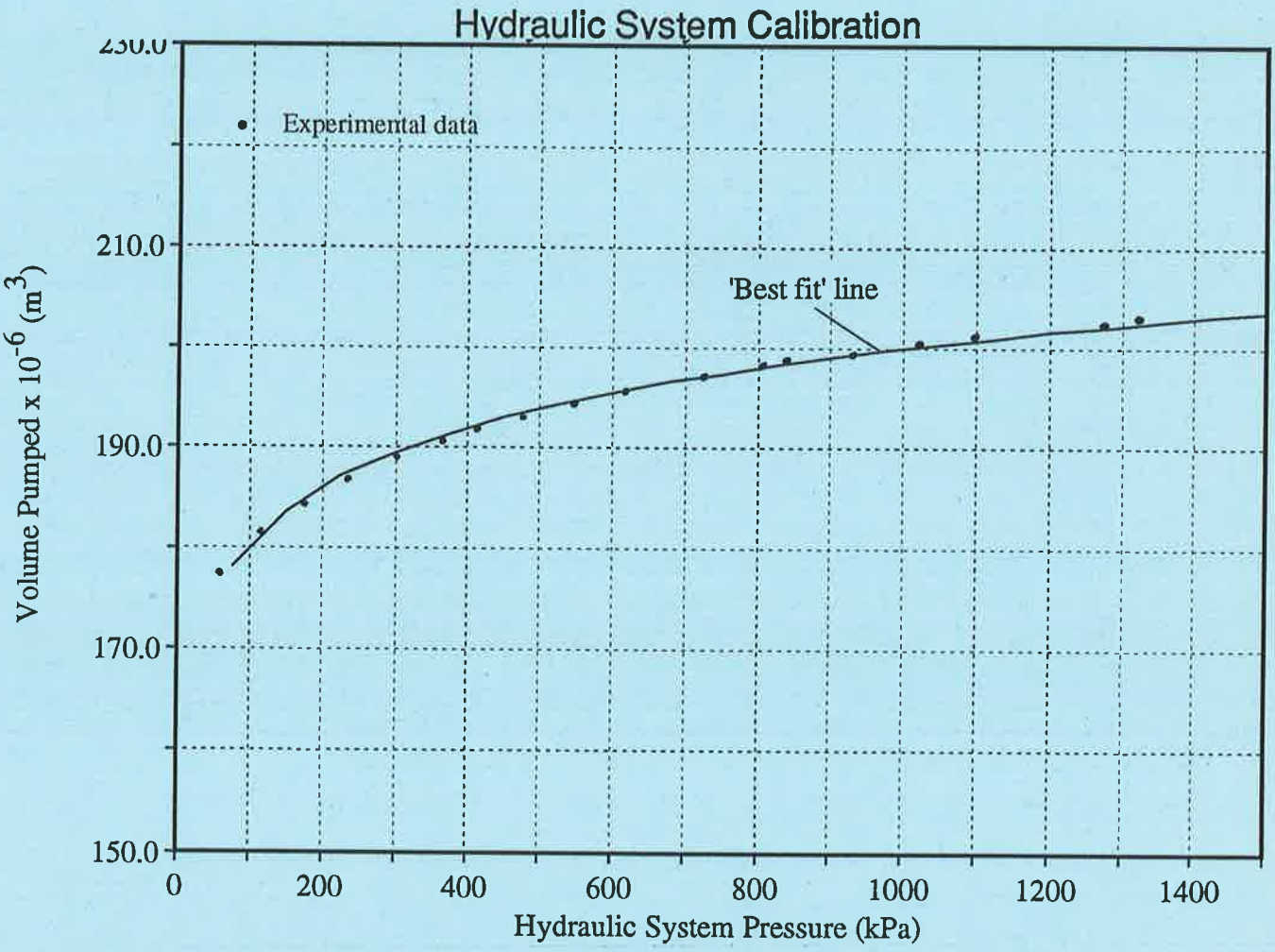

Figure 5.11. Plot showing volume of hydraulic fluid to be pumped in order to achieve a particular system pressure.

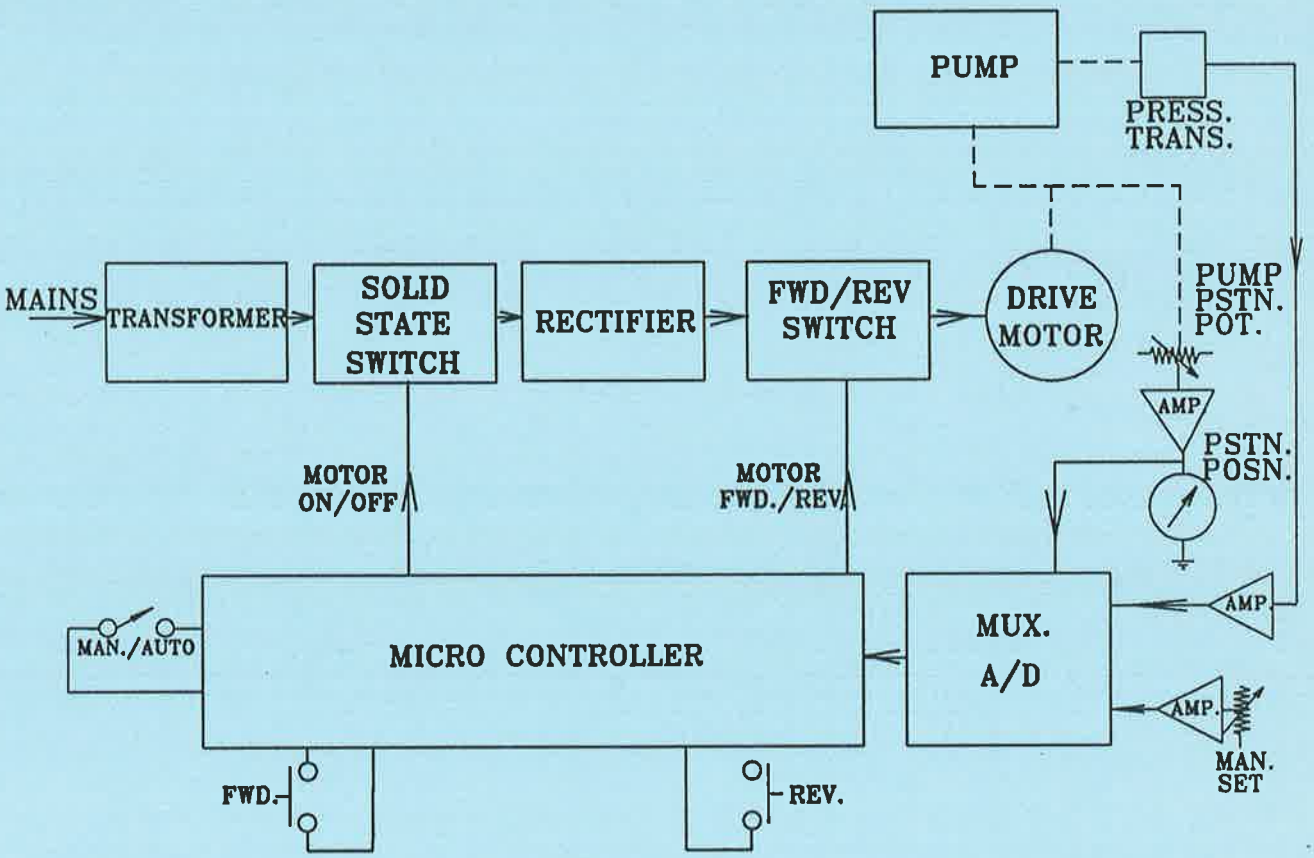

Figure 5.12. Block diagram of pressure controller circuit.

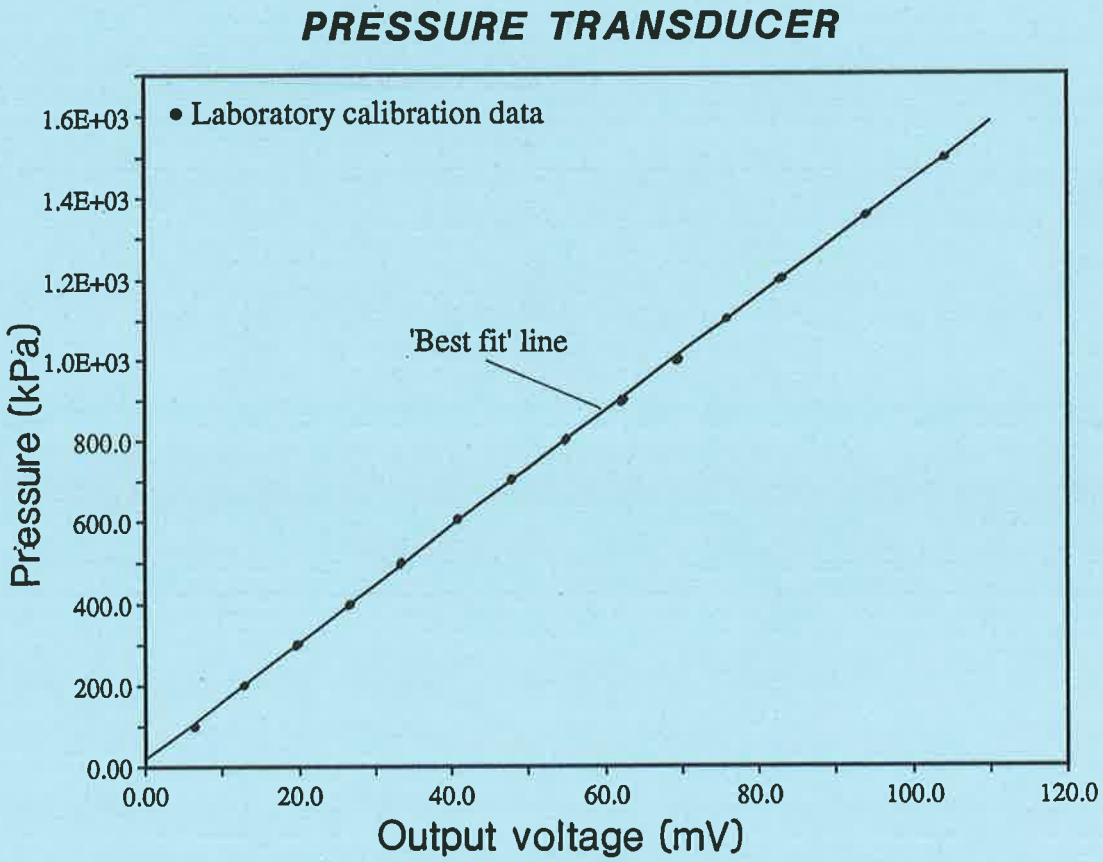

Figure 5.13. Pressure transducer calibration curve.

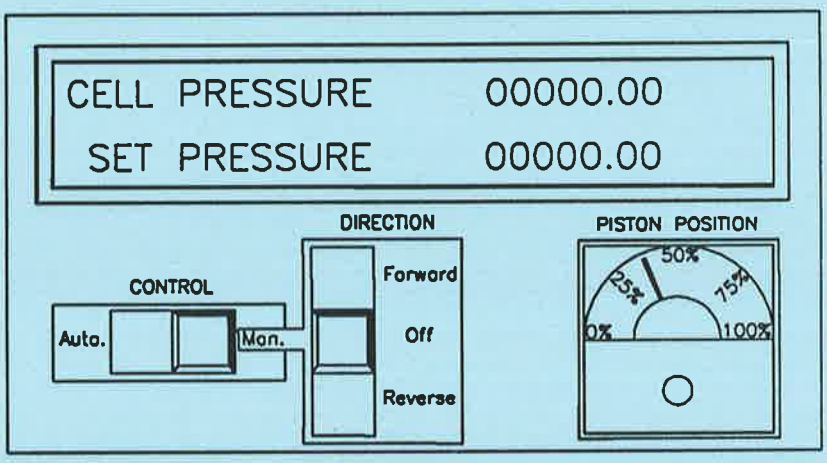

Figure 5.14. Front panel of the linear displacement pump controller.

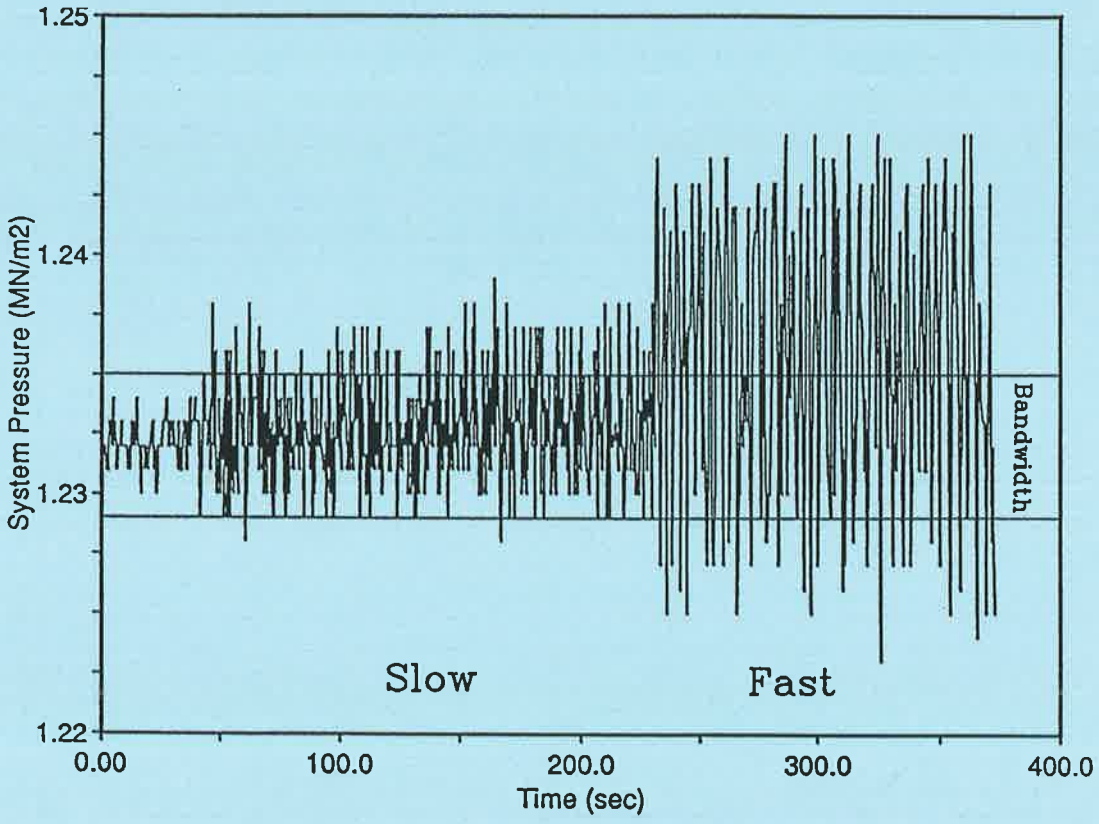

Figure 5.15. Plot showing the influence of motor speed on pressure control.

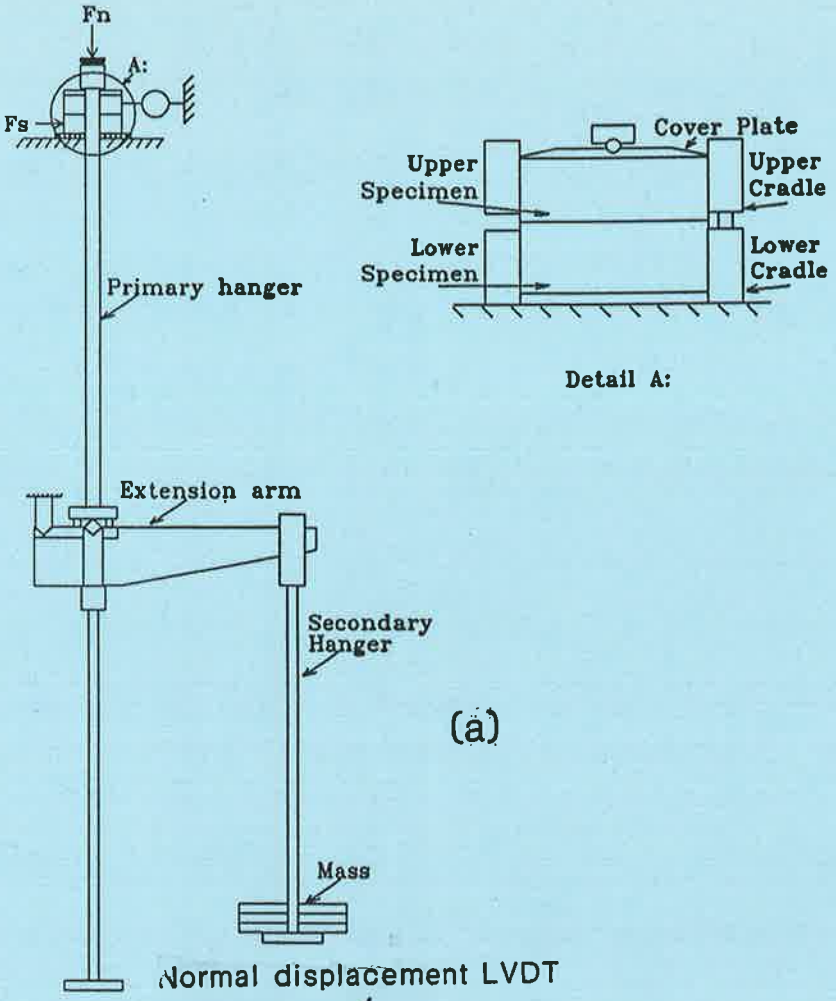

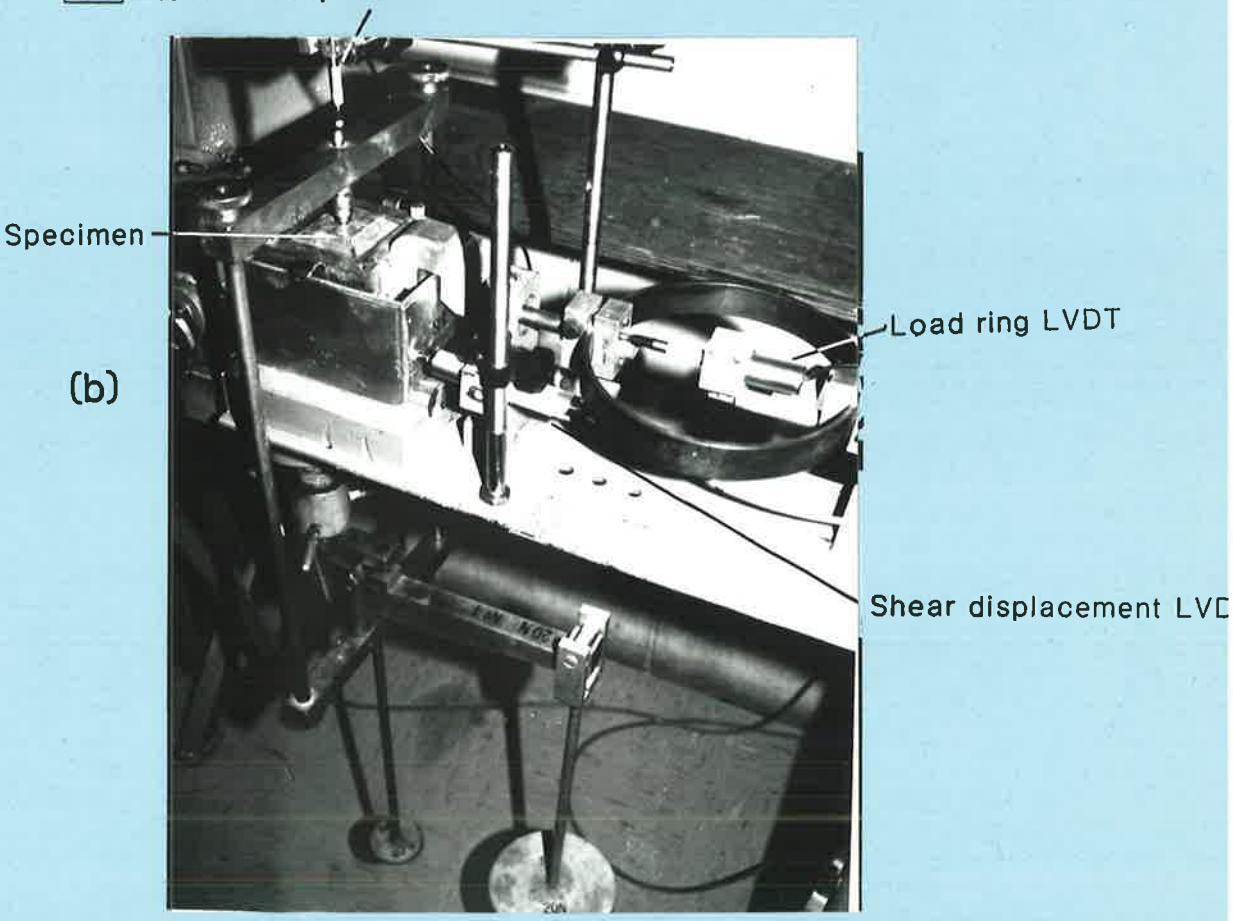

Figure 5.16. (a) Details of the Casagrande shear box apparatus. (b) Modifications to basic shear box apparatus.

Chapter 6.
Experimental Programme - Part 1
Tests to Determine the Properties of the Modelling Material.

Chapter 6. Experimental Programme - Part 1: Tests to Determine the Properties of the Modelling Material.

6.1. Introduction.

There is wide scatter in the data available from other researchers characterising the strength and deformability of neat gypsum cement mortars and little available information for mortars comprised of sand/cement mixtures. Accordingly a testing programme was undertaken to obtain data on the engineering properties of the modelling materials selected in Chapter 4. The characteristic properties of the material and the discontinuities determined from these tests were:

(1) Uniaxial compressive strength of the intact material, σ_c,

(2) Mohr-Coulomb shear strength parameters for the intact material, ϕ_i.and c_i,

(3) Young's modulus and Poisson's ratio of the intact material, E and ν,

(4) Tensile strength of the intact material, σ_t,

(5) Relationship expressing the shear strength parameter ϕ_w in terms of σ_n,

(6) Relationship expressing the shear stiffness, K_s. of the discontinuities in terms of σ_n.

6.2. Results of Material Property Tests on Intact Material

The tests on the intact modelling materials represent a small component of the main aim of this project, that of investigating the behaviour of discontinuous specimens. The details of

the tests are, therefore, not presented in the main body of the text but are, instead, presented in Appendix C. The main results of the tests are summarised in Table 6.1.

Table 6.1. Summary of intact material properties. The results have been compared with typical results for natural material (after Lama and Vutukuri [92]).

Parameter	100% Gypsum cement	50/50 Cement/ sand	Rock (Carbonates Sandstone)
Intact Material			
Compressive Strength, σ_c (MPa)	37.2	23.3	10 - 80
Modulus of Elasticity, E (GPa)	5.6	4.8	1 - 20
Poisson's Ratio, ν	0.26	0.26	0.1 - 0.3
Intact cohesion, c_i (MPa)	9	4.2	n\a
Intact friction angle, ϕ_i	37°	49°	35° - 50°
Tensile strength, σ_t (MPa)	8.6	5.9	1.0 - 15.0
Hoek-Brown parameter, m_i	7.5	17.6	7-15
Density, ρ (kg/m^3)	2400	1734	2000-2600

In Table 6.1 many of the π factors, referred to in Equation 4.2, for the modelling materials are compared to those for rock. The ranges selected for the rock were those applicable to carbonates and weak sandstones (for which $\sigma_c < 40$MPa) as the characteristics of these rocks are similar to those of the modelling materials. The remaining non-test-specific π factors are compared in Table 6.2. The first two factors in Equation 4.2 are defined in the table as the single factor $\left(\frac{\sigma_c}{\sigma_t}\right)$. The factors $\left(\frac{\sigma_3}{\rho g S}\right)$, ε and $\left(\varepsilon\sqrt{\frac{S}{g}}\right)$ are test specific and, because they cannot be compared readily, are not included in the table. Considering that it is impossible to satisfy all the requirements for similitude between a modelling material and rock, a comparison of the π factors show reasonable agreement between them. Both intact materials were, therefore, concluded to satisfy similitude requirements for the purposes of this study.

Table 6.2. Comparison of π factors for modelling and natural rock materials. Refer to Equation 4.2. (Note: A unit discontinuity spacing, S, is assumed in the comparison).

	π Factors		
Factor	Gypsum cement	Cement/ sand	Natural rock
E/σ_c	150	206	100 - 250
σ_c/σ_t	4.3	3.9	5 - 10
$\sigma_c/\rho gS$	1580	1370	500-3000

6.3. Direct Shear Tests on Discontinuities

The mechanical behaviour of a discontinuous rock mass is largely influenced by the shear strength and deformability of the individual discontinuities. In order to properly understand the behaviour of the discontinuous specimens and to obtain data on the shear properties of discontinuities formed through the modelling material for input into the numerical model, it was imperative that studies be conducted into the shear behaviour of the discontinuities.

Each half of a shear box specimen was prepared from a silicon rubber mould utilising the techniques described in Section 4.2. Discontinuities having a Celite infill were prepared using the techniques described in Section 4.5. These procedures ensured that direct shear tests were carried out on discontinuities having similar material properties to those intersecting the discontinuous specimens. The halves of a direct shear specimen were assembled in the shear box apparatus, described in Section 5.7, and a normal stress applied. A shear displacement was applied to the lower half of the specimen at a constant rate of 0.61mm/min. The results of the direct shear tests are presented in Tables C.6, C.7 and C.8. Figures 6.1, 6.2 and 6.3 show typical test results.

6.3.1. Discussion of Results.

The behaviour of the gypsum cement and the cement/sand mixture characteristically displayed an initial linear rise in shear stress, noted by Goodman [57] as being, typical of that

seen with rough, clean discontinuities. The shear stress versus shear deformation behaviour of the discontinuities containing the infill was different to that of the clean discontinuities. This behaviour was characterised by a small initial linear increase in shear stress being followed by convex upward behaviour similar to that displayed by a clay. This result could be expected owing to the silicate nature of the infill (Celite, or diatomaceous earth being made up of tectosilicates and clay minerals of phyllosilicates). Pereira [116] produced similar results using a sand infill with a high clay fraction whereas Papaliangas et al. [113] produced an infill from pulverised fuel ash that did not produce a convex curve. This result suggests that the convex nature of the initial region of the shear stress versus shear displacement curve for infilled discontinuities is due to the nature of the infill material rather than the presence of the infill.

The linear or, in the case of the infill, convex behaviour for all materials was rarely smooth and very often resembled the behaviour for the cement/sand material at σ_n = 140kPa (Figure 6.2) and the infill material as shown in Figure 6.3. In the gypsum cement and cement/sand materials, this behaviour might have occurred when high points in the wall material broke away thereby causing small shear deformations to occur with no associated increase in shear stress. Eventually the fragments were eroded and forced into interstices at which point the shear stress increased with the same slope as previously. With the discontinuities containing the infill material, shear deformation tended to occur along laminations through the infill parallel to the discontinuity wall and at the infill/wall interface. It is reasonable to assume that infill material on either side of the laminations might have been removed and re-deposited as the shear deformation proceeded. This process would cause new laminations to develop along which small scale, plastic deformation could occur.

The value of the shear stiffness of the discontinuities, K_s, is included in Tables C.6, C.7 and C.8. The results obtained for the gypsum cement material are similar to those obtained by Indraratna [71]. Figure 6.4(a)-(c) shows the relationship between the shear stiffness and the normal stress on the discontinuity for each material. Models to define the relationship

between K_s and σ_n for the particular discontinuities were obtained by regression analysis of the test data and take the form of the equation:

$$K_S = a_{(K)}\ \sigma_n^{\ b_{(K)}} \qquad (6.1)$$

The value of the coefficients $a_{(K)}$ and $b_{(K)}$ and the coefficient of determination, r^2, are listed in Table 6.3. Goodness-of-fit is often quoted in terms of the correlation coefficient, r, which can be either positive or negative. In this study, goodness-of-fit is quoted in terms of the coefficient of regression, r^2. This term is always positive and provides a more conservative measure for goodness-of-fit than does the correlation coefficient. If the response (vertical axis) can be defined in terms of the stimulus (horizontal axis) with no scatter then $r^2=1$.

Table 6.3. Coefficients applicable to Equation 6.1 (the units for normal stress are Pa and those for shear stiffness, Pa/m).

Discontinuity Material	$a_{(K)}$ x 10^6	$b_{(K)}$	r^2
gypsum cement	1.18	0.505	0.65
cement/sand	5.02	0.368	0.46
Infill	0.38	0.571	0.83

The 100% cement and the infill material have similar roughness characteristics yet the lower stiffness of the infill material is reflected in the decrease in $a_{(K)}$. The presence of the siliceous sand grains causes $a_{(K)}$ for the cement/sand material to be greater than for the other materials.

The shear strength versus shear deformation characteristic of the discontinuities in the gypsum cement and cement/sand material can be generalised as displaying an initial rise in shear strength preceding the onset of plastic behaviour. Within the plastic region stick-slip oscillations were prevalent for the gypsum cement and the cement/sand materials. The amplitude and frequency of these oscillations decreased significantly in those discontinuities

in which infill material had smoothed the asperities and filled any interstices in the wall material.

From Figures 6.1, 6.2 and 6.3 and the results of the other direct shear tests, details of the ultimate shear stress and the corresponding shear displacements were obtained and have been listed in Tables C.6, C.7 and C.8. Many of the discontinuities displayed pseudo-strain hardening effects rather than displaying pure plastic behaviour. In these cases, a value for the ultimate strength of the discontinuities was determined as the intersection point obtained by extrapolating the elastic and the plastic regions. Figure 6.5(a)-(c) shows that the shear stress at yield can be defined in terms of the normal stress by a Coulomb yield criterion for which the shear strength parameters are as listed in Table 6.4. The value for the friction angle of each material type satisfies the requirements for similitude with natural rock.

After investigating the effect of infill on the shear strength of a discontinuity Ladanyi and Archambault [90] Papaliangas et al. [113], Pereira [116] and Phien-wej et al. [117], concluded that the shear strength of a discontinuity decreased with an increase in fill thickness. They concluded that the shear strength was intermediate between a maximum value that was the strength of the unfilled joint and a minimum value that lay in the range between the shear strength of the infill material and the shear strength of the specimen-infill interface. The shear strength of the discontinuity was independent of the infill thickness once the thickness of the infill, f, was greater than the height of the asperities, a. When the discontinuities containing the infill were prepared, it was difficult to maintain an equal infill material thickness between specimens (ie. $2 \leq f/a \leq 5$). The low scatter in shear strength data, appears to confirm the conclusion that if $f/a > 1$ then changes in the thickness of the infill has little effect on the shear strength of the discontinuity.

It should be pointed out that Indraratna [71] determined the discontinuity friction angle of gypsum cement to be a constant 21.9° for normal stresses up to 370kPa. This result is significantly less than that obtained in the current research. On the basis of a comparison of the results obtained for the joint roughness coefficient in both studies, it does not appear that

Table 6.4. Shear strength parameters for discontinuities.

Material	ϕ_w	c_w (kPa)	r^2
100%	35.1	0.0	0.95
50/50	33.2	18.4	0.94
Infill	32.1	10.7	0.92

the discontinuities used in this investigation were significantly rougher than those in Indraratna's study. In addition, there does not appear to be a difference in the method used to prepare the specimens. The only noticeable difference between the investigations was that Indraratna appeared to base his conclusion on the results of 4 direct shear tests compared to 32 tests conducted in this study.

Efforts were made at the beginning of a number of the shear box tests to estimate normal stiffness by subjecting the discontinuities to normal compression and monitoring the normal stress versus normal strain response. The lack of significant roughness features on the discontinuities made it extremely difficult to distinguish between the compression of the asperities and that of the intact material. Owing to the lack of suitable test data, a value for normal stiffness estimated by Indraratna [71] for gypsum cement of 150GN/m^3 was adopted for the clean discontinuities in this study.

6.4. Discontinuity Behaviour Models

The shear stress versus shear displacement behaviour of discontinuities has been described by other researchers for modelling purposes, by a constant stiffness and a constant residual displacement model. A constant stiffness model assumes that the shear stiffness of the discontinuity remains constant with changes in the normal stress. Figure 6.4(a)-(c) clearly shows this assumption to be inappropriate. A constant residual displacement model, on the other hand, assumes that the shear stiffness of the discontinuity varies with the normal stress,

which is more realistic. This model also assumes that the shear displacement, u_{res}, at which the residual shear strength is first realised remains constant as the normal stress on the discontinuity increases. Figure 6.6 shows a plot of u_{res} versus σ_n. In this figure u_{res} is seen to increase, albeit slightly in the gypsum cement and infilled specimens, with σ_n. The very poor fit of the test data to the envelopes (100% gypsum cement: $r^2 = 0.084$, 50/50 cement/sand: $r^2 = 0.37$, infilled discontinuities: $r^2 = 0.22$) meant that further work would be required if the relationship between the parameters was to be developed further.

Bandis [7] found that the slope of the u_{res} versus σ_n curve is often negative as the shear behaviour of a discontinuity moves from plastic to brittle with increasing normal stress. This negative relationship does not appear to be supported by the cement/sand material for the stress levels used but, with the large amount of scatter, could be supported by the other two materials. An interesting similarity exists between the results obtained in the current investigation and the results obtained by Barton and Bakhtar [12] and described by Bandis [7] when they conducted an investigation into the effect of scale on discontinuity strength by surveying 300 laboratory shear tests. From the results of Barton and Bakhtar, Bandis concluded that 75% of the tests averaged u_{res} at 1.28% of the specimen length. Comparable results were obtained from this study in which u_{res} averaged 1.27% for the gypsum cement material and 1.83% for the cement/sand material.

In Section 2.5 the yield criterion of Barton and Choubey [13] was described. Barton and Choubey described the use of a tilt test for obtaining the shear strength parameters used as input data to the yield criterion defined in Equation 2.13. In order to ascertain the effectiveness of tilt test data for obtaining shear strength parameters for Equation 3.8, a basic tilt test apparatus was constructed and 30 tilt tests were performed on discontinuities intersecting 60 x 60 x 34mm specimens of the gypsum cement and the cement/sand material.

Both fresh discontinuities and discontinuities that had been sheared, to produce a residual surface, were tested. The results are listed in Table 6.5. The residual friction angle for the gypsum cement material agrees well with the value suggested by Barton and Choubey for a

carbonate based material. The value is larger than the value obtained from the shear box tests. The value of the JCS in the table is the value obtained for the material in the uniaxial compressive strength tests. The results were substituted into Equation 2.14 to give the estimate for the JRC listed in the table. The JRC results obtained from the tilt tests confirm that both materials had similar smooth planar roughness profiles. By substituting the results for the JRC, the JCS and $\phi_{w(r)}$ into Equations 2.13, relationships describing the residual shear strength of the discontinuity in terms of the normal stress acting on the discontinuity for each material were established.

Figure 6.7 shows a comparison between the predicted and the measured shear strength envelopes obtained from this analysis and those obtained from the shear box test. It can be seen that Barton's criterion significantly over estimates the shear strength of the discontinuities. The inability of the criterion to reasonably model the behaviour of the discontinuities most likely stems from the difficulties associated with obtaining suitable friction angles from the tilt test rather than with the criterion itself. The criterion has been independently validated (Xu and H.de Freitas [160]).

The reasons why a difference occurred between the values of friction angle obtained from the shear and the tilt tests were discussed in Section 2.5. These reasons relate to the non-linear relationship between the shear stress and the normal stress at low normal stresses and to the fact that shearing through the asperities will only occur at higher normal stresses than can be applied in the tilt test. In conclusion, if tilt test data is to be used to determine shear strength parameters, serious consideration must be given to the range of normal stresses at which the criterion will be applied.

Table 6.5. JRC test results.

Wall Material	$\phi_{w(p)}$	$\phi_{w(r)}$	σ_n (MPa)	JCS (MPa)	JRC
gypsum cement	41.8°	41.7°	0.116	37.6	0.04
cement/sand	41.0°	39.4°	0.255	24.0	0.81

6.5. Summary

The results from a comprehensive investigation to determine the material properties of the intact material and the discontinuities have been discussed. These results have shown that the modelling materials satisfied reasonably the requirements for similitude with natural rock. The shear stiffness of the discontinuities has been defined with respect to the normal stress in terms of a non-linear relationship. The shear strength has been defined with respect to the normal stress in terms of a linear Mohr-Coulomb relationship. A comparison of the results from the direct shear tests was made with results predicted by Barton's yield criterion based on input data from a tilt test. These results have shown that the tilt test over-estimates the frictional component of the shear strength, leading the yield criterion to over-estimate the shear strength of the discontinuities.

The next stage of the research involved testing specimens containing multiple discontinuities to determine the influence of the discontinuities on the strength and deformability of the specimens. The results of this research are described in the following chapter.

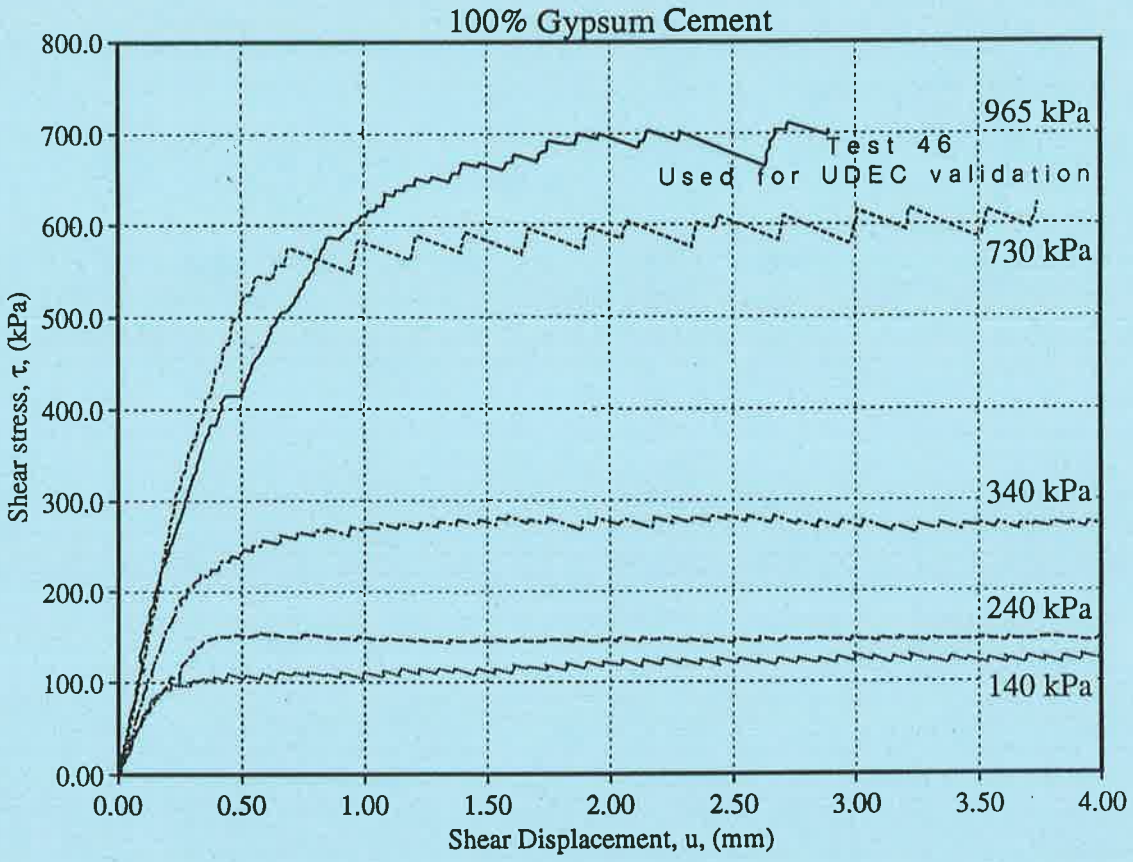

Figure 6.1. Shear stress versus shear displacement plots obtained from shear box tests on discontinuities having gypsum cement wall material.

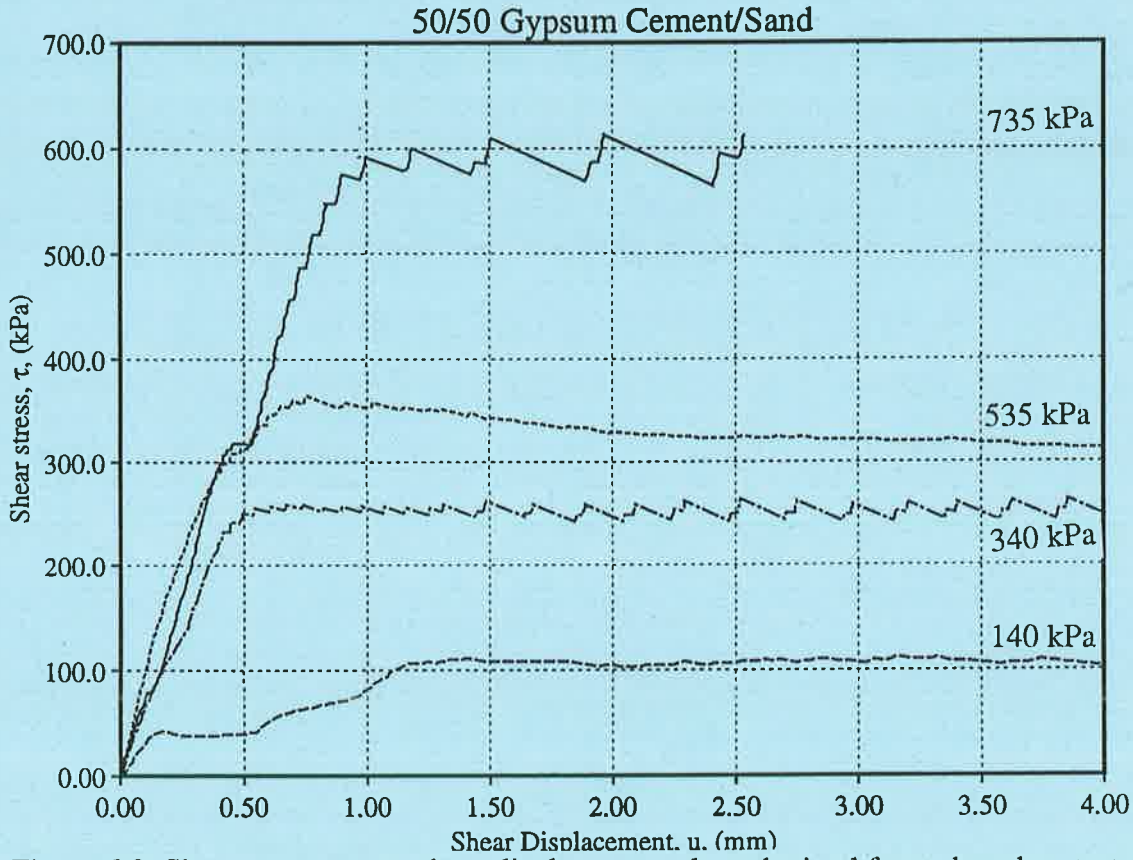

Figure 6.2. Shear stress versus shear displacement plots obtained from shear box tests on discontinuities having cement/sand wall material.

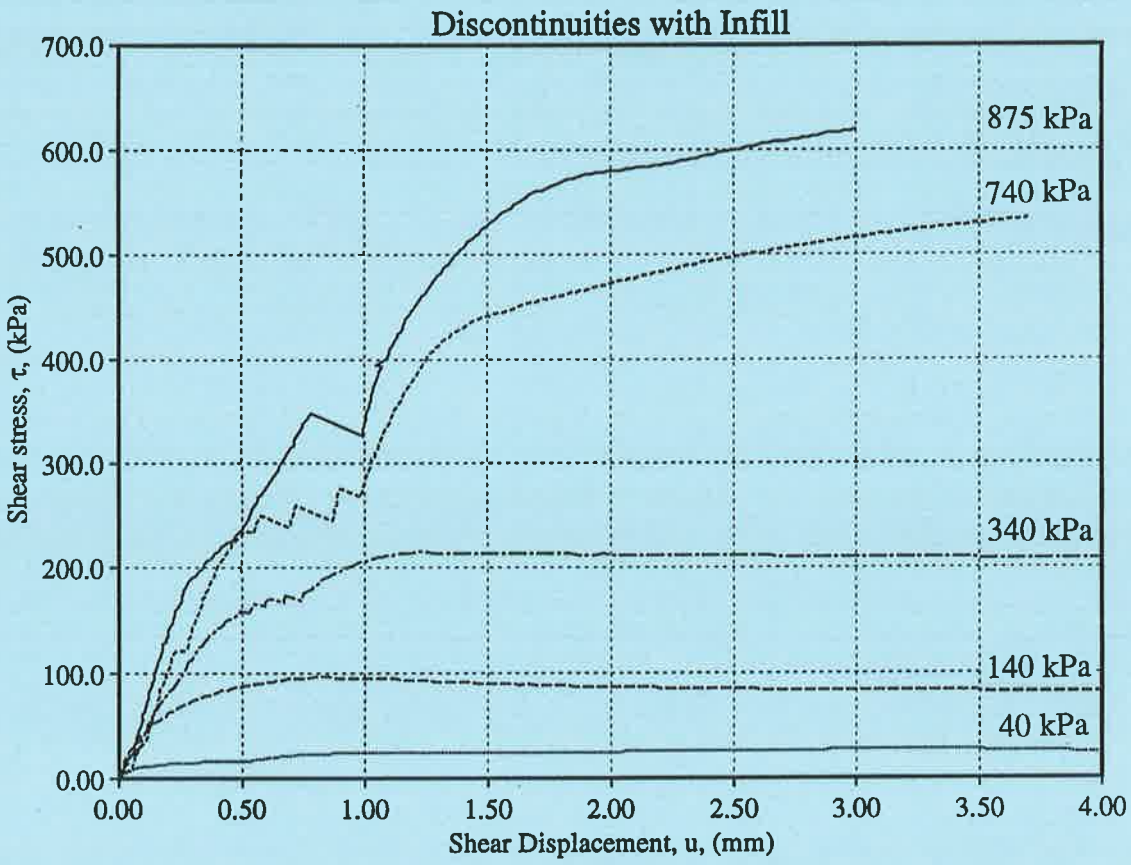

Figure 6.3. Shear stress versus shear displacement plots obtained from shear box tests on discontinuities having Celite infill on a cement/sand wall material.

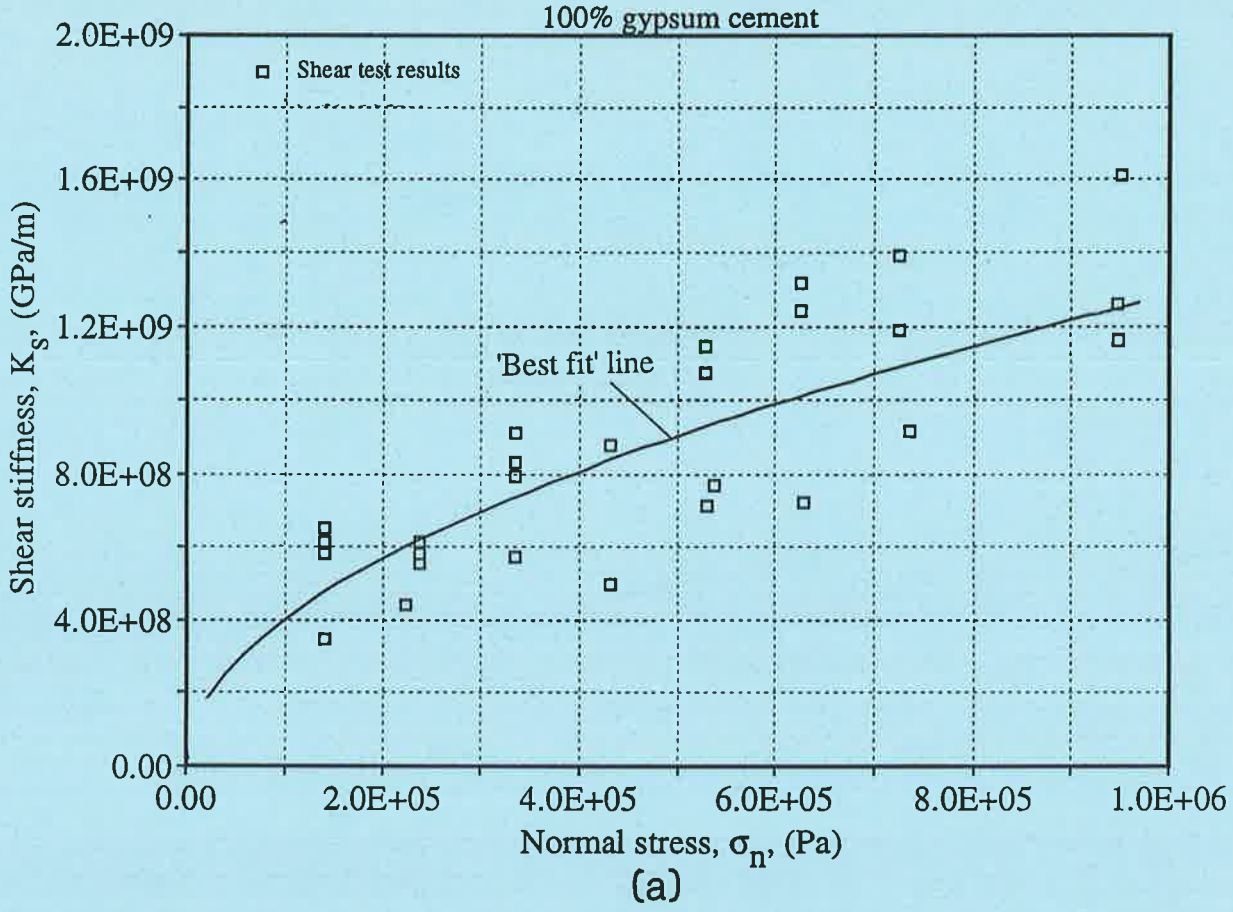

(a)

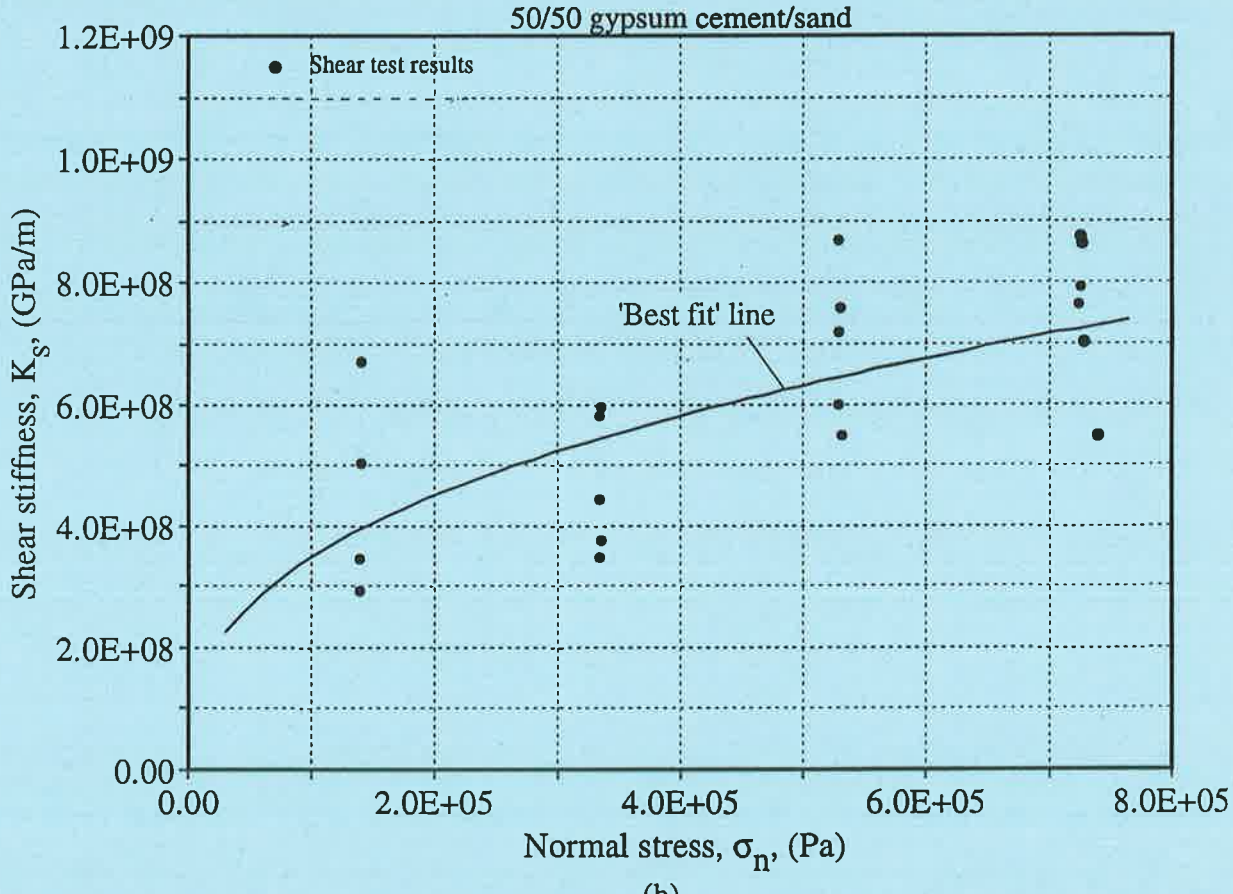

(b)

Figure 6.4(a)-(b). Variation in shear stiffness with normal stress for clean discontinuities intersecting (a) 100% and (b) 50/50 material.

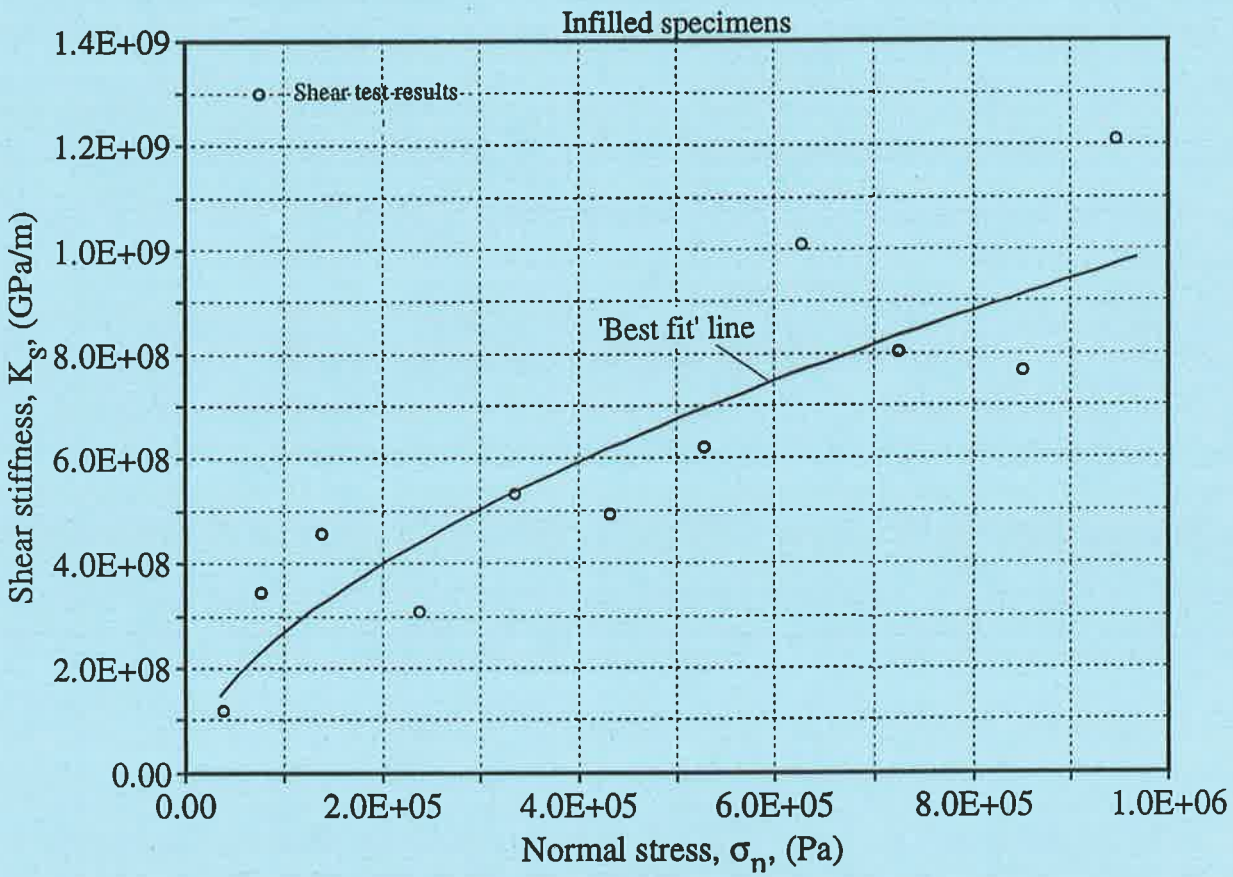

Figure 6.4(c). Variation in shear stiffness with normal stress for discontinuities containing infill.

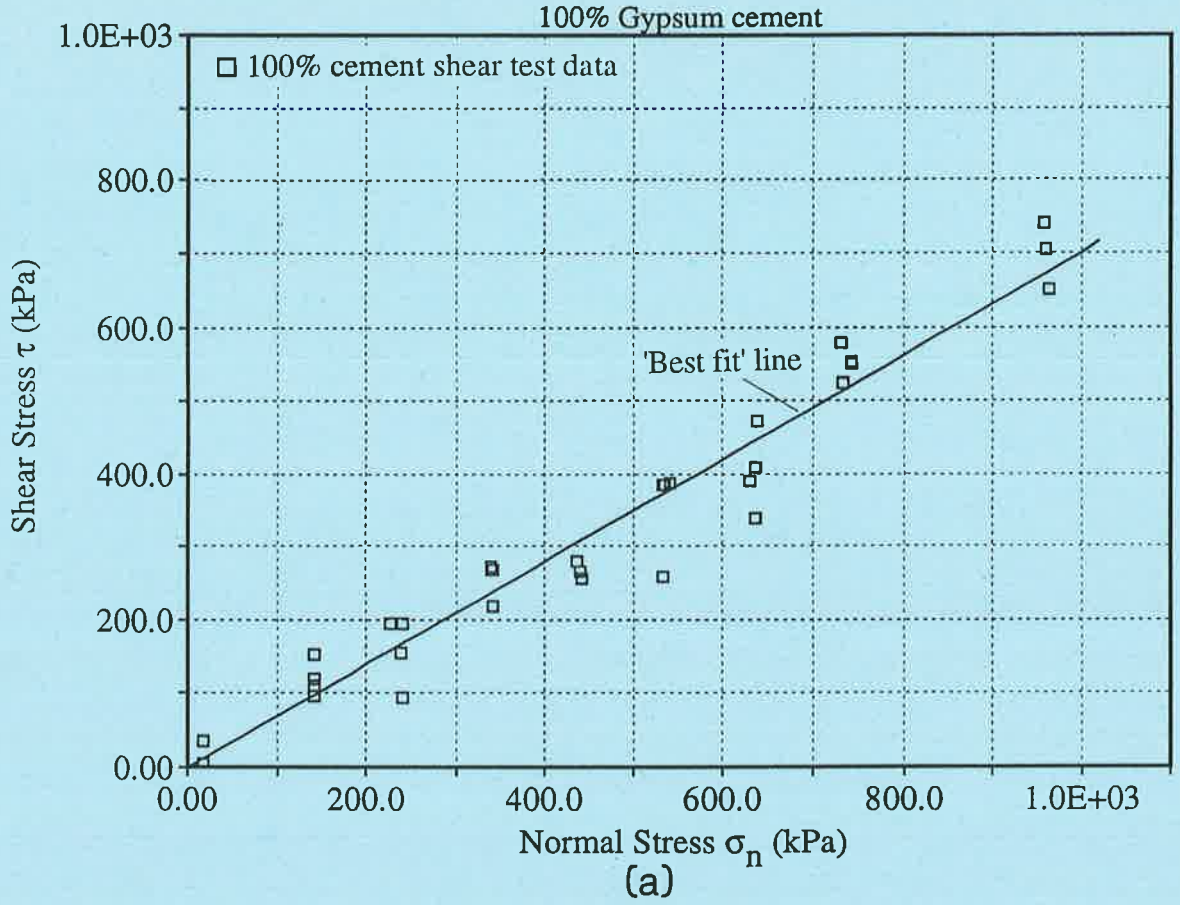

(a)

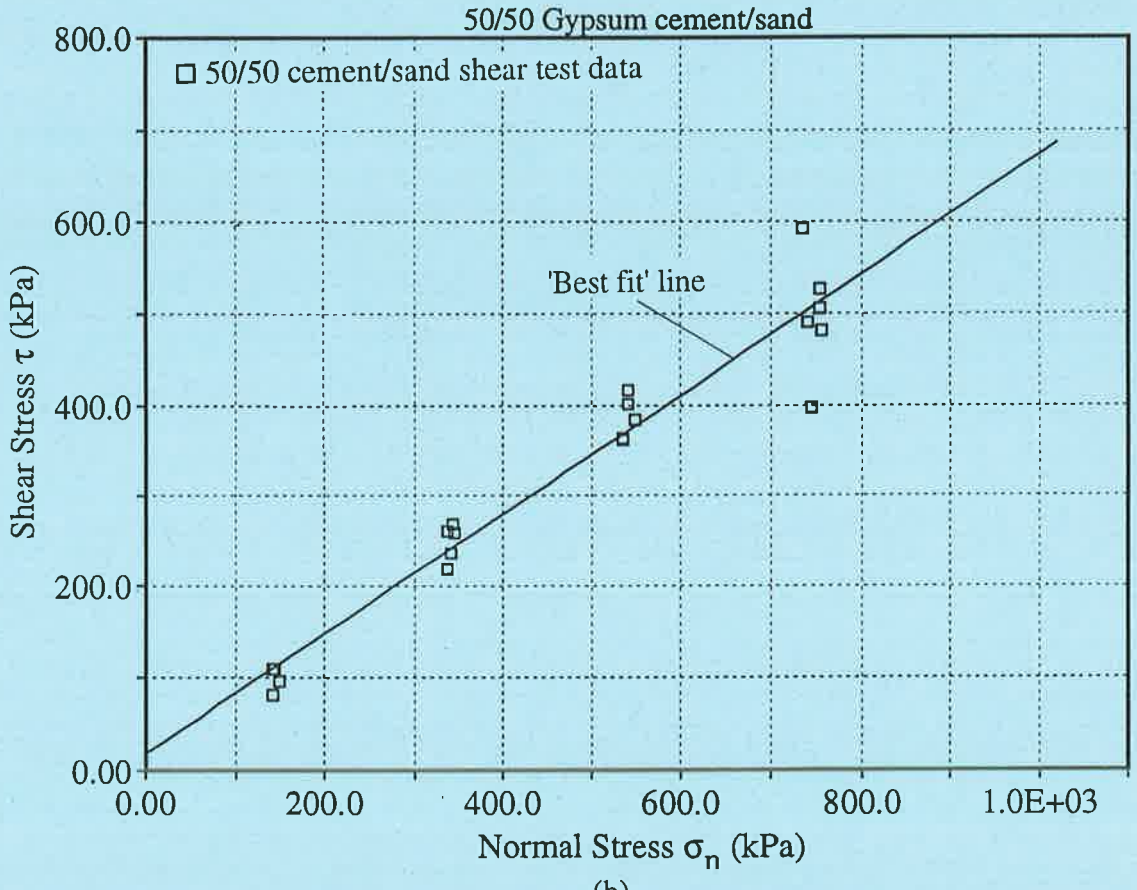

(b)

Figure 6.5(a)-(b). Variation in shear stress at yield with normal stress for discontinuities intersecting (a) 100% and (b) 50/50 material.

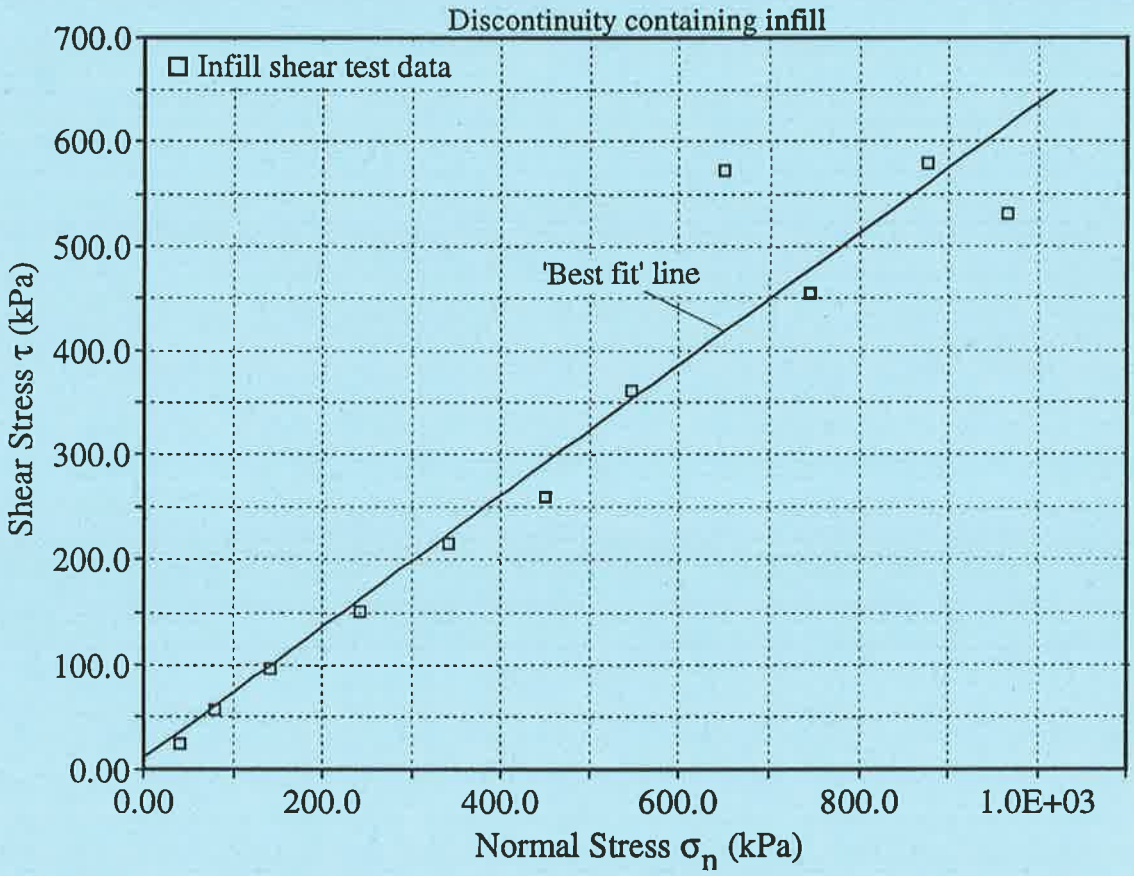

Figure 6.5(c). Variation in shear stress at yield with normal stress for discontinuities containing infill.

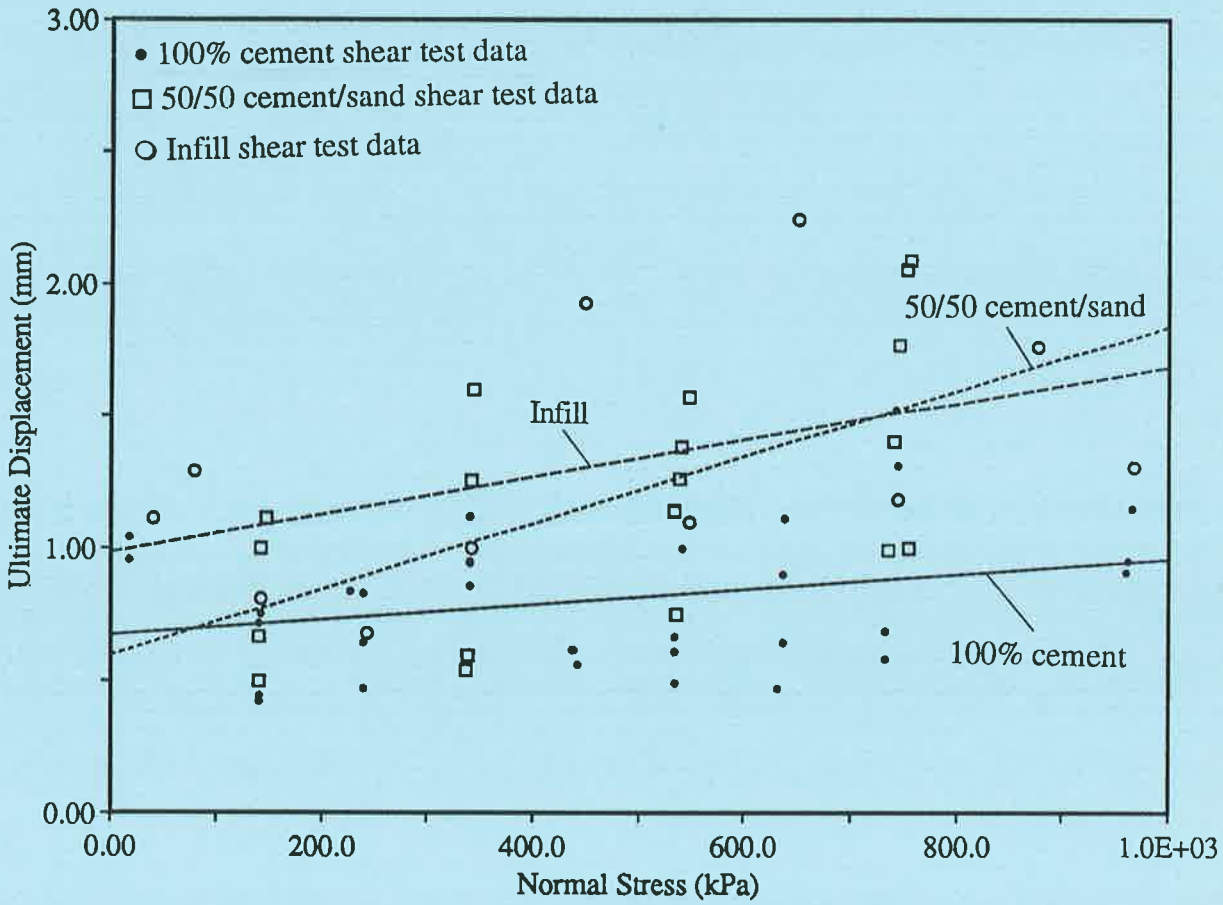

Figure 6.6. Variation in the shear displacement at yield with normal stress for clean discontinuities and discontinuities containing infill.

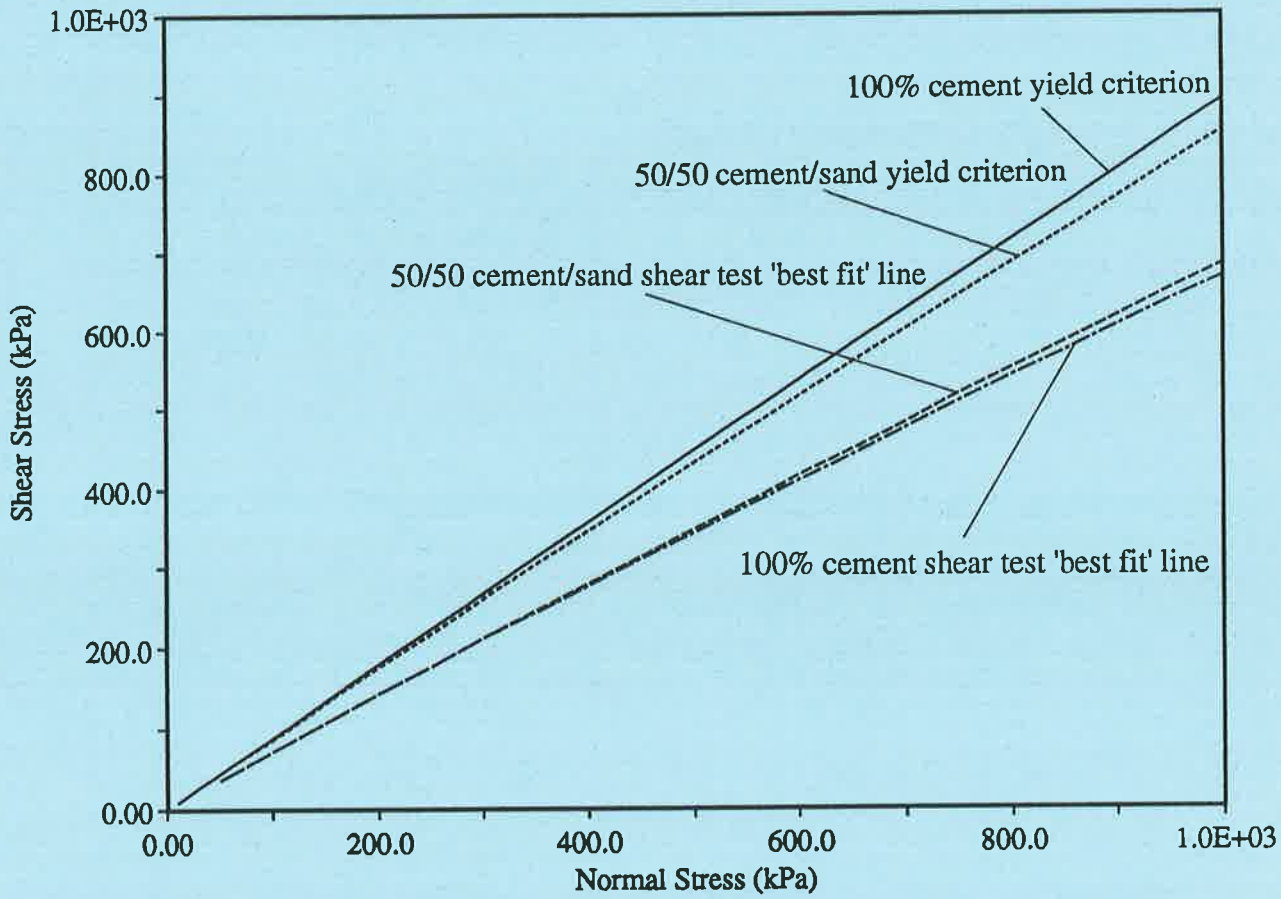

Figure 6.7. Comparison of analytical and laboratory obtained envelopes describing variation in the shear strength of discontinuities at yield with normal stress.

Chapter 7.
Experimental Programme - Part 2
Tests to Determine the Properties of Discontinuous Models.

Chapter 7. Experimental Programme - Part 2: Tests to Determine the Properties of Discontinuous Models.

7.1. Introduction

A series of triaxial tests was carried out to investigate the relationship between major and minor principal stresses and deformation for discontinuous cylindrical specimens. The design of the discontinuous specimens was discussed in Section 3.4 and the manufacture of these specimens was described in Sections 4.4 to 4.6. This chapter describes the setting up of the triaxial cell and the preparation of specimens for testing. The test procedure and the methodology adopted for analysing the test data at the completion of the test are also described. The results from the series of tests are then discussed in detail.

7.2. Triaxial Testing Procedure.

At the start of each test, the top cap of the Hoek cell was screwed anti-clockwise, to raise it to a sufficient height to clean and inspect the top seal. During specimen insertion and removal, the modelling material tended to collect more around this seal than on the bottom seal and hence the simple practice of regularly keeping the seal clean ensured that leakage was minimised. Whenever the rate of leakage increased between tests, the cell was raised from its supporting stand, the bottom piston was removed and the bottom seal was also cleaned.

A paper jacket containing a discontinuous specimen was placed into the lifting frame that was then slowly lowered into the cell. Even though there was little risk of the straps on the frame interfering with specimen deformation or block displacements during a test, care was taken to position the specimen in the frame in a manner designed to reduce this risk. For example, if the dip direction of each discontinuity plane was assumed to be either 0° or 180°, the straps were located at 90° and 270°, respectively. The next stage of the assembly procedure involved fitting the upper piston, complete with the LVDT holding ring, into the cell. The lifting straps were positioned to pass freely through the gap between the upper piston and the top cell cap. The straps were, therefore, able to slide in this gap during triaxial testing and not restrict dilation of the discontinuous specimen.

The plunger on each LVDT was positioned to contact the upper cell cap, thereby enabling any axial displacement of the upper piston during a test to be recorded. The upper spherical seat was placed onto the upper piston and the Hoek cell rolled into position on the Amsler loading frame. The upper platen of the loading frame was then positioned by moving the crosshead until it just touched the upper spherical seat. In all tests, the specimens tended to dilate so the predominant action of the linear displacement pump was to remove fluid from the cell. The piston of the linear displacement pump was, therefore, fully advanced so that the maximum volume of fluid could be withdrawn. Finally, the data logger was initialised to provide a reference mark from which all transducer readings would be based. Following the initialisation, the logger continually monitored the outputs from the transducers and stored the data on disk.

At the beginning of each test, it was desirable to achieve hydrostatic loading of the specimen by increasing the system pressure and the axial load on the specimen simultaneously until the required system pressure was achieved. Hydrostatic conditions could, however, only be achieved if the system pressure and the load frame were automatically controlled in a closed feedback loop. As such equipment was not available, hydrostatic loading conditions could only be approximated.

The manual mode was selected on the controller and the external, electric, gear pump was then used to slowly fill the hydraulic system. At low pressure, air that had entered the annulus of the triaxial cell between tests tended to bleed past the top seal on the membrane and the cell cap. As the pressure increased, the seal became effective. The system pressure was then ramped in steps while being constantly monitored with the Bourdon tube gauge and from the real time display on the data logger. Following each increase in the system pressure, the loading frame was used to increase the axial load on the specimen. Because the helix angle on the threaded column of the loading frame was low, the crosshead could be considered to be fixed with respect to axial forces acting upon it from below. The axial load on the specimen, therefore, increased with each increase in the system pressure, due to the Poisson effect. These increases had the effect of linearising the stepped stress path but not one of creating hydrostatic conditions.

When the system pressure reached a value close to that required for the particular test, minor adjustments of the linear displacement pump enabled the desired specimen confining pressure to be accurately selected. Because these adjustments moved the linear displacement pump piston from its initialised position the adjustments were corrected for when the test data was processed after the test. The automatic mode was then selected on the controller and the pressure in the system at that time became the reference pressure. This pressure would, thereafter, be maintained by the linear displacement pump provided the displacement limits of the pump piston were not exceeded.

The triaxial specimen was subjected to axial loading at a constant rate of 17kN/s as required by the ISRM guidelines [74]. Unlike the Seidner loading frame, the Amsler did not possess a load rate indicator. The loading rate was, therefore, kept within the ISRM guidelines by noting the rate at which the applied load changed with time using a stop-watch, and adjusting the rate accordingly. In order to monitor the load versus deformation behaviour of a specimen during a test, the axial force on the specimen was continually monitored and plotted against the axial deformation on an XY plotter. The test was considered complete when either:

(1) there was no increase in the axial load with increasing axial compression,

(2) axial deformation exceeded the 20mm capacity of the LVDTs or

(3) the cell began to leak as the membrane was forced from its sealing surface as a result of excessive lateral expansion of the specimen.

Due to the limited internal volume of the linear displacement pump, a point was reached during the majority of tests when the fluid in the hydraulic system could no longer be withdrawn by the pump to compensate for the dilation of the specimen. Subsequently, pressure control could only be achieved by opening the bleed off valve by an amount small enough to ensure that fluid was withdrawn at a rate sufficient to maintain the desired pressure. It was, however, impossible to monitor specimen volume changes after this point.

Details regarding the number of tests conducted are summarised in Table 7.1. At the completion of each of these tests, the logger and computer were stopped, the loading frame delivery valve was closed and the bleed off valve opened. The upper platen of the loading frame was then raised. By applying a large system pressure to the cell at this stage, an attempt was made to compress the deformed specimen back to a cylindrical shape in order to facilitate its removal from the cell. The cell was rolled from the loading frame and the system pressure decreased to atmospheric. After the upper spherical seat and piston were removed from the cell, the lifting frame was used to remove the specimen from the cell in the manner described in Section 5.3.2.

7.3. Processing of Test Results.

On completion of a test, the single column sequential raw data file stored on the data logging computer was re-written in tabular format. Each column of the table represented the data from a particular transducer. The method by which the raw tabulated data were then processed for further analysis will be briefly discussed.

Table 7.1. Details of Tests Conducted on Discontinuous Models.

Geo.	Material Type	No. of Tests Conducted	Total
1	100%	11	
	50/50	17	
	Infill	12	40
2	100%	9	
	50/50	14	
	Infill	13	36
3	100%	14	
	50/50	13	
	Infill	12	39
4	100%	14	
	50/50	15	
	Infill	12	41
		Total	156

7.3.1. Axial Deformation.

Each row of the raw data file contained axial displacement values from up to 4 LVDTs. When the raw axial displacements, $\delta_{a(i)}$ (i = 1 to 4), from all LVDTs had been read, the average axial deformation of the specimen, δ_a, was determined.

7.3.2. Volumetric Deformation Ratio.

The change in volume of the specimen, δ_v, is defined as,

$$\delta_v = \delta_{v(i)} + \delta_{v(d)} + \delta_{v(w)} + \delta_{v(a)} \qquad (7.1)$$

where $\delta_{v(i)}$ is the change in volume of the intact material,

$\delta_{v(d)}$ and $\delta_{v(w)}$ are the changes in volume due to the normal and shear deformation of the discontinuities and

$\delta_{v(a)}$ is the change in volume due to the formation of voids between blocks.

Equation 7.1 was solved after initially solving Equation 5.5. In order to solve these equations, the parameters that had to be determined were:

(1) the volume of fluid displaced by the linear displacement pump, V_p,

(2) the volume of fluid that had leaked from the system, V_l and

(3) the volume of penetration of the upper piston into the cell, V_c.

The volume of fluid displaced by the linear displacement pump, V_p, was calculated using the equation,

$$V_p = \delta_p \times A_p \tag{7.2}$$

where A_p is the cross sectional area of the linear displacement pump cylinder and
δ_p is the linear displacement of the linear displacement pump piston.

The method discussed in Section 5.6.2 was used to determine V_l. This method required that the time elapsed since the beginning of the test be known. As a point was logged every 0.45 seconds by the data logger the elapsed time was obtained by multiplying the number of datum by 0.45 seconds.

The volume of penetration of the upper piston of the triaxial cell into the cell, V_c, was determined using,

$$V_c = \delta_{a(ave)} \times A_{piston} \tag{7.3}$$

where A_{piston} is the cross sectional area of the triaxial cell piston.

The volumetric deformation ratio of the specimen, Δ_v , was determined using:

$$\Delta_v = \frac{\delta_v}{V} \tag{7.4}$$

where V is the initial volume of the specimen.

7.3.3. Axial Stress.

The magnitude of the major principal stress on the specimen prior to shear deformations occurring along any pre-existing or newly developed discontinuity was determined by the equation,

$$\sigma_1 = \frac{F_a}{A} \qquad (7.5)$$

where A is the initial cross sectional area of the specimen and

F_a is the force acting through the major principal axis of the specimen.

No allowances were made in the formula given above to account for changes in the cross-sectional area of the specimen. Such corrections assume that the specimen deformed as a right cylinder. This assumption cannot be justified as the influence of platen end effect and the presence of the discontinuities produced shear stresses at the ends of the specimen and significantly altered the stress distribution throughout the specimen.

Equation 7.5 was inappropriate after shear deformations occurred along single or multiple discontinuities because the effective plan area of the specimen, A_{eff}, continually decreased as the specimen axially deformed. Under these conditions, the value of the major principal stress on the specimen was determined by the equation,

$$\sigma_1 = \frac{F_a}{A_{eff}} \qquad (7.6)$$

Head [62] expressed the effective plan area of the specimen, for cases in which shear deformations occur along a single discontinuity, in terms of the equation ,

$$A_{eff} = \tfrac{1}{2} D^2 (\psi - \sin \psi \cos \psi) \qquad (7.7)$$

where D is the diameter of the specimen,

$\psi = acos\left(\delta_a \frac{L}{D} \tan \beta_w\right)$

δ_a is the average axial deformation of the specimen,

L is the original length of the specimen and

β_w is the acute angle between the a unit vector normal to the discontinuity and the major axis through the specimen.

In the present series of tests, where multiple discontinuities intersected the specimens, shear deformation often occurred simultaneously along multiple discontinuities. In these cases it

would have been impractical to estimate the effective area appropriate to each test. Instead, an estimate of the effective area was made, based on the orientation of the single plane along which the majority of the slip had occurred. The orientation of this plane was determined by inspecting the paper jacket after the test and then applying Equations 7.6 and 7.7. The point at which these shear deformations occurred in each of the tests was determined by reference to the volumetric deformation, Δ_v, versus axial deformation, δ_a, plot and the axial force, F_a, versus axial deformation, δ_a, plot. When the slope of the Δ_v versus δ_a plot became positive and stick slip oscillations became apparent on the F_a versus δ_a plot, it was assumed that shear deformations were occurring along one or more discontinuities.

7.4. Discussion of Test Results.

7.4.1. Deformation Mechanisms.

At the end of each test, the paper jacket was inspected and the individual blocks were gently removed from the jacket. As discussed in Section 4.6, the paper jacket ensured that a specimen maintained its integrity during insertion into and removal from the cell. The jacket also retained a record of the relative magnitude and direction of the displacements suffered by the individual blocks during the test. It was, however, inappropriate to use directly any measurements obtained from the jacket as deformations that occurred during the removal of the specimen from the cell were also recorded.

The inspection of the individual blocks after a test ascertained the extent and orientation of any block fracturing that had not been obvious when the jacket had been inspected. Details of all block deformations and fracturing were recorded. Figures 7.1(a)-(d) show typical examples of the results. (Note: In this study the term discontinuity refers to the discontinuities shown in Figure 3.9. The term fracture or crack is used to refer to discontinuities that developed through intact material during testing). By observing the logged results, it was seen that many of the intact blocks forming the Geometry 1 and 2 specimens had deformed during testing and a large number of cracks had developed through intact material. A large amount of the total axial deformation of these specimens appeared to

have been due to shear deformation occurring along cracks. This result appeared to be particularly true for the Geometry 2 specimens. The orientation of the fractures had a common trend and a normal orientated such that β_w ranged from 65° to 75°. This result agrees well with that obtained from the material property tests discussed in Chapter 6 and Appendix C. The noticeable lack of fracturing of the blocks in the Geometry 3 and 4 specimens suggested that the majority of the axial deformation of these specimens was the result of shear deformation occurring along pre-existing discontinuities. In the Geometry 4 model it was obvious that shear deformation had occurred along Discontinuities 1, 2 and 3 after cracks had developed through the intact bridges. In all Geometries there appeared consistently to be heavily crushed zones wherever one discontinuity intersected another. This result suggests that even though shear deformation might have occurred along a particular discontinuity, thereby causing intersecting discontinuities to be terminated, the terminated discontinuities still influenced the behaviour of the shearing discontinuity.

As it was difficult to be definitive about the deformation mechanisms solely by viewing the paper jackets subsequent to a test, an alternative method was developed to assist in this process. This method involved assembling one specimen from each of the four geometries within a thin rubber membrane, axially loading the specimen in stages and photographing the result through the translucent membrane. Figures 7.2(a)-(e) show the final result from each of these studies. Figure 7.2(a) shows that the Geometry 1 specimens deformed as a series of three wedges that formed when shear deformations occurred along Discontinuities 5 and 6. Smaller amounts of shear deformations occurred along Discontinuities 7 and 8. Block rotation and separation is obvious within the centre wedge. The upper wedge shows fractures to have developed through several blocks.

The Geometry 2 specimen (Figure 7.2(b)) was able to sustain a higher axial load than the Geometry 1 specimen for a comparable value of axial deformation. In this case only minor shear deformations along discontinuities were seen with the major amount of axial deformation being the result of shear deformations occurring along fractures. It should be noted that the only geometric difference between Geometries 1 and 2 was that Discontinuity

5 was absent in Geometry 2. The fact that shear deformations occurred along most discontinuities in Geometry 1, yet the same discontinuities did not undergo shear deformations in Geometry 2 highlights the major influence that Discontinuity 5 had on the behaviour of the specimens. One possible scenario that might have caused this result is as follows. Shear deformations occurred along Discontinuity 5 in Geometry 1 specimens and the relative positions of several of the intact blocks on either side of the discontinuity changed. This change in block positions caused the shear stress acting along Discontinuities 6, 7 and 8 to increase until the shear strength of these discontinuities was achieved and shear deformations resulted.

Figures 7.2(c) and 7.2(d) highlight disparate deformation mechanisms that occurred in the Geometry 3 specimens. In Figure 7.2(c) the shear strength of Discontinuity 4 was achieved at a lower value of axial load than for the other discontinuities. Shear deformation along this discontinuity prevented Discontinuities 1, 2 or 3 shearing. An alternative deformation mechanism for Geometry 3 is shown in Figure 7.2(d). This mechanism occurred when Discontinuity 4 was momentarily constrained, thereby allowing shear deformations to occur along Discontinuities 2 and 3. Local zones of crushing were evident whichever deformation mechanism occurred. The inspection of the paper jackets showed that the individual blocks in this specimen were not deformed to the same extent during each test as were those in the tests on the Geometry 1 and 2 specimens.

Figure 7.2(e) shows the deformation mechanism for Geometry 4 specimens. The photo study was not as successful as the other studies because the specimen tended to buckle rather than undergo the deformation mechanism that occurred in the triaxial tests as recorded on the paper jackets. Inspection of the paper jackets showed that the axial deformation of the specimen resulted from shear deformations occurring along Discontinuity 3 after the shear stress within the plane containing the discontinuity was sufficient to cause shearing through the intact bridge. A similar mechanism appeared to have occurred with Discontinuity 2. Several of the thinner blocks were fractured in the plane of maximum shear stress and it can

be assumed that much of this fracturing occurred prior to the discontinuities shearing through the bridges.

7.4.2. Strength and Deformation Relationships.

The tabulated data from each of the tests is presented in Appendix D. A summary of the properties that are tabulated in the Appendix is listed in Table 7.2. It would have been impractical and unhelpful to include 290 plots generated from the 156 tests carried out during this study and, therefore, only those plots required to demonstrate the behaviour of the four geometries and three material combinations at a range of cell pressure have been included. Fifty five axial stress versus axial deformation and volumetric deformation ratio versus axial deformation plots are presented in Appendix E as Figures E.1 to E.55.

The axial stress versus axial deformation plots provide much of the essential information concerning the ability of the specimen to withstand the deformation. Compression was considered to be positive in these plots. The volumetric deformation ratio versus axial deformation plots describe the overall response of the specimens to the deformation. Dilation was considered to be positive in these plots.

The axial stress, σ_1, versus axial deformation, δ_a, curves shown in Figures 7.3(a)-(c) to 7.6(a)-(c) highlight the systematic increase in the strength and decrease in the deformability of the specimens with increases in the confining pressure. Figures 7.7(a)-(b) and 7.8(a)-(b) highlight the influence of the specimen geometry on the strength and deformability of the specimens.

In Figure 7.7(a) and (b), Geometry 2 is seen to have the highest and Geometry 3 the lowest yield strength of the four geometries. This yield strength is compared to the yield strength of an intact specimen in Figure 7.8(a) and (b). This result shows that the yield strength of the Geometry 2 specimen was similar to the residual strength of the intact specimen. In this geometry, axial deformation of the specimen was predominantly a result of failure occurring through intact material. This result was not, however, consistent. The yield strength of all

Table 7.2. Test details tabulated in Appendix D.

Column	Property
1	Test number
2	Confining pressure on the specimen, σ_3,
3	Axial stress at which the specimen began to deform due to shear deformation along discontinuities, $\sigma_{1(slip)}$,
4	Axial stress at which the specimen began to deform due to plastic flow, $\sigma_{1(peak)}$
5	Ratio between the axial deformation at which (3) occurred and the original length of the specimen, $\Delta_{a(peak)}$ (Note: this ratio is expressed as a percentage of the original length)
6	Ratio between the axial deformation at which (4) occurred and the original length of the specimen, $\Delta_{a(peak)}$
7	Axial stiffness of the specimen prior to shear deformations occurring along discontinuities, $K_{a(A)}$
8	Axial stiffness of the specimen subsequent to shear deformations occurring along discontinuities, $K_{a(B)}$
9	Volumetric deformation ratio at which the specimens began to dilate, $\Delta_{v(min)}$ (Note: At this point, $\frac{\partial \Delta_v}{\partial \delta_a} = 0$ and the volume of the specimen is less than the original volume. It is only when $\Delta_v > 0$ that the volume of the specimen is greater than the original volume).

specimens was consistently less than the yield strength of the intact material.

Each of the four geometries had a characteristic shape to its respective axial stress versus axial deformation curve. There were, however, four regions within each curve that were common to all geometries. These regions are highlighted in Figure 7.9. A similar result was found by Einstein and Hirschfeld [50] to occur with models constructed from uniformly shaped parallelepipedal blocks. Figure 7.9 shows a typical axial stress versus axial deformation plot and the associated volumetric change versus axial deformation plot (contraction is -ve).

Region I

Region I is characterised by non-linear axial stress versus axial deformation behaviour and volumetric change versus axial deformation behaviour. This behaviour resulted from the 'loose' blocks making contact with neighbouring blocks as the deviator stress on the specimen was increased. Similar behaviour has been reported in studies with discontinuous specimens by Einstein and Hirschfeld [50] and Yoshinaka and Yamabe [162] and the behaviour has been seen to occur in natural discontinuous rocks (Jaeger [79]). This region was, on average, completed within less than 1mm of axial deformation.

Region II

Within linear Region II the volume of the specimens decreased as the blocks became tightly packed, asperities on the discontinuity surfaces failed and the infill and intact material compressed. The line of best fit through the test data defining σ_3 in terms of the axial stiffness, K_a, of the specimens (Figures 7.10 to 7.13) can be defined by a power curve of the form,

$$K_a = a_{(k)} \sigma_3^{b(k)} \qquad (7.8)$$

where $a_{(k)}$ and $b_{(k)}$ are constants that depend on the geometry and the material type. The values of $a_{(k)}$ and $b_{(k)}$ and the coefficient of regression, are given in Table 7.3.

Geometry 3 and 4 specimens axially deformed as a result of shear deformation along discontinuities. For Geometry 3 specimens the shape of the K_a versus σ_3 curves are similar and hence the parameter $b_{(k)}$ is comparable despite changes in the material type. This result reflects the similar stiffness of the discontinuities for the two materials. For the Geometry 3 and 4 specimens, the lower strength of the infill material reduced $a_{(k)}$ and thereby offset the infill curve from the 50/50 curve. The influence of material strength on stiffness is seen in the results for Geometry 4. As with Geometry 3, the shape of the curves for all materials and hence $b_{(k)}$, is similar. The higher strength of the 100% material, which became significant in the shearing of the bridges, is reflected as an increase in $a_{(k)}$.

The axial deformation of the Geometry 1 and the Geometry 2 specimens involved shearing along fractures through intact material. As the 100% material had a higher strength and a greater shear stiffness than the 50/50 material, $a_{(k)}$ and $b_{(k)}$ are higher. The increase in $a_{(k)}$ for the Geometry 2 specimen, compared to the other specimens, reflects the influence of the discontinuity geometry on the axial stiffness of the specimens. The values of $b_{(k)}$ for the 100% and 50/50 Geometry 1 specimens are similar to the values for the Geometry 2 specimens. A similarity also exists in $b_{(k)}$ for the 100% and the 50/50 Geometry 3 and Geometry 4 specimens. This consistency suggests that $b_{(k)}$ is very dependent on the discontinuity geometry.

Table 7.3.Coefficients applicable to Equation 7.8 that defines the axial stiffness of the specimens in terms of the confining pressure (Units of $a_{(k)}$ are MPa).

	Geometry											
	1			2			3			4		
	100%	50/50	Fill	100%	50/50	Fill	100%	50/50	Fill	100%	50/50	Fill
$a_{(k)}$	1.15	1.90	0.93	2.27	2.17	1.12	1.27	1.22	0.97	1.42	1.15	0.92
$b_{(k)}$	0.41	0.26	0.63	0.43	0.24	0.47	0.57	0.62	0.66	0.64	0.53	0.51
r^2	0.72	0.44	0.81	0.62	0.79	0.59	0.89	0.86	0.85	0.92	0.83	0.89

Analytical decomposition procedures assume that the deformation of a rock mass in any direction is equivalent to the summation of the deformations of the discontinuities and those of the intact material in the same direction. On the basis of this assumption, Yoshinaka and Yamabe [162] showed that the deformation of a specimen constructed from parallelepipedal blocks could be estimated by simple summation (see Equation 2.12).

Table 7.4 compares the average axial stiffness of each geometry, determined from the triaxial tests, as a percentage of the analytical stiffness estimated with Equation 2.12. All results show reasonable agreement between the experimental and the analytical stiffness of the specimens. Geometries 1, 2 and 4 show less agreement with the analytical stiffness than does Geometry 3 due probably to the inability of the equation to account for block to block interaction and for the non-uniform roughness characteristics of fractures through intact material. A limitation of the equation is that while it is suitable for estimating the

Table 7.4. Average axial stiffness of the specimens, K_A, expressed as a percentage of the analytical stiffness determined using Equation 2.12.

	Geometry			
	1	2	3	4
$K_{A(measured)}/K_{A(analytical)}$	93%	93%	97%	81%

deformability of smooth discontinuities it is unable to allow for non-uniform roughness features encountered with natural discontinuities. The limitation of analytical equations, such as Equation 2.12, to model natural discontinuities has encouraged the development and use of numerical techniques for modelling discontinuous rock masses. The ability of the distinct element numerical method to predict the strength and deform mechanisms of the discontinuous specimens is investigated in Chapter 8.

Figures 7.14 to 7.17 show the volumetric contraction of the specimens as a function of σ_3. The average axial deformation at maximum specimen contraction for each of the specimens is listed in Table 7.5. The specimens containing the infill contracted more than the specimens containing clean discontinuities due to the compression of the infill material. The amount of axial deformation, required to achieve maximum contraction of the specimens with clean discontinuities, was independent of geometry. The amount of axial deformation was, however, proportional to β_w, if infill was present.

Region III

Within non-linear Region III stick slip oscillations occurred and the slope of the Δ_v versus δ_a curve became positive as the specimens begun to dilate. This behaviour indicated that the shear strength of pre-existing discontinuities, or that of fractures formed within Region II, had been achieved. Figures 7.18 to 7.21 highlight the change in the axial stiffness of the specimen, K_b, with changes in σ_3. The envelope defining the line of best fit through the test data can be defined by a power curve of the form,

$$K_b = a_{(b)}\, \sigma_3^{b(b)} \qquad (7.9)$$

where $a_{(b)}$, $b_{(b)}$ and the coefficient of regression are given in Table 7.6

Table 7.5. Average axial deformation required to achieve maximum specimen contraction (n/a: not available).

Material	Axial Deformation at Maximum Contraction (mm)			
	Geometry			
	1	2	3	4
100%	n/a	3.0	2.6	2.6
50/50	2.7	3.7	2.1	3.0
Fill	8.9	8.6	4.2	4.0

Table 7.6.Coefficients applicable to Equation 7.9 which defines the axial stiffness of the specimens in terms of the confining pressure (Units of $a_{(b)}$ are MPa).

	Geometry											
	1			2			3			4		
	100%	50/50	Fill	100%	50/50	Fill	100%	50/50	Fill	100%	50/50	Fill
$a_{(b)}$	0.51	0.50	0.44	0.36	0.39	0.33	1.69	1.83	0.68	1.58	1.09	0.79
$b_{(b)}$	0.31	0.29	0.38	0.17	0.57	0.46	0.50	0.34	0.29	0.70	0.10	0.68
r^2	0.17	0.23	0.21	0.11	0.45	0.60	0.52	0.63	0.27	0.84	0.03	0.84

The Geometry 1 and 2 specimens exhibited, on average, three times the stiffness of the Geometry 3 and 4 specimens in which shear deformations occurred primarily along smooth discontinuities. This difference in stiffness is reflected in the values of $a_{(b)}$ in Table 7.6 and in the figures. For all geometries, the material type influenced the value of $b_{(b)}$ to a greater extent than it did the value of $a_{(b)}$. The results do not, however, show a consistent trend in the way that the material type influenced $b_{(b)}$. The stiffness of the Geometry 1 and 2 specimens showed more variability than the Geometry 3 and 4 specimens due to the variation in the roughness of the fractures compared to that of the pre-existing discontinuities. The presence of infill material reduced the stiffness of the Geometry 1 and 2 specimens to a greater extent than it did for the Geometry 3 and 4 specimens. This result possibly occurred when the deformable layer of infill allowed the blocks in the Geometry 1 and 2 specimens to rotate, hinge and displace relative to each other.

Region IV

In non-linear Region IV the specimens achieved their peak axial stress prior to the onset of plastic flow. Figures 7.22 to 7.25 highlight the systematic increase in the strength of the specimens with increases in σ_3. The line of best fit through the test data was defined by a linear curve of the form:

$$\sigma_{1(peak)} = a_{(\sigma)} + b_{(\sigma)}\sigma_3 \qquad (7.10)$$

The value of the coefficients $a_{(\sigma)}$ and $b_{(\sigma)}$ and the coefficient of determination for each specimen, r^2, are listed in Table 7.7. These results show that, for all geometries, infill

generally reduced $b_{(\sigma)}$ from that applicable to specimens with clean discontinuities. The value of $a_{(\sigma)}$, which reflects the unconfined strength of the specimens, was significantly more for the Geometry 1 and 2 specimens than it was for the Geometry 3 and 4 specimens.

Table 7.8 lists the average strength of the specimens as a percentage of the strength of the intact material over the range of confining pressures used in the study. The results show that the presence of discontinuities significantly reduces the strength of an intact material. The amount of the reduction in strength varies, however, with changes in the geometry of the discontinuities. The strength of the material decreases as the angle, β_w, approaches the angle β_{crit} (Note: β_w is the angle between the normal to any fully persistent discontinuity intersecting a specimen and the major principal axis, $\beta_{crit} = 45^\circ + \phi_w/2$ and ϕ_w is the instantaneous friction angle of the discontinuity). In cases such as Geometry 4 where β_w is similar to β_{crit} and the discontinuities are not persistent, the strength of the specimen depends on the ratio between the non-persistent area of the discontinuity and the area of a discontinuity in which $\beta_w = \beta_{crit}$.

The strength of the Geometry 3 and 4 specimens is similar despite being made from dissimilar materials. These specimens deformed as a result of shear displacement occurring along discontinuities and therefore the strength of the specimens was directly related to the

Table 7.7. Strength coefficients applicable to Equation 7.10 that defines the strength of the specimens in terms of the confining pressure (Units of $a_{(\sigma)}$ are MPa).

	Geometry											
	1			2			3			4		
	100%	50/50	Fill	100%	50/50	Fill	100%	50/50	Fill	100%	50/50	Fill
$a_{(\sigma)}$	6.34	5.00	3.58	5.83	8.42	6.07	1.34	0.87	1.64	2.59	1.16	2.70
$b_{(\sigma)}$	6.45	9.57	6.69	10.1	7.88	5.04	7.14	6.02	5.01	7.00	7.47	5.44
r^2	0.94	0.92	0.81	0.98	0.94	0.41	0.98	0.98	0.92	0.82	0.96	0.89

Table 7.8. Average strength of specimens expressed as a percentage of the intact strength over the range 250kPa $\leq \sigma_3 \leq$ 1250kPa.

Geometry											
1			2			3			4		
100%	50/50	Fill	100%	50/50	Fill	100%	50/50	Fill	100%	50/50	Fill
28%	39%	27%	33%	46%	32%	16%	17%	17%	19%	21%	21%

shear strength of the discontinuities that, as shown in Figure 6.5(a)-(c), did not vary significantly between materials.

The strength of the Geometry 1 and 2 specimens, which deformed through a combination of fracture through intact material, block rotation and displacement, was reduced by the presence of the infill material. This behaviour could be explained by reference to the research of Zacas and Knox [163] in which the authors discussed the results from tests on discontinuous rock masses containing weak inclusions. These results highlighted how rock blocks surrounding soft material would rotate and sink into the infill. In relation to the present study, this behaviour could have resulted in an uneven stress distribution developing throughout the blocks and the development of stress concentrations at the contacts. Ultimately this process could have led to the premature failure of the individual blocks and hence the specimen.

This study was primarily concerned with the behaviour of specimens comprised of distinct blocks and, therefore, no tests were carried out on specimens containing a single

discontinuity. The results of tests on anisotropic specimens by other researchers were discussed in Section 2.4.2. An estimate of the yield strength of an anisotropic specimen comprised of material having the same properties as the materials used in this study can be obtained with Equation 2.2. It has been pointed out a number of times in this study that while this equation generally provides an incorrect estimation of the yield strength of a specimen for cases in which $\beta_w \leq \phi_w$, the equation can be applied to cases in which $\beta_w > \phi_w$.

For example, Equation 2.2 predicts that a specimen comprised of 100% gypsum cement material intersected by a discontinuity, in which $\beta_w = 60^o$, and subjected to a confining pressure of 250kPa, would have a yield strength of 0.9MPa. Geometry 3 specimens contained a discontinuity orientated at 60^o and it is along this discontinuity that the major amount of shear deformation occurred. It could, therefore, be expected that this specimen would have a similar yield strength. The yield strength of the Geometry 3 specimen at this confining pressure is found, by the application of Equation 7.10, to be 3MPa . The disparity between the analytical and the experimental results confirms that it is inappropriate to use two-dimensional equations based on anisotropy theory that do not allow for surface roughness features to predict the strength of three-dimensional specimens containing multiple discontinuities. The physical explanation for the results is that if, as in the case of the Geometry 3 specimens, there are discontinuities that intersect the discontinuity along which shear deformation occurs, the shear strength of the discontinuity is increased. This increase in shear strength may occur as small shear deformations along the intersecting discontinuities modify the planar nature of the shearing discontinuity. This result is equivalent to increasing the roughness and hence the shear strength of the shearing discontinuity.

7.5. Summary.

This chapter has discussed the procedure used to prepare the test equipment and discontinuous specimens prior to a test. The test procedure and the methods used to process the test data after each test were also discussed. 156 triaxial tests were carried out on the

discontinuous specimens and the results highlighted the following characteristics of the deformation and yield behaviour of specimens comprised of distinct blocks.

(1) The maximum yield strength of a material is achieved when the material contains no discontinuities. The minimum yield strength is achieved when the material contains a non intersected discontinuity orientated at an angle β_{crit} (where $\beta_{crit} = \phi_w/2 + 45^o$).

(2) In a specimen containing multiple discontinuities orientated so that axial deformation occurs along cracks through intact material, the yield strength is less than that of the intact material. This fact illustrates how the presence of discontinuities will always influence the yield strength of a material. The amount of influence is dependent on the orientation of the discontinuities.

(3) In specimens containing multiple discontinuities, if axial deformation occurs primarily along a single discontinuity, the presence of other discontinuities intersecting the shearing discontinuity will increase the yield strength of the specimen. A specimen containing interlocking discontinuities is stronger than one in which no interlocking occurs.

(4) There is a systematic increase in the strength and decrease in the deformability of discontinuous specimens with increases in the confining pressure prior to and subsequent to, shear deformation occurring along cracks or pre-existing discontinuities.

(5) The axial stress versus axial deformation curves of the four geometries tested had four distinct regions. Non linear Region I occurred as blocks aligned themselves according to the principal stress state. In linear Region II blocks packed together and the volume of the specimens decreased. In non-linear Region III the shear strength of cracks formed through intact material or pre-existing discontinuities was achieved, the specimens began to dilate and stick-slip oscillations occurred. In non-linear Region IV the specimens achieved their yield strength prior to the onset of plastic flow.

(6) Infill reduces the yield strength and increases the deformability of discontinuous specimens. The amount of influence of infill on these parameters is dependent on the orientation of the discontinuities.

(7) The axial stiffness, K, of the specimens prior to and subsequent to, shear deformations occurring along cracks or discontinuities can be defined in terms of the minor principal

stress, σ_3, by a relationship of the form:

$$K = a_{(k)}\sigma_3^{b(k)}$$

(8) Axial stiffness can be reasonably estimated by an analytical decomposition procedure.

(9) The yield strength, $\sigma_{1(peak)}$, of the specimens can be defined in terms of the minor principal stress by an equation of the form:

$$\sigma_{1(peak)} = a_{(\sigma)} + b_{(\sigma)}\sigma_3$$

The techniques developed in this study for manufacturing discontinuous specimens can be used to create specimens with an almost unlimited number of discontinuity geometries. The manufacturing process and the subsequent triaxial testing of the specimens are, however, extremely time consuming. With the development of sophisticated numerical techniques it is now possible to use them in oder to simulate the test procedure. The usefulness of these simulations has been limited traditionally by a lack of suitable verification data. The test results described in the chapter are a particularly valuable as a source of this data and, in the next chapter, numerical tests are carried out to validate the effectiveness of the distinct element method for modelling the behaviour of discontinuous specimens.

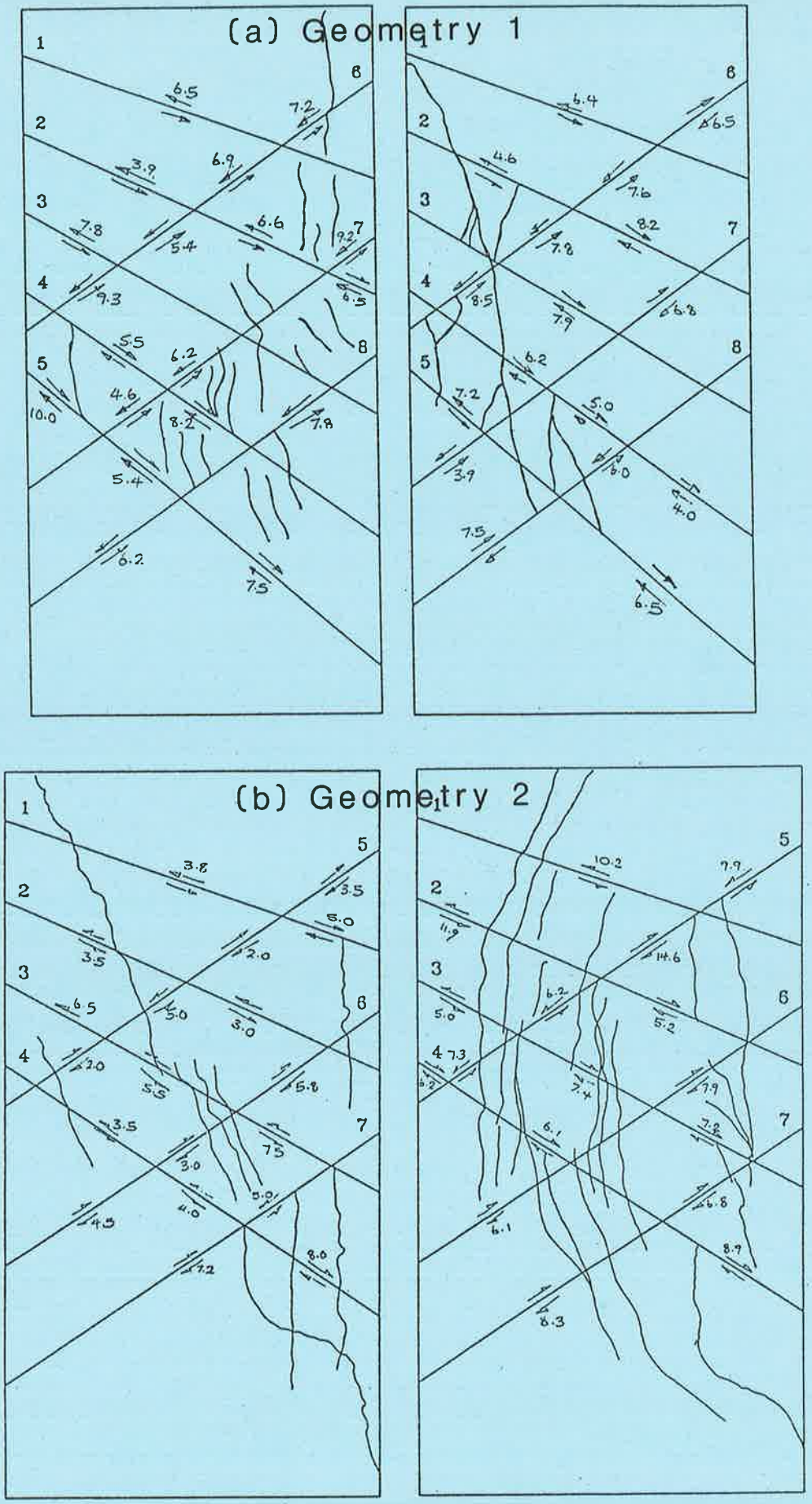

Figure 7.1(a) (b). Typical results for Geometry 1 and 2 specimens obtained from inspection of paper jacket subsequent to a test. Results record direction and magnitude of shear deformation along discontinuities and presence of cracking through intact blocks.

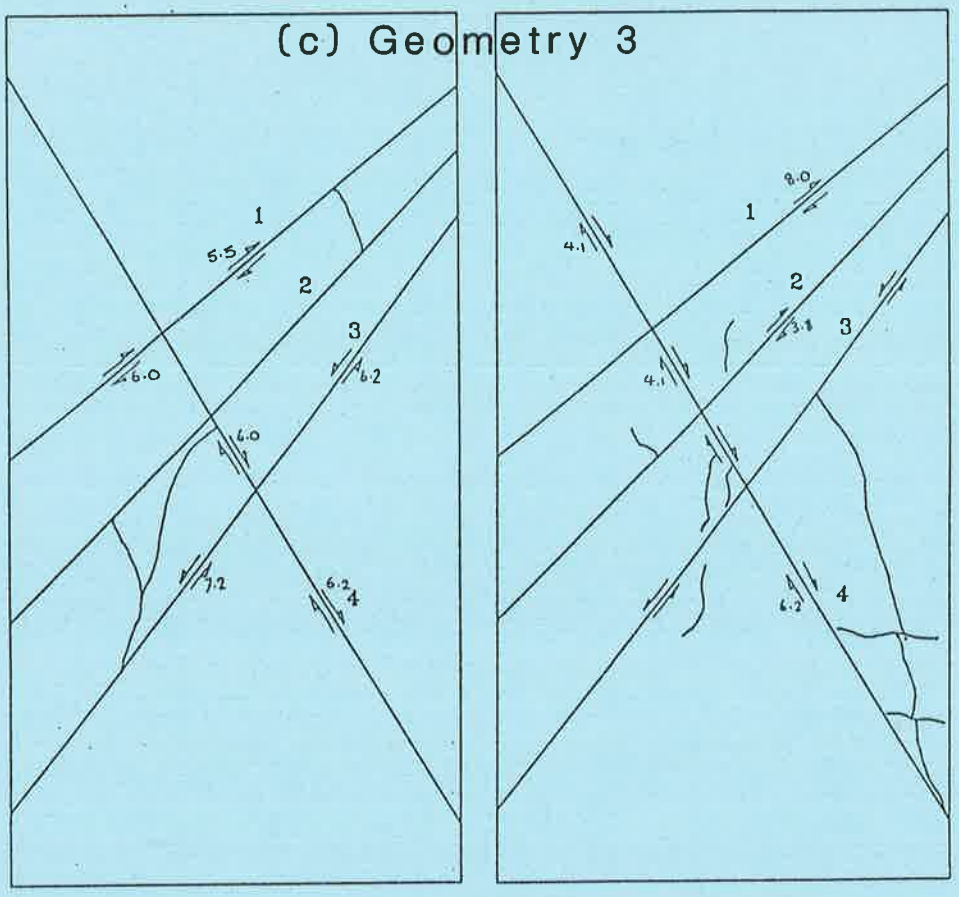

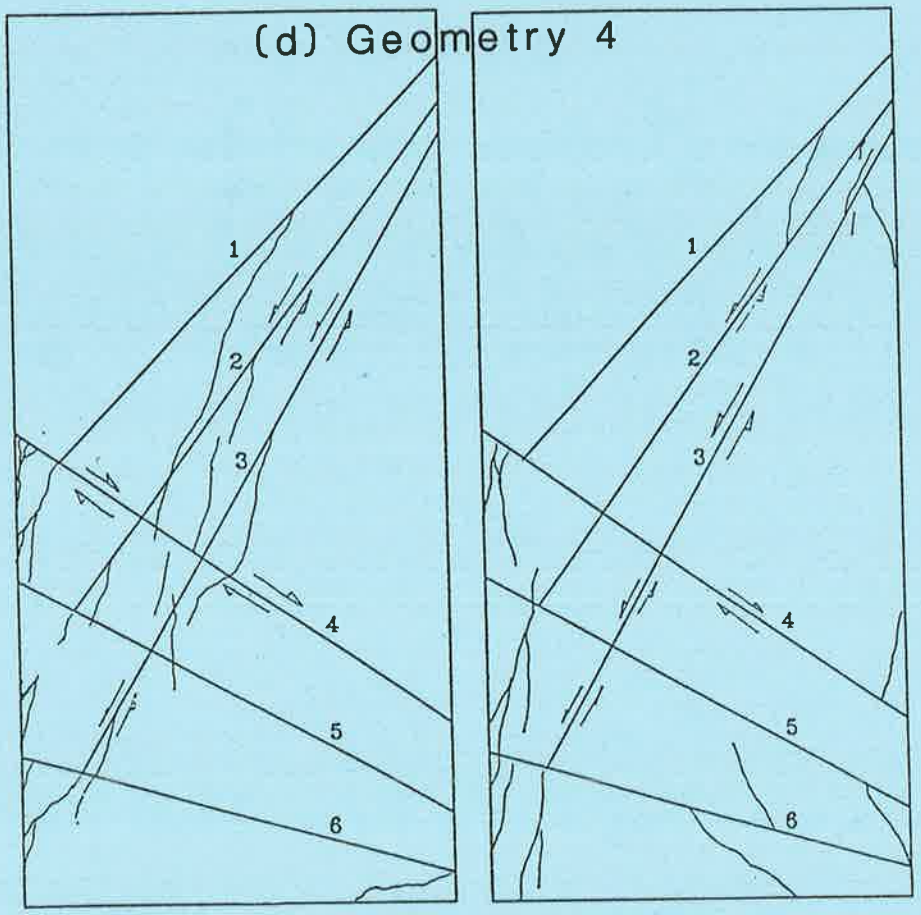

Figure 7.1(c)-(d). Typical results for Geometry 3 and 4 specimens obtained from inspection of paper jacket subsequent to a test.

Figure 7.2(a)-(b). Geometry 1-2 specimens in thin rubber membrane subjected to axial compression.

(c)

(d)

Figure 7.2(c)-(d).Geometry 3 specimen in thin rubber membrane subjected to axial compression.

Figure 7.2(e). Geometry 4 specimen in thin rubber membrane subjected to axial compression.

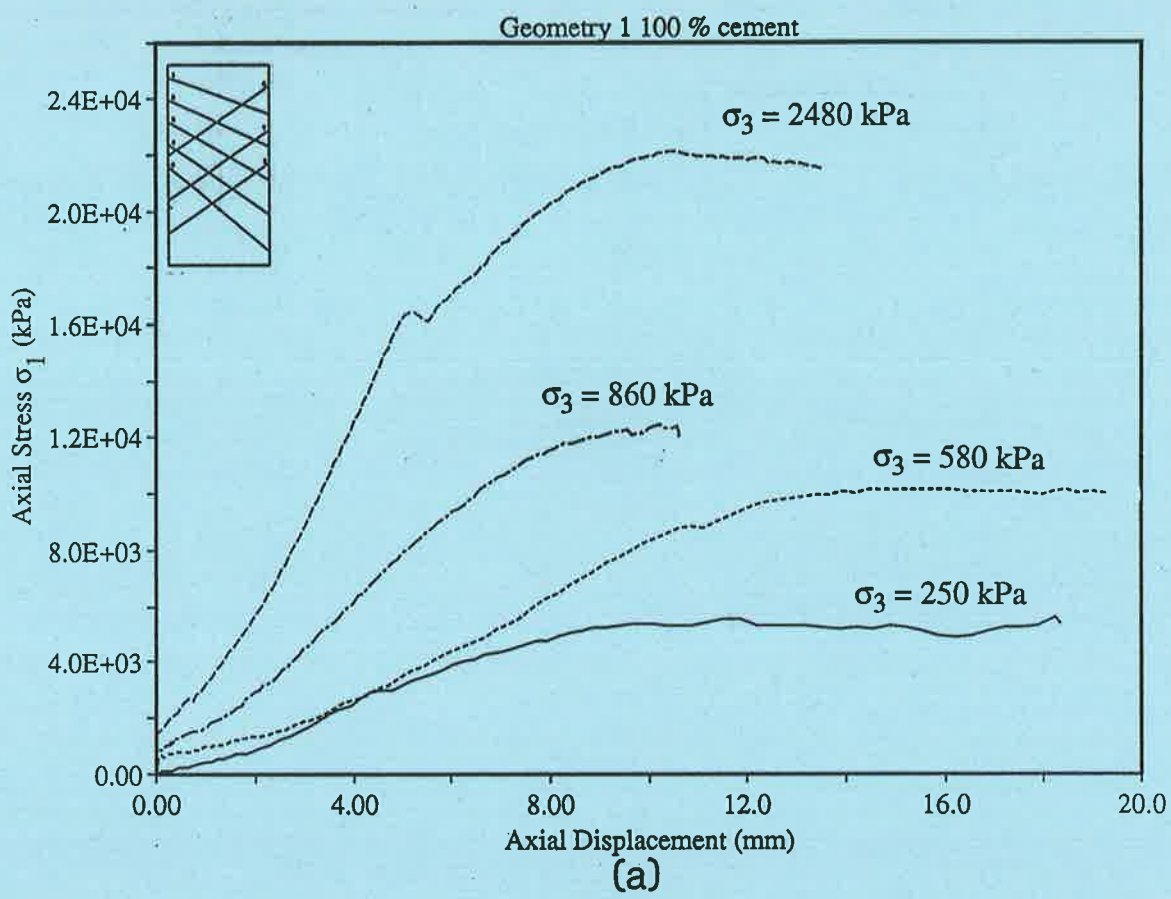

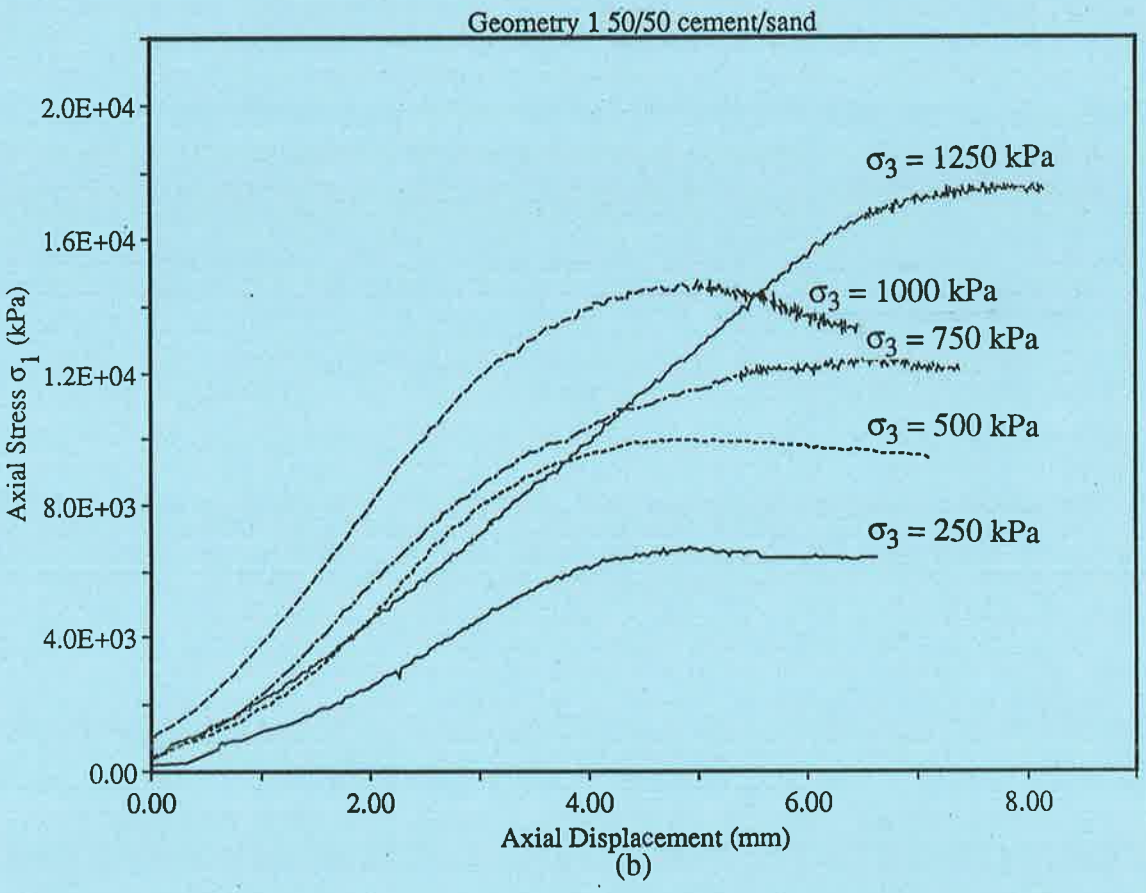

Figure 7.3(a)-(b). Influence of confining pressure on axial stress versus axial deformation behaviour for Geometry 1 specimens of (a) 100% and (b) 50/50 material.

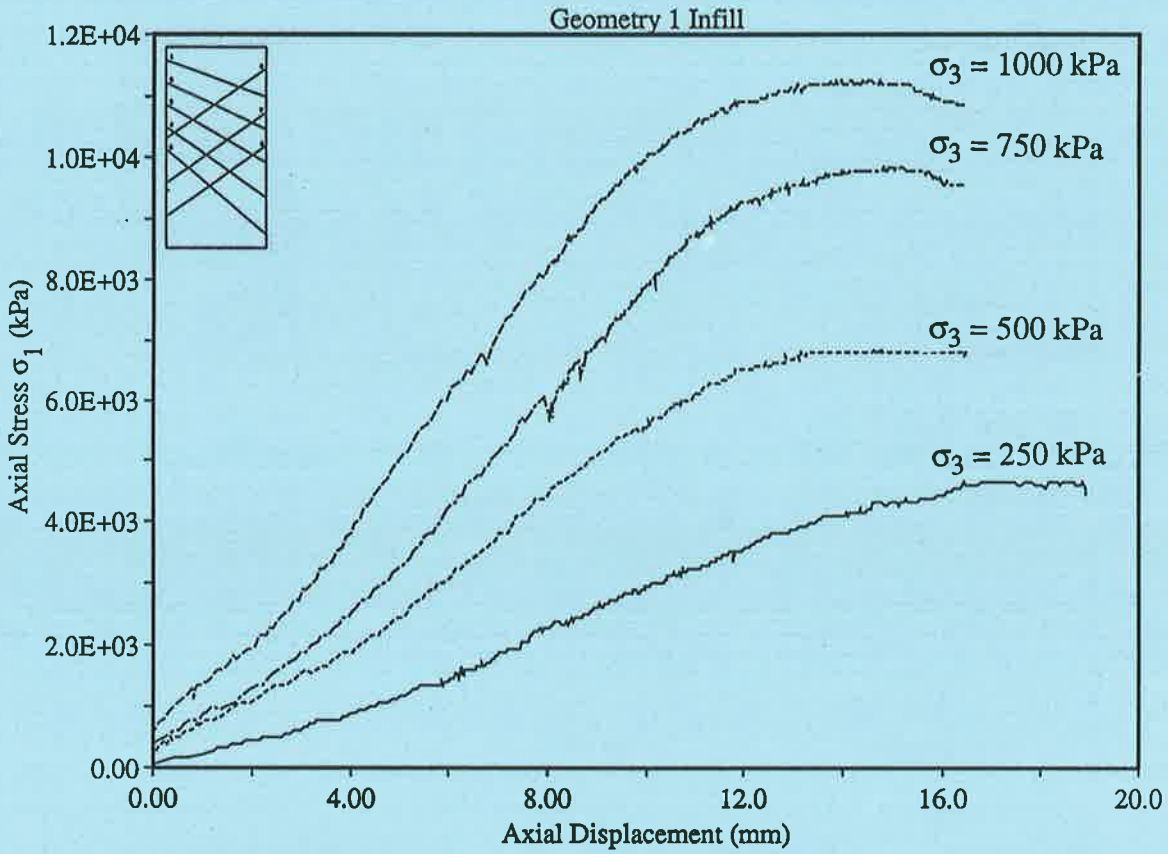

Figure 7.3(c). Influence of confining pressure on axial stress versus axial deformation behaviour for Geometry 1 specimens containing infill.

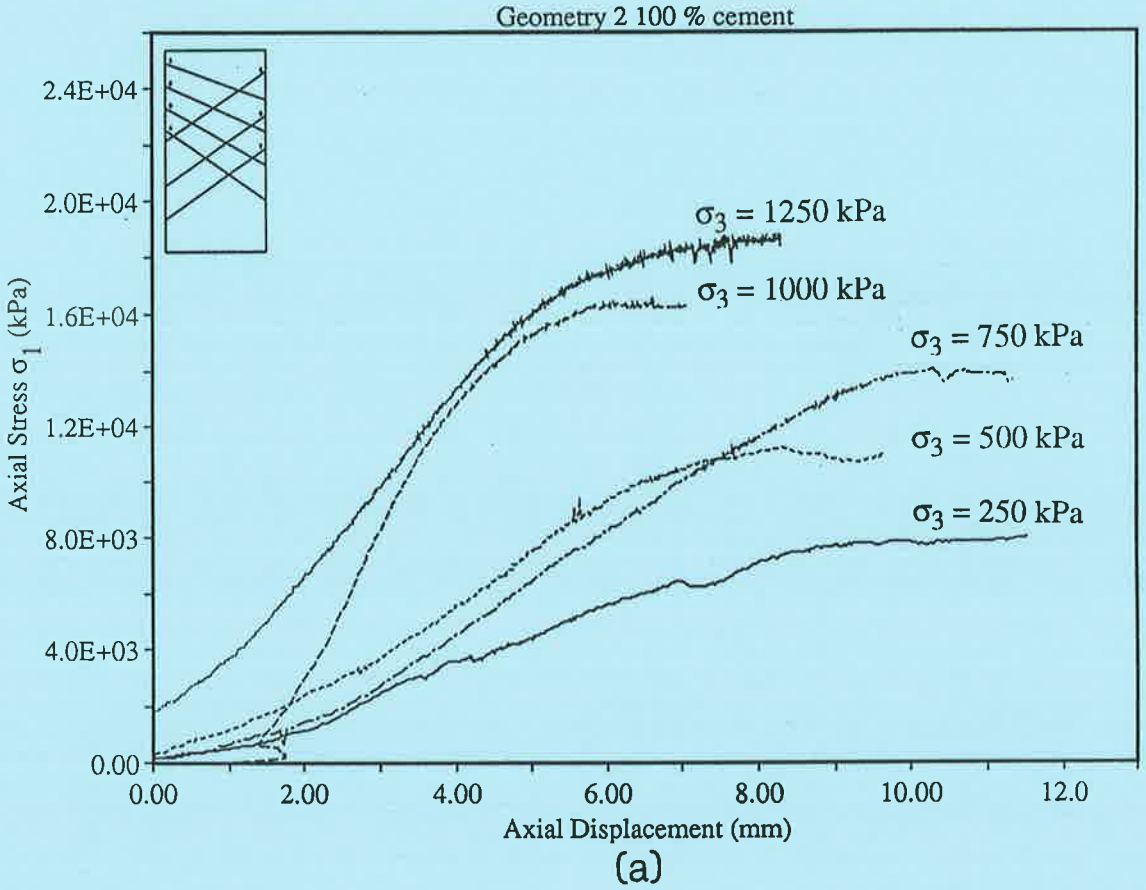

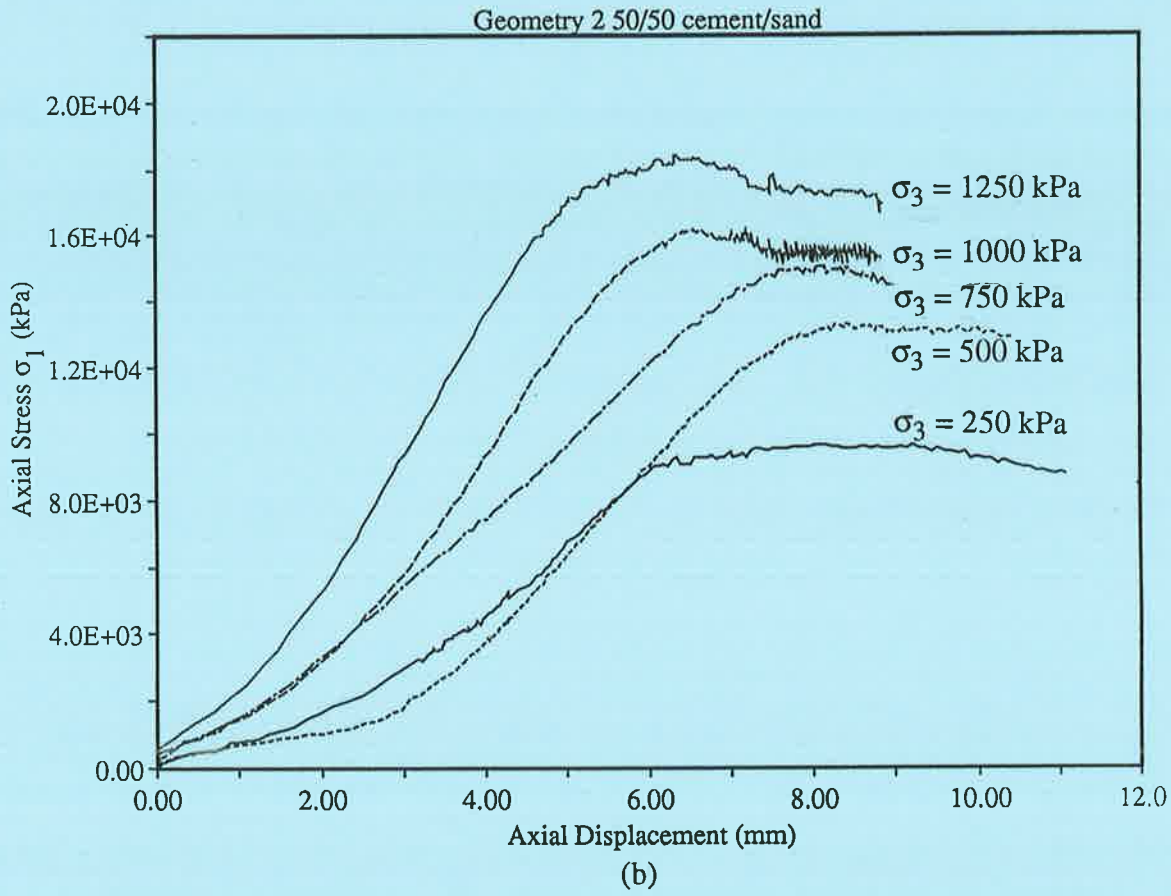

Figure 7.4(a)-(b). Influence of confining pressure on axial stress versus axial deformation behaviour for Geometry 2 specimens of (a) 100% and (b) 50/50 material.

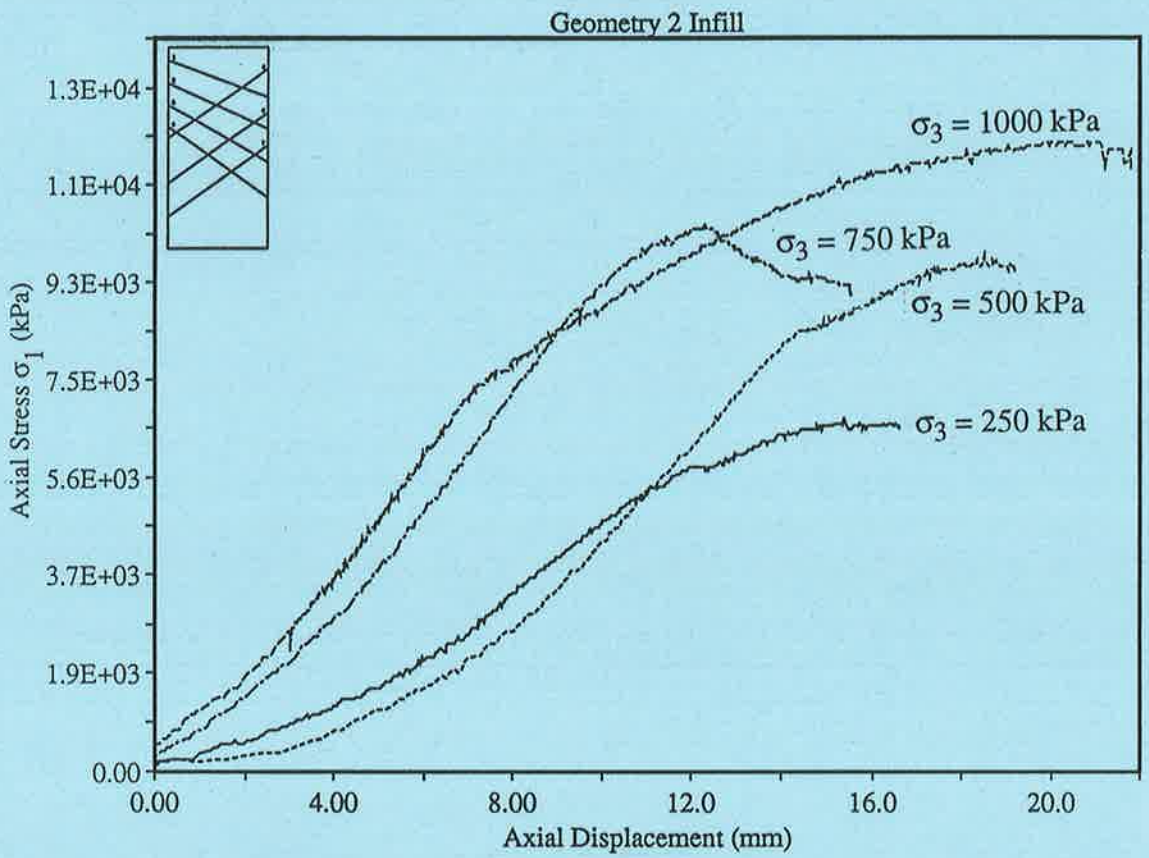

Figure 7.4(c). Influence of confining pressure on axial stress versus axial deformation behaviour for Geometry 2 specimens containing infill.

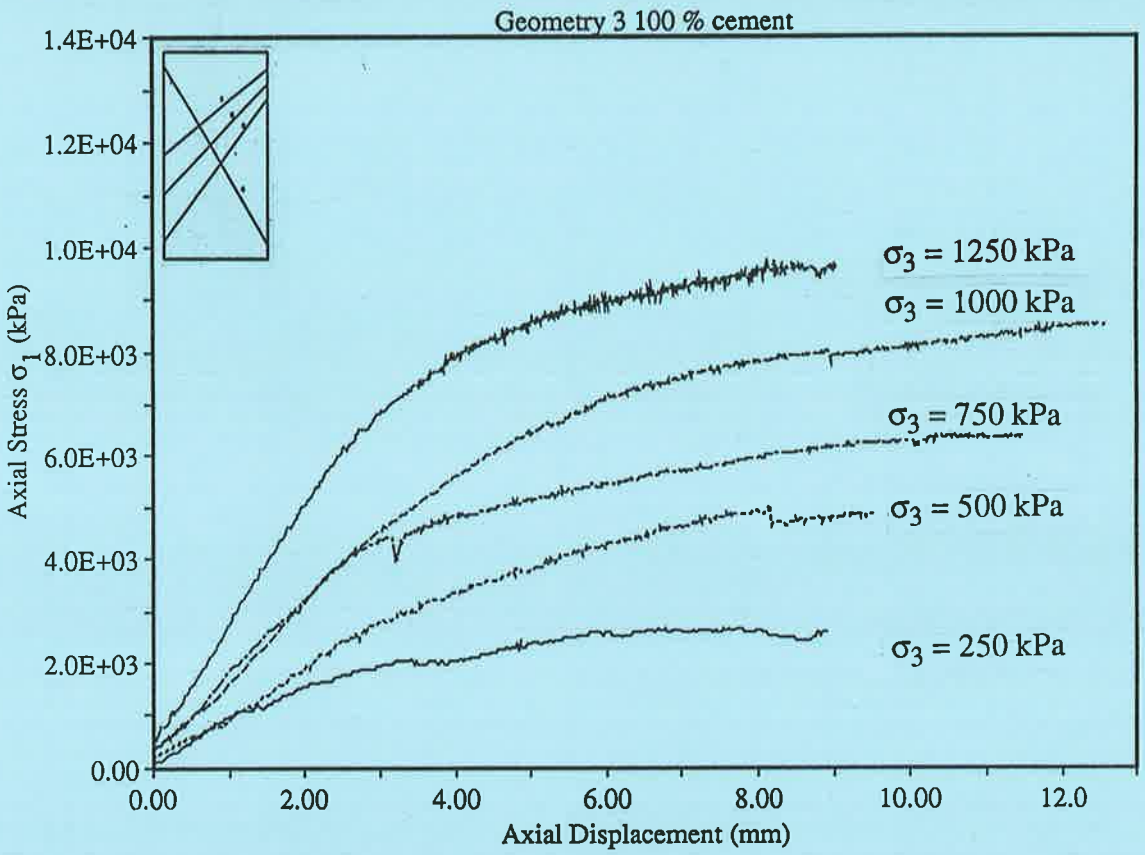

(a)

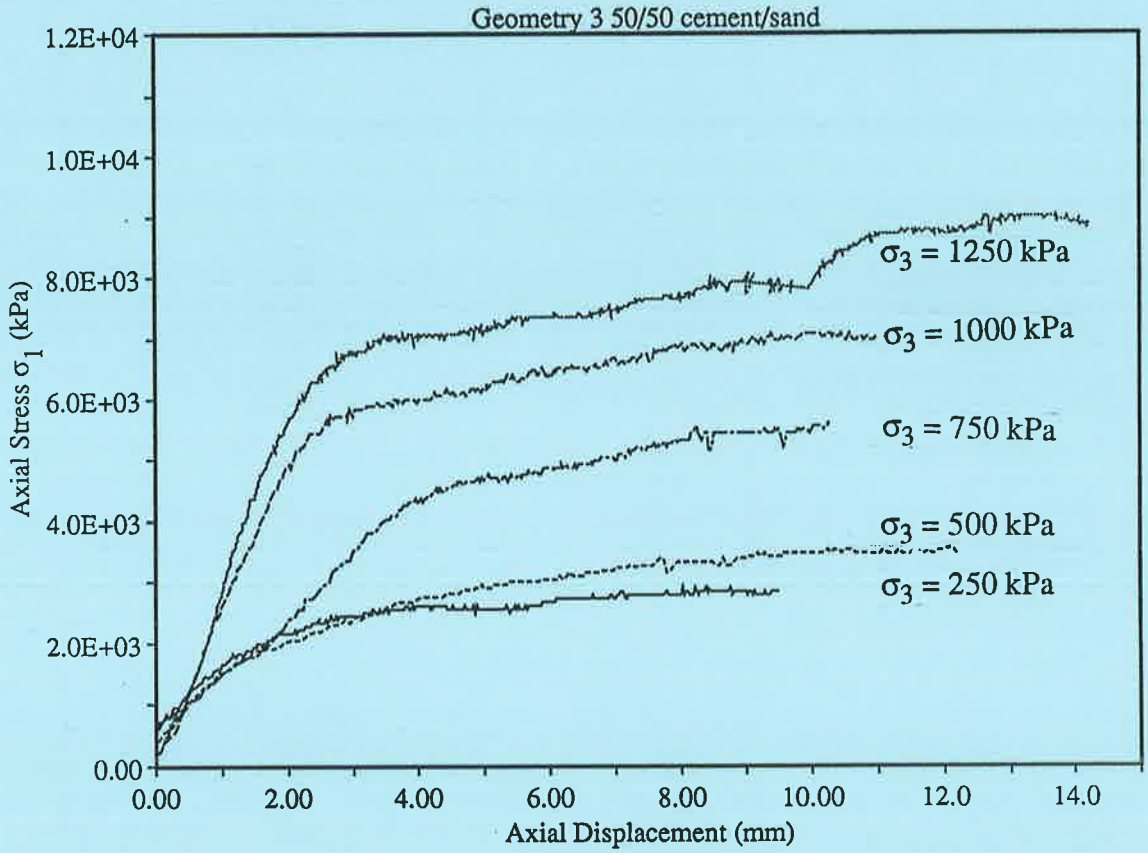

(b)

Figure 7.5(a)-(b). Influence of confining pressure on axial stress versus axial deformation behaviour for Geometry 3 specimens of (a) 100% and (b) 50/50 material.

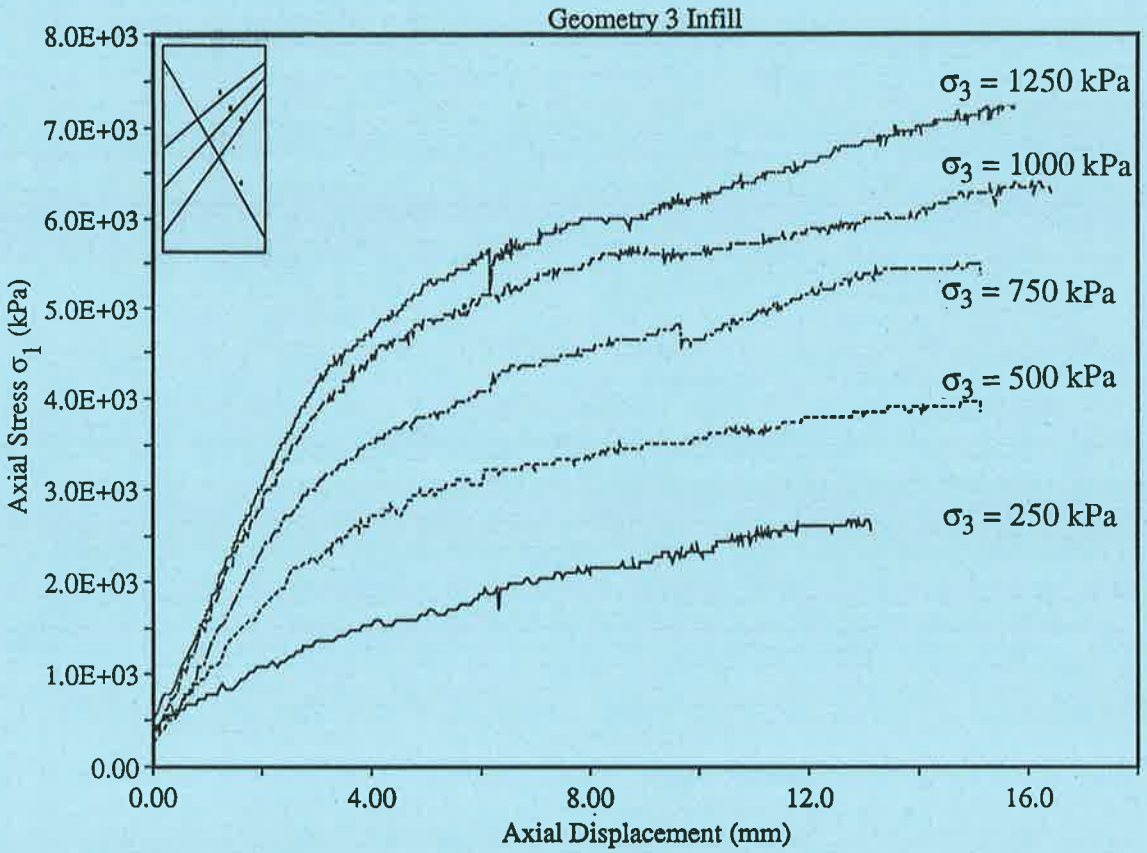

Figure 7.5(c). Influence of confining pressure on axial stress versus axial deformation behaviour for Geometry 3 specimens containing infill.

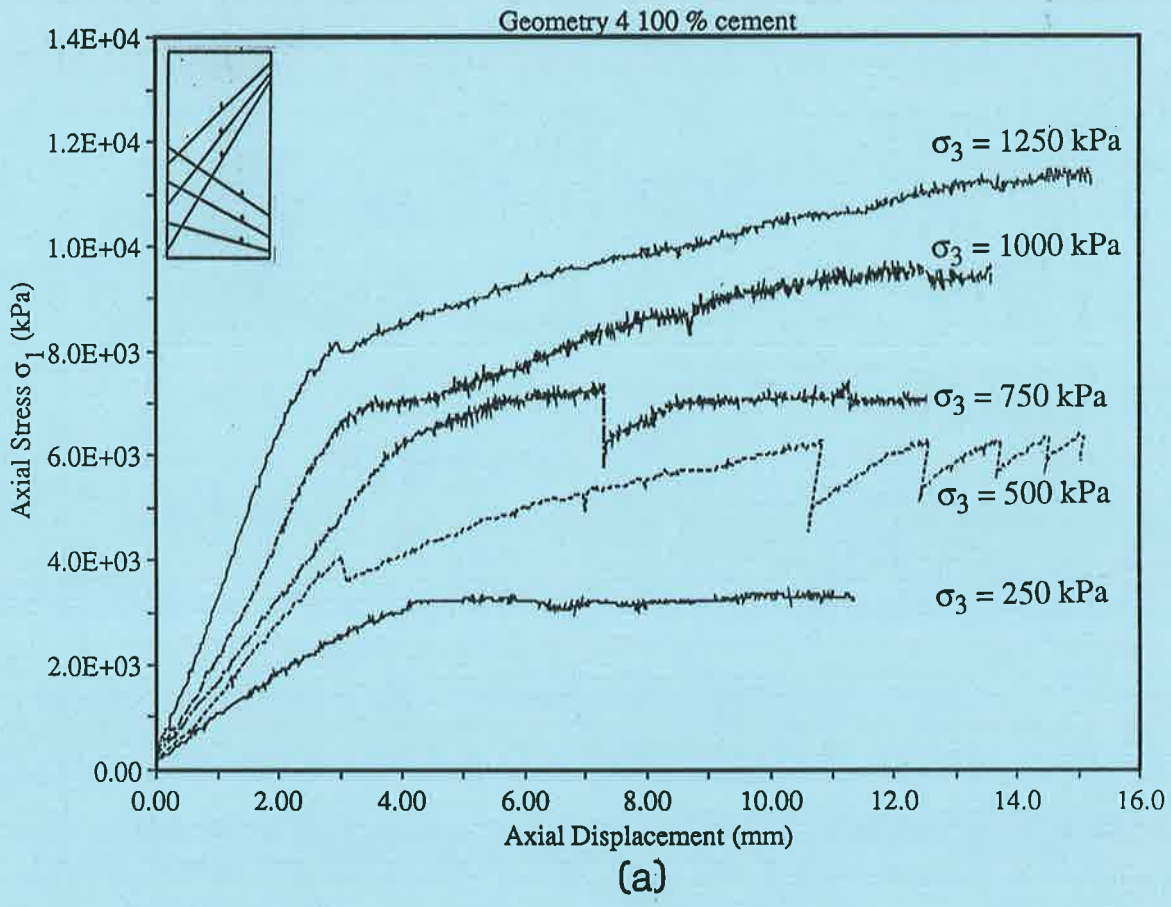

(a)

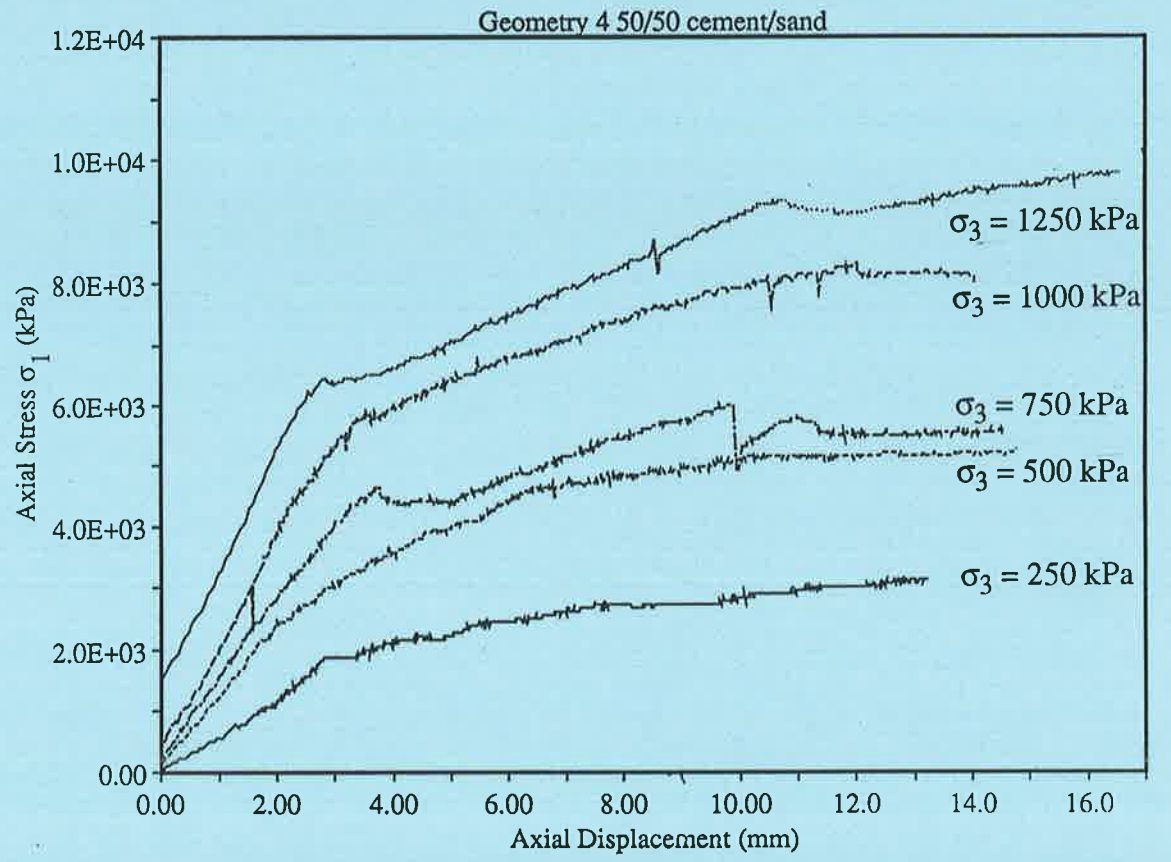

(b)

Figure 7.6(a)-(b). Influence of confining pressure on axial stress versus axial deformation behaviour for Geometry 4 specimens of (a) 100% and (b) 50/50 material.

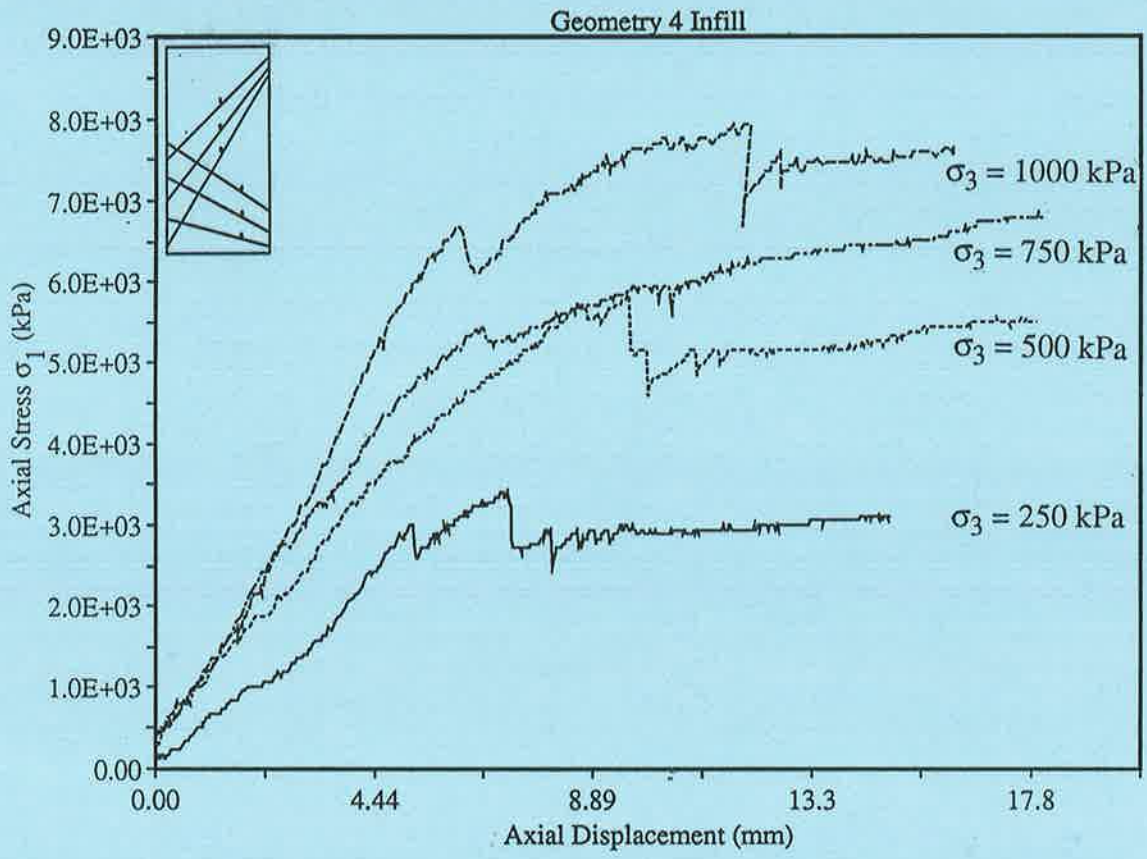

Figure 7.6(c). Influence of confining pressure on axial stress versus axial deformation behaviour for Geometry 4 specimens containing infill.

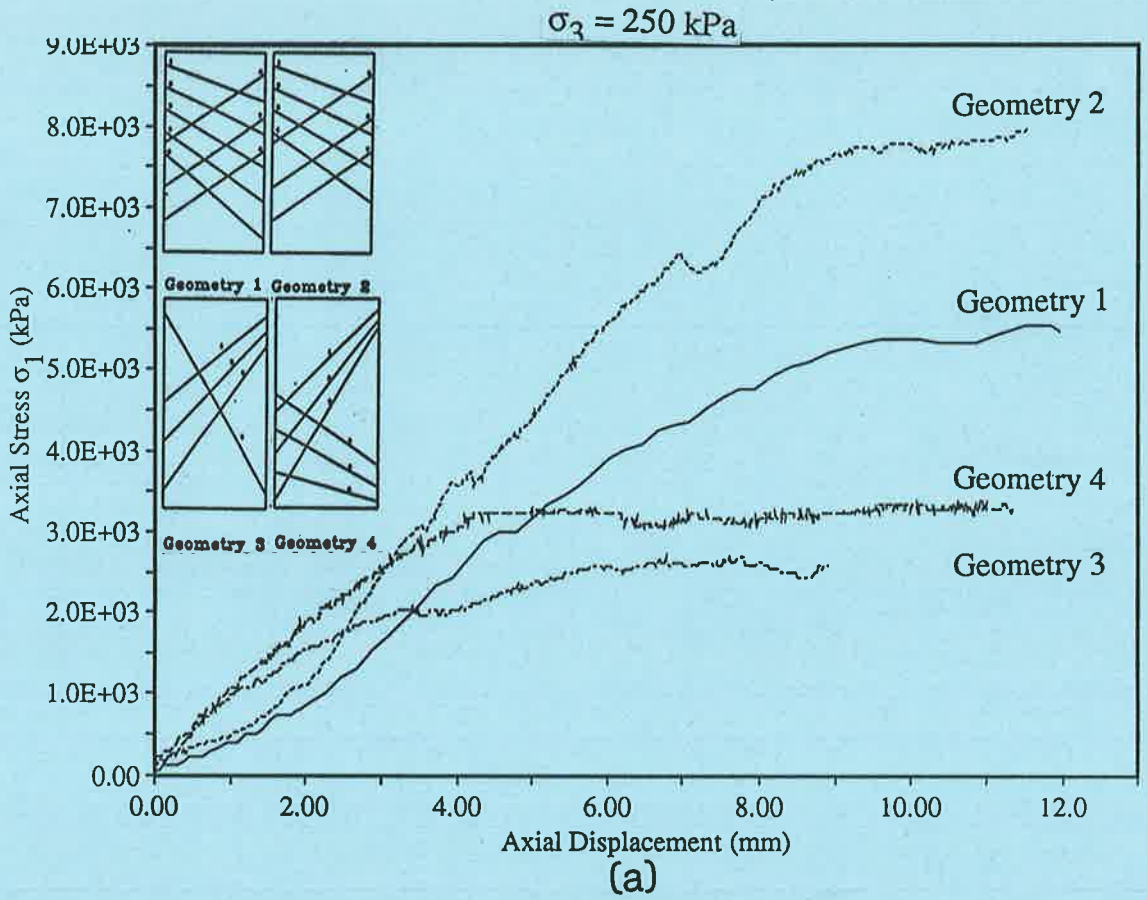

(a)

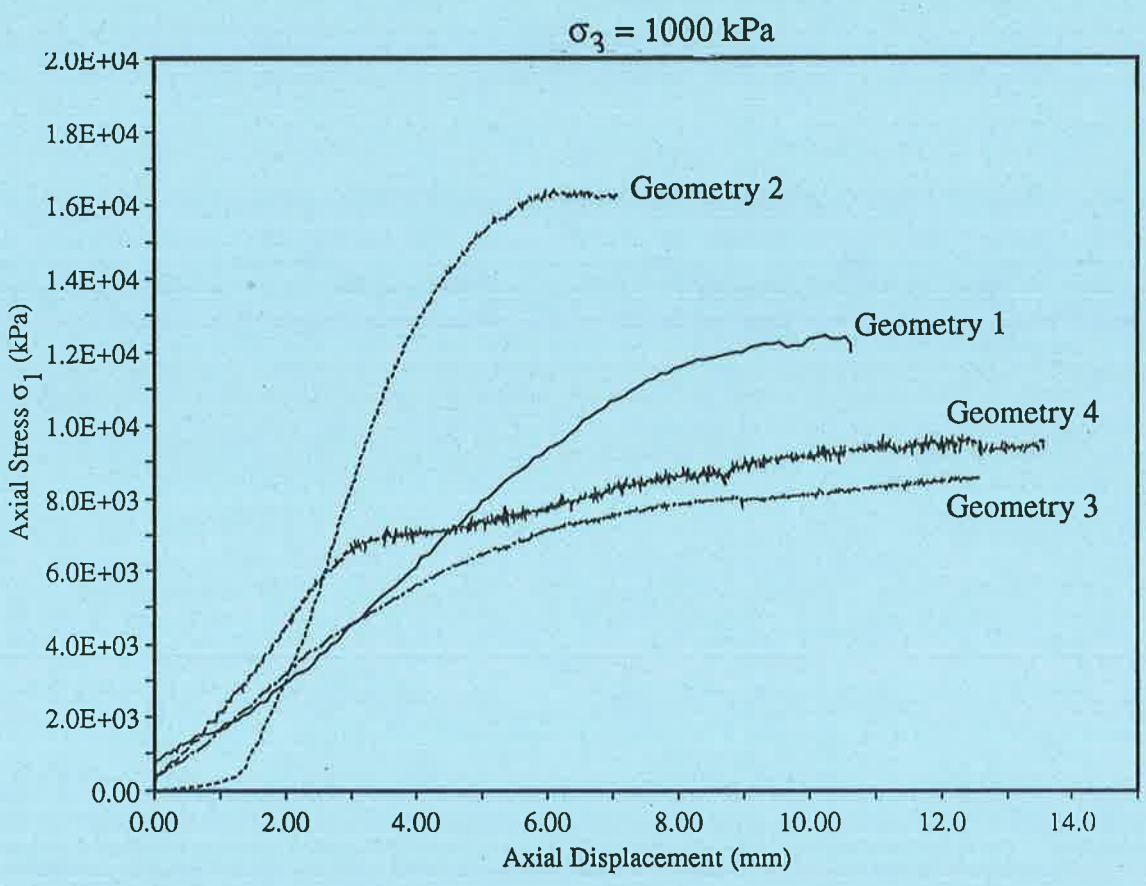

(b)

Figure 7.7(a)-(b). Influence of specimen geometry on the axial stress versus axial deformation behaviour for 100% gypsum cement discontinuous specimens (a) σ_3 = 250kPa and (b) σ_3 = 1000kPa).

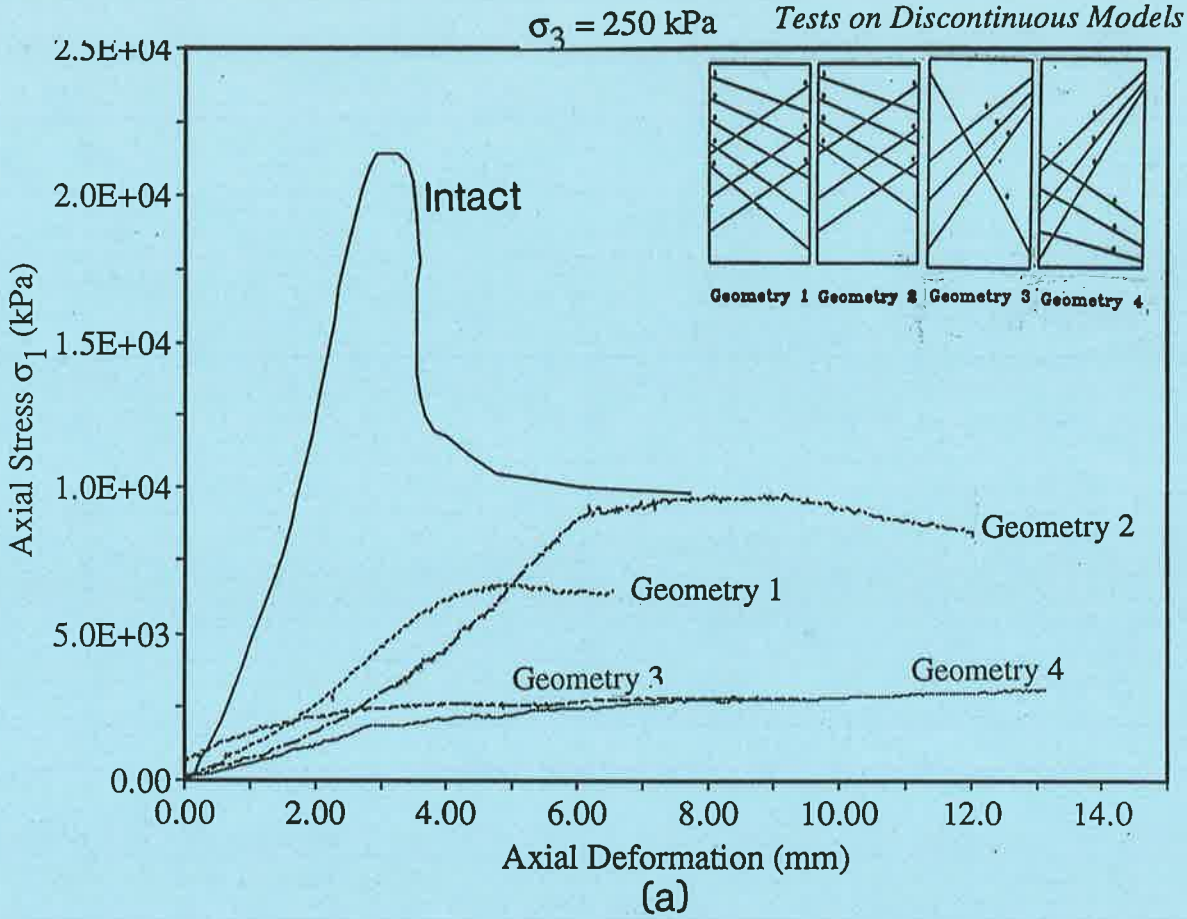

(a)

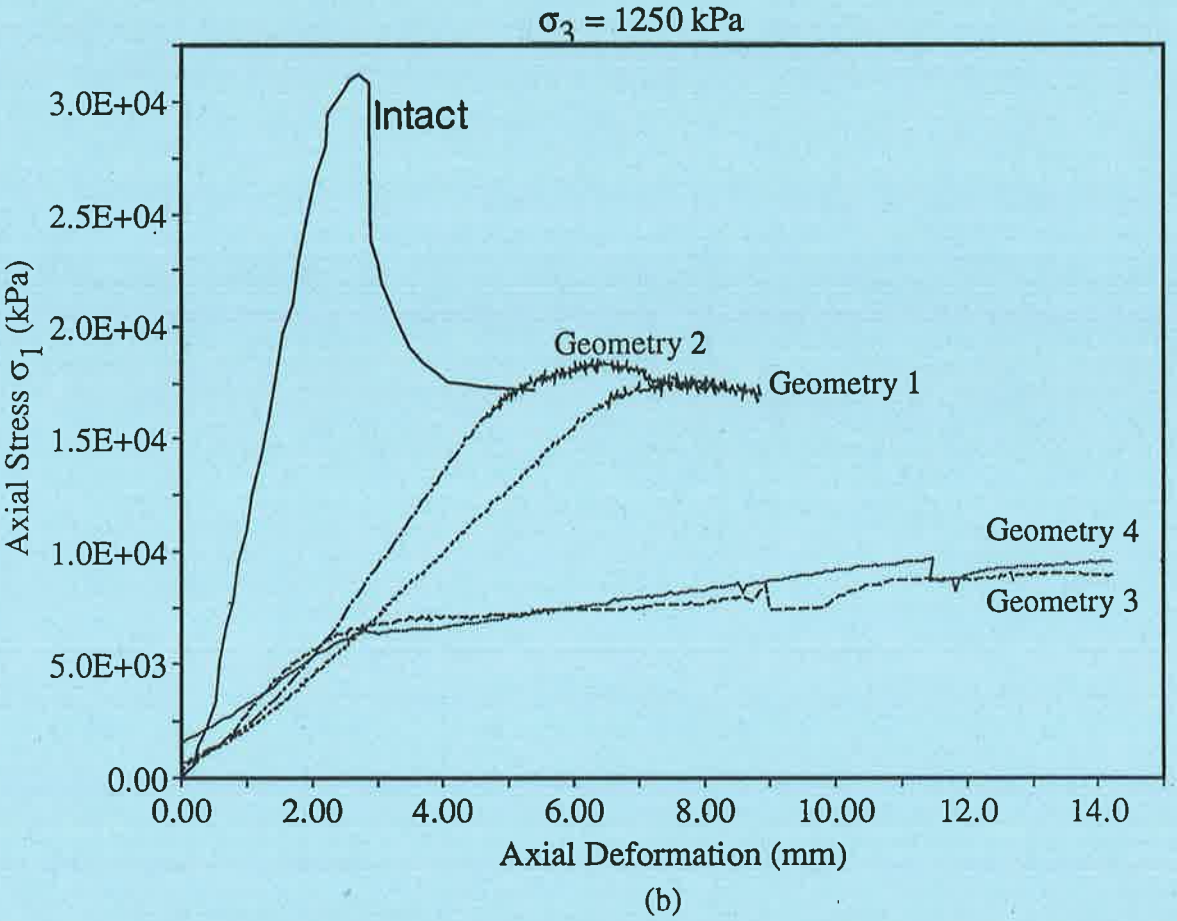

(b)

Figure 7.8(a)-(b). Figure highlighting the influence of specimen geometry on axial stress/deformation behaviour for 50/50 cement/sand discontinuous specimens (a) σ_3 = 250kPa and (b) σ_3 = 1000kPa).

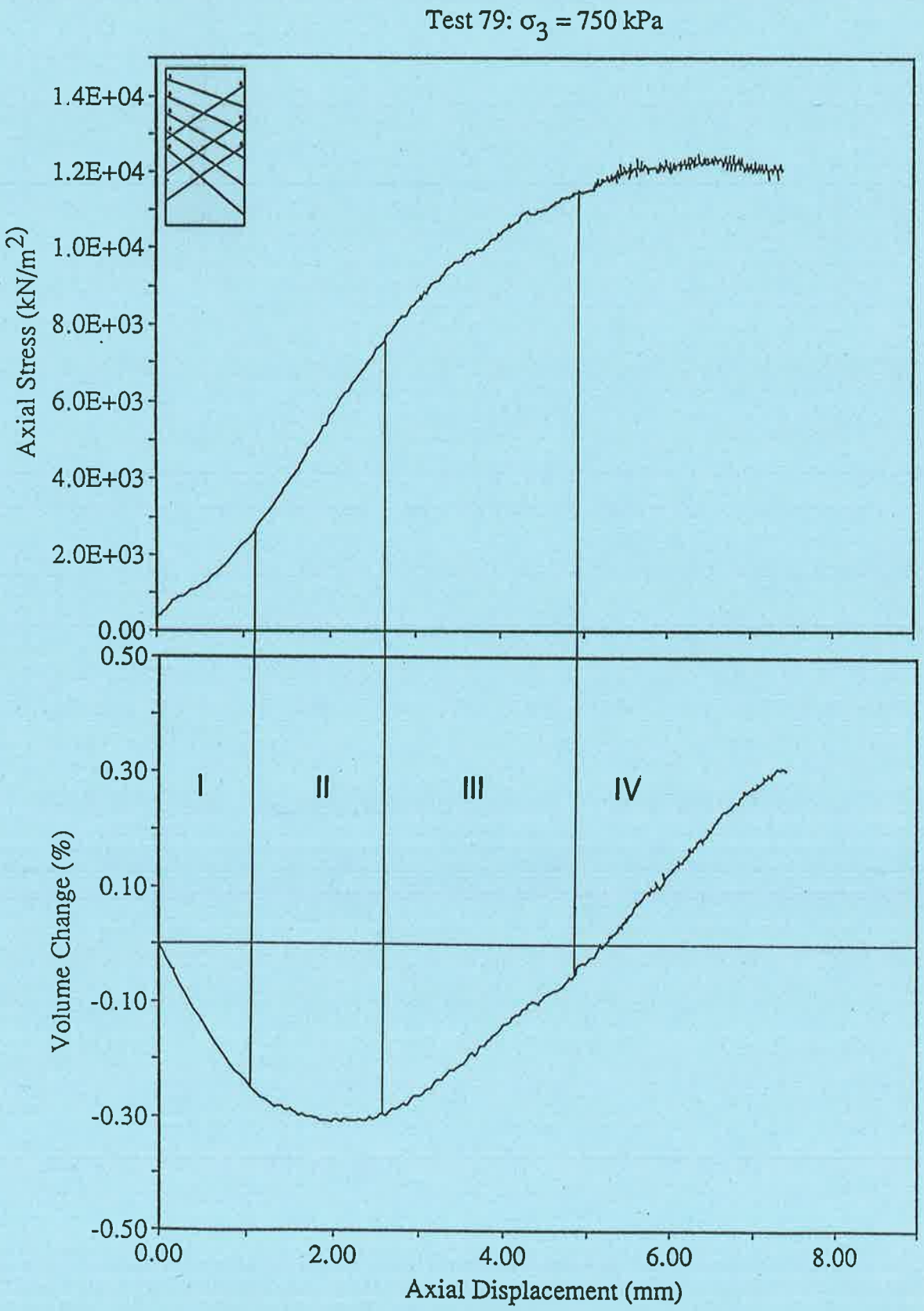

Figure 7.9. Axial stress versus axial deformation and volumetric deformation vs axial deformation plots for Geometry 1 cement/sand specimen at σ_3 = 750kPa showing four distinct regions that were typical for all geometries.

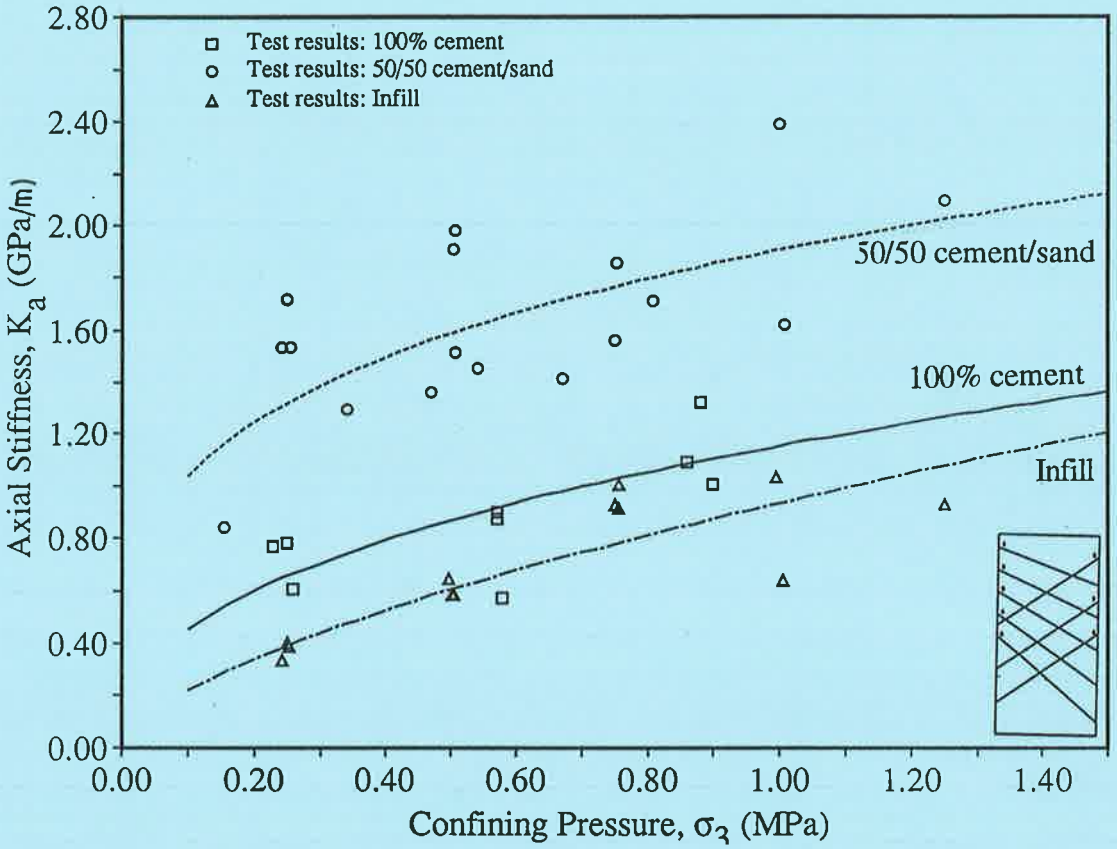

Figure 7.10. Influence of confining pressure on axial stiffness in Region II for Geometry 1 specimens.

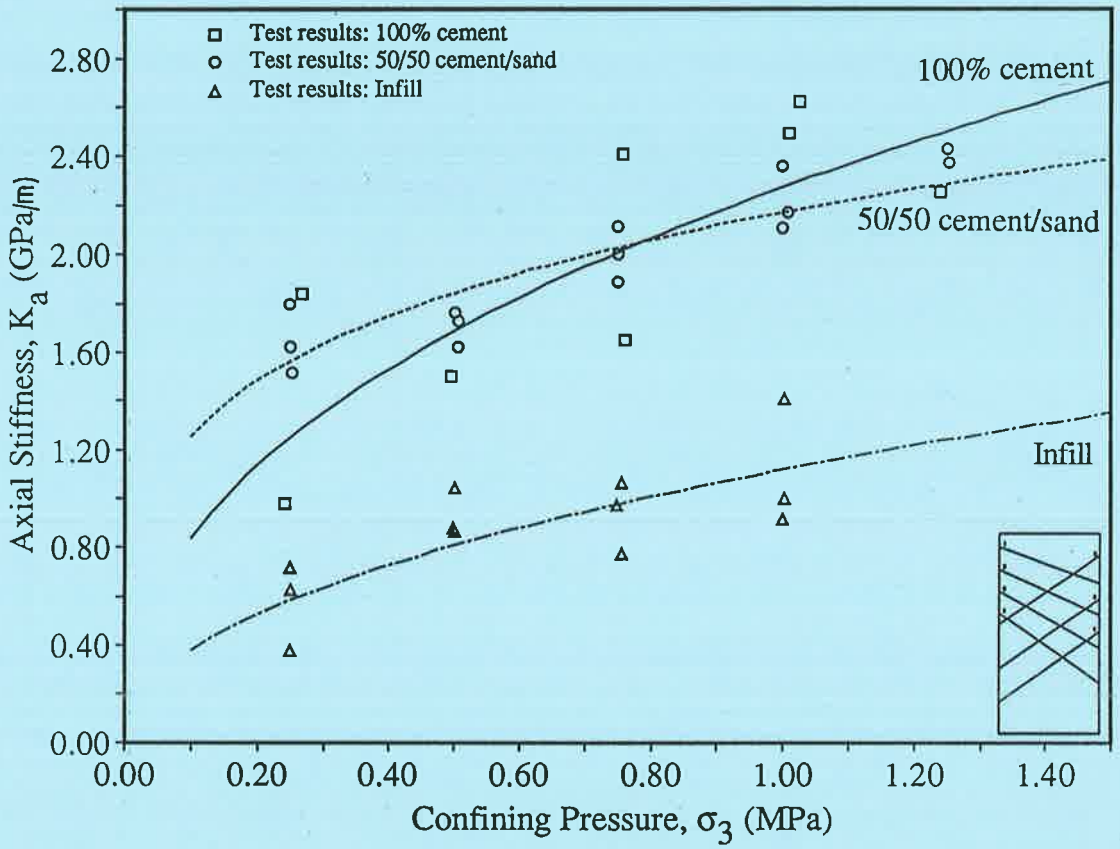

Figure 7.11. Influence of confining pressure on axial stiffness in Region II for Geometry 2 specimens.

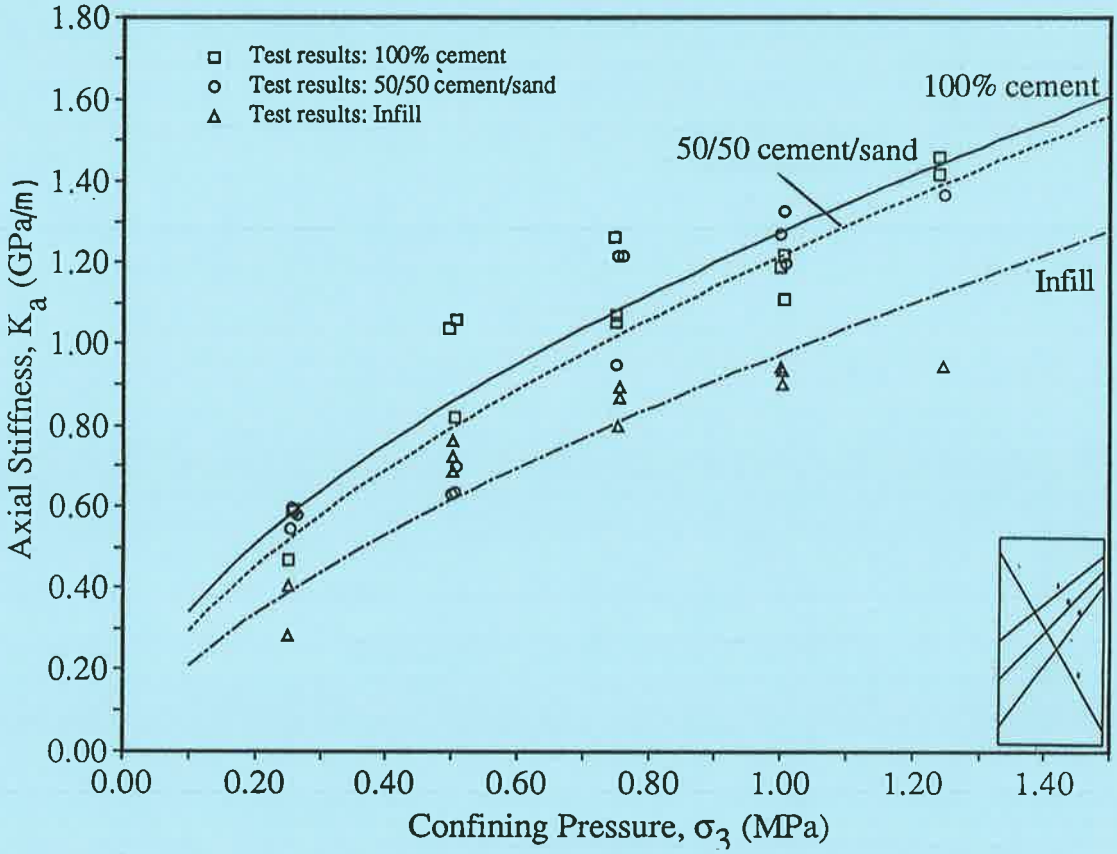

Figure 7.12. Influence of confining pressure on axial stiffness in Region II for Geometry 3 specimens.

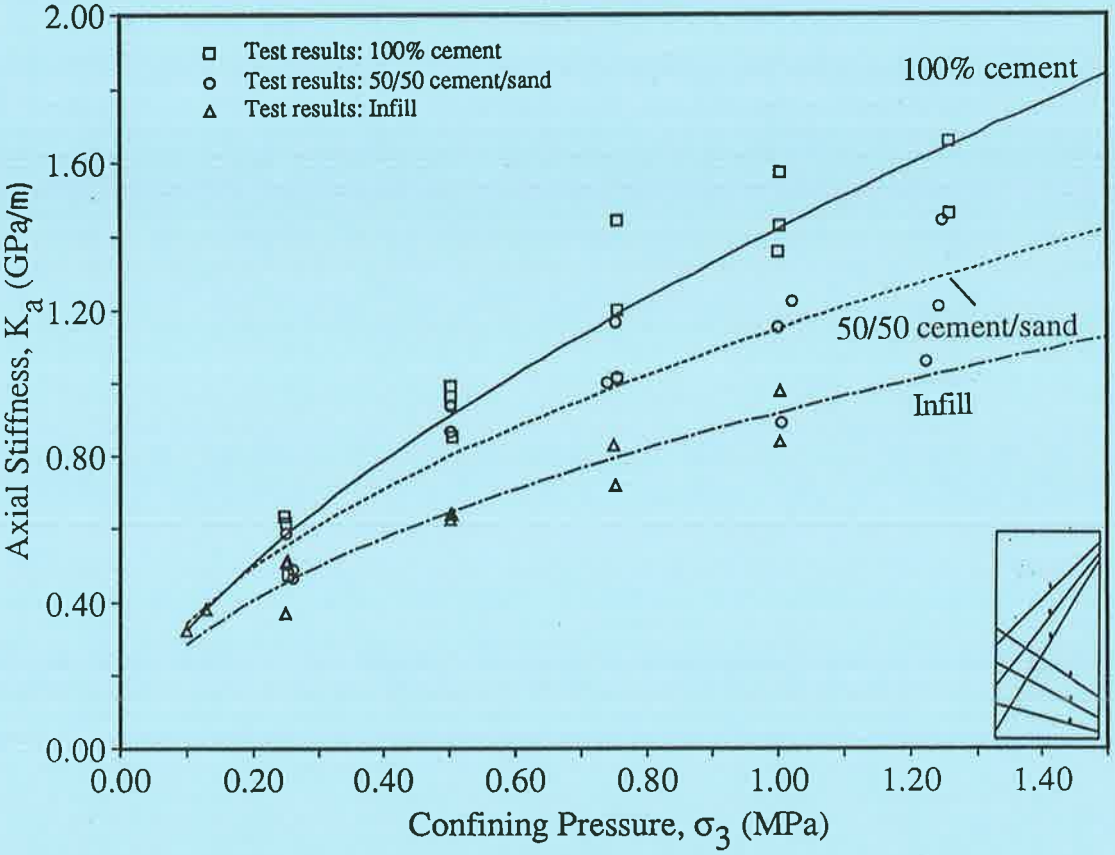

Figure 7.13. Influence of confining pressure on axial stiffness in Region II for Geometry 4 specimens.

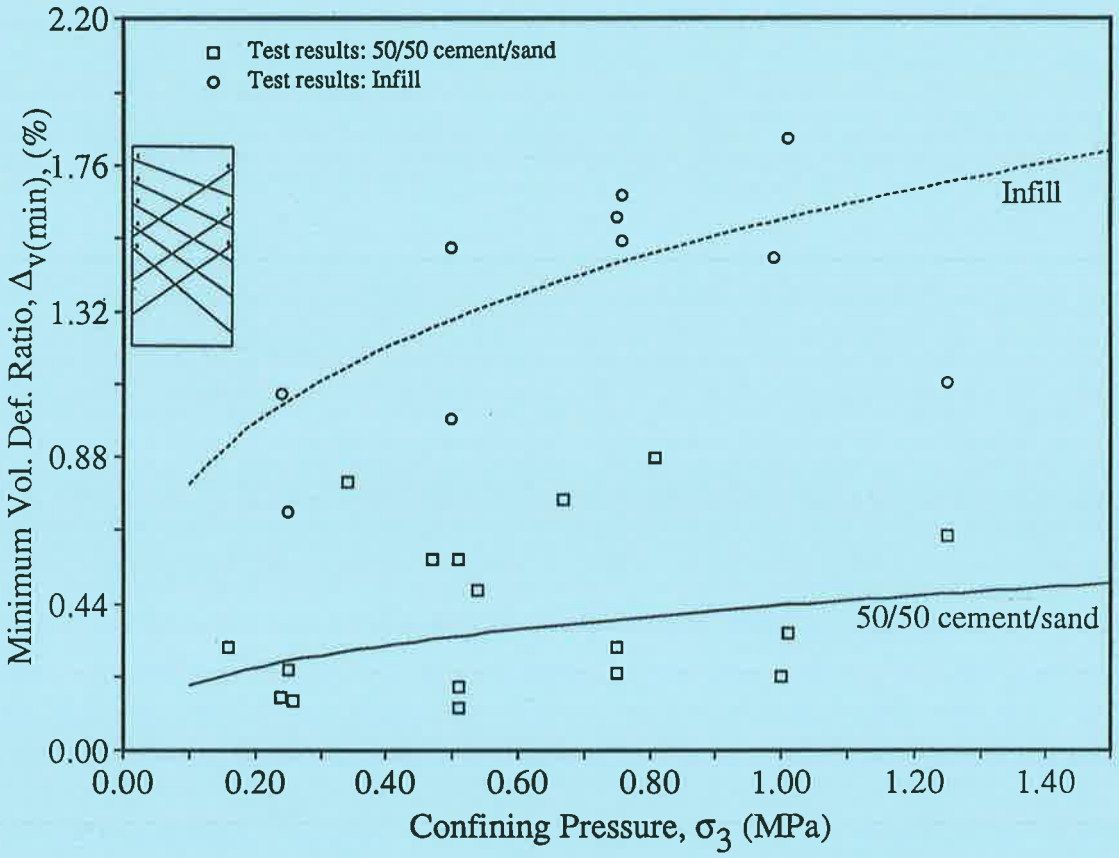

Figure 7.14. Influence of confining pressure on volumetric deformation for the Geometry 1 specimens.

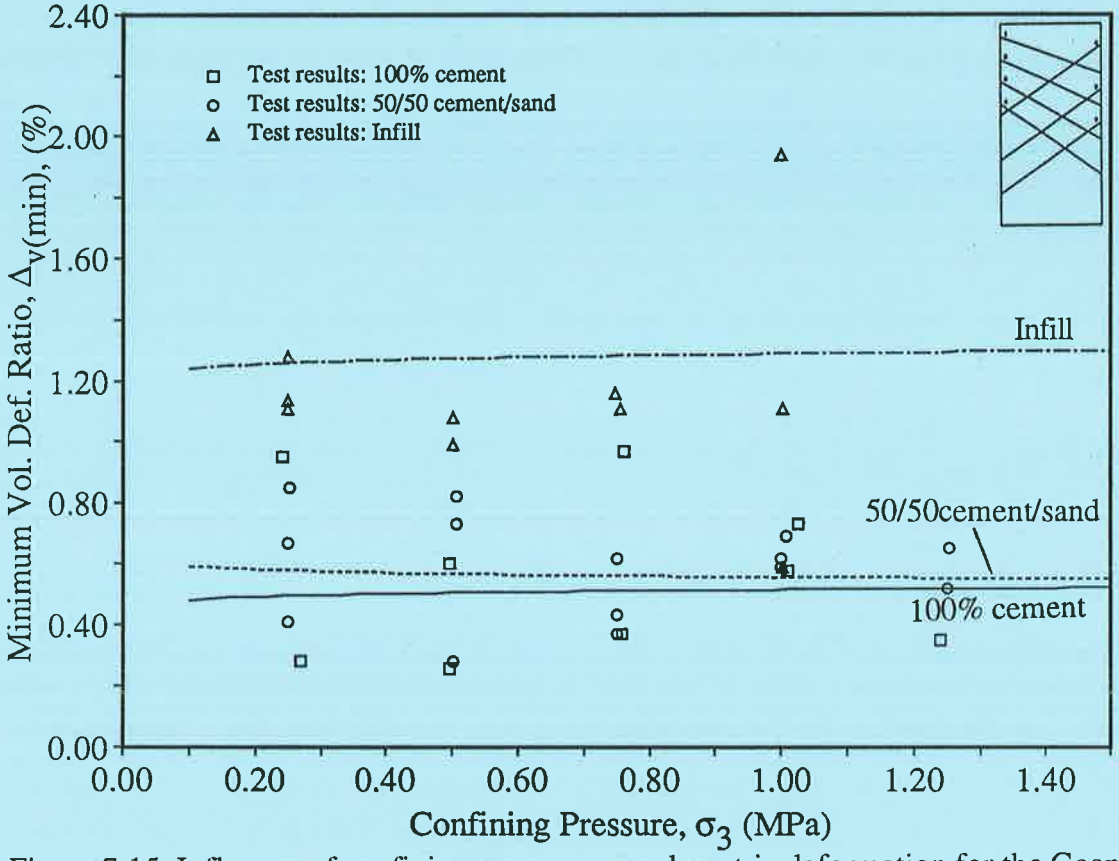

Figure 7.15. Influence of confining pressure on volumetric deformation for the Geometry 2 specimens.

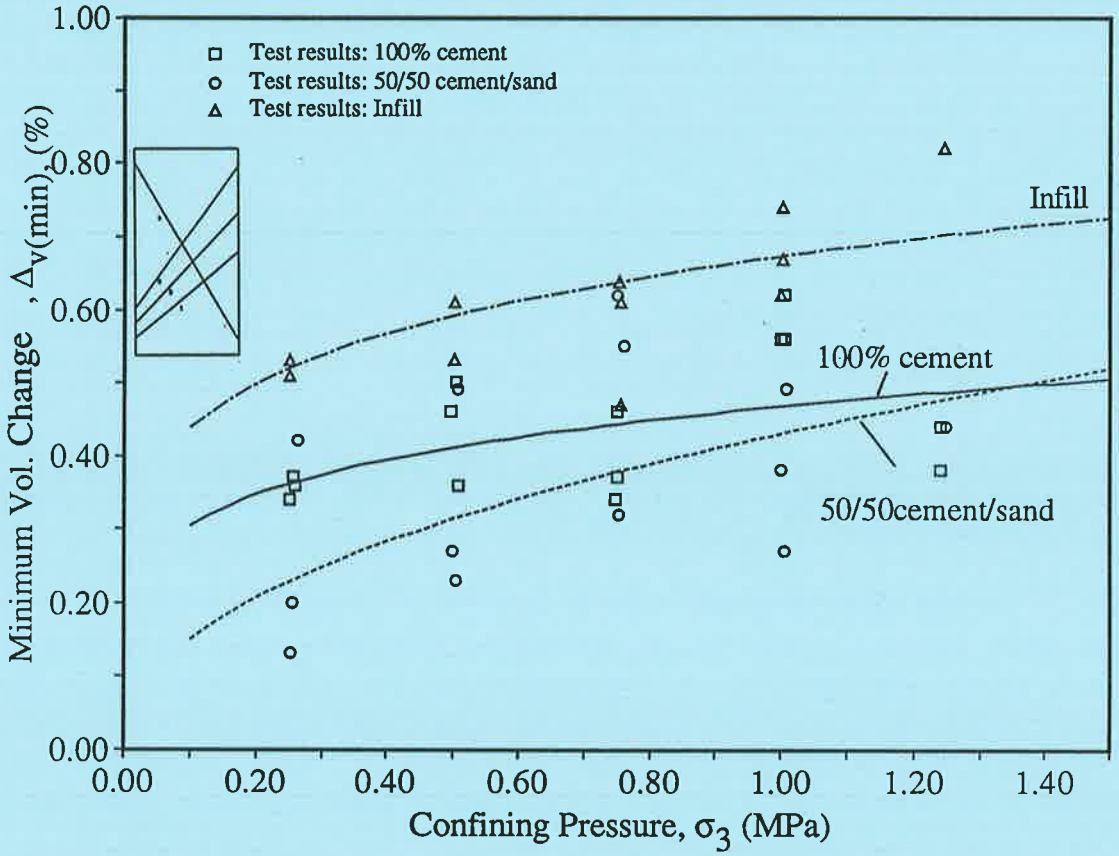

Figure 7.16. Volumetric deformation versus confining pressure for the Geometry 3 specimens.

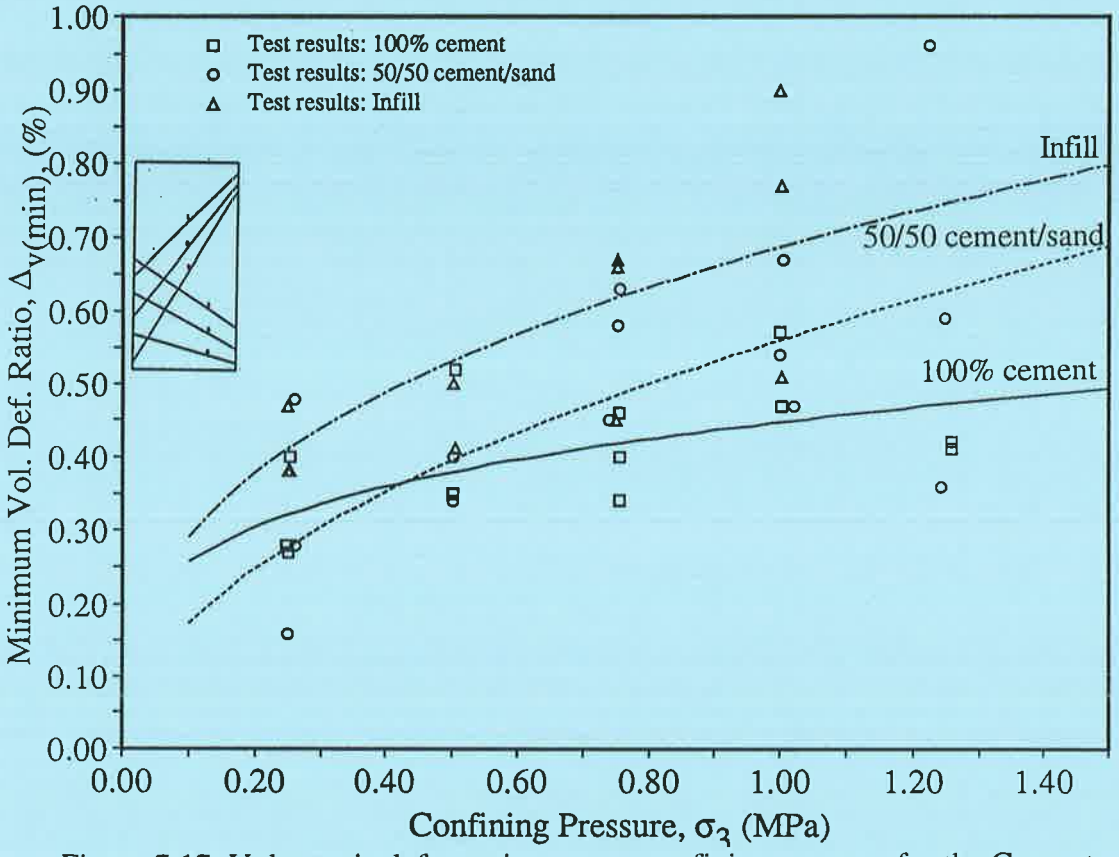

Figure 7.17. Volumetric deformation versus confining pressure for the Geometry 4 specimens.

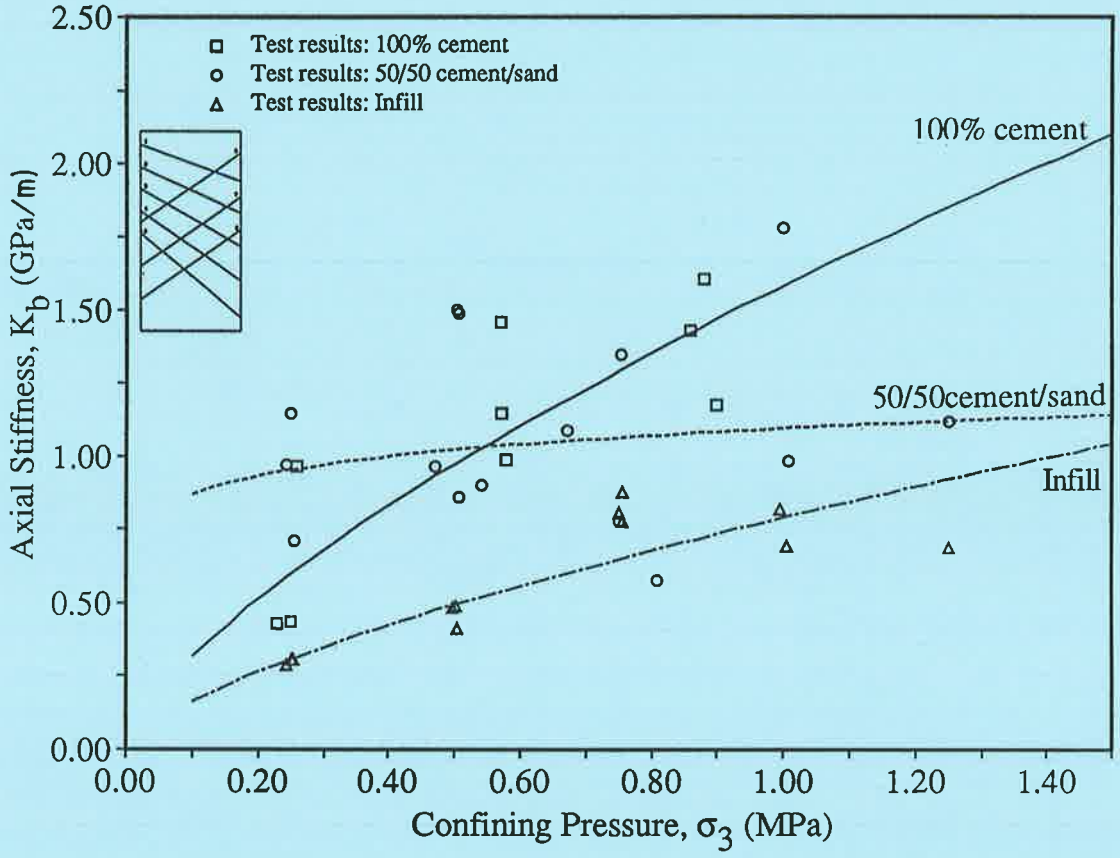

Figure 7.18. Influence of confining pressure on axial stiffness K_R for Geometry 1.

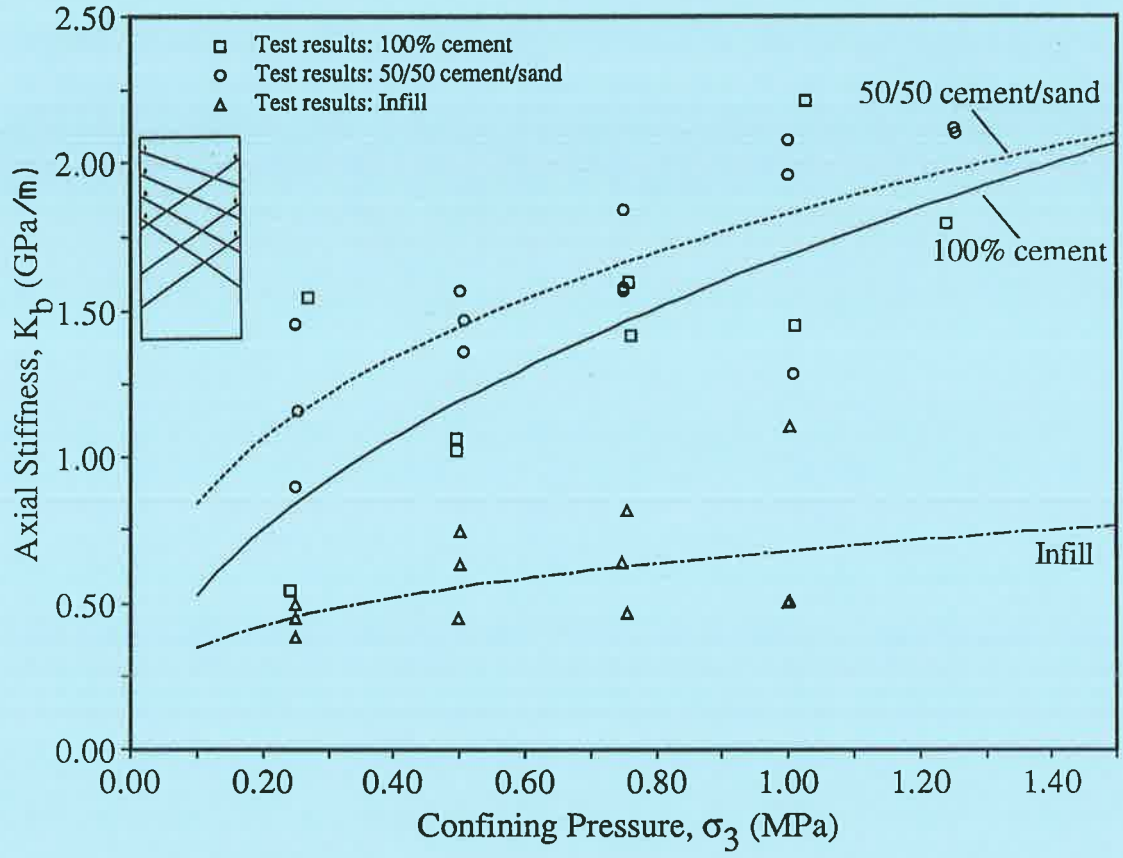

Figure 7.19. Influence of confining pressure on axial stiffness K_R for Geometry 2.

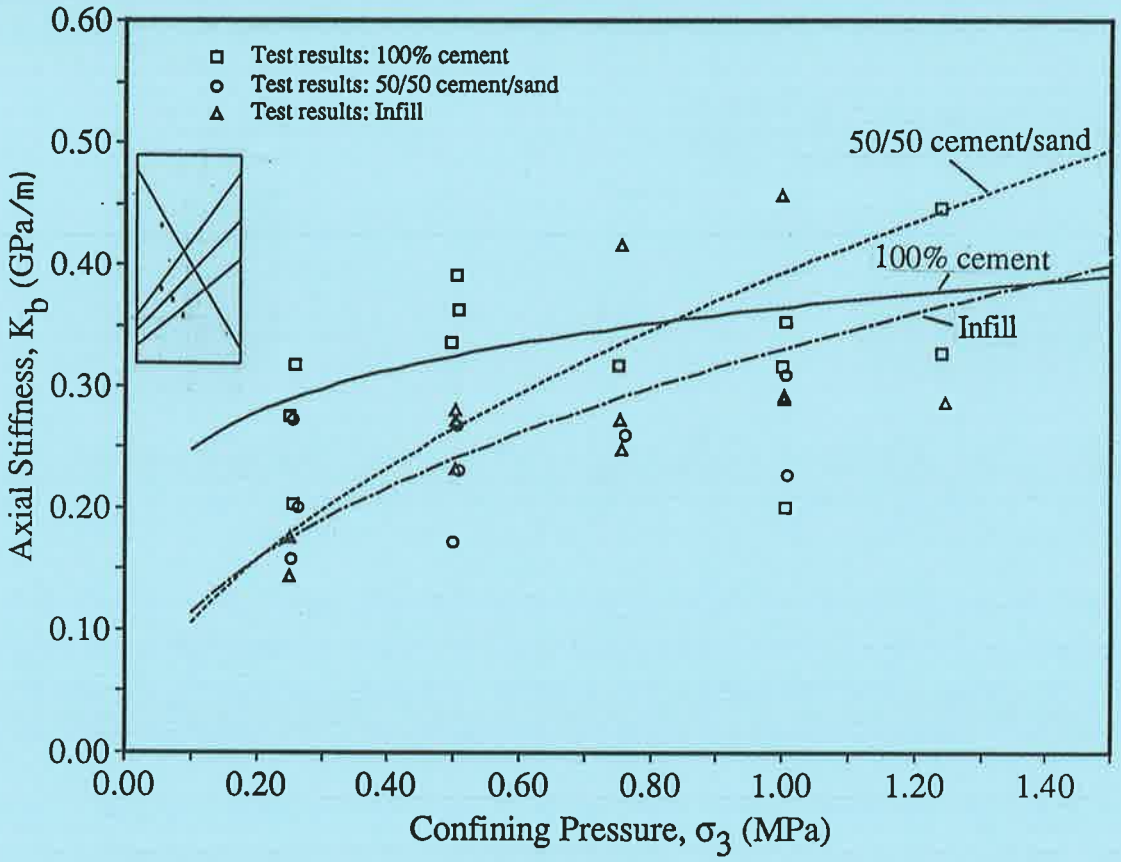

Figure 7.20. Influence of confining pressure on axial stiffness K_R for Geometry 3.

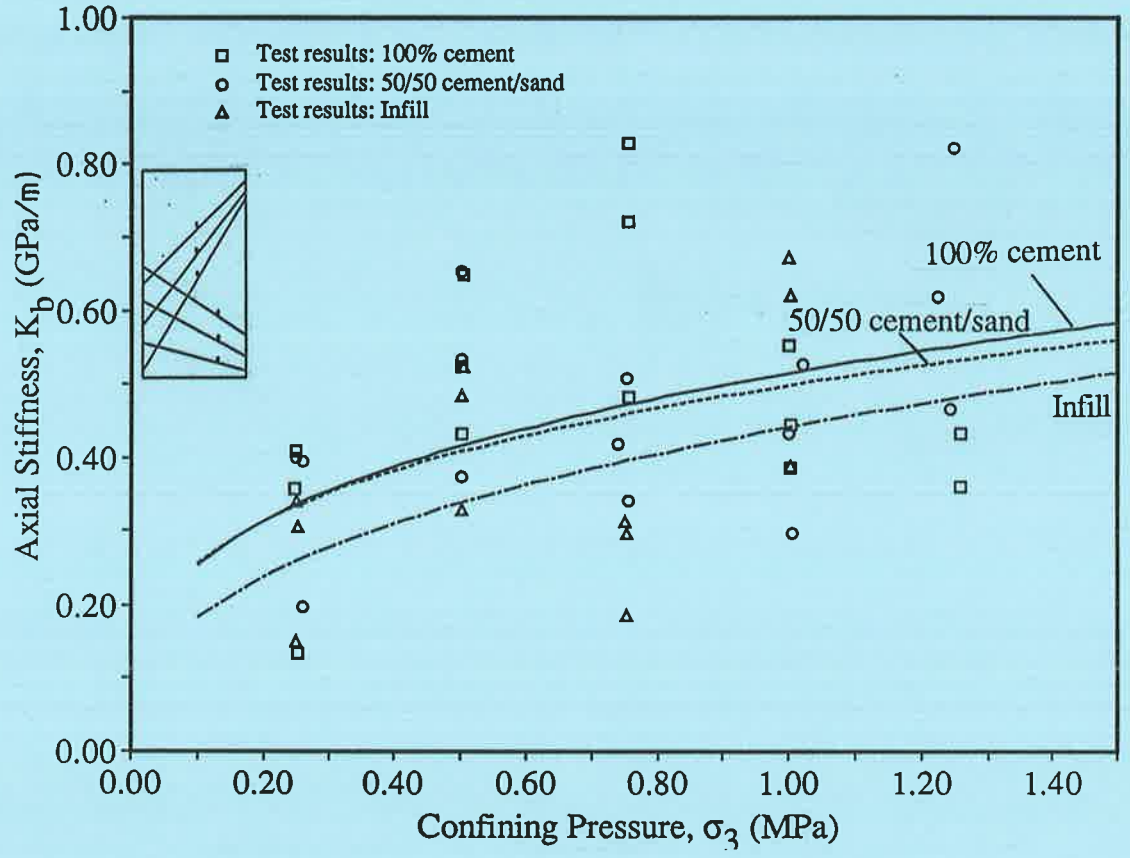

Figure 7.21. Influence of confining pressure on axial stiffness K_R for Geometry 4.

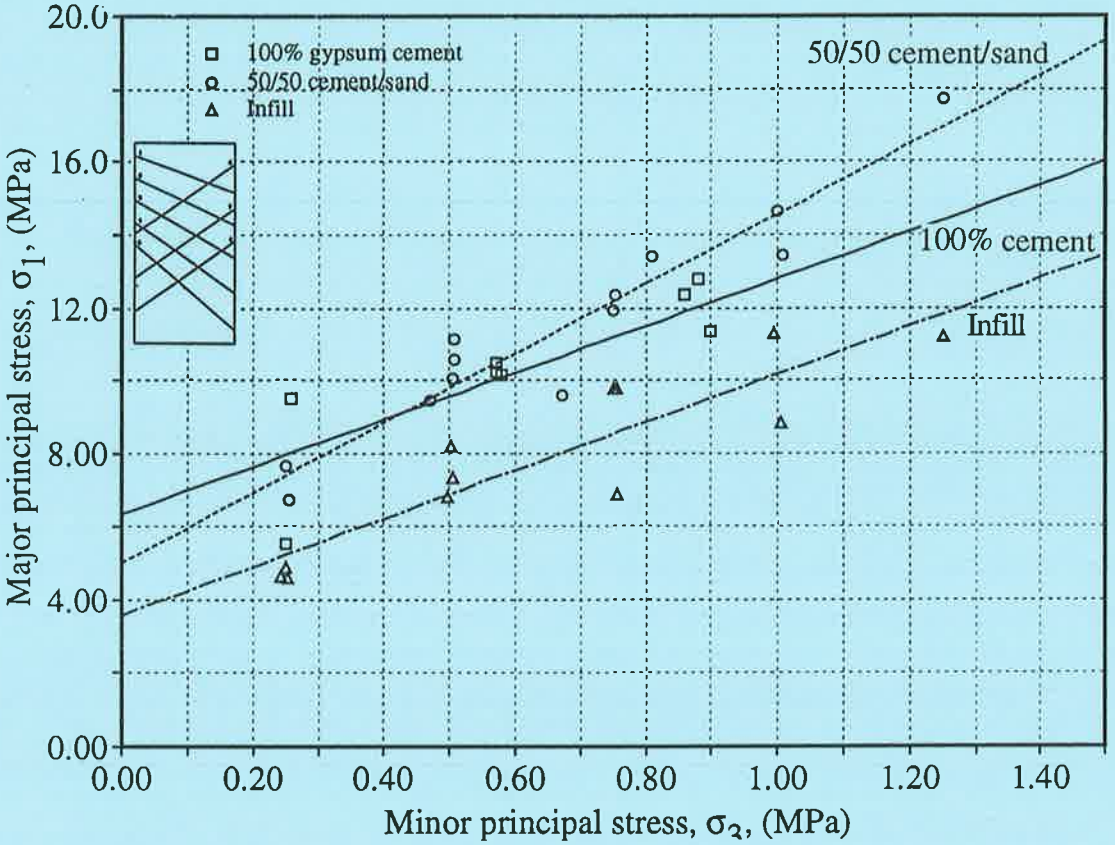

Figure 7.22. Influence of confining pressure on the yield stress of Geometry 1.

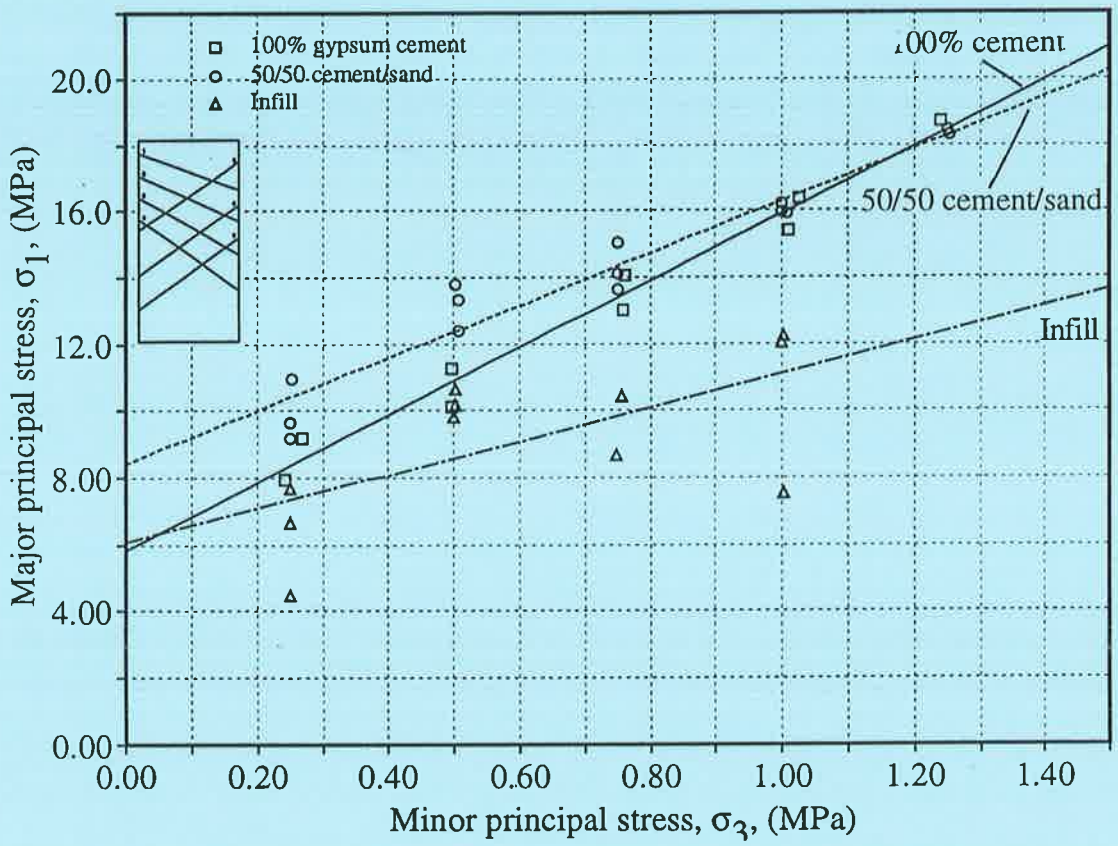

Figure 7.23. Influence of confining pressure on the yield stress of Geometry 2.

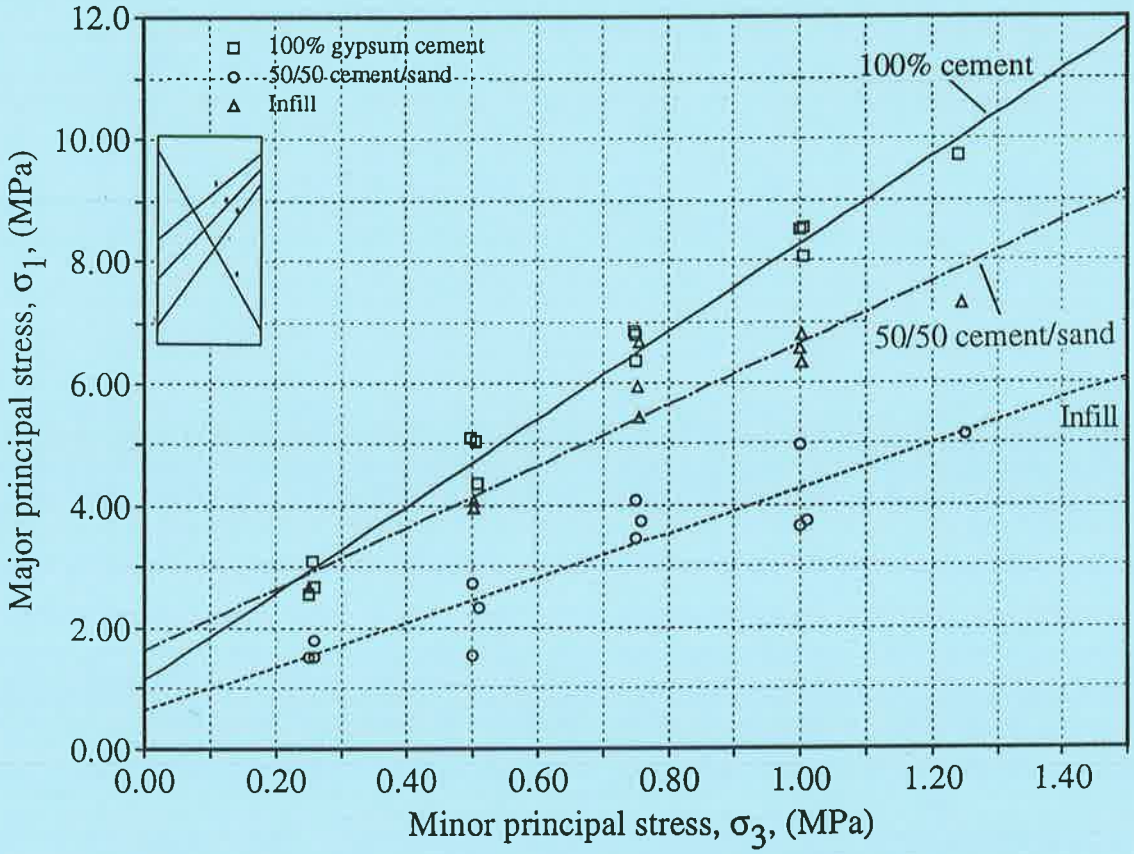

Figure 7.24. Influence of confining pressure on the yield stress of Geometry 3.

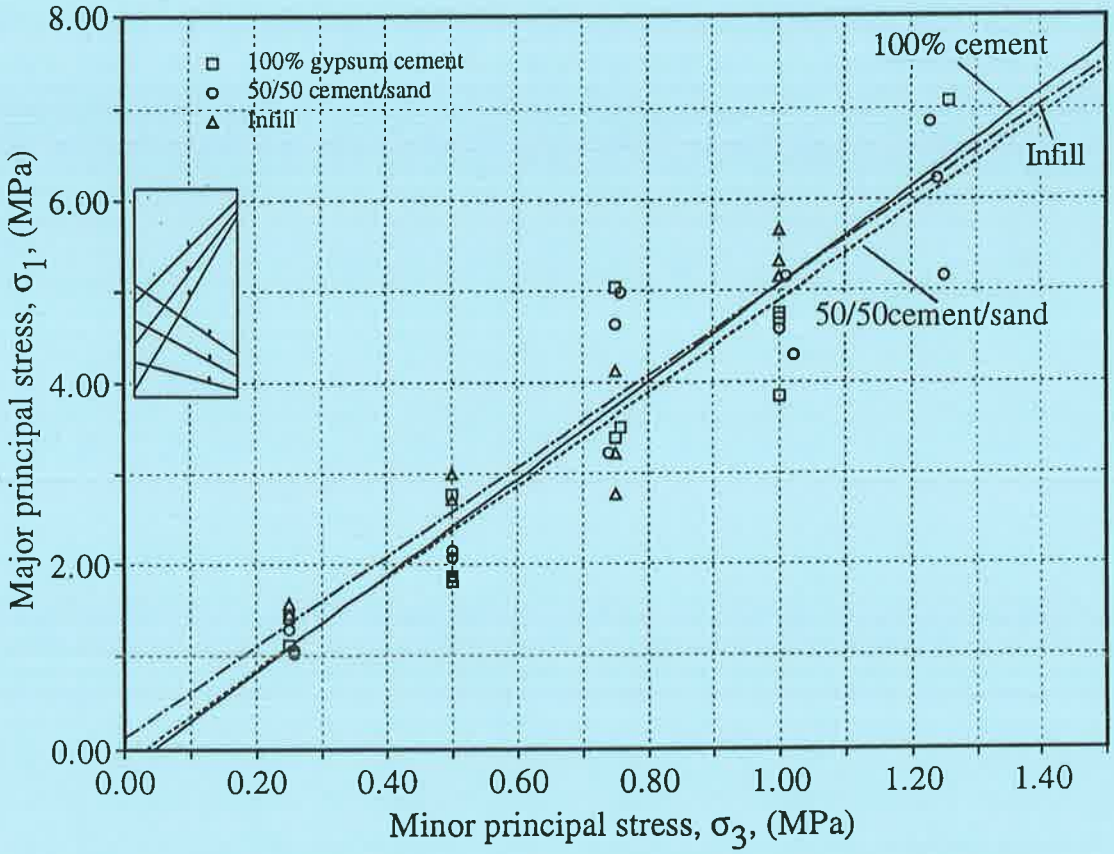

Figure 7.25. Influence of confining pressure on the yield stress of Geometry 4.

Chapter 8.
Numerical Modelling of Discontinuous Specimens.

Chapter 8. Numerical Modelling of Discontinuous Specimens.

8.1. Introduction.

As stated in Chapter 1, the fifth aspect of this study involved using the results obtained in the experimental study to validate a the distinct element method of numerical analysis. If these validations were successful, the numerical procedure could be used as a tool to predict the deformability of other geometries in the field and in the laboratory. The following sections will briefly present the theory upon which the distinct element method is based (ITASCA [77]) and then present four verification tests.

8.2. Description of The Distinct Element Method.

The program having the acronym UDEC (Universal Distinct Element Code) developed by Cundall [39] [40] and Lemos et al. [95] and marketed by ITASCA [77], originated from a project designed to simulate and investigate the behaviour of jointed rock masses when subjected to dynamic loading. A two-dimensional public domain version of UDEC (V1.6) written in Fortran 77 was initially obtained for use in this study. Before this early version of the software could be implemented

(1) a major missing common block had to be written,

(2) the I/O routines had to be structured so they could run under a UNIX operating system,

(3) graphics routines had to be written so output could be viewed on the monitor and produced as hard copy.

While this version of UDEC did not possess all the features of the later two- and three-dimensional versions, it was sufficiently versatile to be a valuable research tool during the early stages of the research. During the later stages of the research a proprietary version of the program (V1.82) was obtained and it was this version that was used for the verification tests.

8.2.1. Block Interface Relations.

The basic assumption in the distinct element method is that it takes a finite time for energy to propagate through a system of blocks. In reality this propagation time is approximately the time which a longitudinal, or P, wave takes to propagate a distance, δ_x, through a block. By selecting a time step, t, such that:

$$t < \frac{\delta_x}{C_p} \tag{8.1}$$

where C_p is the linear velocity of the wave, it can be assumed that the motion of one block occurs independently from that of another block over the time step. This interdependence allows the equations of motion for each individual block to be solved for the particular time step. There is no requirement for large matrices defining the entire domain to be formed and solved, as there is with the finite element method, which makes for a numerically efficient solution. The very small timestep does, however, mean that many iterations are needed before the problem domain either reaches a satisfactory state of equilibrium or failure.

In UDEC, the blocks may be rigid or deformable and a mixture of block types can exist within the same domain. Rigid blocks possess a non-deformable geometry and are suitable for systems controlled by the behaviour of the discontinuities rather than by internal deformation and failure of the blocks. In situations where the stresses are low such as slope stability and similar low stress situations, this generalisation is sufficient. It is often preferable to assume the blocks to be fully deformable. This deformability is allowed for in UDEC by internally discretising a block into finite difference elements and treating the individual block as a continuum.

Each block is defined in two-dimensional Cartesian space by the position of its corners in the space and by the material properties of the block. The material properties can be varied between blocks. Blocks can contact through three mechanisms; corner to corner, corner to edge and edge to edge. Corner to corner and corner to edge contacts are modelled as a single point and edge to edge contacts by two points. Contacts can progressively change between contact types. The shear interaction of each contact point is mechanically represented by a spring-slider system and the normal interaction by a spring. In order to prevent blocks from locking up during corner to corner contact, the block corners are rounded by an arc that is tangential to two adjacent sides. The radius of this arc is variable. If two corners from adjacent blocks contact, the rounding allows the blocks to 'roll' around each other. This action is analogous to the two corners shearing off as they contact.

For the purpose of determining contact forces, two blocks that contact are assumed to penetrate each other. This penetration can be assumed to model inter-asperity or granular penetration. The magnitude of the penetration is determined by considering the geometry of one block with respect to the other and the linear and angular velocity of the centroid of each block over the time period t. The shear and normal displacements of the contact, u_s and u_n respectively, are related to the shear and normal contact velocities, $\hat{u}_s$ and $\hat{u}_n$, as follows,

$$u_s = \hat{u}_s\, t \tag{8.2}$$

and

$$u_n = \hat{u}_n\, t \tag{8.3}$$

The normal and shear forces at a corner to corner or corner to edge contact, F_n, are determined from the relationships,

$$F_S = k_S\, u_S \tag{8.4}$$

and

$$F_n = k_n\, u_n \tag{8.5}$$

where k_n and k_s are the normal and shear spring constants, analogous to the normal and shear stiffness at the contact point. In the case of edge to edge systems this representation is described in terms of stress rather than forces.

A contact can be specified as having a tensile strength, $F_{n(min)}$. The magnitude of $F_{n(min)}$, is often assumed to be zero. If $F_n < F_{n(min)}$ the blocks are assumed to separate and the contact is deleted. The maximum shear strength of a contact, $F_{s(max)}$, is defined according to the Mohr-Coulomb friction criterion (Equation 2.1).

8.2.2. Equations of Motion.

The translation and rotation of a block about its centroid are determined by summing the individual forces and moments on a block and then applying the laws of motion. Consider a block of mass, m, acted upon by gravity, g, a series of forces, F_1, F_2,.....,F_n and moments, M_1, M_2,.....,M_n. The sums of the forces and moments on the block are given by:

$$\sum_{i=1}^{n} F_i = F_1 + F_2 + ...+ F_n \tag{8.6}$$

and

$$\sum_{i=1}^{n} M_i = M_1 + M_2 + ...+ M_n \tag{8.7}$$

The motion of the block can be considered to be opposed by a dashpot at the centroid of the block producing a damping force proportional to the mass of the block and the linear velocity of the block centroid. Damping, in the form of a force that opposes the block velocity, is imposed on the system to ultimately ensure that a steady state condition is reached. At time $T = t_{(n)}$ that is equal to n times a given time step, Δt, the second law of motion can be written for the block as:

$$\frac{\partial \hat{u}}{\partial t} = \frac{\sum_{i=1}^{n} F_i^{t(n)}}{m} - \alpha \hat{u}_i + g \tag{8.8}$$

and

$$\frac{\partial \omega}{\partial t} = \frac{\sum_{i=1}^{n} M_i^{t(n)}}{I} \tag{8.9}$$

where α is the dashpot damping coefficient,

$\hat{u}$ is the linear velocity component of the block centroid,

g is the acceleration of the mass due to gravity,

I is the moment of inertia of the block,

ω is the angular velocity of the block about the centroid and
m is the mass of the block.

If $\hat{u}$ and ω are determined at the half time steps times $t = t_{(n)} + 0.5\,\Delta t$ and $t = t_{(n)} - 0.5\Delta t$ then, based on the central difference theorem, the left hand side of Equations 8.8 and 8.9 can be written as:

$$\frac{\partial \hat{u}_i}{\partial t} = \frac{\hat{u}_i^{(t(n) + 0.5\Delta t)} - \hat{u}_i^{(t(n) - 0.5\Delta t)}}{\Delta t} \tag{8.10}$$

and

$$\frac{\partial \omega_i}{\partial t} = \frac{\omega_i^{(t(n) + 0.5\Delta t)} - \omega_i^{(t(n) - 0.5\Delta t)}}{\Delta t} \tag{8.11}$$

Similarly, $\hat{u}_i$ can be written as:

$$\hat{u}_i = \frac{\hat{u}_i^{(t(n) + 0.5\Delta t)} - \hat{u}_i^{(t(n) - 0.5\Delta t)}}{2} \tag{8.12}$$

Substituting Equations 8.10 and 8.12 into 8.8 and substituting Equations 8.11 into 8.9 and rearranging yields:

$$\frac{\hat{u}_i^{(t(n) + 0.5\Delta t)} - \hat{u}_i^{(t(n) - 0.5\Delta t)}}{\Delta t} = \frac{\sum_{i=1}^{n} F_i^{t(n)}}{m} - \alpha\left(\frac{u_i^{(t(n) + 0.5\Delta t)} - u_i^{(t(n) - 0.5\Delta t)}}{2}\right) + g \tag{8.13}$$

and

$$\frac{\omega_i^{(t(n) + 0.5\Delta t)} - \omega_i^{(t(n) - 0.5\Delta t)}}{\Delta t} = \frac{\sum_{i=1}^{n} M_i^{t(n)}}{I} \tag{8.14}$$

The linear and angular velocity of the block at time $t = t_n + 0.5\Delta t$ can be found by rearranging Equations 8.13 and 8.14 yielding:

$$\hat{u}_i^{(t(n) + 0.5\Delta t)} = \frac{\hat{u}_i^{(t(n) - 0.5\Delta t)}(1 - 0.5\alpha\Delta t) + \left(\frac{\sum_{i=1}^{n} F_i^{t(n)}}{m} + g\right)\Delta t}{(1 + 0.5\alpha\Delta t)} \tag{8.15}$$

and

$$\omega_i^{(t(n) + 0.5\Delta t)} = \omega_i^{(t(n) - 0.5\Delta t)} + \frac{\left(\sum_{i=1}^{n} M_i^{t(n)}\right)\Delta t}{I} \tag{8.16}$$

The position of the block at time $t = t_{(n)} + \Delta t$ can be calculated from the position of the block

at time t_n and the linear and angular velocity of the block. Hence the Cartesian co-ordinate of the centroid on the x-axis, x_i, can be determined by the equation:

$$x_i^{(t(n) + \Delta t)} = x^{t(n)} + \hat{u}_i^{(t(n) + 0.5\Delta t)}\Delta t \qquad (8.17)$$

and the rotation of the block about the centroid, θ_i, by:

$$\theta_i^{(t(n) + \Delta t)} = \theta^{t(n)} + \omega_i^{(t(n) + 0.5\Delta t)}\Delta t \qquad (8.18)$$

An iterative process, summarised in Figure 8.1, is used for solving Equations 8.6 to 8.18. For a particular time step, new contact forces occur as the blocks interact. The magnitude of these forces is determined from Equations 8.4 and 8.5. The resultant of the contact forces is transferred to the centroid of the block that is accelerated accordingly. The magnitude of the linear and angular acceleration is determined from Equations 8.8 and 8.9. The velocities of the block corners are then determined at the half time step by the application of Equations 8.15 and 8.16 and the relative velocity of any block contacts is determined. The sum of the forces at the centroid of the block is then reset to zero. The position of the block is determined from Equations 8.17 and 8.18. This iteration process is repeated for each block in turn. When the equations applying to each block have been solved, the time step is incremented and the process repeated for all blocks.

8.3. Implementation of Program UDEC.

Starfield and Cundall [139] described the first stage of designing any problem domain for numerical modelling as one of visualising the problem and attempting to determine the possible modes of failure. The simplest model is then constructed to verify or eliminate these assumptions. If the model predicts that mechanisms, other than those assumed, occurred then further thought should be given to the problem. Alternatively, if the estimated mechanism appears correct then further complexities can be added to refine the model. A line should be drawn, however, between the practice of adding refinements that may affect the overall behaviour of the model and those added purely to make the model more complex. Starfield and Cundall described the credo that more detail makes a better model as a

carryover from the past when geologic models were considered to be too over-simplified to be useful. They stressed that at best over detailed models were a waste of time and at worst they were counter-productive, by concealing the dominant mechanism by minor mechanisms.

With regard to the present study, the essential components of the problem domain were:

(1) *in situ* and boundary stresses applied parallel to the minor axis of the specimen to simulate the effect of a confining pressure,

(2) a constant axial displacement applied to the upper block parallel to the major axis of the discontinuous specimen to simulate the effect of 'strain controlled' loading conditions,

(3) a lower block fixed in the vertical direction to simulate a stiff lower loading plate and

(4) a series of discontinuities intersecting an intact block.

Before implementing this numerical model a series of tests were carried out to verify the effectiveness of UDEC for modelling the behaviour of the intact material and the discontinuities. A number of verification tests have been presented by ITASCA [77], however, none of the tests:

(1) investigated the elasto plastic stress/deformation characteristics of an intact material,

(2) compared the predicted elasto-plastic deformation of a discontinuity with experimentally obtained results or

(3) investigated the observed change that occurs in the yield strength of an anisotropic specimen with changes in the orientation of the anisotropy.

Three verification tests were, therefore, carried out to investigate these points.

8.3.1 Verification Test 1: Intact Specimens.

This test concerned an elasto-plastic specimen with a horizontal discontinuity subjected to a uniformly increasing biaxial stress differential. (Note: This test was intended to model an intact specimen subjected to axi-symmetric loading conditions. As UDEC is a two-dimensional formulation, biaxial conditions were modelled). The objectives of this test were to assess the ability of UDEC to model:

(1) solid elasto-plastic behaviour,

(2) stress and velocity boundary conditions and

(3) the formation of shear banding.

In a physical triaxial test on an intact specimen, as axial deformation occurs, a crack develops along the plane of maximum shear stress. Thereafter, shear deformation continues along the newly formed discontinuity. As UDEC is essentially a code for modelling a pre-existing discontinuum, it is unable to crack a block. Only those discontinuities that were included in the model at the beginning of a run can exist. Even though blocks cannot crack, the development of shear localisation can be simulated. Shear localisation pre-empts the development of a crack. This effect was modelled by defining all intact blocks as fully deformable and having stress/deformation characteristics defined by an elasto-plastic constitutive model. The accuracy of the plasticity calculation was improved by using diagonally opposed quadrilateral finite difference zones, as shown in Figure 8.2, rather than the traditional triangular finite difference zones. The problem with this approach was that the analysis required the model to be subjected to large strains before shear localisations could be observed. To impose large strains, at a strain rate sufficiently low enough to ensure that shock waves were not introduced into the system, a large number of cycles had to be carried out. The symptoms of a too high strain rate were that either a 'Contact Overlap Too Great' error or undesirable cyclic behaviour occurred.

The mechanical properties of the intact material were assumed to be those of the 100% gypsum cement material used in the laboratory tests. Owing to the discontinuum nature of UDEC, at least one discontinuity was required to intersect the intact block and a horizontal discontinuity was, therefore, included. In order to ensure that compression of the discontinuity had little influence on the deformability of the specimen, a high value for the normal stiffness was applied. The mechanical properties of the intact material and the discontinuity are listed in Table 8.1. A typical UDEC input file is listed in Appendix F.1.

The results obtained from UDEC are compared to the results obtained from Equation 2.2 in Table 8.2. The results are also compared to those obtained from the laboratory tests on the

intact material. The table shows excellent agreement between all results at both extremes of confining pressure. Figure 8.3 indicates the plastic state of the zones. At the points marked (+), the stresses satisfy the continuously yielding joint criterion and it is assumed that plastic flow is occurring. In the upper left corner of the model the zones marked (x) are listed as having 'yielded in past'. According to ITASCA [77] this occurrence is generally the result of zones appearing to have yielded at the beginning of a simulation before stresses are evenly distributed throughout the domain. Once cycling progressed these points 'unloaded' and therefore no longer satisfied the yield criterion.

Throughout the centre of the model a number of zones can be seen to be at the yield surface and it is this surface that governed the failure mechanism of the model. These zones form a shear band and the displacement vectors clearly indicate that the 'flow' of material was influenced by the orientation of this band. Detailed discussion of the theory of localisation, which is the precursor of shear banding, is presented by Vermeer [147] and Vermeer and de Borst [148]. For the particular run shown in the figure, the orientation of the shear bands is from top right to bottom left. In other runs the bands dipped from top left to bottom right or displayed a 'cup and cone' effect. Whichever option predominated for a particular run probably depended on rounding errors that occurred during the simulation and/or the calculation sequence adopted during execution of the program.

A comparison of the axial stress versus axial displacement behaviour of the laboratory specimen and the UDEC model is shown in Figure 8.4. The initial non-linearity of the laboratory plot was due possibly to bedding in of the platens as a result of a slight non-parallelism of the specimen ends. Allowing for this offset, the results show excellent agreement with respect to the axial stiffness. The limitation of the UDEC model with respect to crack development is highlighted subsequent to yield. After yielding, the ability of the laboratory specimen to maintain the axial stress rapidly decreased until the residual shear strength of the newly developed crack was realised. The rate at which the support ability of the specimen decreased was predominantly a function of the stiffness of the testing machine.

The UDEC model was, however, unable to crack and, once the yield strength was realised, plastic deformation of the intact material occurred.

8.3.2 Verification Test 2: Direct Shear Test.

This test concerned a horizontal discontinuity subjected to a shear stress parallel to the discontinuity and a stress normal to the discontinuity (Note: This test was intended to model a direct shear test). ITASCA [77] presented a verification of a direct shear test. This verification test did not compare the results predicted by UDEC with laboratory results.

Table 8.1. Parameters used for UDEC verification tests.

Intact material	Discontinuity
Density = 2400 kg/m^3	Normal stiffness = 150GPa
Bulk modulus = 3.9 GPa	Shear stiffness = 651MPa
Shear modulus = 2.2GPa	Friction angle = 33.8°
Intact cohesion = 9.0MPa	
Tensile strength = 8.6MPa	
Intact friction angle = 37°	

Table 8.2. Comparison of UDEC results with analytical solution and with laboratory results for an intact specimen of 100% gypsum cement in triaxial compression.

	Yield Stress, σ_1, (MPa)		
Confining Pressure, σ_3 (MPa)	Analytic Solution	UDEC Result	Laboratory Result
0.25	37.1	37.1	37.6
1.25	41.1	41.2	39.6

In the shear box tests conducted on the individual discontinuities, the shear stiffness (Figure 6.4(a)-(c)) and the shear strength (Figure 6.5(a)-(c)) were shown to be normal stress dependent. The shear stress versus shear displacement behaviour, described in Section 6.3.1 and shown in Figures 6.1 to 6.3, is also non-linear prior to the shear stress reaching the

residual strength "target" for the discontinuity. The continuously yielding joint model provided in UDEC is considered to model these characteristic discontinuity behaviours better than the standard Mohr-Coulomb model. This improvement occurs because the continuously yielding model is able to model:

(1) non-linear shear stress versus shear deformation behaviour associated with shear stiffness/normal stress interdependence,

(2) changes in the shear strength of the discontinuity as roughness features are modified during shear deformation and

(3) the peak/residual shear strength characteristic of discontinuities that is observed in direct shear tests as discontinuities undergo shear deformation.

For this verification test, UDEC was used to simulate direct shear test number 46 (see Figure 6.1) conducted on a discontinuity intersecting the 100% gypsum cement material. The specimen, having a cross section 60 x 60mm, was subjected to a normal stress of 965kPa.

The continuously yielding model requires that the shear and normal stiffness of a discontinuity be defined by an equation of the form of Equation 6.1. Figure 8.5, obtained from the results of the direct shear test, shows the stiffness of the discontinuity to decrease with shear deformation. The shear stiffness can be seen to decrease from a maximum value of shear stiffness at low displacement to asymptotic to a minimum value. UDEC has the facility for defining both these maximum and minimum values of shear stiffness. For this verification test, the maximum value (MAXJKS) was obtained directly from the plot. In order to choose a suitable minimum value, a linear line of best fit was fitted through the shear stiffness versus normal stress data in Figure 6.4(a) and the intercept on the shear stiffness axis was assumed to represent the minimum shear stiffness for this material (MINJKS).

This continuously yielding model allows for the friction angle of the material to vary from a value that includes the dilation angle of the material down to a residual value. This facility has the effect of simulating damage occurring to the asperities as shear deformation occurs.

In order to determine the maximum and the residual friction angle for the discontinuity, the tangent of the friction angle was plotted in terms of the shear deformation as shown in Figure 8.6. The curve can be seen to increase to a maximum value (JIF) and then to decrease slightly to a lower residual value (JFRIC). Once plastic behaviour occurs, the rate at which JIF reduces to JFRIC is determined by the value of the roughness parameter JR. This parameter quantifies the length between individual roughness profiles. The 100% gypsum cement material had a similar roughness to the infill material and therefore JR was assumed to be the maximum particle size of the material as indicated on the particle size distribution curves shown in Figure 4.7. A typical UDEC input file included the text listed in Appendix F.2.

A comparison of the shear stress versus shear displacement behaviour of the direct shear specimen and the UDEC model is shown in Figure 8.7. The shear stiffness predicted in the elastic region showed excellent agreement with that obtained in the laboratory. In the plastic region, the stiffness prediction was less satisfactory when UDEC predicted a pseudo strain-hardening effect occurring. By extrapolating the elastic and plastic regions to a common point, in order to obtain an estimate of the yield strength of the discontinuity, it was encouraging to see that the predicted and the laboratory results were similar.

8.3.3 Verification Test 3: Anisotropic Specimens.

This test concerned an elasto-plastic specimen with a discontinuity orientated at an angle β_w such that $0^\circ \leq \beta_w \leq 60^\circ$ subjected to a uniformly increasing biaxial stress differential. Larger values of β_w were not tested as values of $\beta_w > 60^\circ$ were not included in the discontinuous laboratory specimens. The objectives of this test were to test the ability of UDEC to model elasto-plastic behaviour in an anisotropic specimen.

The model was divided into fully deformable quadrilateral finite difference zones. Figure 8.8 shows this discretisation applied to a model in which $\beta_w = 35^\circ$. While it was desirable to have uniformity in the shape of the finite difference zones, non-uniformity was not found to cause any difference in the solution. Other than changes in the SPLIT command, which

formed the discontinuity, the UDEC code for these tests was the same as for verification test 1. Eight tests were carried out at angles of 10°, 30°, 35°, 40°, 45°, 50°, 55° and 60° degrees and the results were compared to the analytical results obtained by the application of Equation 2.2.

The results are illustrated in Figure 8.9 for a confining pressure of 250kPa. The results show satisfactory agreement between the analytical and the numerical results for cases in which β_w was greater than the friction angle of the discontinuity, ϕ_w. In these cases the models axially deformed as a result of shear displacement occurring along discontinuities.

The disagreement between the analytical and the UDEC results for cases in which β_w was less than the friction angle was due, not to problems in UDEC but, to the inability of the analytical equation to correctly model the behaviour of anisotropic specimens. In Sections 2.4.1 and 3.2 the results of a number of tests on natural anisotropic materials were discussed. These results confirmed that, rather than there being a sharp change in yield strength of the specimen at $\beta_w = \phi_w$ as predicted by Equation 2.2, the yield strength of a specimen often gradually changed in a manner similar to that predicted by UDEC. In reality, the rate of change in the yield strength of the specimen with changes in β_w depends on the ratio between the shear strength of the intact material and that of the discontinuities. For the cases modelled, there was a combination of slip on the discontinuity and shear deformation of the intact material as illustrated in Figure 8.10. In this figure the upper block is seen to have moved left and the lower block to have moved right along the discontinuity. At the same time the right vertical side of the upper block and the left vertical side of the lower block can be seen to have been slightly distorted by the shear deformations occurring along the shear banding. This complex interplay between the two modes of failure produced the convoluted axial stress versus axial deformation curve in Figure 8.11. This behaviour might have been caused by the discontinuity and the intact material producing the numerical equivalent of stick slip oscillations.

In summary, Verification tests 1 and 2 and 3 showed that UDEC is capable of modelling the

elasto-plastic stress versus deformation behaviour characteristics of intact and anisotropic specimens. The inability of UDEC to crack blocks meant that care had to be taken to identify the development of shear bands which could indicate that the intact material was shearing. The next stage of the study investigated the effectiveness of UDEC in analysing specimens containing multiple discontinuities.

8.3.4. Verification Test 4: Multiple Discontinuities

If a triaxial test is conducted using a 'high pressure' cell (see Section 5.3) in which the specimen is isolated from the confining pressure fluid by a thin membrane fixed to the pistons, it is reasonable to ignore the influence of the membrane on the yield behaviour of the specimen. In this case, it may be acceptable to model the confining pressure acting on the specimen as a boundary condition acting directly upon the blocks. Alternatively, if a Hoek cell is used, the thick membrane remains fixed along its major axis with respect to the specimen and the shear stiffness of the specimen/membrane interface may contribute to the apparent strength of the specimen. If this contribution is significant, the influence of the membrane on the apparent yield strength should not be ignored in the numerical model. A number of simple tests were, therefore, carried out to determine,

(1) the shear stiffness of the specimen/paper jacket interface and the jacket/membrane interface,

(2) the shear strength parameters of the specimen/paper jacket interface and jacket/membrane interface and

(3) the shear and bulk modulus of the membrane.

A 35 x 510mm strip cut from a damaged membrane was installed in a tensile test machine. Four points, two at each end of the membrane and two on opposite edges were drawn on the surface of the membrane in order to enable axial and lateral deformation to be monitored. The resulting stress versus strain curves are shown in Figure 8.12. The slopes of the dotted lines were used to determine the average Young's modulus and Poisson's ratio for the material as 45.2MPa and 0.48 respectively from which the bulk and shear modulus of the material were calculated.

In order to determine the shear strength parameters and shear stiffness of the paper jacket/membrane interface and the jacket/specimen interface, a simple direct shear test was carried out on the materials. These tests involved applying a normal force to the materials with weights and a shear force with a spring balance. The results of the tests are shown in Figures 8.13 and 8.14. Figure 8.13 shows the membrane/jacket interface to have the greatest shear strength of the two interfaces. This shear strength can be defined in terms of a linear Mohr-Coulomb relationship in which the friction angle (JFRIC) is 35° and the apparent cohesion (JCOH) is 964Pa. It was extremely difficult to determine the shear stiffness of the interfaces by this technique as the membrane and the block tended to displace rapidly as soon as the shear strength was realised. Figure 8.14 shows the best results obtainable and these results show both interfaces to have a similar shear stiffness (JKS) in the order of 3.1MPa.

A typical UDEC input file for the discontinuous specimens within the membrane included the text listed in Appendix F.3. The code used for this verification test was essentially the same as that used for Verification test 3 except that the width of the problem domain was extended to include the membrane, the membrane material type was defined and the discontinuities were included. A single interface having the greatest shear strength of the two interfaces and the greatest stiffness of the two interfaces was modelled rather than attempting to model the jacket/membrane interface and the jacket/specimen interface. Although this modelled interface was not an accurate representation of the physical model, for the purposes of this exercise, it was a reasonable assumption.

Figure 8.15(a)-(d) shows the models for Geometries 1-4 prior to the application of boundary conditions. The inclusion of the rubber membrane can clearly be seen in this figure. Figure 8.15(b) highlights the automatically generated finite difference zones for Geometry 2. These zones were given a maximum edge length of 70mm. Smaller zones would have increased the run time and, because the deformability of the specimens was primarily controlled by the discontinuities, would not have contributed to a significantly more accurate solution.

'Hydrostatic' loading conditions on the specimen were modelled by setting the *in situ* stresses

at each of the grid points and all three principal stresses to the same value. (Note: Even though UDEC is a two-dimensional code, it allows a block to fail in the out-of-plane direction. In order to prevent this failure, the out-of- plane stress must be fixed). Even though 'hydrostatic' conditions had been applied, the model had to be cycled, prior to the application of the axial velocity, in order for it to reach an equilibrium state. Had the model not been in equilibrium, the initial stress state at any grid point could have been sufficiently out of balance to invoke a displacement at the grid point or cause the grid point to yield prior to the application of the axial velocity.

During initial implementations of the model, as the model was cycled towards equilibrium, the maximum out-of-balance force that existed at any grid point throughout the domain, was monitored. Equilibrium conditions were reached after approximately 5000 cycles, when the maximum out-of-balance force approached zero.

In order to prevent shock waves throughout the system that might have caused undesirable cyclic behaviour or caused blocks to overlap, a small constant axial velocity of 0.001m/sec was applied to the upper-most block in the model. An axial velocity rather than a boundary stress were applied to simulate the model being tested under 'strain controlled' rather than 'stress controlled' conditions. A fraction of the critical time step for each of the blocks and the zones was selected to further assist in model stability. The implementation of these procedures meant that a very large number of cycles had to be applied to the model if the model was to reach equilibrium under axial loading conditions. The reaction at the centre of the upper boundary was monitored in order for the yield stress at a point under the applied load to be determined.

Figure 8.16(a)-(d) shows the predicted deformation mechanisms for each of the models and Figure 8.17(a)-(d) provides an indication of the plastic state of each of the zones after cycling. The deformation mechanisms indicated in Figure 8.16(a) and (c) agree well with the mechanisms indicated in Figures 7.1(a) and (c) and Figure 7.2(a) and (c). Figure 8.16(a) shows the formation of three wedges as the deformation mechanism is dominated by slip

along Discontinuities 5 and 6, the discontinuities having an orientation closest to b_{crit}. Similarly, Figure 8.16(c) shows that the orientation of Discontinuity 4 with respect to the major principal axis allowed the discontinuity to govern the deformation mechanism of Geometry 3. The shear strength of all discontinuities in Geometry 3 was realised under the imposed stress conditions. Yielding of the intact material was not indicated in Figures 8.17(a) or (c) as deformation of Geometries 1 and 3 was governed by slip along discontinuities.

The most significantly different results from those obtained in the laboratory are shown in Figure 8.16(b) and (d). Figure 8.16(b) indicates that a significant amount of the axial deformation of Geometry 2 occurred along discontinuities in a similar manner to that predicted for the Geometry 1 specimen. This result did not indicate the development of cracks through intact material along which shear deformations were observed in the laboratory. As shown in Verification test 1, this mechanism cannot be modelled by UDEC. Figure 8.17(b) confirms, however, that plastic zones and zones within which tensile failure was predicted, were beginning to form in the specimen. This result indicates that a shear band was beginning to develop from top left to bottom right. No indication of the formation of plastic behaviour, similar to that seen in the Geometry 2 model, is indicated in Figure 8.17(a) for the Geometry 1 model. On the basis of the results of the laboratory tests this result confirmed that UDEC correctly identified the shear failure mechanisms that occurred in the two Geometries.

Like the Geometry 2 specimen, the failure mechanism for the Geometry 4 specimen cannot be correctly modelled owing to the lack of a facility in UDEC to allow intact blocks to crack. For example, in the laboratory, shear deformations along Discontinuity 3 caused a shear fracture to develop in the lower block. The development of this fracture enabled shear deformation along Discontinuity 3 to become the predominant mechanism for the axial deformation of the specimen. Unlike the observed mechanism, Figure 8.16(d), shows that a mechanism was predicted by UDEC that was similar to that seen in Figure 7.2(e). As shown in Figure 8.16(d), UDEC does predict that several zones within those intact blocks that

terminate Discontinuities 1, 2 and 3 had begun to behave plastically prior to the specimen axially deforming by 20mm. While a zone predicted to be in a plastic state does not in itself predict that a fracture had developed, a continuous line of these zones as seen in Figure 8.17(d) is indicative of the development of a fracture. Of course, whether or not a fracture develops in the position in a physical model depends on the elastic properties of the intact material.

Figures 8.18(a)-(d) show examples of the predicted axial stress versus axial deformation behaviour within a zone beneath the velocity boundary for the four geometries. All plots are for the 100% gypsum cement material at a confining pressure of 1250kPa and each numerical model was cycled until at least 12mm of axial deformation had occurred. This deformation was consistent with that observed in the laboratory as being the maximum deformation required to produce plastic behaviour. In order to get UDEC to produce these results and not consistently cause blocks to overlap, the input files had to be slightly modified from that used previously. These modifications involved

(1) increasing the normal stiffness of the discontinuities,
(2) ignoring the influence of the membrane,
(3) fixing the shear stiffness of the discontinuities at a constant value,
(4) reducing the time step with the FRAC command,
(5) setting the CSCAN command to cause the positions of the contact corners to be updated more frequently and
(6) increasing the overlap tolerance with the OVTOL command to allow a greater contact overlap than one half of the rounding length.

Modifications 4, 5 and 6 altered run time parameters and were unlikely to significantly influence the result. Modifications 1, 2 and 3 might have affected the results but, as an acceptable solution could not be obtained without these modifications, it is difficult to quantify the significance of the changes. A constant value of shear stiffness for the discontinuities intersecting each specimen was determined by:

(1) calculating the normal stress along each discontinuity applicable to the chosen principal stress state using the stress transformation equations,
(2) averaging the normal stresses and subsequently,
(3) calculating the shear stress applicable to the average normal stress using Equation 6.1.

Figures 8.18(a)-(d) indicate the onset of slip along the discontinuities although only the simulation of Geometry 3 (Figure 8.18(c)) displayed elasto-plastic behaviour at an axial displacement of approximately that seen in the laboratory. The simulations of Geometries 1, 2 and 4 predicted the onset of discontinuity slip but rather than predict plastic behaviour, displayed a pseudo strain-hardening effect. This result indicates the inability of the code to correctly simulate the combination of intact and discontinuity yield behaviour. The results do, however, indicate a

subtle change in the axial stress versus axial deformation behaviour at an axial deformation similar to that at which plastic behaviour was seen in the laboratory. This point has been indicated on each of the plots.

The yield stress for the Geometry 3 specimen was determined by summing the gridpoint forces acting beneath the velocity boundary under plastic flow condition and dividing the total force by the effective area (0.15m) over which the stress was applied. On average, the yield stress obtained by this method was 8% greater than that indicated in the axial stress versus axial deformation plot. As described previously, being a two dimensional simulation, UDEC models the geometries as strips and assumes a unit third dimension. UDEC is unable to account for the uniform axial load being applied over a circular rather than a square, cross section. A rudimentary correction was, therefore, applied to the predicted yield stress to account for the difference between the actual and the modelled cross sectional area. This correction, of $\frac{4}{\pi}$, is the ratio between the two areas.

The yield stress for Geometries 1, 2 and 4 could not be determined with respect to the gridpoint forces beneath the velocity boundary as these forces did not become constant with the onset of plastic flow but increased with axial deformation. Instead an estimate of the yield stress was obtained by:

(1) determining the axial stress acting within the zone directly beneath the velocity boundary when the change indicating the onset of plastic behaviour occurred,
(2) increasing this stress by 8%, the amount found for the Geometry 3 simulation to be appropriate when gridpoint forces are considered and
(3) applying the $\frac{4}{\pi}$ correction to account for the cross sectional area of the specimen.

The predicted yield stress for each of the specimens are compared in Tables 8.3 and 8.4 to those obtained by the application of Equation 7.10. The table shows two values of the predicted stress. The first value includes the 0.8% correction for Geometries 1, 2 and 4. The second value includes the area correction for all geometries. The error term represents the percentage change in the predicted result from the actual result.

The predicted results for the Geometry 2 specimen were acceptable which indicates that for domains in which axial deformation occurs primarily as a result of the deformation of the intact material, UDEC can provide a reasonable solution. The results for the other geometries show large and unacceptable errors. These results suggest that while UDEC can correctly predict yield stresses for relatively simplistic cases such as direct shear tests, the code becomes less effective as the number of blocks increases.

Table 8.3. Comparison of UDEC and laboratory results for Geometry 1 and 2 specimens of gypsum cement.

Confining Pressure (kPa)	Predicted Yield Stress (MPa)		Actual Yield Stress (MPa)	Error (%)	Predicted Yield Stress (MPa)		Actual Yield Stress (MPa)	Error (%)
	No area corn.	Area corn.			No area corn.	Area corn.		
250	3.3	4.3	7.9	46	5.8	7.4	8.4	12
500	5.4	6.9	9.6	29	8.0	10.2	10.9	6
750	6.2	7.8	11.2	30	10.3	13.0	13.4	3
1000	9.2	11.7	12.8	9	12.7	16.2	15.9	-1.8
1250	10.9	13.8	14.4	4	13.3	16.9	18.5	9

Table 8.4. Comparison of UDEC and laboratory results for Geometry 3 and 4 specimens of gypsum cement.

Confining Pressure (kPa)	Predicted Yield Stress (MPa)		Actual Yield Stress (MPa)	Error (%)	Predicted Yield Stress (MPa)		Actual Yield Stress (MPa)	Error (%)
	No area corn.	Area corn.			No area corn.	Area corn.		
250	1.1	1.4	3.0	53	4.0	5.1	4.3	-18
500	2.1	2.7	4.8	44	6.3	8.0	6.1	-30
750	3.3	4.2	6.6	36	8.0	10.1	7.8	-30
1000	4.4	5.6	8.4	33	9.8	12.5	9.6	-30
1250	5.4	6.9	10.2	32	11.4	14.5	11.3	-29

This limited study highlights some of the limitations of the two dimensional code for simulating complex three dimensional problems. The geometrical limitations have been somewhat addressed in the three dimensional distinct element code 3DEC. Figure 8.19 from Cundall [42] shows the collapse of a discontinuous three-dimensional column obtained by using 3DEC. The deformation mechanism indicated shows the potential for the code to simulate the behaviour of discontinuous specimens such as those investigated in this study.

8.4. Summary

In this chapter, a number of validation tests have been carried out to assess the suitability of using UDEC to simulate the axial stress versus axial deformation behaviour of discontinuous specimens. The results indicate that UDEC can correctly identify deformation mechanisms in specimens in which axial deformation occurs primarily due to slip along pre-existing discontinuities. For specimens in which axial deformation occurs primarily due to cracking of intact blocks, care needs to be taken to identify the formation of shear banding that indicates the onset of plastic flow.

A large amount of time was devoted in this study to obtaining suitable results from the simulation yet the validation indicated an unacceptable disparity between the predicted and the actual yield stresses. UDEC possesses a vast number of features for modifying the problem domain. Time limitations did not, however, permit a more thorough investigation as to the cause of the disparity and the possibility for better results to be achieved by incorporating more of features into the analysis.

The advantage of having the laboratory obtained yield stresses to validate the predicted stresses is obvious. If UDEC was used to simulate a domain in which there was no means of validating the predicted results against physical results, extreme caution would need to be taken before any design could be based on the predicted result. In summary, UDEC provides an excellent tool for indicating failure mechanisms. On the basis of the results obtained in this study, UDEC should not, however, be used to provide definitive analytical solutions for design situations involving complex geometries.

Even without a contribution from UDEC, the results obtained in Chapter 7 could still be used to provide valuable data necessary for the development of the orientation weighting procedure in the next chapter.

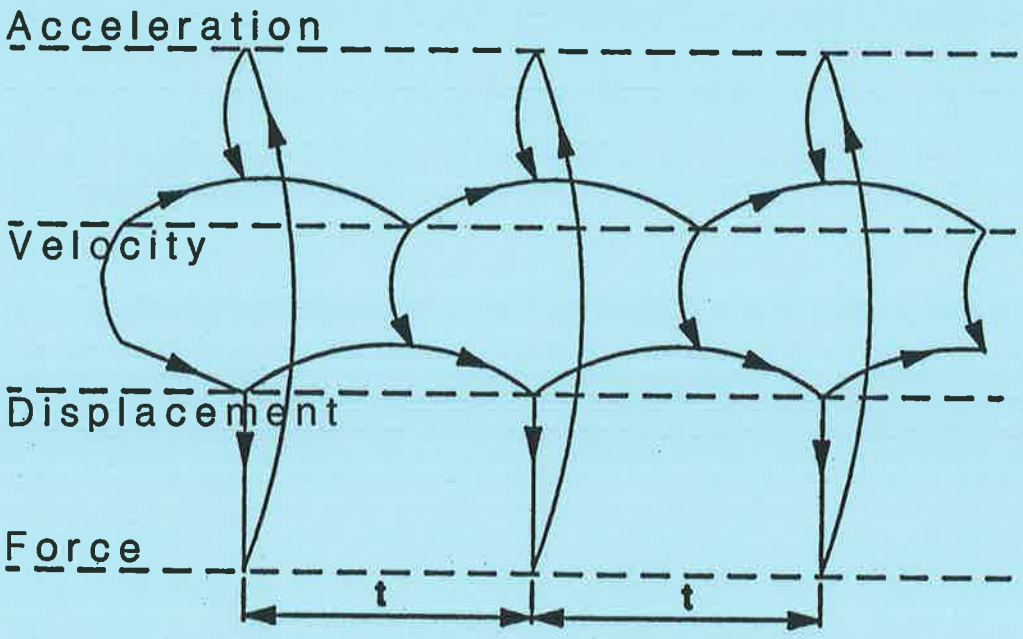

Figure 8.1. Interlaced Nature of Calculation Cycle Used in UDEC. - (after ITASCA [77])

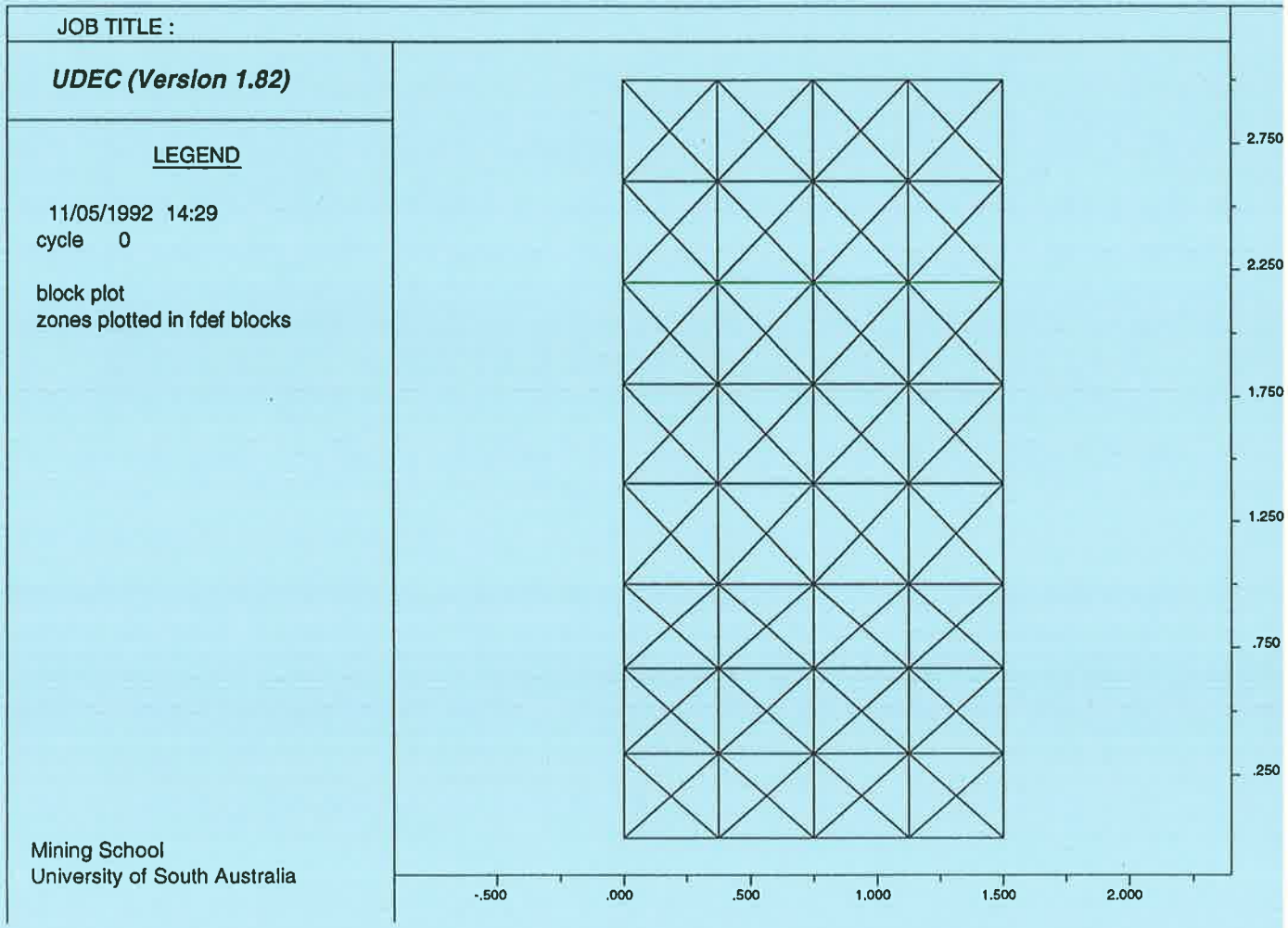

Figure 8.2. Discretisation of elasto-plastic intact block into constant strain diagonally opposed finite difference triangles.

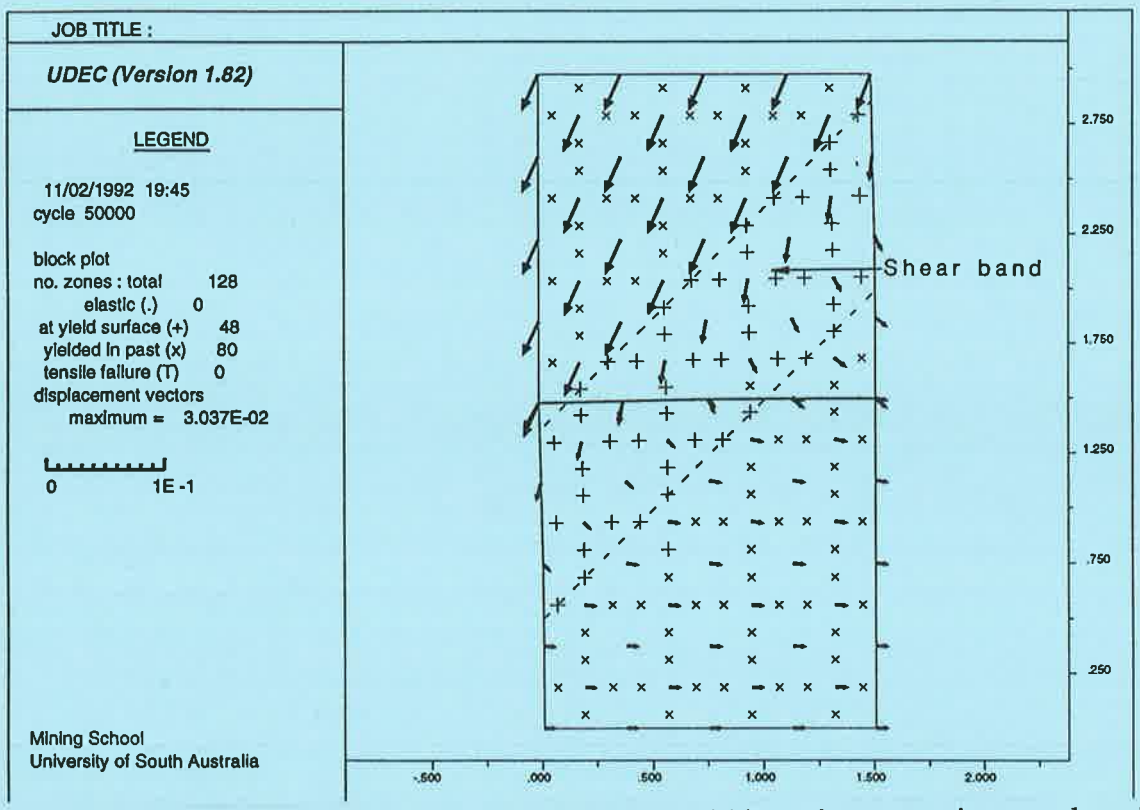

Figure 8.3. Plot indicating the plastic state of the zones within an intact specimen undergoing triaxial compression.

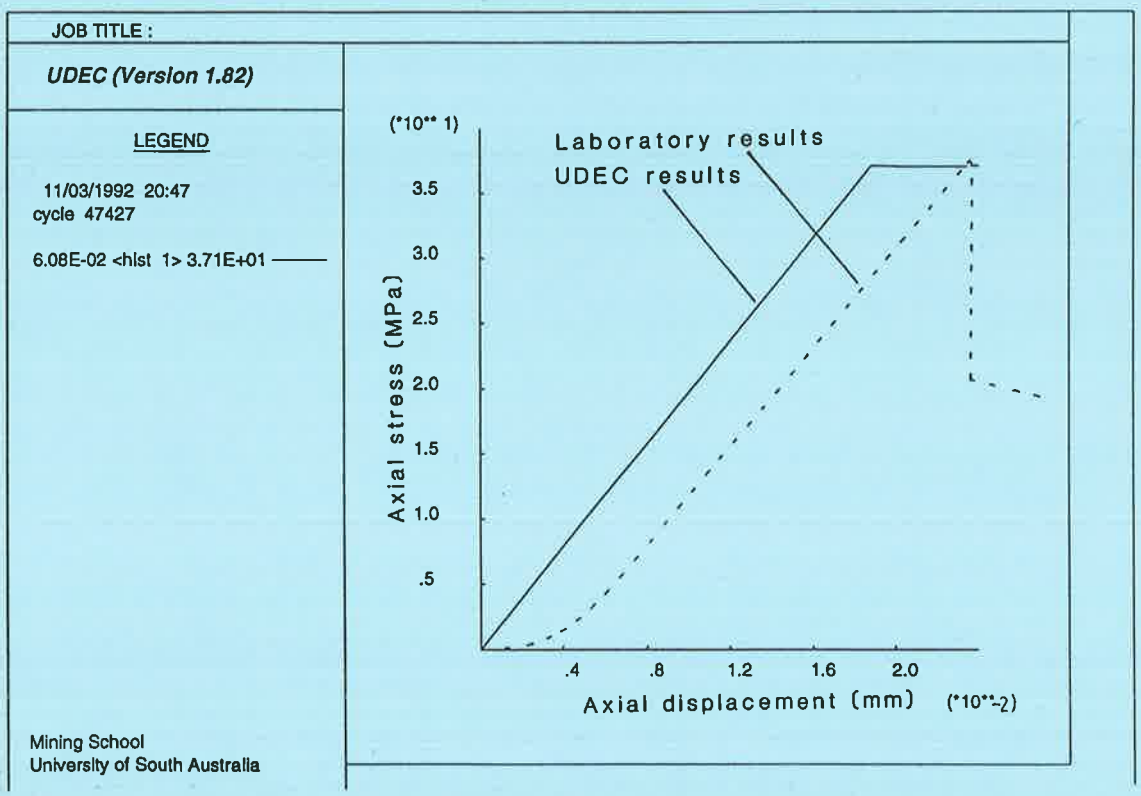

Figure 8.4. Comparison of the axial stress versus axial displacement behaviour of the intact 100% gypsum cement laboratory specimen with that within a zone beneath the applied load in the UDEC model.

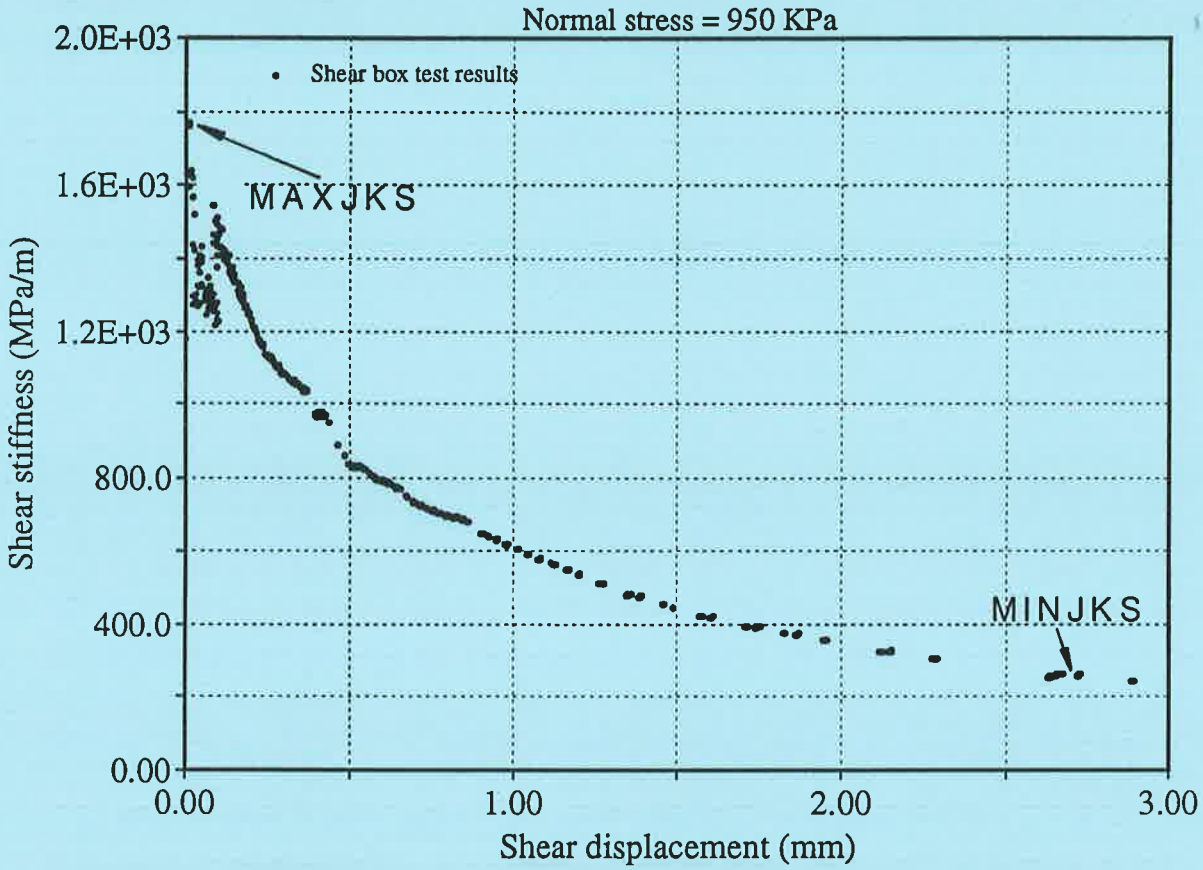

Figure 8.5. Variation in the shear stiffness of the discontinuity with shear displacement for direct shear test 46.

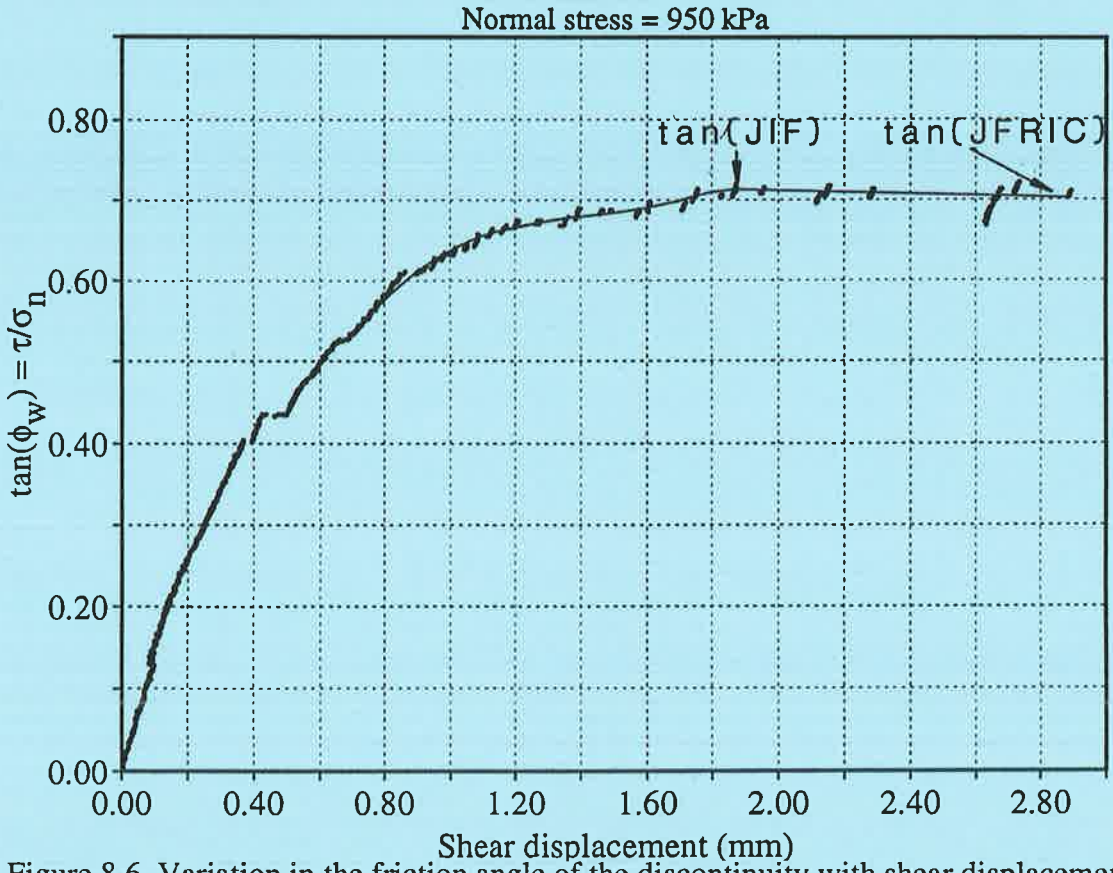

Figure 8.6. Variation in the friction angle of the discontinuity with shear displacement for direct shear test 46.

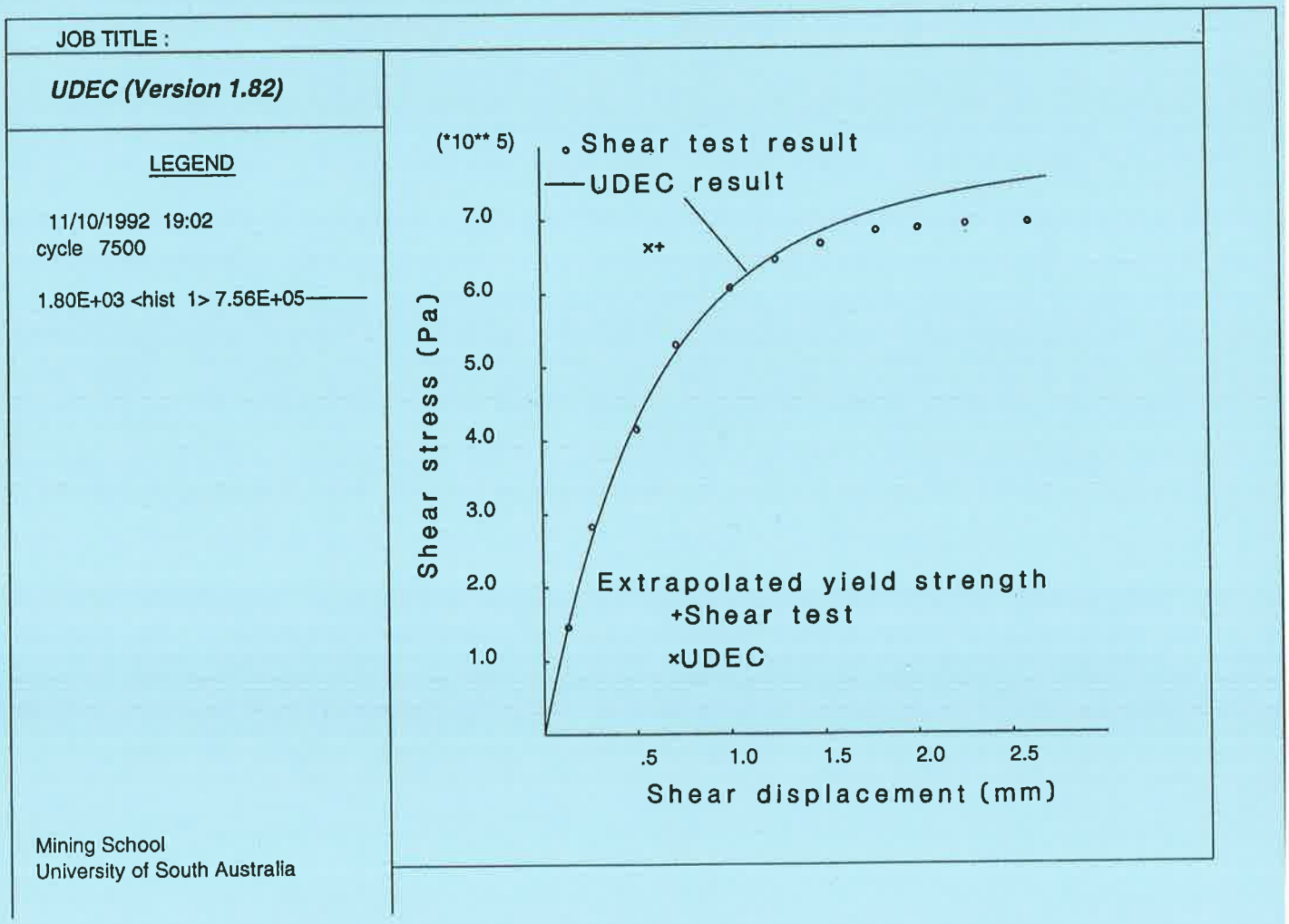

Figure 8.7. Comparison of laboratory direct shear test results with the results predicted by UDEC.

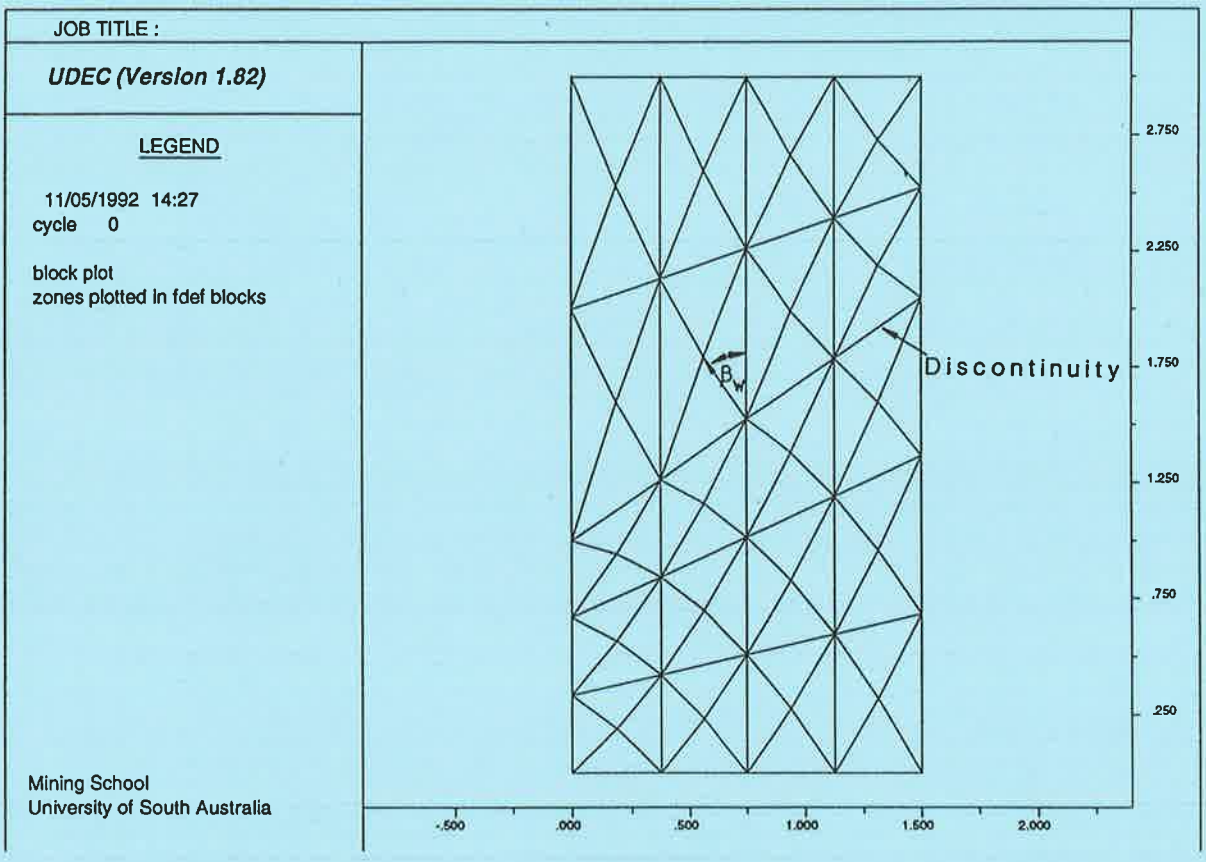

Figure 8.8. Discretisation of elasto-plastic anisotropic block into constant strain diagonally opposed finite difference triangles.

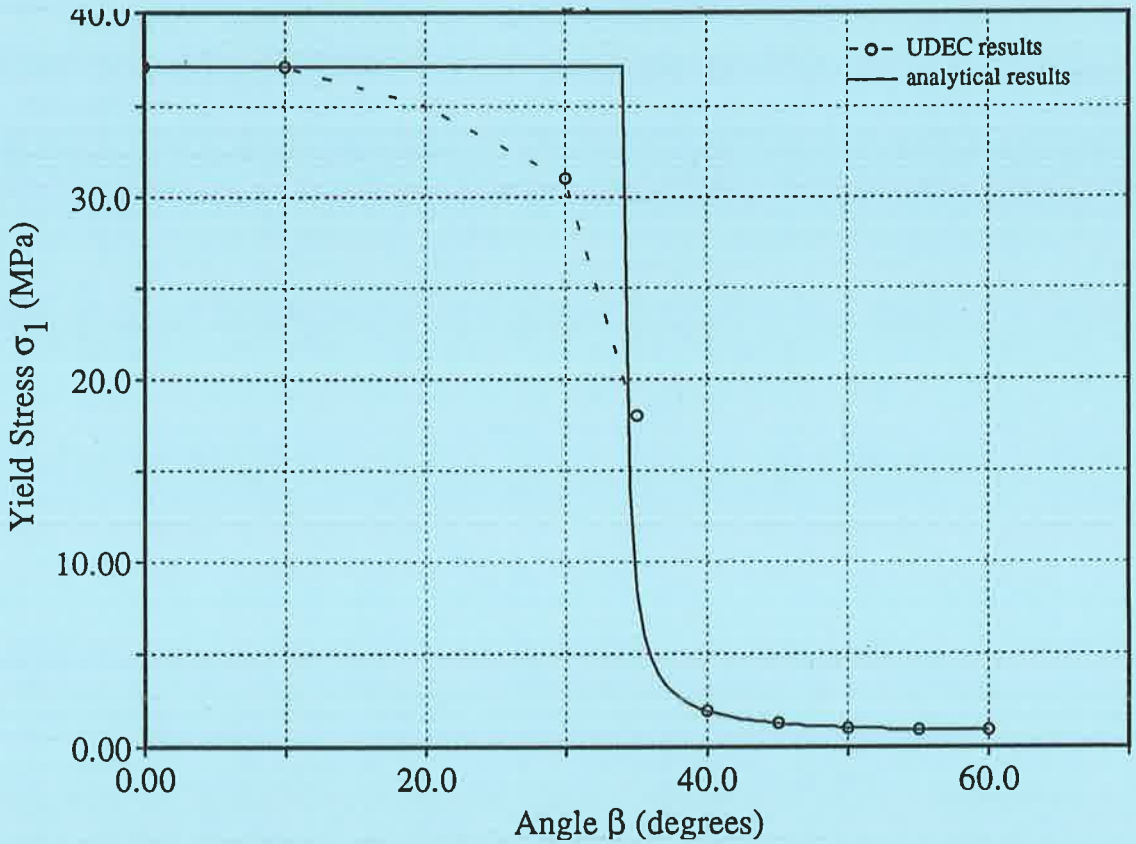

Figure 8.9. Variation in yield stress with discontinuity orientation for analytical and UDEC anisotropic models. σ_3=250kPa.

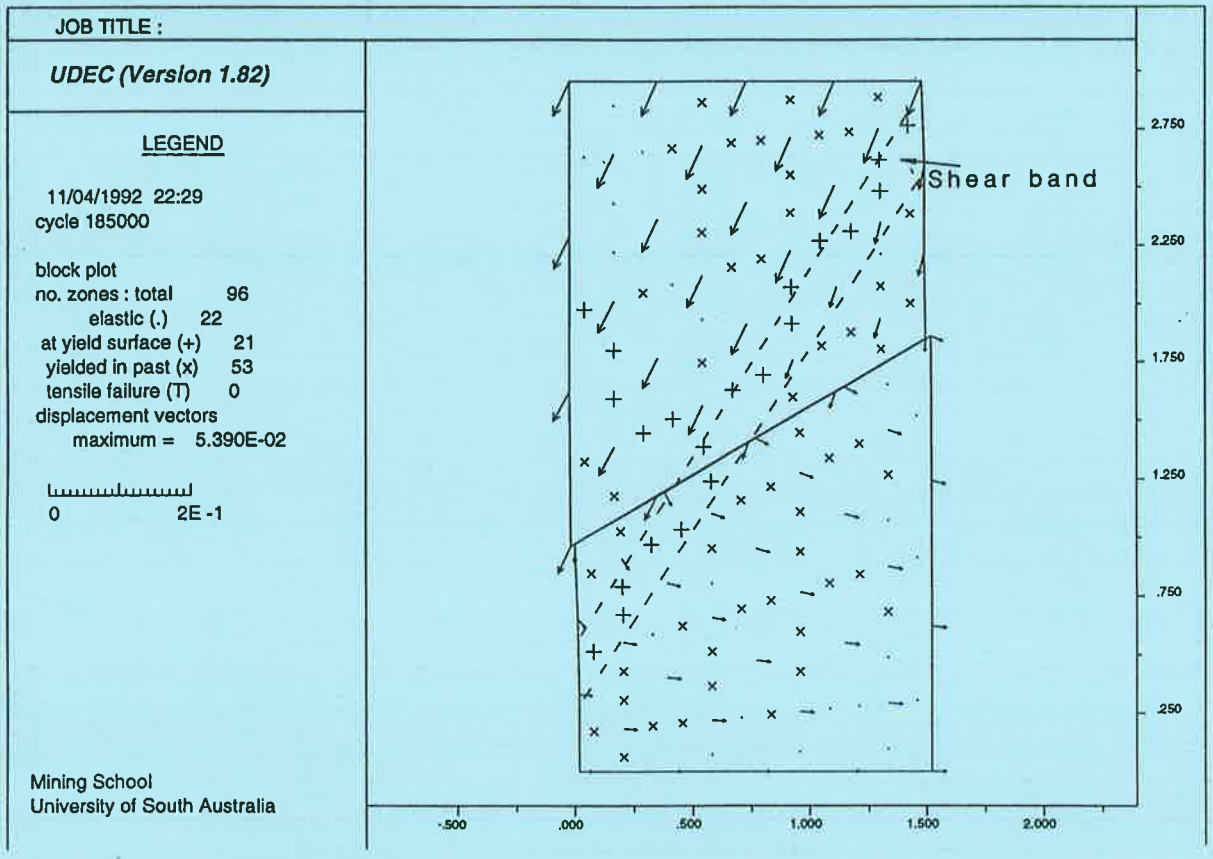

Figure 8.10. Plot indicating the plastic state of the zones within an anisotropic specimen undergoing triaxial compression. β_w=30°, σ_3=250kPa.

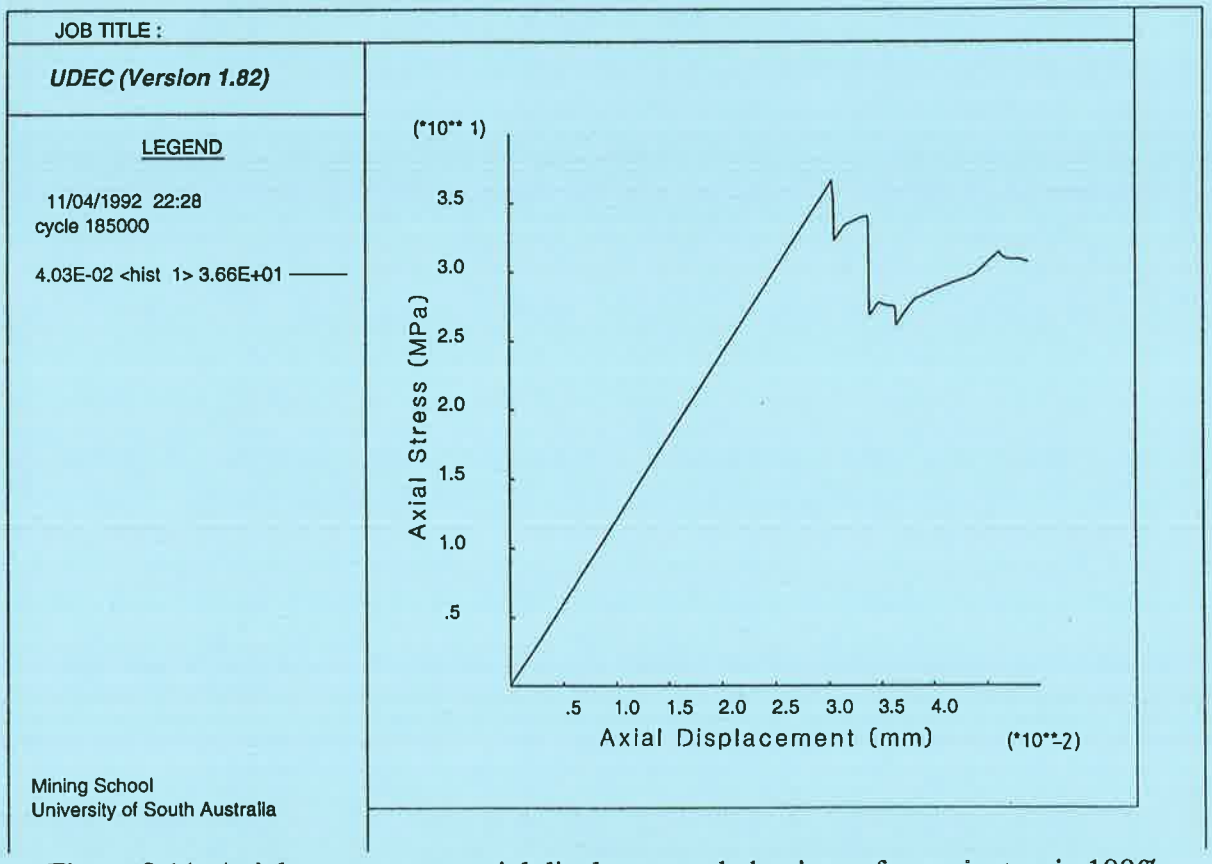

Figure 8.11. Axial stress versus axial displacement behaviour of an anisotropic 100% gypsum cement specimen within a zone beneath the applied load. β_w=30°, σ_3=250kPa.

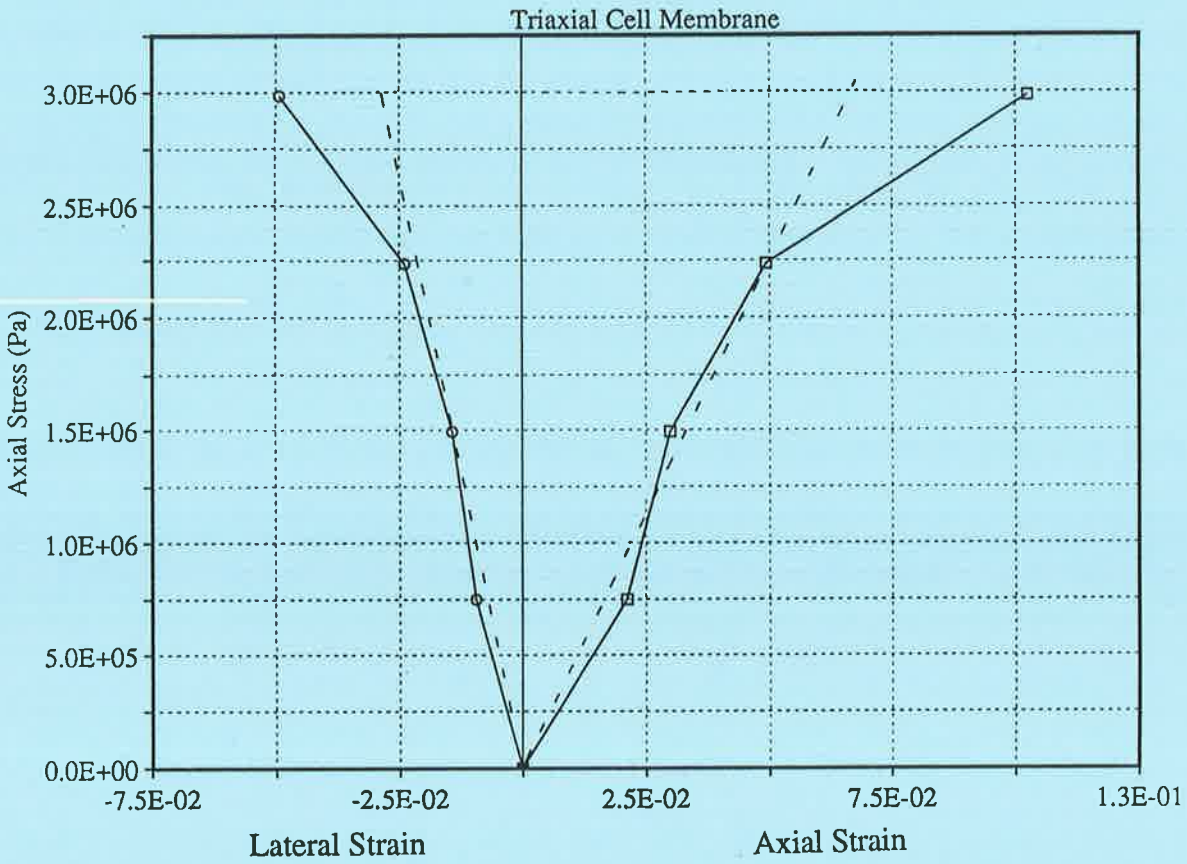

Figure 8.12. Axial stress versus axial and lateral strain curves for the membrane.

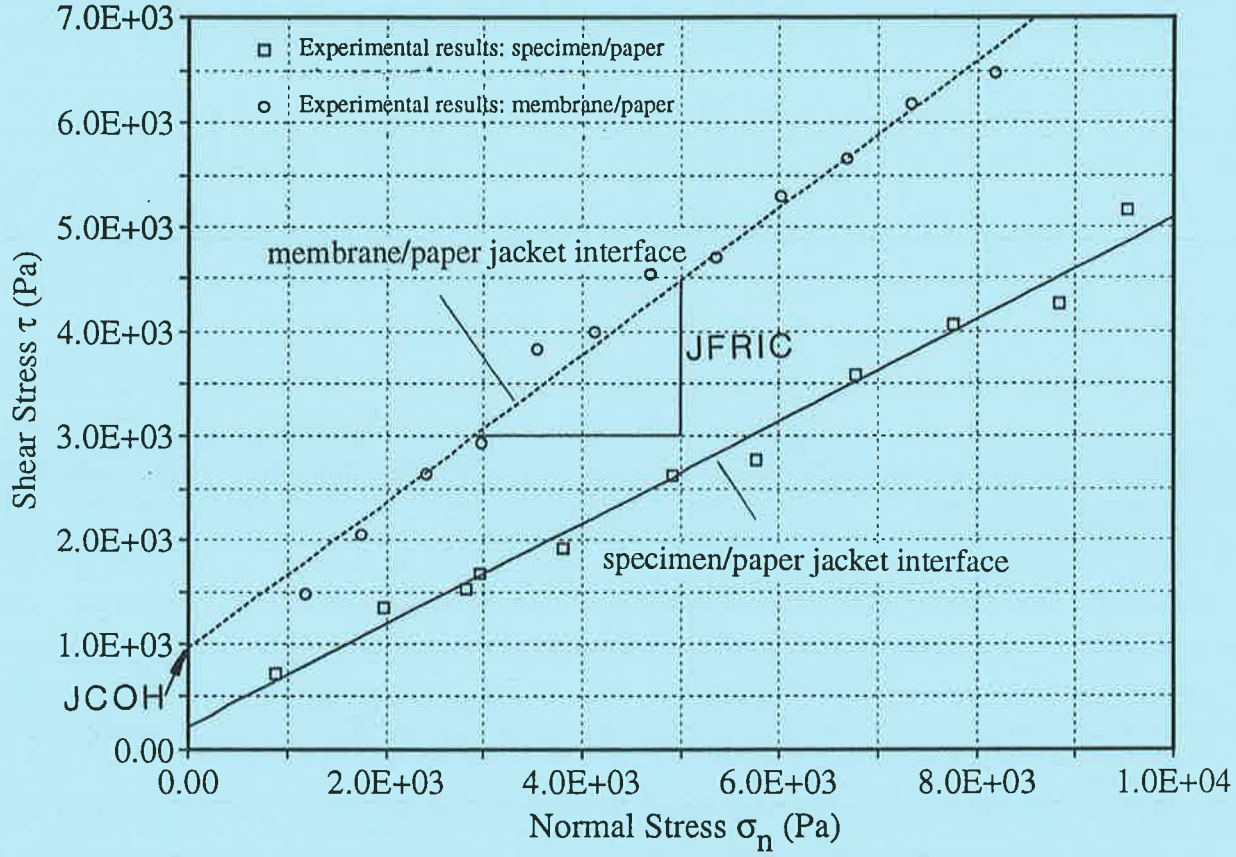

Figure 8.13. Shear versus normal stress results of direct shear test on membrane/paper and specimen/paper interface.

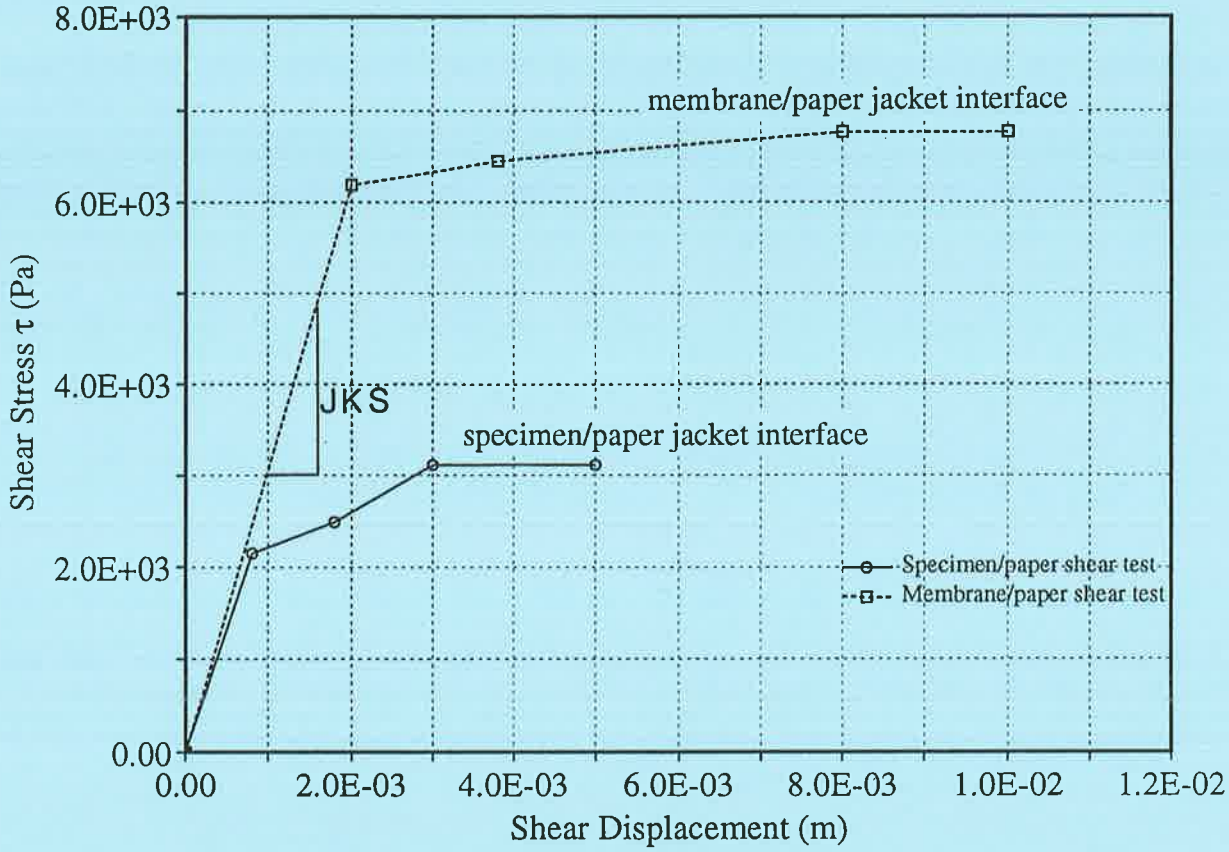

Figure 8.14. Shear stress versus shear deformation results of direct shear test on membrane/paper and specimen/paper interface.

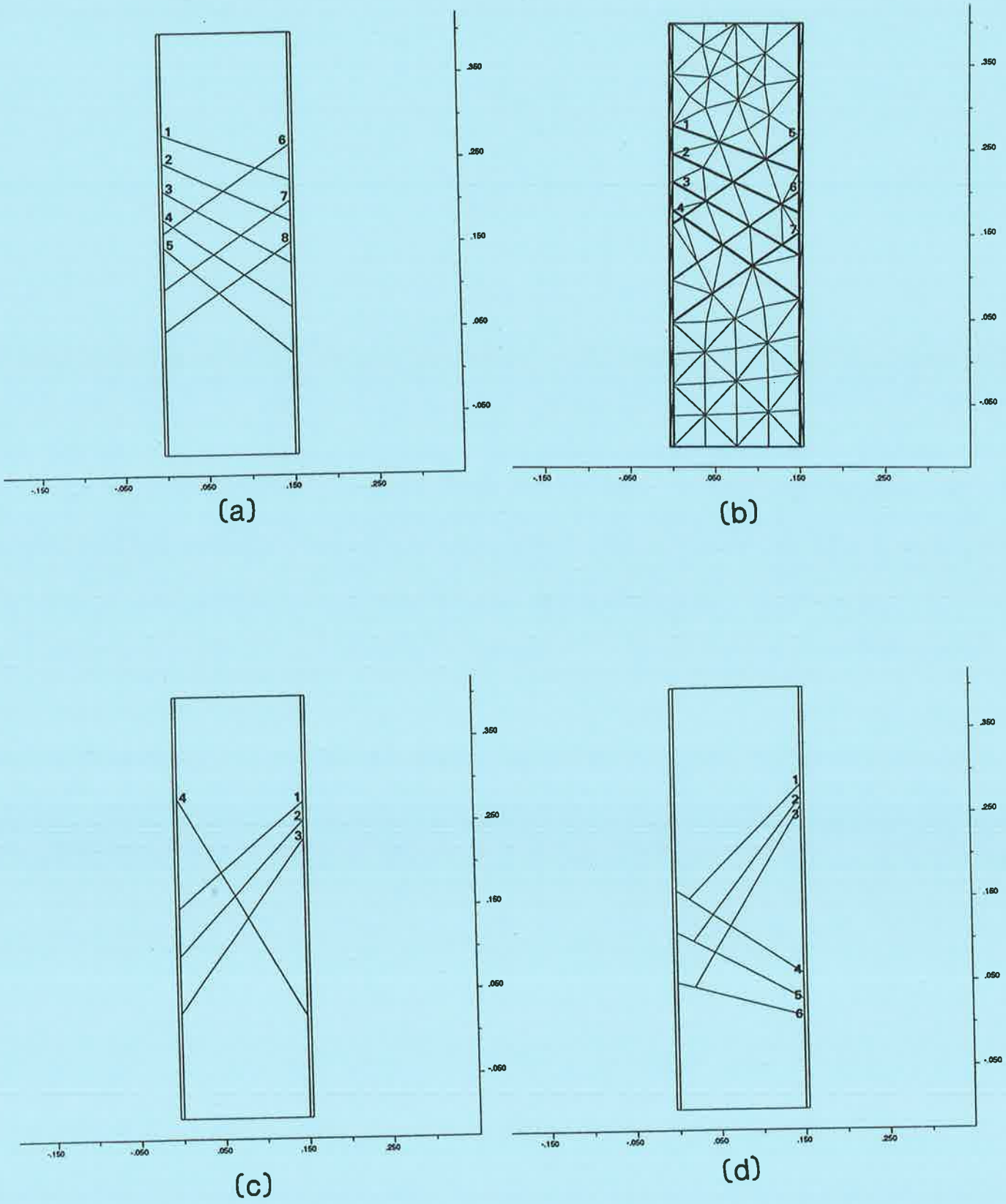

Figure 8.15(a)-(d). Numerical model of Geometry 1-4 specimens prior to the application of boundary conditions.

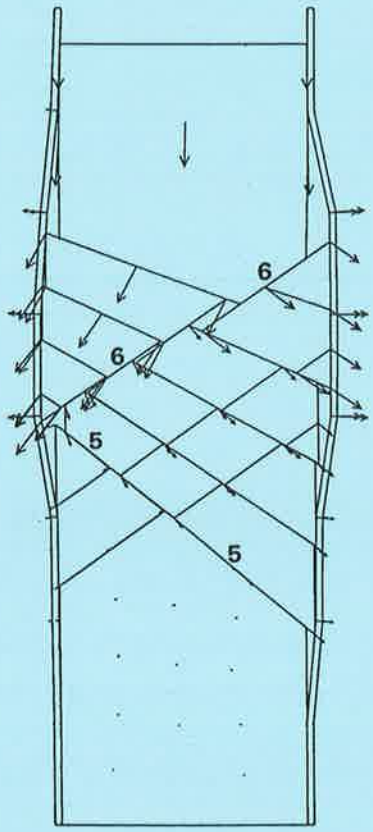

(a)

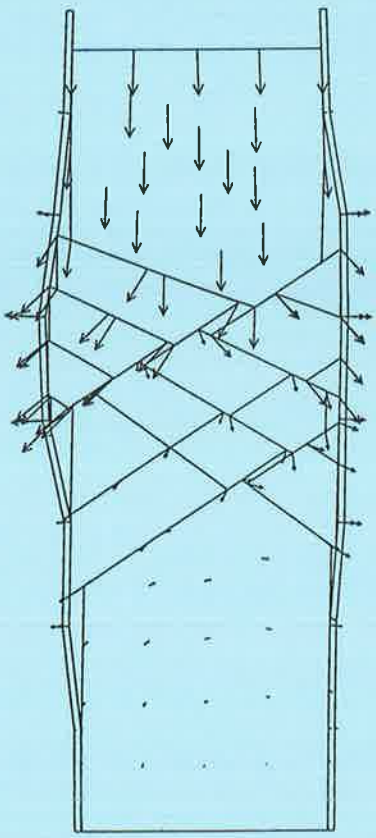

(b)

Figure 8.16(a)-(b). Deformation mechanisms for (a) Geometry 1 and (b) Geometry 2 as predicted by UDEC. Arrows indicate the relative size and direction of gridpoint displacements.

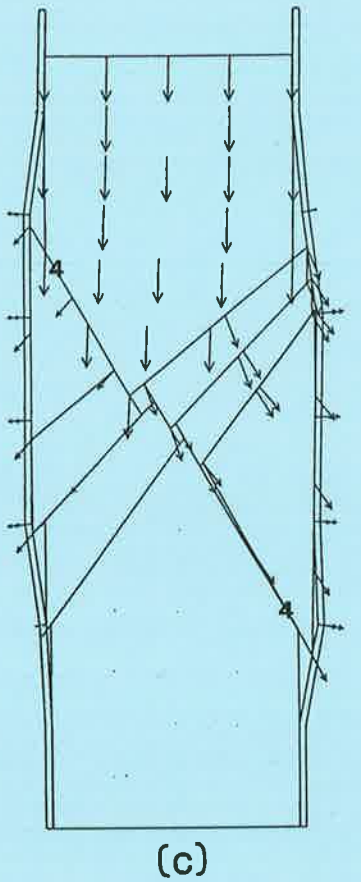

(c)

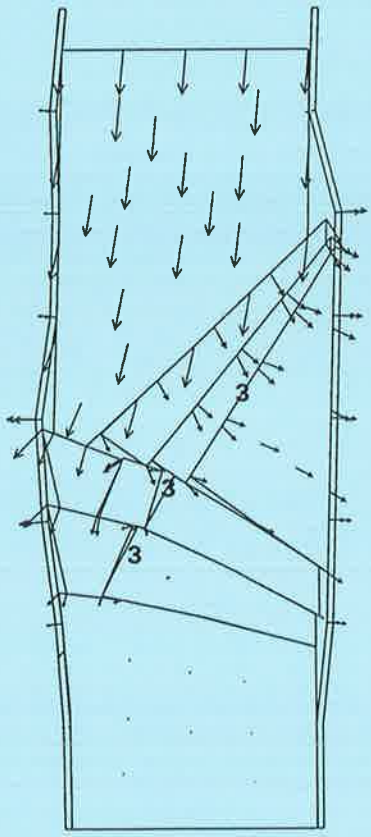

(d)

Figure 8.16(c)-(d). Deformation mechanisms for (c) Geometry 3 and (d) Geometry 4 as predicted by UDEC.

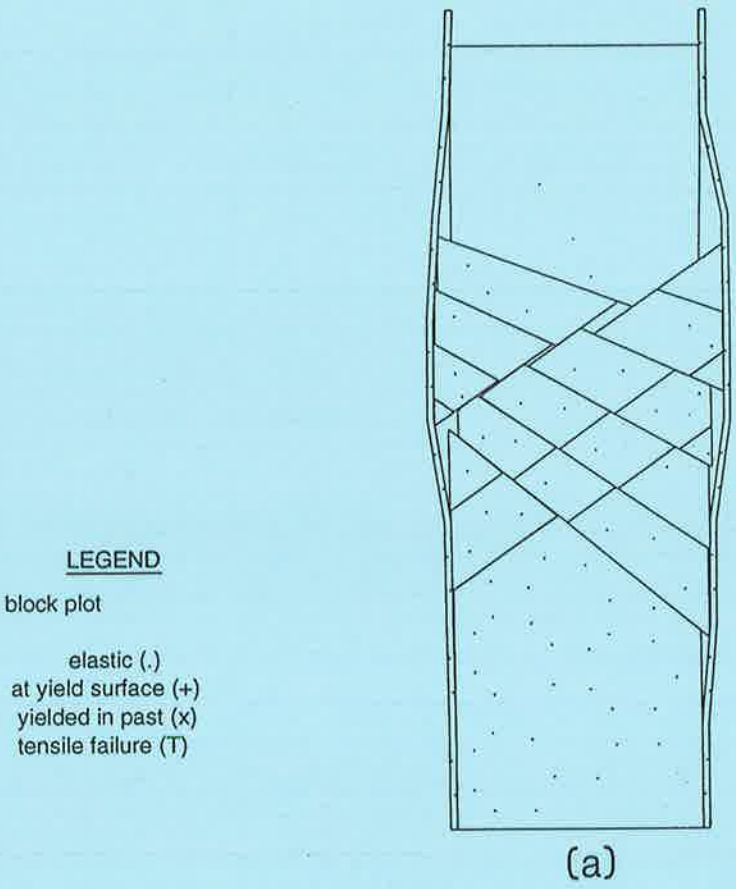

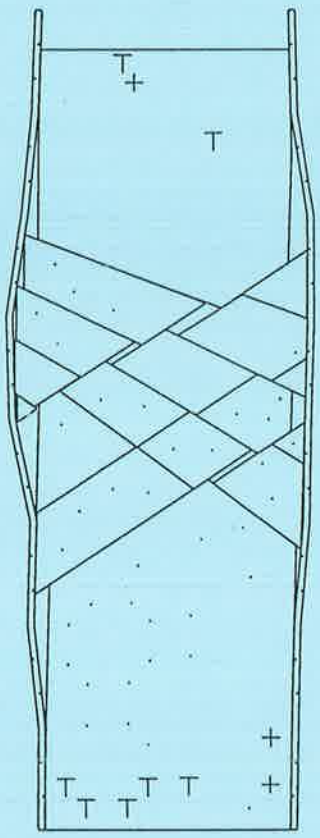

(b)

Figure 8.17(a)-(b). Plastic state in (a) Geometry 1 and (b) Geometry 2 as predicted by UDEC after 50,000 cycles.

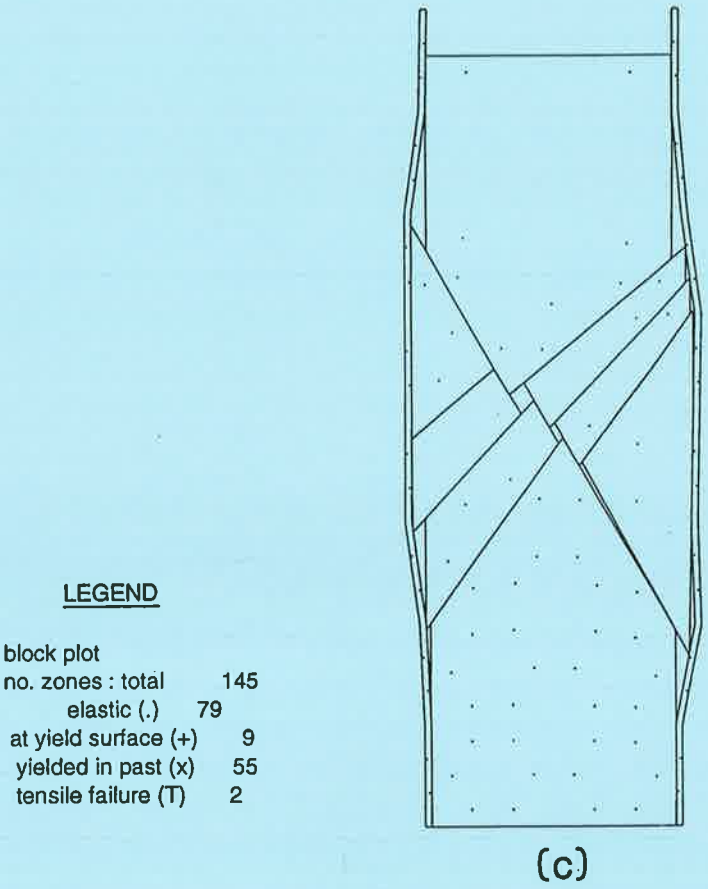

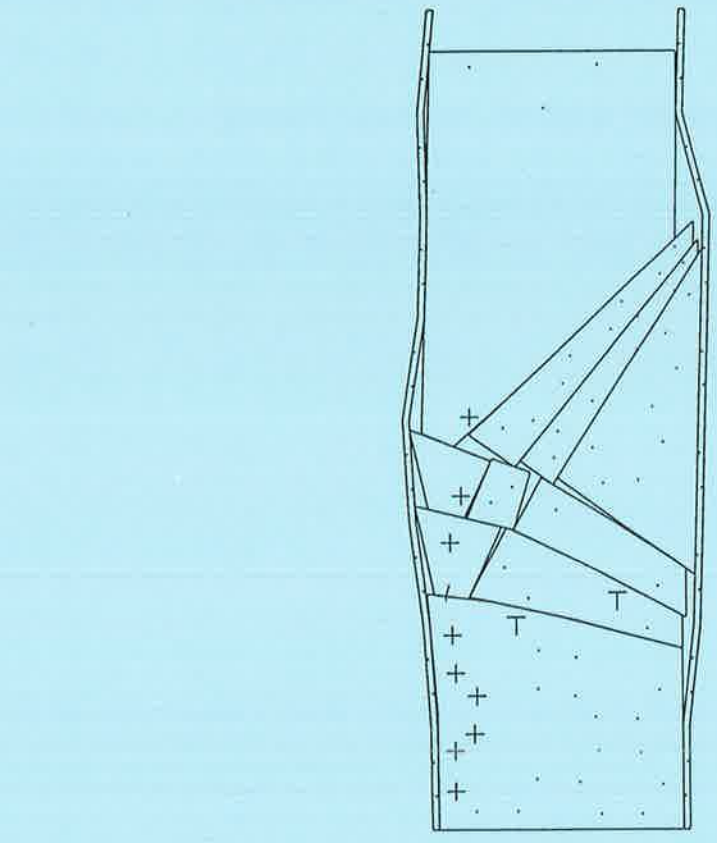

Figure 8.17(c)-(d). Predicted plastic state in (c) Geometry 3 and (d) Geometry 4 after 50,000 cycles.

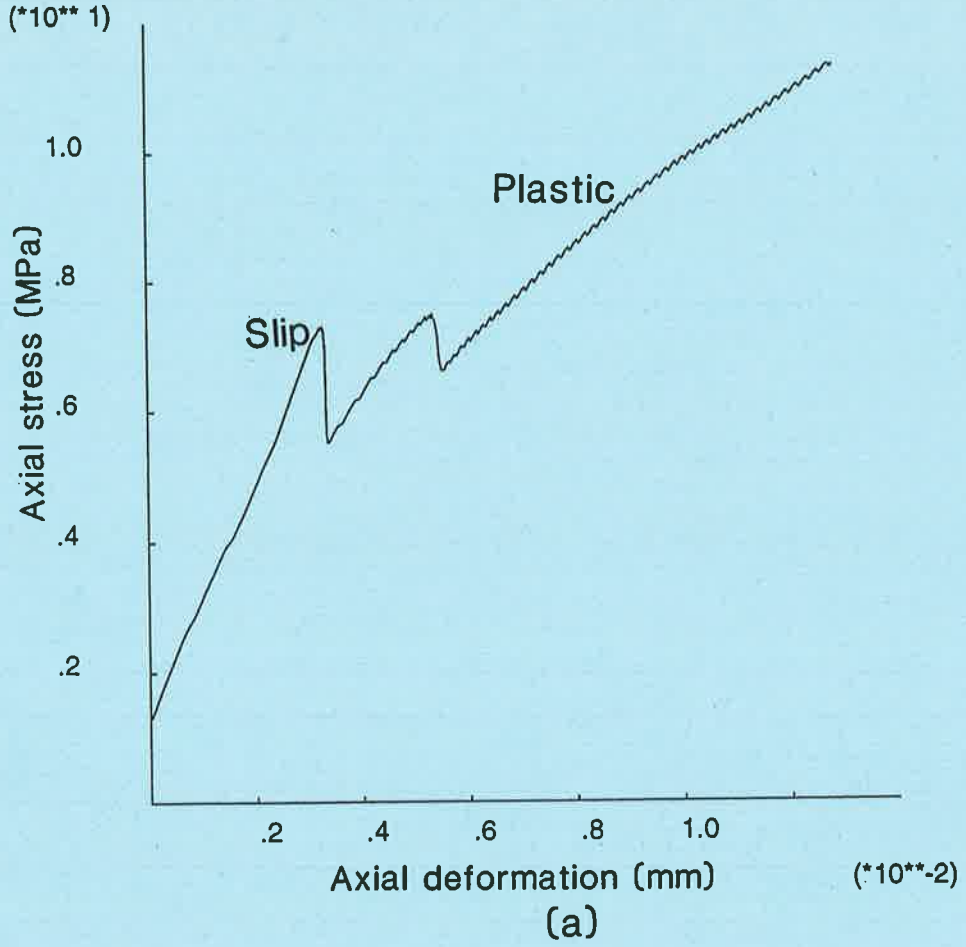

(a)

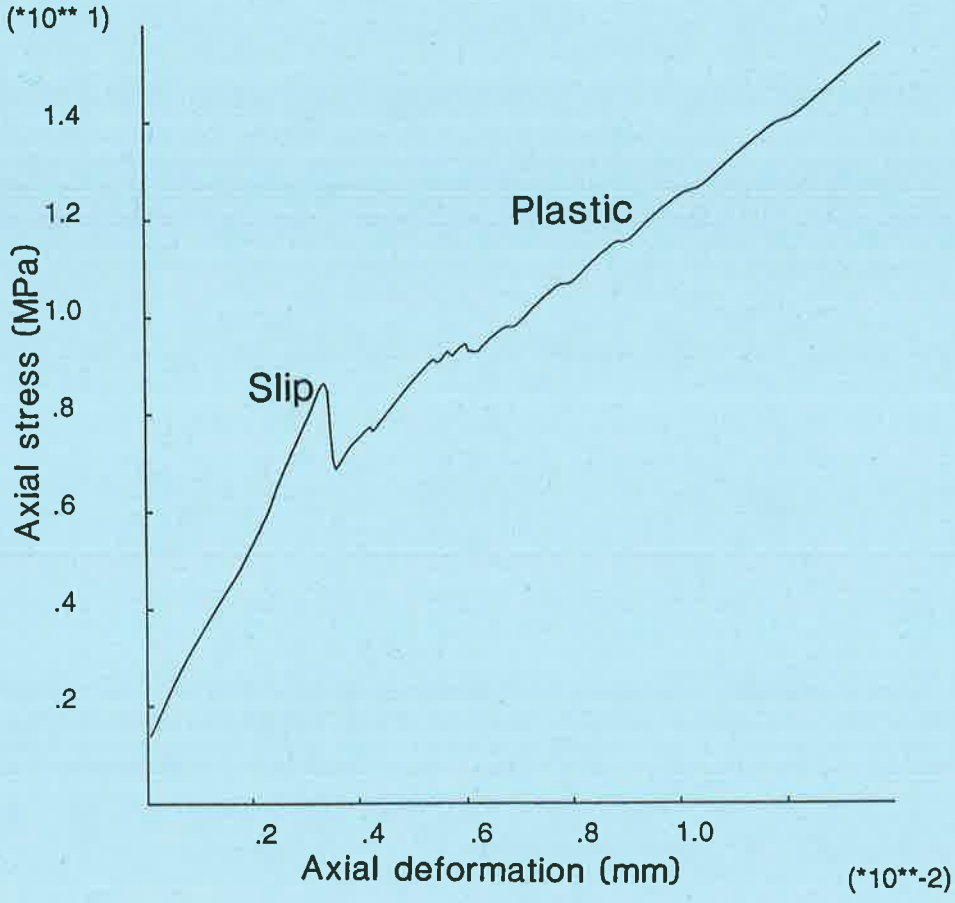

(b)

Figure 8.18 (a)-(b) Predicted axial stress versus axial deformation behaviour within a zone beneath the applied load for (a) Geometry 1 and (b) Geometry 2 specimens.

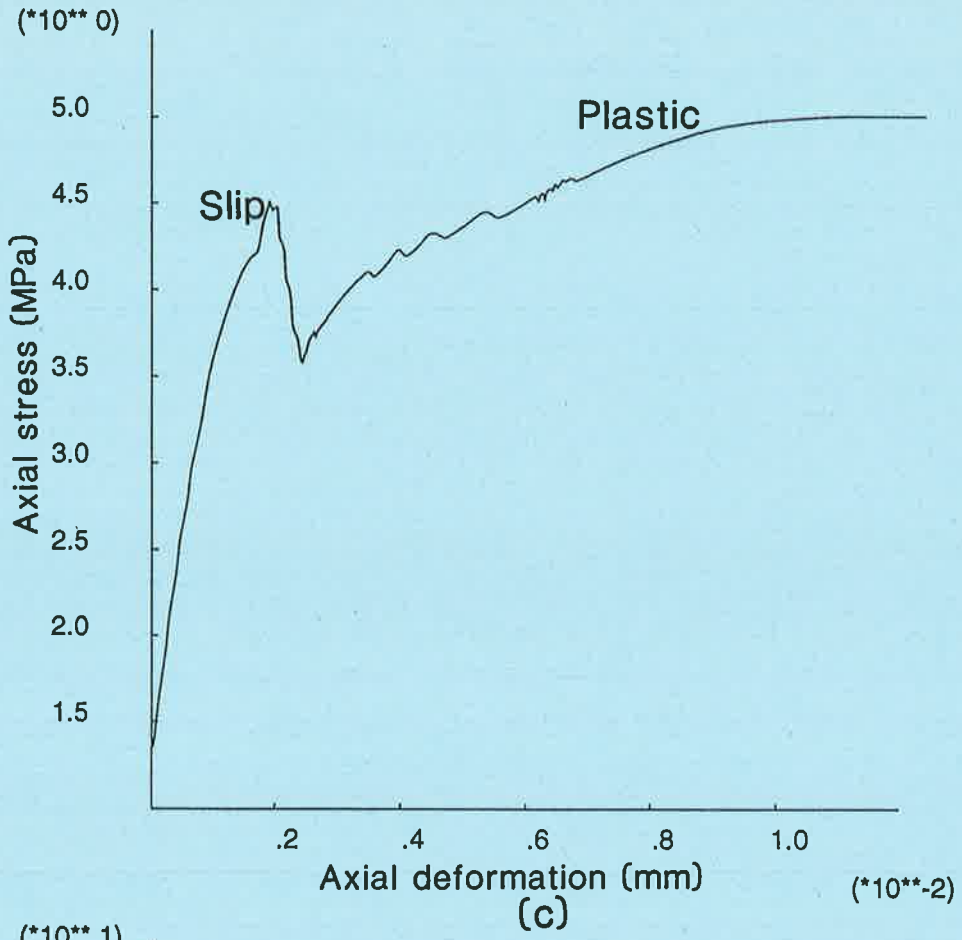

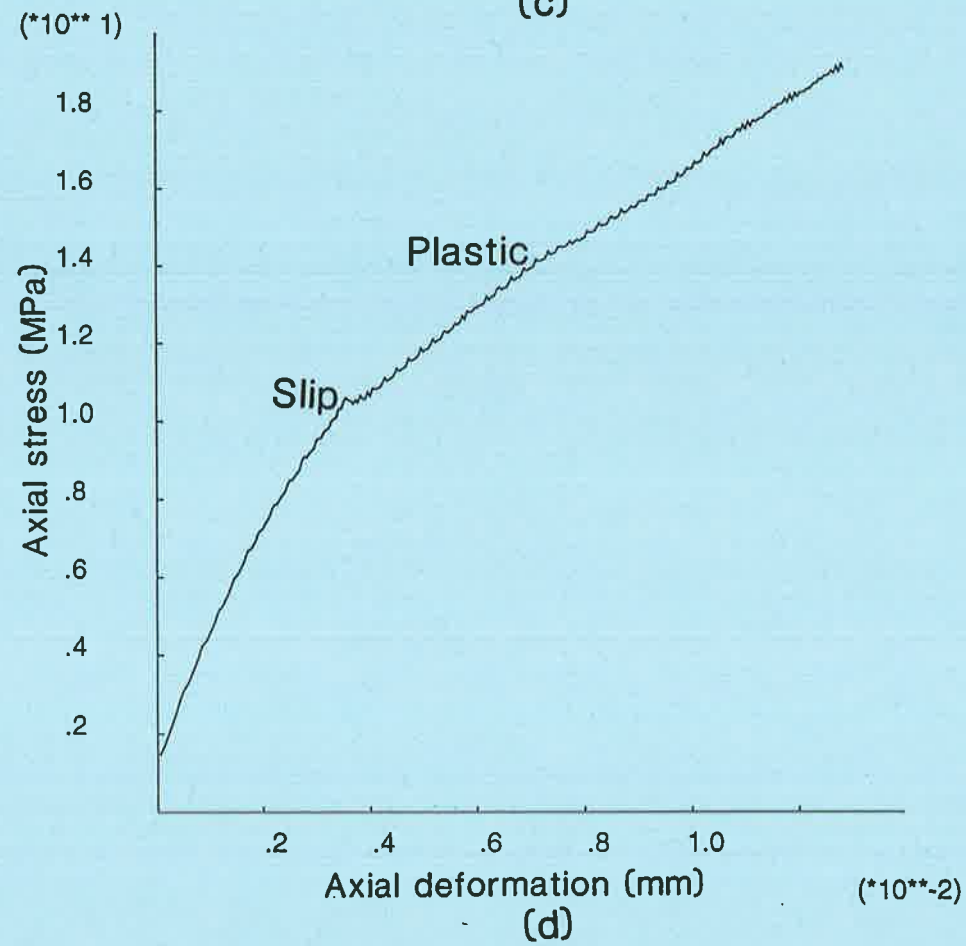

Figure 8.18(c)-(d). Predicted axial stress versus axial deformation behaviour within a zone beneath the applied load for (c) Geometry 3 and (d) Geometry 4 specimens.

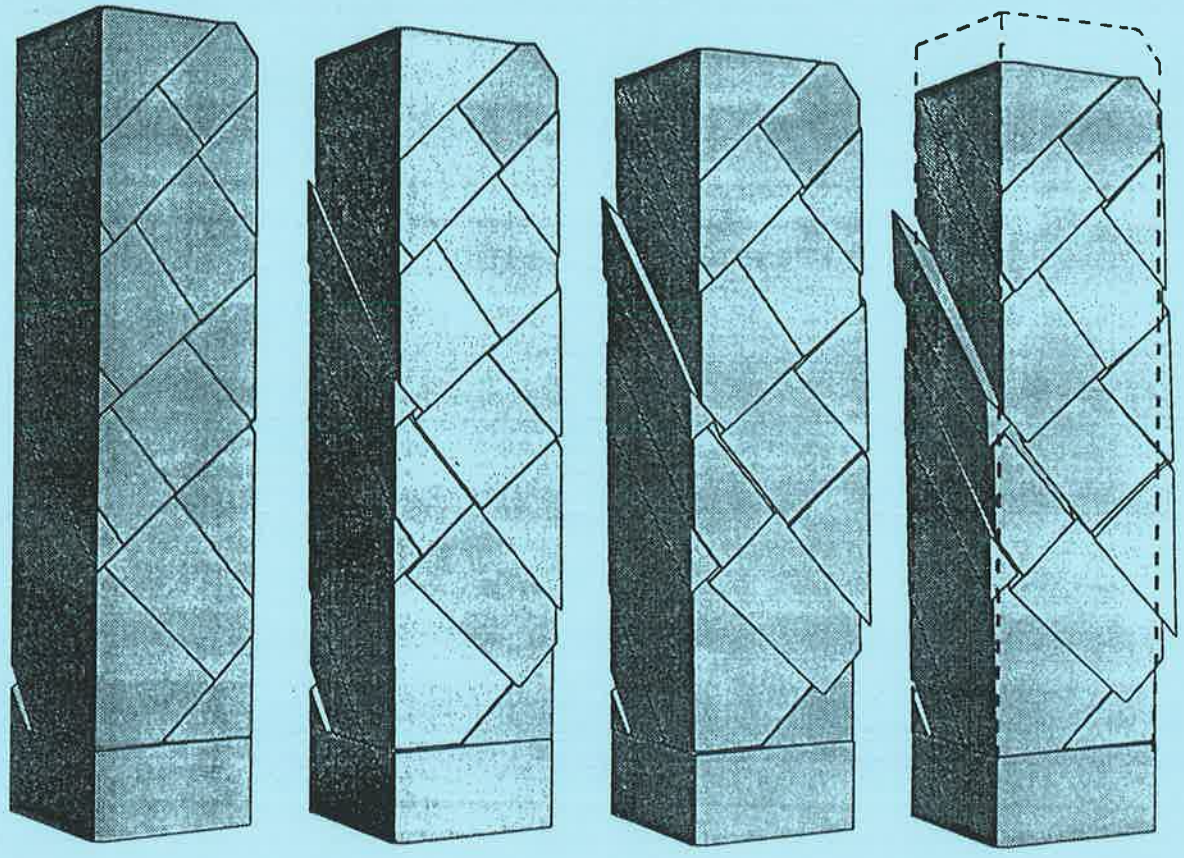

Figure 8.19. Collapse of a discontinuous block using 3-DEC (after Cundall [42]).

Chapter 9.
Application of Rock Mass Rating Theory to Experimental Results.

Chapter 9. Application of Rock Mass Rating Theory to Experimental Results.

9.1. Introduction.

In this Chapter a basic RMR value is obtained for the four hypothetical rock masses described in Section 3.4 and shown in Figures 3.10 to 3.13. A modified RMR is obtained based on the results obtained in Chapter 7. Finally, a case study is presented to demonstrate how the modified RMR procedure can be applied to *in situ* conditions.

9.2. Basic Rock Mass Rating for Specimens.

A basic Rock Mass Rating was obtained for each hypothetical rock mass according to the rating system of Bieniawski [23]. To obtain the basic and, in the next section, the modified RMR values, it is assumed that each rock mass was to be intersected by a near horizontal decline orientated into the page with a trend of $\alpha_e = 270^o$. On the basis of the convention adopted in Section 3.4, all discontinuities strike parallel to the decline. It is assumed that, prior to the excavation, triaxial stress conditions ($\sigma_1 \geq \sigma_2 = \sigma_3 > 0$) exist in the region from which the specimen was obtained. Subsequent to the excavation one of these stresses would reduce ($\sigma_1 \geq \sigma_2 = \sigma_3 \geq 0$). The RMR parameters for each rock mass are listed in Table 9.1 and the rating for the particular parameter is given in parentheses.

The total joint frequency, λ, for each rock mass was assumed to be the total number of discontinuities intersecting the 1m section of scanline AB shown in Figure 3.10 to 3.13. An RQD rating for each rock mass was obtained in terms of λ using Equation 2.8. The average

joint spacing, S, was determined as the inverse of λ. In order to determine the 'joint condition', the discontinuities were rated according to the procedure suggested by Bieniawski [23]. This procedure rates the discontinuities according to a number of criteria. An example of the procedure, applied to the Geometry 1 specimen, is shown in Table 9.2 for Geometry 1. The water content was assumed to be 0% in each case.

The orientation of the discontinuities with respect to the direction of the decline was qualitatively classified according to the criteria established by Wickham et al. [155] and listed in Table 2.2. Bieniawski suggested that if the basic RMR procedure were to be used for the purposes of estimating rock mass strength, then the ratings for discontinuity orientation could be averaged. In contrast, Bieniawski suggested that in other cases, the 'worst case' situation could be chosen. As discussed in Section 2.5, the Author believes that while it is more conservative, the 'worst case' situation should be chosen in all cases. The 'worst case' was, therefore, selected for each of the specimens and a rating adjustment was applied according to the criteria listed in Table 2.1. For example, Specimen 1 contains 8 discontinuities that, according to Table 3.1, plunge at 20°-40°. According to the criteria in Table 2.2, the 20° plunge is a 'fair' orientation. According to Table 2.1, a rating adjustment of -2 is, therefore, assigned for the orientation of this specimen.

By summing the individual ratings in Columns (2), (4), (5), (6) and (7) of Table 9.1 and reducing this sum by the rating adjustment for discontinuity orientation in Column (8), the basic RMR values appropriate to each of the four hypothetical rock masses was determined and is listed in Column (10).

The similarity in the RMR values indicates that, in the case of these specimens, the RMR system is insensitive to changes in the properties of the discontinuities and the intact material. This result can be seen clearly by comparing the strength and deformation behaviour of the Geometry 2 and the Geometry 3 specimens displayed in the tests described

Table 9.1. Theoretical rock masses (Figures 3.10 to 3.13) classified according to the basic RMR system.

(1)	(2)	(3)	(4)	(5)	(6)	(7)	(8)	(9)	(10)
Geo	Mat.	σ_c MPa	λ (/m)	RQD %	S (m)	Joint Con	H_2O	Orient	Basic RMR
1	100%	37.2 (4.4)	36	12.6 (4.3)	0.03 (5.8)	(23)	Dry (15)	Fair (-5)	47.5
	50/50	23.3 (3.1)							46.2
	Infill					Gouge <5mm (10)			33.2
2	100%	37.2 (4.4)	32	17.1 (4.8)	0.03 (5.8)	(23)	Dry (15)	Fair (-5)	48
	50/50	23.3 (3.1)							46.7
	Infill					Gouge <5mm (10)			34.7
3	100%	37.2 (4.4)	16	52.5 (10.5)	0.06 (6.2)	(23)	Dry (15)	Fav. (-2)	57.1
	50/50	23.3 (3.1)							55.8
	Infill					Gouge <5mm (10)			42.8
4	100%	37.2 (4.4)	22	35.5 (7.5)	0.05 (6.2)	(27)	Dry (15)	Fair (-5)	55.1
	50/50	23.3 (3.1)							53.8
	Infill					Gouge <5mm (10)			36.8

Table 9.2. Classification of discontinuity conditions for hypothetical rock mass 1 (after Bieniawski [23]).

Parameter	Value	Rating
Discontinuity length	1-3m	4
Separation (aperture)	None	6
Roughness	Smooth	1
Infilling	None	6
Weathering	Unweathered	6
	Total	23

in Section 7.4.2. According to Table 9.3, Geometries 3 and 4 scored a 'fair' RMR value. For the specimens containing infill, Geometries 1, 2 and 4 scored an 'unfavourable' RMR value due to each specimen having at least one discontinuity set that rated as only 'fair' according to Table 2.2. In contrast, Geometry 3, which had a lower yield strength than the other geometries, rated as consisting of 'fair' rock.

Table 9.3. Rock mass classes determined from total ratings (after Bieniawski [23]).

Rating	100←81	80←61	60←41	40←21	<20
Description	Very good rock	Good rock	Fair rock	Poor rock	Very poor rock

The yield strength for each of the rock masses can be estimated from the basic RMR value using the Hoek-Brown [65] [66] rock mass yield criterion defined in Equation 2.16. The yield criterion parameters m and s in Equation 2.16 were obtained from Equation 2.18(a)-(b) on the assumption that the specimens packed sufficiently tightly under hydrostatic conditions to represent an undisturbed rock mass. The parameter m_i for each of the intact materials was determined in the material property tests and was presented in Table 6.1.

In Figures 9.1 to 9.4 the yield strength curves are compared with the normalised principal stresses obtained from the triaxial tests on the specimens. The yield criterion under-estimates the yield strength of the Geometry 1 and 2 specimens. This result shows that in cases where

$\beta_w \leq \phi_w$ for all discontinuities, the yield criterion provides a conservative lower bound to the rock mass strength. Alternatively, in the Geometry 3 specimen where $\phi_w \leq \beta_w \leq 90^o$ and the discontinuities are fully persistent, the yield criterion over estimates the yield strength. The orientations of three of the discontinuities in the Geometry 4 specimens are similar to those in the Geometry 3 specimens. If the discontinuities were fully persistent, on the basis of the Geometry 3 result, it appears likely that the yield criterion would have over estimated the yield strength. In the Geometry 4 specimen, the non-persistence of the discontinuities provides additional yield strength to the specimen and the yield criterion, therefore, provided a reasonable fit to the experimental data.

Even though these results are based on only four specimen geometries, they do appear to indicate a trend. This trend suggests that, depending on the discontinuity geometry, the well-accepted Hoek-Brown method for assessing the yield strength of the rock mass could be providing either an under estimate as in the case of the Geometry 1 and 2 specimens or, more disturbingly, as in the case of the Geometry 3 specimens, an over estimate of rock mass yield strength. Even though for Geometries 1, 2 and 3, there is a poor fit of the empirical curve to the test data, the curvature in the Hoek-Brown empirical curve does mirror well the curvature required to produce a better fit to the test data. This result confirms that there was no reason to modify the form of the Hoek-Brown equation. The error between the predicted and the yield strength obtained varies with the discontinuity geometry. The geometrical component is assessed in Bieniawski's rating system and it is here that any improvements should be made.

9.3 Modified RMR for Specimens

Additional information to that required for the determination of the basic RMR was required in order to determine a modified RMR for each hypothetical rock mass. In particular, this information defined the orientation and dimensions of the excavation and the orientation of the major principal stress. As the purpose of this exercise was to compare the predicted yield strengths to the yield strengths obtained in the laboratory, the dimensions for the cross

sectional area and the length of the excavation were kept consistent with the dimensions of the specimens. This action was not absolutely necessary as the orientation weighting obtained for each discontinuity would be the same no matter what dimensions were used. What would have changed in this case was the number of discontinuities that were predicted to intersect the excavation.

In order to remain consistent with the scale of the specimens tested, the cross sectional area of the excavation was assumed to be $0.045m^2$ (0.3x0.15). As the spacing of the sets in the third dimension is unknown, it must be assumed to be 0.15m, the diameter of the test specimen. This value is the largest set spacing and $S_{\mu(max)}$ in Equation 3.28 is, therefore, equal to 0.15.

As the major axis through the specimen was equivalent to the major principal axis, it was consistent to assume that the orientation of the decline was horizontal. It was, however, necessary, to have the excavation plunge at 0.5°. Had a small plunge not been provided, Equation 3.16 would, correctly, have predicted that no discontinuities would intersect the decline. This result would have occurred because, this two-dimensional analysis, assumed that all discontinuities had a trend of either 0° or 180°. In a three-dimensional analysis, where even if the mean orientation of the normal to a particular set had a trend of 0° or 180°, the trend of the normals to the individual discontinuities within the set would have varied about this mean and hence intersected the decline.

The classification procedure used to determine the value for the modified RMR value for each of the hypothetical rock masses is tabulated in Table 9.4. Columns (1), (2), (3), (4), (6) and (7) contain the same information as for the basic RMR procedure. The procedures used to determine the modified ratings for discontinuity spacing, $RMR_{(space)}$, are presented in Appendix G and the results are listed in Column (5) of Table 9.4. The mean block volume was determined, not by estimating the volume using Equation 3.26, but by measuring the volume of each block. The ability to accurately determine properties such as block volume is one of the advantages of using models compared to natural discontinuous rock.

The orientation weighting, $w_{\theta(mass)}$, for each specimen is listed in Column (8) and the procedure used to determine these ratings is presented in Appendix G. It will be noticed that the maximum orientation weighting, rather than the mean of all discontinuities or the active discontinuities, was used for each specimen. The reason for this, as explained below, relates to the size of the specimens and the limited number of discontinuities intersecting each specimen. In practical situations the procedure outlined in Section 3.2, Step (17) for determining $w_{\theta(mass)}$ would be used.

Assume that the rock mass in the vicinity of a proposed excavation was divided into many very small sections, each containing only a few discontinuities. Testing each of the sections to determine its yield strength would be like testing one of the specimens tested in Chapter 7. Some of the sections may contain discontinuities having orientation such as Geometry 3, while others may be more like Geometry 2. As shown in Chapter 7, the strength of a specimen, or one of the sections, can be dictated by the behaviour of a single discontinuity, the discontinuity having the greatest orientation weighting. It is this weighting that we should consider for the purposes of this exercise. It would be over conservative to design the entire excavation on the basis of the yield strength of the section having the highest orientation weighting. The best estimate of the yield strength of the entire rock mass would be provided by the mean strength of all sections. The weighting appropriate to this strength is the mean weighting for the rock mass. As suggested in Section 3.2 Step (17), the choice of the design weighting should be based on consideration of the mean weighting for all discontinuities and the mean weighting for the active discontinuities. It is for the purpose of choosing this design weighting that the histogram is such a useful tool.

A relationship defining the Rock Mass Rating for discontinuity orientation, $RMR_{(orient)}$, in terms of the orientation weighting, $w_{\theta(mass)}$, was developed in order to satisfy three requirements. The first requirement was that when $w_\theta = 0$, $RMR_{(orient)} = 20$ points. In the basic RMR system, discontinuity spacing and RQD are both assigned a maximum rating of

Table 9.4. Theoretical rock masses (Figures 3.10 to 3.13) classified according to the modified RMR system.

(1)	(2)	(3)	(4)	(5)	(6)	(7)	(8)
Geo	Mat.	σ_c (MPa)	λ (/m)	$RMR_{(space)}$	Joint Cond	H_2O	$W_{\theta(mass)}$
1	100%	37.2 (4.4)	36	(4.8)	(23)	Dry (15)	0.16
	50/50	23.3 (3.1)					0.14
	Infill				Gouge <5mm (10)		0.18
2	100%	37.2 (4.4)	32	(5.1)	(23)	Dry (15)	0.05
	50/50	23.3 (3.1)					0.04
	Infill				Gouge <5mm (10)		0.06
3	100%	37.2 (4.4)	16	(6.6)	(23)	Dry (15)	0.99
	50/50	23.3 (3.1)					0.98
	Infill				Gouge <5mm (10)		0.99
4	100%	37.2 (4.4)	22	(6.3)	(27)	Dry (15)	0.97
	50/50	23.3 (3.1)					0.96
	Infill				Gouge <5mm (10)		0.98

20 points each. As discussed in Section 3.3, in the modified RMR system, the RQD is not considered and the points allocated to it in the basic system are, instead, allocated as additional points for discontinuity orientation. Table 2.1 presents Bieniawski's recommended rating adjustment for discontinuity orientation. For a 'very favourable' orientation a maximum rating adjustment of zero points is allocated. In the modified system, 'very favourable' conditions are those in which $w_\theta = 0$. This maximum rating for these conditions is, therefore, allocated 20 points.

The second requirement for the relationship defining $RMR_{(orient)}$ in terms of w_θ was that it had to allow a modified RMR value for each of the specimens to be determined that, when used as input to Equations 2.16 and 2.18, provided a better fit to the experimental data shown in Figures 9.1 to 9.4.

In the modified RMR system, 'very unfavourable' conditions, such as those for the Geometry 3 specimens, are those in which $w_\theta \approx 1$. By using an iterative procedure it was found that, in cases such as these, $RMR_{(orient)}$ should be allocated -3 points. This allocation formed the third requirement for the relationship between $RMR_{(orient)}$ and w_θ.

All requirements for the relationship between $RMR_{(orient)}$ and w_θ are satisfied by a curve having a shape of curve A in Figure 9.5. Through the use of an iterative procedure the curve was defined by the relationship,

$$RMR_{(orient)} = 11.75 \cos(180\, w_\theta) + 8.25 \qquad (9.1)$$

Equation 9.1 was applied to the orientation weighting data listed in Column 8 of Table 9.4 to determine $RMR_{(orient)}$. This value is listed for each specimen and material type in Column (3) of Table 9.5. The individual ratings in Columns (3), (5), (6), (7) in Table 9.4 and $RMR_{(orient)}$ in Table 9.5 were summed to produce the modified RMR value for the specimens. The RMR value is listed in Column (4) of Table 9.5.

The yield strength for each of the rock masses was estimated from the modified RMR value using the Hoek-Brown [65] [66] rock mass yield criterion defined in Equation 2.16. In Figures 9.6 to 9.9 the yield strength curves are compared with the normalised principal stresses obtained from the triaxial tests on the specimens. The empirical yield strength curves based on the modified RMR system show a significantly better fit to the test data than those generated using the basic RMR system.

The prediction of the yield strength for the 100% gypsum cement discontinuities and the infilled discontinuities is reasonable, albeit slightly conservative, for all geometries. For Geometries 1 and 2 the yield strength prediction for the 50/50 gypsum cement/sand specimens is significantly better than that predicted in the basic RMR procedure, although, it is still quite conservative. These results suggest that a larger value of $RMR_{(orient)}$ should be applied in cases where $w_{\theta(mass)} \rightarrow 0$.

The theory developed in this chapter and in Chapter 3, for determining a modified RMR value for each specimen, assumed that the maximum value that could be applied to a rock mass was 100 points. This assumption allowed consistency between the basic and the modified RMR systems. In the basic RMR system, Bieniawski [23] based the ranges for each parameter on the subjective recommendations of the ISRM [73] for the Quantitative Description of Discontinuities in Rock Masses. The aim of the present research has been to reduce the reliance on subjective recommendations. In light of the findings that 100 points is not necessarily the most appropriate maximum value, a further 10 points is allocated to discontinuity orientation. The maximum possible RMR value, therefore, becomes 110 points. In this case, when $w_\theta = 0$, $RMR_{(orient)}$=30 points and, as previously required, when $w_\theta = 1$, $RMR_{(orient)} = -3$ points. These ranges ensured that the yield strength predicted for geometries such as Geometry 1 and 2 was greater than that predicted by Equation 9.1 while for geometries such as Geometry 3 and 4, the yield strength remained similar. This condition is satisfied by a curve having a shape of curve B in Figure 9.5. Through the use of aniterative procedure the curve was defined by the relationship,

$$RMR_{(orient)} = 11.75 \cos(180\ w_\theta) + 8.25 \qquad (9.2)$$

Equation 9.2 was applied to the orientation weighting data listed in Column (8) of Table 9.4 to determine $RMR_{(orient)}$. This value is listed for each specimen and material type in Column (5) of Table 9.5. The individual ratings in Columns (3), (5), (6) and (7) in Table 9.4 and $RMR_{(orient)}$ in Table 9.5 were summed to produce the modified RMR value for the specimens. The RMR value is listed in Column (6) of Table 9.5.

In Figures 9.10 to 9.13 the yield strength curves are compared with the normalised principal stresses obtained from the triaxial tests on the specimens. For the Geometry 1 and 2 specimens, the empirical yield strength curves show a significantly better fit to the test data than that generated using either the basic RMR system or the modified system based on Equation 9.1. The predicted yield strength for the 50/50 gypsum cement/sand specimen fits the tests data well while that for the 100% cement specimens in the Geometry 1 model does less so. It is possible that, owing to the excessive deviation in the compressive strength of the 100% material as discussed in Appendix C, the Hoek-Brown parameter m_i used in this analysis might have been in error. Any error in m_i would have influenced the slope of the empirical curve. Time limitations did not permit further investigation of this effect.

For Geometries 1 and 2, the empirical curve for the infill represents an upper bound for the yield strength. This result suggests that the 'joint condition' rating of 10, for joints containing < 5mm of infill material, in the basic and the modified RMR system could be slightly excessive. It is beyond the scope of this study to investigate the relationship between infill thickness and yield strength predicted by either the basic or the modified RMR procedure. Considering that the modified RMR technique was not intended to provide a definitive value for, but rather an improved estimate of, the yield strength of a rock mass, it was encouraging that the predicted and the yield strengths obtained in the laboratory were in close agreement with each other.

Table 9.5. Comparison of modified Rock Mass Ratings for hypothetical rock masses obtained using Equations 9.1 and 9.2.

		Maximum $RMR_{(orient)}$ = 20		Maximum $RMR_{(orient)}$ =30	
Geometry	Material	$RMR_{(orient)}$	Modified RMR	$RMR_{(orient)}$	Modified RMR
	100%	18.6	65.8	27.9	75.1
1	50/50	18.9	64.8	28.4	74.3
	infill	18.2	51.1	27.4	60.3
	100%	19.9	67.4	29.8	77.3
2	50/50	19.9	66.1	29.9	76.1
	infill	19.8	53.0	29.7	62.9
	100%	-3.5	45.5	-3.5	45.5
3	50/50	-3.5	44.2	-3.5	44.2
	infill	-3.5	31.2	-3.5	31.2
	100%	-3.4	49.3	-3.4	49.3
4	50/50	-3.4	48.0	-3.4	48.0
	infill	-3.5	30.9	-3.5	30.9

9.4. Basic vs Modified RMR Procedure: A Case Study.

The site chosen for the geotechnical investigation was a marble quarry (Figure 9.14) in Penrice, a town 50km north of Adelaide, South Australia. The quarry is located in undulating, hilly country on the eastern edge of the Barossa Valley, within the Mount Lofty Ranges. The rock unit being quarried is the Angaston marble that is interbedded with schist and calc-silicate rocks. Stapledon and Stevens [138] described the structure as consisting of beds tightly folded about axes trending approximately north-south. The belt of marble in which the quarry is located is near vertical and is on the eastern limb of a southerly plunging anticline. The major axis of the quarry is 1100m in length and the depth of the pit is 130m. For the purpose of this exercise, it is assumed that a 5m wide x 4m high exploration decline is to be driven in the south east wall of the quarry as shown in Figure 9.14. The decline is to have the orientation $\alpha_e = 205°$ and $\beta_e = 10°$ and a length of 250m.

Shear box and compression tests were conducted on unweathered core obtained from the site

and the marble was found to have a uniaxial compressive strength of 64.4MPa and a residual friction angle, ϕ_w, of 40°. Many of the discontinuities intersecting the rock mass had an aperture size of up to 1mm. The large aperture size would tend to make the rock mass reasonably permeable. A sump at the bottom of the pit is pumped continuously throughout the year indicating that the water table is permanently above the base of the pit. Therefore, depending on the drawdown curve, it is possible that the decline will be permanently wet if not dripping.

The average depth, z, of the decline, with respect to the crest of the pit, is 140m. On the basis of the research by Brown and Hoek [32], an estimate of the vertical stress and the horizontal stress at a depth of 140m would be 3.8MPa (0.027 x 140m) and 10.3MPa (7.26 + 0.022(140m)) respectively. In the absence of data to the contrary, the horizontal stress is assumed to be the major principal stress. As there is a free face north of the decline, the horizontal stress in the north/south direction is assumed to be negligible. Therefore, the major principal stress is assumed to be orientated in the east/west direction at $\alpha_\sigma = 90°$ and $\beta_\sigma = 0°$.

A representative sample of discontinuities was logged with a scanline survey as part of this study and a concurrent project in order to obtain data on the geometric properties of the discontinuities in the region of the proposed decline. Details of the survey are described by Raiseborough [122]. In order to obtain sufficient data, 31 scanlines orientated in approximately three orthogonal directions, were logged. To conduct each survey a measuring tape was established across an exposed face of the rock mass. Each horizontal survey was generally 30m long which enabled data on approximately 150 discontinuities per scanline to be collected. Vertical scanlines could, logistically, only be a maximum of three metres in length and therefore the number of discontinuities sampled by these scanlines was proportionally decreased. In total, 906 discontinuities were sampled.

The normals to the sampled discontinuities are presented in Figure 9.15 in the form of an equal angle equatorial lower hemisphere projection. The orientations of the 31 scanlines are

circled. The software CANDO (Priest [119]) was used to identify the discontinuity sets. A maximum weighting of 10 was applied to the normals to correct for discontinuity orientation bias and a 15° cone angle was used in the clustering algorithm. Figure 9.16 shows the discontinuities allocated to sets. The analysis identified three joint sets and a random component. Details of these sets are presented in Table 9.6. In this table the mean spacing for the sets and the random component is also presented. Fisher's constant in Column (4) provides an indication of how tightly the discontinuities from a set cluster about the mean orientation of the set. As Fisher's constant$\rightarrow\infty$ the discontinuities approach parallelism and, alternatively, as Fisher's constant$\rightarrow$1 the discontinuities become random. The constants for Sets 1 and 3 were sufficiently large to confirm that the calculated mean orientations provided a reasonable estimate of the mean orientation for the respective set. The low value for Fisher's constant for Set 2 meant that, without further sampling, lower confidence had to be placed in the calculated mean orientation providing an estimate of the correct mean orientation. All value were within the order of that expected (Priest [119]).

A basic Rock Mass Rating for the rock mass in the vicinity of the decline was obtained according to the procedure outlined by Bieniawski [19]. The results are presented in Table 9.7. The RQD rating was determined by applying Equation 2.8 to the average of the spacing values listed in Table 9.6. The procedure used to determine the condition of the discontinuities is presented in Table 9.8 and is based on the method described by Bieniawski.

The rating adjustment for discontinuity orientation was made by reference to Figure 9.16 in which the mean orientation of the normals to each of the sets can be viewed in relation to the decline. With reference to Table 2.2, Set 1 strikes perpendicular to the decline, has a dip from 45-90° and the decline is driven with the dip. Set 1, therefore, represented a 'very favourable' condition and was accordingly assigned a rating adjustment of 0. Set 2 strikes parallel to the decline and has a dip from 45-90°. This condition was 'very unfavourable' and was, therefore, assigned a rating adjustment of -12 points. Set 3 strikes parallel to the decline and has a dip from 20-45°. This condition was 'fair' and, therefore, assigned -5 points. These ratings were averaged as recommended by Bieniawski.

Table 9.6. Discontinuity set statistics for Penrice quarry.

(1)	(2)	(3)		(4)	(5)	(6)
Set	Values	Mean orientation of normal to set (degrees)		Fisher's Const.	Mean Spacing, (mm)	Mean Size (m)
		α_k	β_k		S_μ	
1	240	38	7	21.7	203	1.94
2	386	105	17	6.9	339	1.59
3	82	248	66	25.7	257	1.36
random	198	not applicable			178	1.32
Total	906					

Table 9.7. Basic Rock Mass Rating determination for Penrice quarry (after Bieniawski [19])

Parameter	Value	Rating
Strength of intact rock	64.4MPa	7
Drill core quality, RQD	94.0	19
Average spacing of discontinuities	270mm	10
Condition of discontinuities	see Table 9.8	23
Ground water	wet	7
Orient. rating adjustment	(fair)+(v.unfav)+(v.fav)	-7
	Basic RMR	59

Bieniawski suggested that a rock mass having a total rating of 59 would be composed of 'fair' rock and that the recommended average stand up time of a 5 metre span would be 1 week. He also suggested that the rock mass would have a friction angle of 25-35°. This value is lower than the friction angle for the individual discontinuities. The yield conditions for the rock mass can be established in terms of the Hoek-Brown rock mass yield criterion. The Hoek-Brown rock mass yield criterion parameters, m and s, were found from Equation 2.18(a)-(b) to be 1.619 and 0.010 respectively (m_i for intact marble=7). Substituting these

Table 9.8. Classification of discontinuity conditions for Penrice quarry (after Bieniawski [23]).

Parameter	Value	Rating
Discontinuity length	1-3m	4
Separation (aperture)	0.1-1mm	4
Roughness	Slightly	3
Infilling	None	6
Weathering	Unweathered	6
	Total	23

values into Equation 2.16 provides a relationship for the yield strength of the rock mass in the vicinity of the decline in terms of the minor principal stress as:

$$\sigma_1 = \sigma_3 + \sqrt{104.3\sigma_3 + 41.5} \qquad (9.3)$$

To rate the rock mass according to the modified Rock Mass Rating procedure, a value of $RMR_{(orient)}$ and $RMR_{(space)}$ was determined according to the procedures detailed in Sections 3.2. and 3.3. using the program WEIGHTS listed in Appendix A.

The value for $RMR_{(orient)}$ is a function of the orientation weighting for the rock mass. The ultimate choice for an appropriate weighting was determined on the basis of the histogram shown in Figure 9.17. The histogram shows that the majority of discontinuities intersecting the decline have values of $W_{\theta(mass)}$ clustered around $W_{\theta(mass)}=0$ which indicated that the rock mass in the vicinity of the decline was predominantly stable. The mean weighting values for all the discontinuities and for the active discontinuities, are presented in Table 9.9. The histogram shows that 5% of the discontinuities are clustered around $W_{\theta(mass)}=1$. Table 9.10 indicates that these highly active discontinuities come from Set 3 and from the random component. This small percentage of highly active discontinuities was allowed for by choosing an ultimate weighting for the rock mass slightly larger than the mean weighting.

For the purposes of this exercise a value of 0.3 was chosen which is the mean of the two mean values listed in Table 9.9. According to Equation 9.2, the value for $RMR_{(orient)}$ was, therefore, 15.16 (11.75cos(180 x 0.3) + 8.25).

Figure 9.18 and Table 9.9 show how the result could be significantly different if the orientation of the major principal axis was α_s=110°, β_s=30°, rather than the assumed orientation. In this case, there are a significant number of discontinuities clustered around $W_{\theta(mass)} = 1$. It is up to the design engineer to use their judgement in choosing an appropriate weighting for the decline. For example, if it was crucial that the decline remain structurally sound over the entire length, an ultimate weighting for the rock mass of 1 could be chosen.

The value of $RMR_{(space)}$ is a function of the mean block size, the cross sectional area of the excavation and the maximum discontinuity set spacing, as defined in Equation 3.28. According to Equation 3.26, the mean block size is a function of the discontinuity frequency along the excavation which, according to the values listed in Table 9.10, was 8.56/m $\left(\frac{1147 + 82 + 443 + 467}{250m}\right)$. The mean block size was, therefore, $0.003m^3 \left(\frac{6}{\pi(8.56m)^3}\right)$. The maximum discontinuity set spacing is seen in Table 9.6 to be 0.339m and, therefore, the value for $RMR_{(space)}$ was $1.24 \left(20\left(\frac{0.003m^3}{0.339m \times 20m^2}\right)^{0.36}\right)$.

Table 9.11 lists the individual ratings applicable to each of the parameters in the modified RMR procedure. As discussed in Chapter 3.3, no allowance is made for the RQD rating of the rock mass in the modified system.

The sum of the individual rating provided an overall rating for the rock mass. The modified RMR for the rock mass was slightly less than that obtained using the basic RMR system. The Hoek-Brown rock mass yield criterion parameters, m and s, were found from Equation 2.18(a)-(b) to be 1.42 and 0.007 respectively (m_i for marble is 7, Hoek and Brown [66]).

Table 9.9. Influence of the principal stress orientation on $W_{\theta(mass)}$.

	Principal stress orientation	
	α_σ=90° β_σ=0°	α_σ=110° β_σ=30°
Mean Orientation Weighting (all data)	0.17	0.58
Mean Orientation Weighting (active discontinuities)	0.44	0.73

Table 9.10. Results of orientation weighting procedure for individual sets at Penrice.

	Sets			
	1	2	3	random
Mean orientation weighting	0.02	0.07	0.36	0.28
Number of discontinuities to intersect decline	1147	82	443	467

Table 9.11. Modified Rock Mass Rating determination for Penrice quarry.

Parameter	Value	Rating
Strength of intact rock	64.4MPa	7
$RMR_{(space)}$		1.24
Condition of discontinuities	slightly weathered walls separation < 1mm	25
Ground water	wet	7
$RMR_{(orient)}$	0.3	15.16
	Modified RMR	55.4

By substituting these values into Equation 2.16 a relationship for the yield strength of the rock mass in the vicinity of the decline was obtained in terms of the minor principal stress as:

$$\sigma_1 = \sigma_3 + \sqrt{91.7\sigma_3 + 29.0} \qquad (9.4)$$

Figure 9.19 shows a comparison of the predicted yield strengths obtained according to the basic and the modified RMR systems. The predicted minor principal stress at Penrice was 3.8 MPa and this stress is included within the range of minor principal stresses plotted. It

should be noted that the theory developed in this study was based on laboratory tests conducted at lower minor principal stresses. Without further investigation, there is no evidence that the theory would be valid for higher stresses. The results show the modified RMR system predicts a lower mean yield strength for the rock mass than that predicted by the basic RMR system. The result predicted by the modified system would have been lower if the stress conditions that produced Figure 9.18 existed. Owing to the lack of adequate data defining the *in situ* rock mass yield strength, it is difficult to substantiate the results obtained.

9.5 Summary

This chapter and Chapter 3 presented an essential component of the present study. Chapter 3 discussed a modified technique for classifying a rock mass for the purpose of obtaining input data for the Hoek-Brown rock mass yield criterion. This chapter further developed the technique based upon the results obtained from the laboratory studies. The technique follows a logical progression and a case study has been presented to demonstrate how this procedure is implemented.

As the techniques were developed using models of discontinuous rock subjected to a low stress environment, it would be wrong to assume that the results would be applicable to *in situ* rock masses containing highly complex discontinuity networks and subjected to higher stress states. There is, however, a sound basis upon which the recommended techniques were developed and further investigation of the suitability of the techniques should be carried out. This recommendation and a number of other recommendations are presented in Chapter 10.

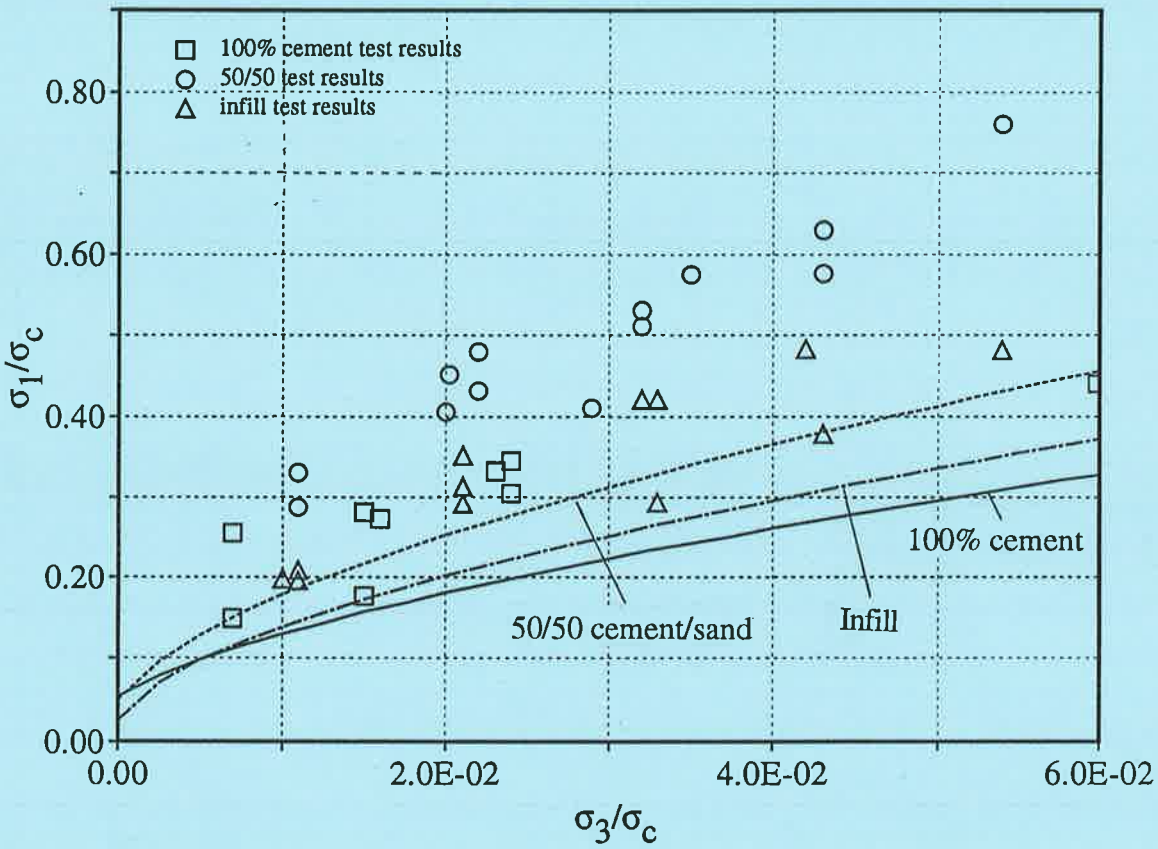

Figure 9.1. Comparison between the predicted normalised principal stresses on the specimens at yield and the experimental results for Geometry 1.

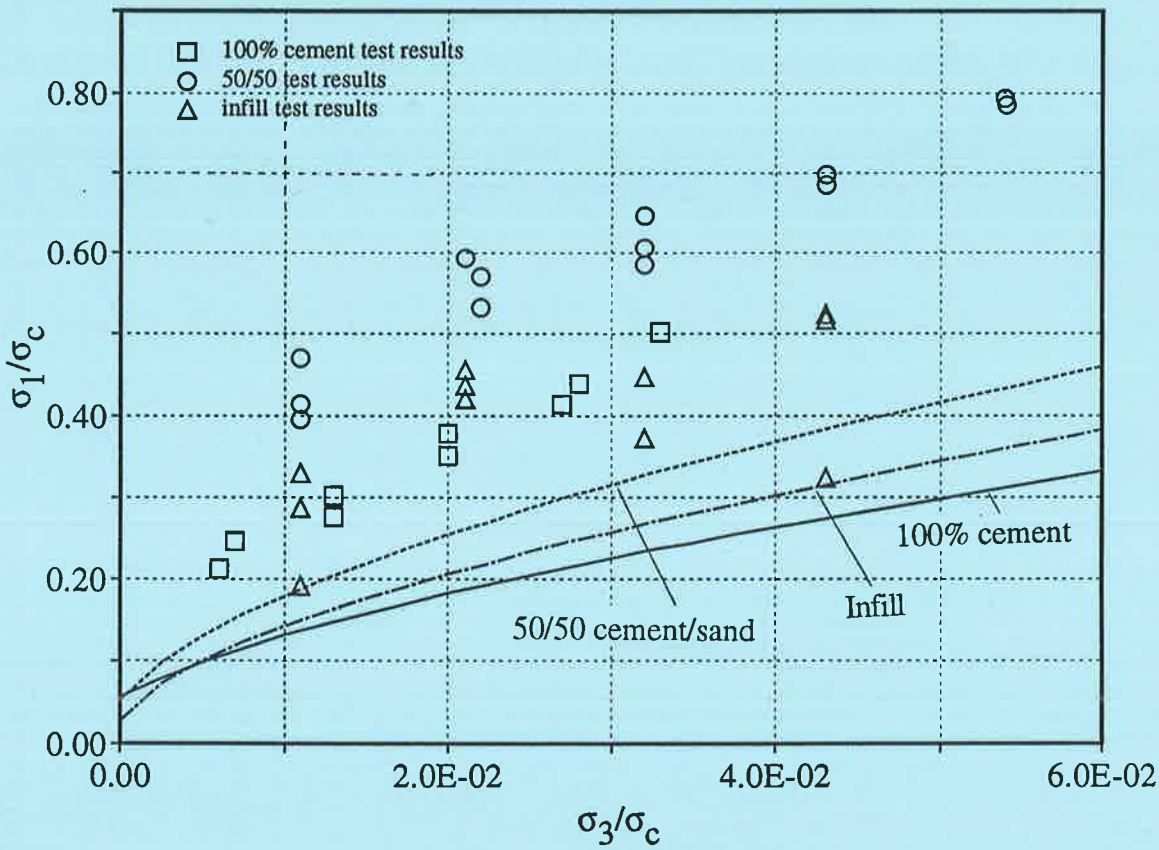

Figure 9.2. Comparison between the predicted normalised principal stresses on the specimens at yield and the experimental results for Geometry 2.

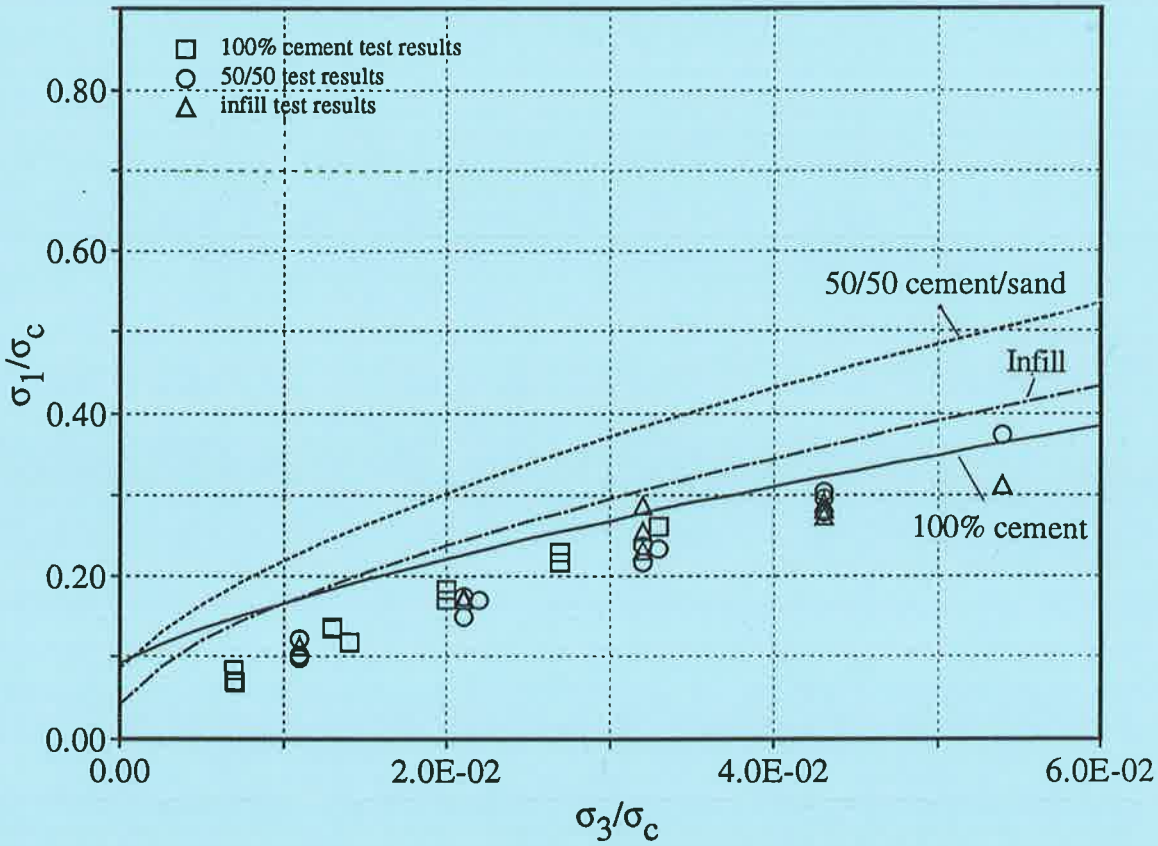

Figure 9.3. Comparison between the predicted normalised principal stresses on the specimens at yield and the experimental results for Geometry 3.

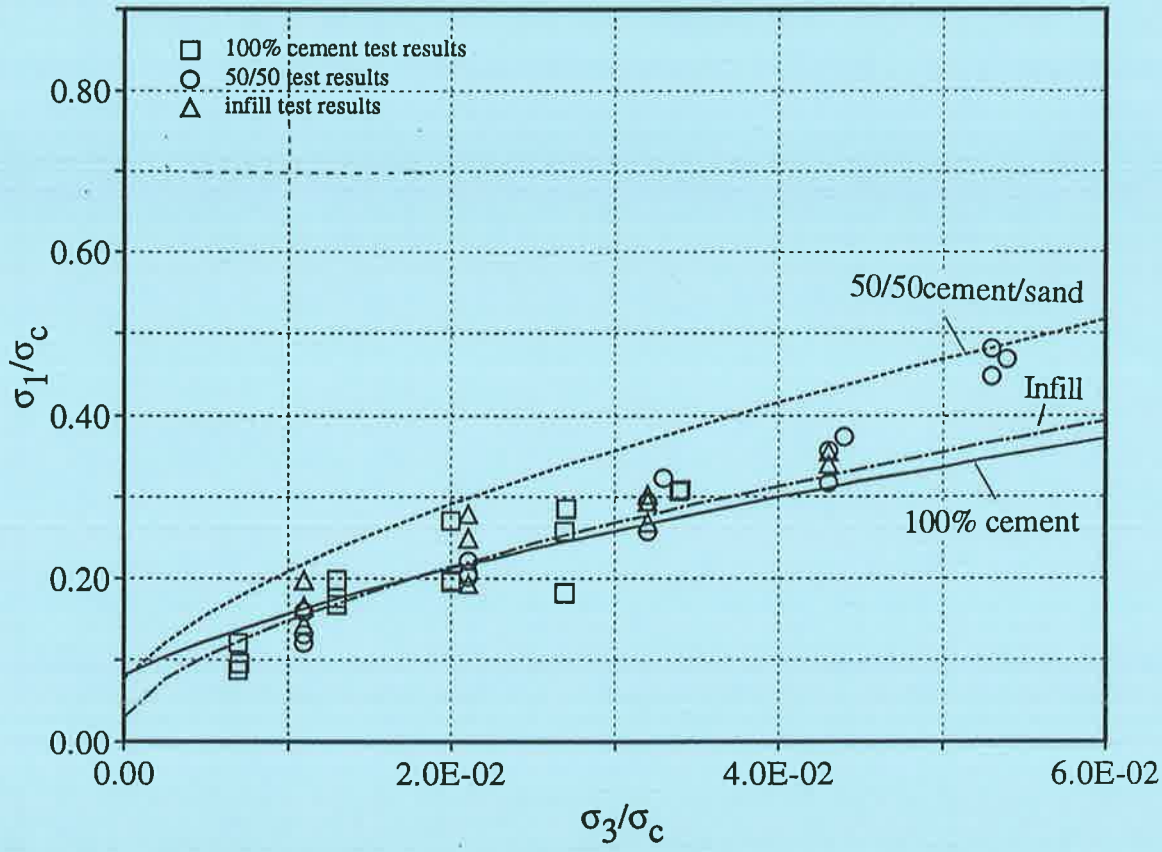

Figure 9.4. Comparison between the predicted normalised principal stresses on the specimens at yield and the experimental results for Geometry 4.

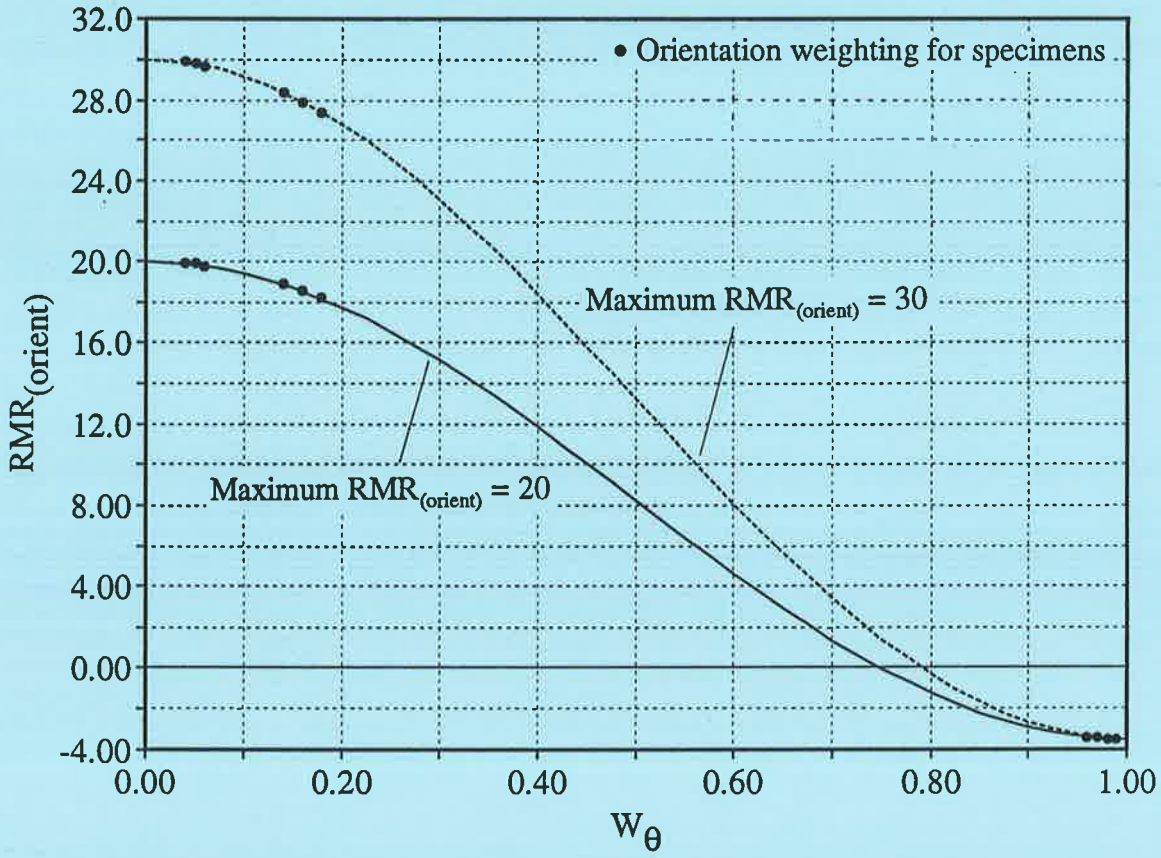

Figure 9.5. Modified RMR adjustment for discontinuity orientation in terms of the orientation weighting, w_θ.

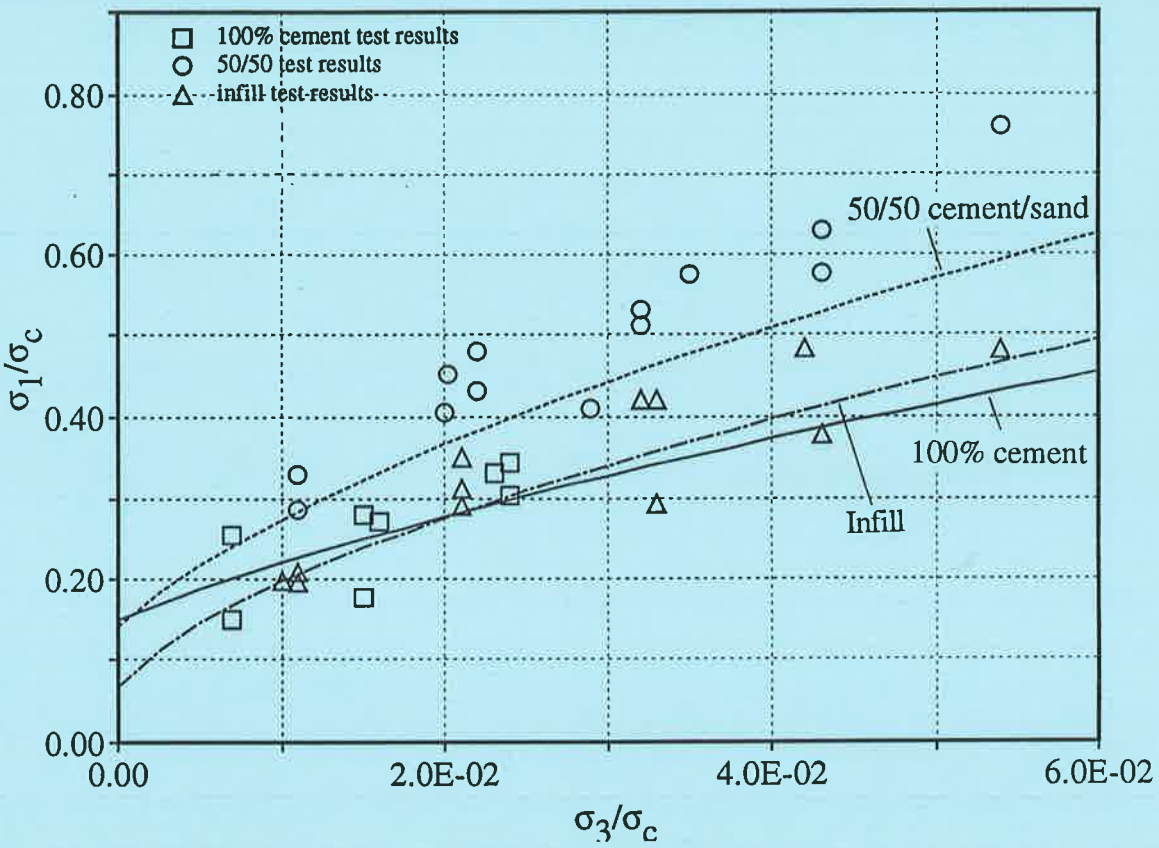

Figure 9.6. Comparison between the predicted normalised principal stresses on the specimens at yield and the experimental results for Geometry 1. Maximum value for $RMR_{(orient)} = 20$

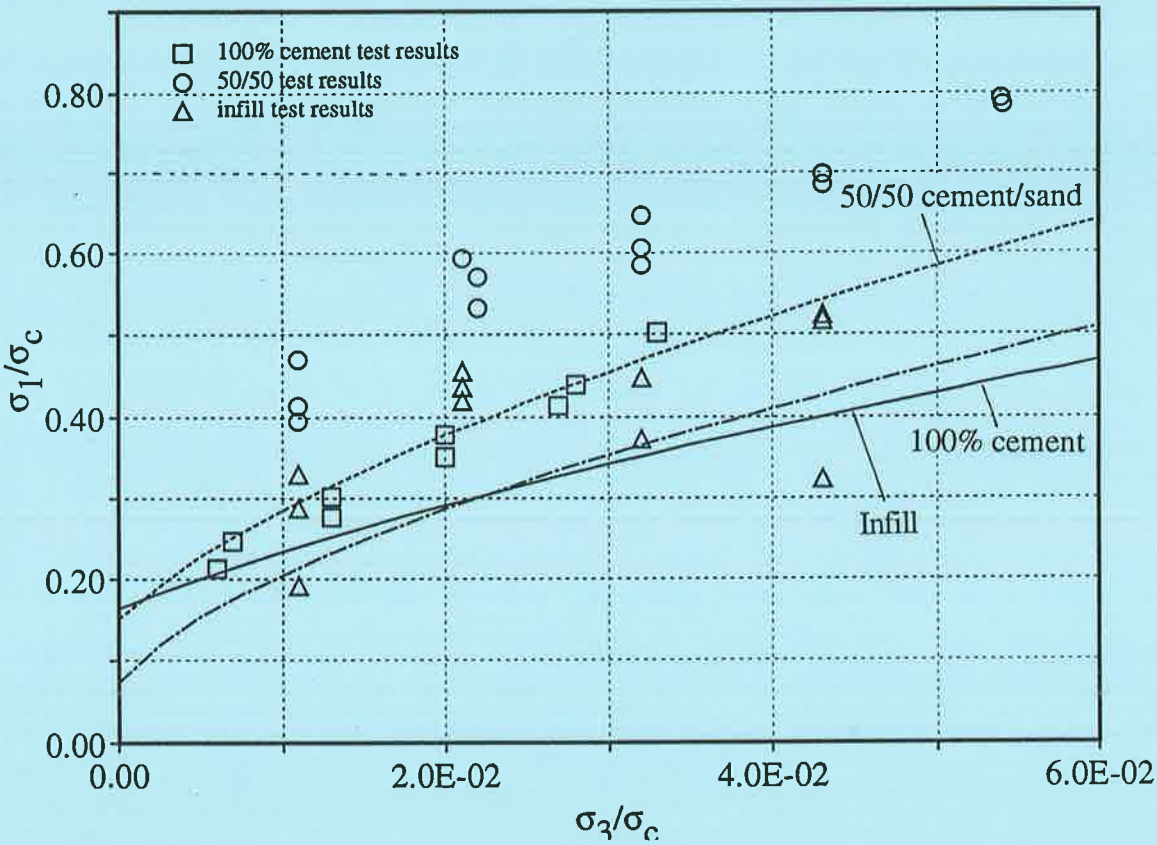

Figure 9.7. Comparison between the predicted normalised principal stresses on the specimens at yield and the experimental results for Geometry 2. Maximum value for $RMR_{(orient)} = 20$

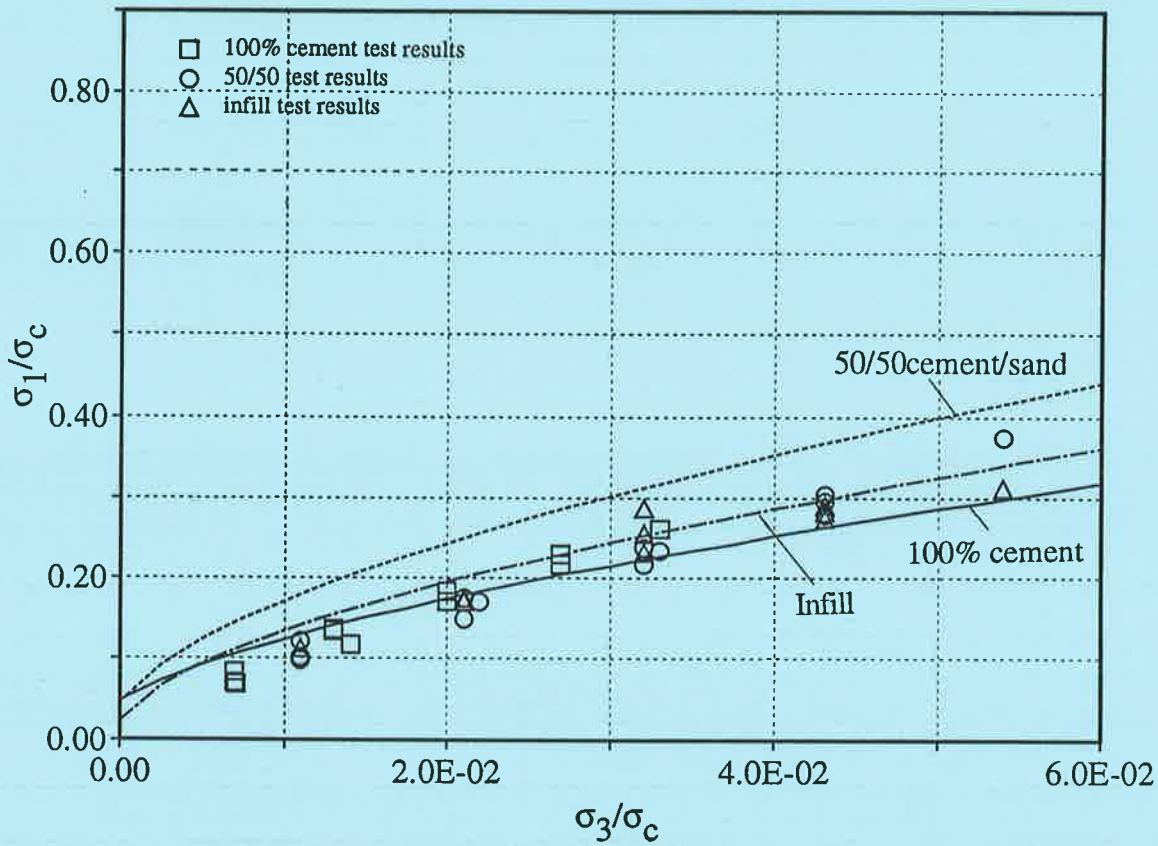

Figure 9.8. Comparison between the predicted normalised principal stresses on the specimens at yield and the experimental results for Geometry 3. Maximum value for $RMR_{(orient)} = 20$

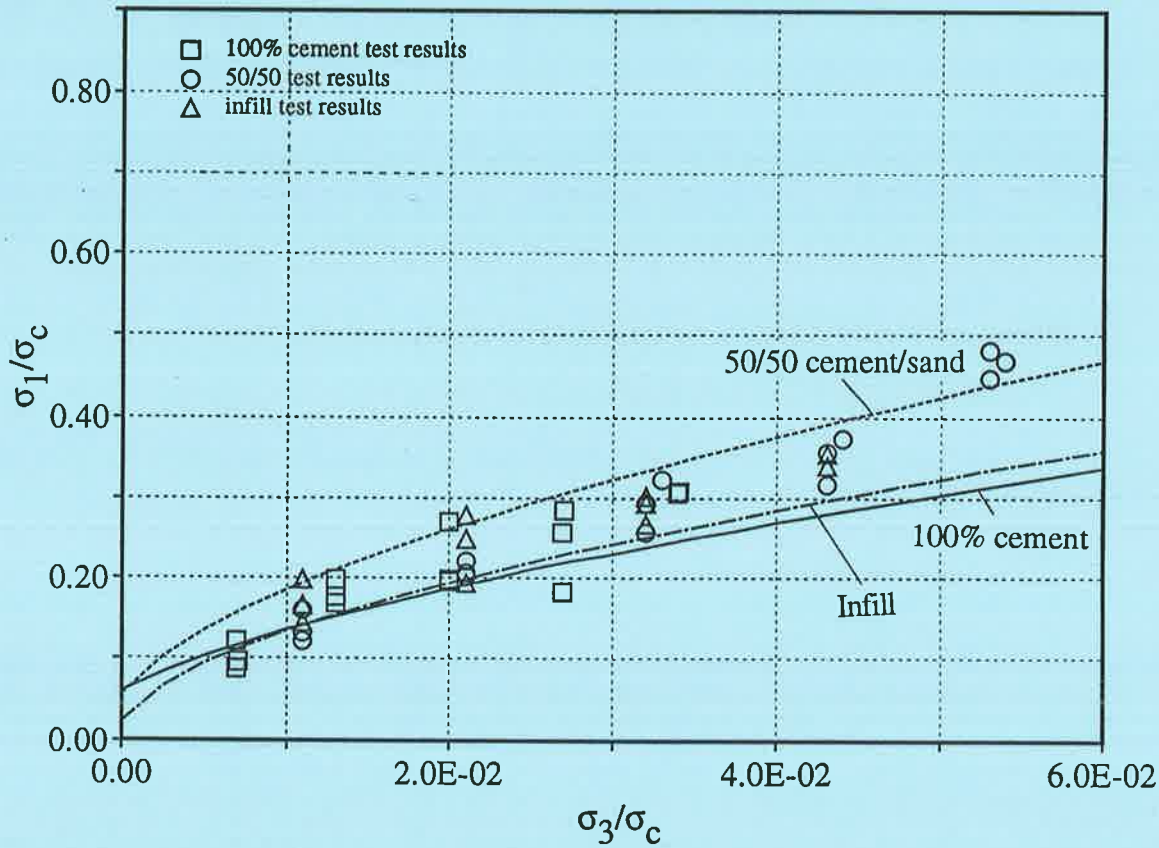

Figure 9.9. Comparison between the predicted normalised principal stresses on the specimens at yield and the experimental results for Geometry 4. Maximum value for $RMR_{(orient)} = 20$

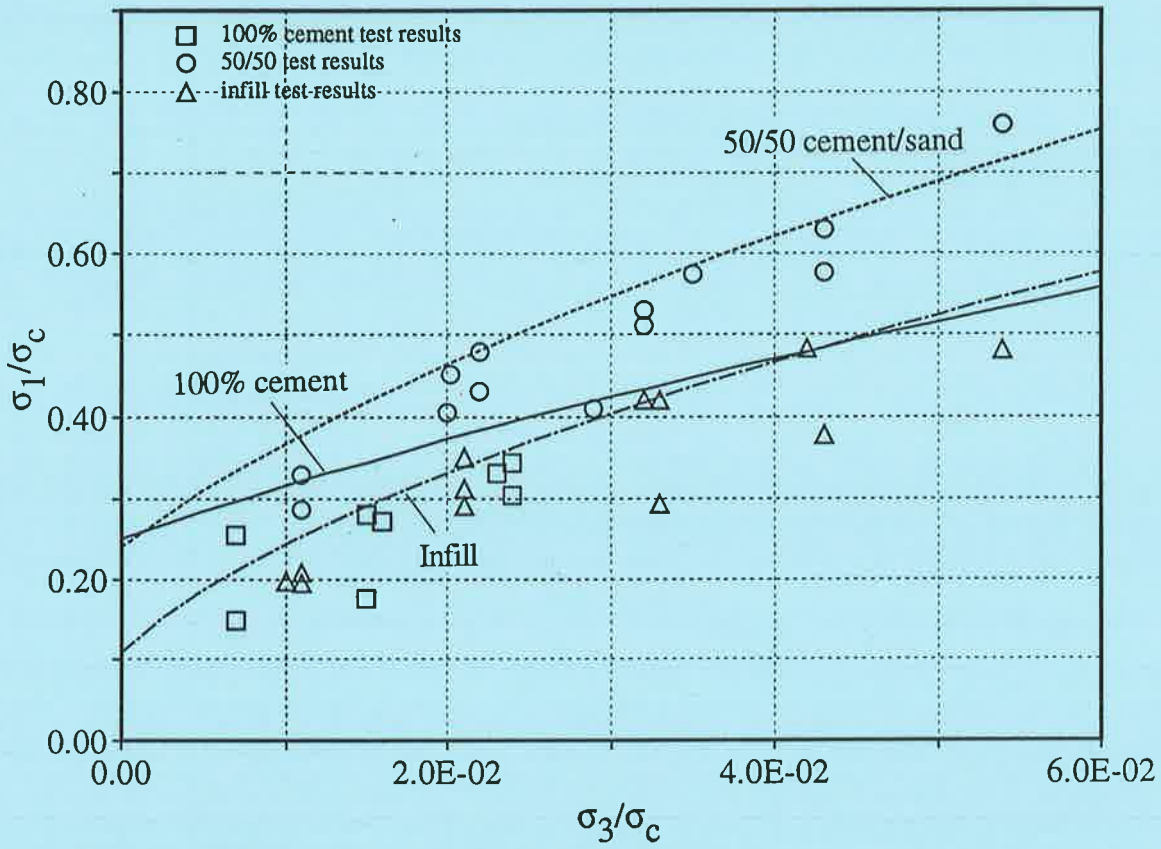

Figure 9.10. Comparison between the predicted normalised principal stresses on the specimens at yield and the experimental results for Geometry 1. Maximum value for $RMR_{(orient)} = 30$

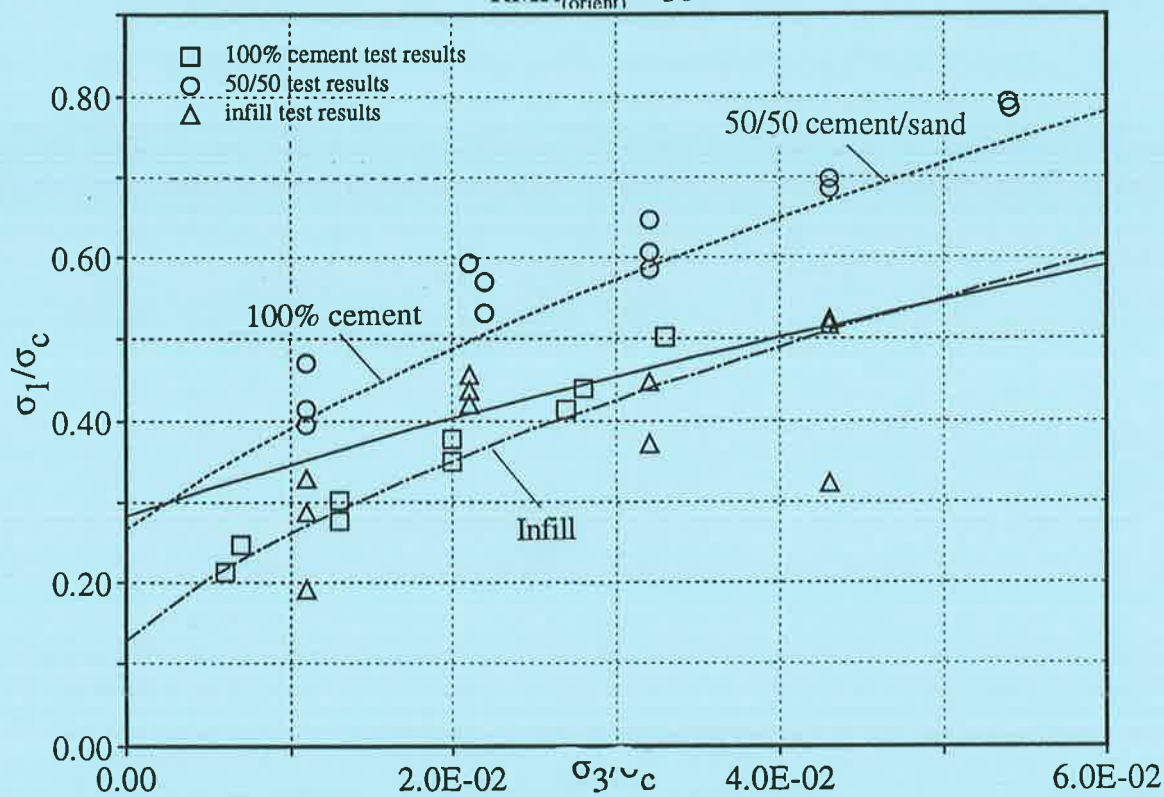

Figure 9.11. Comparison between the predicted normalised principal stresses on the specimens at yield and the experimental results for Geometry 2. Maximum value for $RMR_{(orient)} = 30$

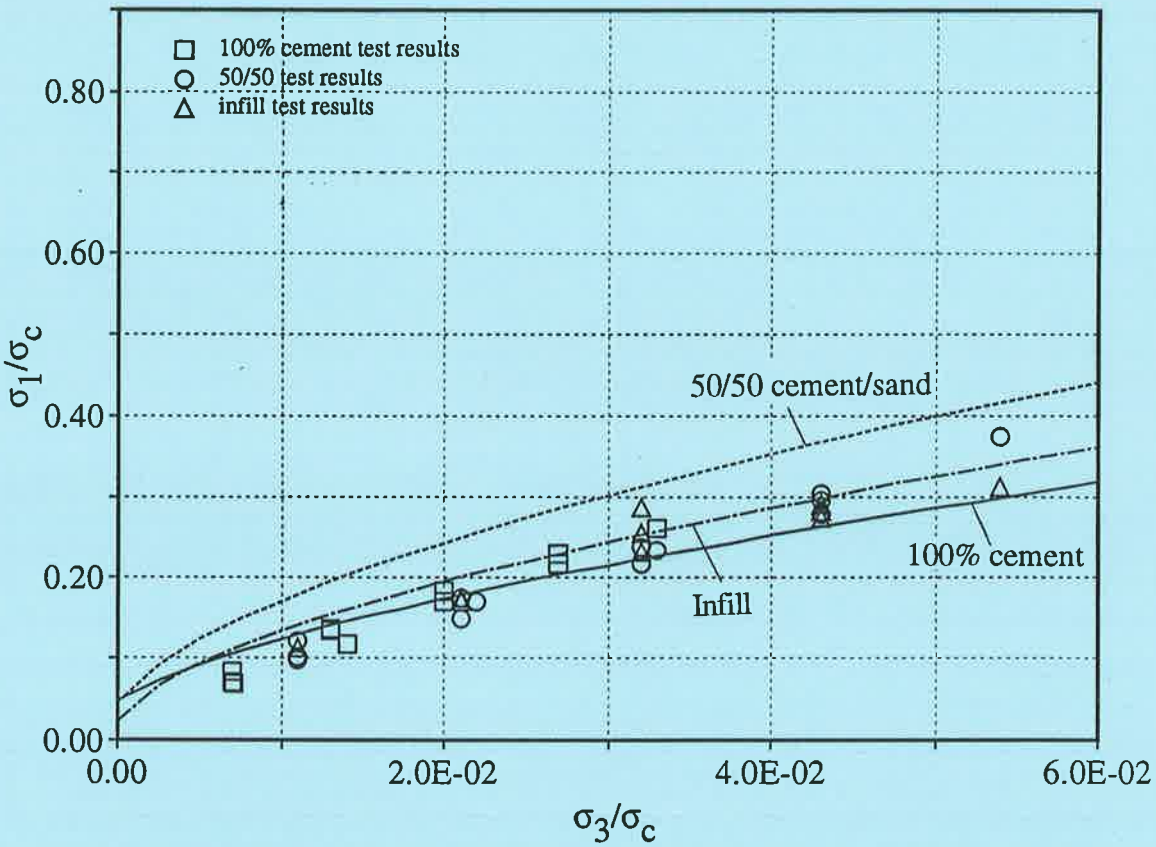

Figure 9.12. Comparison between the predicted normalised principal stresses on the specimens at yield and the experimental results for Geometry 3. Maximum value for $RMR_{(orient)} = 30$

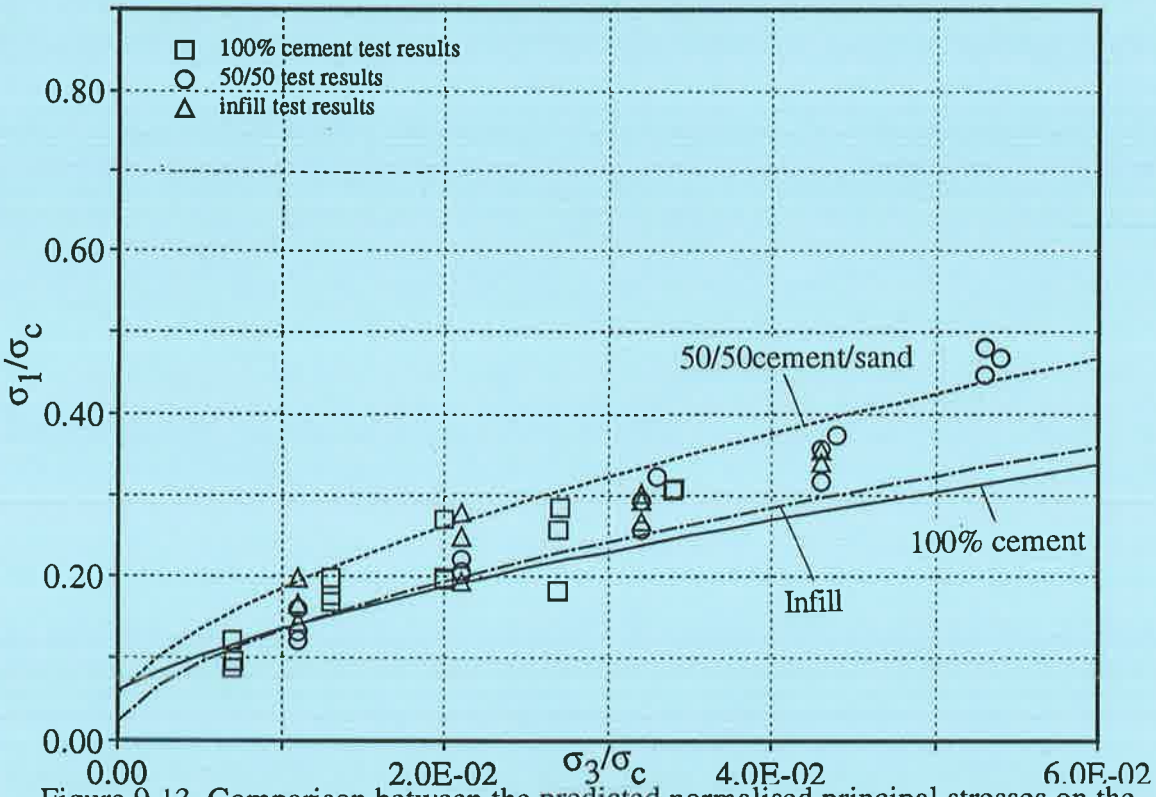

Figure 9.13. Comparison between the predicted normalised principal stresses on the specimens at yield and the experimental results for Geometry 4. Maximum value for $RMR_{(orient)} = 30$

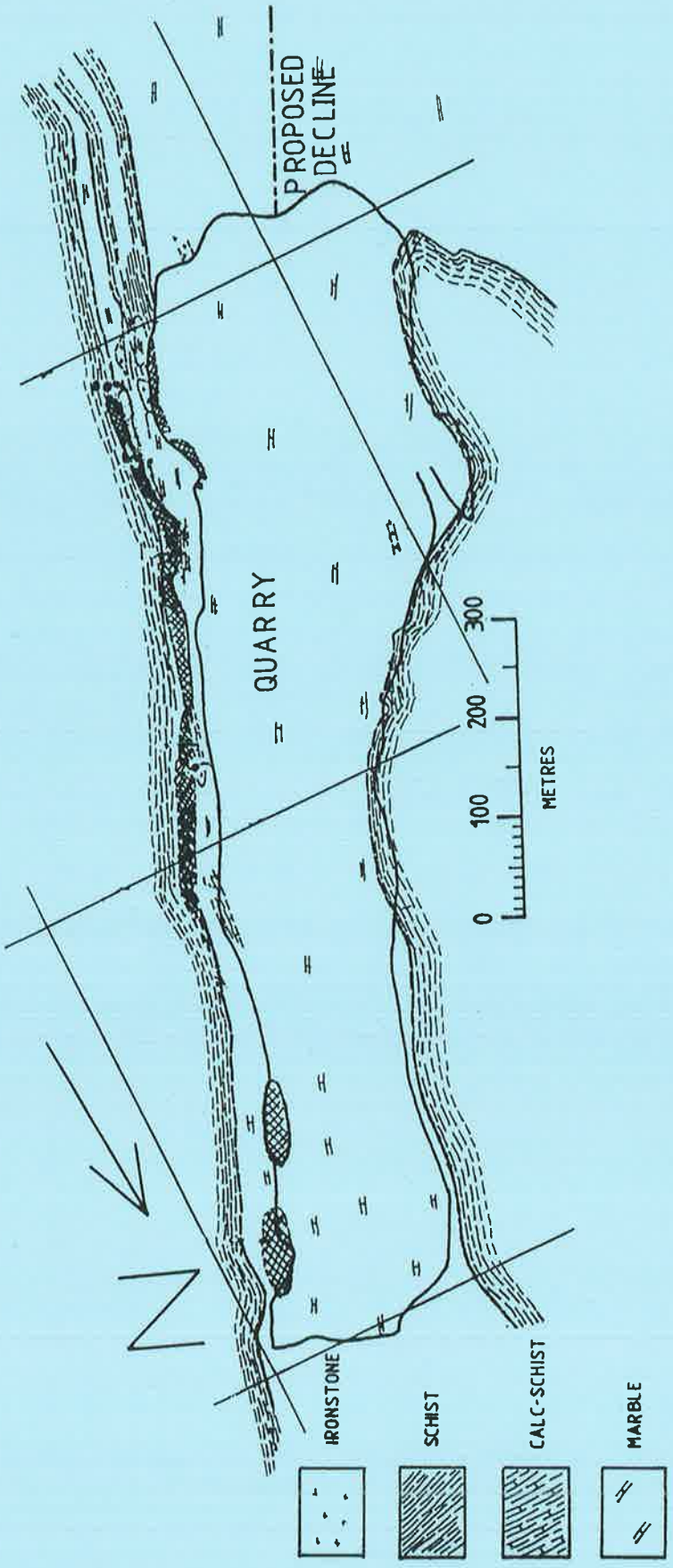

Figure 9.14. Location of geotechnical study (modified after Stapledon and Stevens [138]).

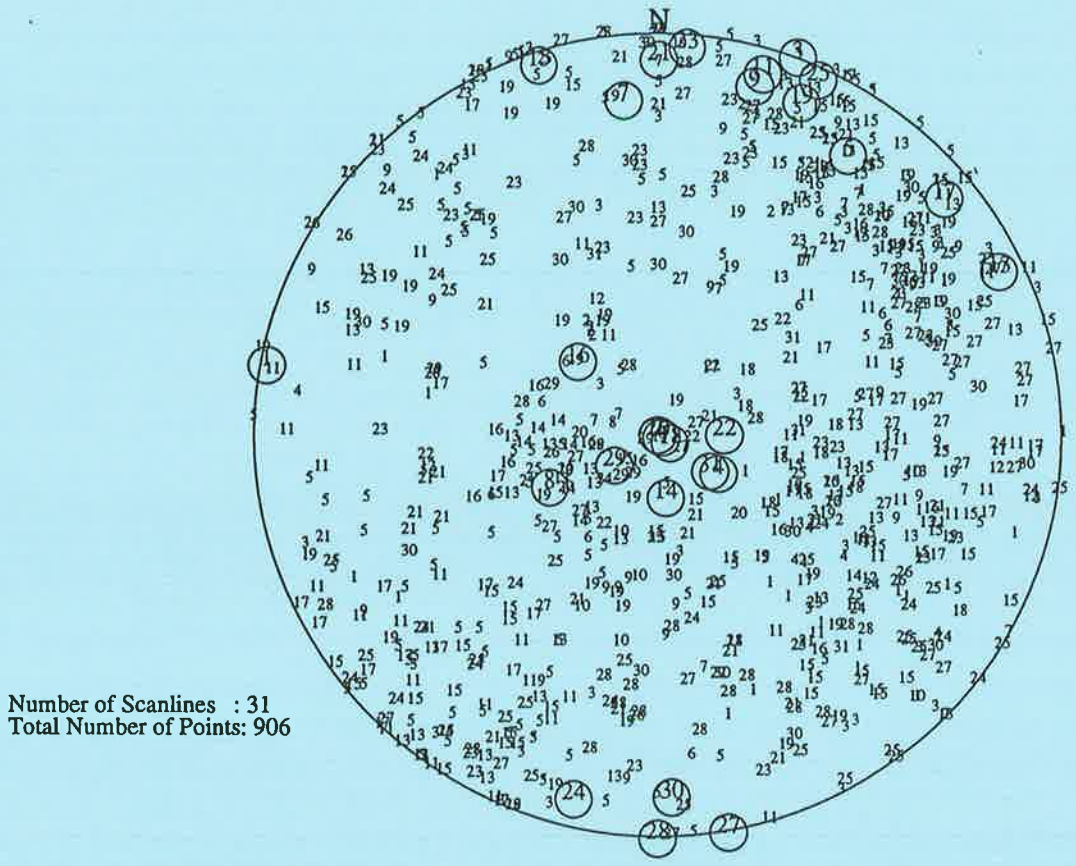

Figure 9.15. Discontinuity data logged during scanline survey presented on hemispherical projection. Scanline positions are circled.

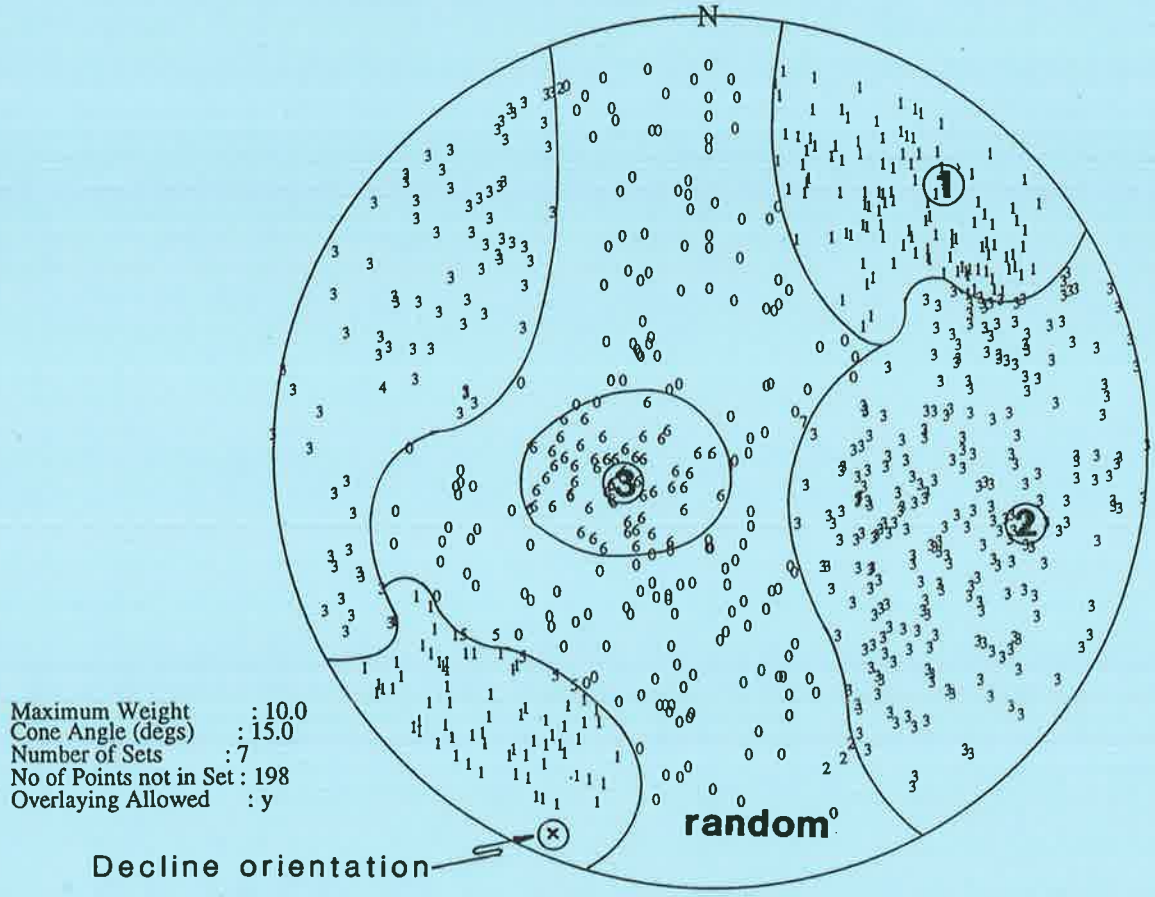

Figure 9.16. Discontinuity data assigned to sets. Mean orientation of each set are circled.

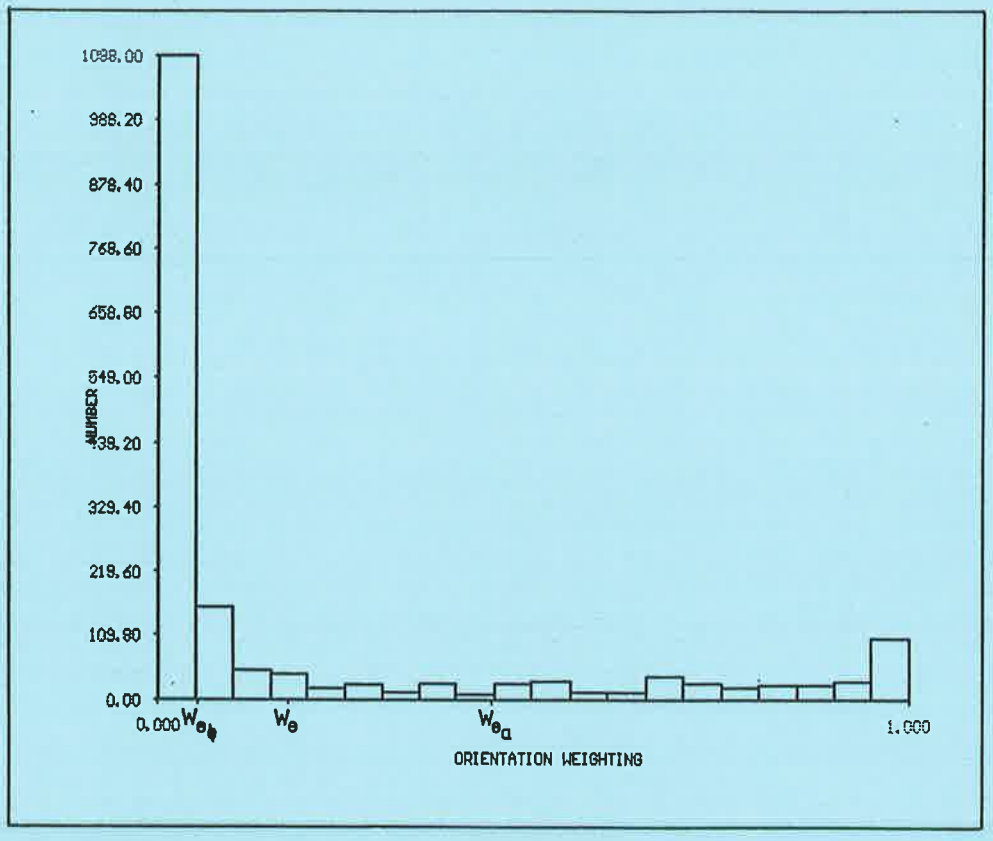

Figure 9.17. Orientation weighting histogram for Penrice Quarry. Orientation of major principal stress is α_s=90°, β_s=0°

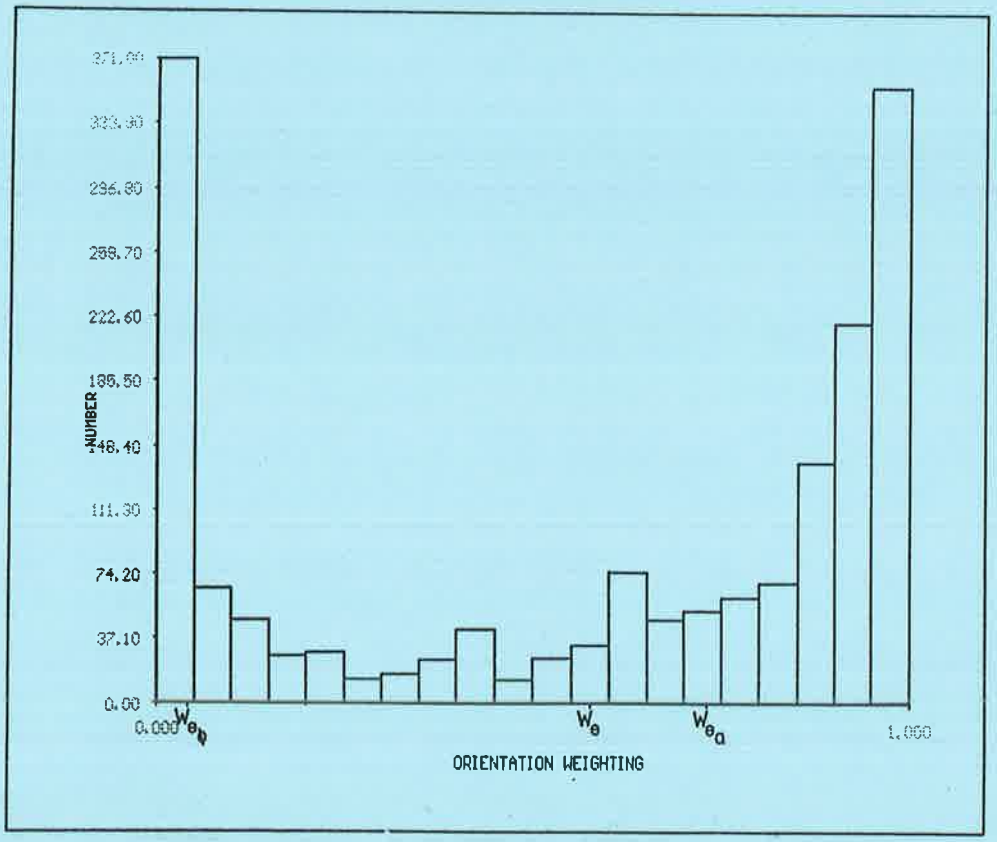

Figure 9.18. Orientation weighting histogram for Penrice Quarry. Orientation of major principal stress is α_s=110°, β_s=30°

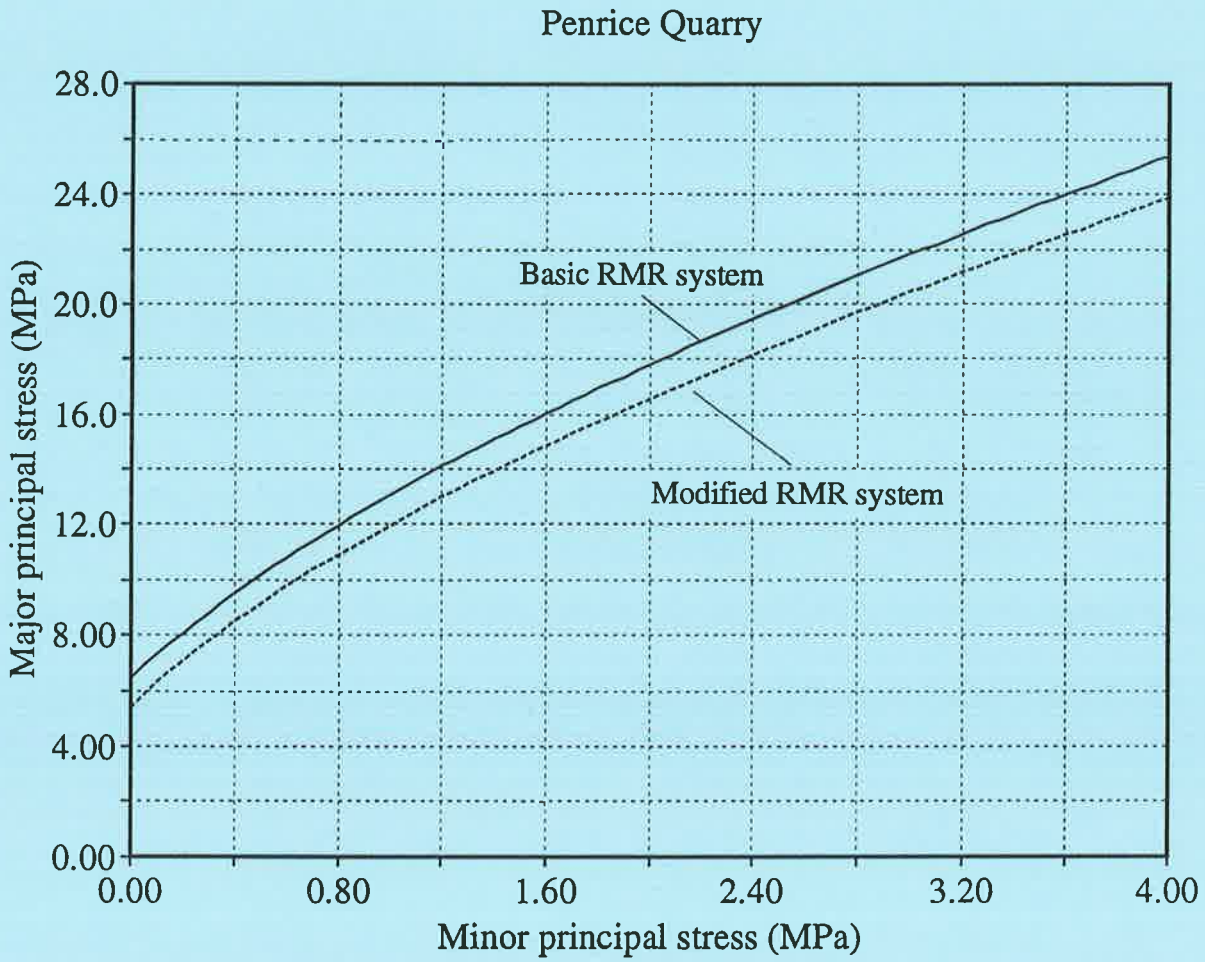

Figure 9.19. Yield strength of the rock mass in the vicinity of the proposed decline at Penrice Quarry. Yield strength predicted by the Hoek-Brown criterion using input data from the basic and the modified RMR systems.

Chapter 10.
Summary and Conclusions.

Chapter 10. Summary and Conclusions.

10.1 Summary

The increased degree of specialisation within the field of rock mechanics reflects the intractability of rock masses to rational engineering design. Rock masses are often heterogeneous and anisotropic, contain discontinuities and have unpredictable spatial variability in the engineering properties of the intact material and the discontinuities. All of these features affect the strength and deformability of the rock mass. The influence of the properties of the discontinuities on the strength and deformability of a rock mass has been researched for many years by many diverse approaches including analytical, numerical, experimental and empirical methods. Many of these approaches were discussed in Chapter 2 of this thesis.

In Chapter 2, analytical solutions were shown to be restricted to fairly simple domains having a small number of discontinuity sets. Numerical methods, such as the distinct element method, were shown to have essentially overcome these restrictions by incorporating the analytical theory into a computational framework that allows large amounts of rock mass structural and material data to be incorporated into the analysis. The major limitation with most numerical methods is that they are restricted to two-dimensional domains. In Chapter 8, an example of the limitation of a two-dimensional analysis for predicting collapse loads in a three-dimensional problem were highlighted. While three-dimensional formulations are available, they are currently expensive and limited by the amount of structural data that can

be incorporated into the analysis.

The effectiveness of laboratory studies conducted on specimens of natural discontinuous rock, for the purposes of determining the yield strength and deformability characteristics of a rock mass, was investigated in Chapter 2. These studies were shown to be of limited practical use owing to the spatial variability in the properties of the intact rock and the discontinuities, the restrictions imposed by the volume of the available test equipment and the influence of scale when extrapolating laboratory results to field conditions. Tests conducted on discontinuous specimens manufactured from a homogeneous modelling material were shown in Chapter 2 to have provided valuable information concerning the behaviour of discontinuous rock masses. These tests were traditionally carried out on specimens having non-representative discontinuity geometries. The strength and deformation behaviour of more realistic specimens was investigated in Chapter 7.

The use of the empirically derived Hoek-Brown rock mass yield strength criterion (Hoek and Brown [65]) using input parameters derived from the Rock Mass Rating (RMR) system developed by Bieniawski [23] has gained widespread acceptance for Civil and Mining Engineering applications as a practical tool for developing a yield criterion applicable to a discontinuous rock mass. A number of deficiencies in the use of this combined procedure were discussed in Chapters 2, 3 and 9 and were shown to be related more to the use of the RMR system than to the yield criterion itself. Three significant deficiencies are:

(1) The combined RMR/yield criterion procedure tends to provide a lower bound to rock mass yield strength leading to conservatism in design. This fact was observed in the results of the laboratory tests discussed in Chapter 7.

(2) The use of the RQD rating in the RMR system is undesirable as it is an unreliable estimator of discontinuity frequency. As discontinuity frequency is a function of discontinuity spacing and RQD, the RMR system effectively rates discontinuity frequency twice.

(3) Neither the RMR system nor the yield criterion were designed to be sensitive to the influence of discontinuity shear strength, or the influence of the principal stress direction

with respect to discontinuity orientation, on the yield strength or deformability of the rock mass.

In Chapters 3 and 9, three modifications to Bieniawski's basic RMR classification system were proposed to partially address these deficiencies with respect to underground excavations. These modifications do not seek to modify all aspects of Bieniawski's system, rather, they seek to modify those aspects considered to be most subjective. In summary, these modifications involve:

(1) Ignoring the rating for drill core quality, RQD.

(2) Determining a discontinuity spacing rating, that seeks to quantify the mean volume of the blocks with respect to the size of the proposed excavation. A maximum rating of 20 points is applied to the rock mass for this parameter. The magnitude of this rating is consistent with that applicable in the basic RMR system.

(3) An orientation weighting is determined for the rock mass in the vicinity of the rock mass that seeks to quantify the likelihood for the discontinuities in the vicinity of the underground excavation to slip. In the modified RMR system, this rating ranges from -3 to 30 points.

A scanline mapping technique is used to determine input data for the suggested procedure. Additional data is also required defining the *in situ* major principal stress direction, the orientation of the proposed excavation and the friction angle for the discontinuities. The shear strength data for the discontinuities is obtained from shear box tests. The scanline data is analysed, using the principles of discontinuity analysis, to provide data defining the mean orientation and spacing of the discontinuity sets in the vicinity of the excavation. Once these properties are known, in order to obtain the orientation weighting for the rock mass, an estimate is made of the number of discontinuities expected to intersect the excavation. Further analysis, based on the shear strength parameters of the discontinuities and the orientation of the excavation and the major principal stress, enables those discontinuities expected to intersect the excavation to be weighted according to the likelihood of slip along the particular discontinuity. This data is plotted in the form of a histogram that provides the

design engineer with a visual aid for assessing the integrity of the rock mass in the vicinity of the excavation. The eventual choice of an appropriate orientation weighting for the rock mass is made after consideration of the long term stability requirements for the particular excavation. Once the orientation weighting has been determined, it is used in place of Bieniawski's 'rating adjustment for discontinuity orientation'.

Four discontinuous specimens, representing core from four hypothetical rock masses, were designed in Chapter 3 to be used in a comprehensive series of triaxial tests. The results of these tests enabled data necessary for the development of the modified rating technique to be obtained and the strength and deformation behaviour of specimens comprised of distinct blocks to be investigated.

In Chapter 4, an original technique for fabricating the cylindrical discontinuous specimens suitable for triaxial testing was presented. This technique briefly involved fabricating a cylinder out of foam and cutting the discontinuities into the cylinder with a hot wire. The foam blocks formed in this process were coated with liquid silicon rubber to create moulds into which a modelling material would be poured. Two materials, one composed of gypsum cement and the other, a 50/50 combination of gypsum cement and sand, were selected as suitable material from which to manufacture the specimens. A diatomaceous earth based material was selected for use as infill.

Considerable time was devoted in this study to develop equipment that could be used to conduct reliable and well-controlled tests. These tests were necessary to investigate the properties of the modelling material to ensure that the material satisfied the requirements for similitude with natural rock and to enable the characteristics of the discontinuous specimens to be tested under triaxial conditions. These tests involved commissioning and instrumenting a 150 mm Hoek cell and designing and constructing a cell pressure control system. This control system was based around a linear displacement pump that was capable of maintaining pressure within closer limits than those required by the ISRM and accurately monitoring changes in the volume of a specimen to within $3.8mm^3$. This value represents an

improvement on the cited systems of other researchers.

The results from a comprehensive investigation to determine the material properties of the intact material and the discontinuities, discussed in Chapter 6, showed that the modelling materials satisfied reasonably the requirements for similitude with natural rock. The shear stiffness of the discontinuities was defined with respect to the normal stress in terms of a non-linear relationship and the shear strength was defined with respect to the normal stress in terms of a linear Mohr-Coulomb relationship.

The results from 156 triaxial tests on the discontinuous specimens enabled a comprehensive discussion of the characteristic deformation and yield behaviour of the specimens to be carried out in Chapter 7. These tests showed that:

(1) The maximum yield strength of a material is achieved when the material contains no discontinuities. The minimum yield strength is achieved when the material contains a non-intersected discontinuity orientated at an angle β_{crit} (where $\beta_{crit} = \phi_w/2 + 45^o$ and ϕ_w is the friction angle of the discontinuity).

(2) In a specimen containing multiple discontinuities, orientated so that axial deformation occurs along cracks through intact material, the yield strength is less than that of the intact material. This fact illustrates how the presence of discontinuities will always reduce the yield strength of a material. The extent of the reduction is dependent on the orientation of the discontinuities.

(3) In specimens containing multiple discontinuities, if axial deformation occurs primarily along a single discontinuity, the presence of other discontinuities intersecting the shearing discontinuity will increase the yield strength of the specimen. A specimen containing interlocking discontinuities is stronger than one in which no interlocking occurs.

(4) There is a systematic increase in the yield strength and decrease in the deformability of discontinuous specimens with increases in the confining pressure prior to and subsequent to shear deformation occurring along cracks or pre-existing discontinuities.

(5) The axial stress versus axial deformation curves of the four geometries tested had four distinct regions. Non-linear Region I occurred as blocks aligned themselves according to

the principal stress state. In linear Region II blocks packed together and the volume of the specimens decreased. In non-linear Region III the shear strength of cracks formed through intact material or pre-existing discontinuities was achieved, the specimens began to dilate and stick slip oscillations occurred. In non-linear Region IV the specimens achieved their yield strength prior to the onset of plastic flow.

(6) Infill reduces the yield strength and increases the deformability of discontinuous specimens. The amount of influence of infill on these parameters is dependent on the orientation of the discontinuities.

(7) The axial stiffness, K, of the specimens prior to and subsequent to shear deformations occurring along cracks or discontinuities can be defined in terms of the minor principal stress, σ_3, by a relationship of the form:

$$K = a_{(k)}\sigma_3^{b(k)}$$

where $a_{(k)}$ and $b_{(k)}$ depend on the specimen geometry and the material properties.

(8) Axial stiffness can be reasonably estimated by an analytical decomposition procedure.

(9) The yield strength, $\sigma_{1(peak)}$, of the specimens can be defined in terms of the minor principal stress by an equation of the form:

$$\sigma_{1(peak)} = a_{(\sigma)} + b_{(\sigma)}\sigma_3$$

where $a_{(\sigma)}$ and $b_{(\sigma)}$ depend on the specimen geometry and the material properties.

(10) The Hoek-Brown rock mass yield criterion, based upon input data obtained from the basic RMR system, tends to provide a conservative estimate of rock mass strength for cases in which $\beta_w < \phi_w$. (where β_w is the acute angle between the normal to a discontinuity and the major principal axis).

(11) A discontinuous specimen contracts prior to slip occurring along discontinuities as the deviator stress increases, blocks pack together and asperities are crushed. The specimen then dilates as slip occurs. This dilation is not due solely to the effect traditionally associated with slip along discontinuities that results from the over-riding of asperities. Although this effect occurs, volumetric change is predominantly associated with the formation of voids within the specimen as blocks separate from each other.

Even though the techniques developed in the study for producing the discontinuous

specimens is capable of being used to manufacture a wide range of discontinuity geometries, the techniques and the subsequent triaxial testing, is extremely time consuming. The number of geometries that can be tested in the available time is, therefore, limited. A further limitation on physical testing is that the size of the available test equipment limits the number of distinct blocks that can be incorporated into discontinuous specimens. These limitations do not apply to the same degree if numerical techniques, such as the distinct element method implemented in the proprietary software UDEC, are used to model the discontinuum. In Chapter 8, the test results described in Chapters 6 and 7 proved to be valuable for validating the effectiveness of the two-dimensional UDEC for modelling three-dimensional problems. These results showed that UDEC:

(1) could provide reasonable predictions of failure mechanisms,

(2) was able to model the elasto-plastic stress versus deformation behaviour characteristics of intact and anisotropic specimens,

(3) was unable to correctly predict the yield strength of non-symmetrical three-dimensional domains because of the necessity to model these domains as two-dimensional strips and

(4) was unable to crack blocks. The necessity that all discontinuities existing in the domain have to be defined prior to UDEC being implemented and that no new discontinuities could develop, means that care has to be taken to identify the development of shear bands during a run which could indicate that the intact material is yielding in shear.

(5) The calculation sequence that UDEC chooses is of paramount importance to the failure mechanism predicted. Once sliding is initiated on a particular discontinuity, other discontinuities are terminated and hence prevented from further sliding. If, as in the case of the Geometry 1 specimens, the calculation sequence was top down, sliding was predicted to occur first on uppermost discontinuities. This mechanism was in contrast to the laboratory tests in which sliding occurred bottom up.

On the basis of the results obtained from the laboratory studies, the procedure developed in Chapter 3 for classifying a rock mass for the purpose of obtaining input data for the Hoek-Brown rock mass yield criterion was completed in Chapter 9. It was shown in Chapter 7, that the Hoek-Brown rock mass yield criterion provided a lower bound to rock mass yield

strength and, depending on the discontinuity orientation, this lower bound could be quite conservative. In Chapter 9, it was shown that, based on the results obtained using models of discontinuous rock subjected to a low stress environment, the suggested procedure could provide a better estimate of yield strength. The suggested procedure follows a logical progression and a case study was presented to demonstrate how this procedure could be implemented.

10.2. Recommendations for Future Work.

The modified RMR system developed in this thesis was developed on the basis of the results from a limited number of triaxial tests conducted at low confining pressures on models of discontinuous rock. For the next stage of the research, it would be desirable to validate the results obtained using specimens of discontinuous rock subjected to a broader range of confining pressures. These specimens should be obtained from a rock mass in which the geometric properties of the discontinuities within the rock matrix were quantified with a scanline survey. In order to obtain a statistically sound distribution of results for a particular site, the spatial variability in rock mass properties would require that a large number of core samples be obtained. It would also be necessary for orientated core to be obtained in such a manner that the major axis through the core was coincident with the major principal direction in the region from which the specimens were obtained. This result would be difficult to achieve in practice because:

(1) of the very limited data usually available defining the stress state at a particular site,
(2) obtaining the sample would, in itself, modify the stress state,
(3) sampling direction is limited by the capabilities of the drilling rig,
(4) quality sampling is a very time consuming and expensive exercise and
(5) of the difficulties involved in obtaining orientated core of sufficient competency to enable discontinuities to be logged.

Owing to a lack of suitable field specimens to test and to the limitations of the two-dimensional version of UDEC, it would be desirable for the results obtained in the laboratory

to be compared with those predicted by the three-dimensional implementation of the distinct element method, 3-DEC. The latest version of 3-DEC is limited by the number of blocks that can be modelled. The number of blocks in the laboratory specimens is, however, well within the capabilities of the software. If it can be shown that 3-DEC can correctly predict the yield strength of the laboratory specimens, a wider numerical study could be implemented for more complex geometries. A comparison would be made between the yield strengths predicted by the modified rating procedure and those predicted by 3-DEC.

At present, the weighting for discontinuity spacing, $RMR_{(space)}$, is based on a simplistic analysis for determining block size and does not consider whether the orientation of the blocks is such that removable or non-removable blocks are formed. Block size and geometry can be determined using block theory as implemented in software such as SAFEX (Thompson and Windsor [143]). It is desirable that aspects of block theory be incorporated into the modified procedure so that it may consider better the significance of blocks with respect to the proposed excavation. It is important that these additional features do not make the modified Rock Mass Rating procedure so cumbersome that it no longer represents a practical tool for obtaining an initial estimate of rock mass yield strength.

The concepts developed in this thesis, defining the strength and deformability of the discontinuous specimens, were developed on the basis of fairly simplistic materials. An important question that arises is how applicable are the results for natural rock materials, especially materials containing discontinuities possessing apparent cohesion and significant roughness features? This question can only be answered by carrying out a more extensive laboratory testing programme using a wider variety of simulated rock types. Roughness features could be added by combining gravel sized particles into a gypsum cement matrix.

The concept that the stiffness of the specimen/rubber jacket interface in a Hoek triaxial cell may contribute significantly to the apparent stiffness of a discontinuous specimen is worthy of investigation. From the attempt to quantify this stiffness in Chapter 8, it appears that this contribution may be significant at low confining pressures. More detailed testing is required

to properly quantify this variable. Another area of potential research involving the Hoek cell is to develop further the concept for monitoring the circumferential strain on a specimen by monitoring the circumferential strain in the rubber membrane.

10.3. Conclusions.

The deformation behaviour of a discontinuous rock mass, containing multiple sets of discontinuities, is highly complex and non-linear. The yield strength of the rock mass cannot be estimated by excessively simplistic analytical techniques owing to the interlocking of blocks. Rock mass yield strength can, however, be estimated using an empirical technique, provided that the technique is based on input data obtained from the application of a non-subjective, Rock Mass Rating system such as that suggested in this thesis.

Appendix A.
Program for Determining the Orientation Weighting Coefficient

Appendix A. Program for Determining the Orientation Weighting Coefficient.

This appendix contains the source code for the program WEIGHTS. This program can be used to determine the orientation weighting, $w_{\theta(mass)}$ and the modified Rock Mass Ratings $RMR_{(orient)}$ and $RMR_{(space)}$ for the rock mass in the vicinity of the proposed excavation. The program is written in Turbo Pascal©[3]. For brevity, plotting and mathematics units have not been included. Details of these units can be obtained from the Author if required.

The program was not designed to be totally stand alone but to be used in conjunction with a program, such as CANDO (Priest [119]), that clusters scanline sampled discontinuities into their respective sets. Once each of the discontinuities is allocated to a set, the scanline data for the discontinuity is written by CANDO to a separate file containing data for only those discontinuities contained within the particular set. For example, if file PENRICE.DAT contains data for all discontinuities sampled in the scanline survey, files PENRICE.1, PENRICE.2,.....,PENRICE.N are generated. These files contain the data on discontinuities in sets 1,2,.....,N respectively. Program WEIGHTS reads data from each of these set files. The parent file name, PENRICE, is prompted for, along with other input data, in the following windows:

[3] Turbo Pascal is a registered trademark of Borland International, Inc. PO. Box 660001, Scotts valley, CA, USA, 95066-0001.

SITE DATA

Trend of excavation ?	205
Plunge of excavation ?	10
Length of excavation ?	250
Trend of major principal stress ?	90
Plunge of major principal stress ?	0
Number of discontinuity sets ?	4
Discontinuity orientation data filename (no extension) ?	penrice
Friction angle of discontinuities ?	40

SET DATA

FOR SET NUMBER **1**

Trend of mean normal ?	37.5
Plunge of mean normal ?	7.4
Mean discontinuity spacing ?	0.203

(this text and data is repeated for the other sets)

Output from WEIGHTS includes the histogram, as shown in Figure 9.17, and the data displayed in the following windows:

SUMMARY 1

Mean orientation weighting (all discontinuities)	0.11
Mean orientation weighting (active discontinuities)	0.42
Orientation weighting at friction angle	0.05
$RMR_{(orient)}$	19.3
Mean block volume	0.003
$RMR_{(space)}$	1.24
Number of discontinuities sampled by scanline	892
Number of discontinuities to intersect excavation	2148

CR to continue

SUMMARY 2

For set 1	
Number of discontinuities sampled	234
Number to intersect excavation	1147
Mean orientation weighting for set	0.01

(this text and data is repeated for the other sets)

CR to continue

Source Code of WEIGHTS

```
program ch3;
{$N+}
uses
        graph,plotlib,crtlib,crt,mathlib;
type
        arr1 = array[1..20] of real;
        arr2 = array[0..1000] of real;
        arr3 = array[1..20] of integer;
var
        Infile,ver,InFileName,OutfileName:string;        {in/out file props.}
        f1:text;
        InputText:char;
        irow,icol:integer;
        NSets,k:integer;                                 {set properties}
        DSet:arr3;
        Ns,MeanWset,alpha,beta,S:arr1;
        N,Wset,S1,S2,S3,NSet,randomNs,dr,RandomE:real;
        Phir,Phid,exponent,RMRorient,lambda:real;        {discontinuity properties}
        i,Dtotal:integer;
        Ntotal,Nactive:real;
        Wall,Wactive,MeanWall,MeanWactive,Wphi:real;
        semi,Li,scanumber,alphan,betan:real;
        Worient,Ne,NePrime:arr2;
        alphae,betae,Le,Ax,Jv,RMRspace:real;             {site properties}
        alphas,betas:real;                               {stress props.}
        ThetaEN,ThetaER,BetaW,psi,betacrit:real;         {angles}
        xmin,xmax,dx,pi,temp1:real;                      {general}
{*************************************************************************}
procedure CalcAngle(var alpha1,beta1,alpha2,beta2:real;var theta:real);
{To determine the acute angle between two lines in space}
begin
        theta:=acos(cos(alpha1-alpha2)*cos(beta1)*cos(beta2)+sin(beta1)*sin(beta2));
end;
{*************************************************************************}
procedure histo(xmin,xmax,dx:real);
{plots discontinuity orientation weightings }
```

```
var
        rangex,rangey,ymax:real;
        maxinterval,interval,jjj:integer;
        number:array[0..1000] of integer;
begin
{sort readings into histogram limits}
        for jjj :=0 to 1000 do number[jjj]:=0;
        ymax:=0;
        maxinterval:=0;
        for i:=1 to Dtotal do
        begin
                interval:=trunc(Worient[i]/dx)+1;
                if interval > maxinterval then maxinterval:=interval;
                number[interval]:=number[interval] + trunc(NePrime[i]);
                if number[interval] > ymax then ymax:=number[interval];
        end;
        rangex:=xmax-xmin;
        rangey:=ymax;
        init;
        windowmap(1,0.0-0.2*rangex,-0.2*rangey,xmax+0.1*rangex,ymax+0.1*rangey,
                1,getmaxy-20,getmaxx-1,1,red);
        remap(1);
        xaxis(0.0,0.0,xmax,0.0,xmax,1,5,3,0.4*xmax,-0.1*rangey,
        'ORIENTATION WEIGHTING',white,green,white);
        yaxis(0.0,0.0,rangey,0.0,rangey*0.1,10,5,2,-0.1*rangex,  0.4*ymax,
        'NUMBER',white,green,white);
        for jjj:=1 to maxinterval do
        begin
                movea(0.0+(jjj-1)*dx,0.0);
                drawa(0.0+(jjj-1)*dx,number[jjj]);
                drawa(0.0+jjj*dx,number[jjj]);
                drawa(0.0+jjj*dx,0.0);
        end;
end;
{*************************************************************************}
{               MAIN PROGRAM                                              }
{*************************************************************************}
begin
        pi := 3.141592653589;
        textbackground(blue);
        clrscr;
        clearwindow(1);
        windowbox(1,1,1,79,25,red,' SITE DATA ',yellow,singlex);
        irow:=5;icol:=5;gotoxy(icol,irow);
        textcolor(white);write('Trend of excavation                    ');
        textcolor(yellow);readln(alphae);
        inc(irow);gotoxy(icol,irow);
        textcolor(white);write('Plunge of excavation                   ');
        textcolor(yellow);readln(betae);
        inc(irow);gotoxy(icol,irow);
        textcolor(white);write('Length of excavation                   ');
        textcolor(yellow);readln(Le);
```

```
inc(irow);gotoxy(icol,irow);
textcolor(white);write('Cross sectional area of excavation          ');
textcolor(yellow);readln(Ax);
inc(irow);inc(irow); gotoxy(icol,irow);
textcolor(white);write('Trend of major principal stress             ');
textcolor(yellow);readln(alphas);
inc(irow);gotoxy(icol,irow);
textcolor(white);write('Plunge of major principal stress            ');
textcolor(yellow);readln(betas);
inc(irow);inc(irow);gotoxy(icol,irow);
textcolor(white);write('Number of discontinuity sets (incl. random set)  ');
textcolor(yellow);readln(NSets);
inc(irow);gotoxy(icol,irow);
textcolor(white);write('Discontinuity orient. data fileneme (no ext)     ');
textcolor(yellow);readln(InFileName);
inc(irow);gotoxy(icol,irow);
textcolor(white);write('Friction angle of discontinuities           ');
textcolor(yellow);readln(Phid);
inc(irow);inc(irow);
textcolor(lightgreen);
gotoxy(icol,irow);write('CR to continue');
hidecursor;
readln;
Phir:=Phid*pi/180;
BetaCrit := pi/4 + (Phir/2.0);          {1.3.1 Determine the critical angle}
exponent := (0.175 * Phid) - 0.250;     {1.3.2 Determine the exponent for orientation
                                        weighting equation}
alphae:=alphae*pi/180;
betae :=betae*pi/180;
alphas:=alphas*pi/180;
betas :=betas*pi/180;
{*****************************************************************
                              SETS
*****************************************************************}
N := 0;
RandomNs := 0;
for k:=1 to NSets-1 do
begin
        clrscr;
        textbackground(blue);
        clearwindow(1);
        str(k,ver);
        windowbox(1,1,1,79,25,red,' SET DATA ',yellow,singlex);
        irow:=5;icol:=5;gotoxy(icol,irow);
        textcolor(white); write('FOR SET NUMBER   ');
        textcolor(yellow);writeln(VER);
        inc(irow);inc(irow);gotoxy(icol,irow);
        textcolor(white);write('Trend of mean normal                ');
        textcolor(yellow);readln(alpha[k]);
        inc(irow);inc(irow);gotoxy(icol,irow);
        textcolor(white);write('Plunge of mean normal               ');
        textcolor(yellow);readln(beta[k]);
```

```
            inc(irow);inc(irow);gotoxy(icol,irow);
            textcolor(white);write('Mean discontinuity spacing              ');
            textcolor(yellow);readln(S[k]);
            inc(irow);inc(irow);
            textcolor(lightgreen);
            gotoxy(icol,irow);write('CR to continue');
            hidecursor;
            readln;
            alpha[k]:=alpha[k]*pi/180;
            beta[k]:=beta[k]*pi/180;
                  {**********STAGE 6*****************}
            {Determine angle between the mean normal to a set and the excavation}
            CalcAngle(alphae,betae,alpha[k],beta[k],ThetaER);
                  {***********STAGE 7****************}
            {Estimate the number of discontinuities from the set that will intersect
            the excavation}
            Ns[k] := Le * cos(ThetaER)/S[k];
                  {************STAGE 8****************}
            {Estimate the total number of discontinuities that will intersect the
            excavation - This total does NOT include the random component}
            N := N + Ns[k];
end;
{Determine how many discontinuities are in the random component}
str(NSets,ver);
InFile:=InFileName+'.'+ver;
assign(f1,InFile);
reset(f1);
repeat
      readln(f1,Li,alphan,betan,semi,scanumber);
      randomNs := randomNs + 1;
until eof(f1);
close(f1);
{*****************************************************************
                        DISCONTINUITIES
*****************************************************************}
for k := 1 to NSets do DSet[k]:=0;
i := 0;
Wall := 0;
Wactive := 0;
Ntotal := 0;
Nactive := 0;
for k:=1 to NSets do
begin
      Nset := 0;
      Wset := 0;
      str(k,ver);
      InFile:=InFileName+'.'+ver;
      assign(f1,InFile);
      reset(f1);
      repeat
            Dset[k] := Dset[k] + 1;
            i := i + 1; {Keep a track of number of discontinuities sampled}
```

```
                readln(f1,Li,alphan,betan,semi,scanumber); {Read data on individual
                                                            discontinuity}
                alphan:= alphan*pi/180;
                betan := betan *pi/180;
                {*******************STAGE 9*******************}
                {Determine angle between discontinuity and excavation}
                CalcAngle(alphan,betan,alphae,betae,ThetaEN);
                {*******************STAGE 10*******************}
                {Estimate number of discontinuities to intersect excavation}
                Ne[i]:= (Le * cos(ThetaEN)/S[k]);
                {*******************STAGE 11*******************}
                {Find total number of discontinuities to intersect the excavation}
                Ntotal := Ntotal + Ne[i];
                Nset   := Nset + Ne[i]; {Determine number of discontinuities in set}
                {*******************STAGE 13*******************}
                {Determine the angle beween the discontinuity and the stress}
                CalcAngle(alphas,betas,alphan,betan,BetaW);
                {*******************STAGE 14*******************}
                {Determine the orientation weighting if BetaW = PhiW}
                psi:= Phir - BetaCrit;
                Temp1:= cos(2 * psi);
                WPhi:=pwr(Temp1,exponent);
                {*******************STAGE 15*******************}
                {Determine the orientation weighting for the discontinuity}
                psi := betaw - BetaCrit;
                If psi <= -1.0 * pi/4
                then Worient[i]:=0
                else
                begin
                        Temp1 := cos(2 * psi);
                        Worient[i]:=pwr(Temp1,exponent);
                end;
                {*******************STAGE 16*******************}
                {Determine the sum of the orientation weightings for the set}
                Wset := Wset + Worient[i] * Ne[i];

                {Determine sum of orientation weightings for all discontinuities}
                Wall:= Wall + Worient[i] * Ne[i];

                {Determine sum of orientation weightings for active discontinuities}
                if Worient[i] >= WPhi then   {Determine how many discontinuities are
                begin                         active}
                        Wactive := Wactive + Worient[i] * Ne[i];
                        Nactive := Nactive + Ne[i]
                end;
        until eof(f1);
        {*******************STAGE 18*******************}
        {Determine the mean orientation weighting for the set}
        MeanWset[k] := Wset / Nset;
end;
Dtotal := i;  {Dtotal is the total number of discontinuities sampled}
{*******************STAGE 17*******************}
```

```
{Determine the mean orientation weightings for all discontinuities}
MeanWall := Wall / Ntotal;

{Determine the mean orientation weightings for active discontinuities}
MeanWactive := Wactive / Nactive;
{*********************STAGE 12*********************}
{Determine weighted number of discontinuities to intersect excavation}
dr := RandomNs/(Dtotal-RandomNs);
RandomE := dr * N;
N  := N + RandomE;
for i:= 1 to Dtotal do Neprime[i] := Ne[i] * N/Ntotal;
{*********************STAGE 16*********************}
{Plot histogram}
dx := 0.05;
xmin := 0;
xmax := 1;
histo(xmin,xmax,dx);
readln;
closegraph;
{*****************************************************************}
{Determine value for,RMR(orient), based on mean weighting}
RMRorient := 11.75 * cos(pi * MeanWAll) + 8.25;
{*****************************************************************}
{DETERMINE SPACING WEIGHTING, RMR(space)}
s1:=0;
{Determine the maximum discontinuity spacings}
for k := 1 to NSets do if (S[k] > s1) then s1:=S[k];
lambda := N/Le;                          {Discontinuity mean frequency}
Jv := 6/(pi * lambda * lambda * lambda);  {Mean block volume}
{Determine RMR value for spacing}
Temp1 := Jv/(Ax*s1);
if Temp1 >= 1
then RMRspace := 20                      {limit RMR(space) to 20}
else RMRspace := 20 * pwr(temp1,0.36);
{*****************************************************************}
{OUTPUT ROUTINE}
restorecrtmode;
textbackground(blue);
clearwindow(1);
windowbox(1,1,1,79,25,red,' SUMMARY 1',yellow,singlex);
irow:=5;icol:=5;gotoxy(icol,irow);
textcolor(white); write('Mean Orientation Weighting (all discs.)                ');
textcolor(yellow);writeln(MeanWall:5:5);
inc(irow);gotoxy(icol,irow);
textcolor(white); write('Mean Orientation Weighting (active discs.)             ');
textcolor(yellow);writeln(MeanWactive:5:5);
inc(irow);gotoxy(icol,irow);
textcolor(white) ;write('Orientation weighting at friction angle                ');
textcolor(yellow);writeln(WPhi:5:3);
inc(irow);gotoxy(icol,irow);
textcolor(white) ;write('RMR(orient)                                            ');
textcolor(yellow);writeln(RMRorient:5:3);
```

```
inc(irow);gotoxy(icol,irow);
inc(irow);gotoxy(icol,irow);
textcolor(white);write('Mean block volume                                    );
textcolor(yellow);writeln(Jv:5:3);
inc(irow);gotoxy(icol,irow);
textcolor(white) ;write('RMR(space)                                          ');
textcolor(yellow);writeln(RMRspace:5:3);
inc(irow);gotoxy(icol,irow);
inc(irow);gotoxy(icol,irow);
textcolor(white);write('Total number of discontinuities sampled by scanline  ');
textcolor(yellow);writeln(Dtotal);
inc(irow);gotoxy(icol,irow);
textcolor(white);write('Number of discontinuities to intersect excavation    ');
textcolor(yellow);writeln(N:5:1);
inc(irow);inc(irow);gotoxy(icol,irow);
textcolor(lightgreen);
gotoxy(icol,irow);write('CR to continue');
hidecursor;
readln;
{*************************************************************}
textbackground(blue);
clearwindow(1);
windowbox(1,1,1,79,25,red,' SUMMARY 2 ',yellow,singlex);
irow:=2;icol:=5;gotoxy(icol,irow);
for k:=1 to NSets do
begin
        inc(irow);gotoxy(icol,irow);
        inc(irow);gotoxy(icol,irow);
        textcolor(white);writeln('For set ',k);
        inc(irow);gotoxy(icol,irow);
        textcolor(white);write('Number of discontinuities sampled            ');
        textcolor(yellow);writeln(DSet[k]);
        if k <> NSets
        then
        begin
                inc(irow);gotoxy(icol,irow);
                textcolor(white);write('Number of discontinuities to intersect
                excavation      ');
                textcolor(yellow);
                writeln(Ns[k]:5:5)
        end
        else
        begin
                inc(irow);gotoxy(icol,irow);
                textcolor(white);write('Total number to intersect excavation ');
                textcolor(yellow);
                writeln(RandomE:5:5);
        end;
        inc(irow);gotoxy(icol,irow);
        textcolor(white);write('Mean weighting for set                       ');
        textcolor(yellow);writeln(MeanWSet[k]:5:5);
end;
```

```
        inc(irow);inc(irow);gotoxy(icol,irow);
        textcolor(lightgreen);
        gotoxy(icol,irow);write('CR to continue');
        hidecursor;
        readln;
end.
```

Appendix B. Membrane Removal and Replacement Procedure.

Appendix B. Membrane Removal and Replacement Procedure.

One of the advantages of a Hoek triaxial cell over a 'high pressure' cell is that there is no need to remove the rubber membrane from the cell unless it is damaged. If removal is required, the mass of the cell (290kg without the pistons) can make membrane removal and the subsequent de-airing of the cell, difficult and time consuming. The manufacturer's handbook suggests a method for carrying out these procedures. The suggested procedure is unsuitable for a cell of this size. An improved method for replacing the membranes was therefore developed and is described as follows.

(1) Both top and bottom pistons are removed from the cell.

(2) The upper cell cap is removed and, after a container is placed below one of the hydraulic couplings, the coupling is removed. Half of the total volume of hydraulic fluid in the annulus then drains from the cell as both of the outlets are located at mid-height. An improved cell design, that would allow all fluid to drain from the cell, would have one outlet located at the base of one side and the other outlet located diametrically opposite at the top. The lower outlet would then be used to fully drain the cell.

(3) Two wooden wedges are placed opposite each other to move the upper membrane seal off the cell body. Sufficient space is produced to allow both hands to grip the membrane and slowly lift it out of the cell. As the membrane is lifted the remaining fluid in the annulus drains. The membrane can be totally removed when all the fluid has drained from the cell.

(4) The sealing surface of a new membrane is lubricated and the new membrane is gently fitted into the cell.

(5) The wooden wedge are again used to move the upper membrane seal a sufficient distance

off the seal surface to allow air to escape. Teflon tape is then wound onto the thread of the hydraulic coupling which is screwed back into the cell.

(6) A hand pump is used to pump clean hydraulic fluid into the cell until fluid leaks from the air bleed hole created by the wedges. The wedges are now removed and the top cap placed back on the cell. The cell is now ready for use.

By carrying out procedures (5) and (6), most of the air could be removed from the cell. A small amount of air did remain trapped in the upper seal of the membrane. This air could be seen through the membrane and by determining the cross sectional area of the region within which the air was trapped and by measuring the depth of the air bubble, it was possible to estimate that about 1ml. of air remained in the cell. This volume of air is absorbed into solution on application of pressure of the order of 200 kPa.

Appendix C.
Intact Material and Discontinuities - Test Results

Appendix C. Intact Material and Discontinuities - Test Results.

C.1. Uniaxial Compression Tests.

A total of 41 cylindrical specimens (107mm x 42mm diameter) composed of gypsum cement and 31 composed of the gypsum cement/sand mixture were prepared. The ISRM guidelines [75] suggest that the minimum diameter of test specimen should be not less than 54mm. A diameter of 42mm was chosen, however, so that the moulds used to form the uniaxial test specimens could also be used to form specimens for the triaxial cell used in the next series of tests. A specimen diameter to length ratio (d:l) of 1:2 is traditionally used for concrete specimen testing although a ratio of 1:3 has been used by many researchers for rock mechanics research. A specimen having a greater ratio may be susceptible to failure through flexure brought about by eccentric loading. A value of 2:5 was chosen according to the ISRM guidelines which indicated that a ratio within the range $2:5 \leq d:l \leq 1:3$ be used.

A lathe, fitted with a high speed grinding wheel positioned perpendicular to the major axis of the specimen, was used to prepare the ends of each specimen. This process ensured uniformity in the length of the specimens with each length being reduced to 105mm. More importantly, this process ensured that the ends of each specimens were smooth and perpendicular to the major axis of the specimen and within the tolerances recommended in the ISRM guidelines.

Each test specimen was placed centrally upon a steel seat of equal diameter on the lower compression platen of the Seidner load frame discussed in Section 5.2. A spherically seated steel platen, also having the same diameter as the specimen, was placed on the upper surface

of the specimen to ensure that the load was applied parallel to the major axis of the specimen. The specimens were tested according to the ISRM guidelines [75] at a constant loading rate of 0.9MPa/s to reduce the influence of loading rate on specimen strength (Bieniawski [16], Sangha and Dhir [131]). The loading rate was monitored by reference to the load rate indicator.

C.1.1. Results of UCS Tests.

The results of the uniaxial compressive strength tests for the gypsum cement specimens are listed in Table C.1. A majority of these specimens (76%) failed in shear producing the familiar 'cup and cone' failure surface. The orientation of the shear surface, β_w, ranged from 60°- 67° with an average of 64.4°. Assuming that failure occurred along the plane at which the shear stress ratio (τ/σ_n) was a maximum, then the angle of internal friction of the material, ϕ_i, given by $\phi_i = 2(\beta_w - 45^\circ)$, fell between 30° and 44°. Flexural failure appeared to cause failure at lower strengths in the remaining (24%) gypsum cement specimens. This result is highlighted in the frequency distribution plot shown in Figure C.1(a) in which the two regions can clearly be distinguished. From this plot the mean compressive strength of those specimens that failed in shear was 37.2MPa with a standard deviation about this mean of 1.4 MPa.

The results of the uniaxial compressive strength tests for the gypsum cement specimens/sand specimens are listed in Table C.2. The majority of these specimens, (75%), failed in shear along a single predominant plane such that β_w ranged from 48° to 67°. This result suggested that ϕ_i fell between 6° and 44°. The frequency distribution plot shown in Figure C.1(b) highlights the wide variation in the compressive strength of the specimens. Two distinct compressive strengths for the material are indicated by this plot. The average compressive strength of the stronger specimens was 23.3MPa with a standard deviation about this mean of 2.4MPa. The lower strength region of the plot should have contained 25% of the total number of specimen, that is, those specimens observed to have failed through flexure. Instead, it contained 52% of the specimens.

Table C.1. Uniaxial compressive strength test results for intact gypsum cement specimens.

Test No.	UCS (MPa)	Test No.	UCS (MPa)	Test No.	UCS (MPa)
1	37.5	16	37.0	31	39.9
2	38.8	17	37.4	32	26.3
3	37.4	18	37.0	33	28.3
4	36.7	19	40.0	34	35.3
5	37.9	20	37.1	35	28.3
6	29.5	21	37.6	36	35.9
7	39.2	22	32.3	37	29.9
8	38.8	23	37.9	38	38.4
9	38.8	24	37.9	39	38.4
10	28.9	25	38.1	40	37.0
11	39.0	26	36.3	41	39.7
12	38.5	27	34.5	42	30.1
13	36.1	28	36.6	43	30.5
14	35.4	29	39.7	44	27.1
15	38.4	30	38.1		

Table C.2. Uniaxial compressive strength test results for intact gypsum cement/sand specimens.

Test No.	UCS (MPa)	Test No.	UCS (MPa)	Test No.	UCS (MPa)
1	22.3	12	19.5	23	26.1
2	7.4	13	7.1	24	25.7
3	22.8	14	7.4	25	7.9
4	6.5	15	23.0	26	5.0
5	28.4	16	26.9	27	23.8
6	4.7	17	7.9	28	23.9
7	6.1	18	5.2	29	5.2
8	23.7	19	22.1	30	25.1
9	7.9	20	8.4	31	6.2
10	25.8	21	20.7		
11	6.5	22	8.2		

It is difficult to explain why 27% (52% - 25%) of the specimens failed in shear at the lower strength but some possible reasons may be:

(1) incomplete mixing of the dry materials which produced zones of almost pure sand within competent zones and

(2) incomplete combination of the dry materials with the water which produced zones of improperly cured material.

As there were no obvious heterogeneous regions about the failure surfaces the items listed above appeared not to have significantly influenced the shear strengths. Nevertheless, efforts were made to minimise both of these occurrences in later batches by assuring proper mixing at all stages. Other possible reasons for the lower strengths are:

(3) the presence of excessive air bubbles. The possibility of this result occurring was reduced in later batches by improving the technique used to fill and vibrate the moulds containing the wet mixture and

(4) a gradation of material density throughout the specimen. This result was considered to be a distinct possibility as the wet mixture tended to sit for a sufficiently long time to allow the heavier sand particles to settle out before the mixture could set.

In order to determine if this latter behaviour occurred, a cylindrical specimen was sawn in four equi-distant places to create five discs of material. The volume of each of these discs was accurately determined by the mercury displacement method and the densities of each disc calculated. The results of this study are plotted in Figure C.2. It is apparent from this plot that the specimen did become denser with depth with a 7% increase in density between the lower (0-17mm) and the upper disc. The largest increase occurred at a height of approximately 21mm. This gradation of material would have formed an anisotropy perpendicular to the major principal axis of the specimen. Studies into the affect of anisotropy on the behaviour of material (Jaeger [80], McLamore and Gray [98]) have shown that, in cases in which $\beta_w = 0^\circ$, it is unlikely that the reduction in strength would have been in the order experienced.

The reduction in strength of many of the gypsum cement/sand specimens might have been due, instead, to the influence of density on the shear strength of gypsum cement based materials. Because of the gradation, more than half of the total volume of a graded specimen would have had a lower density than the mean density of the specimen and, hence, a lower strength. In order to minimise gradation in later batches, care was taken to ensure that each batch was completely mixed in the wet and the dry state and that the viscosity of the mix was sufficiently high before pouring the wet mix.

C.2. Determination of Young's Modulus.

In order to determine Young's modulus and Poisson's ratio for each material in uniaxial compression, 3 cylindrical specimens (300mm x 150mm diameter) were fitted with 4 Kyowa (model KFC-30) 30mm strain gauges, 2 to monitor axial and 2 to monitor circumferential strain. The axial deformation and load were monitored by a data logger from an LVDT and a load cell respectively. The specimens were initially loaded and unloaded several times in uniaxial compression until consistent axial load versus axial deformation results were obtained. Each specimen was then slowly loaded to failure.

Figure C.3 shows a typical axial stress versus axial strain and axial stress versus circumferential strain plot for a gypsum cement specimen. The curve shows a typical result obtained when a testing frame is used that is soft relative to the specimen. The tangent elastic modulus, E, was measured as the slope of the linear section of the axial stress versus axial strain curve at approximately 50% of the peak strength. The magnitude of E averaged at 5.6GPa for the gypsum cement specimens yet tended to vary with the strength of the specimen. For the cement/sand specimens the average value of E was 4.8GPa. The average value of Poisson's ratio, ν, for both materials was 0.26.

C.3. Triaxial Tests.

A 42mm diameter Hoek cell was used for the triaxial tests on the intact material. Cylindrical specimens (90mm x 42mm in diameter) suitable for triaxial testing were formed in a similar manner to those specimens used for the uniaxial compressive strength tests. The 90mm length was the maximum suitable for the Hoek cell. This length resulted in a d:l ratio within the range of $1{:}2 \leq d{:}l \leq 1{:}3$ recommended by the ISRM [74] for triaxial testing. Because of the large percentage of low strength cement/sand specimens encountered during the uniaxial compressive strength tests, a greater number of these specimens than the gypsum cement specimens were tested to allow for any variation in strength. The ends of the specimens were prepared following the same procedures as those for specimens used for the UCS tests.

The Hoek cell was cleaned and inspected before a specimen and a pair of spherically seated piston, were inserted into the cell. In a uniaxial compressive strength test the top half of the spherical seat is able to move perpendicular to the major axis of the specimen in order to align the major axis with the compression platens. Likewise, in a triaxial test using a Hoek cell, one spherical seat is sufficient to ensure that alignment is achieved up to the point when the axial deformation of the specimen occurs as a result of shear deformation occurring along discontinuities. After this deformation occurs, two spherically seated pistons are required to ensure that full contact is maintained over the sliding surfaces (Brady and Brown [27]).

The triaxial cell was placed into the load frame on a support designed to ensure that the specimen was placed at the correct height with respect to the rubber membrane. A calibrated LVDT connected into the data logger and XY plotter was mounted between the upper and lower load frame platens to monitor the axial deformation. Confining pressures ranging from 200kPa to 1250kPa were applied and maintained by the linear displacement pump, described in Section 5.6. The axial load on the specimen was increased in accordance with the ISRM guidelines [74]. At the completion of each test the cell was disassembled and the specimen removed for inspection.

C.3.1. Results of Triaxial Tests.

The results of the tests are tabulated in Tables C.3 and C.4. The axial stress versus axial strain behaviour of the material tended to be linear until yielding and those tests that produced non-linear results still had linear regions up to approximately 50% of the peak strength. The peak and residual stresses at yield can be described for both materials by the equations:

$$\sigma_{1(peak)} = a_{(p)} + b_{(p)}\sigma_3 \qquad (C.1)$$

and

$$\sigma_{1(res)} = a_{(r)} + b_{(r)}\sigma_3 \qquad (C.2)$$

The coefficients $a_{(p)}$, $b_{(p)}$, $a_{(r)}$ and $b_{(r)}$ and the coefficient of determination, r^2, are listed in Table C.5.

The shear stress on the plane of failure can be described in terms of the normal stress for both materials by a linear Mohr-Coulomb relationship as shown in Figures C.4(a)-(b). For the gypsum cement, the internal friction angle, ϕ_i, was 37° and the cohesion, c_i, was 9MPa. For the gypsum cement/sand material ϕ_i was 49° and c_i was 4.2MPa.

Figure C.5 shows the relationship between the tangent elastic modulus, E, and the confining pressure σ_3 for the two materials. It is difficult to establish firm conclusions from the results because of the large amount of scatter but they appear to show that the elastic modulus and in particular that of the gypsum cement material, is not significantly affected by changes in the confining pressure for the range used. Indraratna [70] concluded that this result was preferred for geomechanics modelling materials where variation in the elastic modulus with the confining pressure could cause problems with satisfying strain similitude requirements between natural rock and the modelling material.

For the cement/sand material the Hoek-Brown rock material constant m_i value (Figure C.6) was 17.6 which was within the expected range for natural materials including sandstones. For the gypsum cement, m_i was 2.4, a value lower than would have been expected for a natural sulphate based material. This result might have been due in part to the difficulties involved in trying to synthesise a natural material under laboratory conditions, but the result was more likely due to the large scatter in the test data.

C.4. Tensile Strength.

The tensile strength of the intact material was determined by conducting a Brazil test on 6 specimens (300mm x 150mm diameter) of the gypsum cement and the cement/sand material in accordance with Australian Standard 1012.10.

The average tensile strength of the gypsum cement was 8.6MPa and, for the cement/sand material, 5.9MPa. The result for the cement/sand material is consistent with that expected of a sandstone. The result for the gypsum cement was 200% greater than that which would be

expected for a similar natural material. While this result suggests that the cement/sand material is more suitable than the gypsum cement for modelling natural rock, it is important to consider the results in terms of the ability of the two materials to satisfy similitude requirements. One of these requirements is that similitude exists between the modelling material and the natural material with respect to the ratio σ_c/σ_t. In natural rock, this ratio generally falls in the range 5-45. Based on the test results, this ratio for the gypsum cement is 4.3 and for the cement/sand material the ratio is 3.9. These ratios are slightly less than the minimum ratio for natural material. The results were close enough to be considered acceptable for the purposes of this study as it was not expected that tensile failure would be the predominant mode of failure in the triaxial tests on the discontinuous specimens.

Table C.3. Triaxial test results for intact gypsum cement specimens (n/a: not available).

Test No.	Principal Stresses (MPa)			E (GPa)	Test No.	Principal Stresses (MPa)			E (GPa)
	σ_3	$\sigma_{1(peak)}$	$\sigma_{1(res)}$			σ_3	$\sigma_{1(peak)}$	$\sigma_{1(res)}$	
1	0.2	32.8	23.1	4.85	15	0.8	31.8	23.5	5.35
2	0.2	37.8	23.7	5.15	16	0.8	36.4	25.0	5.22
3	0.2	32.0	21.6	5.25	17	0.8	37.7	29.6	n/a
4	0.2	29.7	19.2	n/a	18	0.8	35.6	24.8	n/a
5	0.4	46.6	30.0	4.96	19	1.0	43.4	29.9	6.30
6	0.4	38.8	25.1	5.10	20	1.0	39.3	28.2	5.22
7	0.4	43.2	27.6	5.54	21	1.0	43.0	28.7	5.48
8	0.4	37.2	24.3	n/a	22	1.0	35.4	25.0	n/a
9	0.6	43.0	28.6	5.29	23	1.25	38.6	32.0	5.82
10	0.6	35.7	24.0	5.37	24	1.25	35.0	33.3	5.59
11	0.6	31.0	21.4	5.49	25	1.25	46.1	35.0	5.71
12	0.6	39.6	28.5	n/a	26	1.25	37.0	24.5	n/a
13	0.6	36.5	25.0	n/a	27	1.25	42.4	30.5	n/a
14	0.8	47.3	30.1	n/a					

Table C.4. Triaxial test results for intact gypsum cement/sand specimens (n/a: not available).

Test No.	Principal Stresses (MPa)			E (GPa)	Test No.	Principal Stresses (MPa)			E (GPa)
	σ_3	$\sigma_{1(peak)}$	$\sigma_{1(res)}$			σ_3	$\sigma_{1(peak)}$	$\sigma_{1(res)}$	
1	0.2	22.9	13.5	3.57	20	0.6	25.2	n/a	n/a
2	0.2	22.3	n/a	n/a	21	0.8	26.7	18.8	4.76
3	0.2	22.3	n/a	n/a	22	0.8	29.0	18.7	3.75
4	0.2	24.2	n/a	n/a	23	0.8	30.4	15.5	5.27

Table C.4. (continued) Triaxial test results for intact gypsum cement/sand specimens (n/a: not available).

Test No.	Principal Stresses (MPa)			E (GPa)	Test No.	Principal Stresses (MPa)			E (GPa)
	σ_3	$\sigma_{1(peak)}$	$\sigma_{1(res)}$			σ_3	$\sigma_{1(peak)}$	$\sigma_{1(res)}$	
5	0.3	24.0	n/a	n/a	24	0.8	31.9	18.4	5.08
6	0.3	23.9	n/a	n/a	25	0.8	31.3	n/a	n/a
7	0.3	23.3	n/a	n/a	26	0.9	30.4	n/a	n/a
8	0.4	24.6	16.1	2.86	27	0.9	28.4	n/a	n/a
9	0.4	25.6	n/a	3.87	28	0.9	27.8	n/a	n/a
10	0.4	31.4	n/a	3.57	29	1.0	29.5	19.0	6.05
11	0.4	27.4	n/a	3.99	30	1.0	33.6	23.0	n/a
12	0.4	27.1	n/a	n/a	31	1.0	32.8	21.3	11.1
13	0.4	31.7	n/a	n/a	32	1.0	30.2	n/a	5.55
14	0.6	25.7	13.5	4.90	33	1.0	35.1	n/a	5.07
15	0.6	28.7	16.7	n/a	34	1.25	33.8	21.0	5.32
16	0.6	28.8	14.6	n/a	35	1.25	36.9	23.2	4.44
17	0.6	27.4	n/a	5.67	36	1.25	32.8	19.0	4.70

Table C.5. Coefficients applicable to Equations. C.1 and C.2 (units of $a_{(peak)}$ and $a_{(res)}$ are MPa).

Material	$a_{(peak)}$	$b_{(peak)}$	$r^2_{(peak)}$	$a_{(res)}$	$b_{(res)}$	$r^2_{(res)}$
100%	37.28	4.09	0.09	21.57	7.11	0.44
50/50	23.38	9.81	0.68	11.34	8.27	0.67

C.5. Shear Box Tests.

Discussion of the shear box test results is included in the main body of the text.

Table C.6. Shear box test results for gypsum cement/sand specimens.

Test No.	Shear Displ. u_s	Shear Stress $\tau_{(ult)}$	Norm. Stress σ_n	Shear Stiff. K_s
	(mm)	(kPa)		(GPa/m)
2	1.00	506.3	755.2	0.548
3	2.06	526.4	753.4	0.791
4	1.77	398.8	745.0	0.764
5	2.09	480.4	757.0	0.873
6	1.10	489.7	740.3	0.703

Table C.6. (continued) Shear box test results for gypsum cement/sand specimens.

Test No.	Shear Displ. u_s (mm)	Shear Stress $\tau_{(ult)}$ (kPa)	Norm. Stress σ_n (kPa)	Shear Stiff. K_s (GPa/m)
7	1.57	384.7	548.5	0.600
8	1.11	96.9	148.5	0.293
9	1.00	110.1	143.1	0.347
10	1.14	363.1	534.9	0.719
11	1.36	258.9	344.9	0.446
18	1.00	416.6	540.0	0.869
19	0.60	260.1	337.5	0.584
20	1.04	269.1	343.3	0.377
22	0.87	401.6	541.1	0.550
15	0.87	591.5	735.2	0.862
16	0.39	83.0	141.3	0.670
17	0.75	364.9	535.3	0.758
12	0.54	219.0	337.2	0.597
13	0.50	110.3	140.9	0.503
14	1.15	236.4	341.3	0.349

Table C.7. Shear box test results for gypsum cement specimens.

Test No.	Shear Displ. u_s (mm)	Shear Stress τ_{ult} (kPa)	Norm. Stress σ_n (kPa)	Shear Stiff. K_s (GPa/m)
23	0.58	524.1	732.4	1.188
24	1.31	551.2	743.6	0.616
25	0.69	577.0	731.5	1.391
26	0.47	390.3	630.8	1.317
27	0.90	408.6	636.9	1.238
28	1.11	472.0	638.4	0.725
29	1.00	387.1	540.9	0.772
30	0.49	384.0	534.1	1.146
31	0.61	258.6	534.0	1.077
32	0.56	254.8	442.0	0.146
33	0.62	265.1	439.2	0.498
35	0.62	280.1	436.3	0.877
36	0.86	266.9	339.8	0.574
37	0.95	268.0	340.7	0.794
38	0.94	271.6	339.5	0.829
39	0.83	94.0	240.3	0.616
40	0.65	195.0	239.6	0.581
41	0.47	154.6	238.8	0.552
42	0.42	94.4	141.0	0.348
43	0.75	119.2	141.8	0.616

Table C.7. (continued) Shear box test results for gypsum cement specimens.

Test No.	Shear Displ. u_s (mm)	Shear Stress τ_{ult} (kPa)	Norm. Stress σ_n (kPa)	Shear Stiff. K_s (GPa/m)
44	0.44	110.0	140.8	0.651
45	0.65	337.5	635.6	0.448
46	1.15	651.6	964.7	1.160
47	0.91	740.0	959.0	1.610
48	0.95	704.7	960.5	1.260
51	0.63	152.9	141.4	0.580
52	0.84	195.3	227.1	0.441
53	1.12	217.6	340.5	0.909
54	0.67	384.1	534.9	0.712
55	0.92	550.3	741.9	0.914

Table C.8. Shear box test results for gypsum cement/sand specimens containing infill.

Test No.	Shear Displ. u_s (mm)	Shear Stress $\tau_{(ult)}$ (kPa)	Norm. Stress σ_n (kPa)	Shear Stiff. K_s (GPa/m)
56	1.30	530.7	966.2	1.209
57	1.76	579.2	876.7	0.766
58	1.18	455.0	744.1	0.801
59	2.25	573.0	650.2	1.011
60	1.10	362.0	547.5	0.622
61	1.93	260.0	450.2	0.492
62	1.00	214.5	341.2	0.532
63	0.68	150.8	242.5	0.308
64	0.81	96.1	141.6	0.456
65	1.85	56.3	78.9	0.344
66	0.85	24.0	39.6	0.116

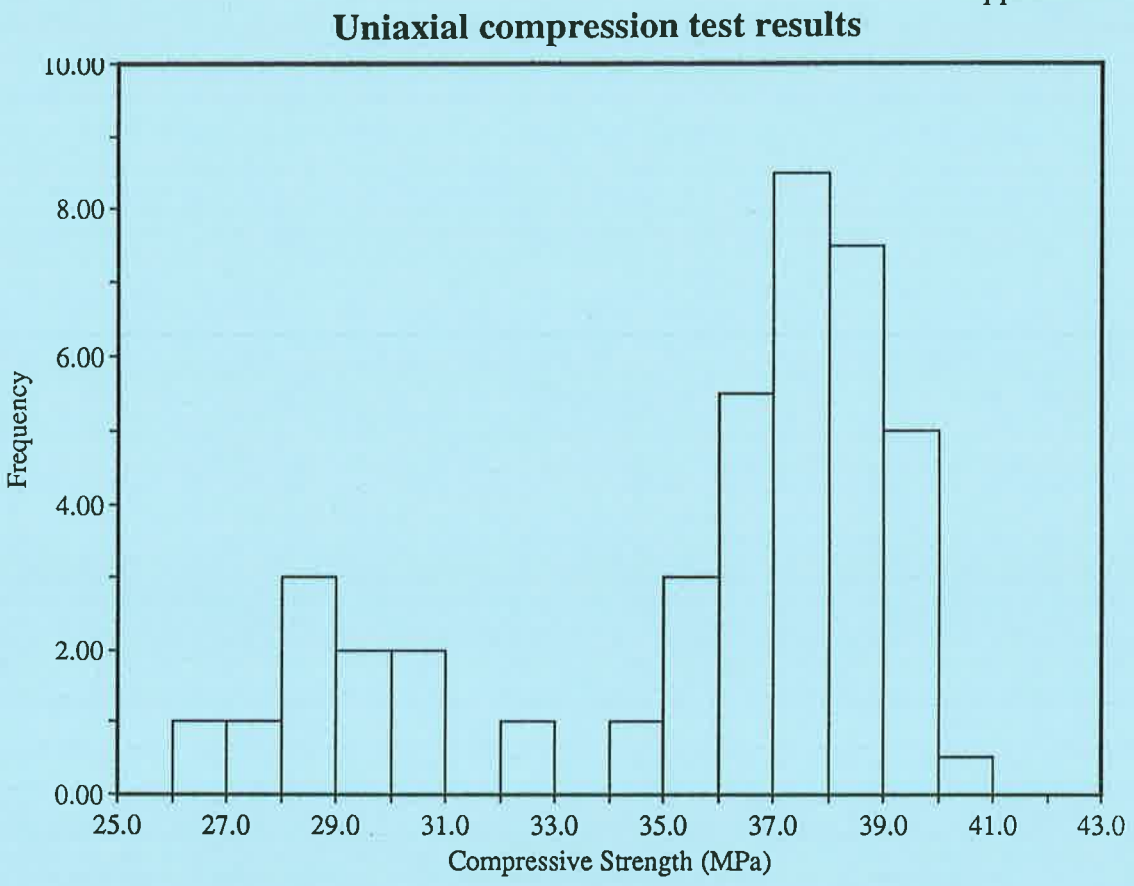

(a)

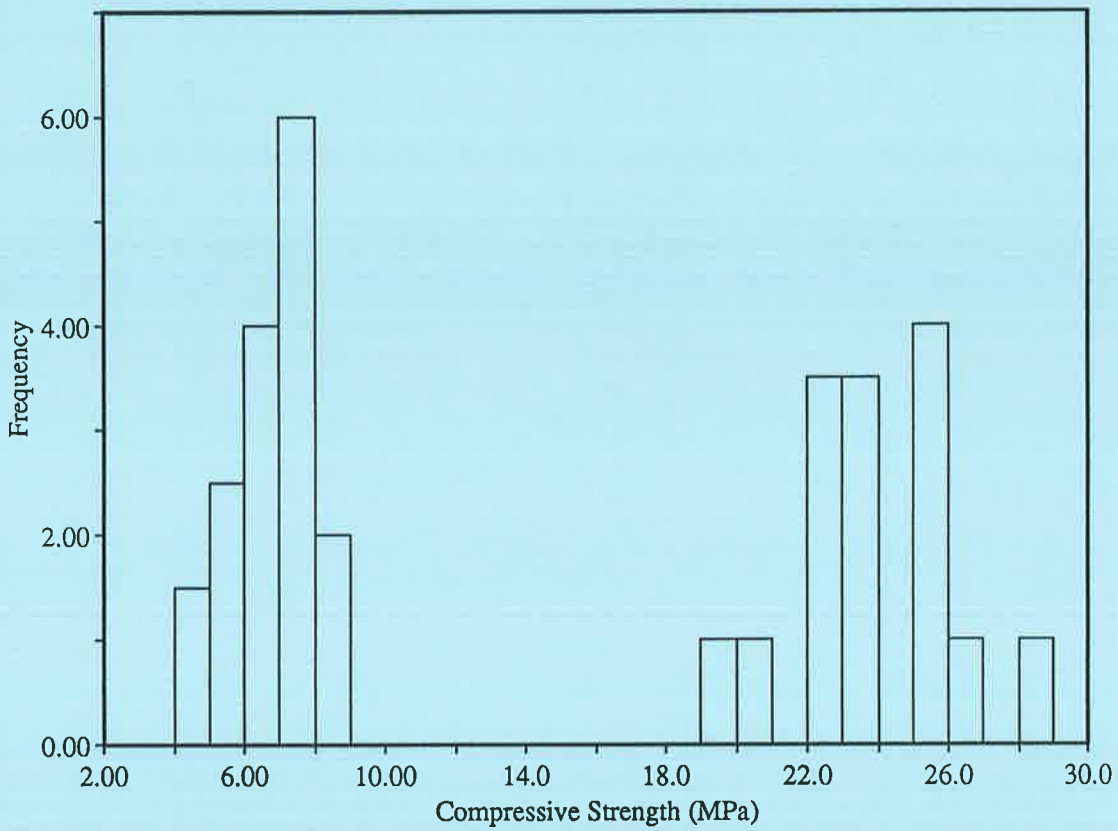

(b)

Figure C.1. Frequency distribution plot obtained from the results of uniaxial compressive strength tests on 42mm diameter specimens of (a) intact gypsum cement and (b) cement/sand material.

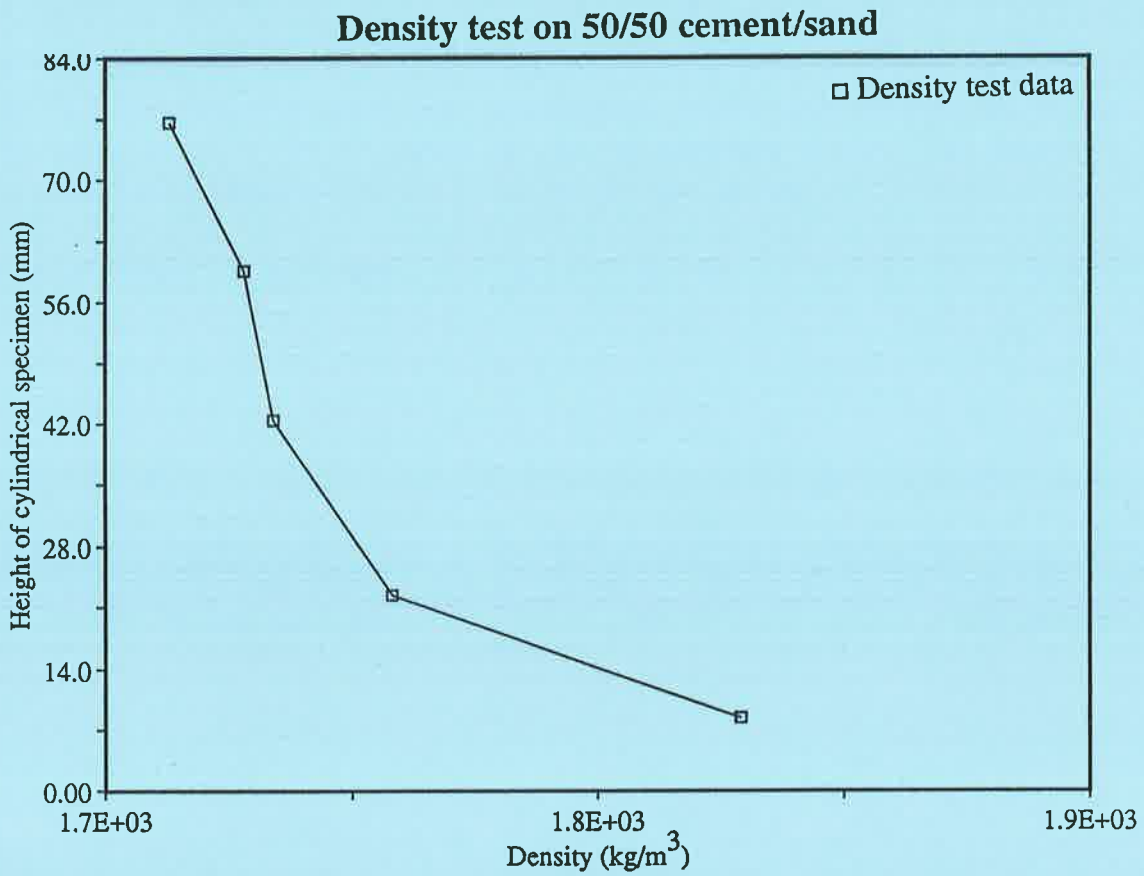

Figure C.2. Variation in density with height for a 42mm diameter specimens of intact 50/50 cement/sand material.

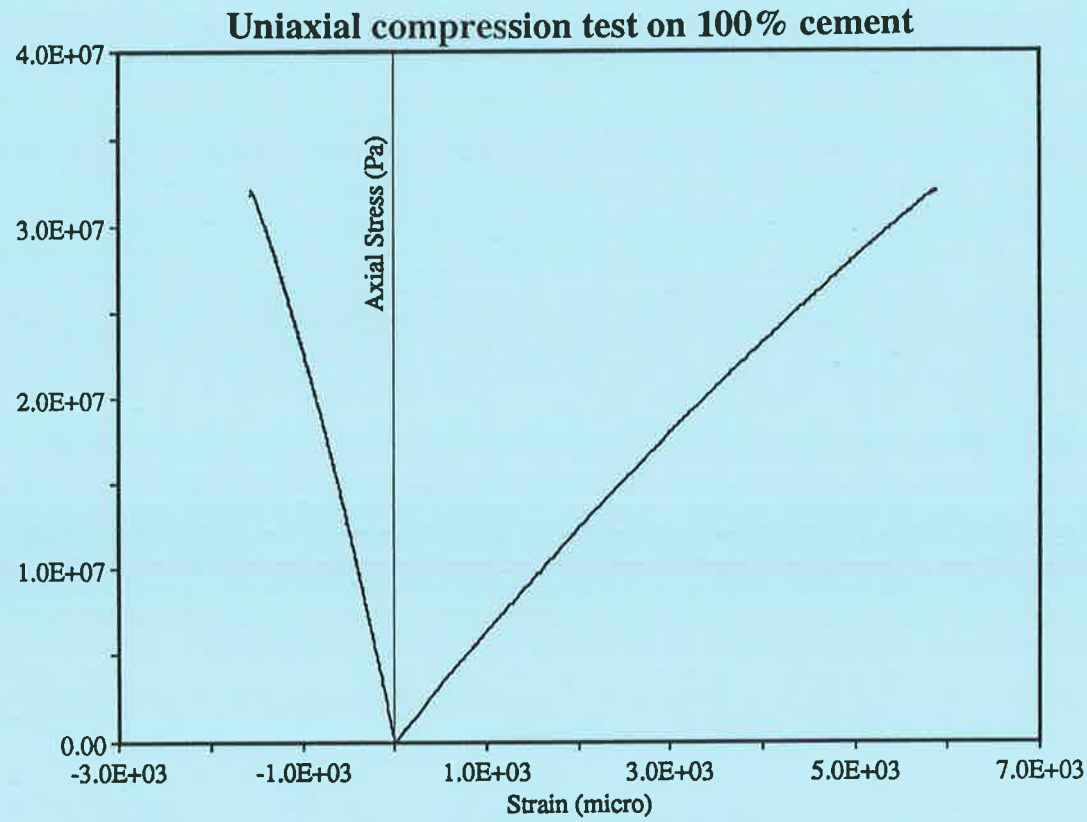

Figure C.3. Circumferential strain versus axial stress and axial strain versus axial stress curves for gypsum cement under uniaxial compression.

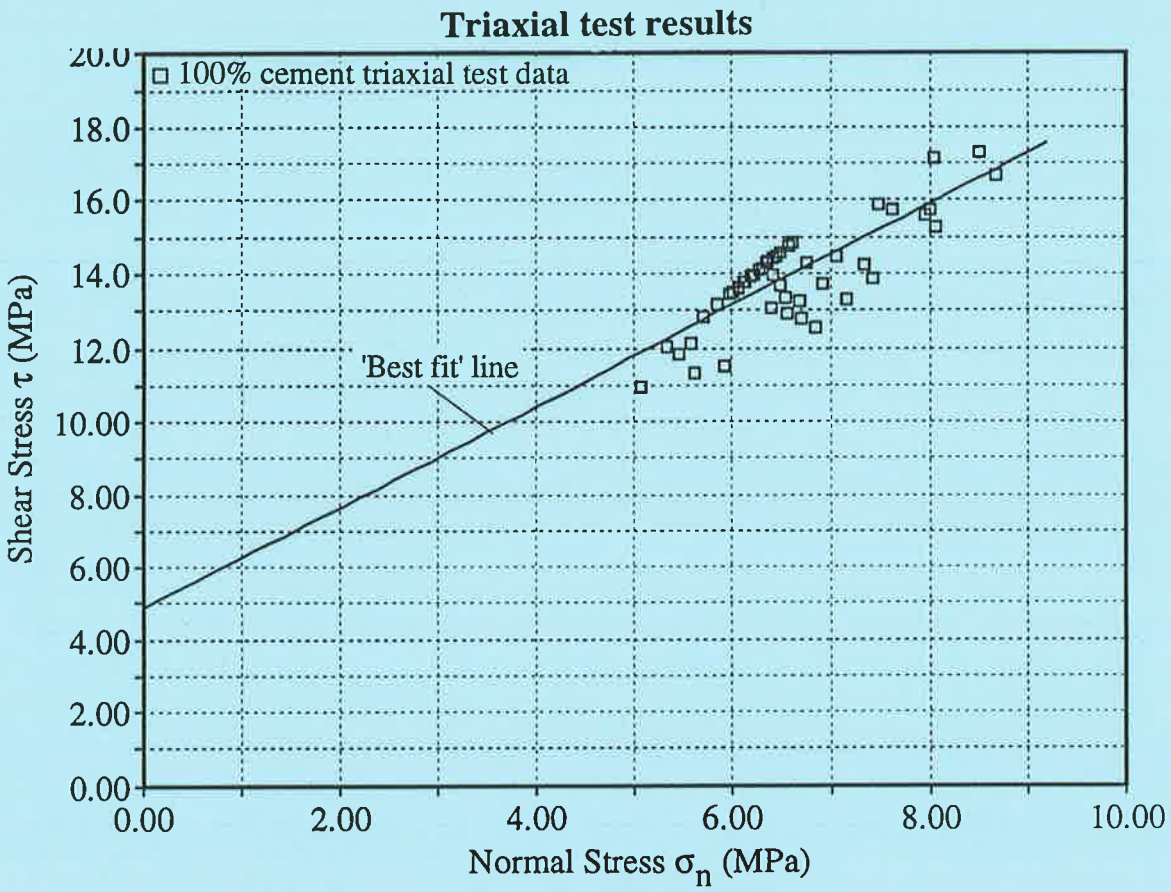

(a)

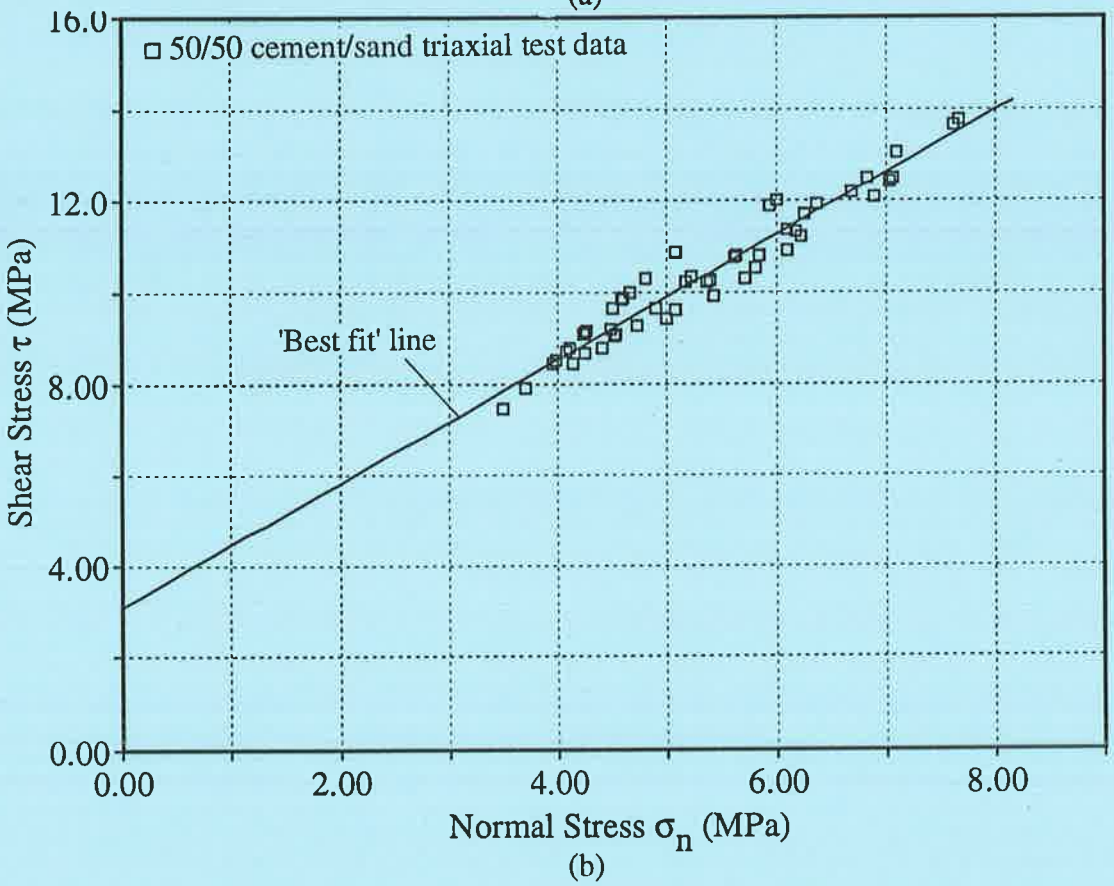

(b)

Figure C.4(a)-(b). Mohr-Coulomb plots for (a) gypsum cement (ϕ_i = 37°, c_i = 9MPa) and (b) cement/sand (ϕ_i = 49°, c_i = 4.2MPa) intact specimens.

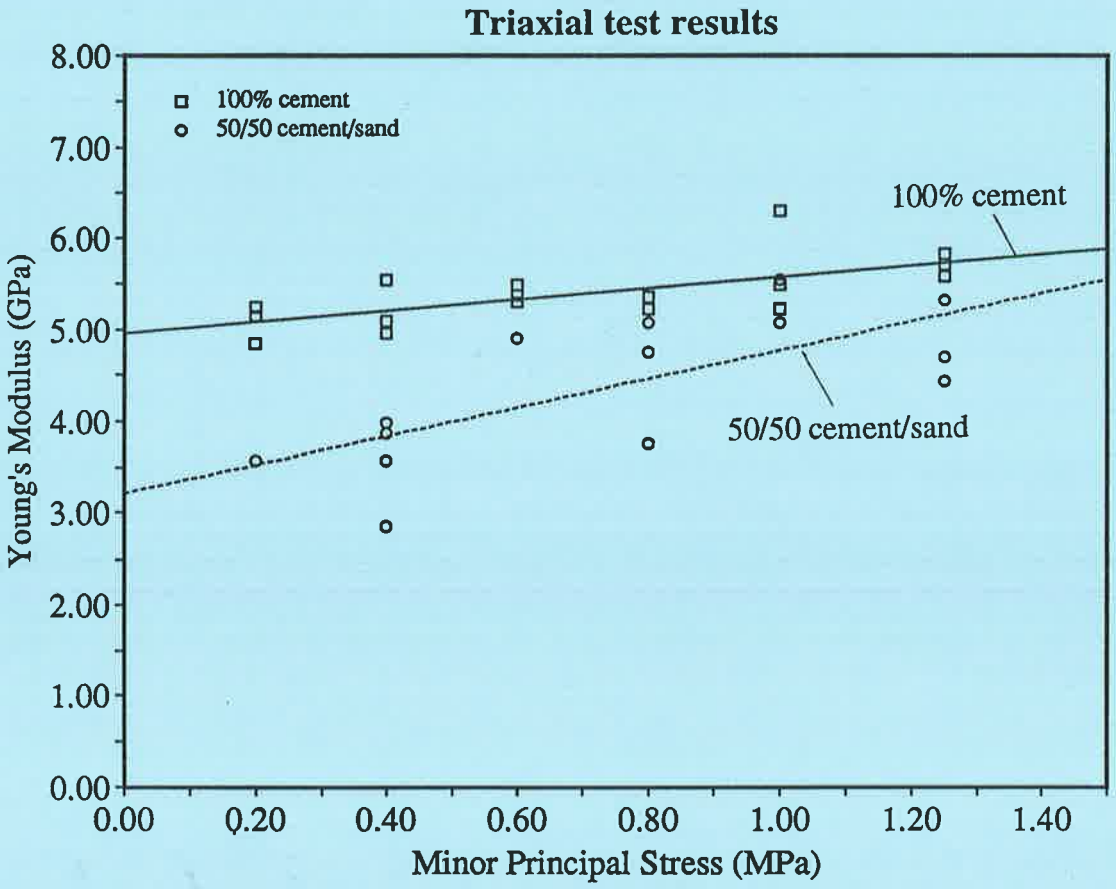

Figure C.5. Variation in Young's modulus with confining pressure for intact specimens.

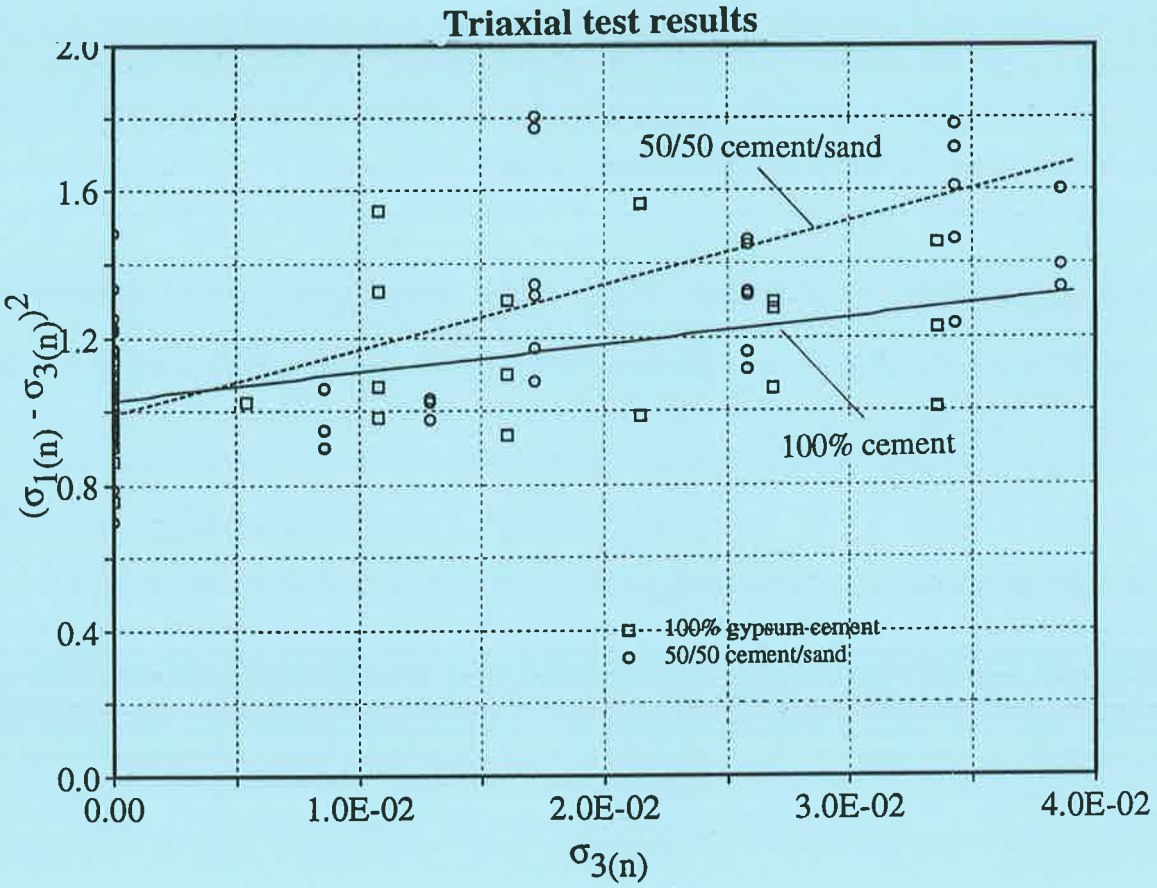

Figure C.6. Hoek-Brown yield curves for gypsum cement (m=33, s=1) and cement /sand (m=17.6, s=1) intact specimens.

Appendix D.
Discontinuous Models - Triaxial Test Results

Appendix D. Discontinuous Models - Triaxial Test Results

This appendix contains the tabulated results from the triaxial tests on the discontinuous specimens. Each section contains the results for a particular geometry and each section is divided up into sub-sections for the various material types.

(Note: n/a refers to "Not Available".)

D.1. Geometry 1.

Table D.1. Triaxial test results for Geometry 1 gypsum cement specimens.

Test No.	Principal Stresses (MPa)			Ax. Def. Ratio (%)		Axial Stiffness (GPa/m)	
	σ_3	$\sigma_{1(slip)}$	$\sigma_{1(peak)}$	$\Delta_{a(slip)}$	$\Delta_{a(peak)}$	K_A	K_B
12	0.23	4.53	n/a	2.85	n/a	0.77	0.43
13	0.25	3.90	5.54	2.01	3.83	0.78	0.44
15	0.26	5.83	9.50	2.75	7.14	0.60	0.96
16	0.57	7.07	10.47	1.77	3.95	0.87	1.46
17	0.58	8.43	10.13	3.37	4.81	0.57	0.99
18	0.57	6.62	10.24	1.79	3.35	0.90	1.14
19	0.90	7.75	11.32	2.23	3.81	1.01	1.17
20	0.86	8.66	12.34	1.83	3.34	1.09	1.43
22	0.88	8.94	12.79	1.74	3.30	1.32	1.60
23	2.00	17.09	n/a	1.60	n/a	1.81	2.80
25	2.48	16.41	22.13	1.72	3.46	1.68	2.62

Table D.2. Triaxial test results for Geometry 1 gypsum cement/sand specimens.

Test No.	Principal Stresses (MPa)			Ax. Def. Ratio (%)		Axial Stiffness (GPa/m)		Vol. Def. Rat. (%)
	σ_3	$\sigma_{1(slip)}$	$\sigma_{1(peak)}$	$\Delta_{a(slip)}$	$\Delta_{a(peak)}$	K_A	K_B	Δ_v
26	0.24	3.34	n/a	0.72	n/a	1.53	0.97	0.16
27	0.47	7.02	9.45	1.97	2.65	1.36	0.96	0.57
28	0.67	8.32	9.56	2.39	2.78	1.42	1.09	0.75
29	0.54	9.05	n/a	2.08	n/a	1.46	0.90	0.48

Table D.2. (continued) Triaxial test results for Geometry 1 gypsum cement/sand specimens.

Test No.	Principal Stresses (MPa)			Ax. Def. Ratio (%)		Axial Stiffness (GPa/m)		Vol. Def. Rat. (%)
	σ_3	$\sigma_{1(slip)}$	$\sigma_{1(peak)}$	$\Delta_{a(slip)}$	$\Delta_{a(peak)}$	K_A	K_B	Δ_v
30	0.34	6.79	n/a	2.11	n/a	1.29	n/a	0.80
31	0.81	11.43	13.40	2.15	3.03	1.71	0.57	0.87
32	0.51	9.00	11.15	0.91	1.66	2.00	1.48	0.13
33	0.16	n/a	n/a	n/a	n/a	0.84	n/a	0.31
77	0.26	5.44	6.70	1.15	1.64	1.53	0.71	0.15
78	0.51	7.41	10.03	0.93	1.56	1.90	1.50	0.19
79	0.75	8.20	12.38	0.95	2.15	1.86	1.35	0.31
80	1.00	11.15	14.67	0.93	1.67	2.39	1.78	0.22
81	0.25	5.22	7.67	1.12	2.02	1.71	1.14	0.24
82	0.51	7.92	10.55	1.79	3.61	1.51	0.86	0.57
83	0.75	9.80	11.91	1.69	2.35	1.56	0.78	0.23
84	1.01	11.95	13.45	1.41	2.02	1.62	0.98	0.35
96	1.25	15.50	17.71	1.99	2.53	2.09	1.12	0.64

Table D.3. Triaxial test results for Geometry 1 gypsum cement/sand specimens containing infill.

Test No.	Principal Stresses (MPa)			Ax. Def. Ratio (%)		Axial Stiffness (GPa/m)		Vol. Def. Rat. (%)
	σ_3	$\sigma_{1(slip)}$	$\sigma_{1(peak)}$	$\Delta_{a(slip)}$	$\Delta_{a(peak)}$	K_A	K_B	Δ_v
134	0.25	3.45	4.87	0.46	2.05	0.40	0.30	n/a
135	0.50	5.43	6.79	3.15	4.38	0.64	0.48	0.99
136	0.76	6.11	9.79	2.65	4.66	0.91	0.87	1.53
137	0.99	8.32	11.26	2.69	4.61	1.03	0.82	1.48
138	1.25	10.07	11.20	2.86	3.58	0.92	0.68	1.10
139	0.24	2.87	4.64	3.24	5.48	0.33	0.29	1.07
140	0.50	5.72	8.15	3.79	5.43	0.58	0.48	1.51
141	0.76	5.55	6.85	2.41	3.15	1.01	0.78	1.67
142	1.01	6.45	8.83	2.83	5.98	0.64	0.69	1.84
143	0.25	2.72	4.58	2.58	4.84	0.38	0.30	0.71
144	0.50	6.28	7.30	3.71	5.12	0.58	0.41	2.32
145	0.75	5.72	9.79	2.34	4.75	0.92	0.80	1.60

D.2. Geometry 2.

Table D.4. Triaxial test results for Geometry 2 gypsum cement specimens.

Test No.	Principal Stresses (MPa)			Ax. Def. Ratio (%)		Axial Stiffness (GPa/m)		Vol. Def. Rat. (%)
	σ_3	$\sigma_{1(slip)}$	$\sigma_{1(peak)}$	$\Delta_{a(slip)}$	$\Delta_{a(peak)}$	K_A	K_B	Δ_v
45	0.24	6.42	7.97	2.31	3.85	0.98	0.54	0.95
46	0.50	9.42	11.25	2.02	3.23	1.50	1.06	0.60
47	0.76	11.30	14.06	2.60	3.43	1.65	1.42	0.97
48	1.01	13.36	15.42	1.26	1.98	2.49	1.45	0.58
49	0.27	7.45	9.18	1.40	1.90	1.84	1.55	0.28
50	0.50	8.62	10.31	1.38	2.24	1.50	1.02	0.26
51	0.76	9.84	13.03	0.93	1.78	2.41	1.60	0.37
52	1.03	11.44	16.36	1.22	1.99	2.62	2.21	0.73
97	1.24	15.11	18.73	1.52	2.62	2.26	1.80	0.35

Table D.5. Triaxial test results for Geometry 2 gypsum cement/sand specimens.

Test No.	Principal Stresses (MPa)			Ax. Def. Ratio (%)		Axial Stiffness (GPa/m)		Vol. Def. Rat. (%)
	σ_3	$\sigma_{1(slip)}$	$\sigma_{1(peak)}$	$\Delta_{a(slip)}$	$\Delta_{a(peak)}$	K_A	K_B	Δ_v
69	0.25	9.56	10.97	2.37	2.99	1.52	1.16	0.85
70	0.51	12.05	13.31	2.42	2.82	1.73	1.36	0.82
71	0.75	11.62	14.11	1.77	2.52	2.00	1.57	0.37
72	1.01	15.00	15.94	2.13	2.41	2.17	1.28	0.69
73	0.25	7.83	9.18	2.63	3.17	1.80	0.90	0.67
74	0.51	10.78	12.42	2.33	2.72	1.62	1.47	0.73
75	0.75	11.58	13.64	1.69	2.46	2.11	1.84	0.43
76	1.0	11.15	15.99	1.67	2.49	2.10	1.96	0.59
85	0.25	7.75	9.68	1.82	2.67	1.62	1.46	0.41
86	0.50	11.71	13.81	1.71	2.29	1.76	1.56	0.28
87	0.75	13.47	15.05	2.21	2.66	1.89	1.58	0.62
88	1.00	13.64	16.24	1.75	2.16	2.36	2.08	0.62
89	1.25	15.56	18.45	1.51	2.09	2.43	2.12	0.52
90	1.25	15.90	18.28	1.73	2.17	2.38	2.10	0.65

Table D.6. Triaxial test results for Geometry 2 gypsum cement/sand specimens containing infill.

Test No.	Principal Stresses (MPa)			Ax. Def. Ratio (%)		Axial Stiffness (GPa/m)		Vol. Def. Rat (%)
	σ_3	$\sigma_{1(slip)}$	$\sigma_{1(peak)}$	$\Delta_{a(slip)}$	$\Delta_{a(peak)}$	K_A	K_B	Δ_v
146	0.25	2.21	4.47	2.28	4.29	0.38	0.45	1.28
147	0.50	8.38	9.79	4.80	6.16	0.88	0.45	2.35
148	0.75	6.73	10.41	4.16	7.10	0.77	0.46	2.79
149	1.00	n/a	n/a	n/a	n/a	1.00	n/a	n/a
150	1.00	10.24	12.22	1.81	3.89	1.41	1.10	0.59
151	0.25	5.15	6.68	3.53	5.11	0.62	0.38	1.14
152	0.50	7.75	10.19	3.65	5.97	0.86	0.63	1.08
153	0.75	8.72	10.41	3.11	4.10	1.06	0.82	1.11
154	1.00	6.22	7.53	2.16	5.32	1.00	0.51	1.11
155	0.25	7.02	7.70	4.17	4.90	0.72	0.50	1.11
156	0.50	9.00	10.64	3.61	4.40	1.04	0.74	0.99
157	0.75	7.07	8.66	2.57	5.00	0.97	0.64	1.16
158	1.00	7.36	12.05	2.41	6.64	0.91	0.51	1.94

D.3. Geometry 3.

Table D.7. Triaxial test results for Geometry 3 gypsum cement/sand specimens.

Test No.	Principal Stresses (MPa)			Ax. Def. Ratio (%)		Axial Stiffness (GPa/m)		Vol. Def. Rat. (%)
	σ_3	$\sigma_{1(slip)}$	$\sigma_{1(peak)}$	$\Delta_{a(slip)}$	$\Delta_{a(peak)}$	K_A	K_B	Δ_v
53	0.25	1.50	2.43	0.33	1.41	0.54	1.58	0.13
54	0.50	1.55	3.47	0.33	3.06	0.63	1.72	0.27
55	0.76	3.75	5.48	0.93	3.38	1.22	0.26	0.55
56	1.00	3.66	6.89	0.38	3.16	1.32	0.31	0.27
57	0.26	1.50	2.29	0.53	1.95	0.58	0.20	0.42
58	0.51	2.34	3.98	0.60	1.81	0.70	0.23	0.49
59	0.75	3.47	5.06	0.44	2.50	1.22	0.53	0.32
60	1.01	3.75	6.51	0.68	3.70	1.20	0.23	0.49
91	0.26	1.81	2.83	0.41	2.60	0.60	0.27	0.20
92	0.50	2.72	4.07	0.58	2.77	0.64	0.27	0.23
93	0.75	4.08	5.54	1.20	3.32	0.95	0.32	0.62
94	1.00	4.98	7.07	0.69	3.14	1.27	0.51	0.38
95	1.25	5.15	8.72	0.59	3.66	1.36	0.82	0.44

Table D.8. Triaxial test results for Geometry 3 gypsum cement specimens.

Test No.	Principal Stresses (MPa)			Ax. Def. Ratio (%)		Axial Stiffness (GPa/m)		Vol. Def. Rat. (%)
	σ_3	$\sigma_{1(slip)}$	$\sigma_{1(peak)}$	$\Delta_{a(slip)}$	$\Delta_{a(peak)}$	K_A	K_B	Δ_v
61	0.26	1.55	3.09	0.52	2.57	0.58	0.20	0.37
62	0.51	2.01	4.36	0.41	2.56	1.06	0.36	0.36
63	0.75	2.76	6.84	0.41	3.04	1.26	0.54	0.34
64	1.00	3.47	8.06	0.61	4.33	1.22	0.35	0.56
65	0.26	1.02	2.67	0.37	2.23	0.59	0.32	0.36
66	0.50	2.25	5.11	0.51	2.82	1.03	0.34	0.46
67	0.75	3.98	6.37	0.84	3.45	1.07	0.32	0.37
68	1.00	3.84	8.53	0.82	4.05	1.11	0.20	0.62
98	0.25	2.15	2.55	1.22	1.87	0.47	n/a	0.34
99	0.50	2.72	5.04	0.96	2.72	0.82	0.39	0.50
100	0.75	3.23	6.79	0.79	3.03	1.05	0.52	0.46
101	1.00	5.09	n/a	1.04	n/a	1.19	0.32	0.56
102	1.24	5.05	9.73	0.74	2.74	1.42	0.33	0.38
103	1.24	6.00	9.73	0.72	2.69	1.46	0.47	0.44

Table D.9. Triaxial test results for Geometry 3 gypsum cement/sand specimens containing infill.

Test No.	Principal Stresses (MPa)			Ax. Def. Ratio (%)		Axial Stiffness (GPa/m)		Vol. Def. Rat. (%)
	σ_3	$\sigma_{1(slip)}$	$\sigma_{1(peak)}$	$\Delta_{a(slip)}$	$\Delta_{a(peak)}$	K_A	K_B	Δ_v
159	0.25	1.58	2.66	1.36	4.23	0.28	0.14	0.51
160	0.50	2.15	3.96	0.85	4.92	0.68	0.23	0.78
161	0.75	2.77	5.43	0.82	4.41	0.86	0.25	0.61
162	1.00	3.00	6.38	0.69	5.10	0.93	0.29	0.67
163	1.25	3.51	7.30	0.78	5.17	0.94	0.29	0.82
164	0.25	1.08	2.66	0.57	4.98	0.40	0.18	0.53
165	0.50	2.15	3.96	0.81	4.81	0.76	0.28	0.53
166	0.75	2.66	5.94	0.85	4.42	0.80	0.72	0.64
167	1.00	2.72	6.79	0.54	5.18	0.90	0.29	0.74
168	0.50	1.58	4.07	0.59	5.05	0.72	0.27	0.61
169	0.75	3.00	6.68	0.76	4.32	0.89	0.42	0.47
170	1.00	2.49	6.56	0.56	5.94	0.94	0.46	0.62

D.4. Geometry 4.

Table D.10. Triaxial test results for Geometry 4 gypsum cement/sand specimens.

Test No.	Principal Stresses (MPa)			Ax. Def. Ratio (%)		Axial Stiffness (GPa/m)		Vol. Def. Rat. (%)
	σ_3	$\sigma_{1(slip)}$	$\sigma_{1(peak)}$	$\Delta_{a(slip)}$	$\Delta_{a(peak)}$	K_A	K_B	Δ_v
104	0.25	1.30	3.73	0.38	1.96	0.59	0.40	0.16
105	0.50	1.87	4.81	0.50	2.86	0.94	0.65	0.40
106	0.74	3.22	6.00	0.75	3.22	1.00	0.42	0.45
107	1.00	4.58	8.32	0.76	3.99	1.15	0.43	0.54
108	1.23	6.85	11.20	1.71	4.95	1.06	0.62	0.96
109	0.26	1.02	3.11	0.56	4.18	0.47	0.20	0.48
110	0.50	2.09	5.15	0.56	3.33	0.93	0.53	0.34
111	0.75	4.64	6.85	1.05	3.01	1.16	0.51	0.58
112	1.02	4.30	8.71	0.63	3.30	1.22	0.53	0.47
113	1.25	5.15	10.92	0.90	3.62	1.44	0.82	0.59
114	0.26	1.07	2.83	0.47	4.49	0.49	0.39	0.28
115	0.50	2.15	4.70	0.64	3.86	0.86	0.37	0.40
116	0.76	4.98	7.53	1.17	4.38	1.02	0.34	0.63
117	1.01	5.15	7.36	1.39	4.60	0.88	0.30	0.67
118	1.24	6.22	10.41	0.85	5.69	1.21	0.46	0.36

Table D.11. Triaxial test results for Geometry 4 gypsum cement specimens.

Test No.	Principal Stresses (MPa)			Ax. Def. Ratio (%)		Axial Stiffness (GPa/m)		Vol. Def. Rat. (%)
	σ_3	$\sigma_{1(slip)}$	$\sigma_{1(peak)}$	$\Delta_{a(slip)}$	$\Delta_{a(peak)}$	K_A	K_B	Δ_v
119	0.25	1.42	3.28	0.47	1.66	0.62	0.41	0.27
120	0.50	1.87	6.56	0.49	4.50	0.99	0.43	0.35
121	0.75	3.40	7.30	0.69	2.31	1.01	0.48	0.40
122	1.00	4.70	9.56	0.70	3.92	1.57	0.44	0.47
123	1.26	7.07	11.43	0.73	4.85	1.66	0.43	0.41
124	0.25	1.47	4.53	0.51	3.30	0.63	0.36	0.28
125	0.50	2.77	7.36	0.91	4.27	0.85	0.65	0.52
126	0.75	5.04	10.07	0.87	2.92	1.44	0.72	0.34
127	1.00	4.75	10.64	0.86	4.98	1.43	0.38	0.47
129	0.25	1.13	3.62	0.73	3.40	0.47	0.13	0.40
130	0.50	1.81	6.28	0.41	3.61	0.96	0.52	0.35
131	0.76	3.51	7.36	0.77	4.51	1.20	0.83	0.46
132	1.00	3.85	6.79	0.71	2.91	1.36	0.55	0.57
133	1.26	7.07	11.50	1.01	4.83	1.46	0.36	0.42

Table D.12. Triaxial test results for Geometry 4 gypsum cement/sand specimens containing infill.

Test No.	Principal Stresses (MPa)			Ax. Def. Ratio (%)		Axial Stiffness (GPa/m)		Vol. Def. Rat. (%)
	σ_3	$\sigma_{1(slip)}$	$\sigma_{1(peak)}$	$\Delta_{a(slip)}$	$\Delta_{a(peak)}$	K_A	K_B	Δ_v
171	0.25	1.58	4.64	0.82	3.53	0.51	0.30	0.38
172	0.50	2.72	6.51	0.88	4.62	0.64	0.52	0.41
173	0.75	4.13	7.02	1.12	3.77	0.82	0.31	0.45
174	1.00	5.15	8.26	1.03	4.39	0.98	0.62	0.51
175	0.25	1.58	3.90	1.05	5.49	0.37	0.15	0.47
176	0.50	3.00	5.83	1.21	3.19	0.62	0.48	0.50
177	0.75	2.77	6.85	0.85	5.97	0.72	0.30	0.67
178	1.00	5.66	8.26	1.52	5.63	0.84	0.39	0.77
179	0.25	1.47	3.40	1.03	2.34	0.51	0.34	0.38
180	0.50	1.87	4.53	0.97	4.71	0.64	0.33	0.81
181	0.75	3.22	6.22	1.32	3.38	0.82	0.18	0.66
182	1.00	5.32	7.92	1.52	3.93	0.98	0.67	0.90

Appendix E. Triaxial Test Plots for Discontinuous Models

This section contains typical axial stress versus axial deformation plots and volumetric change versus axial deformation plots for 54 of the 156 triaxial tests carried out on the discontinuous specimens. The linear displacement pump was not available for the tests on the Geometry 1 100% gypsum cement models and therefore no volumetric change versus axial deformation plots are available for these tests.

E.1. Geometry 1

E.1.1. Geometry 1 100% Gypsum Cement

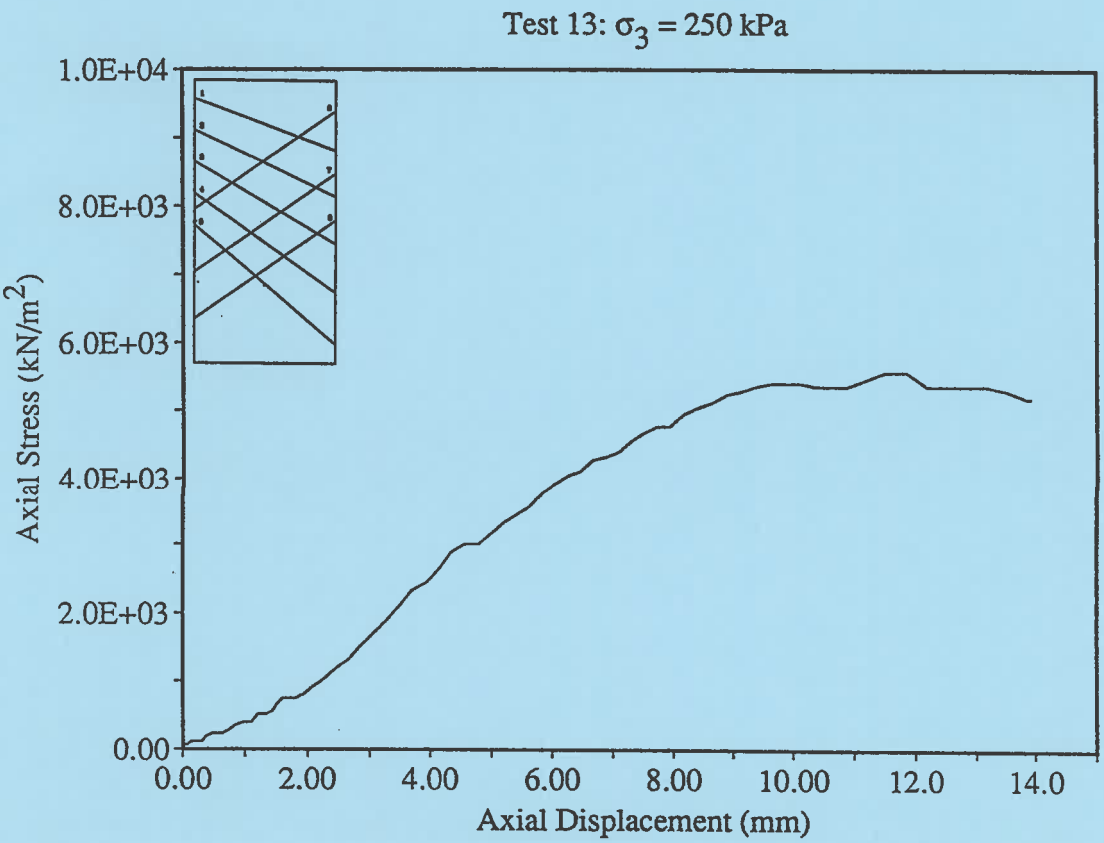

Figure E.1. Test 13, Geometry 1, 100% cement, σ_3 = 250 kPa

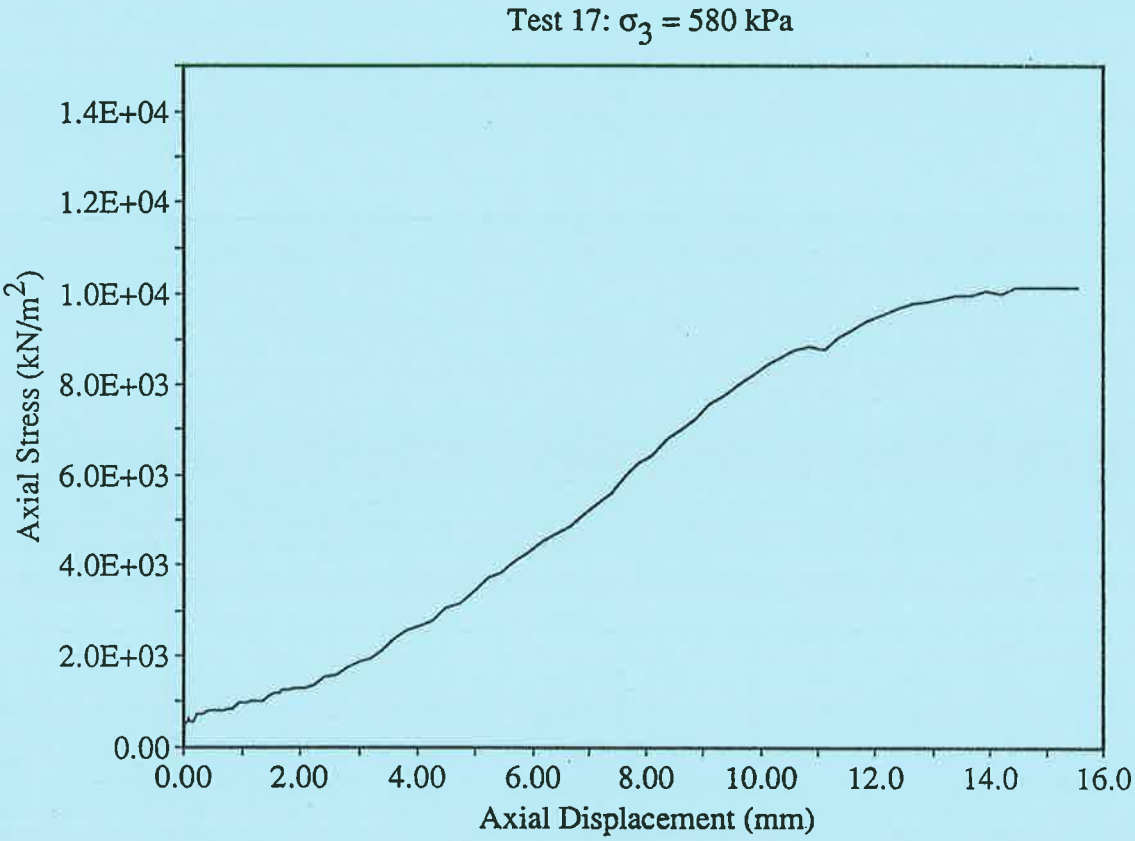

Figure E.2. Test 17, Geometry 1, 100% cement, σ_3 = 580 kPa

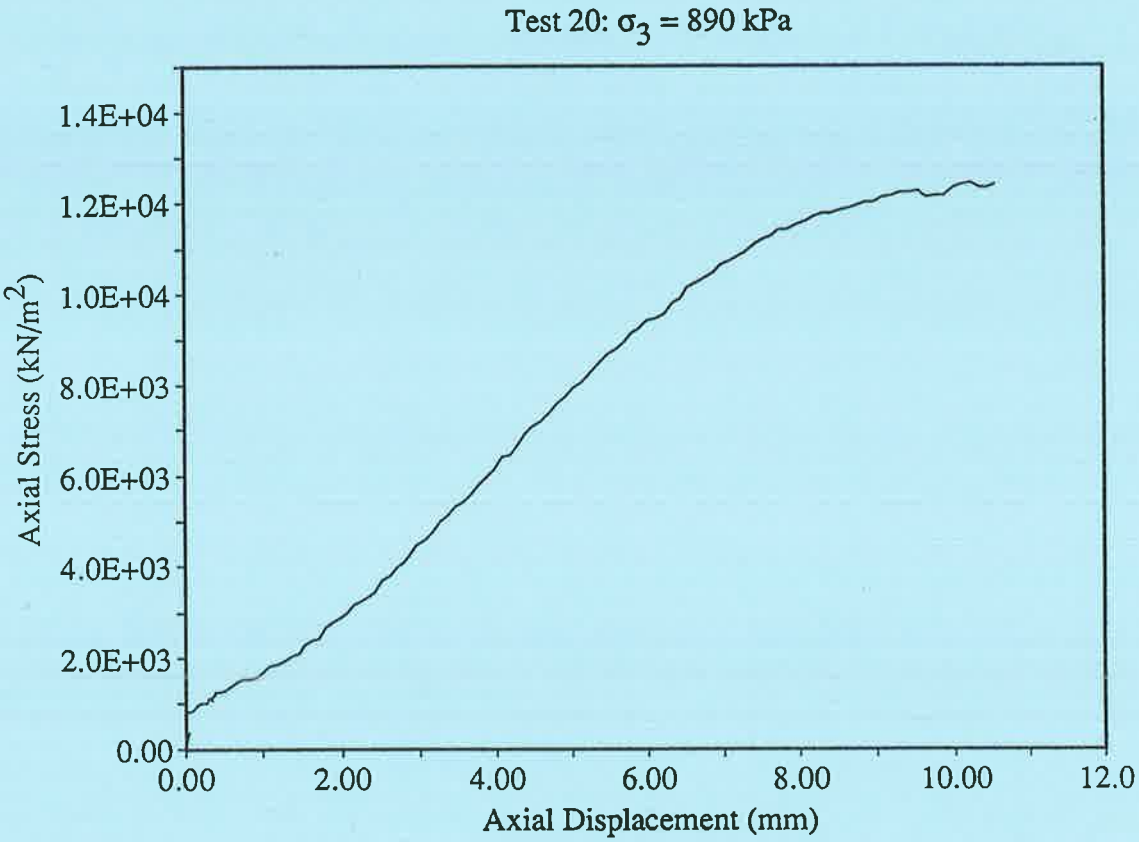

Figure E.3. Test 20, Geometry 1, 100% cement, σ_3 = 890 kPa

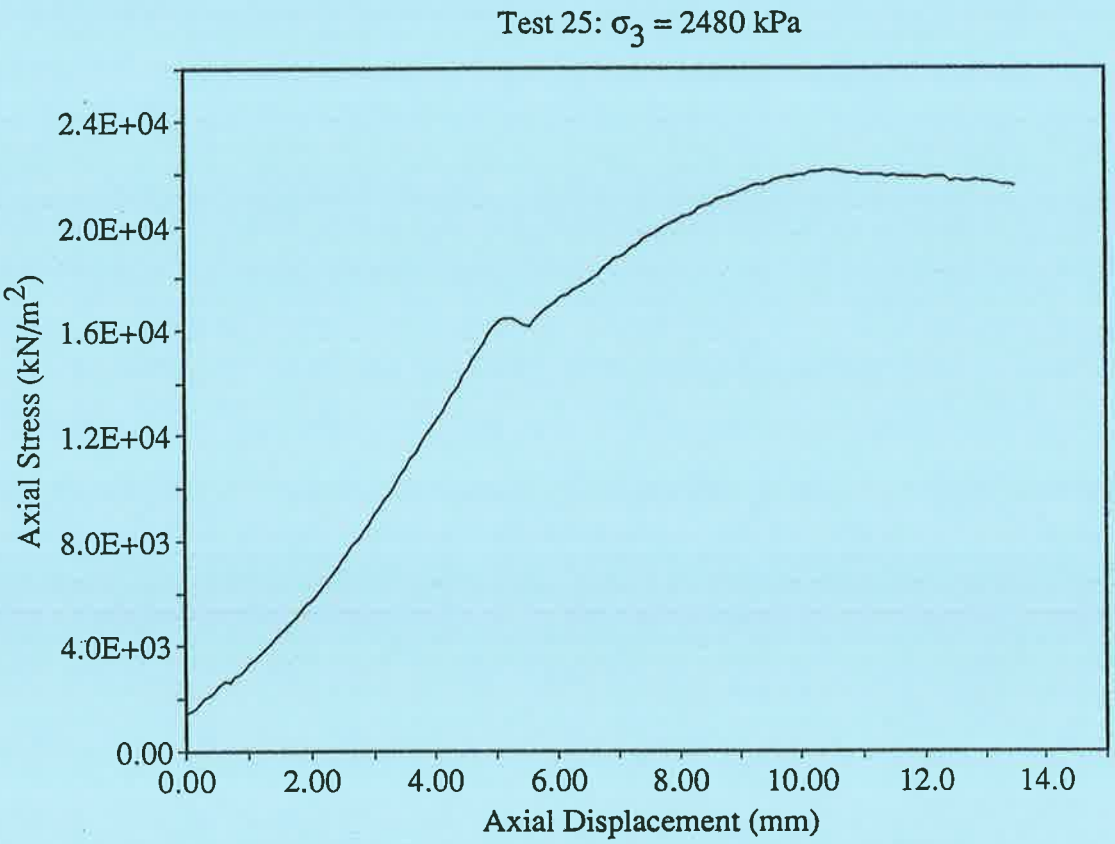

Figure E.4. Test 25, Geometry 1, 100% cement, σ_3 = 2480 kPa

E.1.2. Geometry 1 50/50 Gypsum Cement/Sand

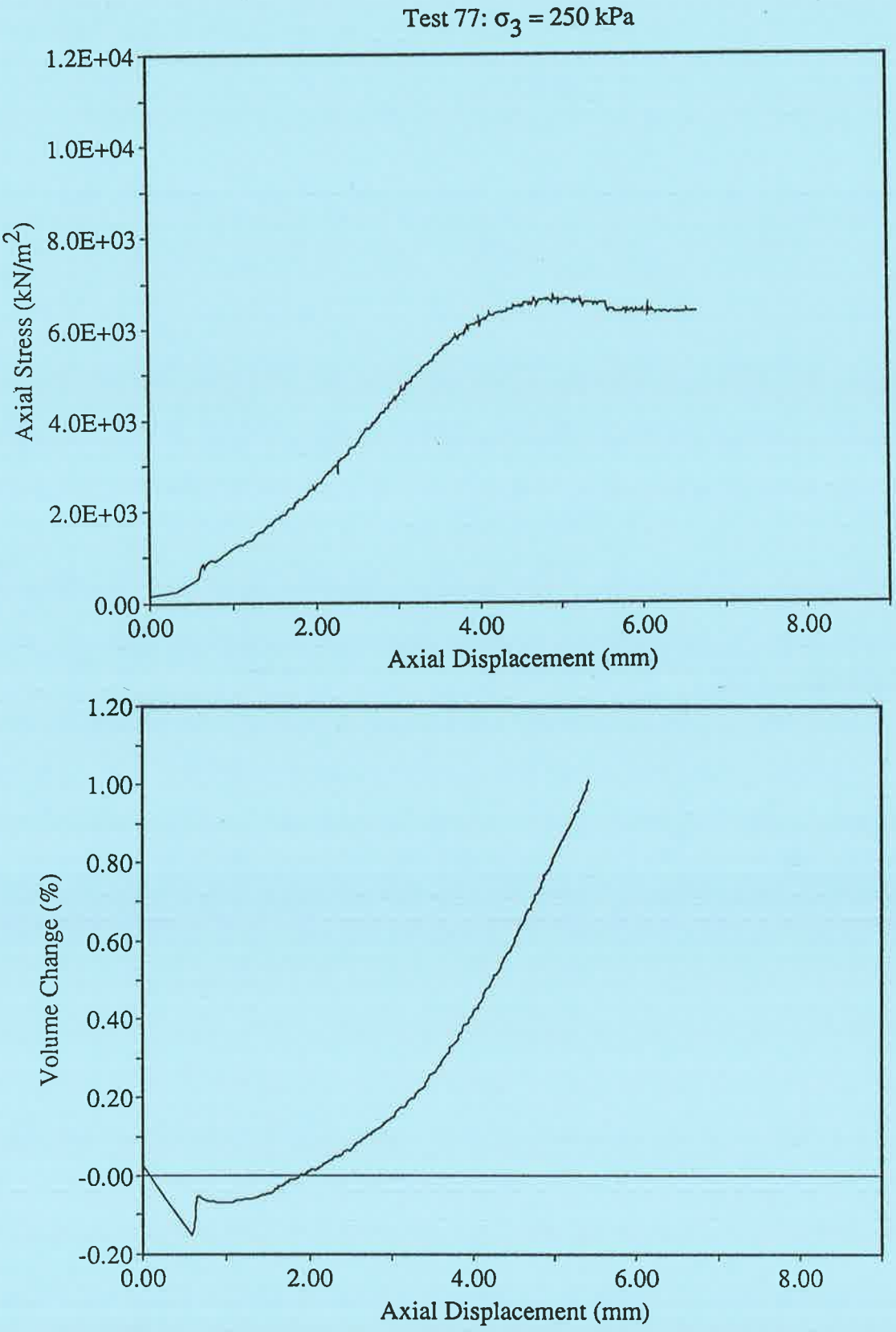

Figure E.5. Test 77, Geometry 1, 50/50 cement/sand, σ_3 = 250 kPa

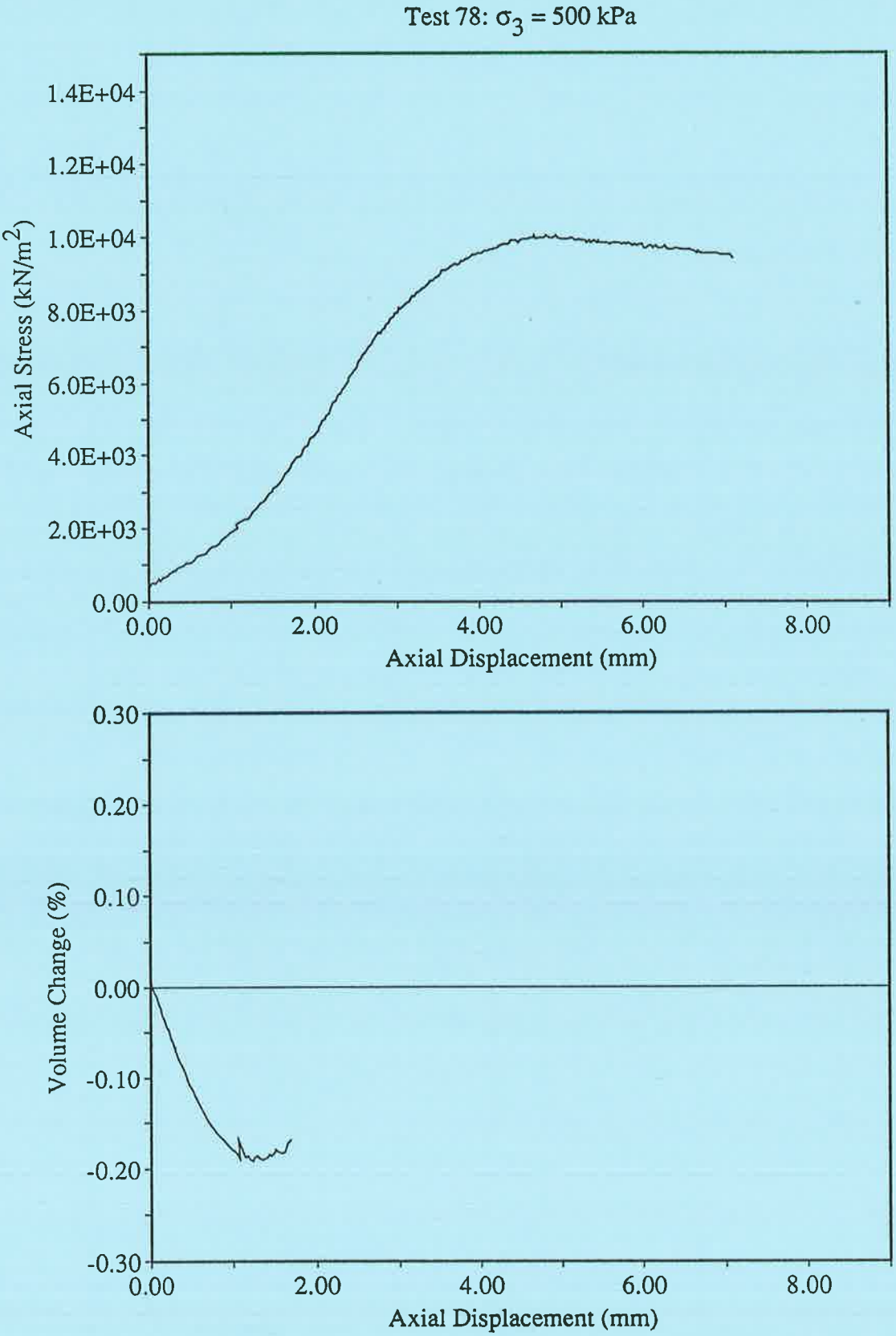

Figure E.6. Test 78, Geometry 1, 50/50 cement/sand, σ_3 = 500 kPa

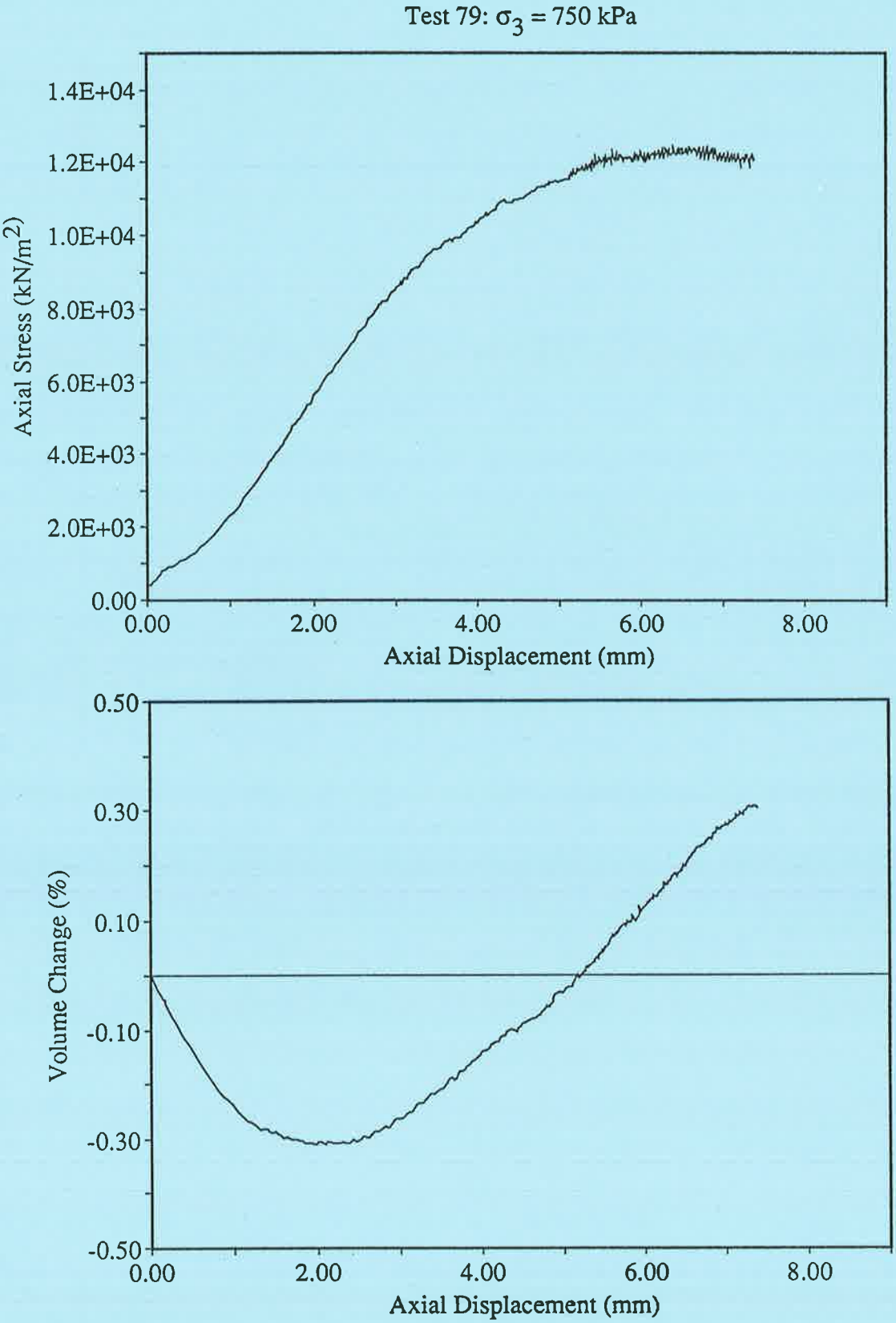

Figure E.7. Test 79, Geometry 1, 50/50 cement/sand, σ_3 = 750 kPa

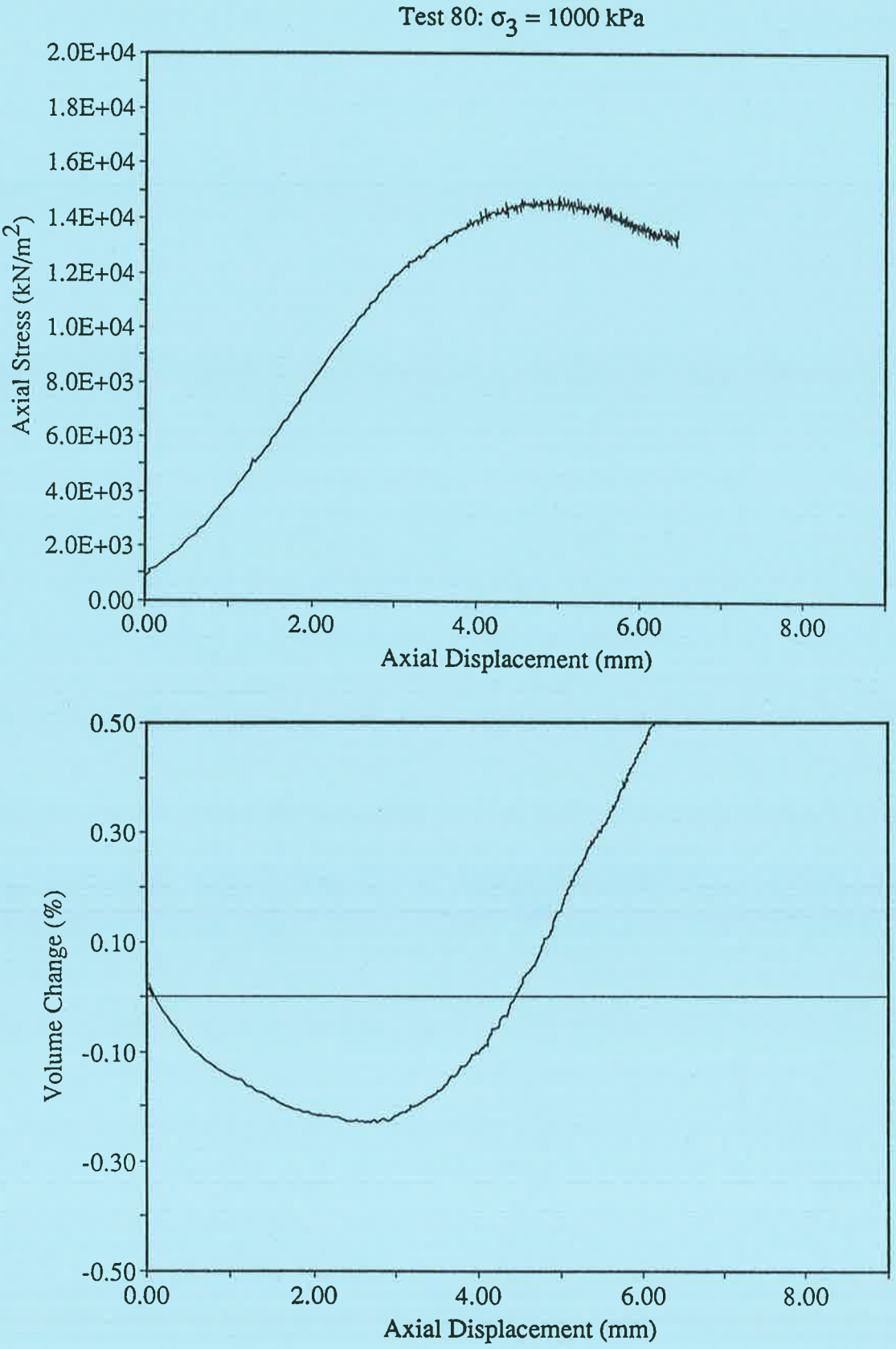

Figure E.8. Test 80, Geometry 1, 50/50 cement/sand, σ_3 = 1000 kPa

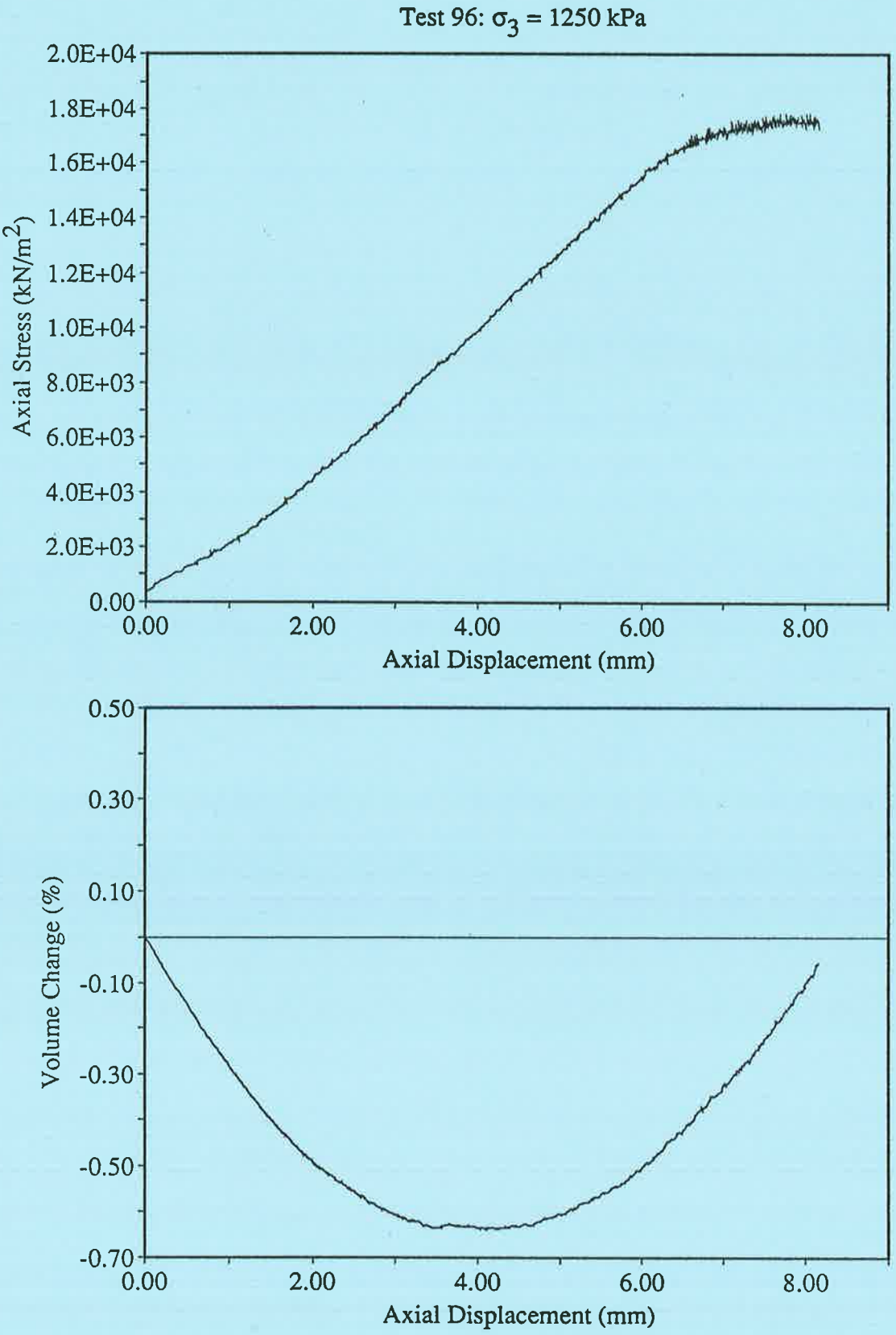

Figure E.9. Test 96, Geometry 1, 50/50 cement/sand, σ_3 = 1250 kPa

E.1.3. Geometry 1 Specimens with Infill

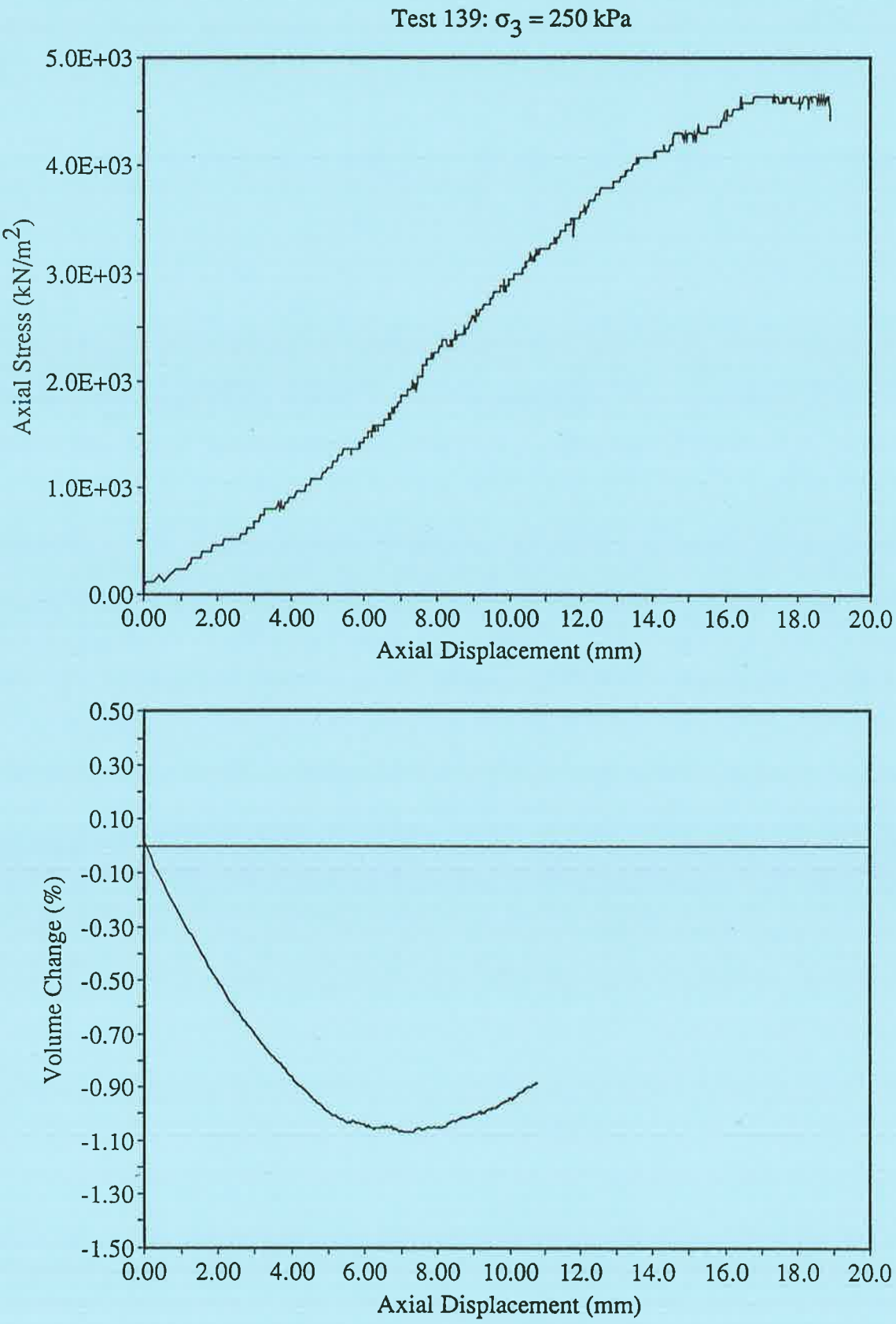

Figure E.10. Test 139, Geometry 1, 50/50 cement/sand specimens with infill, σ_3 = 250 kPa

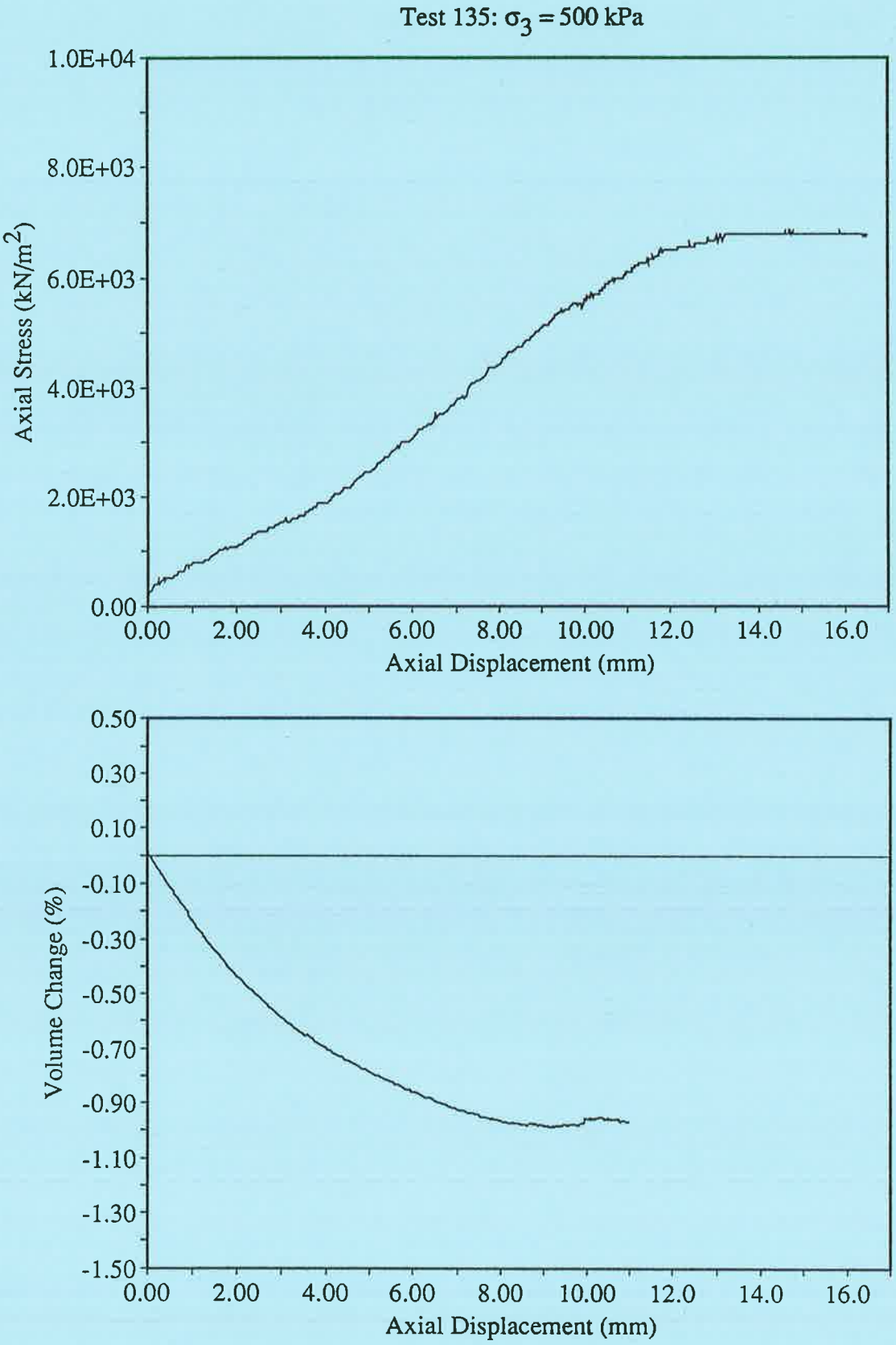

Figure E.11. Test 135, Geometry 1, 50/50 cement/sand specimens with infill, σ_3 = 500 kPa

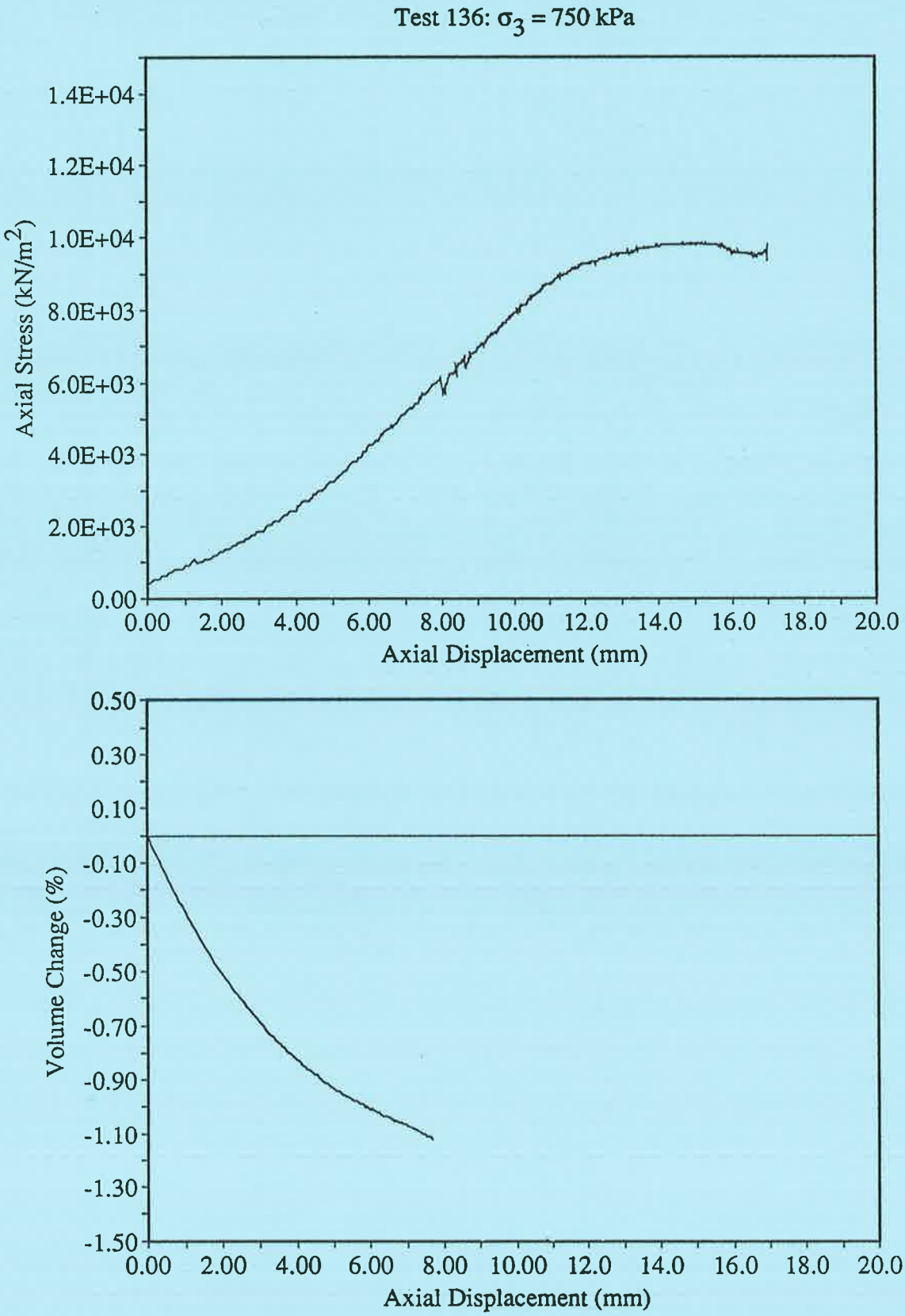

Figure E.12. Test 136, Geometry 1, 50/50 cement/sand specimens with infill, σ_3 = 750 kPa

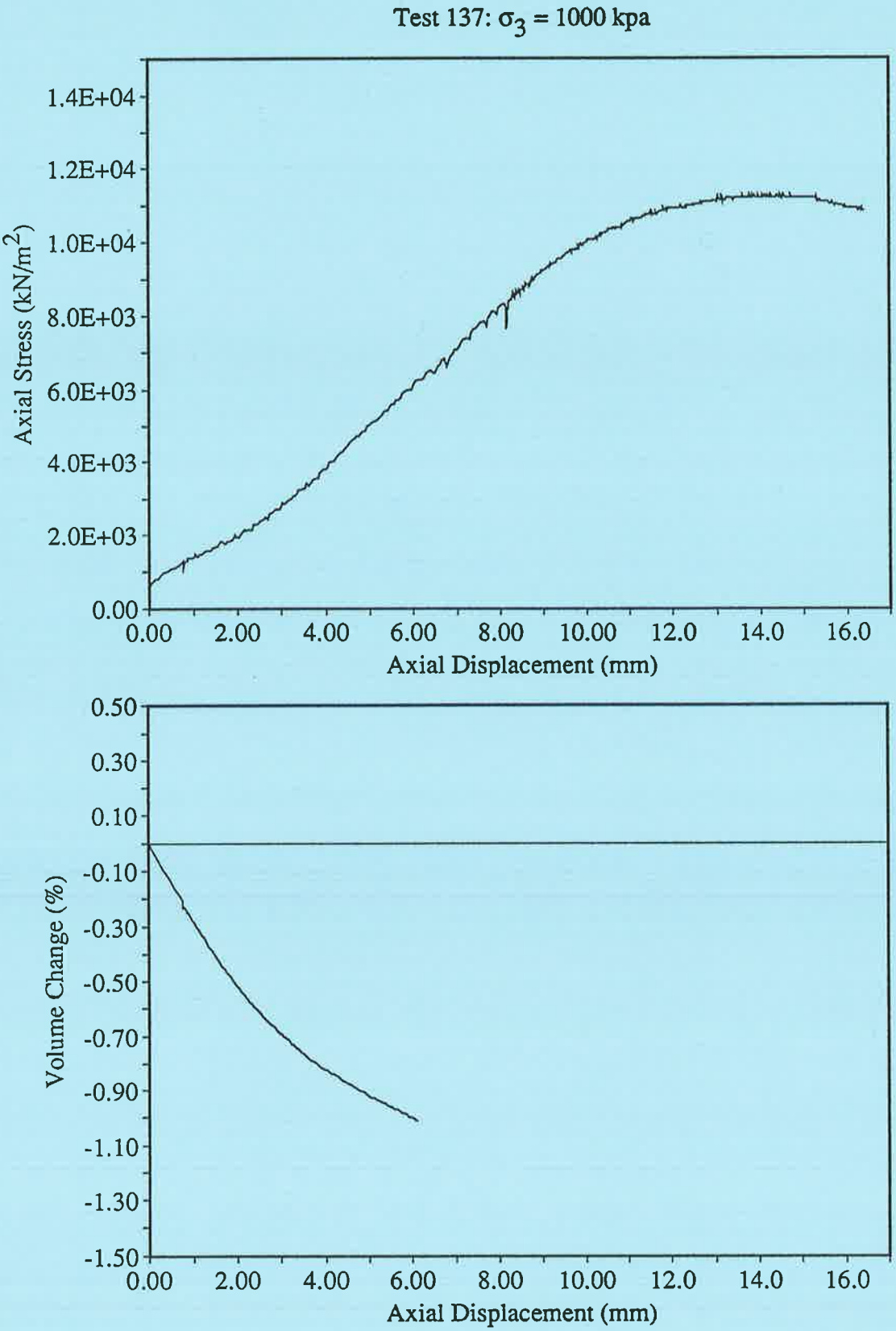

Figure E.13. Test 137, Geometry 1, 50/50 cement/sand specimens with infill, σ_3 = 1000 kPa

E.2. Geometry 2

E.2.1. Geometry 2 100% Gypsum Cement Specimens

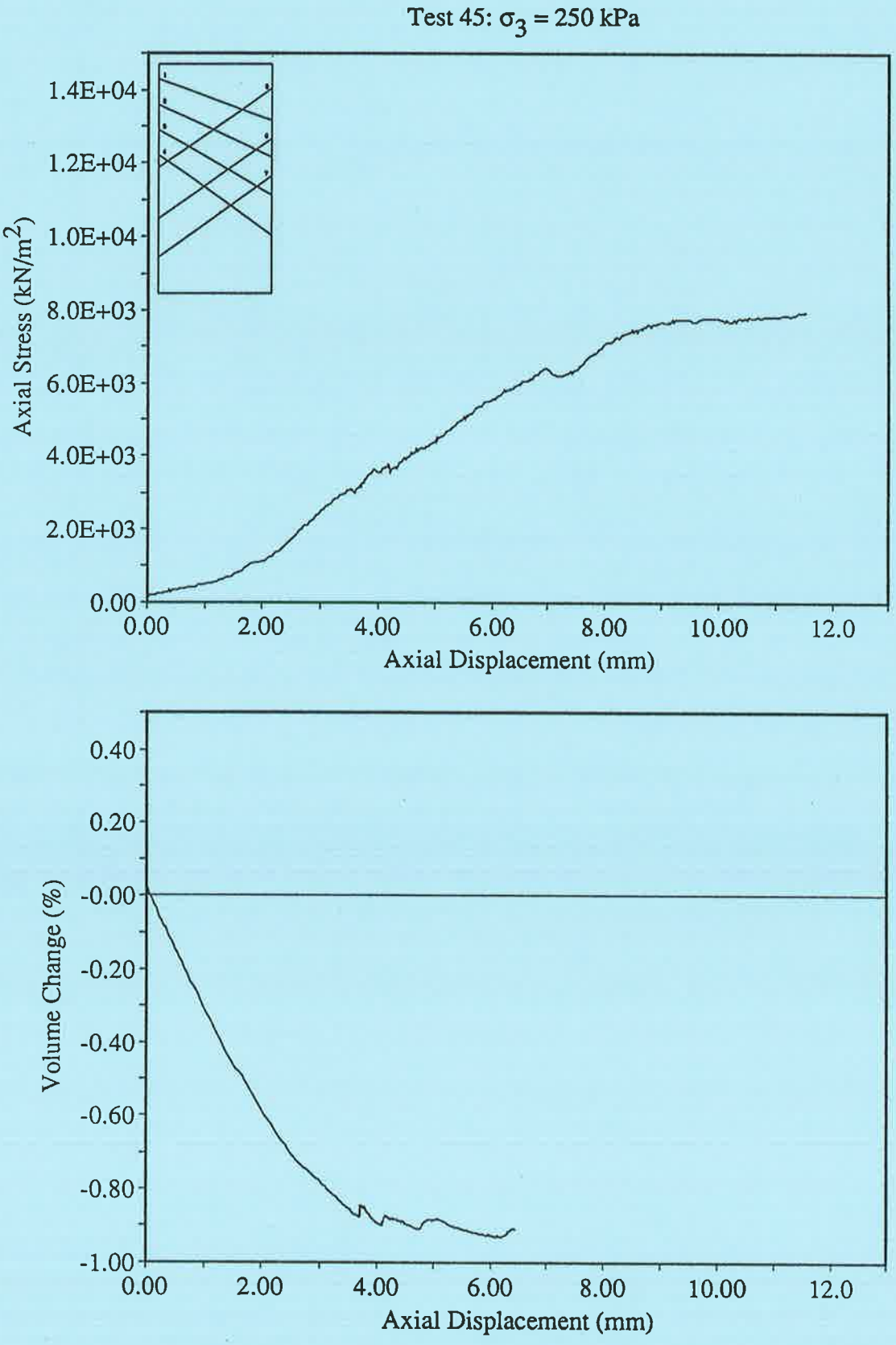

Figure E.14. Test 45, Geometry 2, 100% cement specimens, σ_3 = 250 kPa

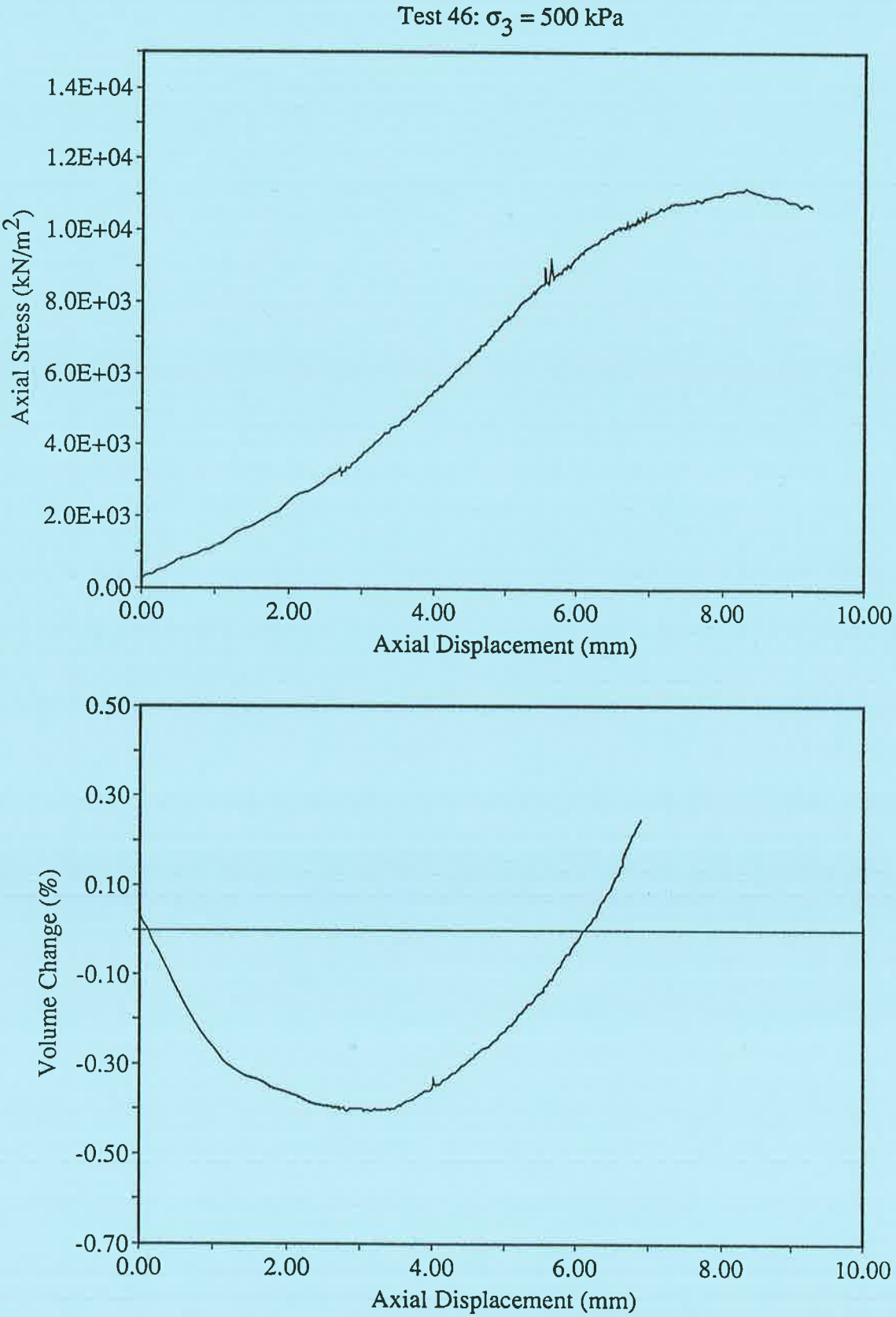

Figure E.15. Test 46, Geometry 2, 100% cement specimens, σ_3 = 500 kPa

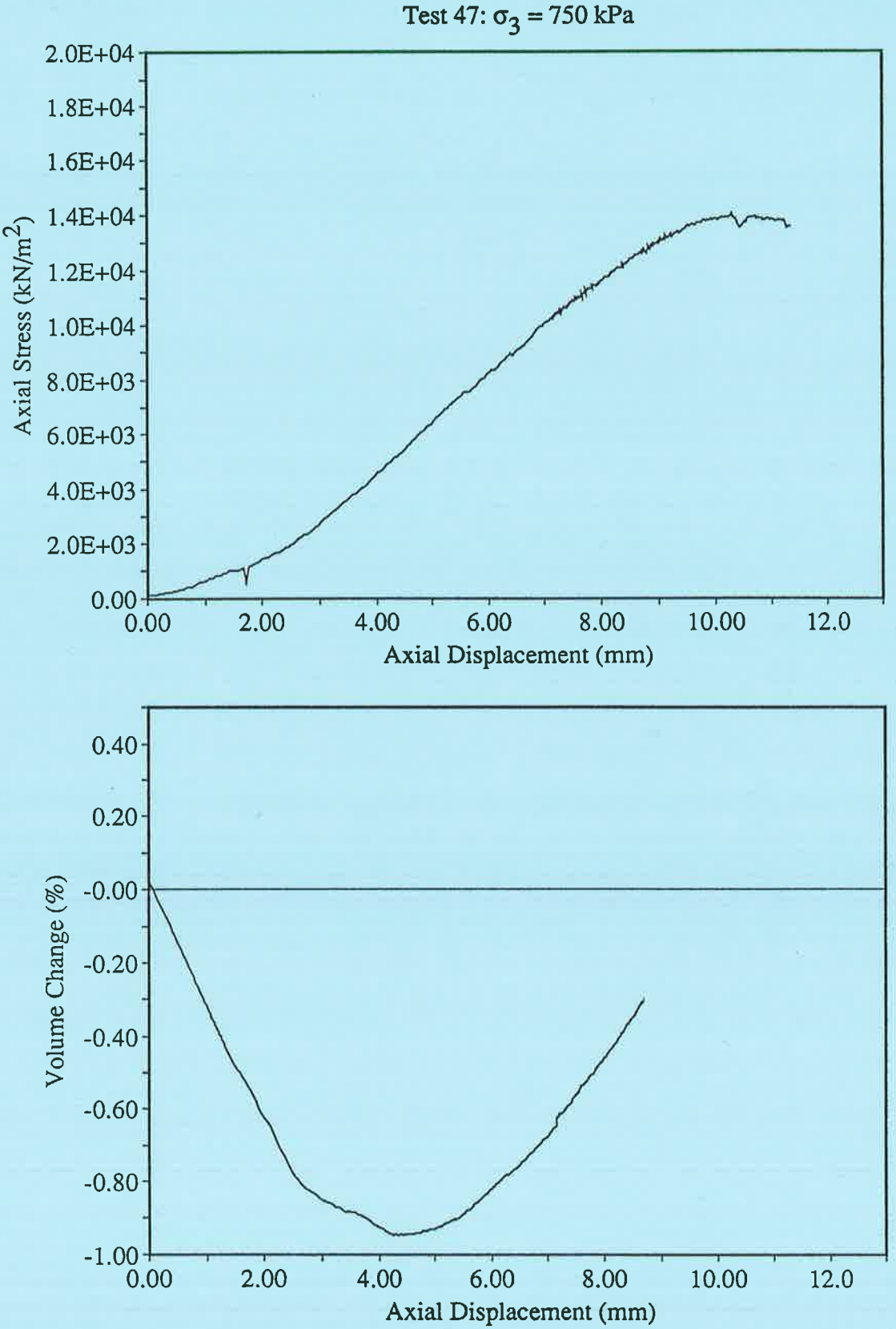

Figure E.16. Test 47, Geometry 2, 100% cement specimens, σ_3 = 750 kPa

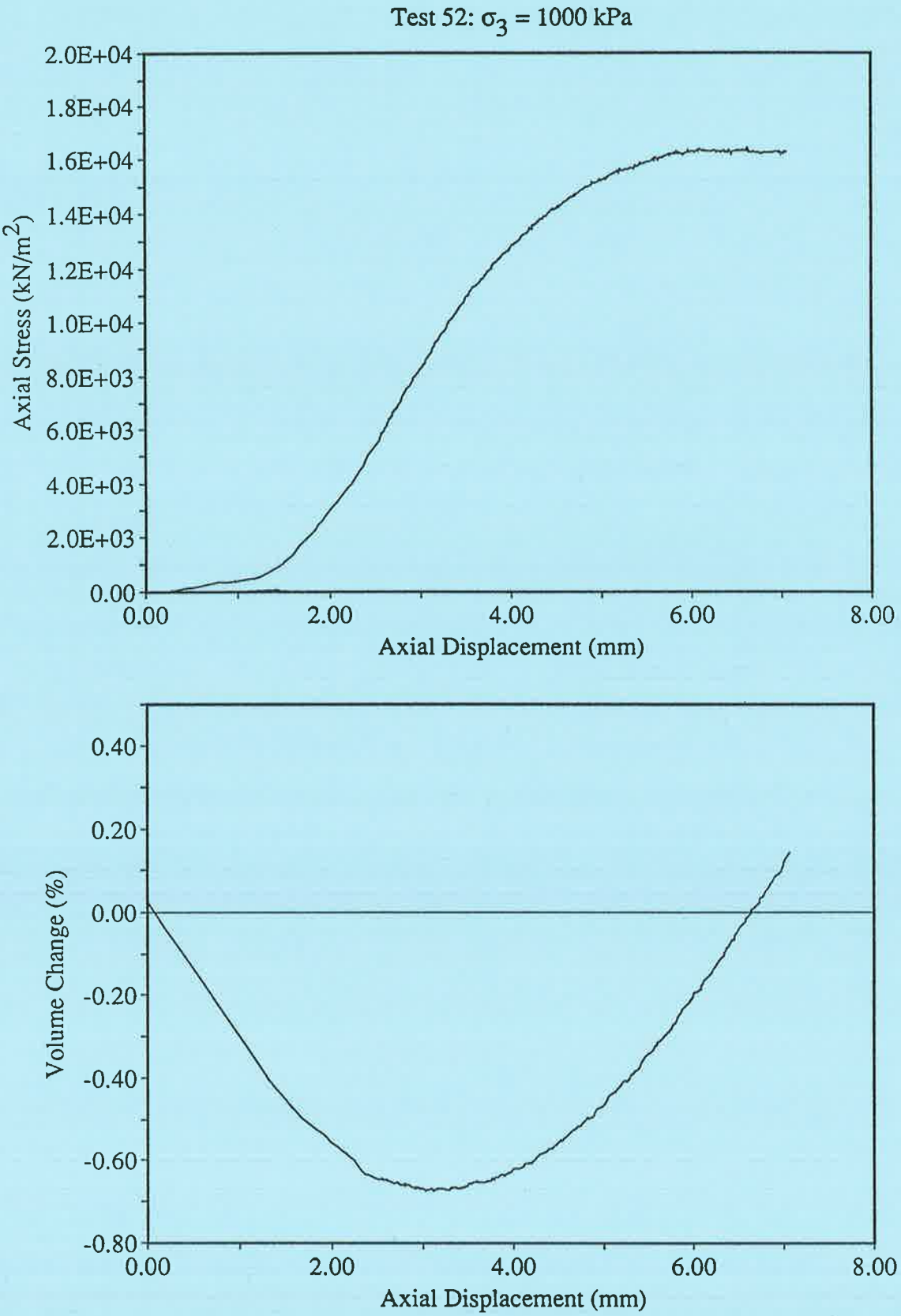

Figure E.17. Test 52, Geometry 2, 100% cement specimens, σ_3 = 1000 kPa

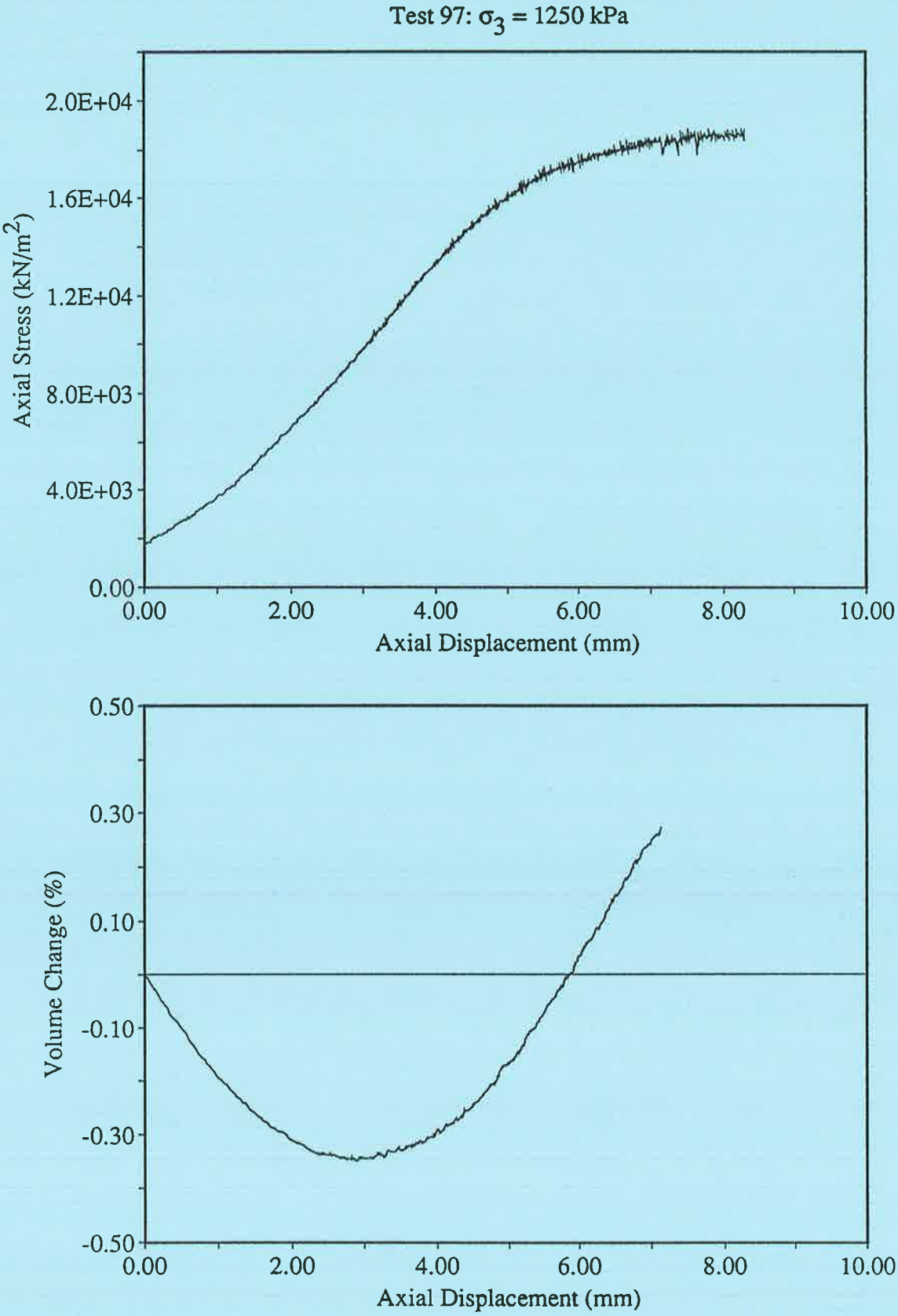

Figure E.18. Test 97, Geometry 2, 100% cement specimens, σ_3 = 1250 kPa

E.2.2. Geometry 2 50/50 Gypsum Cement/Sand Specimens

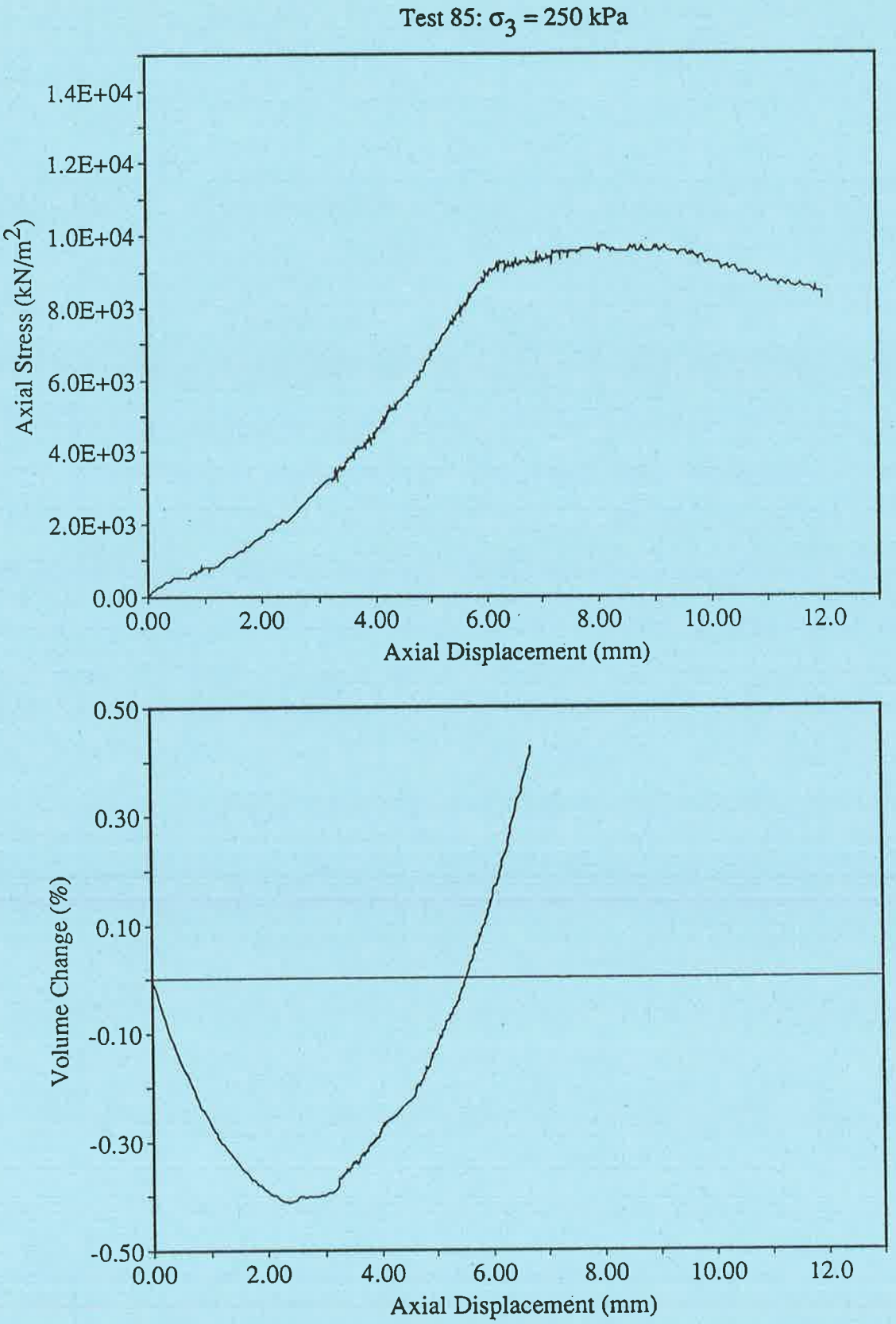

Figure E.19. Test 85, Geometry 2, 50/50 cement/sand specimens, σ_3 = 250 kPa

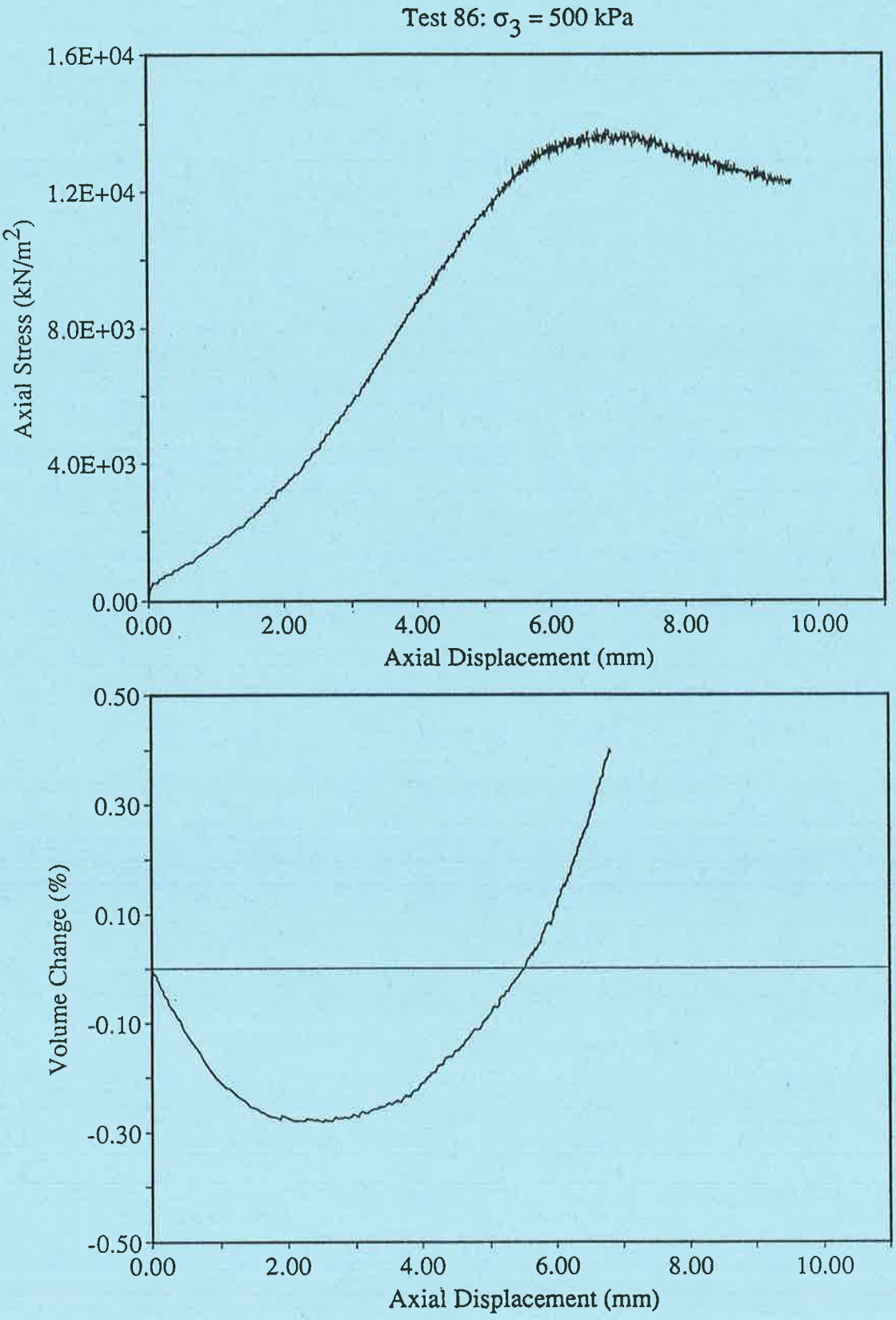

Figure E.20. Test 86, Geometry 2, 50/50 cement/sand specimens, σ_3 = 500 kPa

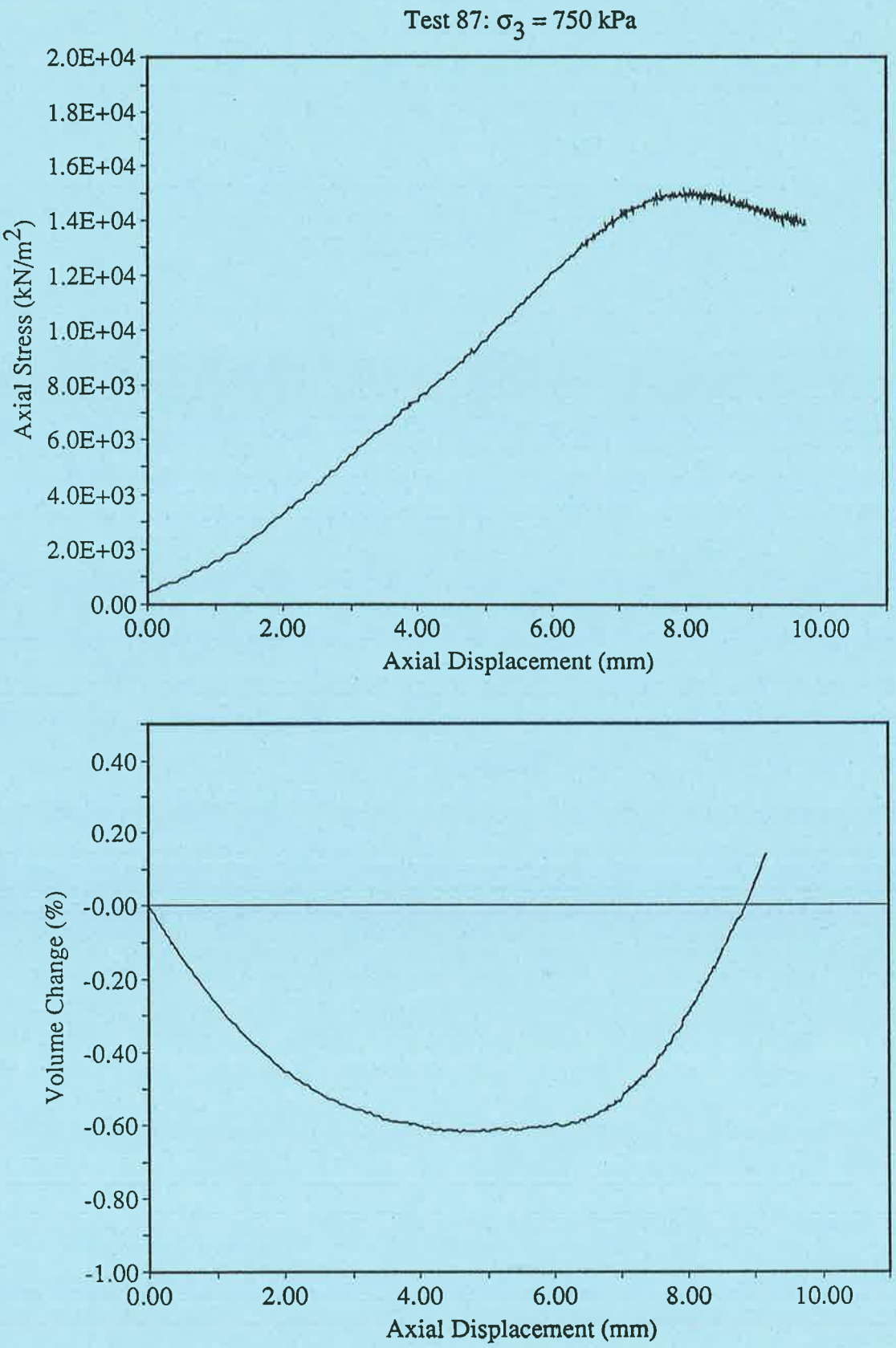

Figure E.21. Test 87, Geometry 2, 50/50 cement/sand specimens, σ_3 = 750 kPa

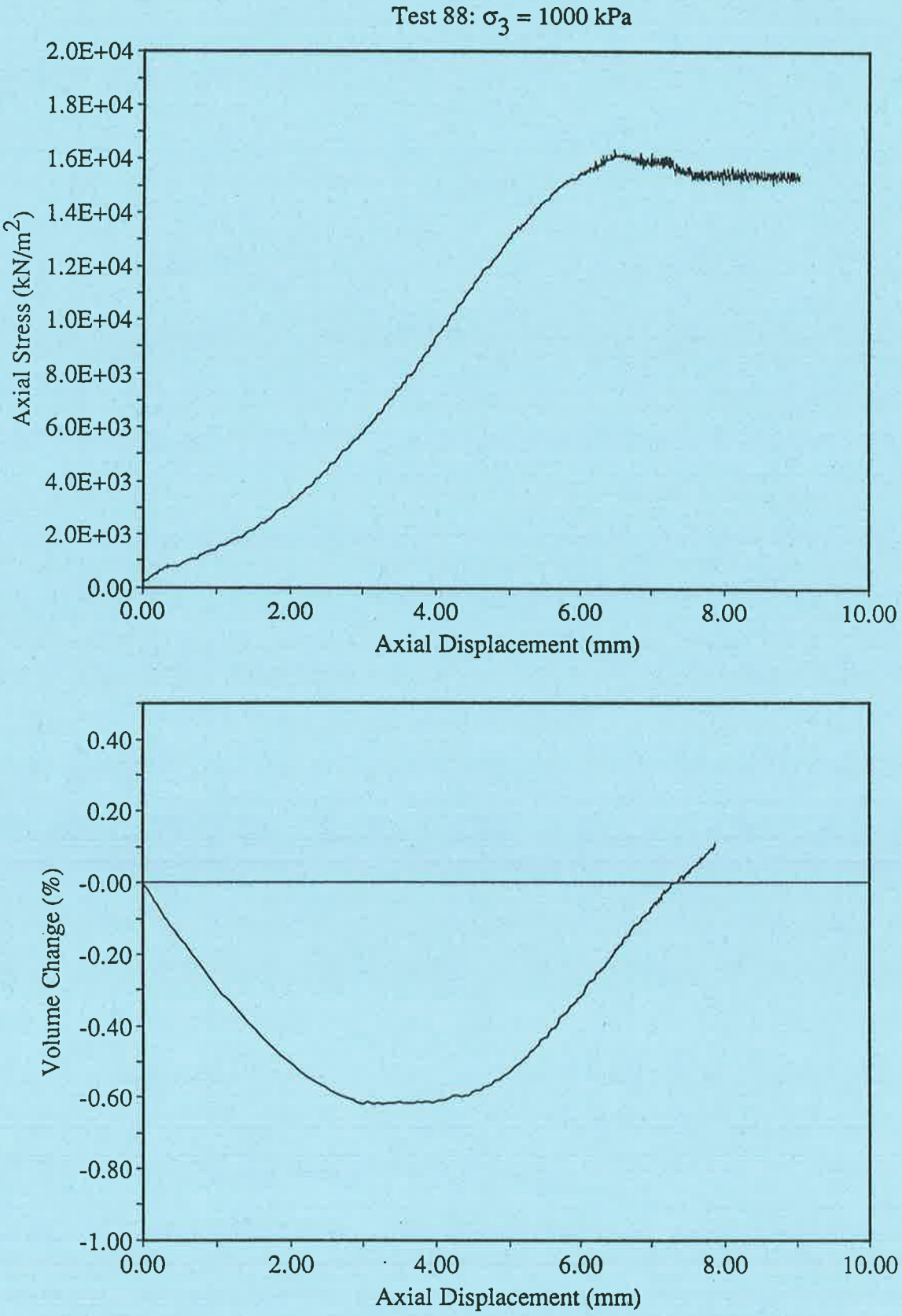

Figure E.22. Test 88, Geometry 2, 50/50 cement/sand specimens, σ_3 = 1000 kPa

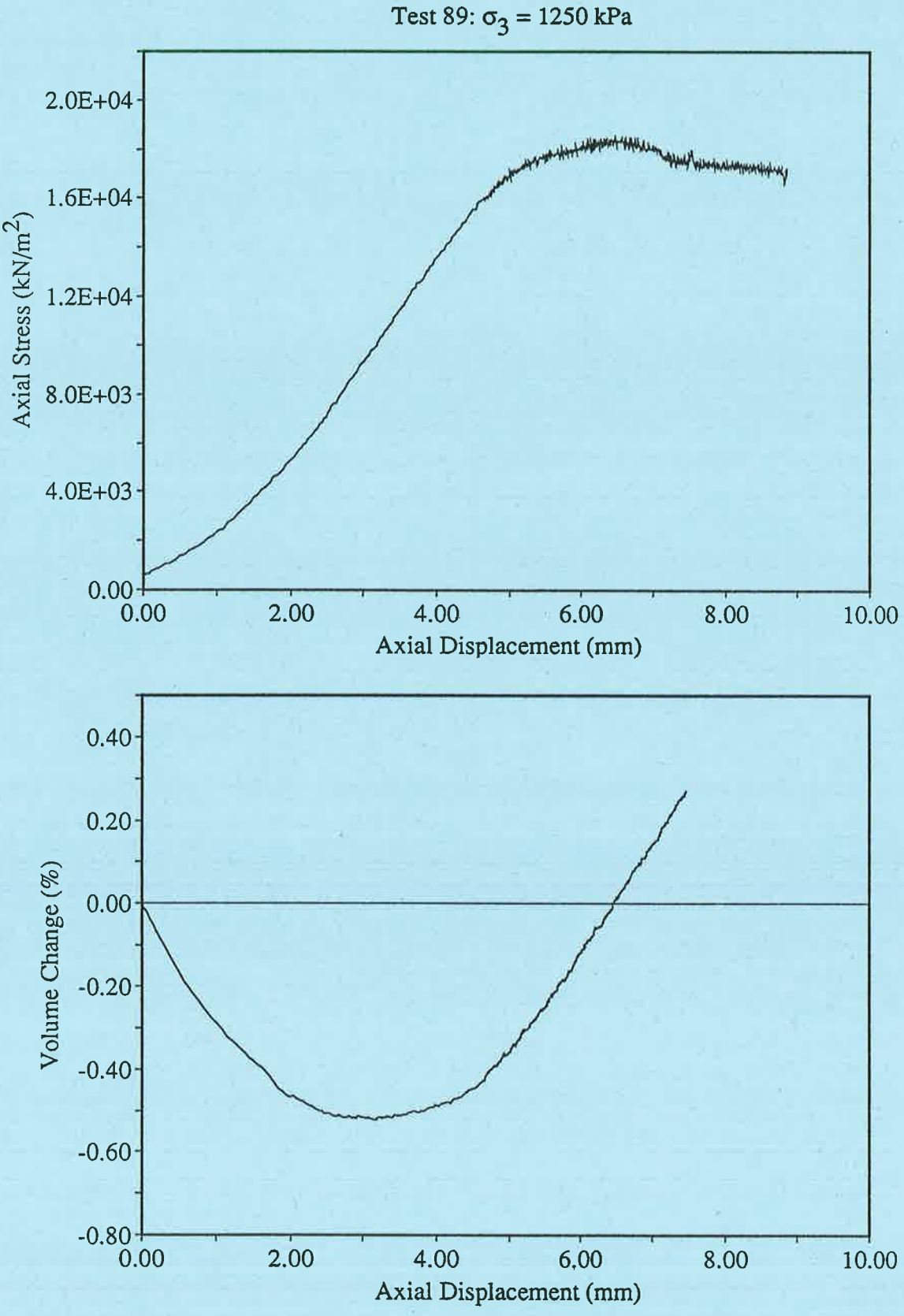

Figure E.23. Test 89, Geometry 2, 50/50 cement/sand specimens, σ_3 = 1250 kPa

E.2.3. Geometry 2 Specimens with Infill

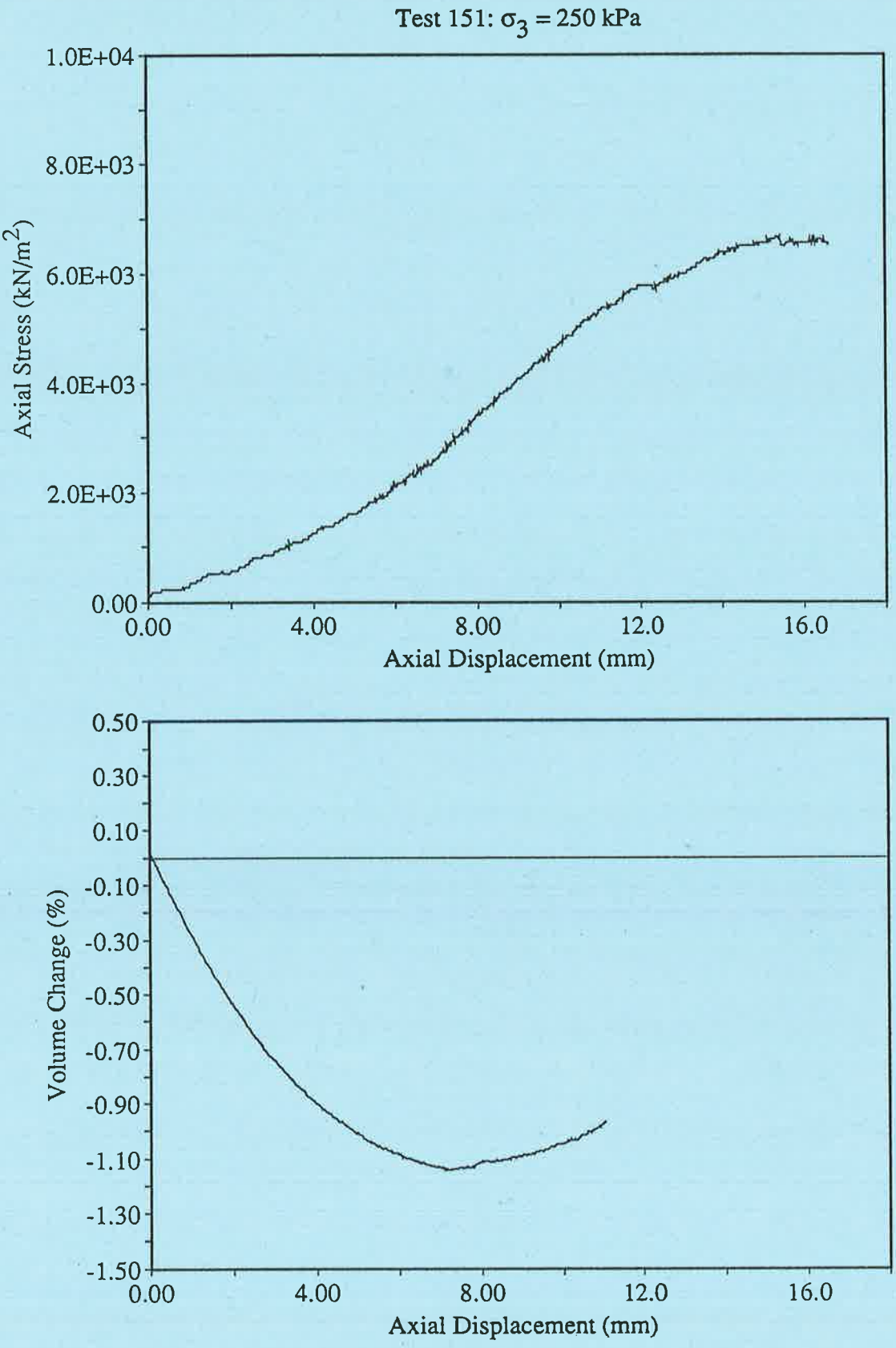

Figure E.24. Test 151, Geometry 2, 50/50 cement/sand specimens with infill, σ_3 = 250 kPa

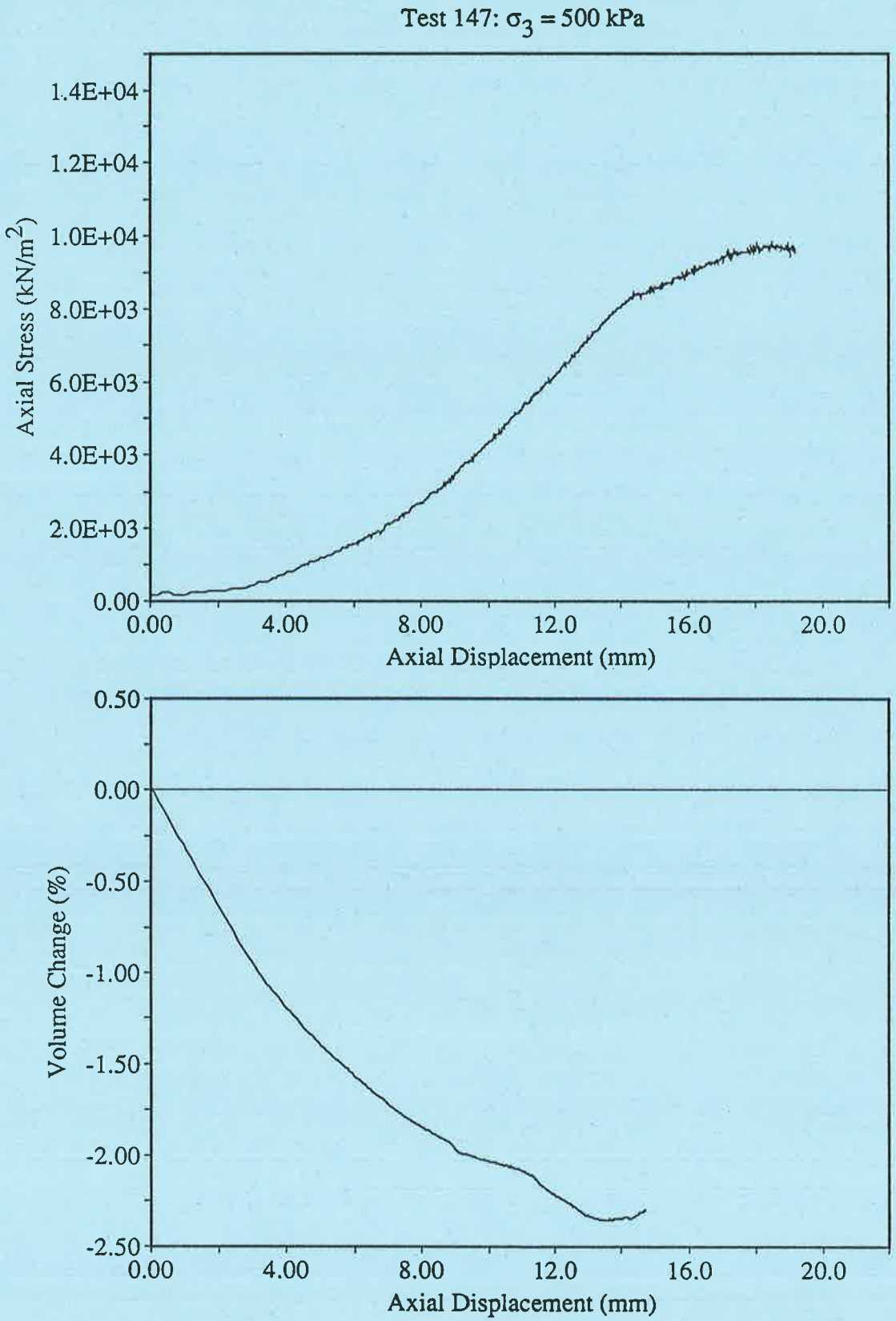

Figure E.25. Test 147, Geometry 2, 50/50 cement/sand specimens with infill, σ_3 = 500 kPa

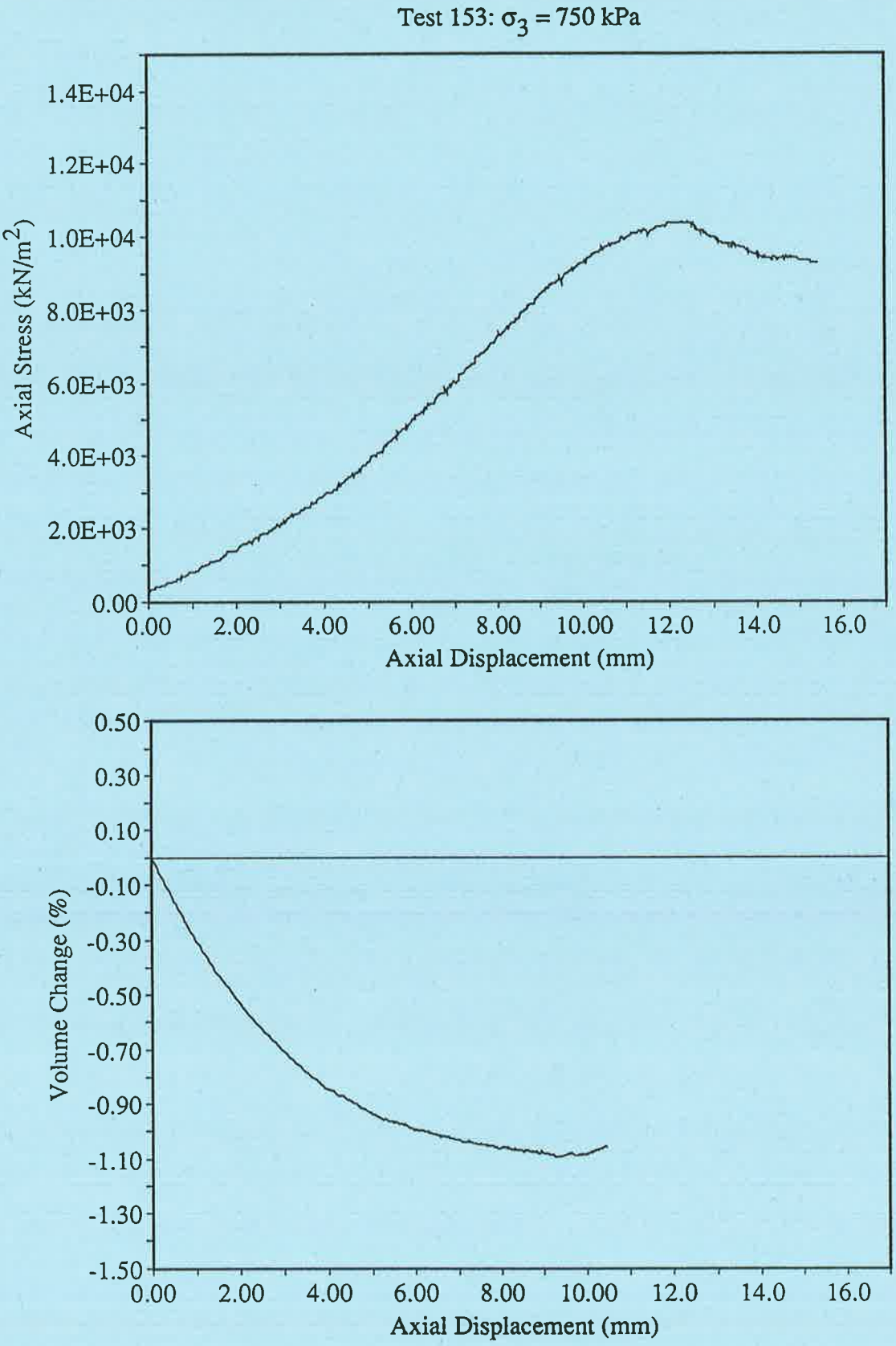

Figure E.26. Test 153, Geometry 2, 50/50 cement/sand specimens with infill, σ_3 = 750 kPa

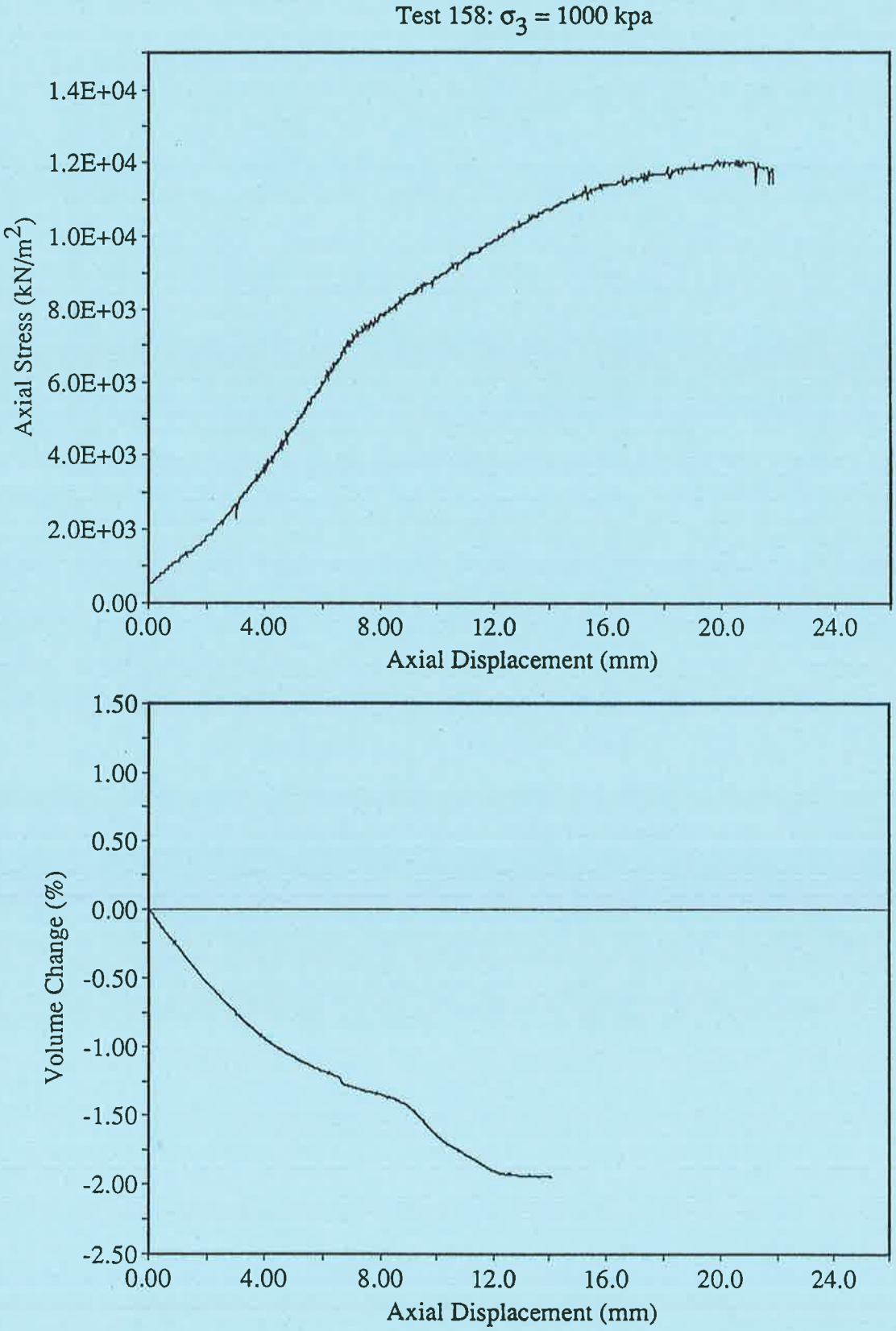

Figure E.27. Test 158, Geometry 2, 50/50 cement/sand specimens with infill, σ_3 = 1000 kPa

E.3. Geometry 3

E.3.1. Geometry 3 100% Gypsum Cement Specimens

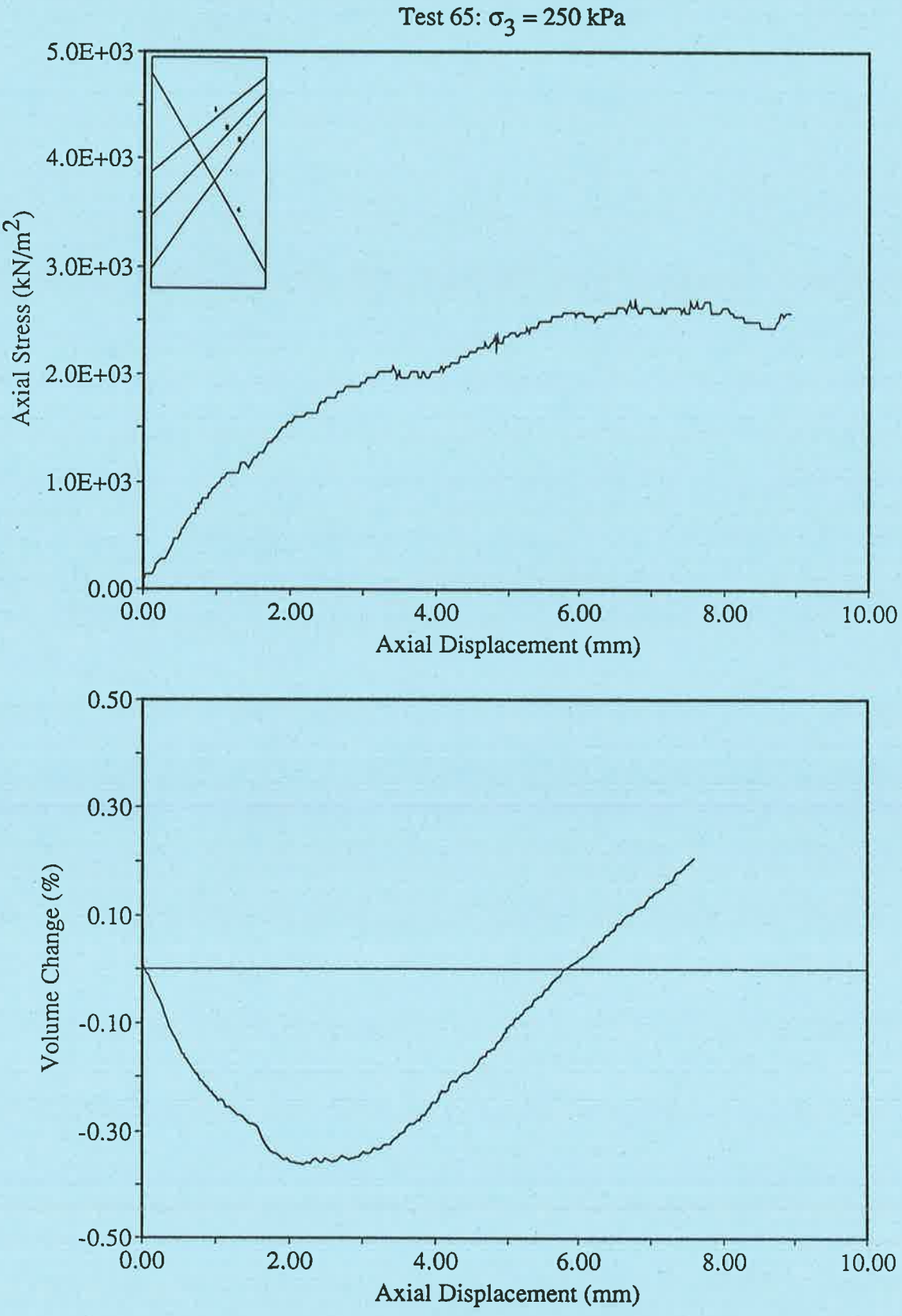

Figure E.28. Test 65, Geometry 3, 100% cement specimens, σ_3 = 250 kPa

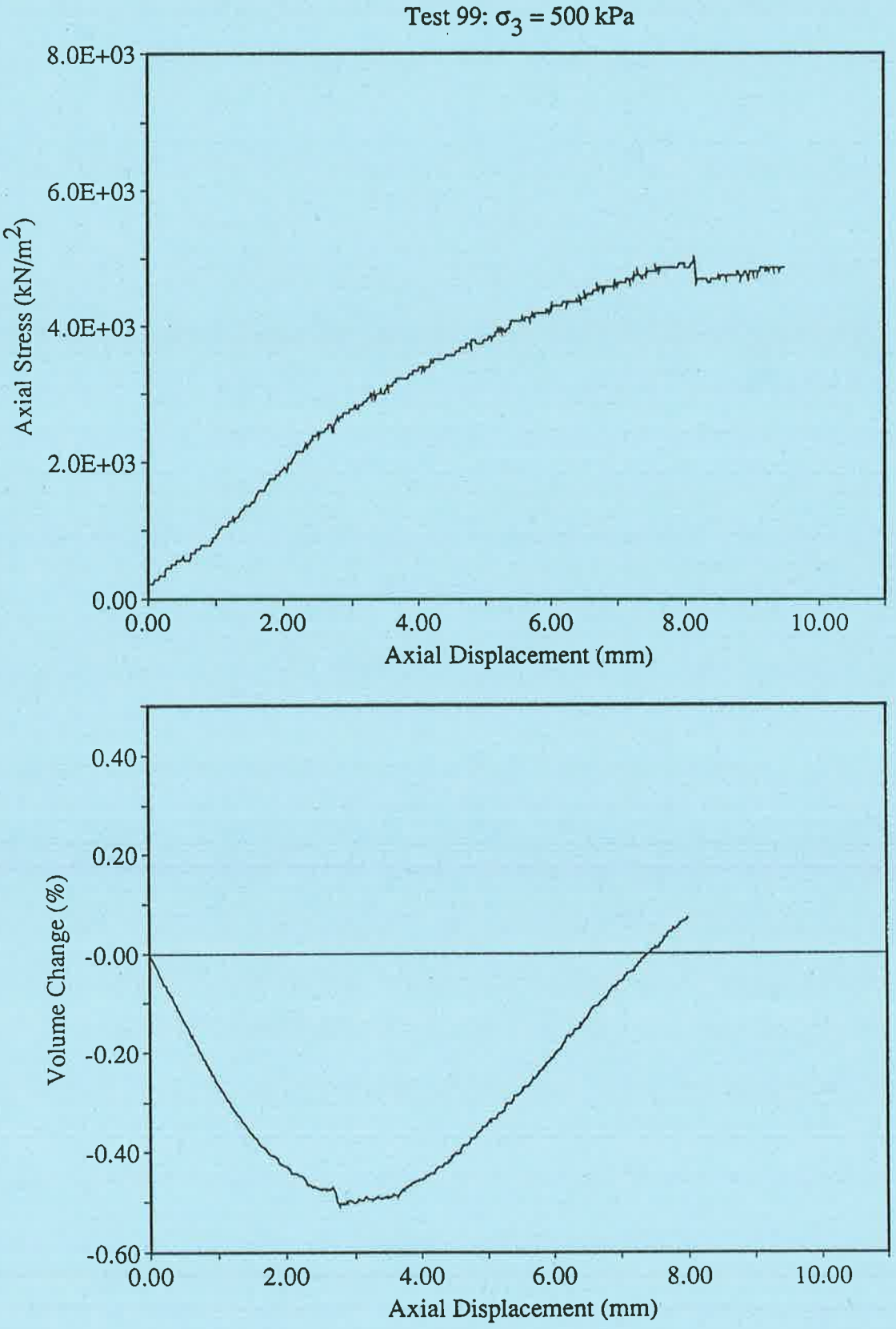

Figure E.29. Test 99, Geometry 3, 100% cement specimens, σ_3 = 500 kPa

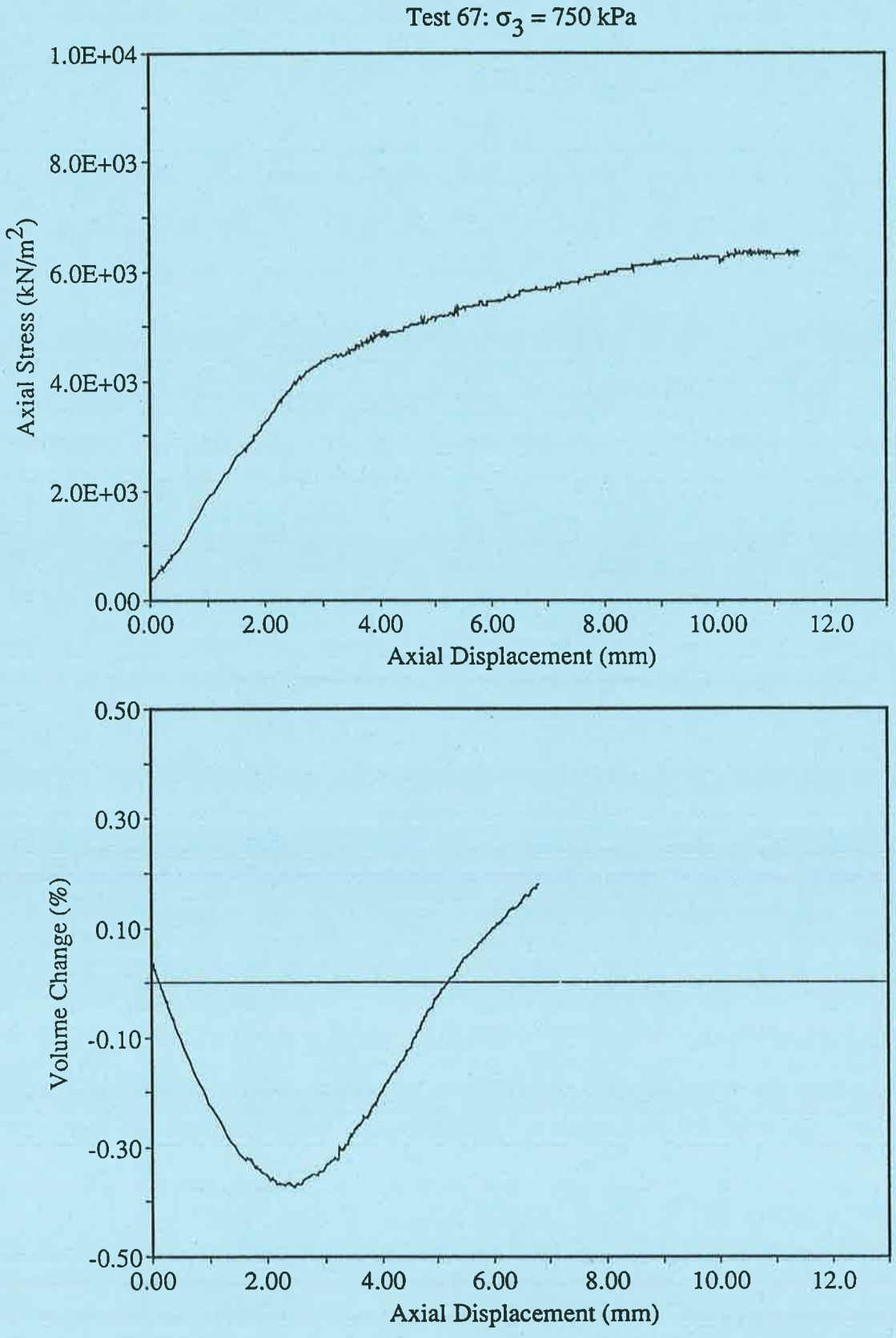

Figure E.30. Test 67, Geometry 3, 100% cement specimens, σ_3 = 750 kPa

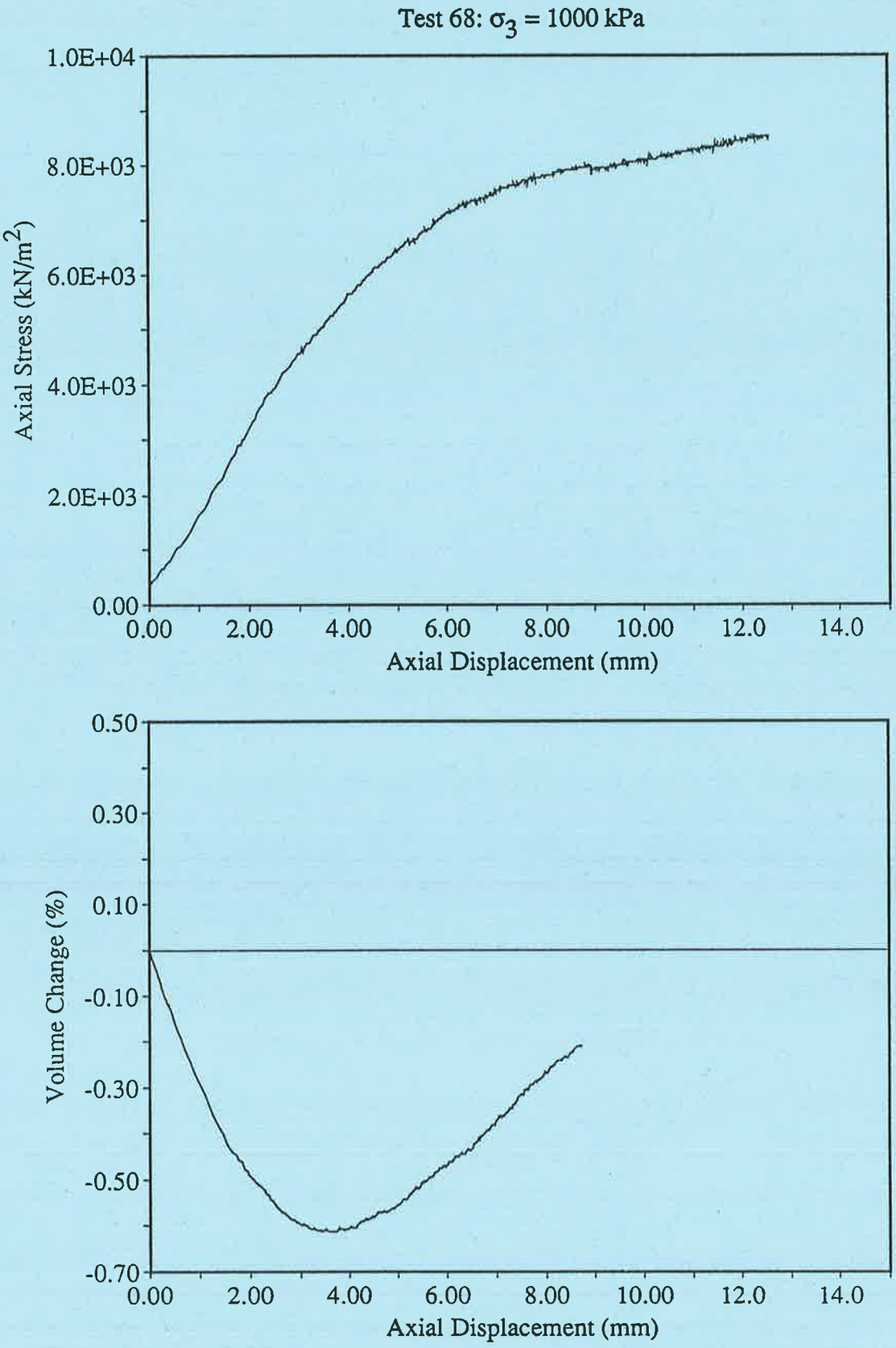

Figure E.31. Test 68, Geometry 3, 100% cement specimens, σ_3 = 1000 kPa

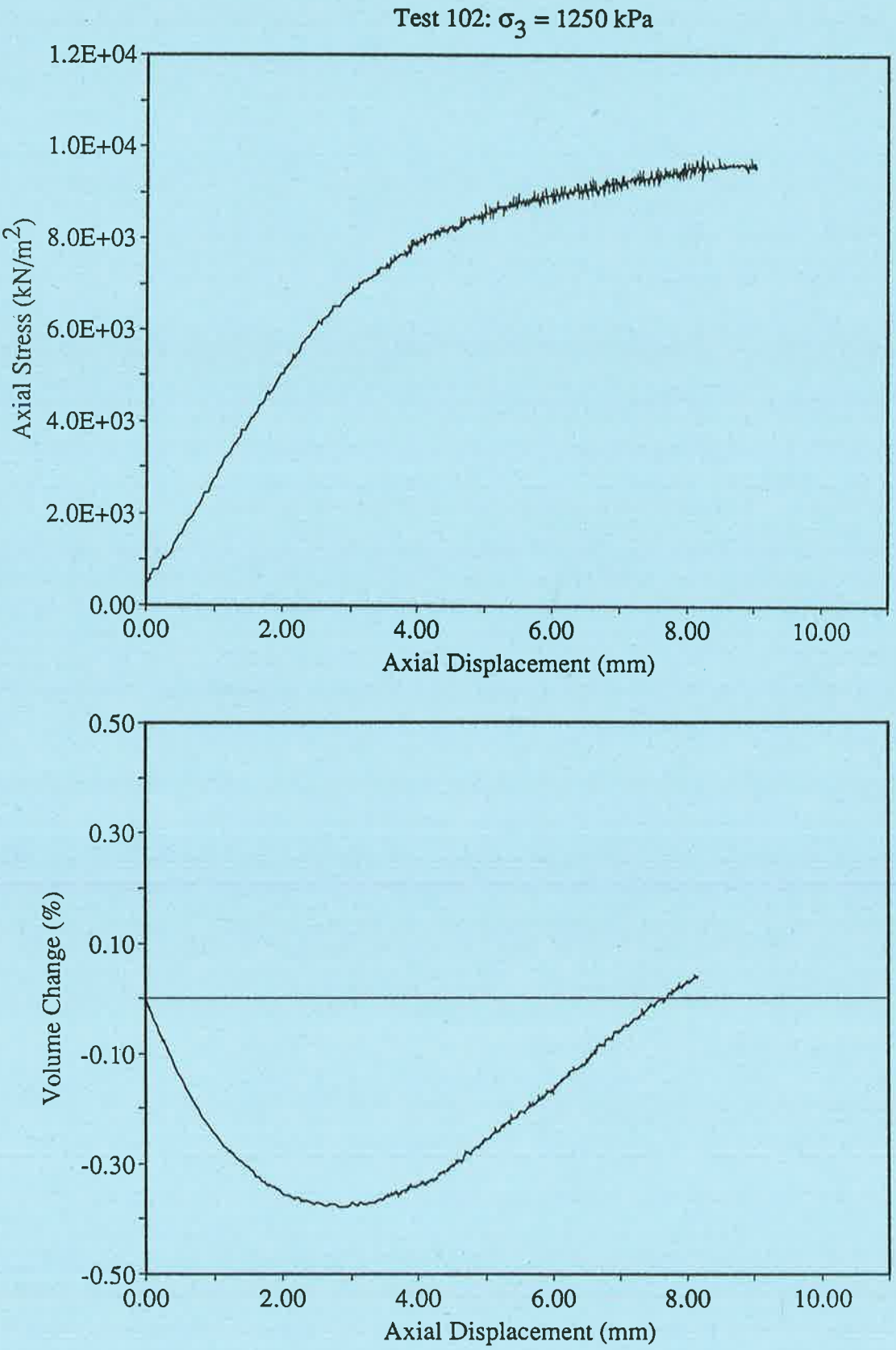

Figure E.32. Test 102, Geometry 3, 100% cement specimens, σ_3 = 1250 kPa

E.3.2. Geometry 3 50/50 Gypsum Cement/Sand Specimens

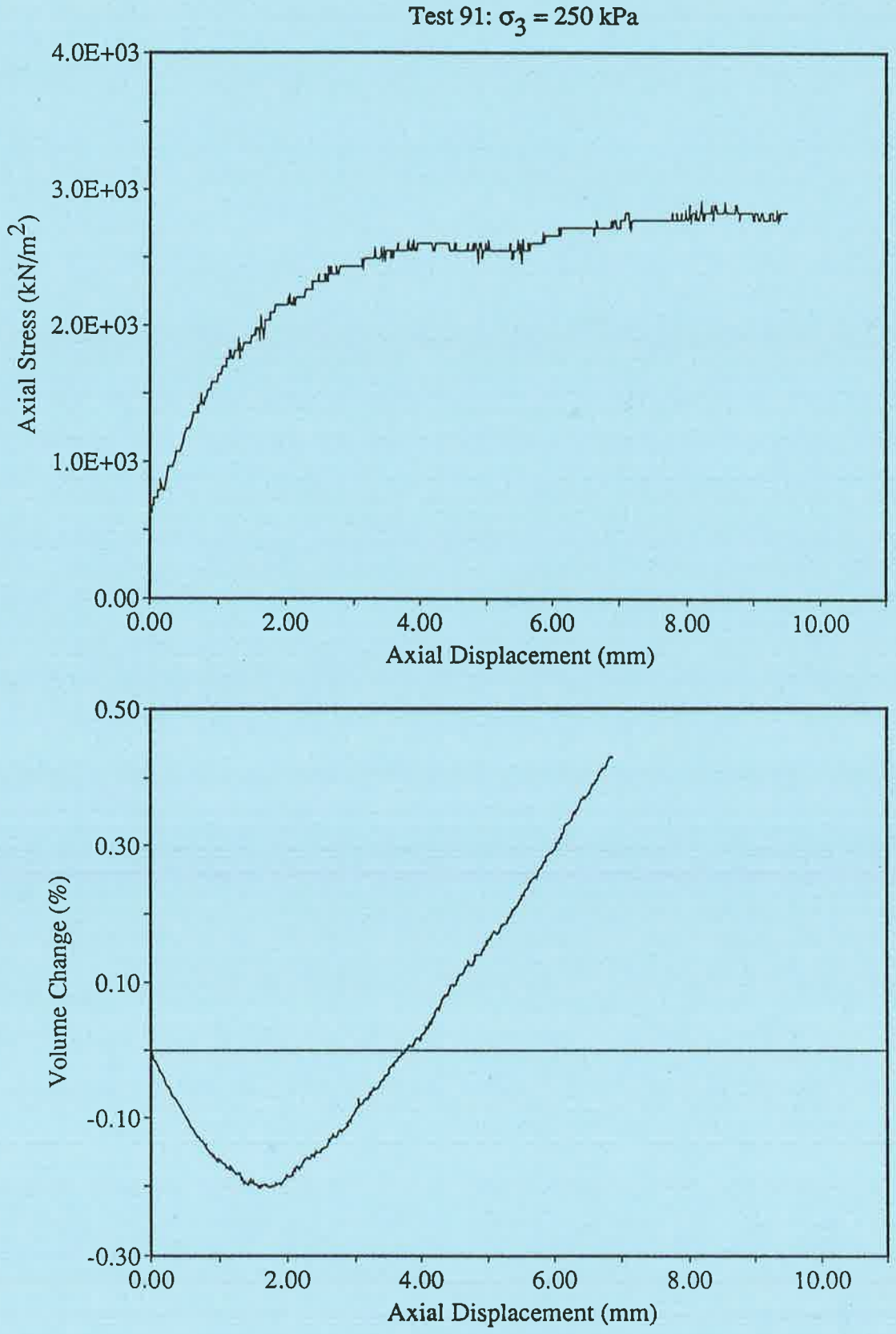

Figure E.33. Test 91, Geometry 3, 50/50 cement/sand specimens, σ_3 = 250 kPa

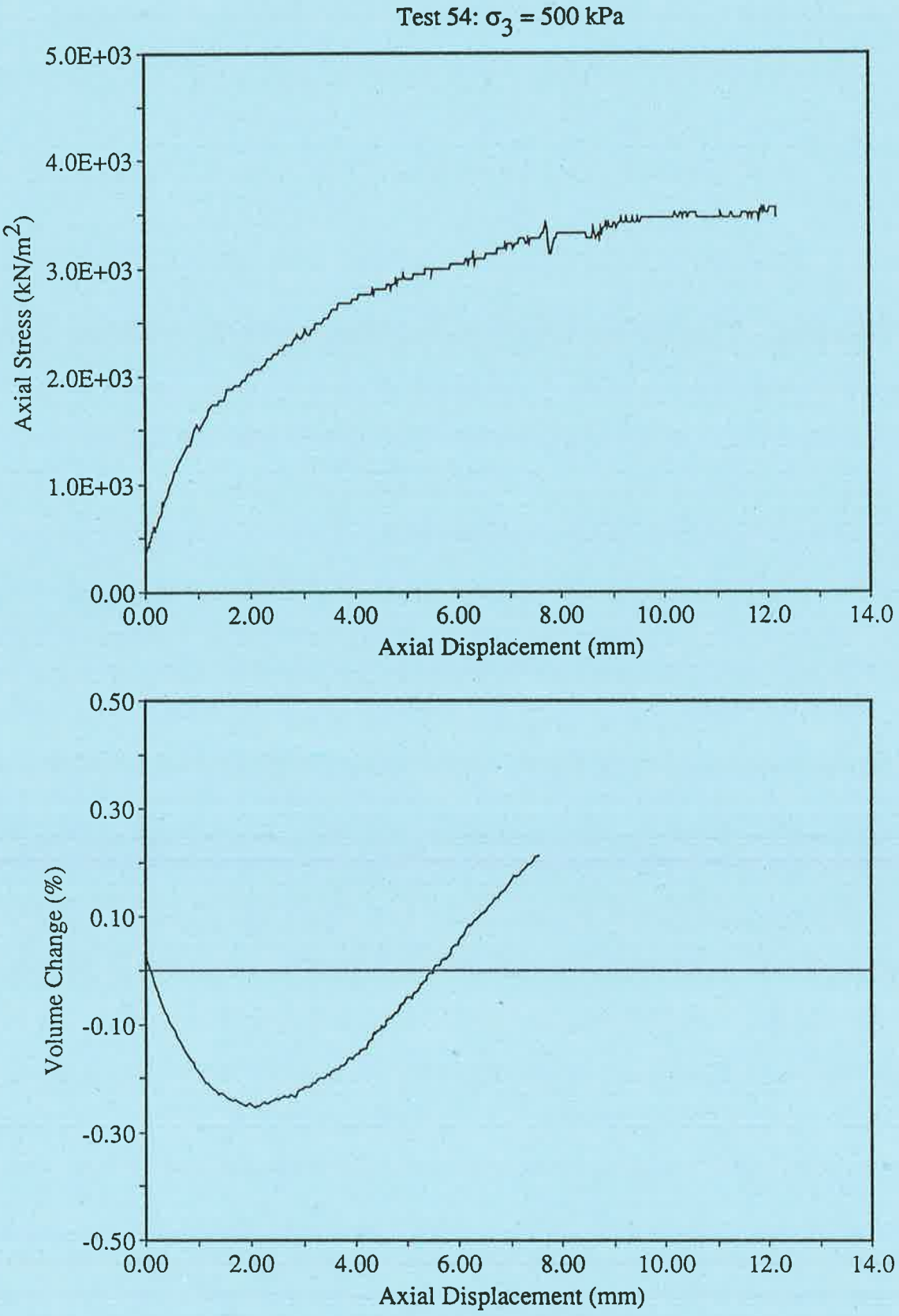

Figure E.34. Test 54, Geometry 3, 50/50 cement/sand specimens, σ_3 = 500 kPa

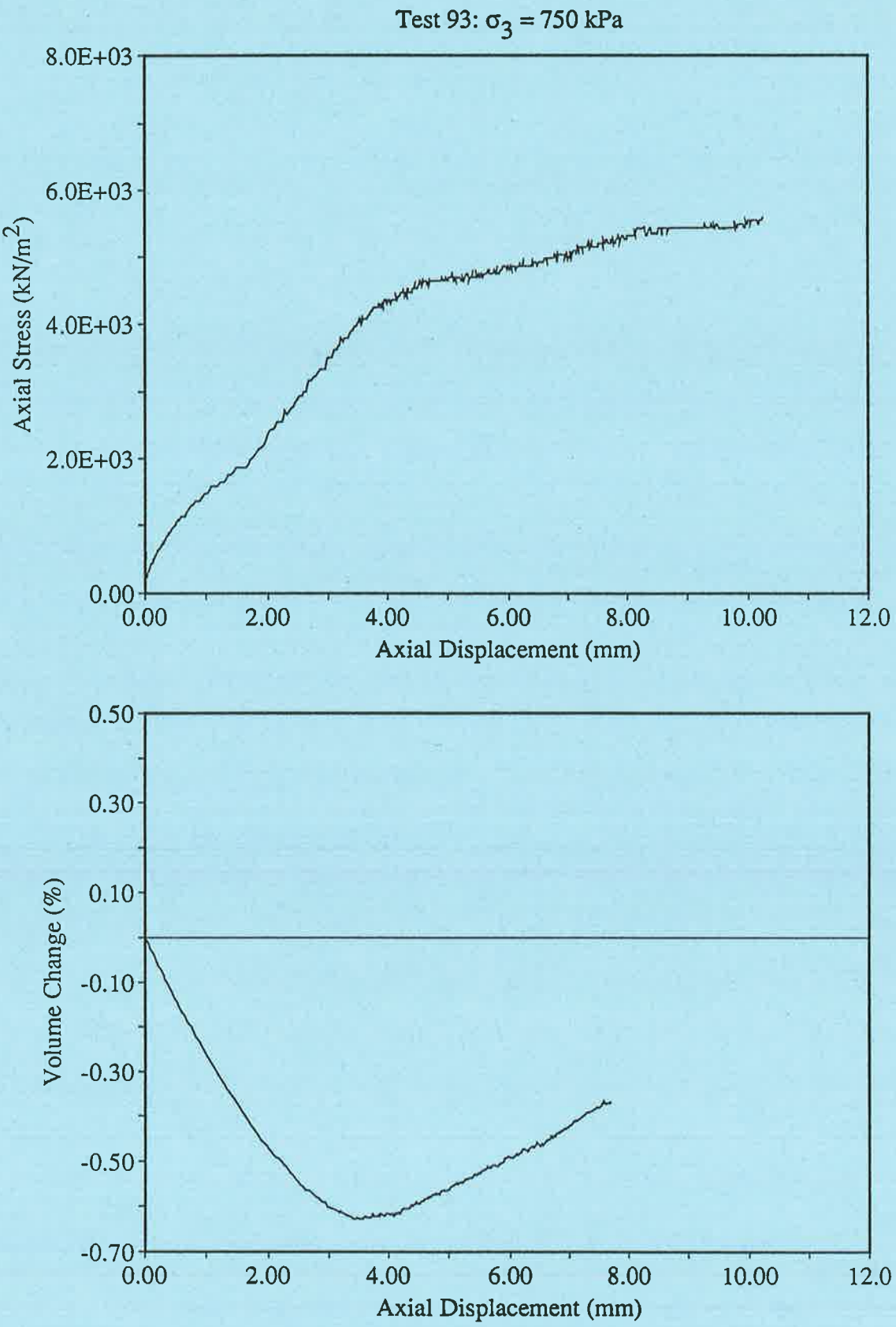

Figure E.35. Test 93, Geometry 3, 50/50 cement/sand specimens, σ_3 = 750 kPa

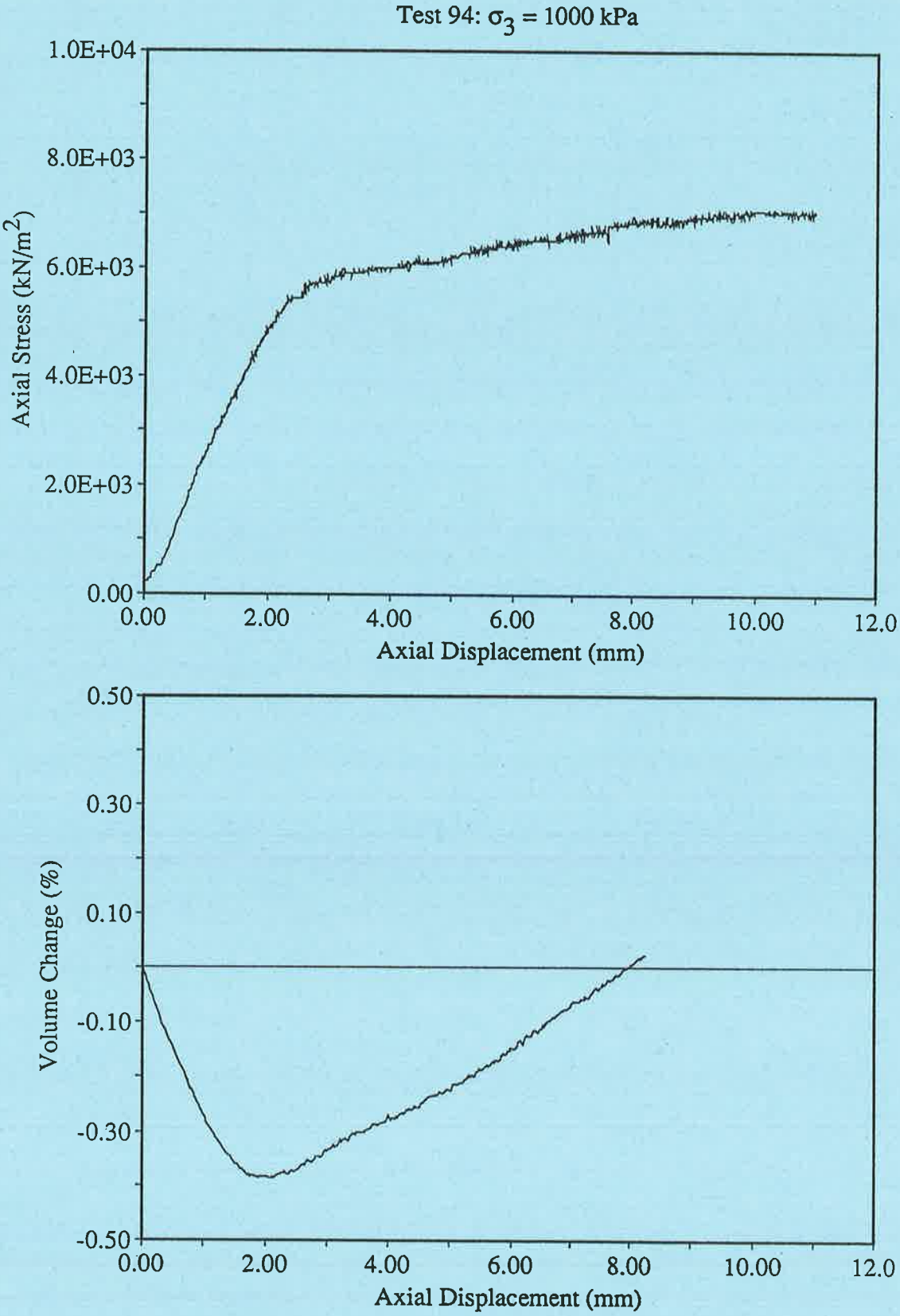

Figure E.36. Test 94, Geometry 3, 50/50 cement/sand specimens, σ_3 = 1000 kPa

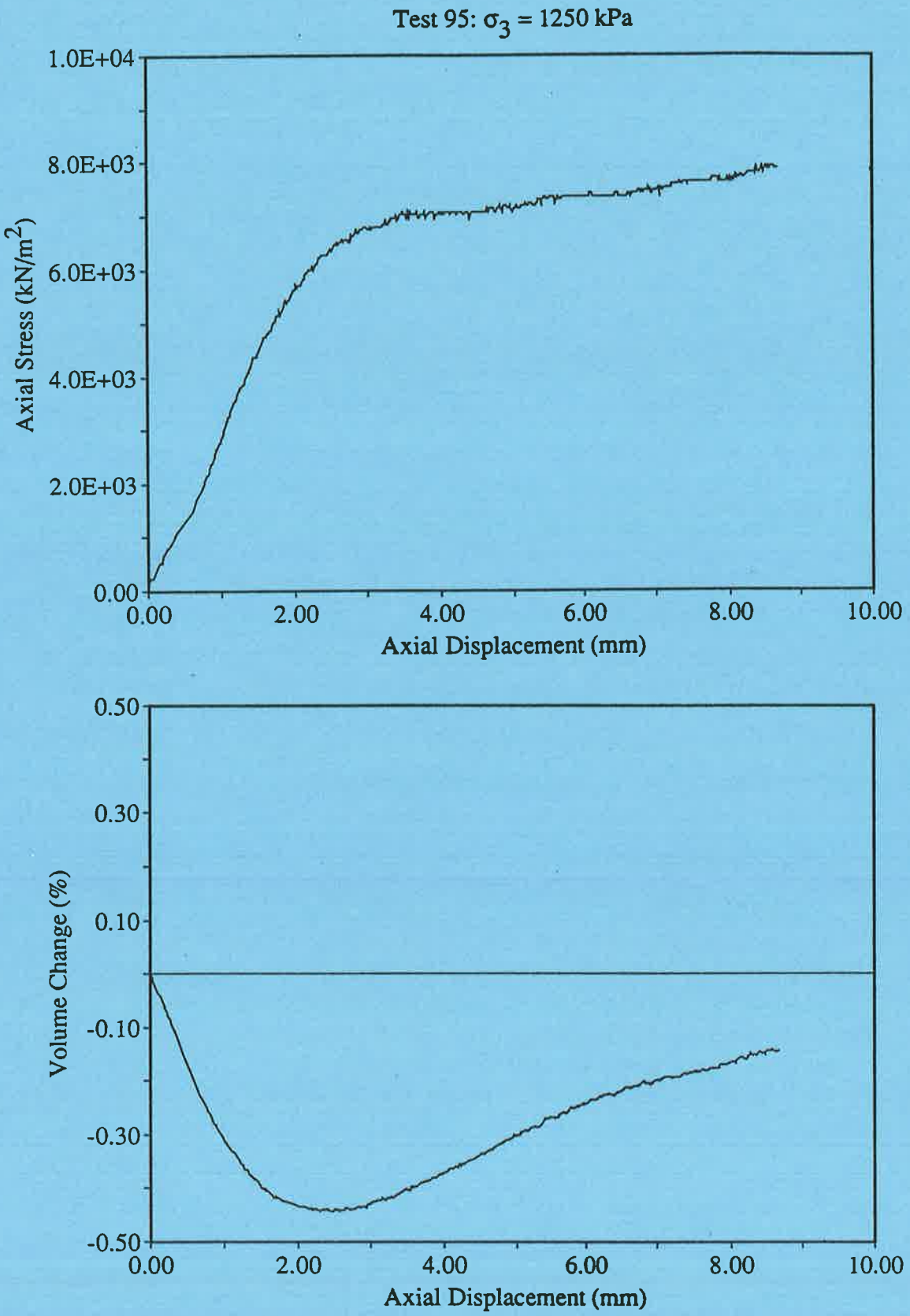

Figure E.37. Test 95, Geometry 3, 50/50 cement/sand specimens, σ_3 = 1250 kPa

E.3.3. Geometry 3 Specimens with Infill

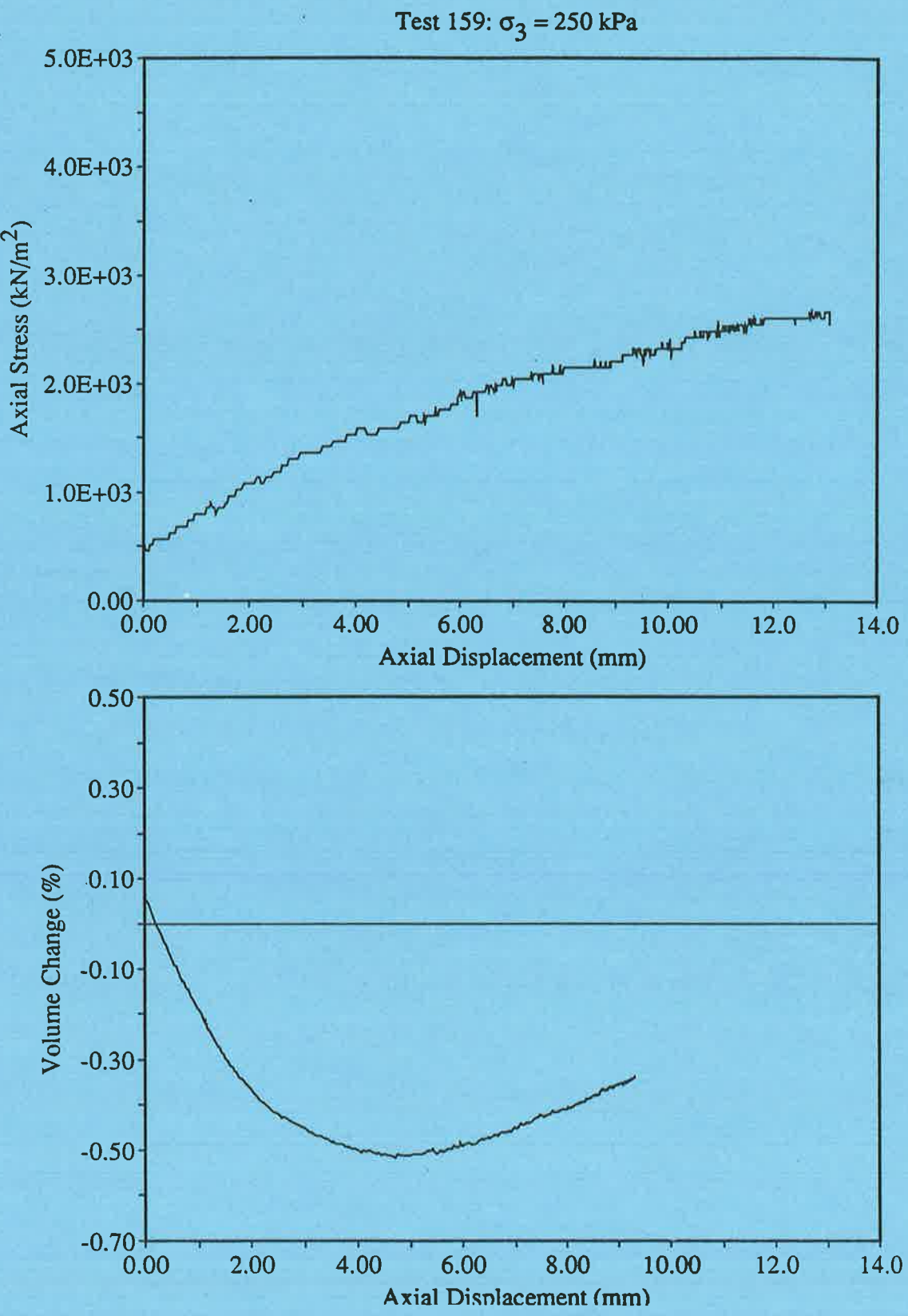

Figure E.38. Test 159, Geometry 3, 50/50 cement/sand specimens with infill, σ_3 = 250 kPa

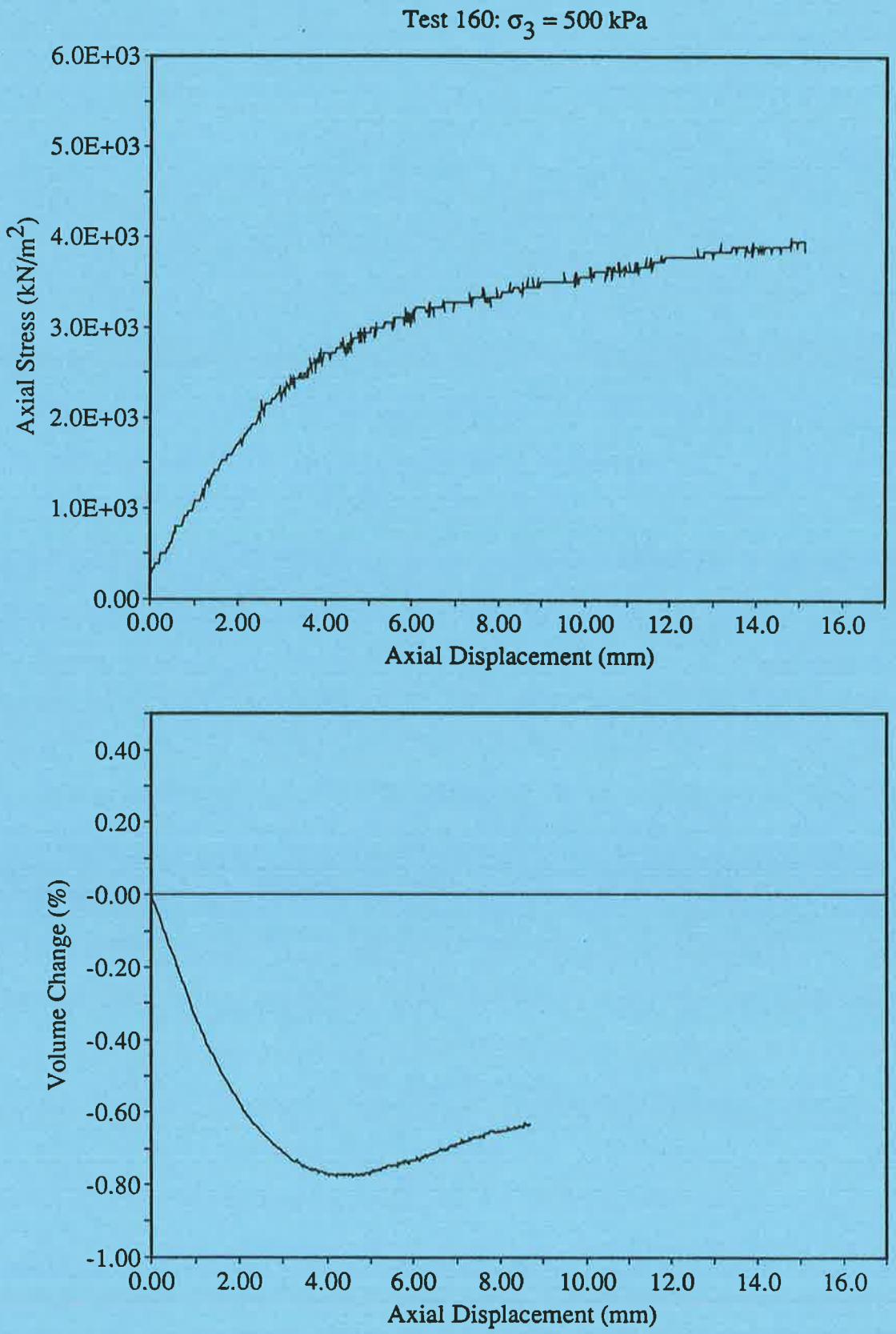

Figure E.39. Test 160, Geometry 3, 50/50 cement/sand specimens with infill, σ_3 = 500 kPa

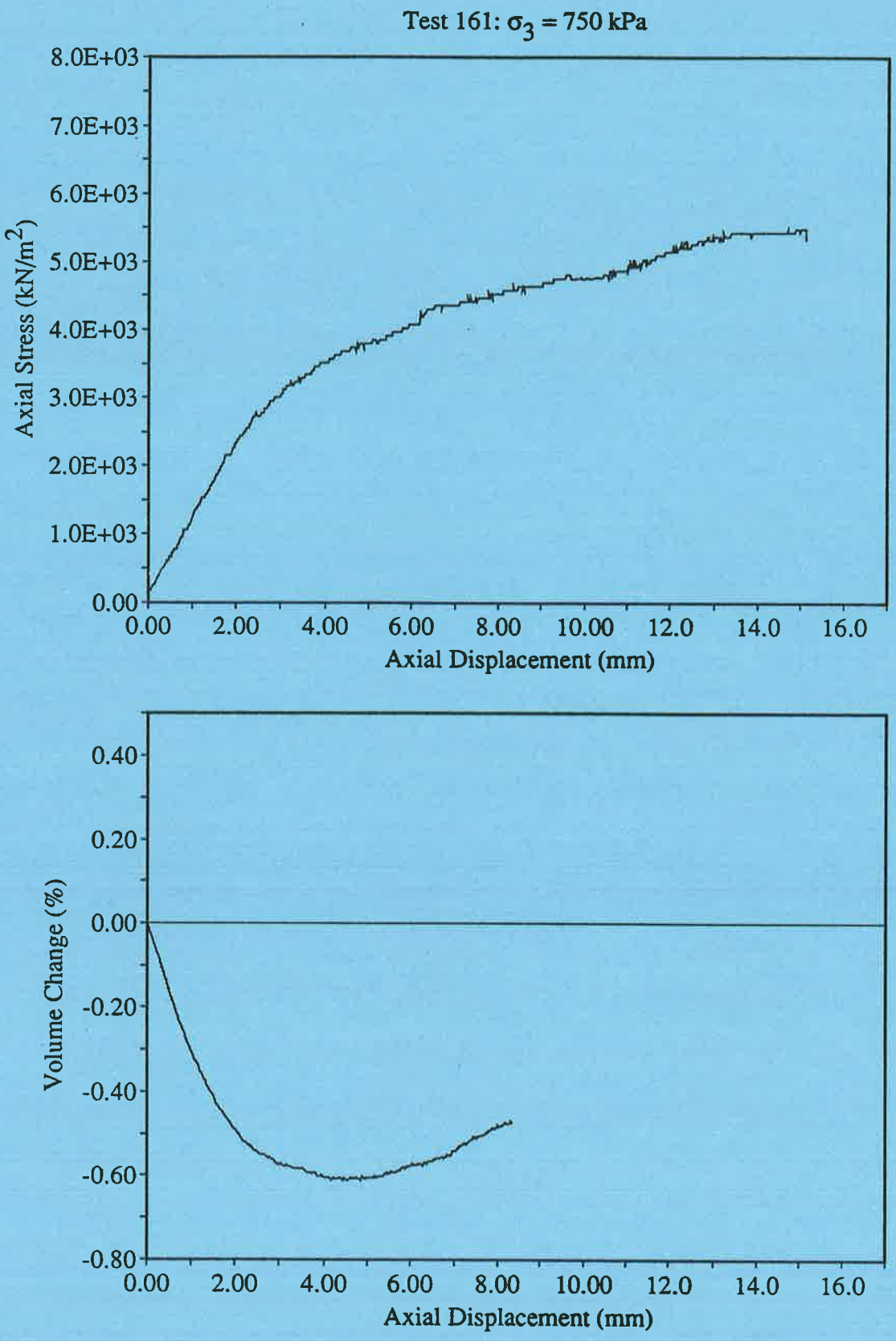

Figure E.40. Test 161, Geometry 3, 50/50 cement/sand specimens with infill, σ_3 = 750 kPa

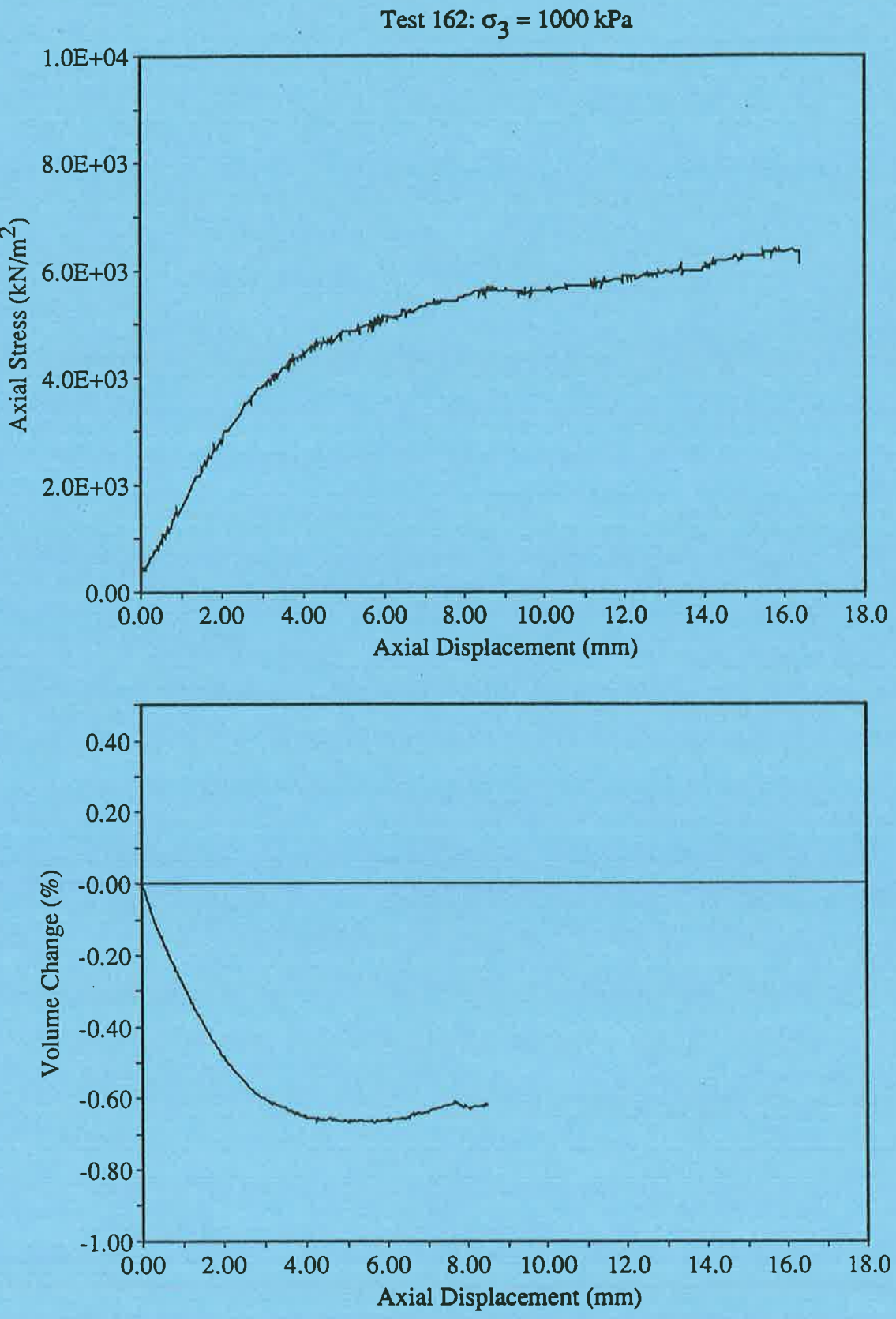

Figure E.41. Test 163, Geometry 3, 50/50 cement/sand specimens with infill, σ_3 = 1250 kPa

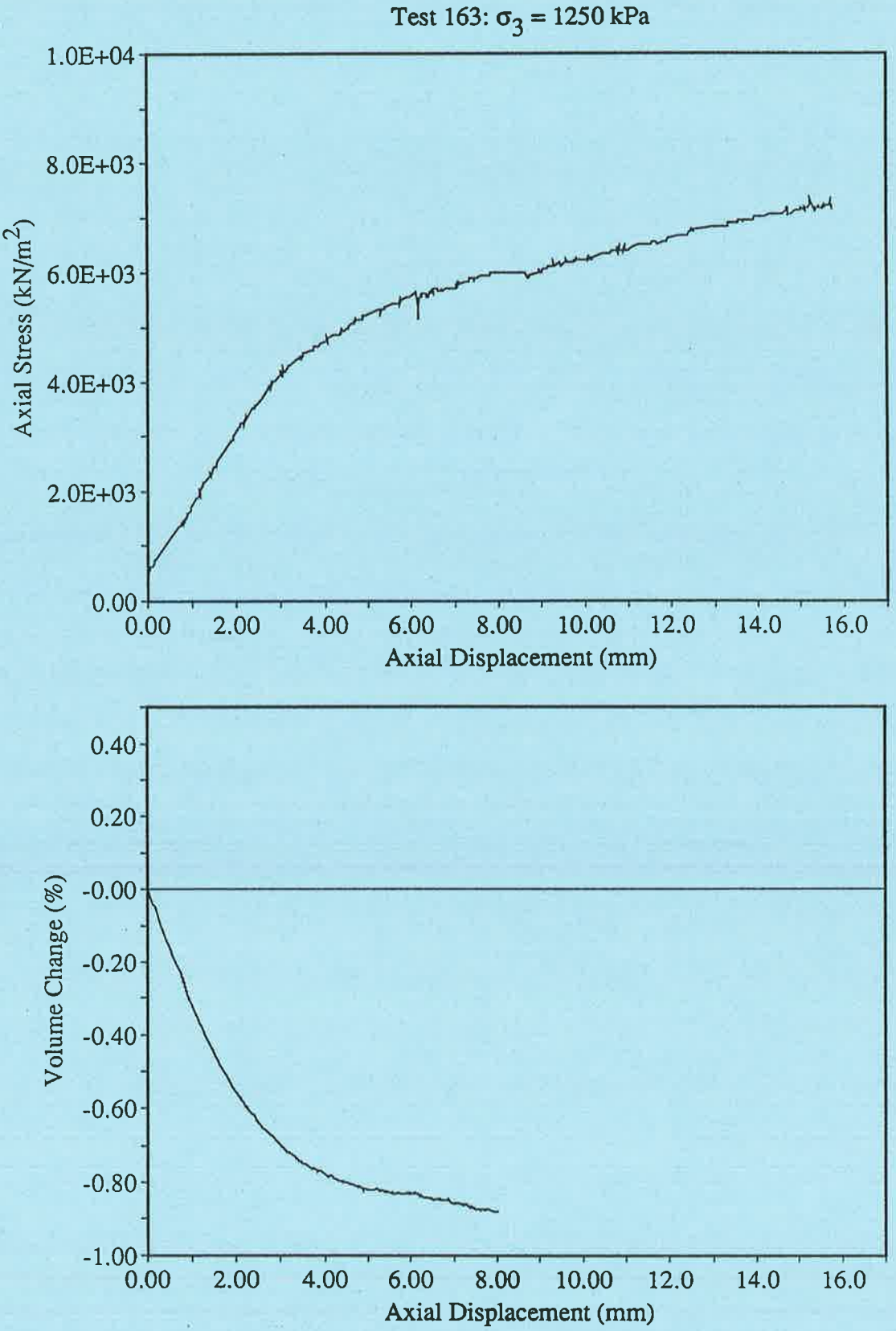

Figure E.41(b) Test 163 Geometry 3, 50/50 cement/sand specimens with infill, σ_3 = 1250 kPa

E.4. Geometry 4

E.4.1. Geometry 4 100% Gypsum Cement Specimens

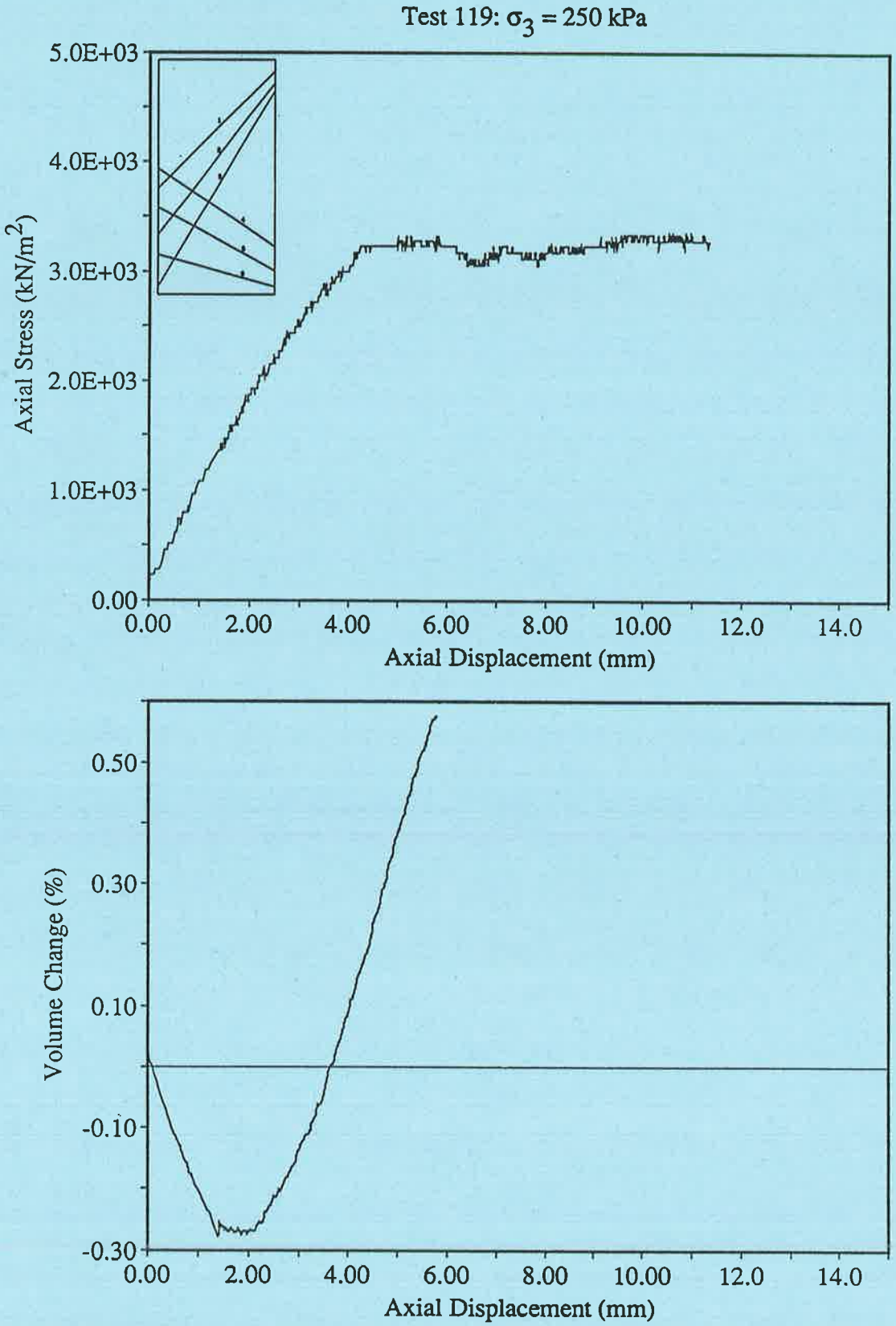

Figure E.42. Test 119, Geometry 4, 100% cement specimen, σ_3 = 250 kPa

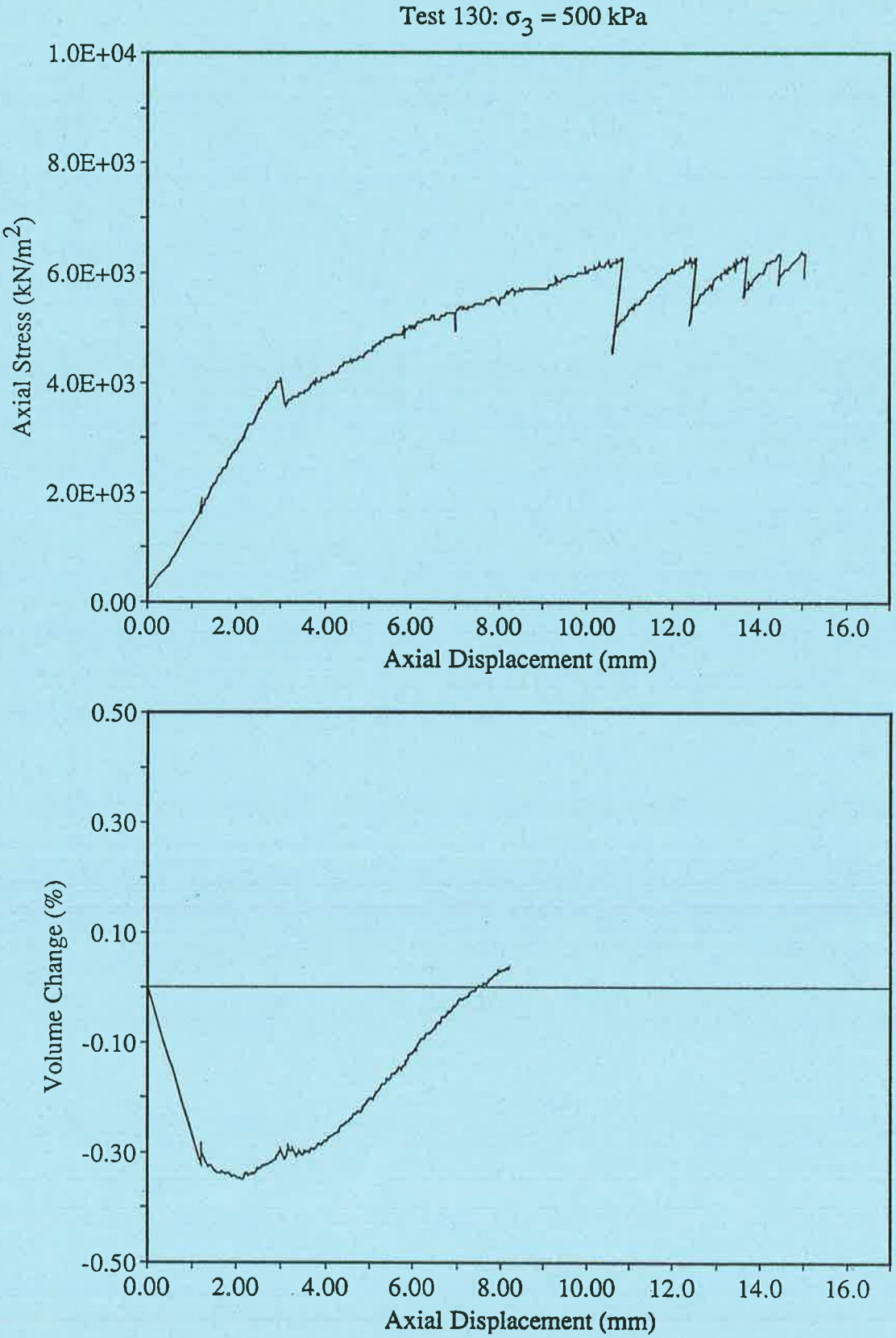

Figure E.43. Test 130, Geometry 4, 100% cement specimen, σ_3 = 500 kPa

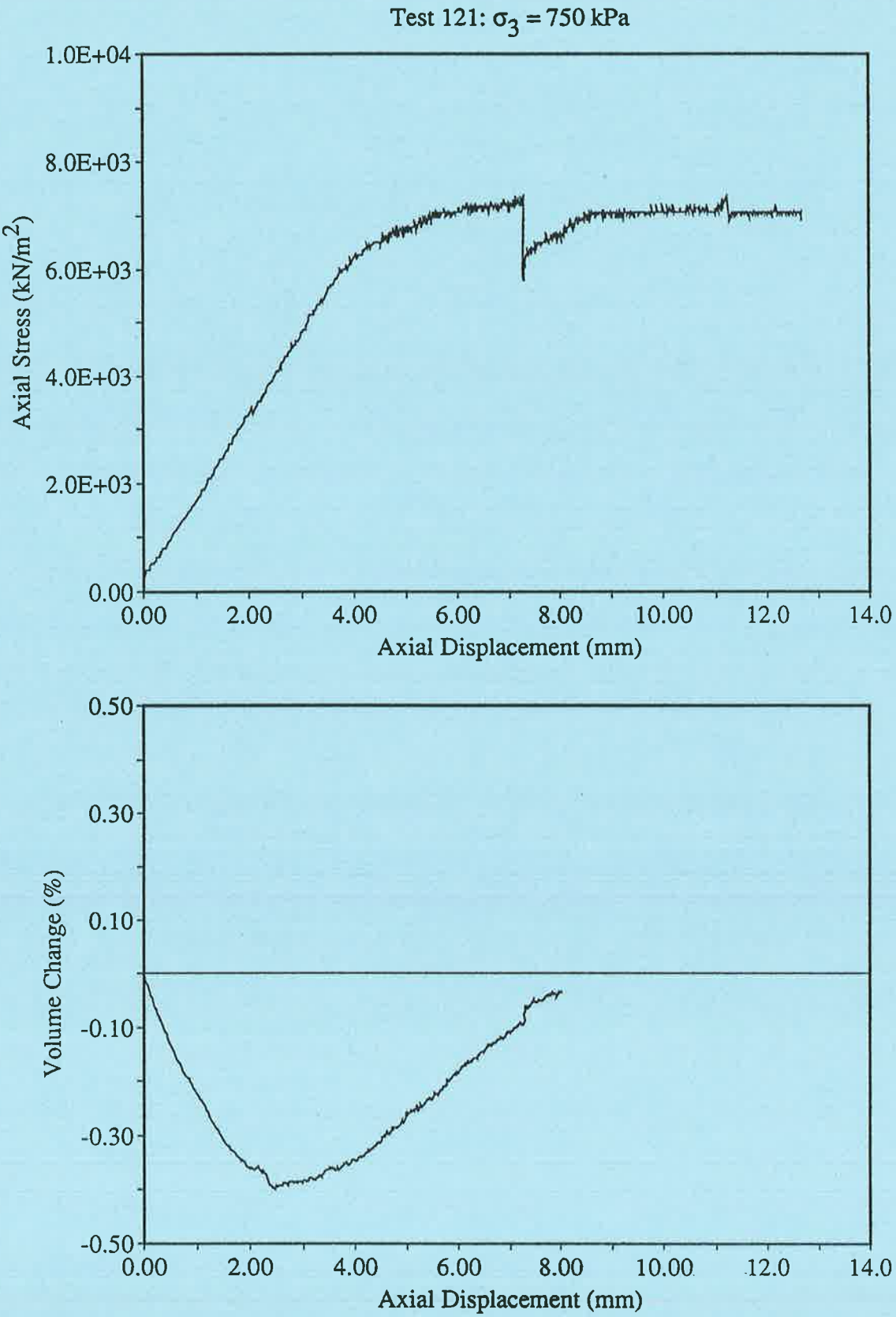

Figure E.44. Test 121, Geometry 4, 100% cement specimen, σ_3 = 750 kPa

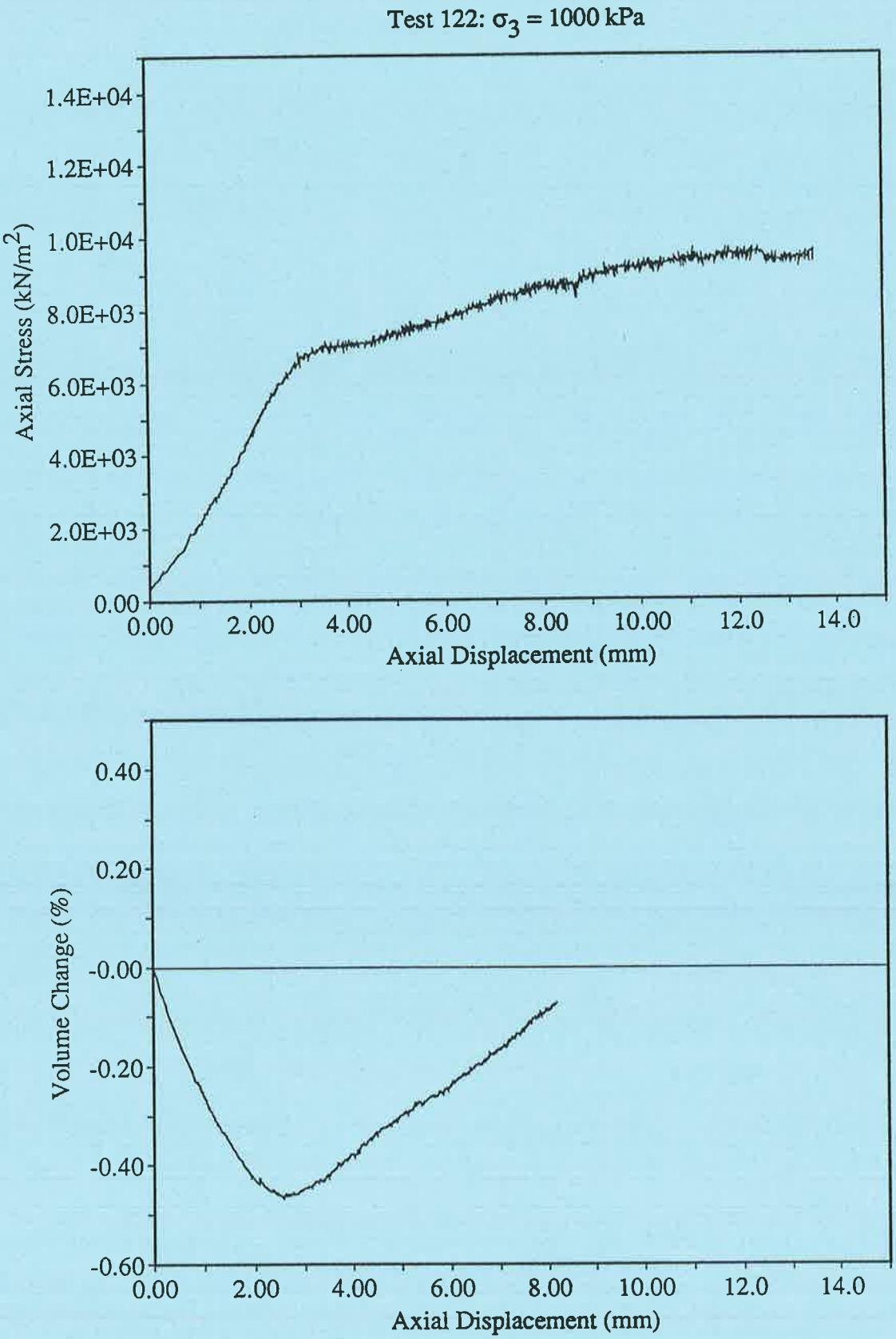

Figure E.45. Test 122, Geometry 4, 100% cement specimen, σ_3 = 1000 kPa

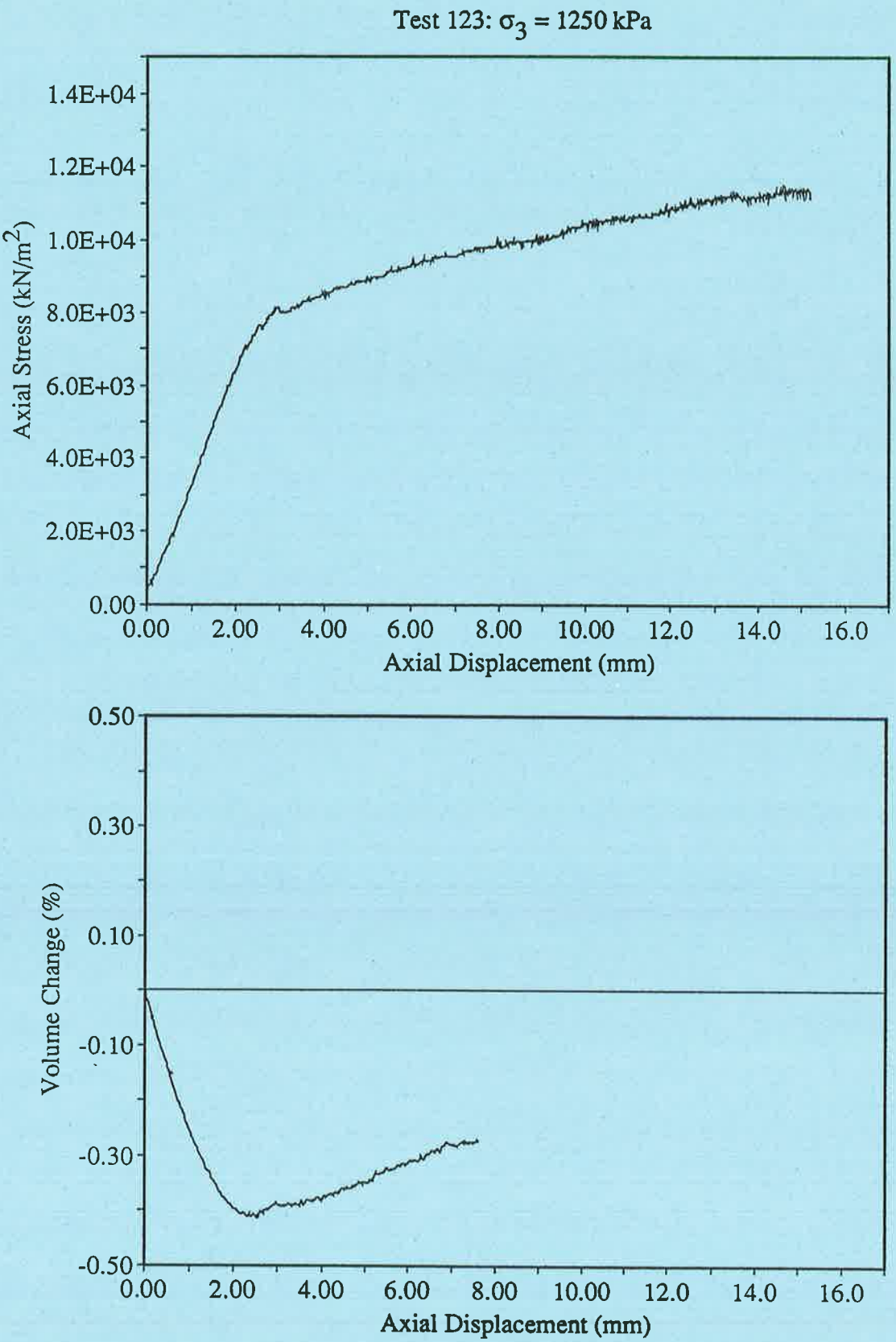

Figure E.46. Test 123, Geometry 4, 100% cement specimen, σ_3 = 1250 kPa

E.4.2. Geometry 4 50/50 Gypsum Cement/Sand Specimens

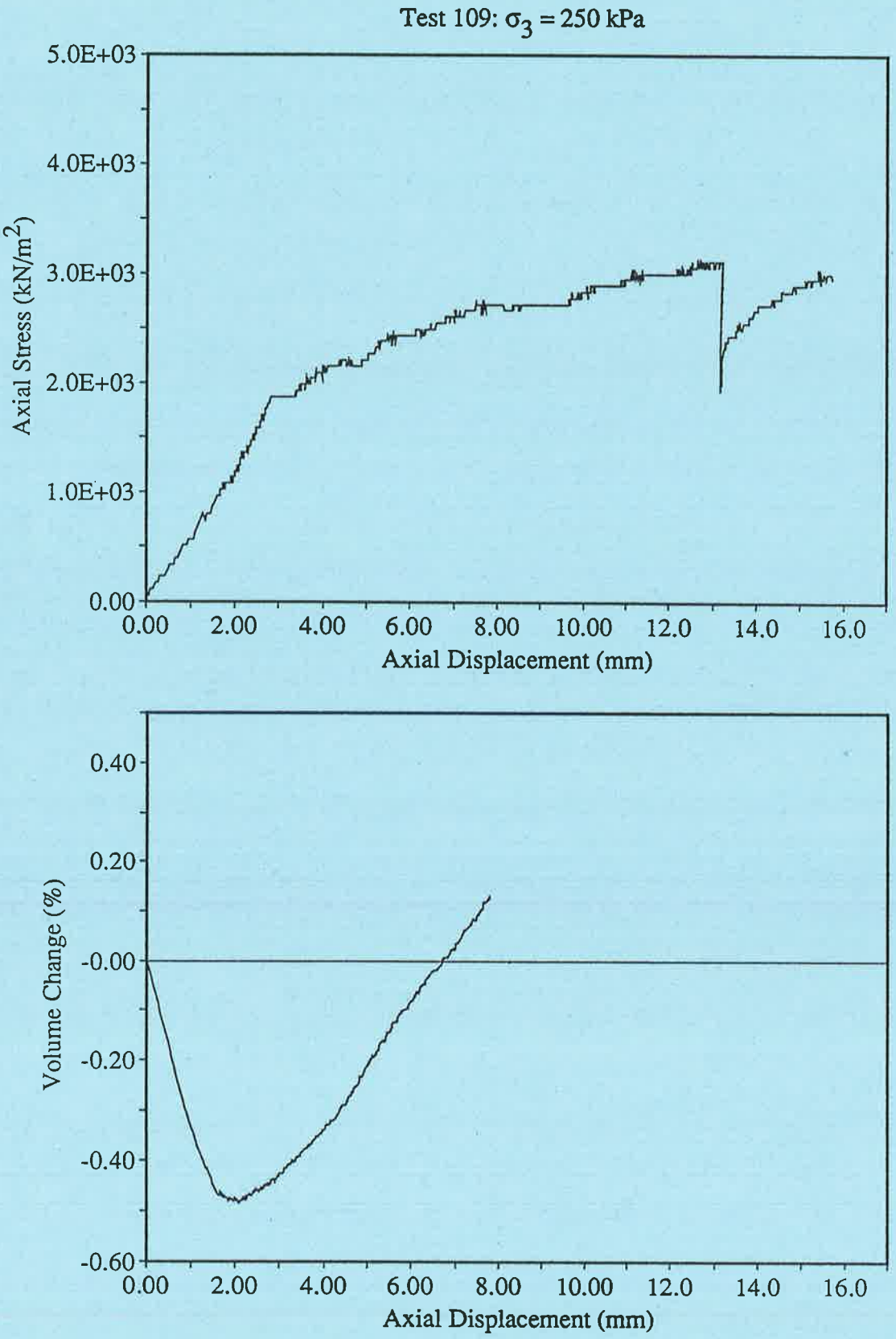

Figure E.47. Test 109, Geometry 4, 50/50 cement/sand specimen, σ_3 = 250 kPa

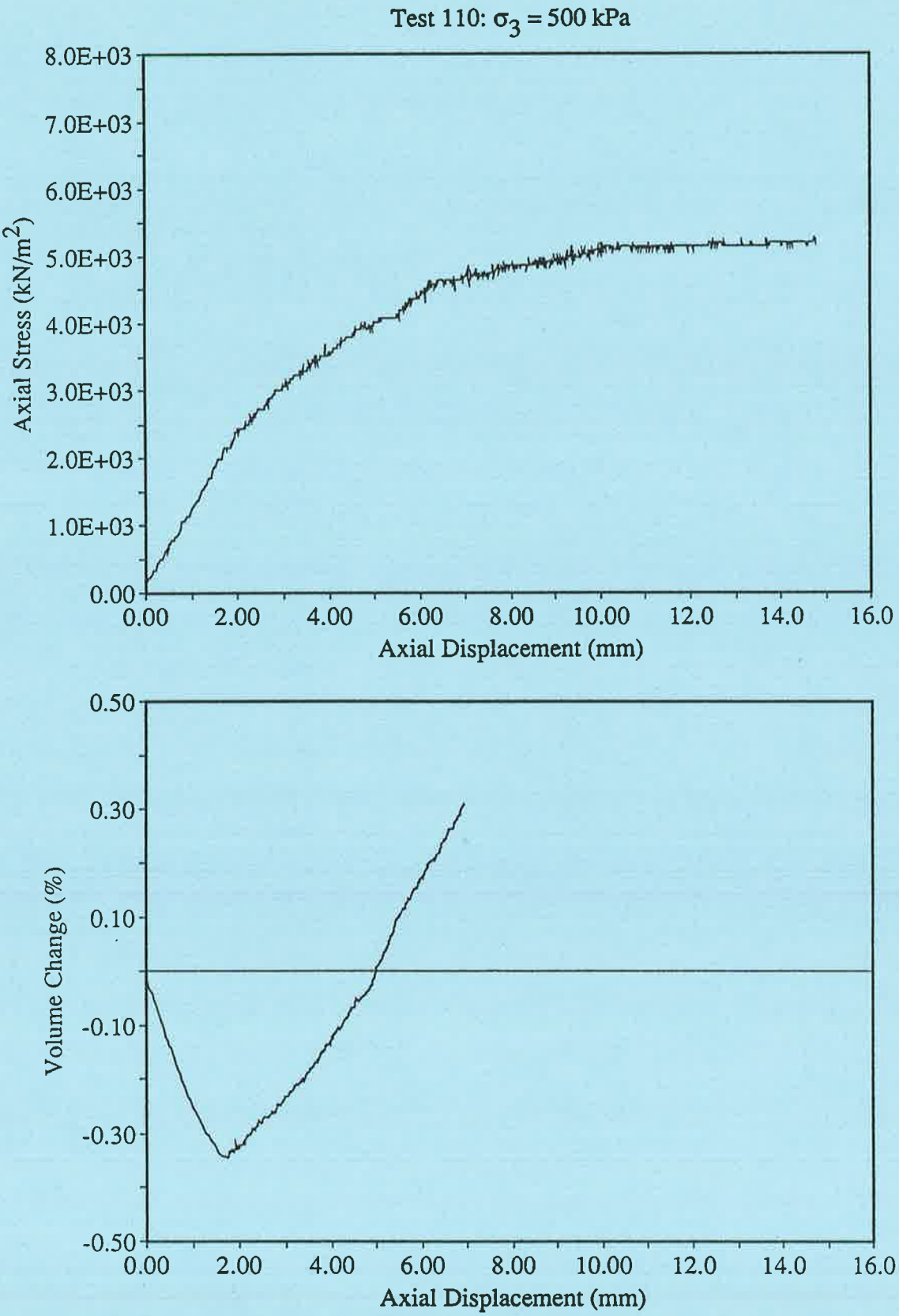

Figure E.48. Test 110, Geometry 4, 50/50 cement/sand specimen, σ_3 = 500 kPa

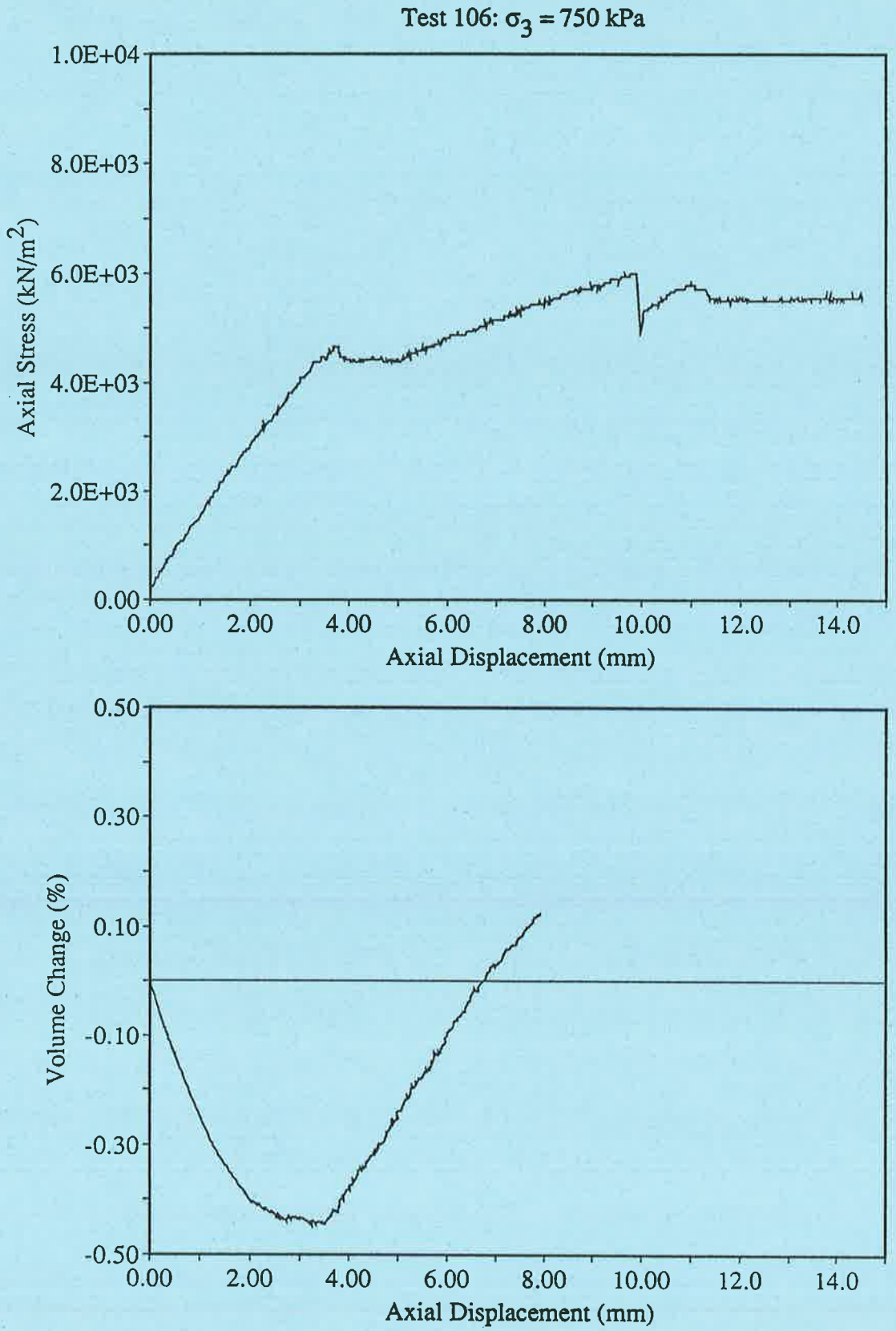

Figure E.49. Test 106, Geometry 4, 50/50 cement/sand specimen, σ_3 = 750 kPa

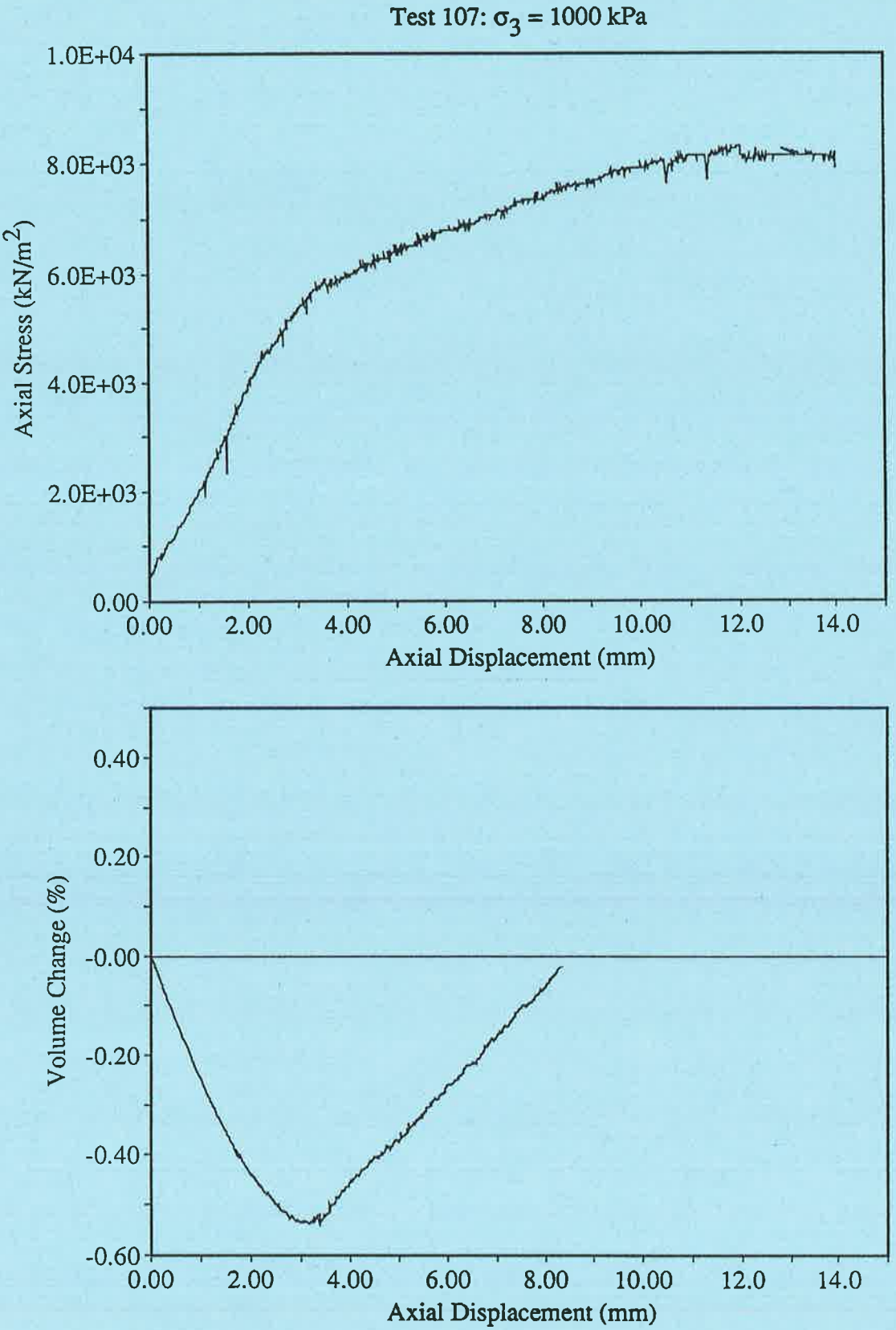

Figure E.50. Test 107, Geometry 4, 50/50 cement/sand specimen, σ_3 = 1000 kPa

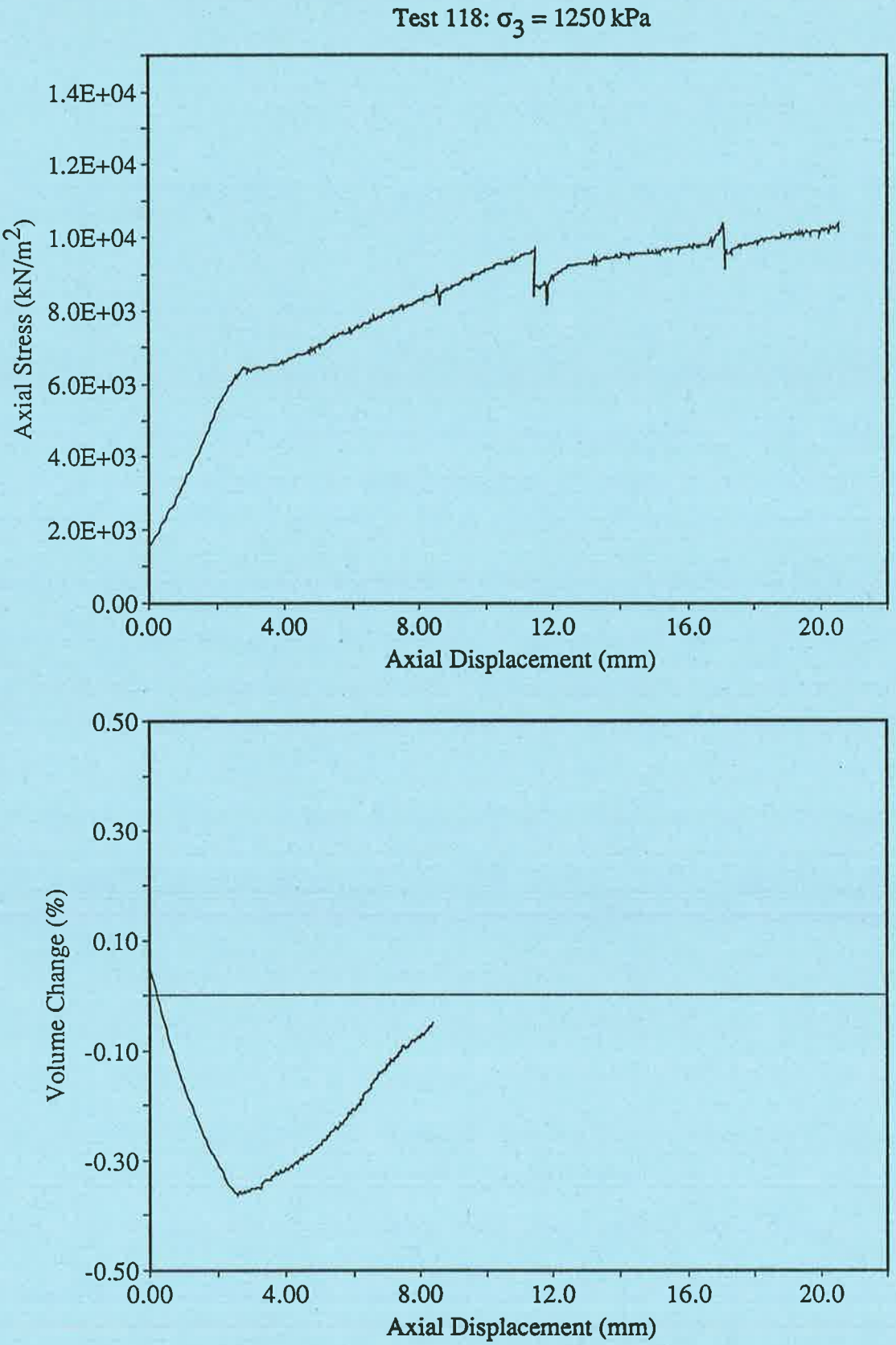

Figure E.51. Test 118, Geometry 4, 50/50 cement/sand specimen, σ_3 = 1250 kPa

E.4.3. Geometry 4 Specimens with Infill

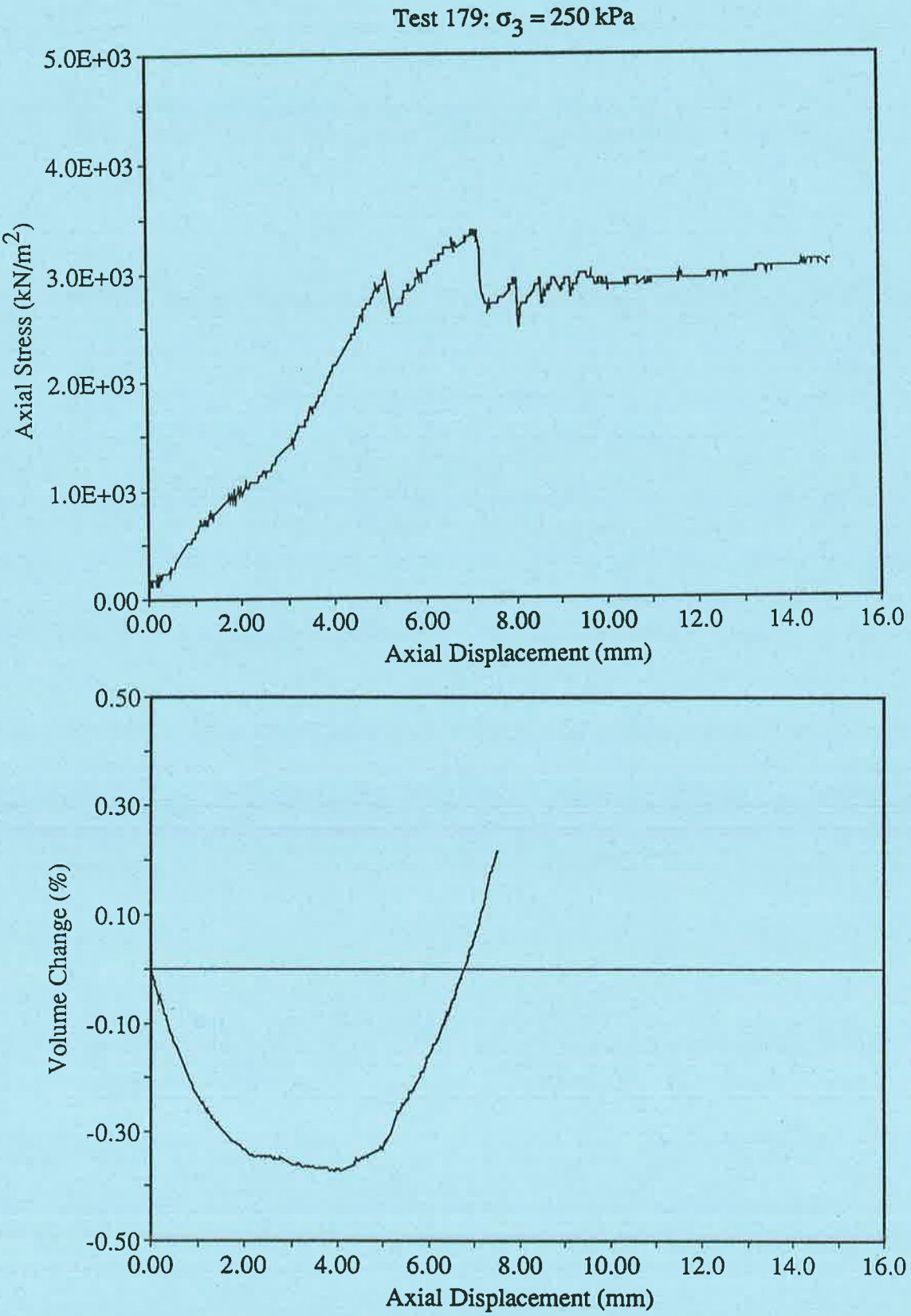

Figure E.52. Test 179, Geometry 4, 50/50 cement/sand specimen with infill, σ_3 = 250 kPa

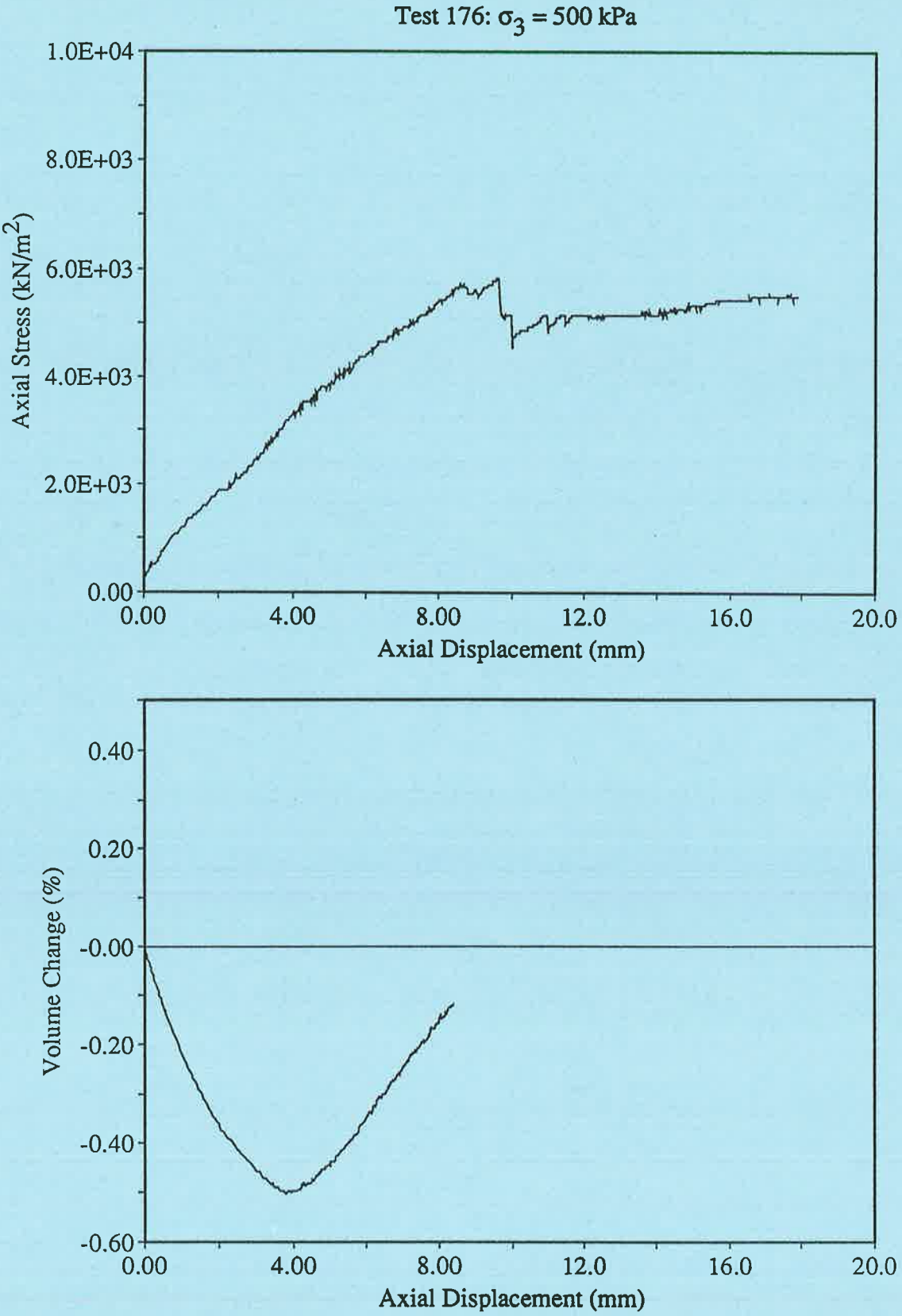

Figure E.53. Test 176, Geometry 4, 50/50 cement/sand specimen with infill, σ_3 = 500 kPa

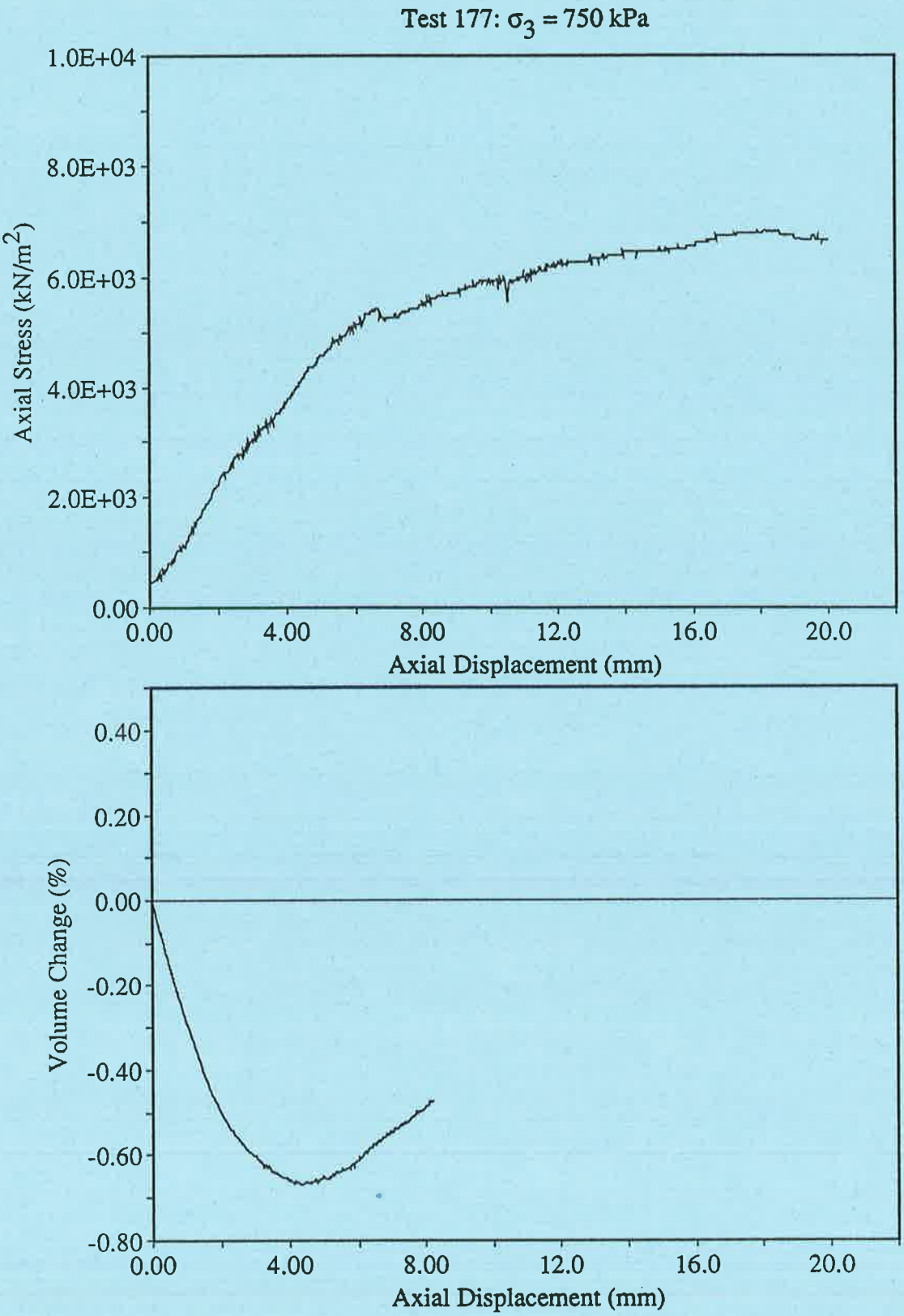

Figure E.54. Test 177, Geometry 4, 50/50 cement/sand specimen with infill, σ_3 = 750 kPa

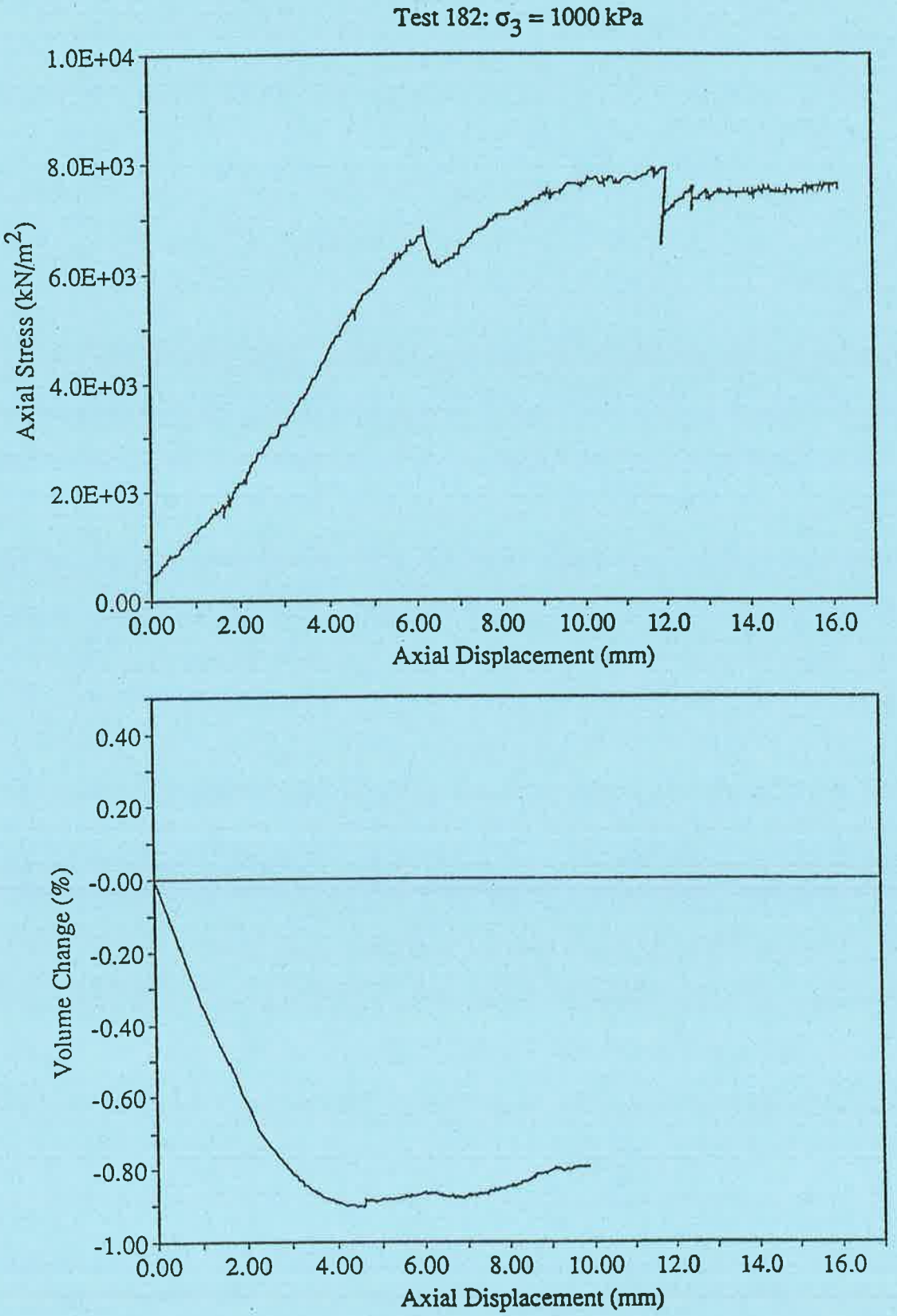

Figure E.55. Test 182, Geometry 4, 50/50 cement/sand specimen with infill, σ_3 = 1000 kPa

Appendix F.
UDEC Input Files

Appendix F. UDEC Input Files.

This appendix contains examples of the UDEC input files used in the verification tests discussed in Chapter 8.

F.1. Verification Test 1: Intact Material.

```
* Specify block corner rounding length and domain dimensions
round          0.001
block          (0,0) (0,3) (1.5,3) (1.5,0)
* Create a single horizontal discontinuity
split          (0,1.0) (1.5,1.0)
* Make blocks fully deformable with quadrilateral finite difference zones
gen quad       0.5 0.5
* Define properties of intact material and discontinuities
prop mat=1     dens=2.4e-3  k=3900  g=2200  coh=9.0  tens=8.6  fric=37
+              jkn=150e9  jks=651 jf=33.8
* Apply hydrostatic stress conditions and fix lower boundary
bound stress   -0.25  0  -0.25
insitu stress  -0.25  0  -0.25
bound          -0.1 1.6 -0.1 0.1 yvel=0
* cycle to equilibrium
cycle          5000
* apply a constant velocity to upper boundary
bound          -0.1 1.6  2.9 3.1 yvel=-0.01
* cycle to equilibrium
cycle          45000
```

F.2. Verification Test 2: Direct Shear Test

```
* Specify domain dimensions and block corner rounding size
round          0.001
block          (0.00 0.00) (0.00 0.06) (0.06 0.06) (0.06 0.00)
* Intersect block by a single horizontal discontinuity
crack          -0.01 0.03  0.07 0.03
* Material properties of block and discontinuity
prop mat=1     d=2400  k=3.9e9  g=2.2e9  jkn=150e9  jen=0.0  jks=1.18e6  jes=0.505
+              minjks=0.365e9  maxjks=1.8e9  jfric=35.4  jif=35.75  jr=1e-4
* Make block fully deformable and assign joint constitutive model
gen edge       0.07
change         jcons=3
* Apply hydrostatic boundary and in situ stress conditions
insitu stress  -965e3 0 -965e3
bound          -0.01 0.07 -0.01 0.07 stress -965e3 0 -965e3
* Apply velocity boundaries to lower block
bound          -0.01 0.07 -0.01 0.01 yvel=0
bound          cor=135,109 xvel=0 yvel=0
* Cycle to equilibrium
cycle          500
* Apply shearing velocity
bound          cor=148,122 xvel=-0.05
```

F.3. Verification Test 4: Multiple Discontinuities

```
* Specify block corner rounding size
round          0.005
* Specify domain size
block          (-0.004,-0.1) (-0.004,0.4) (0.154,0.4) (0.154,-0.1)
* Create membrane
split          0.000 -0.100 0.000 4.00
split          0.150 -0.100 0.150 4.00
* Create discontinuities
crack          0,0.2800 0.150,0.2254
crack          0,0.2465 0.150,0.1765
crack          0,0.2130 0.150,0.1264
crack          0,0.1795 0.150,0.0745
crack          0,0.1460 0.150,0.0201
crack          0,0.1627 0.150,0.2677
```

```
crack          0,0.0960 0.150,0.2010
crack          0,0.0465 0.150,0.1515
* Specimen intact material properties
prop mat=1     d=2400  k=3.89e9  g=2.22e9  coh=9.0e6  tens=8.6e6  fric=37
prop jmat=1    jkn=150e9  jen=0.0  jks=1.18e6  jes=0.505  minjks=0.365e9  maxjks=1.8e9
+              jfric=35.4  jif=35.75  jr=1.0e-4  jcoh=40e3
* Membrane material properties
prop mat=2     d=900  k=377e6  g=15e6  coh=68e6  tens=50e6  fric=20
prop jmat=2    jkn=150e12  jks=3.1e6  jfric=35  jcoh=964
* Assign all blocks as being fully deformable
gen edge       0.07
* Assign material types to blocks and joints and assign constituve model
change  0.000  0.150  -0.10  0.40  jcons=3  jmat=1  cons=3  mat=1
change -0.004  0.000  -0.10  0.40  jmat=2  cons=3  mat=2
change  0.150  0.154  -0.10  0.40  jmat=2  cons=3  mat=2
set jcondf     3
* Assign hydrostatic stress boundary conditions
insitu stress  -250e3  0  -250e3
insitu szz     -250e3
bound stress   -250e3  0  -250e3
* Assign fixed boundaries
bound cor      63     24     yvel=0.0  xvel=0.0
bound cor      37     22     yvel=0.0  xvel=0.0
bound cor      286    50     yvel=0.0  xvel=0.0
* Cycle to equilibrium under hydrostatic conditions
cycle          5000
* Apply a fixed velocity to upper-most block
bound cor      135    273    yvel=-0.001
* Monitor reaction stress and deformation at upper boundary
hist syy(0.075,0.4) ydis(0.075,0.4)
* Cycle to equilibrium using half critical time steps
frac  0.5 0.5
cycle 200000
```

Appendix G. Calculation of Weighting Factors for Specimens.

Appendix G. Calculation of Weighting Factors for Specimens.

This appendix outlines the procedure used for determining the orientation and the spacing weightings for each of the discontinuous specimens. The columns in the orientation weighting calculation spreadsheet are placed in the logical order for determining the orientation weighting coefficient for each specimen as presented in Section 3.2. The procedure for determining the spacing rating is presented in Section 3.3. In these tables presented in the following sub-sections the discontinuity numbers relate to the numbers shown in Figure 3.9. The discontinuity set numbers relate to the set numbers shown in Table 3.1. Additional data required for the analysis is,

- Orientation of the major principal stress: α_s=0°, β_s=90°.
- Orientation of the decline: α_e=270°, β_e=0.5°
- Length of the decline: 0.15m
- Cross sectional area of the decline: 0.045m.

G.1. Geometry 1

Table G.1. Geometry 1 set details.

Set	Orientation α_s β_s	Spacing (m)
1	180°/70°	0.282
2	180°/65°	0.282
3	180°/60°	0.272
4	180°/55°	0.278
5	180°/50°	0.276
6	0°/55°	0.304

Mean block volume, $J_v = 266.3 \times 10^{-6}\ m^3$

$$RMR_{(space)} = 20\left(\frac{266.3 \times 10^{-6}}{0.045 \times 0.304}\right)^{0.36}$$

$$= 4.84$$

Table G.2. Geometry 1 orientation weighting calculation spreadsheet.

Set (k)	cos $\theta_{er(k)}$ $x10^{-3}$	$N_{s(k)}$ $x10^{-3}$	Dis (i)	$\alpha_{n(i)}$ /$\beta_{n(i)}$ (deg)	cos $\theta_{en(i)}$ $x10^{-3}$	$N_{e(i)}$ $x10^{-3}$	$N_{e(i)}'$ $x10^{-3}$	$\beta_{w(i)}$ deg	W_θ 100%	50/50	infill
1	8.20	4.36	1	180/70	8.20	4.36	3.36	20	0.000	0.000	0.000
2	7.91	4.21	2	180/65	7.91	4.21	3.25	25	0.000	0.000	0.001
3	7.56	4.17	3	180/60	7.56	4.17	3.22	30	0.010	0.007	0.014
4	7.15	3.86	4	180/55	7.15	3.86	2.98	35	0.052	0.040	0.064
5	6.68	3.63	5	180/50	6.68	3.63	2.80	40	0.160	0.135	0.185
6	7.15	3.53	6	0/55	7.15	3.53	2.72	35	0.052	0.040	0.064
	$N_{(k)total}$	23.76	7	0/55	7.15	3.53	2.72	35	0.052	0.040	0.064
			8	0/55	7.15	3.53	2.72	35	0.052	0.040	0.064
					N_{total}	30.82	23.76				

G.2. Geometry 2

Table G.3. Geometry 2 set details.

Set	Orientation α_S β_S	Spacing (m)
1	180°/70°	0.282
2	180°/65°	0.282
3	180°/60°	0.272
4	180°/55°	0.278
5	0°/55°	0.304

Block volume, $J_v = 313 \times 10^{-6}$ m^3

$$RMR_{(space)} = 20\left(\frac{313 \times 10^{-6}}{0.045 \times 0.304}\right)^{0.36}$$

$$= 5.14$$

Table G.4. Geometry 2 orientation weighting calculation spreadsheet.

Set (k)	cos $\theta_{er(k)}$ x10^{-3}	$N_{e(k)}$ x10^{-3}	Dis (i)	$\alpha_{n(i)}$ /$\beta_{n(i)}$ (deg)	cos $\theta_{en(i)}$ x10^{-3}	$N_{e(i)}$ x10^{-3}	$N_{e(i)}'$ x10^{-3}	$\beta_{w(i)}$ deg	W_θ 100%	50/50	infill
1	8.20	4.36	1	180/70	8.20	4.36	3.23	20	0.000	0.000	0.000
2	7.91	4.21	2	180/65	7.91	4.21	3.12	25	0.000	0.000	0.001
3	7.56	4.17	3	180/60	7.56	4.17	3.09	30	0.010	0.007	0.014
4	7.15	3.86	4	180/55	7.15	3.86	2.86	35	0.052	0.040	0.064
5	7.15	3.53	6	0/55	7.15	3.53	2.61	35	0.052	0.040	0.064
	$N_{(k)total}$	20.13	7	0/55	7.15	3.53	2.61	35	0.052	0.040	0.064
			8	0/55	7.15	3.53	2.61	35	0.052	0.040	0.064
					N_{total}	27.19	20.13				

G.3. Geometry 3

Table G.5. Geometry 3 set details.

Set	Orientation α_S β_S	Spacing (m)
1	0°/50°	0.314
2	0°/43°	0.269
3	0°/36°	0.263
4	180°/30°	0.274

Block volume, $J_v = 666.8 \times 10^{-6}\ m^3$

$$RMR_{(space)} = 20\left(\frac{666.8 \times 10^{-6}}{0.045 \times 0.314}\right)^{0.36}$$

$$= 6.62$$

Table G.6. Geometry 3 orientation weighting calculation spreadsheet.

Set (k)	cos $\theta_{er(k)}$ $x10^{-3}$	$N_{s(k)}$ $x10^{-3}$	Dis (i)	$\alpha_{n(i)}$ /$\beta_{n(i)}$ (deg)	cos $\theta_{en(i)}$ $x10^{-3}$	$N_{e(i)}$ $x10^{-3}$	$N_{e(i)}'$ $x10^{-3}$	$\beta_{w(i)}$ deg	W_θ 100%	50/50	infill
1	6.68	3.19	1	0°/50°	6.68	3.19	3.19	40	0.160	0.135	0.185
2	5.95	3.32	2	0°/43°	5.95	3.32	3.32	47	0.451	0.412	0.480
3	5.13	2.86	3	0°/36°	5.13	2.86	2.86	54	0.807	0.775	0.833
4	4.36	2.39	4	180°/30°	4.36	2.39	2.39	60	0.988	0.980	0.994
	$N_{(k)total}$	11.8			N_{total}	11.8	11.8				

G.4. Geometry 4

Table G.7. Geometry 4 set details.

Set	Orientation α_s β_s	Spacing (m)
1	0°/45°	0.287
2	0°/37.6°	0.287
3	0°/31.0°	0.291
4	180°/56°	0.266
5	180°/61.9°	0.281
6	180°/75.1°	0.270

Block volume, $J_v = 531.2 \times 10^{-6}\ m^3$

$$RMR_{(space)} = 20\left(\frac{531.2 \times 10^{-6}}{0.045 \times 0.291}\right)^{0.36}$$

$$= 6.31$$

Table G.8. Geometry 4 orientation weighting calculation spreadsheet.

Set (k)	cos $\theta_{er(k)}$ $x10^{-3}$	$N_{e(k)}$ $x10^{-3}$	Dis (i)	$\alpha_{n(i)}$ /$\beta_{n(i)}$ (deg)	cos $\theta_{en(i)}$ $x10^{-3}$	$N_{e(i)}$ $x10^{-3}$	$N_{e(i)}'$ $x10^{-3}$	$\beta_{w(i)}$ deg	W_θ 100%	50/50	infill
1	6.17	3.23	1	0°/45°	6.17	3.23	3.23	45	0.354	0.316	0.389
2	5.32	2.78	2	0°/37.6°	5.32	2.78	2.78	52.4	0.731	0.695	0.762
3	4.49	2.32	3	0°/31.0°	4.49	2.32	2.32	59.0	0.972	0.960	0.982
4	7.23	4.08	4	180°/56°	7.23	4.08	4.08	34.0	0.039	0.030	0.050
5	7.70	4.11	5	180/61.9	7.70	4.11	4.11	28.1	0.004	0.003	0.007
6	8.43	4.69	6	180/75.1	8.43	4.69	4.69	14.9	0.000	0.000	0.000
	$N_{(k)total}$	21.2			N_{total}	21.2	21.2				

Table G.9. Orientation weightings for specimens.

Legend

all: mean of all discontinuities

active: mean of active discontinuities

max: maximum weighting.

	Geometry 1			Geometry 2			Geometry 3			Geometry 4		
	100%	50/50	infill	100%	50/50	infill	100%	50/50	infill	100%	50/50	infill
all	0.045	0.036	0.054	0.029	0.022	0.036	0.569	0.542	0.592	0.264	0.251	0.278
active	0.074	0.059	0.088	0.052	0.040	0.064	0.569	0.542	0.592	0.450	0.622	0.472
max.	0.160	0.135	0.185	0.052	0.040	0.064	0.988	0.980	0.994	0.972	0.960	0.982

References

References.

[1] Archambault, G., Fortin, M., Gill, D.E., Aubertin, M. and Ladanyi, B. Experimental Investigations for an Algorithm Simulating the Effect of Variable Normal Stiffness on Discontinuities Shear Strength. In *Rock Joints* Barton and Stephansson (eds) A.A.Balkema Rotterdam, pp.141-149, (1990).

[2] Attewell, P.B. and Sandford. The Influence of Anisotropy on the Strength and Deformability of Penrhyn Slate (1974).

[3] Attewell, P.B. and Woodman, J.P. Stability of Discontinuous Rock Masses Under Polyaxial Stress Systems. In *Stability of Rock Slopes, 13th Symp. on Rock Mech*, ASCE., August (1971).

[4] Amadei, B. Strength of a Regularly Jointed Rock Mass Under Biaxial and Axisymmetric Loading Conditions. *Int. J. Rock Mech. Min. Sci. and Geomech. Abstr.* Vol.25, pp.3-13, (1988).

[5] Baczynski, N., Walker, S. and Rajkowski, M. Large Scale Shear Testing at Leigh Creek in South Australia, 20p., (1992) in preparation.

[6] Baleshta, J.R. and Dusseault, M.B. Triaxial Testing of Intact Salt Rocks: Pressure Systems, Cell and Frame. *Advanced Triaxial Testing of Soil and Rock,* ASTM STP 977, Donaghe, R.T. Chaney, R.C. and Silver, M.L. (Eds.), ASTM, Philadelphia, pp.155-168, (1988).

[7] Bandis, S.C. Mechanical Properties of Rock Joints. In *Rock Joints* Barton and Stephansson (eds) A.A.Balkema Rotterdam, pp.125-141, (1990).

[8] Bandis, S.C., Lumsden, A.C. and Barton, N.R. Fundamentals of Rock Joint Deformation. *Int. J. Rock Mech. Min. Sci. and Geomech. Abstr.*, Vol.20, No. 6, pp.249-268, (1983).

[9] Bardet, J.P. and Scott, R.F. Seismic Stability of Fractured Rock Masses with the Distinct Element Method. *Proc. 26th US Symp. on Rock Mech., Rapid City, SD.* pp. 139-149, June 26-28, (1985).

[10] Barton, N.R, Review of a New Shear Strength Criterion for Rock Joints. *Eng. Geol.* Vol.7, pp. 287-332, (1973).

[11] Barton, N.R. A Model Study of Rock Joint Deformation. *Int. J. Rock Mech. and Min. Sci.* Vol.9, pp. 579-672, (1977).

[12] Barton, N.R. and Bakhtar,K. Rock Joint Description and Modelling for the Hydrothermomechanical design of nuclear waste repositories. Terra Tek Engineering, TRE 83-100, Part 1-4, (1983).

[13] Barton, N.R. and Choubey, V. The Shear Strength of Rock Joints in Theory and Practice. *Rock Mechanics* Vol.10, No. 1-2, pp. 1-54, (1977).

[14] Barton, N.R., Lien, R. and Lunde, J. Engineering Classification of Rock Masses for the

Design of Tunnel Supports. *Rock Mechanics* Vol.6, No. 4, pp. 183-236, (1974).

[15] Benjelloun, Z.H., Boulon, M. and Billaux, D. Experimental and Numerical Investigations on Rock Joints. In *Rock Joints* Barton and Stephansson (eds) A.A.Balkema Rotterdam, pp.171-179, (1990).

[16] Bieniawski, Z.T. Time Dependant Behaviour of Fractured Rock.*Rock Mechanics* Vol.2, No.3, pp.123-137, (1970).

[17] Bieniawski, Z.T. Geomechanics Classification of Rock Masses and its Application in Tunnelling. In *Tunnelling in Rock*, 2nd Ed., Z.T. Bieniawski (ed), Sth. Afr. Instit. Civil. Engin. (Pub.) pp.89-103, (1974).

[18] Bieniawski, Z.T. and Orr, C.M. Rapid Site Appraisal for Dam Foundations by the Geomechanics Classification. *Proc. 12th Congr. Large Dams, ICOLD*, Mexico City, pp.483-501, (1976).

[19] Bieniawski, Z.T. Rock Mass Classification in Rock Engineering. *Proc. of the Symp. on Exploration for Rock Engineering* Z.T. Bieniawski (ed), Cape Town: A.A. Balkema Vol.1, pp.97-106, (1976).

[20] Bieniawski, Z.T. The Geomechanics Classification in Rock Engineering Applications. In *Proc. 4th Int. Cong. Rock Mech.*, ISRM, Montreux, Vol. 2, pp. 41-48, (1979).

[21] Bieniawski, Z.T.(1) Strength and Deformability of Rock Masses. (2) Empirical Methods of Design. In *Rock Mechanics Design in Mining and Tunneling*, Z.T. Bieniawski (ed), Pub. A.A. Balkema, Rotterdam, (1984).

[22] Bieniawski, Z.T., Denkhaus, H.G. and Vogler, U.W. Failure of Fractured Rock. *Int. J. Rock Mech. Min. Sci.* Vol.6, pp.323-341, (1969).

[23] Bieniawski, Z.T. *Engineering Rock Mass Classification: A Complete Manual for Engineers and Geologists in Mining, Civil and Petroleum Engineering*, John Wiley and Sons, (1989).

[24] Blejwas, T.E. and Hanson, F.D. Scale Effects in the Shear Behaviour of Joints under Multi-axial Loading. In *Rock Joints* Barton and Stephansson (eds) A.A.Balkema Rotterdam, pp.185-191, (1990).

[25] Boral Investo, Hints For Use and Care (of Patternstone), Nov. (1988).

[26] Brace, W.F., Paulding, B.W.Jnr. and Scholtz, C. Dilatancy in the Fracture of Crystalline Rocks. *J. Geophysical Res* Vol.71, No. 6, pp. 3939-3953, (1966).

[27] Brady, B.H.G. and Brown, E.T. *Rock Mechanics for Underground Mining.* George Allen and Unwin, (1985).

[28] Bray, J.W. A Study of Jointed and Fractured Rock. Part 1. Fracture Patterns and their Failure Characteristics. *Felsmechanik und Ingenieurgeologie (Rock Mechanics and EngineeringGeology)* Vol.2-3, pp.117-136, (1967).

[29] Bray, J.W. Personal communication with S.D. Priest. (1984).

[30] Bro, A. Three-dimensional Styrofoam Models of Blocky Rock Masses. *Int. J. Rock Mech. Min. Sci. and Geomech. Abstr. Vol.*28, (1), 109-113. (1991).

[31] Brown, E.T. Strength of Models of Rock with Intermittent Joints. *J. Soil Mech.*

Foundns. Div., Am. Soc. Civ. Engrs. Vol.96, SM6, pp. 1935-1949, (1970).

[32] Brown, E.T. and Hoek, E. Trends in Relationships between Measured *In situ* Stresses and Depth, *Int. J. Rock Mech. Min. Sci. and Geomech. Abstr.* Vol. 15, pp.211-215 (1978).

[33] Brown, E.T. and Trollope, D.H. Strength of a Model of Jointed Rock. *J. Soil Mech. Foundns. Div., Am. Soc. Civ. Engrs.* Vol.96, pp. 685-703, (1970).

[34] Cain, P., Yuen, C.M.K., LeBel, G.R., Crawford, A.M., Lau, D.H.C. Triaxial Testing of Brittle Sandstone Using a Multiple Failure State Method. *Geotechnical Testing Journal GTJODJ* Vol.10, No. 4, pp.213-217, (1987).

[35] Coulomb, C.A. Essai sur une application des r`egles de maximis et minimis `a. quelques.probl`e.mes de statique, relatifs `a. l'architecture. *M`emoirs de Math`ematique et de Physique*, l'Acad`emie Royale des.Sciences. Vol.7, pp.343-382, (1776).

[36] Coulthard, M. UDEC formulation for simply deformable blocks Private discussion (1992).

[37] Cramer, M.L. and Black, M.T. The design and construction of a block test in closely jointed rock. In *26th US. Symp. on Rock Mechanics, Rapid City, SD.* 26-28 June, (1985).

[38] Crouch, S.L. Experimental Determination of Volumetric Strain in Failed Rock. *Int. J. Rock Mech. Min. Sci.* Vol.7, pp.589-603, (1970).

[39] Cundall, P.A. A Computer Model For Simulating Progressive Large Scale Movement in Blocky Rock. *Rock Fracture. Proc. Intl. Symp. on Rock Fracture. Nancy, France*, Paper 2-8, (1971).

[40] Cundall, P.A. Development of Generalized 2-D and 3-D Distinct Element Programs for modelling of Jointed Rock. *U.S. Army Eng. Waterways Exp. Stn. Final Tech. Rpt.*, (1983).

[41] Cundall, P.A. Numerical Modelling of Jointed and Faulted Rock. *Proc. Int. Conf. on Jointed and Faulted Rock, Vienna, Austria.* April 18-20, (1990).

[42] Cundall, P.A. Latest Developments in Stress Analysis Using FLAC, UDEC and 3DEC.*Notes from Seminar*, Melbourne, Dec. (1990).

[43] Cundall, P.A., Maini, T., Beresford, P.J., Last, N.C. and Asgian, M.I. Computer Modelling of Jointed Rock Masses. *U.S. Army Waterways Exp. Stn. Tech. Rpt.* N-78-4, (1971).

[44] Deere, D.U. Technical Description of Rock Cores for Engineering Purposes. *Rock Mechanics and Engineering Geology* Vol.1, No.1, pp. 17-22, (1964).

[45] Deere, D.U. Geological Considerations. In *Rock Mechanics in Engineering Practice*, K. G. Stagg and O. C. Zienkiewicz (eds), pp.1-20, London, Wiley (Pub), (1968).

[46] Desai, C.S., Janardahanam, R. and Sture, S. High Capacity Multiaxial Testing Device. *Geotechnical Testing Journal, GTJODJ* Vol.5, No. 1/2, pp. 26-33, (1982).

[47] Diederichs, M.S. and Hoek, E. *DIPS Ver. 2.2 Software Manual.* Dept. of Civil Engineering, University of Toronto, (1989).

[48] Donath, F.A. Effects of Cohesion and Granularity on Deformation Behaviour of Anisotropic Rock. In *Studies in Mineralogy and Precambrian Geology. Geol. Soc. Am. Memoir*, Doe, B.R and Smith, D.K. (Ed) Vol.135 pp. 95-128.

[49] Einstein, H.H., Nelson, R.A., Bruhn, R.W. and Hirschfeld, R.C. Model Studies of Jointed Rock Behaviour. *Proc. 11th Symp. Rock Mech. Berkeley, Calif.* pp.83-103, (1970).

[50] Einstein, H.H. and Hirschfeld, R.C. Model Studies on Mechanics of Jointed Rock. *J. Soil Mech. Foundns. Div., Am. Soc. Civ. Engrs.* Vol.99, pp.229-248, (1973).

[51] Elliot, G.M. An Investigation of a Yield Criterion for porous Rock. *PhD. thesis* Imperial College, London, pp.91-105, (1982).

[52] Foppl, A. Mitteilungen Aus Dem Mechanik. *Technischen Laboratorium Der Koenig Technische* Hochschule, Munchen, Hefte Vol.28, pp,44-48, (1902).

[53] Fossum, A.F. Effective Elastic Properties for a Randomly Jointed Rock Mass. *Int. J. Rock Mech. Min. Sci. and Geomech. Abstr.* Vol.22, pp.467-470, (1985).

[54] Gerrard, C.M. Equivalent Elastic Modulii of a Rock Mass Consisting of Orthorhombic Layers. *Int. J. Rock Mech. Min. Sci. and Geomech. Abstr.* Vol.19, pp.10-14, (1982).

[55] Gerrard, C.M. Elastic Models of Rock Masses Having One, Two and Three Sets of Joints. *Int. J. Rock Mech. Min. Sci. and Geomech. Abstr.* Vol.19, pp.15-23, (1982).

[56] Gonzalez de Vallejo, L.I. A New Rock Classification System for Underground Assessment Using Surface Data, *Int. Symp. Eng. Geol. Underground Constr.* LNEC., Lisbon, Vol.1, pp. II.85-II94, (1983).

[57] Goodman, R.E. The Mechanical Properties of Joints. In *Advances in Rock Mechanics. Proc 3rd Cong. of the ISRM, Denver, Col.* Sept 1-7, pp.127-140, (1974).

[58] Goodman, R.E. and Shi, G. *Block Theory and its Application to Rock Engineering*, Prentice-Hall Inc. New Jersey, (1985).

[59] Goodman, R.E., Taylor, R.L. and Brekke, T.L. A Model for the Mechanics of Jointed Rock. *J. Soil Mech. Foundns. Div.*, Am. Soc. Civ. Engrs. Vol.94, No. SM3, Proc. Paper 5937, pp.637-659, (1968).

[60] Haberfield, C.M. and Johnston, I.W. Young's Modulii of a Soft Rock in Compression, Bending and Tension. In *5th Australian-New Zealand Conf. on Geomechanics, Sydney*, pp. 243-246, Aug 22-23, (1988).

[61] Hart, R.D., Cundall, P.A. and Cramer, M.L. Analysis of a Loading Test on a Large Basalt Block. In *26th US. Symp. on Rock Mechanics, Rapid City, SD.* 26-28 June, (1985).

[62] Head, K.H. *Manual of Soil Laboratory Testing*. Pentech Press, pp. 889-891, (1982).

[63] Hencher, S.R. and Richards, L.R. Laboratory Direct Shear Testing of Rock Discontinuities. *Ground Engineering* Vol. 22, No.2, pp.24-31, (1989).

[64] Hoek, E. Strength of Jointed Rock Masses. *G`eotechnique*. Vol.33, No. 3, p.210, (1983).

[65] Hoek, E. and Brown, E.T. Empirical Strength Criterion for Rock Masses. *Journal of the*

Geotechnical Engineering Div. ASCE. Vol.106, No. GT9, pp. 1013-1035, (1980).

[66] Hoek, E. and Brown, E.T. The Hoek-Brown Failure Criterion - a 1988 Update. In *15th Canadian Rock Mechanics Symp.*, pp. 31-38, (1988).

[67] Hoek, E. and Franklin, J.A. Simple Triaxial Cell For Field or Laboratory Testing *Trans. Inst. Min. Metal.* Vol.77, pp.a22-a26, (1968).

[68] Hojem, J.P. and Cook, N.G. The Design and Construction of a Triaxial and a Polyaxial Cell for Testing Rock Specimens. *S.A. Mech. Eng.* Vol.18, No. 2, pp. 57-61, (1968)

[69] Hoskins, E.R. The Failure of Thick Walled Hollow Cylinders of Isotropic Rock. *Int. J. Rock Mech. Min. Sci.* Vol.6, No. 1, pp. 99-125, (1969)

[70] Indraratna, B. Development and Applications of a Synthetic Material to Simulate Soft Sedimentary Rocks. *G`eotechnique*, Vol.40, No. 2, pp. 189-200, (1990).

[71] Indraratna, B. Laboratory Simulation of Joints and Their Influence on Rock Mass Behaviour. In *Rock Joints* Barton and Stephansson (eds) A.A.Balkema Rotterdam, pp.235-243, (1990).

[72] International Society of Rock Mechanics Commission on Standardisation of Laboratory and Field Tests 1974. Suggested methods for determining shear strength. Doc. No. 1. Reprinted in *Rock characterization, testing and monitoring - ISRM suggested methods* E.T.Brown (ed) 129-140. Oxford: Pergamon (Pub.), (1981).

[73] International Society of Rock Mechanics Commission on Standardisation of Laboratory and Field Tests 1978a. Suggested Methods for the Quantitative Description of Discontinuities in Rock Masses. *Int. J. Rock Mech. Min. Sci. and Geomech. Abstr.* Vol.15, pp.319-368, (1978).

[74] International Society of Rock Mechanics Commission on Standardisation of Laboratory and Field Tests 1978. Vogler, U.W. and Kovari, K. Suggested Methods for Determining The Strength of Rock Materials in Triaxial Compression: Revised Version. *Int. J. Rock Mech. Min. Sci. and Geomech. Abstr.* Vol.20, No. 6, pp.283-290, (1983).

[75] International Society of Rock Mechanics Commission on Standardisation of Laboratory and Field Tests 1978a. Suggested Methods for Determining the Uniaxial Compressive Strength and Deformability of Rock Materials. *Int. J. Rock Mech. Min. Sci. and Geomech. Abstr* Vol.16, pp.135-140, (1979).

[76] International Society of Rock Mechanics Commission on Standardisation of Laboratory and Field Tests 1989. Natau, O.P. and Mutschler, T.O. Suggested Method for Large Scale Sampling and Triaxial Testing of Jointed Rock. *Int. J. Rock Mech. Min. Sci. and Geomech. Abstr.* Vol.26, No.5, pp.427-434, (1989).

[77] Itasca Consulting Group. Universal Distinct Element Code (UDEC Ver. 1.8a), *User Manual* Minnesota, USA., (1992).

[78] Jaeger, J.C. Shear Failure of Anisotropic Rock. *Geological magazine* Vol.97, (1960).

[79] Jaeger, J.C. Behaviour of Closely Jointed Rock. *Proc. 11th Symp. Rock Mech., Berkeley, Calif.* pp57-68, (1970).

[80] Jaeger, J.C. and Cook, N.G.W. Sliding on a Plane of Weakness: Two-dimensional

Theory. *Fundamentals of Rock Mechanics* 3rd edn. London: Chapman and Hall (1976).

[81] Johnston, I.W. and Lam, T.S.K. Frictional characteristics of planar concrete-rock interfaces under constant normal stiffness conditions. *Proc. 4th Australia-New Zealand Geomechanics Conf.*, Perth Vol.**2**, pp.397-401.

[82] Johnston, I.W. and Choi, S.K. A Synthetic Soft Rock for Laboratory model Studies. *G`eotechnique* Vol.36, No.2, pp. 251-263, (1986).

[83] Kaiser, P.K., MacKay, C. and Gale A.D. Evaluation of Rock Classification at B.C. Rail Tumbler Ridge Tunnels. *Rock Mechanics and Rock Engineering* Vol.19, pp. 205-234, (1986).

[84] Kendorski, F., Cummings, R., Bieniawski, Z.T. and Skinner, E. Rock Mass Classification for Block Caving Mine Drift Support. *Proc. 5th Int. Congr. Rock Mech.*, ISRM, Melbourne, pp. B51-B63, (1983)

[85] Krauland, N., Soder, P. and Agmalm, G. Determination of Rock Mass Strength by Rock Mass Classification - Some Experiences and Questions from Boliden Mines *Int. J. Rock Mech. Min. Sci. and Geomech. Abstr.* Vol.26, No. 1, pp.115-123, (1989).

[86] Kulhawy, F.H. Geomechanical Model for Rock Foundation Settlement. *J. Geotech. Eng. Div.* (ASCE), Vol.104, (GT2), pp.211-227, (1978).

[87] Kulhawy, F.H. and Goodman, R.E. Design of Foundations on Discontinuous Rock. In *Proc. Int. Conf. on Structural Foundations on Rock, Sydney, Australia.* Pells, P.J.N. (Ed), A.A. Balkema/Rotterdam (Pub), May 7-9, (1980).

[88] Kulhawy, F.H. and Ingraffea, A.R. Geomechanical Model for Settlement of Long Dams on Discontinuous Rock Masses. In *Proc. ISRM Int. Symp. on Rock Mech. Related To Dam Foundations, Rio De Janeiro, Brazil.*, Kanji, M.A. and Abrahas R.A. (Ed), Sept 27-29, (1978).

[89] Ladanyi, B. and Archambault, G. Evaluation de la Resistance au Cisaillement d'une Massif Rocheux Fragments (In french). *Proc. 24th Int. Geol. Cong.*, Sect. 13d, pp. 249-260, (1977).

[90] Ladanyi, B. and Archambault, G. Shear Strength and Deformability of Filled Indented Joints. *Proc. Int. Symp. on Goetechnics of Structurally Complex Formations,* Associazione Geotechnica Italiana, Vol.1, pp. 317-326, (1977).

[91] Lajtai, E.Z. The Influence of Interlocking Rock Discontinuities on Compressive Strength (Model Experiments). *Felsmechanik und Ingenieurgeologie (Rock Mechanics and Engineering Geology* Vol.5, No.4, (1967).

[92] Lama, R.D. and Vutukuri, V.S. *Handbook on the Mechanical Properties of Rocks. Vol.*IV - Testing Techniques and Results. Switzerland, Trans Tech. Publications, (1978).

[93] Laubscher, D.H. Geomechanics Classification of Jointed Rock Masses - Mining Applications. *Trans. Inst. Min. Metall.* Vol.86, pp. A1-A7, (1977).

[94] Laubscher, D.H. Design Aspects and Effectiveness of Support Systems in Different Mining Situations. *Trans. Inst. Min. Metall.* Vol.93, pp. A70-A81, (1984).

[95] Lemos, H.V., Hart, R.D. and Cundall, P.A. A Generalized Distinct Element Program for Modelling Jointed Rock Mass: A Keynote Lecture. *Proc. Int. Symp. on Fundamentals of Rock Joints, Bj`orkliden* pp.335-343, 15-20 Sept, (1985)

[96] Lenoe, E.M. Deformation and Failure of Granular Media under Three-dimensional Stresses. *Experimental Mechanics* pp.99-105, Feb. (1966).

[97] Makurat, A., Barton, A., Vik, G., Chrssanthakis, P. and Monsen, K. Jointed Rock Mass Modelling. In *Rock Joints* Barton and Stephansson (eds) A.A.Balkema Rotterdam, pp.647-657, (1990).

[98] McLamore, R. and Gray, K.E. The Mechanical Behaviour of Anisotropic Sedimentary Rocks. *J. Engng for Industry. Trans. Am. Soc. of Mech. Eng., Ser. B* Vol.89, pp.62-73, (1967).

[99] McMahon, B. Indices Related to the Mechanical Properties of jointed rock. In. *Status of Practical Rock Mechanics: Proc. 9th Symp. on Rock Mech.*, Chap. 6, April (1967).

[100] Meyers A.G. and Priest S.D. The Prediction of Rock Mass Strength and Deformability for Engineering Design - Laboratory Practice. *Proc. Western Australian Conference on Mining Geomechanics,* Kalgoorlie, June 8-10 (1992).

[101] Meyers A.G. and Priest S.D. A Micro-Processor Controlled Pump for Triaxial Cell Pressure Control, *Int. J. Rock Mech. Min. Sci. & Geomech. Abstr.* Vol.29, No.2, pp.187-191, (1992).

[102] Meyers A.G. and Priest S.D. A Technique for Moulding Cylindrical Discontinuous Models, *Rock Mechanics*, (1992).

[103] Michelis, P. A True Triaxial Cell for Low and High Pressure Experiments. *Int. J. Rock Mech. Min. Sci. and Geomech. Abstr.* Vol.22, No. 3, pp.183-188, (1985).

[104] Miles, R.E. The Random Division of Space. *Suppl. Adv. Appl. Prob.*, pp.263-266, (1972).

[105] Mogi, K. Effect of the Triaxial Stress System on Rock Failure. *Rock Mechanics in Japan* Vol.1, pp. 53-55, (1970).

[106] Mustoe, G.G.W., Williams, J.R., Hocking, G. and Worgan, K. Penetration and Fracturing of Brittle Plates Under Dynamic Impact. *NUMETA '87. 2nd. Int. Conf. on Advances in Numerical Methods in Engineering: Theory and Applications,* Swansea, U.K, (1987).

[107] Newman, D.A. and Bieniawski, Z.T. Modified Version of the Geomechanics Classification for Entry design in Underground Coal Mines. *Trans. Soc. Min. Eng. AIME* Vol.280, pp.2134-2138, (1986).

[108] Obert, L. and Duvall, W.I. Rock Model Studies. In *Rock Mechanics and the Design of Structures in Rock* pp.387-401, Wiley, (1967).

[109] Oda, M., Yamabe, T. and Kamemura, K. A Crack Tensor and its Relation to Wave Velocity Anisotropy in Jointed Rock Masses. *Int. J. Rock Mech. Min. Sci. and Geomech. Abstr.* Vol.23, No.6, pp387-397, (1986).

[110] Ohmachi, T. and Arai, Y. On the Distinct Element Parameters Used for Earthquake

Ground Motion Simulation. *Computers and Geotechnics* Vol.2, pp. 329-345, (1986).

[111] Ohnishi, Y. and Dharmaratne, P.G.R. Shear Behaviour of Physical Models of Rock Joints Under Constant Normal Stiffness Conditions. In *Rock Joints* Barton and Stephansson (eds) A.A.Balkema Rotterdam, pp.267-275, (1990).

[112] Ooi, L.H. and Carter, J.P. A Constant Normal Stiffness Direct Shear Device for Static and Cyclic Loading. *Univ. of Sydney, School of Civil and Mining Engineering, Research Report.* Vol.520, pp.3-13, (1988).

[113] Papaliangas, T., Lumsden, A.C., Hencher, S.R. and Manolopoulou, S. Shear Strength of Modelled Filled Rock Joints. In *Rock Joints* Barton and Stephansson (eds) A.A.Balkema Rotterdam, pp.275-283, (1990).

[114] Paterson, M.S. *Experimental Rock Deformation - The Brittle Field.* Berlin: Springer, (1978).

[115] Patton, F.D. Multiple Modes of Shear Failure in Rock. *Proc. 1st Int. Conf. on Rock Mechanics, Lisbon*, pp.509-513, (1966).

[116] Pereira, J.P. Shear Strength of Filled Discontinuities. In *Rock Joints* Barton and Stephansson (eds) A.A.Balkema Rotterdam, pp.283-289, (1990).

[117] Phien-wej, N., Shrestha, U.B. and Rantucci, G. Effect of Infill Thickness on Shear Behaviour of Rock Joints. In *Rock Joints* Barton and Stephansson (eds) A.A.Balkema Rotterdam, pp.289-295, (1990).

[118] Pinnaduwa, H.S.W. and Kulatilake, A.M. Estimating Elastic Constants and Strength of Discontinuous Rock. *J. Geotech. Eng* Vol.111, No.7, pp.847-864, (1985).

[119] Priest, S.D. *Hemispherical Projection Methods in Rock Mechanics.* George Allen & Unwin, London, pp.44-49, (1985).

[120] Priest, S.D. *Discontinuity Analysis for Rock Engineering.* Chapman and Hall, London, (1992).

[121] Priest, S.D. and Hudson, J.A. Discontinuity Spacing in Rock. *Int. J. Rock Mech. Min. Sci. and Geomech. Abstr.* Vol.13, pp. 135-148, (1976).

[122] Raisborough, S. Evaluation of Geotechnical Mapping Software, *BE. Thesis,* Dept. of Mining Engineering, University of SA. (1992).

[123] Ramamurthy, T., Venkatappa Rao, G. and Singh, J. A Strength Criterion for Anisotropic Rocks. In *5th Australia-New Zealand Conf. on Geomechanics*, Sydney, pp.253-257 (1988).

[124] Reik, G. and Hesselmann, F.J. Methods for the Determination of Rock Mass Strength of Sedimentary Rock *Rock Mechanics* Suppl. Vol.11, pp.59-71, (1981).

[125] Reik, G. and Zacas, M. Strength and Deformation Characteristics of Jointed Media in True Triaxial Compression. *Int. J. Rock Mech. Min. Sci. and Geomech. Abstr.* Vol.15, pp.295-303, (1978).

[126] Romana, M. New Adjustment Ratings for Application of Bieniawski Classification to Slopes. *Proc. Int. Symp. Rock Mech. in Excav. Min. Civ. Works*, ISRM Mexico City, pp.59-68, (1985).

[127] Ross-Brown, D.M. and Walton, G. A Portable Shear box for Testing Rock Joints. *Rock Mechanics* Vol.7, pp.129-153, (1975).

[128] Russack, A. B. Triaxial Cell Controller, *BE Thesi,* School of Electrical Engineering, University of Adelaide, (1989).

[129] Sacchi Landriani, G. and Taliercio, A. A Failure Condition for Layered Rocklike Material. *Int. J. Rock Mech. Min. Sci. and Geomech. Abstr.* Vol.19, No. 7, pp.285-305, (1986).

[130] Saeb, S. and Amadei, B. Modelling Joint Response Under Constant or Variable Normal Stiffness Boundary Conditions *Int. J. Rock Mech. Min. Sci. and Geomech. Abstr.* Vol.27, No.3, pp.213-217, (1990).

[131] Sangha, M. and Dhir, K. Strength and Deformation of Rock subject to Multiaxial Compressive Stresses. *Int. J. Rock Mech. Min. Sci. and Geomech. Abstr.*Vol.12, pp.277-282, (1975).

[132] Santos, C. Determination of the Rock Mass Rating based on the Geomechanics Classification of Bieniawski. In *Engineering Rock Mass Classifications* Z. T. Bieniawski (Ed.) pp. 222-237, (1988)

[133] Sargand, S.M. and Hazen, G.A. Deformation Behaviour of Shales *Int. J. Rock Mech. Min. Sci. and Geomech. Abstr.* Vol.24, No. 6, pp.365-370, (1987).

[134] Serafim, J.L. and Pereira, J.P. Consideration of the Geomechanics Classification of Bieniawski. *Proc. Intl. Symp. Engng. Geol. and Underground Construction,* Lisbon, Portugal, pp. 1133-44, (1983)

[135] Singh, M. M. and Huck, P. J. Large Scale Triaxial Tests on Rock. *Proc. 14th Symposium on Rock Mechanics* June 11-14 1972. Ed. Hardy, H.R. et al. ASCE (1973).

[136] Singh, J., Ramamurthy, T. and Vankatappa Rao, G. Strength Anisotropies in Rocks, *Indian Geotechnical Journal* Vol. 19, No. 2, pp.147-166, (1989).

[137] Skinas, C.A., Bandis, S.C. and Demiris, C.A. Experimental Investigation and Modelling of Rock Joint Behaviour Under Constant Stiffness. In *Rock Joints* Barton and Stephansson (eds) A.A.Balkema Rotterdam, pp. 301-309, (1990).

[138] Stapledon, D.H. and Stevens, B.G. *Penrice Marble Quarry - Geotechnical Studies. Report on Stages 1 and 2*, (1982-83).

[139] Starfield, A.M. and Cundall, P.A. Towards a Methodology for Rock Mechanics Modelling. *Int. J. Rock Mech. Min. Sci. and Geomech. Abstr.* 25, No.3, pp.99-106, (1988).

[140] Stimpson, B. A New Approach to Simulating Rock Joints in Physical Models. *Int. J. Rock Mech. Min. Sci. and Geomech. Abstr.* Vol.16, pp. 215-216, (1979).

[141] Stimpson, B. Modelling Materials for Engineering Rock Mechanics. *Int. J. Rock Mech. Min. Sci* Vol.7, pp. 77-121, (1986).

[142] Terzaghi, K. Rock Defects and Loads on Tunnel Support. *Rock tunneling with steel supports*, Proctor, R.V. and White, T., (Eds.), Commercial Shearing Co., Ohio, pp. 15-99, (1946).

[143] Thompson,A.G. and Windsor,C.R. SAFEX Stability Assessment for Excavations in Rock Software, CSIRO Division of Geomechanics, (1992).

[144] Trollope, D. H. The Stability of Trapezoidal Openings in Rock Masses *Felsmechanik und Ingenieurgeologie* Vol.4, No.3, (1966).

[145] Trueman, J. and Follington, K. Underground Pillar Strength Determination, In proc. *W.A.Conf. on Min. Geomechanics*, Kalgoorlie, W.A. pp.135-142, (1992).

[146] Van Sint Jan, M.L. Shear Test of Modelled Rock Joints Under Stiff Normal Loading. In *Rock Joints*, Barton and Stephansson (eds), A.A.Balkema, Rotterdam, pp. 323-329, (1990).

[147] Vermeer, P.A. A Simple Shear Band Analysis Using Compliances. In P.A. Vermeer and H.J. Luger (eds.), *Deformation and failure of granular material*, pp 493-499, Rotterdam: Balkema.

[148] Vermeer, P.A. and de Borst, R. Non-associated plasticity for soils, concrete and rock. *Heron*, Vol.29, pp.1-64, (1984).

[149] Villaescusa, E. and Landmark,G.L. Geotechnical Mapping at Mount Isa Mines, In *W.A.Conf. on Mining Geomechanics*, Kalgoorlie, pp. 329-334, June 8-10, 1992

[150] Walton, O.R. Explicit Particle Dynamics Model for Granular Materials. In *Numerical Methods in Geomechanics* Z. Eisenstein, (ed.), A.A. Balkema, Rotterdam, pp.1261-1268, (1982).

[151] Warburton, P.M. Applications of a New Computer Model for Reconstructing Blocky Rock Geometry-Analysing Single Block Stability and Identifying Keystones. *5th International Congress on Rock Mechanics*, ISRM, Melbourne, pp.225-230, (1983).

[152] Wawersik, W. R. Technique and Apparatus for Strain Measurements on Rock in Constant Confining Pressure Experiments. *Rock Mechanics* Vol.7, pp.231-241, (1975).

[153] Weaver, J. Geological Factors Significant in the Assessment of Rippability. *Civ. Eng. S. Afr.* Vol.17, No.12, pp.313-316, (1975).

[154] Wei, Q., Liu, G. and Chen, X. The Discrete Element Method and its Application in Jointed Rock Stability of Hydopower Projects. In *Rock Joints*, Barton and Stephansson (eds), A.A.Balkema, Rotterdam, pp. 759-765, (1990).

[155] Wickham, G.E., Tiedemann, H.R. and Skinner, E.H. Support Determination Based on Geologic Predictions. *Proc. Rapid Excavation and Tunneling Conf., AIME*, New York, pp.43-64, (1972).

[156] Wickham, G.E., Tiedemann, H.R. and Skinner, E.H. Ground Support Prediction Model - RSR Concept. *Proc. Rapid Excavation and Tunneling Conf., AIME*, New York, pp.691-707, (1972).

[157] Williams, J.R., Hocking, G. and Mustoe, G.G.W. The Theoretical Basis of the Discrete Element Method. *Proc. of the NUMETA '85 Conference*, Swansea, pp. 897-906, (1985).

[158] White, R.N. and Sabnis, G.M. Size Effects in Gypsum Mortars. *Journal of Materials* Vol.3, No.1, pp.163-177, (1968).

[159] Windsor, C.R. and Robertson, W.V. Rock Structure Mapping Using an Electronic Compass and an Electronic Logging System. In *Proc. W.A. Conf. on Mining Geomechanics*, Kalgoorlie June 8-10, (1992).

[160] Xu,S. and H.de.Freitas,M. Kinematic Mechanisms of Shear Deformation and the Validity of Barton's Shear Models. In *Rock Joints*, Barton and Stephansson (eds), A.A.Balkema, Rotterdam, pp. 767-774, (1990).

[161] Young, L.E. and Stoek,H.H. Subsidence Resulting from Mining.Engineering *Experiment Station Bulletin* Vol.91, University of Illinois, (1916).

[162] Yoshinaka, R. and Yamabe, T. Joint Stiffness and the Deformation Behaviour of Discontinuous Rock. *Int. J. Rock Mech. Min. Sci. and Geomech. Abstr* Vol.23, No. 1, pp.19-28, (1986).

[163] Zacas, M. and Knox, W.R.A. Behaviour of Multi-layered Rock Masses with Weak Inclusions. In *Proc. Int. Conf. on Structural Foundations on Rock, Sydney, Australia.* Pells, P.J.N. (Ed), A.A. Balkema/Rotterdam (Pub), May 7-9, (1980).